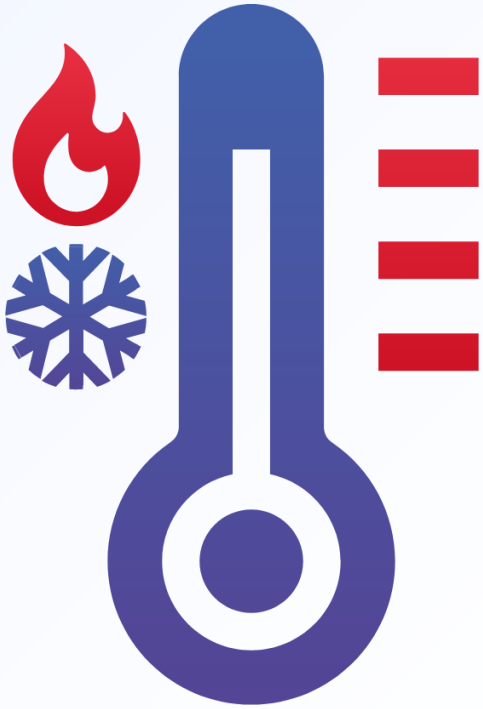
Vol. 45 No. 2 (2024)

ARCHIVES OF THERMODYNAMICS

ISSN: 1231-0956
ISSN: 2083-6023 (Online)



Co-published by

Institute of Fluid Flow Machinery
Polish Academy of Sciences

Committee on Thermodynamics and Combustion
Polish Academy of Sciences

WYDAWNICTWO IMP PAN

Aims and Scope

The aim of the quarterly journal Archives of Thermodynamics (AoT) is to disseminate knowledge between scientists and engineers worldwide and to provide a forum for original research conducted in the field of thermodynamics, heat transfer, fluid flow, combustion and energy conversion in various aspects of thermal sciences, mechanical and power engineering. Besides original research papers, review articles are also welcome.

The journal scope of interest encompasses in particular, but is not limited to:

- Classical and extended non-equilibrium thermodynamics
- Thermodynamic analysis including exergy
- Thermodynamics of heating and cooling
- Thermodynamics of nuclear power generation
- Thermodynamics in defense engineering
- Advances in thermodynamics
- Experimental, theoretical and numerical heat transfer
- Thermal and energy system analysis
- Renewable energy sources including solar energy
- Secondary fuels and fuel conversion
- Heat and momentum transfer in multiphase flows
- Nanofluids
- Energy transition
- Advanced energy carriers
- Energy storage and efficiency
- Energy in buildings
- Hydrogen energy
- Combustion and emissions
- Turbomachinery
- Thermal and energy system analysis
- Integrated energy systems
- Distributed energy generation
- Thermal incineration of wastes
- Waste heat recovery.

Supervisory Editors

- T. Bohdal, Koszalin University of Technology, Poland
- M. Lackowski, Institute of Fluid Flow Machinery, Gdańsk, Poland

Honorary Editor

- J. Mikielewicz, Institute of Fluid Flow Machinery, Gdańsk, Poland

Editor-in-Chief

- P. Ocłoń, Cracow University of Technology, Cracow, Poland

Guest Editor

- J. Wajs, Gdańsk University of Technology, Gdańsk, Poland

Section Editors

- P. Lampart, Institute of Fluid Flow Machinery, Gdańsk, Poland
- S. Polesek-Karczewska, Institute of Fluid Flow Machinery, Gdańsk, Poland
- I. Szczygieł, Silesian University of Technology, Gliwice, Poland
- A. Szlęk, Silesian University of Technology, Gliwice, Poland

Technical Editors

- J. Frączak, Institute of Fluid Flow Machinery, Gdańsk, Poland
- S. Łopata, Institute of Fluid Flow Machinery, Gdańsk, Poland

Members of Programme Committee

- P. Furmański, Warsaw Univ. Tech., Poland
- J. Badur, Inst. Fluid Flow Mach., Gdańsk, Poland
- T. Chmielniak, Silesian Univ. Tech., Gliwice, Poland
- D. Kardaś, Inst. Fluid Flow Mach., Gdańsk, Poland
- S. Pietrowicz, Wrocław Univ. Sci. Tech., Poland
- R. Kobyłecki, Częstochowa Univ. Tech., Poland
- J. Wajs, Gdańsk Univ. Tech., Poland

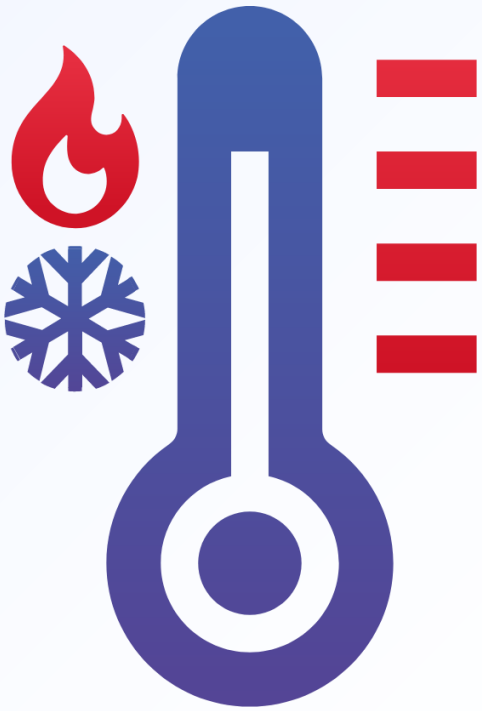
International Advisory Board

- J. Bataille, Ecole Centr. Lyon, France
- A. Bejan, Duke Univ., Durham, USA
- W. Błasiak, Royal Inst. Tech., Stockholm, Sweden
- G.P. Celata, ENEA, Rome, Italy
- L.M. Cheng, Zhejiang Univ., Hangzhou, China
- M. Colaco, Federal Univ. Rio de Janeiro, Brazil
- J.M. Delhaye, CEA, Grenoble, France
- M. Giot, Univ. Catholique Louvain, Belgium
- K. Hooman, Univ. Queensland, Australia
- D. Jackson, Univ. Manchester, UK
- D.F. Li, Kunming Univ. Sci. Tech., China
- K. Kuwagi, Okayama Univ. Science, Japan
- J.P. Meyer, Univ. Pretoria, South Africa
- S. Michaelides, Texas Christian Univ., USA
- M. Moran, Ohio State Univ., USA
- W. Muschik, Tech. Univ., Berlin, Germany
- I. Müller, Tech. Univ., Berlin, Germany
- H. Nakayama, JAEA, Japan
- S. Nizetic, Univ. Split, Croatia
- H. Orlande, Federal Univ. Rio de Janeiro, Brazil
- M. Podowski, Rensselaer Polyt. Inst., USA
- R.V. Rao, Sardar Vallabhbhai Nat. Inst. Techn., India
- A. Rusanov, Inst. Mech. Eng. Probl., Kharkiv, Ukraine
- A. Vallati, Sapienza Univ. Rome, Italy
- M.R. von Spakovsky, Virginia Polyt. Inst., USA
- H.R. Yang, Tsinghua Univ., Beijing, China

Vol. 45 No. 2 (2024)

ARCHIVES OF THERMODYNAMICS

ISSN: 1231-0956
ISSN: 2083-6023 (Online)



Co-published by

Institute of Fluid Flow Machinery
Polish Academy of Sciences

Committee on Thermodynamics and Combustion
Polish Academy of Sciences

WYDAWNICTWO IMP PAN

Editorial Office
IMP PAN Publishers
Institute of Fluid Flow Machinery, Fiszera 14, 80-231 Gdańsk, Poland,
Phone: (+48) 58-341-12-71 int. 230, e-mail: redakcja(at)imp.gda(.)pl
https://www.imp.gda.pl/archives-of-thermodynamics/
Journals PAS – Electronic Library Polish Academy of Sciences
https://journals.pan.pl/ather

Subscription outside Poland
From 2024, Archives of Thermodynamics appear only in electronic version as an open access journal. However, printed archive volumes or issues are still available. The price of a full volume outside Poland is **120 EUR**. The price of a single issue is **30 EUR**. Archived volumes or issues are available on request. Orders should be sent directly to IMP PAN Publishers:
Institute of Fluid-Flow Machinery,
Fiszera 14, 80-231 Gdansk, Poland,
e-mail: redakcja(at)imp.gda.pl or jfrk(at)imp.gda(.)pl or jrybka(at)imp.gda(.)pl.
Payments should be transferred to the bank account of IMP PAN:
IBAN 28 1130 1121 0006 5498 9520 0011 at Bank Gospodarstwa Krajowego; Code SWIFT: GOSKPLPW.

Prenumerata w Polsce
Od 2024, czasopismo ukazuje się tylko w formie elektronicznej otwartej. Osiągalne są jednak wydania papierowe archiwalne. Cena pojedynczego numeru wynosi **50 PLN**. Cena rocznika **200 PLN**. Zamówienia z określeniem numeru (rocznika), nazwiskiem i adresem odbiorcy należy kierować bezpośrednio do Wydawcy:
Instytut Maszyn Przepływowych PAN
ul. Fiszera 14, 80-231 Gdańsk,
e-mail: redakcja(at)imp.gda(.)pl lub jfrk(at)imp.gda(.)pl lub jrybka(at)imp.gda(.)pl.
Wpłaty prosimy kierować na konto Instytutu Maszyn Przepływowych PAN:
nr 28 1130 1121 0006 5498 9520 0011 w Banku Gospodarstwa Krajowego.

Articles in Archives of Thermodynamics are abstracted and indexed within:
Applied Mechanics Reviews • Arianta • Baidu Scholar • BazTech • Cabell's Directory • Celdes • Chemical Abstracts Service (CAS) – CAplus • CNKI Scholar (China National Knowledge Infrastucture) • CNPIEC • EBSCO (relevant databases) • EBSCO Discovery Service • Elsevier – SCOPUS • ESCI (Emerging Sources Citation Index) • Genamics JournalSeek • Google Scholar • Inspec • Index Copernicus • J-Gate • Journal TOCs • Naviga (Softweco) • Paperbase • Pirabase • POL-index • Polymer Library •Primo Central (ExLibris) • ProQuest (relevant databases) • ReadCube • Referativnyi Zhurnal (VINITI) • SCImago (SJR) • Summon (Serials Solutions/ProQuest) • TDOne (TDNet) • TEMA Technik und Management • Ulrich's Periodicals Directory/ulrichsweb • WorldCat (OCLC)

ISSN 1231-0956
ISSN 2083-6023 (Online)
Copyright © 2024 by the Authors under license CC BY 4.0.
Publication funding of this journal is provided by resources of the Polish Academy of Sciences and the Institute of Fluid Flow Machinery

Contents

Selected papers from the 25th Jubilee Congress of Thermodynamicists, 11–14 September, Gdańsk, Poland

1) Jan Wajs, Jakub Łukasik
Assessment of the impact of jet impingement technique on the energy efficiency of air-cooled BIPV/T roof tile 5–18

2) Małgorzata Sikora, Tadeusz Bohdal, Grzegorz Ligus, Stanisław Witczak
Flow maps in multiphase flows 19–28

3) Magdalena Piasecka, Kinga Strąk
Effect of flow orientation in experimental studies on FC-770 boiling heat transfer in asymmetrically heated minichannels 29–39

4) Robert Kaniowski
Pool boiling for water on surfaces with inclined microchannel 41–49

5) Dariusz Mikielewicz, Mikielewicz Jarosław
Influence of thermodynamics on the development of technology and science 51–61

6) Maria Karolina Tychanicz-Kwiecień, Witold Rajmund Rybiński
Experimental and statistical determination of thermal characteristics of the special design minichannel heat exchanger 63–71

7) Romuald Mosdorf, Gabriela Rafałko, Iwona Zaborowska, Paweł Dzienis, Hubert Grzybowski
Complexity of two phase flow dynamics using the recurrence and high speed video analysis 73–81

8) Gabriela Rafałko, Romuald Mosdorf, Hubert Grzybowski, Paweł Dzienis, Grzegorz Górski
Multiscale entropy applications in complexity analysis of two-phase flow 83–90

9) Rafał Gałek, Joanna Wilk
Investigations of the specific heat capacity of selected heterogeneous materials 91–98

10) Krzysztof Badyda, Artur Harutyunyan, Marcin Wołowicz
Repowering strategies: Analysis of gas turbine integration with steam cycle for enhanced power plant performance 99–106

11) Jakub Ochmann, Henryk Łukowicz, Sebastian Lepszy, Łukasz Bartela
Repowering a coal-fired power plant according to the coal-to-nuclear pathway – analysis of nuclear unit development from the perspective of cooling water availability 107–115

12) Agnieszka Kijo-Kleczkowska, Adam Gnatowski, Marcin Gajek, Jarosław Krzywański, Magdalena Szumera, Krzysztof Knaś, Dariusz Kwiatkowski
Coal-plastic waste blendings. Experimental research and prediction of the thermal process 117–128

13) Sławomir Wiśniewski, Michał Bańkowski
Effectiveness analysis of a binary ORC power plant with zeotropic organic fluid 129–138

Contents (*cont'd*)

Other papers

14) Irshad Irshad, Shah Jahan, Ahmed Zubair Jan, Krzysztof Kędzia, Afraz Hussain Majeed, Fiza Khan
Fractional order transient free-convection flow in a channel: application of the optimal homotopy asymptotic method 139–144

15) Jacek Kalina, Michał Rabiej, Carlos Santos Silva
Simulations and techno-economic analysis of solar cooling system 145–155

16) Piotr Tarnawski
Determination of the heat capacity of a water-ice reservoir as a lower heat source for heat pump – Numerical analysis 157–163

17) Kishor Vishwanath Mane, Yevhenii Alekseik
Comprehensive parametric and design review for reducing pulsating heat pipes dependence on space orientation 165–182

18) Yellu Kumar, Adnan Qayoum, Shahid Saleem
Enhancement of adiabatic effectiveness in a combustion chamber liner with effusion cooling through conical and fan shaped holes 183–193

19) Md Atiqur Rahman
Thermal performance of tubular heat exchangers with the discontinuous swirl-inducing conical baffle with opposite-oriented flow deflectors 195–204

20) Shivasheesh Kaushik, Vikas Singh Mahar, Satyendra Singh, Rahul Kshetri, Bhupendra Kumar, Jagdish Singh Mehta, Ashwarya Raj Paul, Satish Kumar, Samriddhi Vashisth, Raj Singh Pundir, Amit Kumar
Comparative experimental analysis of fluid flow in concentric tube exchanger having semi hollow cylindrical macro inserts with nanofluid and base fluid 205–212

21) Karol Mzyk
Possibilities of energy storage in residential photovoltaic installations - overview 213–230

22) Dodeye Ina Igbong, Mafel Obhuo, Oku Ekpenyong Nyong
Parametric multi-response optimization on various organic Rankine cycle configuration for geothermal heat source application using Taguchi – grey relational analysis 231–246

23) Saravanan Jagadha, Batina Madhusudhan Rao, Putta Durgaprasad, Degavath Gopal, Putta Prakash, Naikoti Kishan, Krishnan Muthunagai
Darcy-Forchheimer two-dimensional thin flow of Jeffrey nanofluid with heat generation/absorption and thermal radiation over a stretchable flat sheet 247–259

24) Pranjal Sarmah, Ravi Kumar, Amrit Thakur, Mohit Sharma, Surendra Kumar Yadav, Virendra Kumar
Finite element analysis of femur bone fracture – modelling and analysis 261–268

25) Piotr Koniorczyk, Mateusz Zieliński, Judyta Sienkiewicz, Janusz Zmywaczyk
Thermophysical properties and microstructure of 32CrMoV12-28 hot-work tool steel 269–277

26) Hanlin Song, Zhanghao Lu, Zheshu Ma, Xinjia Guo, Qilin Guo
Thermodynamic analysis of the performance of an irreversible ammonia-fed solid oxide fuel cell 279–290

27) K. Muthukrishnan, C. Ramesh Kumar
Study on the effect of tab cooling on lithium-ion battery pack life cycle 291–299

28) Y.X. Liu, H. Wu, J. Zhang, P.X. Xu, S. Chen, X.H. He, Z.D. Sun
Effects of cooling methods and key parameters on the cooling performance of oil-cooling motor with hairpin windings 301–309

29) B.S. Bibin, Elena Ionela Chereches, Arkadiusz Mystkowski, Kamil Śmierciew, Adam Dudar, Edison Gundabattini
Thermo-physical properties, heat transfer characteristics and performance of nano-enhanced refrigerants: A review 311–322

Co-published by
Institute of Fluid-Flow Machinery
Polish Academy of Sciences
Committee on Thermodynamics and Combustion
Polish Academy of Sciences

Copyright©2024 by the Authors under licence CC BY 4.0.

http://www.imp.gda.pl/archives-of-thermodynamics/

Assessment of the impact of jet impingement technique on the energy efficiency of air-cooled BIPV/T roof tile

Jan Wajs[a*], Jakub Lukasik[a]

[a]Faculty of Mechanical Engineering and Ship Technology, Gdańsk University of Technology, Narutowicza 11/12, 80-233 Gdańsk, Poland
*jan.wajs@pg.edu.pl

Received: 19.11.2023; revised: 19.02.2024; accepted: 04.03.2024

Abstract

The paper concerns a numerical analysis of cooling of the hybrid photovoltaic (PV) modules dedicated to Building-Integrated Photovoltaic/Thermal (BIPV/T) systems. Attention was focused on the photovoltaic roof tiles, using a jet impingement technique, in which the intensification of heat transfer is ensured by streams of air hitting the heat exchange partition. A series of numerical simulations were carried out to assess an influence of the distance of the nozzle outlet from the absorber surface on the values of selected thermal-hydraulic performance indicators and the electrical parameters of the roof tile. The results confirmed the high effectiveness of the proposed method. The best effect was obtained for the case in which the relative distance of the nozzle from the partition to the nozzle diameter was equal to 1. For the mentioned configuration, an over 4 times increase in the value of the heat transfer coefficient was obtained in relation to the reference variant of cooling roof tiles. At the same time, the relative increase in the value of the generated electrical power was from 2.9 to 7.8%, depending on the value of the Reynolds number characterising the flow.

Keywords: Impinging jet; Building-Integrated Photovoltaic/Thermal (BIPV/T); Numerical analysis; Photovoltaic roof tile; Air cooling

Vol. 45(2024), No. 2, 5–18; doi: 10.24425/ather.2024.150847

Cite this manuscript as: Wajs, J., & Lukasik, J. (2024). Assessment of the impact of jet impingement technique on the energy efficiency of air-cooled BIPV/T roof tile. *Archives of Thermodynamics*, 45(2), 5–18.

1. Introduction

The photovoltaics sector is experiencing dynamic development, stimulated by the implementation of subsequent pro-ecological energy strategies. Investors expect an increase in energy efficiency while reducing costs and improving the aesthetics of the installation. In response, Building-Integrated Photovoltaic (BIPV) systems are becoming an interesting option and an increasingly developed branch of photovoltaics (PV). Due to the limited possibility of natural cooling, they are operating under high temperature conditions, leading to a drop in generated power and a reduction in electrical efficiency. To improve the performance of various cooling systems, an effective management of the transferred heat is proposed. Such hybrid systems are known as Building-Integrated Photovoltaic/Thermal (BIPV/T). Air cooling is considered as one of the most promising and practical methods of cooling photovoltaic modules.

Nomenclature

a – absorption coefficient, 1/m
D_h – hydraulic diameter of the air duct at the inlet, m
D_j – nozzle outlet diameter, m
D_{nb} – nozzle base diameter, m
e – specific energy, J/kg
$\vec{g}$ – vector of gravity acceleration, m/s^2
G – distance of the nozzle outlet from the absorber plate, m
G_{sun} – value of the solar irradiance at the front surface of the PV roof tile, W/m^2
h – average heat transfer coefficient from the absorber surface, W/(m^2·K)
H – air duct height, m
H_j – nozzle height, m
h_w – heat transfer coefficient on the front surface of the module, W/(m^2·K)
I – radiation intensity, W/m^2
k_{eff} – effective thermal conductivity coefficient including molecular and turbulent conductivity, W/(m·K)
L – air duct length, m
$\dot{m}$ – air mass flow rate, kg/s
Ma – Mach number
n_{ref} – refractive index
Nu – Nusselt number
δNu – relative increase of Nusselt number compared to a straight channel collector
p – pressure, Pa
Δp – pressure loss, Pa
$\Delta P_{\%}$ – percentage increase in electrical power generation in relation to the reference variant, %
P_{mpp} – temperature coefficient at the point of maximum power, %/K
P_{nom} – nominal power, W
q – heat flux, W/m^2
$\vec{r}$ – position vector
Re – Reynolds number
s – path length, m
$\vec{s}$ – direction vector, m
$\vec{s}'$ – scattering direction vector, m
S_1 – distance of the first transverse row of nozzles from the air duct inlet, m
S_2 – distance of the first longitudinal row of nozzles from the air duct edge, m
T – local temperature, K
T_{abs} – average temperature at the back wall of the absorber, K
T_b – average air temperature between the inlet and outlet, K
ΔT_{cells} – difference in average temperature of the silicon layer between the selected jet impingement variant and the reference variant, K
T_{cells} – average temperature of the silicon layer in selected jet impingement variant, K
T_{cells_EVA} – average temperature at the interface between silicon layer and EVA foil layer, K
T_{cells_ref} – average temperature of the silicon layer in reference variant, K
T_{EVA_cells} – average temperature at the interface between EVA foil layer and silicon layer, K
T_{out} – average air temperature at the outlet of the flow duct, K
T_{surf} – average surface temperature of the PV roof tile, K
$\vec{v}$ – velocity vector, m/s
V_{ch} – channel inlet velocity, m/s
v_{in} – average air velocity at the inlet to the flow duct, m/s
V_j – nozzle outlet velocity, m/s
v_w – wind speed, m/s
W – air duct width, m
X – distance between nozzles in the longitudinal direction, m
Y – distance between nozzles in the transverse direction, m
y^+ – dimensionless wall distance

Greek symbols

α_P – temperature coefficient at the point of max. power, %/K
η_{el_STC} – electrical efficiency of the module in Standard Test Conditions (STC), %
η_{th} – thermal efficiency, %
λ – air thermal conductivity, W/(m·K)
$\mu|_{t=25°C}$ – dynamic viscosity coefficient of air at 25°C, kg/(m·s)
ρ – fluid density, kg/m^3
$\rho|_{t=25°C}$ – air density at 25°C, kg/m^3
σ – Stefan-Boltzmann constant, W/(m^2·K^4)
σ_s – scattering coefficient, 1/m
$\bar{\bar{\tau}}$ – shear stress tensor, Pa
τ_{eff} – total viscous stress tensor, Pa
Φ – phase function
Ω – solid angle, sr

Abbreviations and Acronyms

ASHRAE – American Society of Heating, Refrigerating and Air-Conditioning Engineers
BIPV – Building-Integrated Photovoltaic
BIPV/T – Building-Integrated Photovoltaic/Thermal
DO – Discrete Ordinates
EVA – Ethylene-Vinyl Acetate
PEC – Performance Evaluation Criteria
PV – Photovoltaic
PVF – Polyvinyl Fluoride
RANS – Reynolds Averaged Navier-Stokes
RTE – Radiative Transfer Equation
SAH – Solar Air Heater
SST – Shear Stress Transport
STC – Standard Test Conditions
THPP – Thermo-Hydraulic Performance Parameter

It has several advantages, such as unlimited availability, no cost of acquiring the medium, no negative impact on the environment, low system cost, and no problems with moisture, boiling, and freezing. On the other hand, the major disadvantage of this system is a low value of the heat transfer coefficient. Therefore, effective methods of intensifying heat transport are being sought. In the authors' opinion, one of the most promising directions of improvement in this field is the application of the jet

impingement technique. The air stream hitting the absorber surface creates a thin layer with a high turbulence intensity near the point of impact, which, as a result of the high local values of the heat transfer coefficient, allows for effective heat removal.

There are publications available in the literature on the use of impinging jets to intensify the heat transfer from solar air heaters (SAH). One of the first works in this area was presented by Choundhury and Garg [1]. A perforated plate was a partition for generating the streams. The use of the jet impingement technique in the tested system allows for an increase in the temperature of the air leaving the duct by 15.5 K and an increase in the thermal efficiency of the system by 26.5%, compared to the system with airflow through a straight duct. Zukowski [2] proposed the construction of a microjet SAH, in which the air hitting the flat surface of the absorber plate ensures intensified heat removal. The experimental tests showed that the solar energy conversion efficiency using this solution ranged from 66% to 90%, which allows it to compete with the best solutions available on the market while being characterised by low pressure losses.

Current work on the use of jet impingement technology to remove heat from solar air heaters includes research on various geometric configurations of nozzles that direct the medium and their impact on the energy effects obtained. Chauhan et al. [3] examined the influence of the geometric parameters of the impinging jet system on the thermal efficiency and pressure losses of investigated SAH. The tests were carried out for a straight channel in the range of Reynolds number values from 3 800 to 16 000 determined at the inlet. The generation of air streams was ensured by a perforated plate placed halfway up the duct, at a distance of 25 mm from the absorber heat exchange surface. Attention was focused on the evaluation of geometric parameters in the form of the ratio of the longitudinal spacing of the holes to the duct hydraulic diameter (X/D_h), the ratio of transverse spacing to the duct hydraulic diameter (Y/D_h), as well as the ratio of the nozzle outlet diameter to the duct hydraulic diameter (D_j/D_h). The variant described by the parameters: $X/D_h = 0.435$, $Y/D_h = 0.869$, and $D_j/D_h = 0.065$ was considered as the optimal configuration with the Reynolds number equal to 16 000.

Yadav and Saini [4] using ANSYS 18.1 software conducted numerical studies on the impact of various configurations of dimensionless parameters describing the nozzle geometry on the efficiency of a solar air heater. The variables tested were the ratio of the nozzle height to the duct hydraulic diameter (H_j/D_h) and the ratio of the nozzle outlet diameter to the hydraulic diameter (D_j/D_h). The hydraulic diameter was specified at the inlet cross-section, and the lower part of flow duct was a straight channel with fixed dimensions. Simulations were performed at the Reynolds number range from 3 500 to 17 500. The results indicated that the recommended configuration that provided a favourable balance between the improvement of cooling efficiency and pressure drop was the ratio $H_j/D_h = 0.216$ and $D_j/D_h = 0.065$.

In the study conducted by Pazarlioglu et al. [5], the influence of various nozzle heights on the thermal efficiency of a SAH was assessed. The variable parameter in the tests was the dimensionless ratio of the distance of the nozzle outlet to the absorber plate to the constant diameter of the nozzle (G/D_j). The research was carried out based on numerical analysis for the values of Reynolds numbers defined at the inlet in the range from 10 000 to 25 000. The best configuration for all the conditions tested at the inlet turned out to be the value of $G/D_j = 2$, which, despite generating the highest pressure drop values, achieved the highest value of the performance evaluation criteria (PEC) index.

Hai et al. [6] compared 7 configurations of parallel or crossing nozzles with different inclination angles. The thermo-hydraulic performance parameter (THPP) of the system was investigated for various geometric variables ($0.024 \le D_j/D_h \le 0.144$; $0.30 \le X/D_h \le 0.60$; $0.30 \le Y/D_h \le 0.60$), Reynolds numbers ($10\,000 \le \mathrm{Re} \le 30\,000$), and the ratio of nozzle outlet velocity to the channel inlet velocity ($1 \le V_j/V_{ch} \le 25$). For low values of the V_j/V_{ch} ratio, higher THPP values were obtained for parallel configurations, while for high values, cross-shaped configurations performed better. It was also observed that the change in transverse and longitudinal nozzle spacing had no significant influence on the friction factor. In comparison with a smooth channel in conventional solar air heater, the best configuration caused an increase of the Nusselt number by up to 4.26 times.

Das et al. [7] presented a numerical parametric investigations on a SAH equipped with a perforated plate and conical protruded nozzles. The research focused on evaluating the influence of selected dimensionless parameters on the THPP indicator within a Reynolds number range from 2 900 to 14 300, defined at the channel inlet. Experimental validation of the results was also performed. The best configuration was found to be the variant described by the parameters $H_j/D_h = 0.2608$, $D_j/D_h = 0.0217$, and $D_{nb}/D_h = 0.0652$ (the ratio of nozzle base diameter to hydraulic diameter). For this configuration, at the maximum investigated Reynolds number, the Nusselt number value of 223.18 and a thermal efficiency of 91.25% were gained.

Ewe et al. [8] conducted numerical and experimental thermo-electro-hydraulic analysis of a jet impingement bifacial photovoltaic thermal collector. Configurations with different longitudinal ($0.09 \le X \le 0.126$ m) and transverse ($0.081 \le Y \le 0.1134$ m) jet hole spacings were investigated at two solar irradiance values (700 and 900 W/m^2) and the Reynolds numbers ranging from 1 409 to 28 404. The system performance evaluation took into account a pressure drop and fan power required for flow circulation. The configuration with 36 jet holes reached the highest electrical energy output at a Reynolds number of 5 667, while the maximum thermal energy output was obtained at Re = 9 929. The highest thermal, electrical, and thermo-electro-hydraulic efficiencies were equal to 57.3%, 10.36% and 83.93%, respectively.

Only a few studies in the literature refer to the use of a jet impingement technique for cooling PV modules, especially for removing heat from BIPV/T systems. A significant gap in this matter is confirmed by Ewe et al. [9]. The novelty of the presented paper is the presentation of the results of own work on the assessment of the impact of selected configurations of the cooling system with the jet impingement technique on the electrical and thermal-hydraulic parameters of the BIPV/T module in the form of a PV roof tile. The various nozzle length values, described in dimensionless form as the ratio of the nozzle outlet distance from the absorber surface to the nozzle diameter, were

taken into consideration. The approach proposed in this work is based on multivariant, numerical thermal-flow analyses. The simulations were carried out in the ANSYS Fluent software with the implemented Discrete Ordinates (DO) radiation model and the Solar Load module, allowing for a better representation of real atmospheric conditions. Analyses were carried out at a constant solar irradiance of 1 000 W/m^2 and the Reynolds numbers in the range of 5 000–25 000 for cooling airflow. The results were compared to the reference variant in which air flows freely through the channel and the rear wall of the absorber. The obtained distributions of temperature and velocity fields of the cooling medium were also visualised.

2. Scope of research and methodology

The research was carried out using the Monier Brass PV Premium roof tile model, with cells made of monocrystalline silicon. The technical parameters of investigated roof tile are listed in Table 1.

Table 1. Technical parameters of the tested photovoltaic roof tile [10].

Parameter	Value
Nominal power (P_{nom})	100 W
Electrical efficiency of the module in STC (η_{el_STC})	16.34%
Temperature coefficient of maximum power (P_{mpp})	–0.42%/K
Module dimensions	1 825 x 454 mm
Dimensions of a single cell	156 x 156 mm
Number of cells	22

To intensify heat transfer, 240 symmetrically arranged cylindrical nozzles were used, directing air streams to the module's absorber. The research focused on comparing the results obtained for variants with different nozzle lengths, marked as A, B, and C in Fig. 1, which visualises the tested flow systems with jet impingement technique. The selected configurations were described by the dimensionless parameter G/D_j, defined as the ratio of the distance of the nozzle outlet from the absorber surface (G) to the nozzle diameter (D_j). Variant C, described as G/D_j = 12.61, is a system with a perforated partition to generate streams (holes in the partition take over the function of the nozzles).

For reference purposes, the analyses of cooling under airflow conditions through a straight duct with a height of H = 37.83 mm (variant D, where the aspect ratio W/H = 12) and a double-height duct, that is, H = 75.66 mm (variant E, where W/H = 6) were carried out. The adopted aspect ratio values were obtained from the literature [7, 11, 12, 13] and refer to the ASHRAE 93–97 standard dedicated to solar air heaters [14]. The remaining geometric parameters, listed in Table 2, were taken from the literature [3, 5, 7] and were not optimised at the current stage of the investigation.

The Reynolds number values characterising the air flow were determined at the inlet to the duct using the equation:

$$\mathrm{Re} = \frac{\rho|_{t=25°C} \cdot v_{in} \cdot D_h}{\mu|_{t=25°C}}, \qquad (1)$$

where: $\rho|_{t=25°C}$ – air density at 25°C [kg/m^3]; v_{in} – average air velocity at the inlet [m/s]; D_h – hydraulic diameter of the air duct at the inlet [m]; $\mu|_{t=25°C}$ – dynamic viscosity coefficient of air at 25°C [kg/(m·s)].

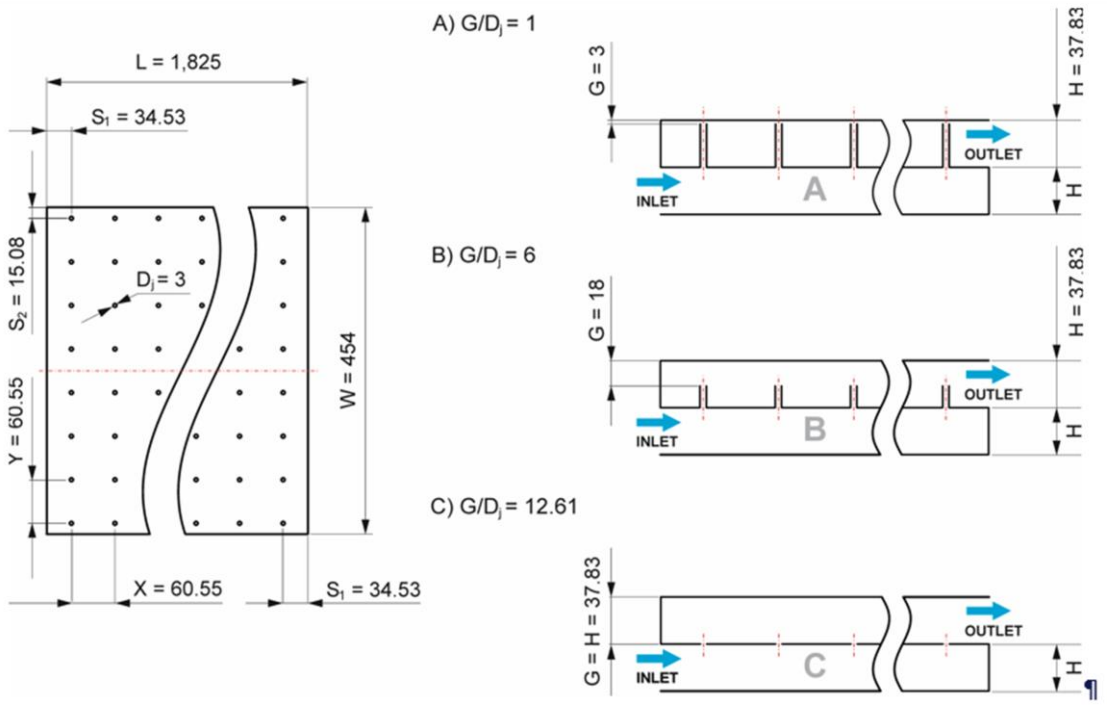


Fig. 1. Geometry of considered airflow ducts with jet impingement technique (variants A, B, C represent various nozzle lengths).

Table 2. Geometric parameters of the tested configurations.

	Variants A, B, C	Variant D	Variant E
Height of the airflow duct (H, mm)	37.83	37.83	75.66
Hydraulic diameter (D_h, m)	0.07	0.07	0.13
Air duct aspect ratio (W/H)	12	12	6
Nozzle diameter (D_j, mm)	3	n/a	n/a
Nozzle diameter to hydraulic diameter ratio (D_j/D_h)	0.043	n/a	n/a
Nozzle spacing in the longitudinal direction (X/D_h)	0.867	n/a	n/a
Nozzle spacing in the transverse direction (Y/D_h)	0.867	n/a	n/a

The values of Reynolds numbers analysed in each configuration, defined at the inlet to the airflow duct, correspond to the values of mass flow rates listed in Table 3.

Table 3. Mass flow rate values corresponding to the analysed Reynolds number values.

Re [–]	$\dot{m}$ [kg/s]	
	Variant A, B, C, D (H = 37.83 mm)	Variant E (H = 75.66 mm)
5000	0.0226	0.0243
10000	0.0451	0.0486
15000	0.0678	0.0729
20000	0.0903	0.0971
25000	0.1128	0.1215

The heat transfer coefficient at the front surface of the module was determined according to the correlation proposed in [15]:

$$h_w = 5.7 + 3.8 \cdot v_w, \tag{2}$$

where: v_w is the wind speed [m/s]. An extreme theoretical case was assumed in which the wind speed is 0 m/s.

The average coefficient of heat transfer at the absorber surface was determined from the relationship:

$$h = \frac{q}{T_{abs} - T_b}, \tag{3}$$

where: q – transferred heat flux [W/m^2]; T_{abs} – average temperature at the back wall of the absorber [K]; T_b – average air temperature between the duct inlet and outlet [K].

The Nusselt number was defined as:

$$\mathrm{Nu} = \frac{h \cdot D_h}{\lambda}, \tag{4}$$

where: λ is the air thermal conductivity [W/(m·K)].

The thermal efficiency of the individual variants was determined from the formula:

$$\eta_{th} = \frac{q}{G_{sun}}, \tag{5}$$

where: G_{sun} – value of the solar irradiance at the front surface of the PV roof tile (1 000 W/m^2).

To consider the improvement of the power generation of the photovoltaic roof tile, its structure has to be taken into account. The cross-section of the photovoltaic roof tile is presented in Fig. 2, including the thicknesses of each layer and the key temperatures marked.

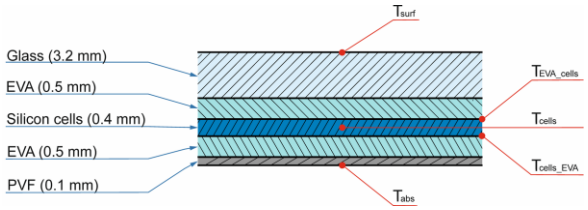


Fig. 2. Modelled layers of photovoltaic roof tile [17].

The estimation of an increase in the electrical power generation in the variants with jet impingement technique (A–C), compared to the reference variant with a straight channel (D), was described by the formula:

$$\Delta P_{\%} = \alpha_P \cdot \Delta T_{cells}, \tag{6}$$

where: α_P – temperature coefficient at the point of maximum power [%/K], ΔT_{cells} – difference in average temperature of the silicon layer between the selected jet impingement variant and the reference variant [K].

To determine ΔT_{cells}, the temperature of silicon layer for each variant with jet impingement technique (A–C) as well as the reference variant (D) must be known:

$$\Delta T_{cells} = T_{cells} - T_{cells_ref}, \tag{7}$$

where: T_{cells} – average temperature of the silicon layer in selected jet impingement variant [K]; T_{cells_ref} – average temperature of the silicon layer in reference variant [K].

The average temperature of the silicon layer was determined as the arithmetic one between the averaged temperature at the interface of the EVA foil layer - silicon layer and silicon layer - EVA foil layer. It was calculated using the formula:

$$T_{cells} = \frac{T_{EVA_cells} + T_{cells_EVA}}{2}, \tag{8}$$

where: T_{EVA_cells} – average temperature at the interface between EVA foil layer and silicon layer [K]; T_{cells_EVA} – average temperature at the interface between silicon layer and EVA foil layer [K].

The above temperature values for each individual layers of the PV module were obtained numerically as the averages over total layer surface.

Taking the temperature of the silicon layer as an average in calculation of electrical power increase was a simplification introduced to determine the overall effect. This assumption was necessary because the local temperature distribution in particular cells was variable as a result of cooling. It leads to different voltage-current operating points. Therefore, to evaluate the operation of the entire module, the averaging procedure was conducted.

Numerical calculations were performed using ANSYS Fluent 2021 R1 software. Constant values of the thermophysical properties of the materials used, taken from the literature, were assumed for the calculations. They are summarised in Table 4.

All layers of the photovoltaic module except the protective glass were modelled using a 2D shell conduction approach. The glass layer, as a semi-transparent material, was modelled using a classic 3D approach. A conformal polyhedral mesh was used. To maintain satisfactory values of the quality of the skewness and orthogonality coefficient, the mesh size was locally refined. For variant A (G/D_j = 1) and variant D (H = 37.83 mm), at the Re = 25 000, a mesh independence test was performed. In variant A, meshes with a number of cells ranging from 2.25 million to 6.65 million were tested, with steps of approximately 0.7 million, and in variant D from 0.18 million. to 1.28 million, in steps of approximately 0.18 million. The condition ending the tests was the conjunction of events, defined as a relative difference of the Nusselt number value between the previous and current results less than 1% and a relative difference of the heat flux transferred by the air between the previous and current results less than 1%. Table 5 presents the results of the mesh sensitivity analysis.

Ultimately, the adapted meshes, ensuring a compromise between the accuracy of the results and the calculation time, consisted of approximately 5.47 million cells. The coefficient y^+ = 0.991 averaged for all analysed Reynolds number values for variant A, and approximately 1.08 million cells, with the coefficient y^+ = 0.847 for variant D was obtained. Ten levels within the boundary layer were created using a constant growth rate of 1.3. The visualisation of the mesh prepared for variant A is presented in Fig. 3.

The finite-volume method for 3D geometry was used to solve the thermal-flow model. Due to the low velocity value (Ma < 0.2), the flow was treated as incompressible. A pressure-based solver, the Reynolds Averaged Navier-Stokes (RANS) equations, and the shear stress transport (SST) k-ω turbulence model suggested by Hussein et al. [23] and Tepe et al. [24] were used. Stationary simulations were performed, without internal sources of heat and mass. The boundary conditions at the inlet were set in the form of a constant value of the mass flow rate to maintain the individual values of the Reynolds numbers and a constant inlet air temperature of 25°C. A fully developed velocity profile prepared using a translational periodic interface was used. The pressure at the outlet from the flow duct was assumed to be equal to atmospheric pressure. The equations of continuity, momentum, and energy have the following form [23, 25, 26]:

Continuity equation:

$$\nabla \cdot \vec{v} = 0, \tag{9}$$

where: $\vec{v}$ – velocity vector [m/s].

Table 4. Thermophysical properties of the materials used [16–22].

Material	Density [kg/m³]	Specific heat [J/(kg·K)]	Thermal conductivity [W/(m·K)]	Refractive index [–]	Emissivity [–]
Air (at 25°C)	1.185	1 005	0.0263	1	–
Glass	3 000	500	1.8	1.5	0.94
EVA foil	960	2 090	0.35	1.5	0.94
Silicon cells	2 330	677	148	–	0.9
PVF	1 200	1 250	0.2	–	0.98

Table 5. Results of the mesh independence test for the case with Re = 25 000.

	Mesh No.	Number of cells	y^+	Nu	δNu%	q [W/m²]	δq%
Variant A (G/D_j = 1)	Mesh 1	2 252 793	7.283	651.45	–	740.86	–
	Mesh 2	3 298 981	4.125	443.35	–31.94%	739.61	–0.17%
	Mesh 3	3 889 612	3.046	391.14	–11.78%	739.41	–0.03%
	Mesh 4	4 454 470	2.316	371.86	–4.93%	740.78	0.15%
	Mesh 5	4,955,807	2.276	367.50	–1.17%	740.39	–0.05%
	Mesh 6	**5 472 638**	**2.232**	**364.64**	**–0.78%**	**740.11**	**–0.04%**
	Mesh 7	6 646 577	2.186	361.91	–0.75%	740.02	–0.01%
Variant D (H = 37.83 mm)	Mesh 1	180 813	7.912	111.33	–	602.46	–
	Mesh 2	371 959	2.662	103.85	–6.72%	625.57	3.69%
	Mesh 3	489 004	2.182	97.56	–6.06%	619.86	–0.92%
	Mesh 4	601 102	1.924	95.33	–2.29%	618.38	–0.24%
	Mesh 5	877 811	1.576	94.14	–1.25%	619.29	–0.15%
	Mesh 6	**1 078 662**	**1.428**	**93.75**	**–0.41%**	**619.90**	**–0.10%**
	Mesh 7	1 283 286	1.377	93.51	–0.25%	620.05	0.02%

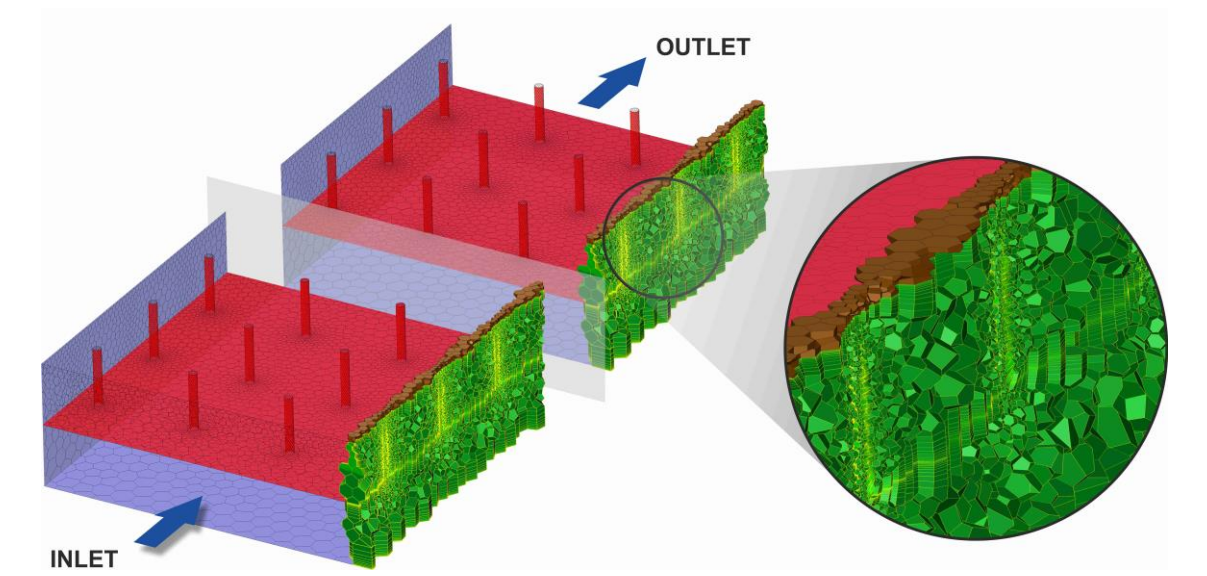


Fig. 3. Longitudinal cross-section of the mesh generated for variant A.

Momentum conservation equation:

$$\nabla \cdot (\rho \vec{v} \vec{v}) = -\nabla p + \nabla \cdot \bar{\bar{\tau}} + \rho \vec{g}, \quad (10)$$

where: ρ – fluid density [kg/m^3]; p – pressure [Pa]; $\bar{\bar{\tau}}$ – shear stress tensor [Pa]; $\vec{g}$ – vector of gravity acceleration [m/s^2].

Energy conservation equation:

$$\nabla \cdot \left(\vec{v}(\rho e + p)\right) = \nabla \cdot \left(k_{eff} \nabla T + \bar{\bar{\tau}}_{eff} \cdot \vec{v}\right), \quad (11)$$

where: e – specific energy [J/kg]; k_{eff} – effective thermal conductivity coefficient including molecular and turbulent conductivity [W/(m·K)]; T – local temperature [K]; $\bar{\bar{\tau}}_{eff}$ – total viscous stress tensor [Pa].

All external walls of the system, except the front surface of the module, were considered adiabatic. The partition between the upper and lower part of the duct was also considered adiabatic. The internal walls at the boundary between the solid and fluid domains were treated as no-slip walls [27]. To reflect the solar radiation falling at the front surface of the module, the Discrete Ordinates radiation model was used, enabling modelling of semi-transparent domains. The Solar Load extension has also been implemented. Radiation modelling is based on the radiative transfer equation (RTE), which determines the intensity of radiation transported from position $\vec{r}$ towards direction $\vec{s}$. In accordance with literature [25,26,28], radiation intensity (I [W/m^2]) is defined using equation (12), where: $\vec{r}$ – position vector [m]; $\vec{s}$ – direction vector [m]; s – path length [m]; a – absorption coefficient [1/m]; σ_s – scattering coefficient [1/m]; n_{ref} – refractive index [–]; σ – Stefan-Boltzmann constant [W/(m^2·K^4)]; $\vec{s}'$ – scattering direction vector; Φ – phase function [–]; Ω – solid angle [sr].

It was assumed that the radiation falls on the front surface of the PV roof tile in the normal direction and there is no reflected radiation. A constant solar irradiance equal to 1 000 W/m^2 was assumed. The calculations used a coupled solver and double precision of numerical notation. Due to the satisfactory values of aspect ratio, orthogonal quality, and skewness, the second-order upwind discretisation scheme was used.

3. Results and discussion

The obtained values of thermal-hydraulic performance indicators were presented as graphs plotted as a function of the Reynolds number. Figure 4 (a) shows the profiles of the average air temperature at the outlet of the flow duct (T_{out}) and the received heat flux (q). Figure 4 (b) presents the profiles of the average temperature at the module front surface (T_{surf}) and the average heat transfer coefficient from the absorber surface (h). Figure 5 (a) shows the profiles of the Nusselt number (Nu) and the thermal efficiency values of the photovoltaic roof tile (η_{th}). Figure 5 (b) presents the characteristics of pressure drops in the flow channel (Δp) and the absolute temperature difference of the module in the silicon cells layer (ΔT_{cells}) between the variants with the jet impingement technique (A, B, C) and the reference variant (D).

In terms of thermal performance, the best results in the entire range of tested Reynolds number values were achieved for variant A with the outlet of the nozzle placed the closest to the absorber (G/D_j = 1). Compared to the reference variant with a straight channel (D) and a height of H = 37.83 mm, the temperature of the air leaving the flow duct increased by 5.7 K, 1.3 K, and 0.6 K at Reynolds numbers of 5 000, 15 000 and 25 000, respectively.

$$\frac{dI(\vec{r},\vec{s})}{ds} = -(a+\sigma_s)I(\vec{r},\vec{s}) + a\frac{{n_{ref}}^2 \sigma T^4}{\pi} + \frac{\sigma_s}{4\pi}\int_0^{4\pi} I(\vec{r},\vec{s}')\Phi(\vec{s}\cdot\vec{s}')d\Omega' \quad (12)$$

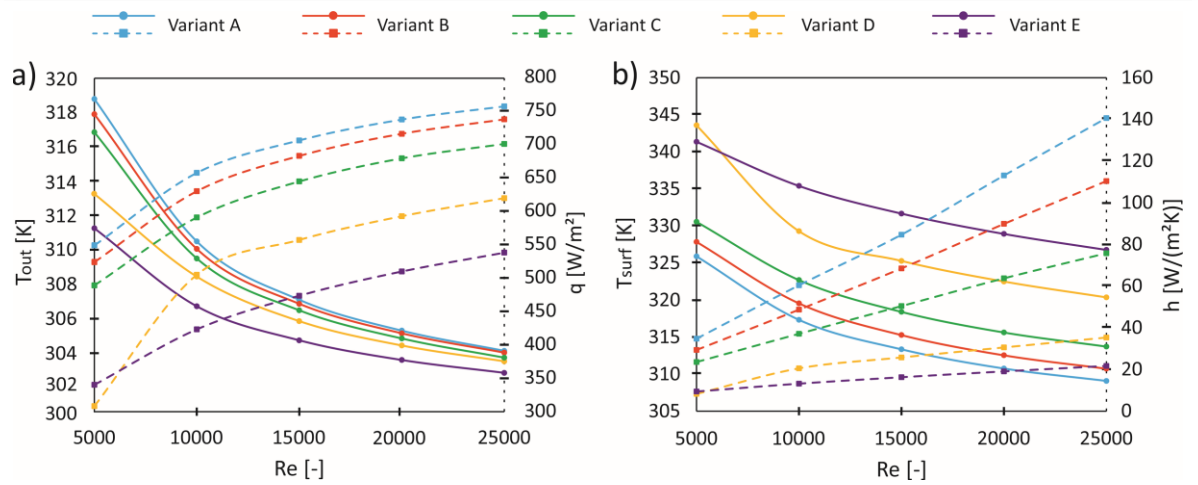


Fig. 4. Characteristics of: (a) average air temperature at the outlet and heat flux transferred by the air; (b) average temperature at the front surface of the module and average heat transfer coefficient at the absorber surface.

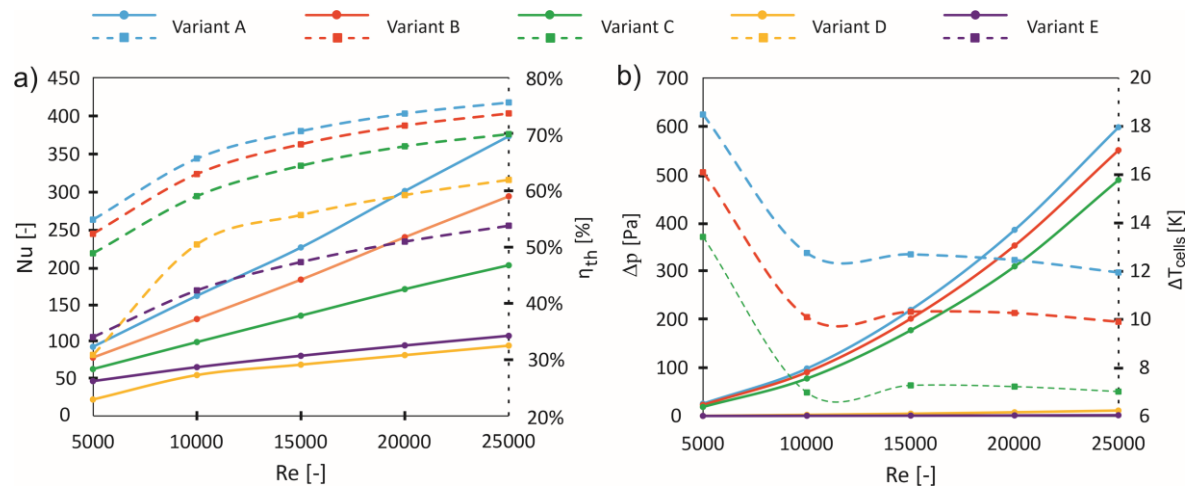


Fig. 5. (a) Profiles of the Nusselt number and thermal efficiency values of the photovoltaic roof tile; (b) Characteristics of pressure drops in the flow channel and the module temperature difference in the silicon layer between the variants with the jet impingement technique and the reference variant.

The temperature drops at the front surface module were 17.7 K, 11.9 K, and 11.3 K, respectively. Heat flux in-creased by 240.9 W/m^2 (78.1%), 149.22 W/m^2 (26.8%), and 137.6 W/m^2 (22.2%). The value of the heat transfer coefficient increased by 26.5 W/(m^2·K), 58.9 W/(m^2·K), and 105.3 W/(m^2·K), and the Nusselt number by 70.4 (320.7%), 156.4 (228.5%) and 279.6 (298.1%).

In the case of variant C, with a perforated plate without noz-zles, the temperature of the air leaving the system increased by 3.7 K, 0.7 K, and 0.2 K, while the temperature drop on the sur-face was reduced by 13.0 K, 6.9 K, and 6.6 K at Reynolds num-bers of 5 000, 15 000, and 25 000, respectively. The heat flux increased by 181.0 W/m^2 (58.7%), 87.6 W/m^2 (15.7%), and 81.3 W/m^2 (13.1%). The heat transfer coefficient increased by 15.3 W/(m^2·K), 24.6 W/(m^2·K), and 40.4 W/(m^2·K), and the Nusselt number increased by 40.6 (185.1%), 65.4 (95.6%) and 107.4 (114.5%). Intermediate points for Re = 10 000 and Re = 20 000 are also presented in the graphs shown in Figs. 4 and 5 for each configuration.

The results indicate that the differences in the temperature of the air leaving the flow channel, the heat flux transferred by the air, and the temperature at the front surface of the module be-tween the leading variant A and the reference variant D decrease with an increase in the Reynolds number. The largest differences occur for the configuration with the lowest considered Reynolds number. Significantly smaller differences are observed between configurations with Reynolds number in the range of 10 000–25 000. This allows to assume that in practical applications, in the thermal aspect related to the potential use of heated air, taking into account the energy required to force the flow and overcome hydraulic resistance, increasing the velocity of the air above a certain limit may not be justified. A significant increase in hy-draulic resistance is noticeable, which for variant A, compared to the reference variant D, resulted in an increase in the pressure drop in the flow channel by 28.8 Pa (79 times), 245.9 Pa (46

times), and 670.3 Pa (53 times), at the Reynolds number values of 5 000, 15 000 and 25 000 respectively. The thermal efficiency values for variants A and D presented in the analogous Reynolds number convention were 54.9%, 70.7%, and 75.8% for variant A and 30.8%, 55.8%, and 62.0% for variant D.

Table 6 shows the estimated increase in electrical power generated by the PV roof tile compared to the reference variant (D).

Table 6. Estimated increase in generated electrical power compared to the reference variant (D).

Re [–]	Variant A	Variant B	Variant C
5 000	7.77%	6.76%	5.64%
10 000	5.36%	4.24%	2.93%
15 000	5.33%	4.33%	3.05%
20 000	5.22%	4.31%	3.03%
25 000	5.02%	4.16%	2.95%

The results obtained indicate a significant increase in the electrical power generated by the PV roof tile, in relation to the configuration with straight cooling channel (variant D). The highest increase in a power is characterised by variant A, which allows to increase the power supply to the system by approximately 7.8%, 5.3%, and 5.0% at the Reynolds number values of 5 000, 15 000, and 25 000, respectively. The variant with an intermediate nozzle length (B) and the variant with a perforated partition generating the streams (C) reached an increase approximately 1% and 2% lower, respectively, compared to the leading variant (A).

The differences in the estimated electrical power generated in variants A–C result from the temperature of the silicon cell layer, achieved by varying the distance between the nozzle outlet and the lower surface of the absorber. Similar to the module surface temperature, the silicon cell layer temperature is the lowest in variant A. This translates to the highest potential for increasing the generated power compared to the reference variant with a straight channel (D). In each configuration with jet impingement, it is also observed that the relative increase in generated power decreases with increasing Reynolds number, particularly in the Reynolds number range of 10 000–25 000. This is due to the diminishing difference between the average silicon cell layer temperature in the different jet impingement variants and the average cell layer temperature in the reference variant D, as the Reynolds number increases. As a result, the increase in Reynolds number has a progressively smaller impact on the relative increase in electrical power of the photovoltaic roof tile compared to the straight channel variant. This provides a field for future system optimisation based on the adopted objective function.

Figures 6–10 present local distributions of selected thermal-hydraulic parameters for the analysed variants. Figures 6 and 7 show the temperature distributions at the front surface of the

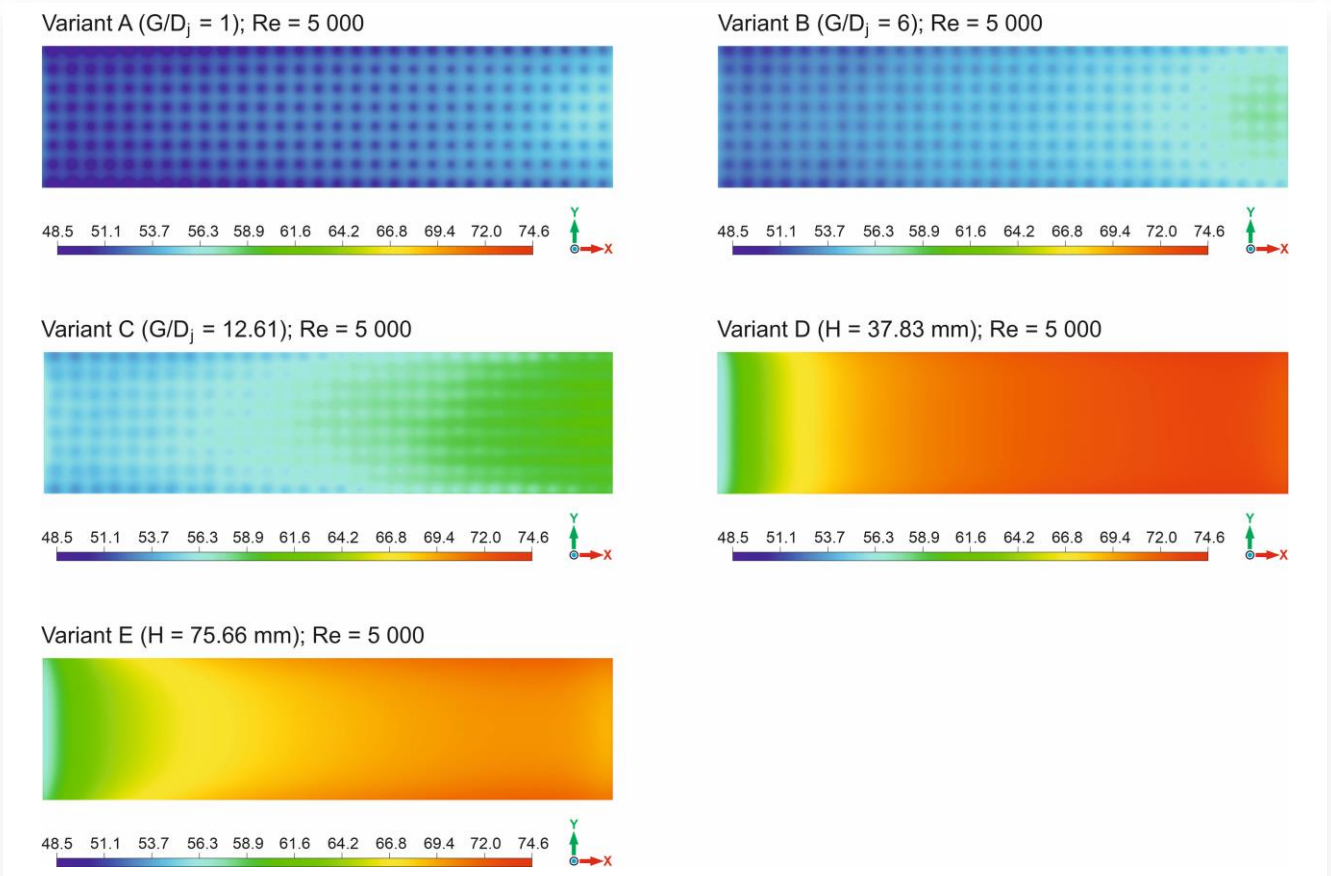


Fig. 6. Temperature distributions at the front surface of the module at Re = 5 000.

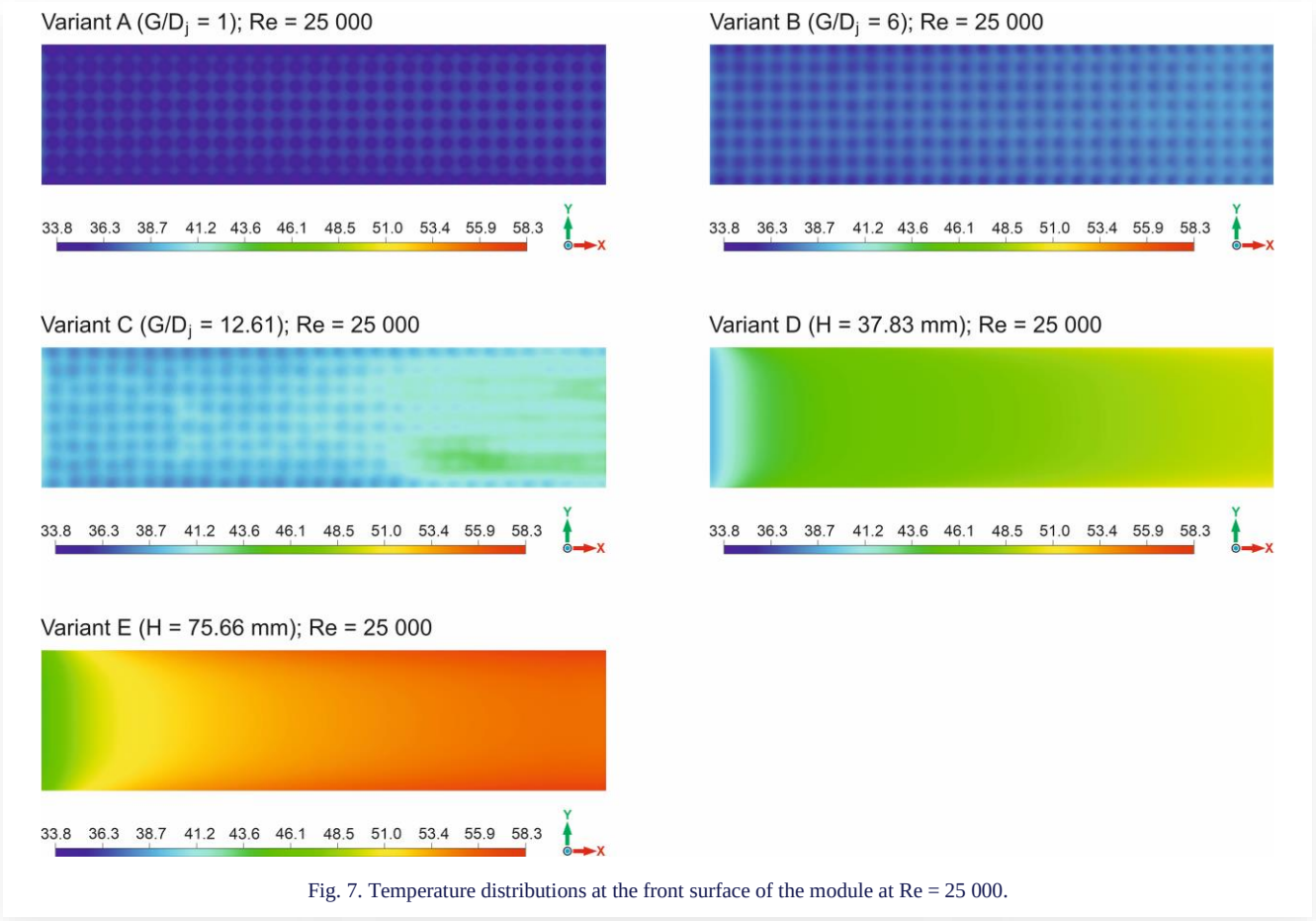


Fig. 7. Temperature distributions at the front surface of the module at Re = 25 000.

module for the flow characterised by the limiting tested Reynolds number of 5 000 and 25 000, respectively for all configurations of flow duct. The graphics presented in Figures 8–10 exhibit the longitudinal cross-section (*zx*) of a PV roof tile. They include 5 rows of nozzles located in the centre of the flow channel (lateral rows 13–17). The cross-section with the *zx* plane represents the 4th longitudinal row. Figure 8 shows the local temperature distribution, while Figure 9 shows the local velocity distribution, and Figure 10 presents the vector velocity field (*x* and *z* components). For graphics referring to the same value of the Reynolds number, a uniform colour scale is used to facilitate the capture of differences between individual configurations.

The temperature distribution at the front surface of the photovoltaic roof tile shows a change in the temperature field directed from the inlet to the outlet, along the x-axis, towards higher values. It is a result of the combined effects of the gradual heating of the air flowing along the absorber through the channel towards the outlet and, in the case of variants with the jet impingement technique, mixing of cold air supplied from the lower part of the duct with the heated air in the upper part. The effect of a local increase in the heat transfer coefficient, manifested by a lower temperature in the area affected by the air flowing from the nozzles, is smaller when the nozzle outlet is located farther from the absorber surface.

For the longitudinal cross-section presented (Fig. 8) in the area from the 13th to the 17th row of nozzles, there is a uniform temperature distribution in each nozzle, resulting from the assumption of adiabaticity of the partition separating the channels and adiabaticity of the nozzles themselves. At the same time, much lower temperature values are observed in the upper part of the flow duct for the configuration with higher Reynolds number values. Moreover, for the variant C with a perforated partition and Re = 5 000 a rapid heating of the air flowing from the holes is visible. Near the absorber, the air discharged from the holes reached a temperature close to the average air temperature in the upper part of flow duct considered in a given cross-section. This is due to the low velocity at which the air moves out the holes, which quickly mixes and exchanges heat with the air transported in the upper channel. A general deviation of the air stream leaving the holes in the perforated partition toward the outlet is observed, as illustrated in Fig. 9.

Figure 10 presents the velocity vector fields taking into account the *x* and *z* components. The deviation of the vectors in the area of air impact on the module absorber presents the air vortices occurring near the nozzle outlet. In the upper part of the duct, a vector velocity field was directed towards the outlet. In the lower part of duct, a velocity profile developed from the lower wall of the flow channel towards the flow core, and air rotation occurring in the area of air attack at the lower edges of the nozzles is observed.

The obtained results were compared with the achievements reported in the literature concerning the application of jet impingement technique in solar systems. According to the authors' best knowledge, publications specifically dedicated to air-based jet impingement adopted to PV/T and BIPV/T systems are very limited. Therefore, reference was also made to studies regarding solar air heaters. Table 7 presents a comparison of the authors' results, with those reported in the literature.

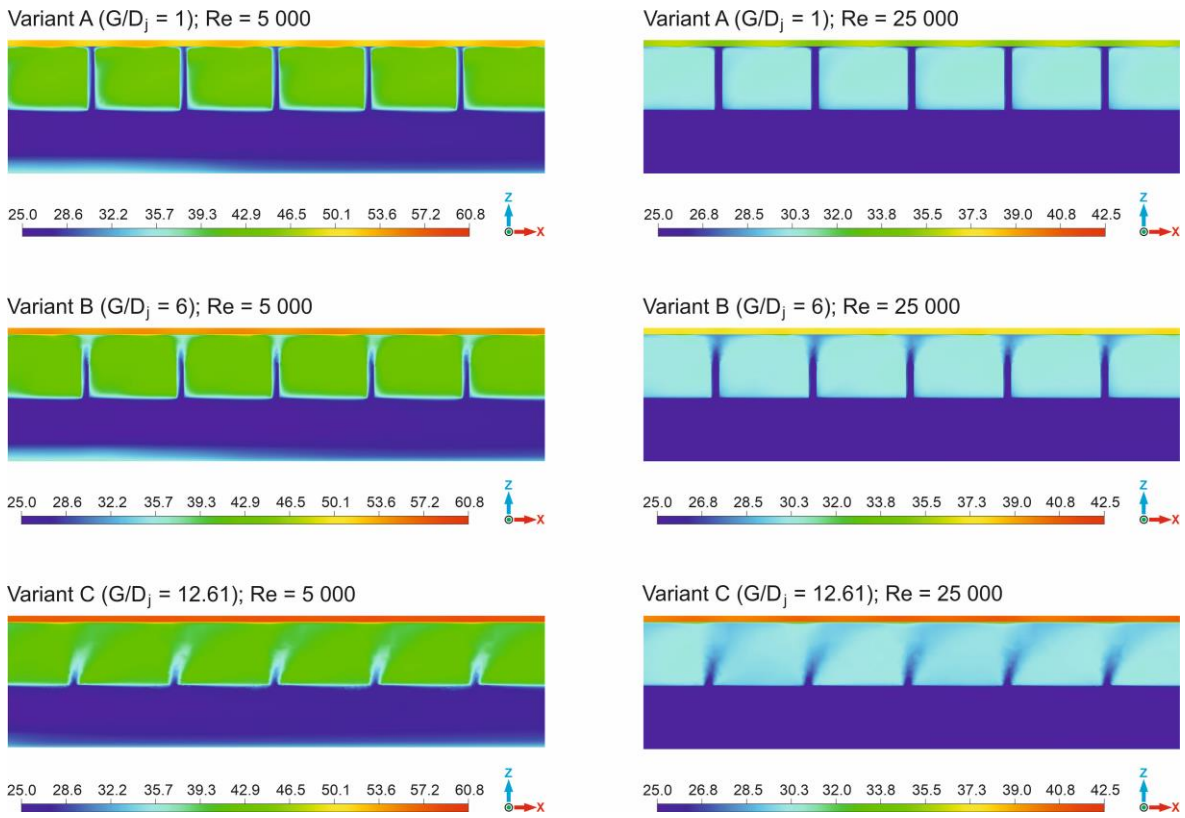


Fig. 8. Temperature distributions in the longitudinal cross-section for variants with the jet impingement technique.

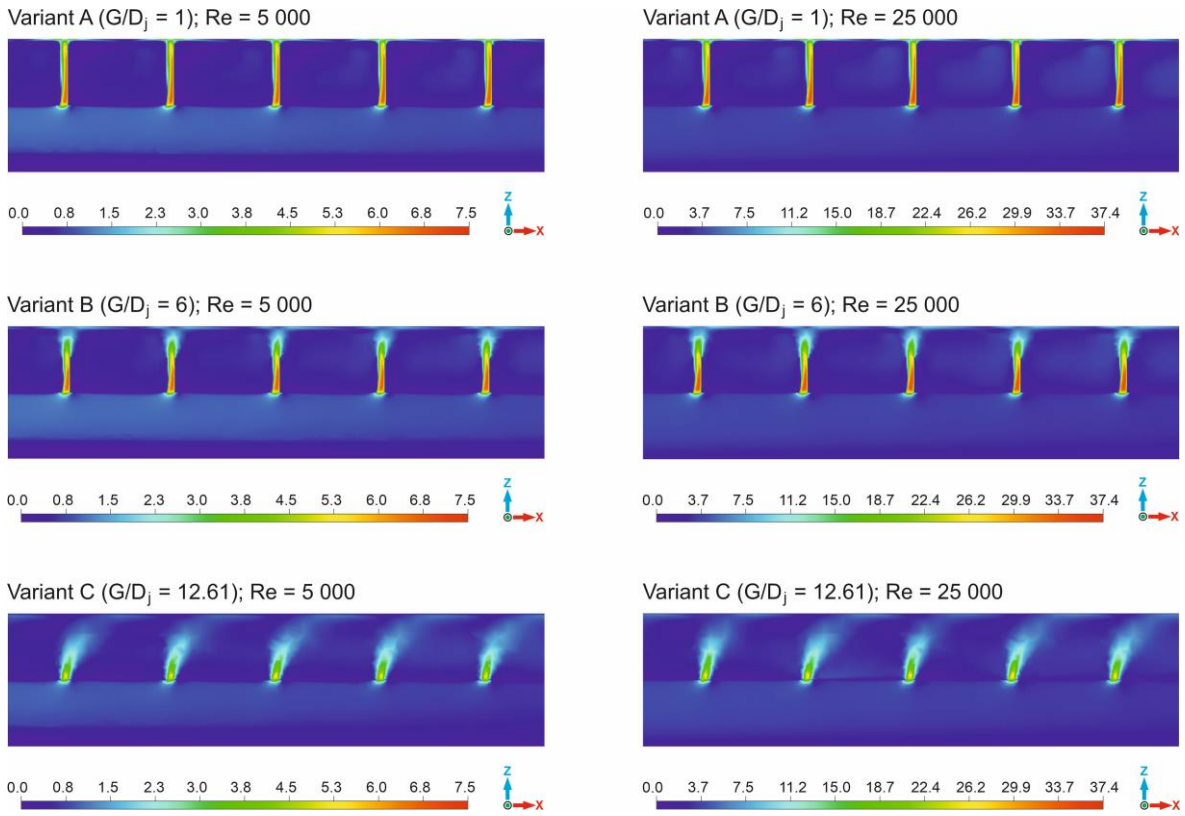


Fig. 9. Velocity distributions in the longitudinal cross-section for variants with the jet impingement technique.

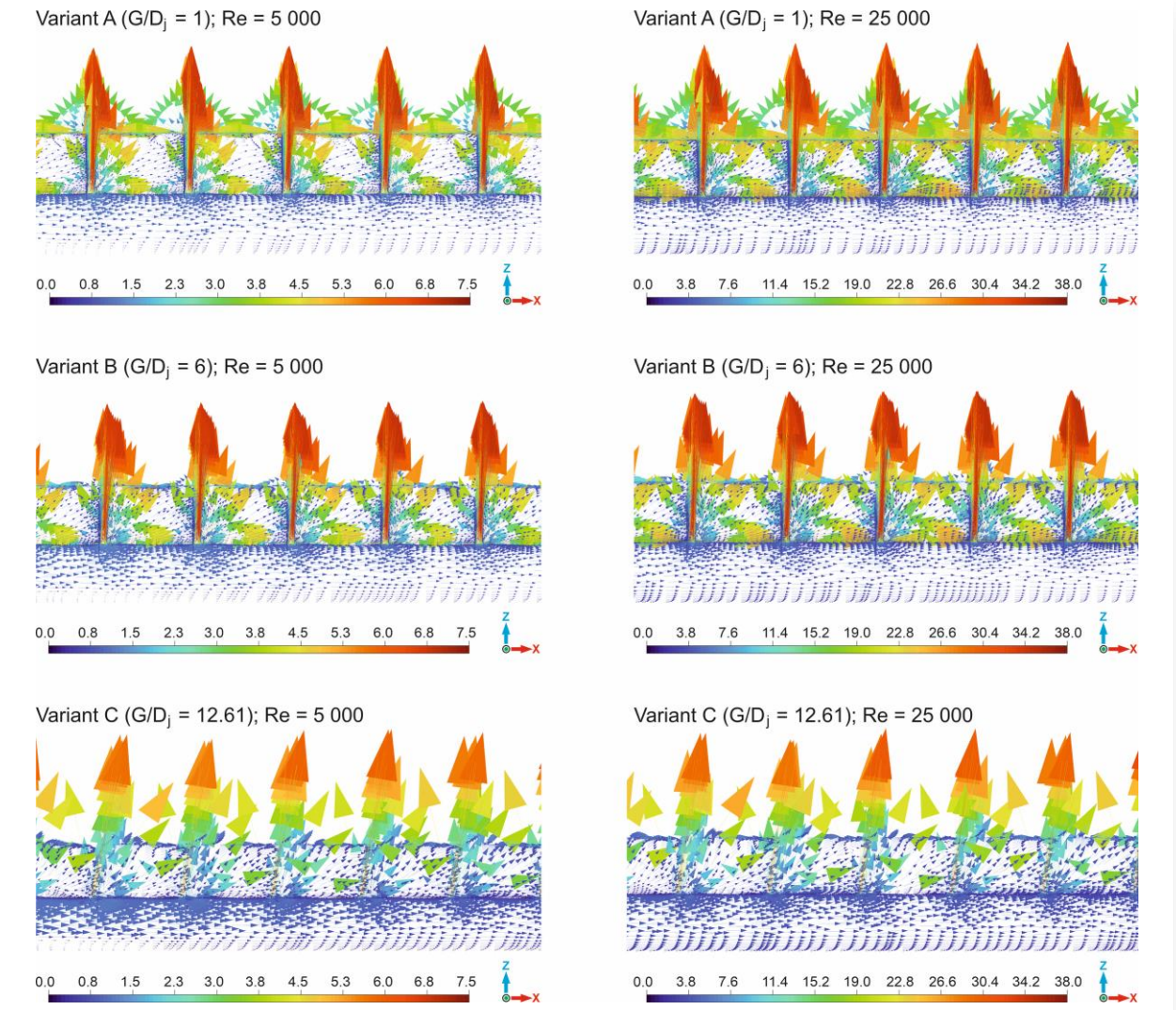


Fig. 10. Vector velocity field for variants with the jet impingement technique.

Table 7. Comparison with previous studies.

Reference / Year	Type of study		Re [–]	Nu [–] (δNu [%])	Thermal efficiency [%]	Remarks
	Exp.	Num.				
Present study	–	+	5 000–25 000	62.6–373.4 (80.8–320.7)	48.9–75.8	BIPV/T collector with elongated nozzles
[6] / 2023	–	+	10 000–30 000	(117–426)	–	SAH with inclined nozzles
[7] / 2023	+	+	2 900–14 300	135–223.2 (202.4–400.0)	42–91	SAH with conical protruded nozzles
[8] / 2022	+	+	1 409–28 404	–	36.5–65.0	Bifacial PV/T with jet plate
[5] / 2022	–	+	10 000–25 000	78.5–232.1	65.4–74.9	SAH with elongated nozzles
[4] / 2020	–	+	3 500–17 500	44–355 (454–758)	–	SAH with elongated nozzles

In Table 7 only values associated with jet impingement configurations were considered. In the Nusselt number column, relative increase compared to a straight channel collector with the same inlet dimensions and similar input parameters is given in parentheses. Validation of the results obtained in this study confirms that the application of jet impingement technique is an effective and promising solution for enhancing heat transfer in solar systems. The own research results are fully reflected in the achievements presented in the literature. However, it should be noted that the studies presented in the literature are of a numerical or experimental nature, involving different geometric configurations and varied input parameter configurations. Therefore, direct comparison of values obtained by different authors and drawing general conclusions without individual analysis of specific cases is not recommended.

4. Conclusions

At the current stage of research, a numerical thermal-flow model of the proposed photovoltaic roof tile cooling system, based on the jet impingement technique, has been developed to fill the gap existing in the literature. The simulations performed confirm the high efficiency of heat transfer intensification using air streams hitting the module absorber. The following are the study's key findings:

I. In terms of thermal performance, the best results in the entire range of tested Reynolds numbers were achieved for variant A with the outlet of the nozzle closest to the absorber ($G/D_j = 1$).

II. The thermal benefits obtained vary in terms of the input conditions, characterised by the Reynolds number defined at the inlet to the flow channel. In each case, the results significantly exceeded the parameters obtained for the reference variant D, with the flow carried out through a straight duct with a height of $H = 37.83$ mm.

III. At the Re = 5 000, a decrease in the average temperature on the module surface by 17.7 K and an increase in the average air temperature at the outlet of the flow channel by 5.7 K were achieved. The value of the heat flux increased by 78.1%, and the relative increase in the value of the heat transfer coefficient and Nusselt number was 320.7%. The thermal efficiency of the system increased by 24.1%.

IV. In the case of higher values of the analysed Reynolds numbers, the relative increases, in relation to the reference variant D, were not so high, but the absolute values of the thermal parameters reached even more favourable values.

V. At all analysed values of the Reynolds number, the pressure drop in the airflow channel was several dozen times higher than for the reference variant D, drawing attention to the importance of the issue of hydraulic resistance occurring as a result of used technique.

VI. The estimated electrical benefits showed that by using the jet impingement technique, depending on the Reynolds number and the configuration of the dimensionless parameter G/D_j, it is possible to obtain an increase in the generated electrical power in the range from 2.9% to 7.8% in relation to the reference variant.

In the next steps, it is planned to compare the results obtained for different nozzle shapes and optimize the geometric parameters of the photovoltaic roof tile cooling system based on the jet impingement technique, focused on maximising energy benefits in practical applications

Acknowledgements

The authors extend their appreciation to Krzysztof Abucewicz for his support with the preparation of drawings.

References

[1] Choudhury, C., & Garg, H.P. (1991). Evaluation of a jet plate solar air heater. *Solar Energy*, 46, 199-209. doi: 1016/0038-092X(91)90064-4.

[2] Zukowski, M. (2015). Experimental investigations of thermal and flow characteristics of a novel microjet air solar heater. *Applied Energy*, 142, 10-20. doi: 10.1016/j.apenergy.2014.12.052.

[3] Chauhan, R., Singh, T., Thakur, N.S., & Patnaik, A. (2016). Optimization of parameters in solar thermal collector provided with impinging air jets based upon preference selection index method. *Renewable Energy*, 99, 118-126. doi: 10.1016/j.renene. 2016.06.046.

[4] Yadav, S., & Saini, R.P. (2020). Numerical investigation on the performance of a solar air heater using jet impingement with absorber plate. *Solar Energy*, 208, 236-248, doi: 10.1016/ j.solener.2020.07.088.

[5] Pazarlıoğlu, H.K., Tepe, A.Ü., Tekir, M., & Arslan, K. (2022). Effect of new design of elongated jet hole on thermal efficiency of solar air heater. *Therm. Sci. Eng. Prog*., 36, 101483. doi: 10.1016/j.tsep.2022.101483.

[6] Hai, T., B Mansir, I., Alshuraiaan, B., M Abed, A., Elhosiny Ali. H., Dahari M., & Albalawi H. (2023). Numerical investigation on the performance of a solar air heater using inclined impinging jets on absorber plate with parallel and crossing orientation of nozzles. *Case Studies in Thermal Engineering*, 45, 102913. doi: 10.1016/j.csite.2023.102913.

[7] Das, S., Biswas, A., & Das, B. (2023). Parametric investigation on the thermo-hydraulic performance of a novel solar air heater design with conical protruded nozzle jet impingement. *Applied Thermal Engineering*, 219, Part B, 119583. doi: 10.1016/j.applthermaleng.2022.119583.

[8] Ewe, W.E., Fudholi, A., Sopian, K., Moshery, R., Asim, N., Nuriana, W., & Ibrahim, A. (2022). Thermo-electro-hydraulic analysis of jet impingement bifacial photovoltaic thermal (JIBPVT) solar air collector. *Energy*, 254, Part B, 124366. doi: 10.1016/ j.energy.2022.124366.

[9] Ewe, W.E., Fudholi, A., & Sopian, K.B. (2022). Jet impingement cooling applications in solar energy technologies: Systematic literature review. *Thermal Science and Engineering Progress*, 34, 101445. doi: 10.1016/j.tsep.2022.101445.

[10] BMI Brass – Photovoltaic Systems brochure, https://www.monier.pl/produkty/systemy-fotowoltaiczne/energia-elektryczna/braas-pv-premium.html [accessed 16 Oct. 2023].

[11] Maithani, R., Sharma, S., & Kumar, A. (2021). Thermo-hydraulic and exergy analysis of inclined impinging jets on absorber plate of solar air heater. *Renewable Energy*, 179, 84-95. doi: 10.1016/j.renene.2021.07.013.

[12] Nadda, R., Kumar, A., & Maithani, R. (2017). Developing heat transfer and friction loss in an impingement jets solar air heater with multiple arc protrusion obstacles. *Solar Energy*, 158, 117-131. doi: 10.1016/j.solener.2017.09.042.

[13] Chauhan, R., Thakur, N.S., Singh, T., & Sethi, M. (2018). Exergy based modeling and optimization of solar thermal collector provided with impinging air jets. *Journal of King Saud University - Engineering Sciences*, 30, 355-362. doi: 10.1016/j.jksues. 2016.07.003.

[14] ASHRAE Standards Committee. (1997). *Methods of testing to determine the thermal performance of solar collectors*. https://www.ashrae.org/.

[15] McAdams, W.H. (1954). *Heat transmission*, 3rd Edn. McGraw-Hill, Tokyo, Japan.

[16] Engineering ToolBox (2001). https://www.engineeringtoolbox.com [accessed 06 Apr. 2023].

[17] Hernandez-Perez, J.G, Carrillo, J.G., Bassam, A., Flota-Banuelos, M. & Patino-Lopez, L.D. (2021). Thermal performance of a discontinuous finned heatsink profile for PV passive cooling. *Applied Thermal Engineering*, 184, 116238. doi: 10.1016/j.applthermaleng.2020.116238.

[18] Leow, W.Z., Irwan, Y.M., Safwati, I., Irwanto, M., Amelia, A.R., Zhubir, N.S., Fahmi, M.I., & Rosle, N. (2020). Simulation study on photovoltaic panel temperature under different solar radiation using computational fluid dynamic method. *Journal of Physics:*

Conference Series. 1432:012052. doi: 10.1088/1742-6596/1432/1/012052.
[19] Thomson, A., Ernst, M., Haedrich, I., & Quian, J. (2017). Impact of PV module configuration on energy yield under realistic conditions. *Optical and Quantum Electronics*, 49, 82. doi: 10.1007/s11082-017-0903-0.
[20] Shamim, A., Noman, M., Zubair, M., Khan, A.D., & Saher, S. (2018). A facile approach to determine the unknown refractive index (n) and extinction coefficient (k) of novel encapsulant materials used in back contact PV modules. *Applied Physics A*, 124, 542. doi: 10.1007/s00339-018-1974-x.
[21] Emissivity factor of common materials. Fluke Corporation, https://www.flukeprocessinstruments.com/en-us/service-and-support/knowledge-center/infrared-technology/emissivity-metals [accessed: 27 Aug. 2023].
[22] Guarracino, I., Mellor, A., Ekins-Daukes, N.J., & Markides, C. (2016). Dynamic coupled thermal-and-electrical modelling of sheet-and-tube hybrid photovoltaic/thermal (PVT) collectors. *Applied Thermal Engineering*, 101, 778-795. doi: 10.1016/j.applthermaleng.2016.02.056.
[23] Hussien, A., Eltayesh, A., & El-Batsh, H.M. (2023). Experimental and numerical investigation for PV cooling by forced convection. *Alexandria Engineering Journal*, 64, 427-440. doi: 10.1016/j.aej.2022.09.006.
[24] Tepe, A.Ü., Uysal, Ü., Yetişken, Y., & Arslan, K. (2020). Jet impingement cooling on a rib-roughened surface using extended jet holes. *Applied Thermal Engineering*, 178, 115601. doi: 10.1016/j.applthermaleng.2020.115601.
[25] Ansys Fluent Theory Guide, 2023, https://www.ansys.com/
[26] Pawlucki, M., & Krys, M. (2020). *CFDs for engineers. Practical exercises on the example of the Ansys Fluent system* (in Polish), Helion SA, Gliwice, pp. 249-256.
[27] Karava, P., Jubayer, C.M., & Savory, E. (2011). Numerical modelling of forced convective heat transfer from the inclined windward roof of an isolated low-rise building with application to photovoltaic/thermal systems. *Applied Thermal Engineering*, 31, 1950-1963. doi: 10.1016/j.applthermaleng.2011.02.042.
[28] Lamaamar, I., Tilioua, A., & Hamdi Alaoui, M. A. (2022). Thermal performance analysis of a poly c-Si PV module under semi-arid conditions. *Materials Science for Energy Technologies*, 5, 243-251. doi: 10.1016/j.mset.2022.03.001.

Co-published by
Institute of Fluid-Flow Machinery
Polish Academy of Sciences
and
Committee on Thermodynamics and Combustion
Polish Academy of Sciences

http://www.imp.gda.pl/archives-of-thermodynamics/

ARCHIVES OF THERMODYNAMICS

Flow maps in multiphase flows

Małgorzata Sikora[a*], Tadeusz Bohdal[a], Stanisław Witczak[b], Grzegorz Ligus[b]

[a]Politechnika Koszalińska, Katedra Energetyki, ul. Śniadeckich 2, 75-453 Koszalin, Poland
[b]Katedra Inżynierii Procesowej i Środowiska, Politechnika Opolska, ul. St. Mikołajczyka 5, 45-271 Opole, Poland
*Corresponding author email: malgorzata.sikora@tu.koszalin.pl

Received: 23.01.2024; revised: 18.03.2024; accepted: 09.04.2024

Abstract

Flow structure maps are the most useful tool in the process of identifying structures formed in multiphase flows. They can be defined as a graphical way to present the transition boundaries of flow structures, depending on the characteristic parameters of the phase transformation or flow, such as the vapor quality, the void fraction, the mass flow density, or the velocities of individual phases. Maps are usually two-dimensional drawings, described with a minimum of two selected parameters or quantities describing the phenomenon. The oldest maps of flow structures concerned adiabatic flows, mainly two-phase water-air systems or three-phase water-oil-air systems in conventional channels. Maps of nonadiabatic flow structures are simple and allow the selection of an appropriate model to determine the heat transfer coefficient as well as the flow resistance of the refrigerant. This has a major impact on the design of flow devices, where two- and even three-phase flows. This paper includes reviews of proposed maps of multiphase flow structures by various authors.

Keywords: Multiphase flows; Flow structures; Flow maps

Vol. 45(2024), No. 2, 19–28; doi: 10.24425/ather.2024.150848

Cite this manuscript as: Sikora, M., Bohdal, T., Witczak, S., & Ligus, G. (2024). Flow Maps in Multiphase Flows. *Archives of Thermodynamics*, 45(2), 19–28.

1. Introduction

The term "two-phase flow" of a refrigerant means the flow of two phases in a system of any geometry. A distinction can be made between a continuous phase (liquid or gas) and a dispersed phase (liquid, gas or solid). The dispersed phase occurs in the form of drops, bubbles or particles and is suspended in the continuous phase. A phase boundary separates both phases. During two-phase flow, the phase separation boundary changes its shape and thus various two-phase flow structures are created. The situation is similar in the case of three-phase flow structures, but in this case, there are more possibilities for phase configuration. In this case, the phases in the flow are two immiscible liquids and a gas, or less commonly a liquid, a gas and a solid.

Figures 1 and 2 show examples of two-phase flow structures occurring in horizontal and vertical channels [1–3]. Some of these structures disappear when the channel diameter decreases or the mass flow density G increases. In the case of flows in vertical channels, the flow structures depend on the flow direction and the mutual density ratio of both phases. The relationship between the formation of water-oil flow structures depending on the flow velocity is shown in Fig. 3 [4]. As can be seen, at higher velocities the structures combine into larger agglomerates.

Nomenclature

A – cross section area, m^2
d – internal diameter, mm
G – mass flux density, kg/(m^{2}s)
j – apparent velocity, m/s
L – length, m
q – heat flux, W/m^2
T – temperature, °C
u – apparent velocity, m/s
$\dot{V}$ – volume flow, m^3/s
x – vapour quality

Greek symbols

λ – coefficient defined by Baker, $\lambda_B = \sqrt{\frac{\rho_v}{\rho_p} \cdot \frac{\rho_l}{\rho_w}}$
μ – viscosity, Pa·s
ρ – density, kg/m^3
σ – surface tension, N/m
φ – void fraction
χ_{tt} – Lockhart Martinelly parameter
ψ – coefficient defined by Baker, $\psi_B = \frac{\sigma_w}{\sigma_l}\left[\frac{\mu_l}{\mu_w}\left(\frac{\rho_w}{\rho_l}\right)^2\right]^{1/3}$

Subscripts and Superscripts

g,o – gas-oil domination
h – hydraulic
l – liquid
o,o – oil domination
s – saturation
v – vapour
w – water
w,o – water-oil domination
$3F,o$ – three-phase flow with dominant oil

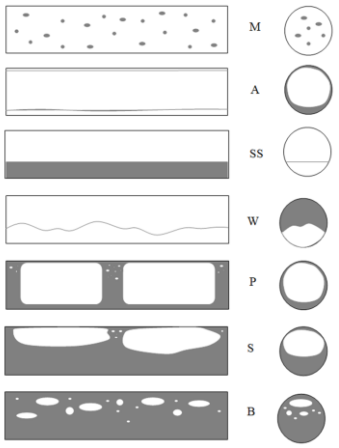


Fig. 1. Schematic diagram of two-phase adiabatic flow in conventional horizontal channel: M – mist flow, A – annular, SS – stratified, W – wavy, S – slug, P – plug, B – bubbly [1].

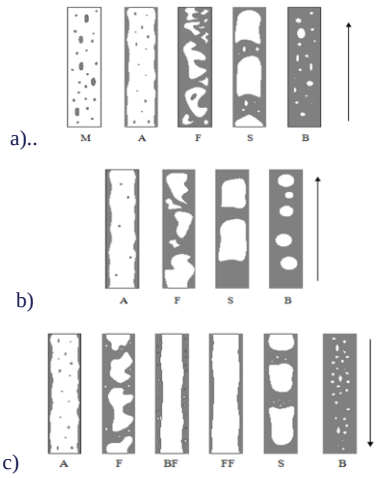
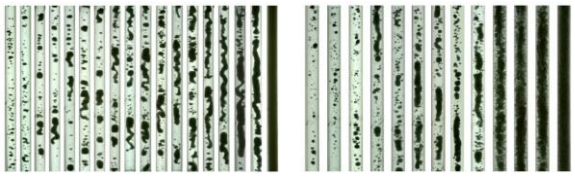


Fig. 2. Schematic diagram of two-phase adiabatic flow in the conventional vertical channel by Dziubiński and Prywer [2] and Ulbrich [3]: a) upflow; b) upflow involving a very viscous fluid; c) downflow. M – mist flow, A – annular, F – frothy, S – slug, B – bubbly, FF – liquid film flow, BF – bubbly-film.



(a) (b)

Fig. 3. Structures of water-oil upflow by Zhang et al. [4]: (a) v = 0.28 m/s; (b) v = 0.57 m/s.

Figure 4 shows the three-phase upflow structures for vertical channels published by Bannwart et al. [5]. They isolated an annular flow A with an oil core and gas bubbles in water forming the ring. They also observed the occurrence of an intermittent structure I, where gas bubbles are separated by oil, and water in the form of a thin layer that adheres to the channel wall.

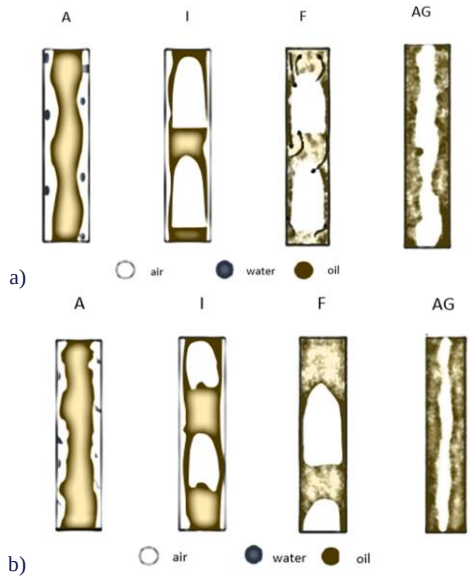


Fig. 4. Three-phase upflow structures air-water-petroleum flow in the vertical channel by Bannawart et al. [5]: a) d = 28.4 mm; b) d = 10 mm.

Another type of flow is the frothy structure F, in which the flow is pulsating and it is difficult to distinguish the liquid phases that mix. The occurrence of an annular gas phase AG was also observed, where a mixture of small oil and water droplets flows on the wall, and gas flows through the middle of the channel. At high velocities, the water and oil mixture may form an emulsion [6]. The same authors published the structures of three-phase water-oil-air flow in horizontal channels, shown in Fig. 5.

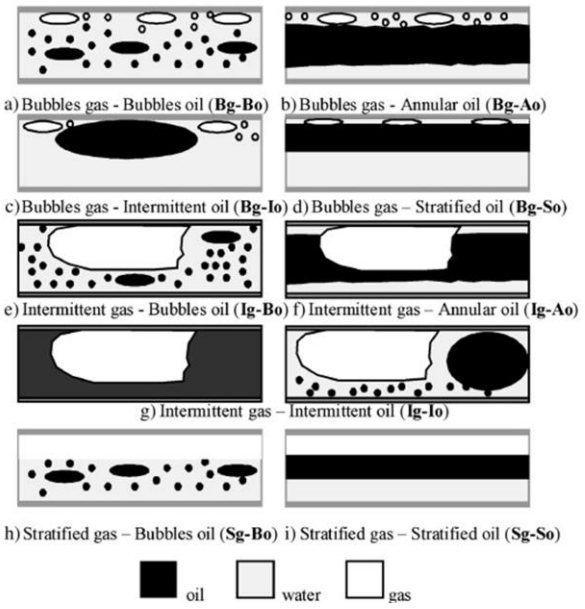


Fig. 5. Three-phase flow structures in horizontal channel by Bannawart et al. [5].

2. Maps of two-phase flow structures

Flow structure maps are the most useful tool in the process of identifying structures formed in multiphase flows. A flow structure map is a graphical way of presenting the transition boundaries of flow structures, depending on the flow parameters. They are two-dimensional drawings, described with a minimum of two characteristic parameters or quantities describing the phenomenon. The oldest maps of flow structures concerned adiabatic flows, mainly the water-air system in conventional channels.

Two-phase flow is the flow of two immiscible substances or the same substance in different states of matter in one system. Two-phase flows can be divided into adiabatic (without heat exchange) and non-adiabatic (phase changes of condensation and boiling).

2.1. Adiabatic flow

The most common adiabatic flows in the literature are liquid-liquid (e.g. water-oil) or liquid-gas flows (water-air). Liquid-liquid flows are most often implemented in horizontal and vertical channels with upflow or downflow. The first published flow map was Baker's map (Fig. 6) [7]. The oldest map of the rising flow of liquid-liquid mixtures in a vertical channel was published by Charles et al. [8], it is a map of the two-phase oil-water mixture, presented in Fig. 7a. Figure 7b shows a map of the flow in a vertical pipe of a mixture of water and oil with a density higher than the density of water, published by Troniewski et al. [9] and Xu et al. [10] modified the two-phase liquid-liquid flow maps by Flores [11] in vertical ascending and descending flow. Figure 8 shows Flores′ maps with the red modification by Xu et al. [10]. These maps were prepared for the oil-water flow at the density ratio ρ_o/ρ_w = 0.85 and the channel diameter d = 50.8 mm, where the transitional flow was marked as C.

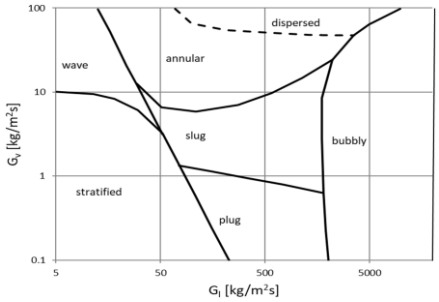


Fig. 6. Two-phase flow map by Baker [7].

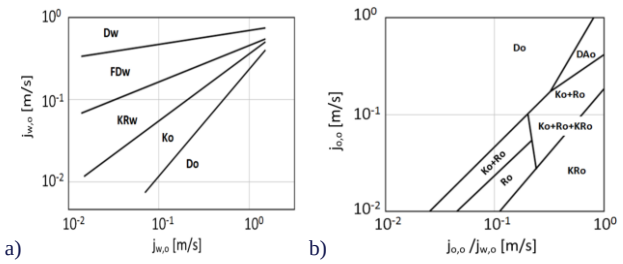


Fig. 7. Maps of liquid-liquid flow by: a) Charles et al. [8]; b) Troniewski et al.[9]. Dw – dispersive flow of water, Do – dispersive flow of oil, DAo – dispersive – annular flow of oil, FDw – film-dispersion water flow, KRw – droplet-slug flow of water, Ko – droplet oil flow, KRo – droplet-slug flow of oil, Ro – stratified oil flow [12].

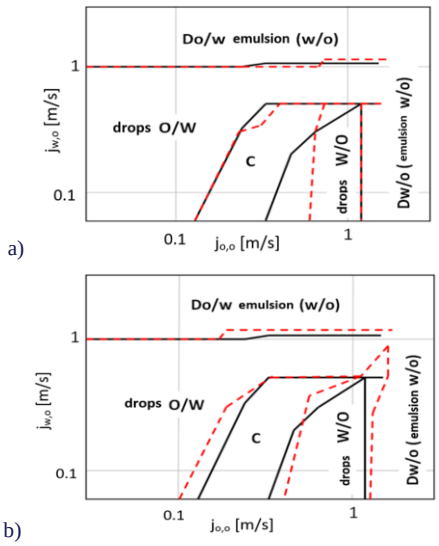


Fig. 8. Maps of vertical two-phase flow by Flores [11] and Xu et al. [10]:

A more frequently studied case of two-phase adiabatic flow is the water-air flow. Hawitt and Roberts [13] proposed a map of the adiabatic upflow during the two-phase flow of a mixture of water and air in vertical channels with a hydraulic diameter of d = 10 and 30 mm, shown in Fig. 9a. To describe the boundaries of the flow structures, the densities ρ and apparent velocities j of individual phases were used:

$$j_l = \frac{\dot{V}_l}{A}, \tag{1}$$

$$j_v = \frac{\dot{V}_v}{A}. \tag{2}$$

The most popular map in comparative analysis of two-phase flow structures is the map of Taitel and Dukler [14] presented in Fig. 9b.

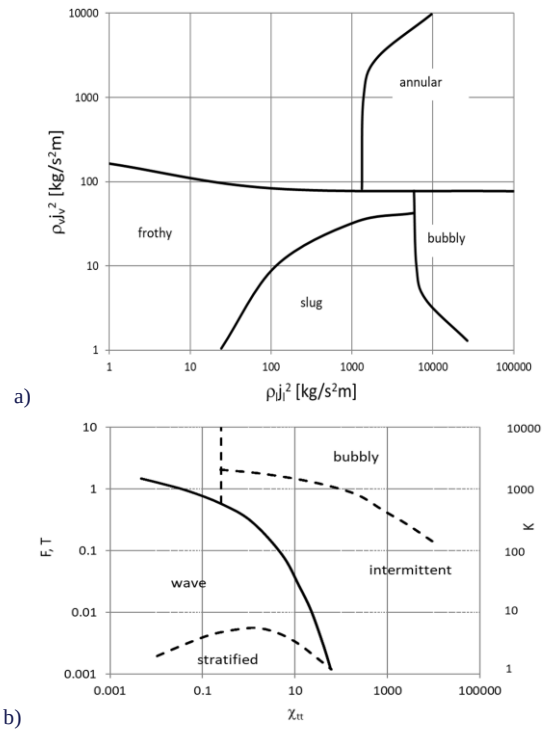


Fig. 9. Adiabatic two-phase flow map of water-air flow according to: (a) Hewitt and Roberts [13]; (b) Taitel and Dukler [14].

The map was developed for two-phase adiabatic systems in the range of hydraulic diameter d = 4.8–22 mm, mass flow density G = 18–990 kg/(m^2·s) and pressure p = 108–1249 kPa [12]. Four characteristic quantities marked with the symbols: F, T, K and Y were used in the construction of this map. These are functions of the Lockhart - Martinelli parameter χ_{tt}, determined as follows:

$$F = \frac{j_v}{(d_h \cdot g \cdot \cos\Theta)^{0.5}} \cdot \left(\frac{\rho_v}{\rho_l - \rho_v}\right)^{0.5}, \tag{3}$$

$$T = \left[\frac{(\mathrm{d}p/\mathrm{d}z)_l}{(\rho_l - \rho_v) g \cdot \cos\Theta}\right]^{0.5}, \tag{4}$$

$$\chi_{tt} = \left(\frac{1-x}{x}\right)^{0.875} \cdot \left(\frac{\rho_v}{\rho_l}\right)^{0.5} \cdot \left(\frac{\mu_l}{\mu_v}\right)^{0.125}. \tag{5}$$

Figure 10a shows a map of the structures of a two-phase, adiabatic flow in a horizontal channel, and Fig. 10b shows a map of the upflow structures in a vertical channel by Ulbrich [15].

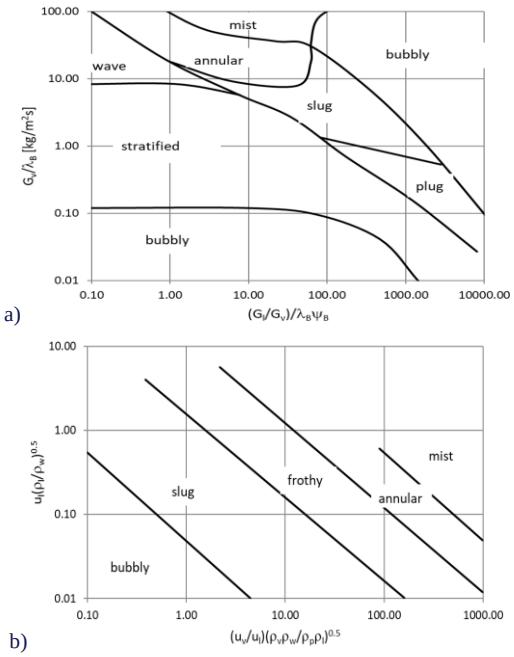


Fig. 10. Generalized structure map of two-phase adiabatic flow by Ulbrich [15] in: a) horizontal channel; b) vertical channel.

2.2. Nonadiabatic flow

Flow structures during condensation or boiling differ significantly from those observed in two-phase adiabatic flows. For this reason, the maps of two-phase flow structures for adiabatic flow, as well as for boiling and condensation, differ from each other. The limits of occurrence of individual structures are most often described using quantities such as void fraction φ, vapour quality x, mass flow density G, apparent velocity of individual phases j_v and j_l, as well as the Lockhart-Martinelli parameter χ_{tt}. These parameters allow for taking into account, in addition to the flow conditions, parameters characterizing heat transfer. The first structure map of two-phase nonadiabatic flow was published in 1980 by Breber et al. [16]. Maps for flow in conventional channels during condensation were also published by Soliman [17] and Teitela and Duklera [18]. These maps are most often modified by other authors.

In small diameter channels, viscosity forces and surface tension have a significant impact on the mechanism of momentum and energy change. The influence of gravity and inertia forces is less important here. These interactions cause the boundaries of the occurrence of individual flow structures to shift, which can be seen in Fig. 11 and Fig. 12.

Figure 11 shows the map published by El Hajal et al. [19] as well as its modifications for different heat flux densities compared with the Steiner map (Fig. 11b). Figure 12(a) shows the map by Coleman and Garimella [20], unlike the maps shown in Fig. 11 and Fig. 12b, this is a map for the condensation process. Figure 12b shows a comparison of flow structure maps by

Wojan et al. [21] and Yang et al. [22] for the boiling process of the R410A refrigerant in the channel d = 6.3 mm.

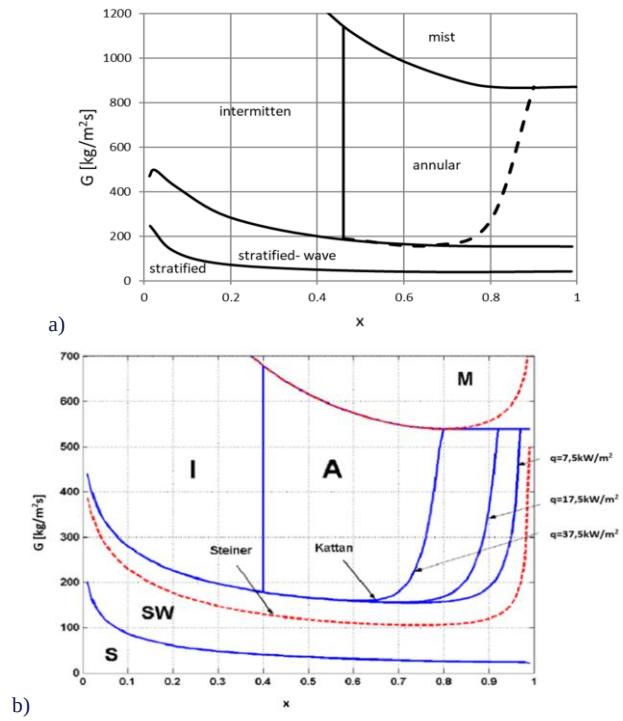


Fig. 11. Two-phase flow map by Kattan et al. [24]: a) for NH_3, R134a and R404A during flow in minichannel; b) for 3 heat flux density compared to the adiabatic flow map by Steiner for R410A refrigerant during boiling in a channel with internal diameter 13.84 mm.

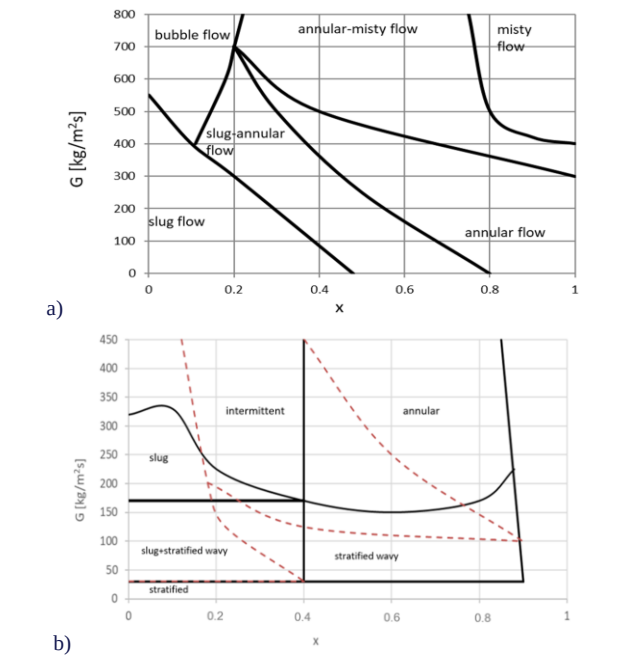


Fig. 12. Two-phase nonadiabatic flow map by: a) Coleman and Garimella [20]; b) comparison of Wojtan et al. [21] (black line) and Yang et al. [22] (red line) flow maps; d = 6.3 mm, R410A refrigerant, T_s = 10 °C.

Maps of flow structures for the boiling process were also published by Turgut and Asker [23]. This flow structure map has been tested for the following refrigerants: R22, R134a, R290, R404a, R410a, R600, R507, R717, and R744 and compared with multi-author correlations. Figure 13 shows the Turgut and Akers map for the R22 and R10A refrigerants. One can see a change in the transition boundary between dry out and mist flow structures, as well as a shift in the boundary between intermittent flow and annular flow. The authors also observed similar shifts for other tested refrigerants.

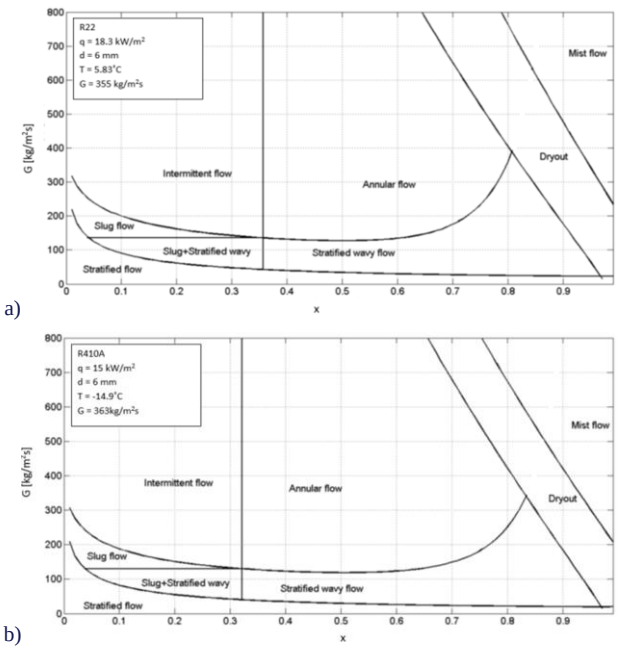


Fig. 13. Flow map by Turgut and Asker [23].

Unfortunately, the limits of the phase transition depend not only on the size of the channel or heat transfer but also on the refrigerant used, as presented by Nema et al. [25] (Fig. 14).

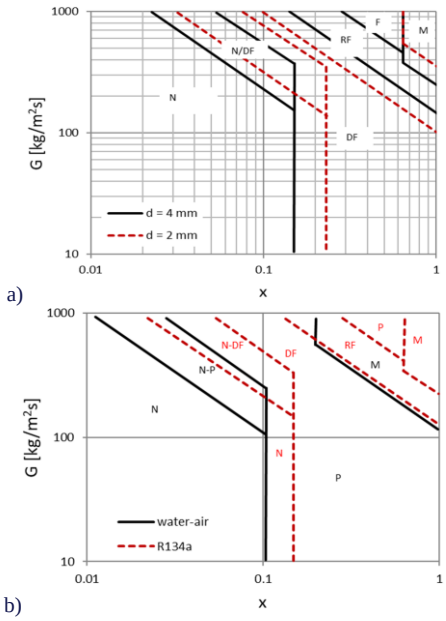


Fig. 14. Two-phase flow map by Nema et al. [25] according to flow kind (adiabatic and nonadiabatic) and kind of refrigerant in terms of d = 1–4.91 mm, G = 150–750 kg/(m²s).

Figure 15a shows the map of Mishima et al. [26], which applies to two-phase flows in vertical gaps with a height in the range of 0.3–17 mm. The apparent velocities of the vapour and liquid phases were used to describe the transition boundaries of flow structures. This map applies to the following structures: bubbly, slug, frothy and annular, mist flow is not included here. This may be due to difficulties in observing this structure. Figure 15b shows the flow structure map of Sikora [27]. This is a map for two-phase condensation flow, constructed based on tests on the condensation of HFE7000, HFE7100 and Novec649 refrigerants in pipe minichannels with an internal diameter of less than 2 mm. To describe the limits, the author used the void fraction φ as a more universal value and less dependent on the properties of the refrigerant than the vapour quality. This is quite a detailed division compared to maps by other authors such as Wojtan or Yang (Fig. 12).

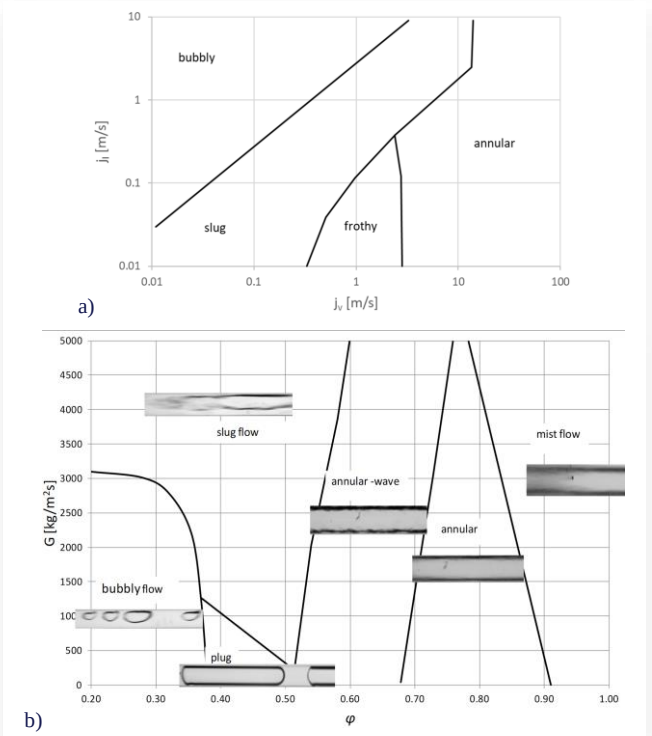


Fig. 15. Two-phase flow map: a) in the gap by Mishima et al. [26], gap height 0.3–17 mm; b) in pipe minichannal with internal diameter d = 2.0–0.5 mm by Sikora [27], for HFE7000, HFE7100 and Novec649 refrigerant condensation.

3. Three-phase Flow Structure Maps

There are two basic types of three-phase flow: two-component and three-component. In the case of a three-phase two-component mixture, two liquids and vapour one of them flow through the channel; in the case of a three-component flow, each phase is a different, mutually immiscible component. The three-phase flow of immiscible liquids and gas is characterized by high complexity, the interaction of phases at the interface and turbulence present in the flow make the process analysis difficult.

The first attempt to develop three-phase flow maps was made by Açikgöz et al. [28]. They published three maps of three-phase flow in the system of apparent velocities of air and water. Two of these maps are shown in Fig. 16. Since each of the maps published by Açikgöz et al. is valid only for constant oil velocity, determining the type of structure for any flow conditions would be problematic and would require a very large number of maps.

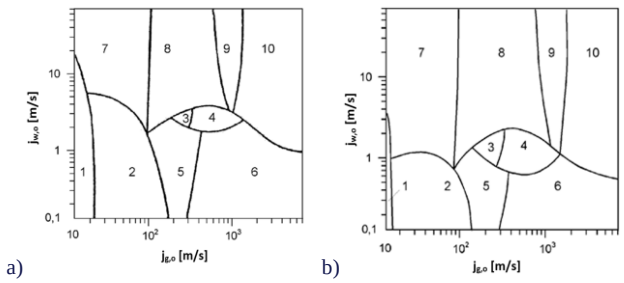


Fig. 16. Flow map of air-water-oil mixture: a) $j_{o,o}$ = 0.043 m/s; b) $j_{o,o}$ = 0.09 m/s according to Açikgöz et al.[28] (Table 1 presents an explanation of the symbols)

Woods et al. [29] developed flow maps for the air-water-oil mixture for three apparent oil velocities ($j_{o,o}$ = 0.00475 m/s, $j_{o,o}$ = 0.0794 m/s, $j_{o,o}$ = 0.1673 m/s), where the occurrence boundaries of the individual flow structures are marked. Examples of map constructions by Woods et al. are shown in Fig. 17.

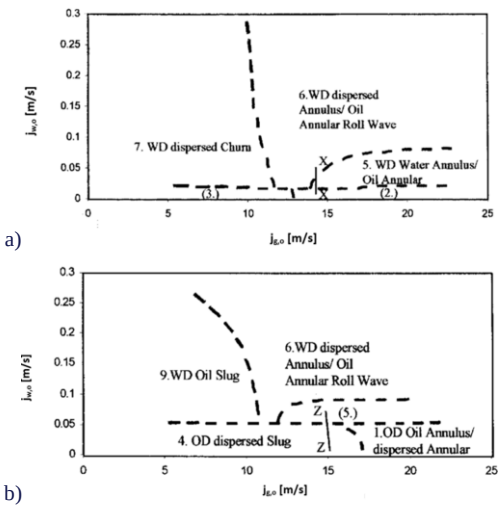


Fig. 17. Three-phase flow map of air-water-oil by Woods et al. [29] for oil velocity: a) $j_{o,o}$ = 0.00475 m/s; b) $j_{o,o}$ = 0.1673 m/s; (2.) – dispersed - annular flow, (3.) – dispersed - annular slight wave flow, (5.) – dispersive-semi-annular flow.

These maps were developed in a coordinate system including the apparent velocities of air and water, commonly used for two-phase flows, which means that the authors attempted to describe the three-phase flow as a classic two-phase gas-liquid flow. Woods et al. also proposed the following relationship:

$$j_{w,o} = 0.32 j_{o,o}\,, \tag{6}$$

to calculate the boundary between flows with the dominant oil and water phases.

Cazarez et al. [30] published a three-phase flow map based on their experimental research (Fig. 18a). It shows the areas

where pseudo-two-phase flow structures occur. In this case, the role of the liquid is played by a mixture of two heterogeneous liquids. The relationship between the velocities of individual components of a three-phase mixture and the apparent air velocity were used to describe the structures.

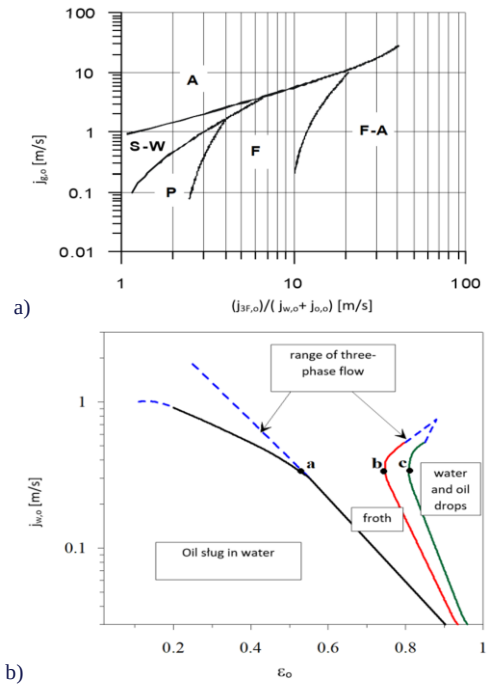


Fig. 18. Three-phase flow map by: a) Cazarez et al. [30]; b) Shean [31]. A – annular flow; F – frothy flow; F-A – frothy - annular flow; P – plug flow; S-W – stratified – wave flow.

There are few published maps of three-phase ascending flow in the literature. One such map is Shean's map [31] (Fig. 18b). This map is an adaptation, for three-phase air-water-oil flow conditions, of the Govier end Aziz map [32] developed for vertical two-phase oil-water flow. The map was built in the coordinate system of the concentration of the oil phase in the liquid and the apparent velocity of water. The boundaries of the flow structures observed by the authors are marked with lines on the map. The authors justified the possibility of adapting Govier's map to the description of three-phase flow, taking into account the observed similarity in the course of the two- and three-phase total pressure loss curves, especially at critical points a, b, c (Fig. 18b). The modification consisted in expanding the area of slug and frothy flow with the dominant water phase. The limit value of oil concentration in the flow is determined using the relationship:

$$\varepsilon_{o,gr} = 0.6 + 0.315\left\{\tanh\left[0.272\left(j_{g,o} - 17\right)\right] + \tanh\left(17.25 - j_{g,o}\right)\right\} \quad (7)$$

However, Spedding et al. [33] presented three maps of three-phase flow (two of them are shown in Fig. 19), in which they marked the boundaries of the occurrence of three-phase structures. Table 1 presents an explanation of the symbols shown on Spedding's maps from Fig. 19. The apparent gas velocity and the concentration of oil in the liquid were used to describe the maps.

As can be seen in the maps, when the proportion of oil in water increases, the oil phase becomes dominant. Flow structures with a dominant water phase cover almost 40% of the map area. The increase in the velocity of the liquid above does not cause such visible changes in the phase dominance. The authors noticed that the location of the transition boundary between the dispersed-slug and dispersed-frothy structures does not change at a gas velocity of 2 m/s for all considered water velocities and low values of oil concentration in water.

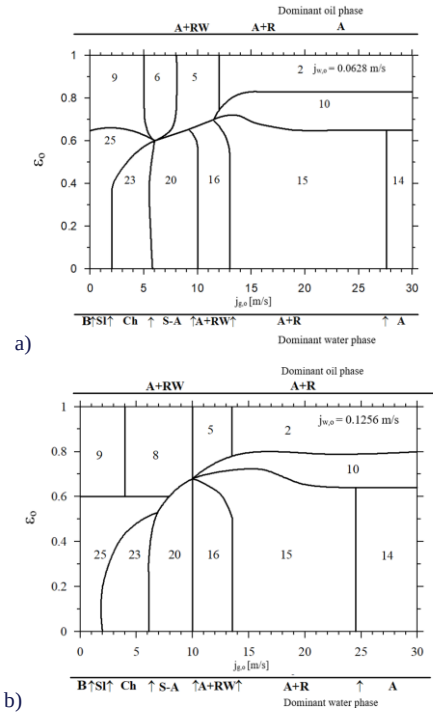


Fig. 19. Three-phase flow map for constant apparent velocity of water, by Spedding et al. [33]: a) $j_{w,o}$ = 0.0628 m/s; b) $j_{w,o}$ = 0.1256 m/s; B - bubbly, Sl – slug, Ch – churn, S-A - semi-annular, A+RW - annular roll wave, A+R - annular ripple, dis A - dispersed annular, A - annular.

Table 1. Designations of three-phase flow structures for Figs. 16 and 19 [34].

Dominant oil phase - OD		Dominant water phase - WD	
1	oil-annular / dispersed-annular	11	water-annular oil-annular
		12	water-annular/oil-annular slightly wavy
2	dispersed-annular	13	water-annular/oil-annular strongly wavy
3	dispersed-annular, slightly wavy	14	dispersed-annular/oil-annular
		15	dispersed-annular/oil-annular slightly wavy
4	dispersed-annular, strongly wavy	16	dispersed - annular/oil-annular, strongly wavy
5	dispersed-semi-annular	17	dispersed - annular
		18	dispersed - annular, slightly wavy
6	dispersed-semi-annular, strongly wavy	19	dispersed - annular, strongly wavy
		20	dispersed - semi-annular
		21	dispersed - semi-ring, slightly wavy
7	dispersed-frothy	22	dispersed - semi-annular, strongly wavy
8	dispersed-annular/dispersed-plug	23	dispersed - frothy
		24	dispersed - annular/dispersed-plug
9	dispersed-plug	25	dispersed - slug
10	fracture-annular	26	oil-slug

Figure 20 shows the investigation results of Pietrzak et al. [35] for three-phase flow, water – air - oil. As can be seen, structures for three-phase flow are more complicated than those for two-phase flow. There are more configurations of every fluid geometrical structure and it depends on the concentration of every phase. The velocities of every phase influence the geometrical configuration of this phase. When the mass flow is very high, in this kind of multi-phase flow an emulsion can be formed. It is very hard to describe on one flow map.

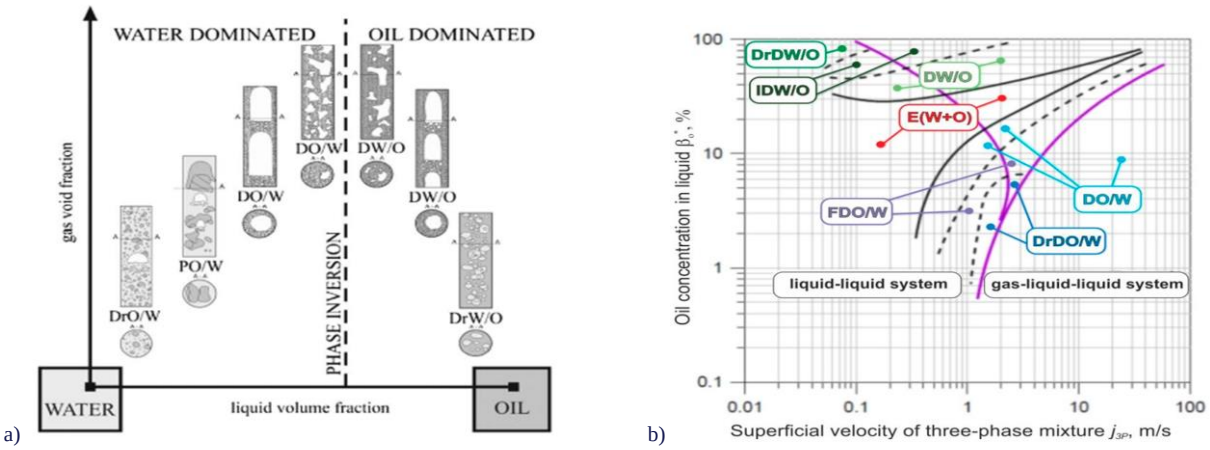


Fig. 20. Investigation results of Pietrzak et al. [35]: a) phase inversion in three-phase flow [35];
b) gas–liquid–liquid three-phase flow map for annular falling flow [36];
B-DrO/W – gas bubbles (B) and drops of oil (DrO) in water continuum (W).
B-PO/W – gas bubbles (B) and plugs of oil (PO) in water continuum (W).
P-DrO/W – plugs of gas (P) and discrete oil droplets (DrO) in water continuum (W).
F-DO/W – breaking up and coalescence of gas bubbles; irregularly shaped gas bubbles flowing with high velocity; an oscillating fluid flow contributes to the formation of multi-phase mixture with froth characteristics (F); oil is dispersed (DO) in water continuum (W).
A-DO/W – annular (A) air-liquid mixture flow; oil dispersed (DO) in water (W).
B-DrW/O – gas bubbles (B) and drops of water (DrW) in oil continuum (O).
P-DrW/O – gas plugs (P) and drops of water (DrW) in oil continuum (O).
F-DW/O – breaking and connecting gas bubbles with irregularly shape flowing at a high velocity, with an oscillating fluid flow contributes to the formation of multi-phase mixture with foam characteristics (F); water dispersed (DW) in oil continuum (O).
A-DW/O – annular (A) air-liquid mixture flow; water dispersed (DW) in oil (O).

4. Summary and conclusions

To sum up, the occurrence of multiphase flow structures depends on several phases and affects the functioning of many flow machines. Therefore, flow structure maps are a very important tool for both scientists and engineers, they allow determining flow conditions only by measuring a few basic parameters such as flow rate, pressure, temperature and flow speed. Unfortunately, there are no unified maps, so we have to look for maps prepared for the fluid used in a given process. Based on the analysed literature, several conclusions can be drawn:

1. Maps of multiphase flow structures are the best tool to determine the flow structures occurring in given conditions. They are simple and allow to select the appropriate model to determine the heat transfer coefficient and the flow resistance of the fluid. This has a major impact on the design of refrigeration and air conditioning equipment.
2. For flow structure maps to be useful in practice, they should be as generalized as possible, and the boundaries of individual structures' occurrence should be described using parameters that are easy to determine in practice. As can be seen, the use of complex quantities makes the practical use of maps of multiphase flow structures difficult. To construct a good flow map it is necessary to connect a lot of flow and heat parameters, which is difficult.
3. The type of multiphase flow structure depends primarily on the diameter of the channel, the orientation of its axis, the type of fluid, its concentration and density, and process parameters (saturation pressure and temperature, mass flow density, phase velocity, heat flux density). These quantities influence the balance of forces acting on all phases and their interface surfaces, as well as the vapour quality x, the void fraction of the channel φ, and define the share of the number of phases flowing through the channel.
4. Unfortunately, there are many discrepancies in the literature as to the scope of occurrence of individual flow structures in given conditions, therefore efforts should be made to simplify and standardize the construction of maps of multiphase flow structures.

References

[1] Sikora, M. (2020). *Modeling of two-phase flow structures during condensation in mini-channels*. Koszalin University of Technology (in Polish).
[2] Dziubiński, M., & Prywer, J. (2009). *Two-phase fluid mechanics.* Scientific and Technical Publishing House, Warsaw (in Polish).
[3] Ulbrich, R. (2014). *Modern research methods for flows in multiphase systems.* Publishing House of the Opole University of Technology (in Polish).

[4] Zhang, J., Xu, J.Y., Wu, Y.X., Li, D.H., & Li, H. (2013). Experimental validation of the calculation of phase holdup for an oil–water two-phase vertical flow based on the measurement of pressure drops. *Flow Measurement and Instrumentation*, 31, 96–101. doi: 10.1016/j.flowmeasinst.2012.08.002

[5] Bannwart, A.C., Rodriguez, O.M.H., Trevisan, F.E., Vieira, F.F., & de Carvalho, C.H.M. (2009). Experimental investigation on liquid–liquid–gas flow: Flow patterns and pressure-gradient. *Journal of Petroleum Science and Engineering*, 65(1–2), 1–13. doi: 10.1016/j.petrol.2008.12.014

[6] Płaczek, M., Pietrzak, M., & Witczak, S. (2018). A conductometric method for determining the upward gas-liquid-liquid three-phase flow. *Archives of Thermodynamics*, 39(3), 97−110. doi: 10.1515/aoter-2018-0022

[7] Baker, O. (1954). Simultaneous flow of oil and gas. *Oil and Gas Journal*, 53, 185–190.

[8] Charles, M.E., Govier, G.W., & Hodgson, G.W. (1961). The horizontal pipeline flow of equal density oil-water mixtures. *Canadian Journal of Chemical Engineering*, 39, 27–36. doi: 10.1002/cjce.5450390106

[9] Troniewski, L., Witczak, S., & Trębacz, J. (2000). Two-phase water-oil flow in vertical channels. *Science Notebooks Mechanics. Opole University of Technology*, 65, 39–54 (in Polish).

[10] Xu, J., Li, D., Guo, J., & Wu, Y. (2010). Investigations of phase inversion and frictional pressure gradients in upward and downward oil–water flow in vertical pipes. *International Journal of Multiphase Flow*, 36, 930–939. doi: 10.1016/j.ijmultiphaseflow.2010.08.007

[11] Flores, J.G. (1997). *Oil–Water Flow in Vertical and Deviated Wells*. University of Tulsa.

[12] Brandt, A. (2014). *Annular flow of a multiphase mixture in the pipes of thin-film apparatus*. PhD thesis, Opole University of Technology (in Polish).

[13] Hewitt, G.F., & Roberts, D.N. (1969). *Studies of Two-Phase Flow Patterns by Simultaneous X-Ray and Flash Photography*. Berkshire: Atomic Energy Research Establishment. Harwell, England.

[14] Taitel, Y., & Dukler, A.E. (1976). A model for predicting flow regime transitions in horizontal and near horizontal gas-liquid flow. *AIChE Journal, American Institute of Chemical Engineers*, 22(1), 47–55. doi: 10.1002/aic.690220105

[15] Ulbrich, R. (1989). *Identification of two-phase gas-liquid flow*. Studies and Monographs, 32, WSI, Opole (in Polish).

[16] Breber, G., Palen, J.W., & Taborek, J. (1980). Prediction of Horizontal Tubeside Condensation of Pure Components Using Flow Regime Criteria. *Journal of Heat Transfer*, 102, 471–476. doi: 10.1115/1.3244325

[17] Soliman, H.M. (1982). On the annular-to-wavy flow pattern transition during condensation inside horizontal tubes. *Canadian Journal of Chemical Engineering*, 60, 475–481. doi: 10.1002/cjce.5450600405

[18] Taitel, Y., & Dukler, A.E. (1976). A model for predicting flow regime transitions in horizontal and near horizontal gas-liquid flow. *AIChE Journal, American Institute of Chemical Engineers, American Institute of Chemical Engineers*, 22, 47–55. doi: 10.1002/aic.690220105

[19] El Hajal, J., Thome, J.R., & Cavallini, A. (2003). Condensation in horizontal tubes, part 1: two-phase flow pattern map. *International Journal of Heat and Mass Transfer*, 46, 3349–3363. doi: 10.1016/S0017-9310(03)00139-X

[20] Coleman, J.W., & Garimella, S. (2003). Two-phase flow regimes in round, square and rectangular tubes during condensation of refrigerant R134a. *International Journal of Refrigeration*, 26, 117–128. doi: 10.1016/S0140-7007(02)00013-0

[21] Wojtan, L., Ursenbacher, T., & Thome, J.R. (2005). Investigation of flow boiling in horizontal tubes: Part I–A new diabatic two-phase flow pattern map. *International Journal of Heat and Mass Transfer*, 48, 2955–2969. doi: 10.1016/j.ijheatmasstransfer.2004.12.012

[22] Yang, C.M., & Hrnjak, P. (2020). A new flow pattern map for flow boiling of R410A in horizontal micro-fin tubes considering the effect of the helix angle. *International Journal of Refrigeration, 109*, 154–160. doi: 10.1016/j.ijrefrig.2019.09.013

[23] Turgut, O.E., & Asker, M. (2022). Flow boiling behaviors of various refrigerants inside horizontal tubes: a comparative research study. *Eskişehir Technical University Journal of Science and Technology A - Applied Sciences and Engineering*, 23, 1–20. doi: 10.18038/estubtda.749040

[24] Kattan, N., Thome, J.R., & Favrat, D. (1998). Flow Boiling in Horizontal Tubes: Part 1–Development of a Diabatic Two-Phase Flow Pattern Map. *Journal of Heat Transfer*, 120, 140. doi: 10.1115/1.2830037

[25] Nema, G., Garimella, S., & Fronk, B.M. (2014). Flow regime transitions during condensation in microchannels. *International Journal of Refrigeration*, 40, 227–240. doi: 10.1016/j.ijrefrig.2013.11.018

[26] Mishima, K., Hibiki, T., & Nishihara, H. (1993). Some characteristics of gas-liquid flow in narrow rectangular ducts. *International Journal of Multiphase Flow*, 19, 115–124. doi: 10.1016/0301-9322(93)90027-R

[27] Sikora, M. (2021). Flow Structure Investigations during Novec Refrigerant Condensation in Minichannels. *Materials*, 14, 6889. doi: 10.3390/ma14226889

[28] Açikgöz, M., França, F., & Lahey, R.T. (1992). An experimental study of three-phase flow regimes. *International Journal of Multiphase Flow*, 18, 327–336. doi: 10.1016/0301-9322(92)90020-H

[29] Woods, G.S., Spedding, P.L., Watterson, J.K., & Raghunathan, R.S. (1998). Three-Phase Oil/Water/Air Vertical Flow. *Chemical Engineering Research and Design*, 76, 571–584. doi: 10.1205/026387698525252

[30] Cazarez, O., Montoya, D., Vital, A.G., & Bannwart, A.C. (2010). Modeling of three-phase heavy oil–water–gas bubbly flow in upward vertical pipes. *International Journal of Multiphase Flow*, 36, 439–448. doi: 10.1016/j.ijmultiphaseflow.2010.01.006

[31] Shean, A.R. (1976). *Pressure drop and phase fraction in oil-water-air vertical pipe flow*. Thesis, Department of Mechanical Engineering, Massachusetts Institute of Technology, Cambridge.

[32] Govier, G.W., & Aziz, K. (2008). *The Flow of Complex Mixtures in Pipes*. (2nd Edn.). Society of Petroleum Engineers.

[33] Spedding, P.L., Woods, G.S., Raghunathan, R.S., & Watterson, J.K. (2000). Flow Pattern, Holdup and Pressure Drop in Vertical and Near Vertical Two- and Three-Phase Upflow. *Chemical Engineering Research and Design*, 78, 404–418. doi: 10.1205/026387600527301

[34] Nowak, M. (2007). *Volume share and resistance of three-phase flow in the vertical channel*. Opole University of Technology (in Polish).

[35] Pietrzak, M., Płaczek, M., & Witczak, S. (2017). Upward flow of air-oil-water mixture in vertical pipe. *Experimental Thermal and Fluid Science*, 81, 175–186. doi: 10.1016/j.expthermflusci.2016.10.021

[36] Brandt, A., Czernek, K., Płaczek, M., & Witczak, S. (2021). Downward Annular Flow of Air–Oil–Water Mixture in a Vertical Pipe. *Energies*, 14(1), 30. doi: 10.3390/en14010030

Co-published by
Institute of Fluid-Flow Machinery
Polish Academy of Sciences
and
Committee on Thermodynamics and Combustion
Polish Academy of Sciences

http://www.imp.gda.pl/archives-of-thermodynamics/

ARCHIVES OF THERMODYNAMICS

Effect of flow orientation in experimental studies on FC-770 boiling heat transfer in asymmetrically heated minichannels

Magdalena Piasecka[a*], Kinga Strąk[a]

[a]Kielce University of Technology, al. Tysiaclecia Panstwa Polskiego 7, PL-25-314 Kielce, Poland
*Corresponding author email: tmpmj@tu.kielce.pl

Received: 31.12.2023; revised: 25.03.2024; accepted: 30.04.2024

Abstract

The article presents experimental results of boiling heat transfer during FC-770 flow in a group of five minichannels with a common heated wall. The flow orientation was changed from 0º to 180º, with a 15° increment. During the experiments, the temperature of its outer heated wall surface was measured by an infrared camera. At the same time, flow patterns were captured through the glass plate opposite the heated wall using a high-speed camera. The purpose of the calculations was to determine local heat transfer coefficients on the contact surface between the working fluid and the heated surface in the central minichannel, using a simplified 1D calculation method. The results in the form of dependences of the temperature of the heated wall and the heat transfer coefficient as a function of the distance from the channel inlet for various flow orientations were analysed. Furthermore, typical boiling curves and two-phase flow patterns were presented. The mean relative error of the heat transfer coefficient was determined for various flow orientation. The dependence of the void fraction as a function of heat flux was illustrated for various angles of minichannel inclination to the horizontal plane. It was observed that the void fraction increased with heat flux and with increasing angle of inclination of the minichannel to the horizontal plane.

Keywords: Heat transfer; Flow boiling; Minichannel; Flow orientation; Flow pattern

Vol. 45(2024), No. 2, 29–39; doi: 10.24425/ather.2024.150849

Cite this manuscript as: Piasecka, M., & Strąk, K. (2024). Effect of flow orientation in experimental studies on FC-770 boiling heat transfer in asymmetrically heated minichannels. *Archives of Thermodynamics*, 45(2), 29–39.

1. Introduction

Due to the rapid advancement of modern technologies, the miniaturisation of devices and components is progressing in engineering applications. Reliable and efficient heat transfer in flowing fluids is crucial in various industrial processes, including high-power electronics, microelectronics, IT microprocessors, and microfluidics. The study of flow boiling heat transfer in small-dimension channels is of great interest to scientists, especially for cooling miniature high-power components. Many research centres are investigating factors that influence the intensification of heat transfer, particularly during phase change processes such as boiling and condensation. One significant aspect under investigation is the impact of different orientations of the heat exchanger on the heat transfer coefficient.

A brief review of the literature on flow boiling heat transfer during refrigerant flow in channels of small dimensions.

In [1], an experimental study was conducted to investigate

Nomenclature

A – channel cross-sectional area, m^2
G – mass flux, kg/(m^2·s)
I – current, A
MRE_α – mean relative error of the heat transfer coefficient, %
ONB – onset of nucleate boiling
p – pressure, Pa
q_w – heat flux (density), W/m^2
T – temperature, K
T_s – ambient temperature, K
x – distance from the minichannel inlet along the direction of flow, m

Greek symbols

α – heat transfer coefficient, W/(m^2·K)
α_s – heat transfer coefficient at the interface between the heated wall and the surroundings, W/(m^2·K)
Δ – absolute error
ΔT_{sub} – inlet liquid subcooling, K, $\Delta T_{sub} = T_{sat,in} - T_{f,in}$
ΔU – voltage drop, V
δ – thickness, m
λ – thermal conductivity, W/(m·K)

Subscripts and Superscripts

f – fluid
in – at the inlet
$loss$ – heat loss
sat – saturation
w – heated wall

bubble dynamics and flow patterns during flow boiling of HFE-7000 in high aspect ratio microchannels of various channel orientations. The test section utilized a transparent glass minichannel with a width-to-height aspect ratio of 10 and a hydraulic diameter of 909 μm. The channel received uniform heating, and a tantalum layer coating facilitated observations. The study focused on the growth of a single bubble and the influence of mass flux and heat flux on bubble behaviour. Additionally, the paper explored the impact of channel orientation on bubble behaviour, considering aspects such as bubble evolution, shape, and nose velocity. No significant differences in flow patterns were observed when comparing horizontal and vertical upward orientations. The study identified two types of instabilities associated with the dominant flow pattern during flow boiling.

Considering the same test section with channels of 5 mm width and 0.5 mm depth, authors in [2] addressed the pressure and thermal characterization of dynamic instabilities during flow boiling of FC-72, exploring different channel orientations. One-sided heating at various channel orientations relative to gravity was considered, ranging from bottom heating (0°) to top heating (180°) in 30° increment. For each channel orientation, the study examined various combinations of heat flux and mass flux leading to categorized flow instabilities. Generally, orientations with a horizontally heated surface (0° and 180°) were more susceptible to flow instability, while intermediate azimuthal rotations (30°, 60° and 90°) showed flow instability only at the highest mass flow rates. At the highest mass flow rates, the horizontal orientation of 180° and heating from the top showed an increase in the heat transfer coefficient (during instability) of up to 77% and 275% in single-phase and two-phase regions, respectively, compared to stable initial conditions.

The authors of [3] discussed modifications to the inlet and outlet plenum, as well as the outlet port orientations, to address instabilities in two-phase microchannel heat sinks. The study explored four orientations: horizontal flow (+0°), downward-facing horizontal flow with downward orientation (–0°), and vertically aligned upward (+90°) and downward flows (–90°). The orientation of the inlet-outlet port was perpendicular to the plane of the microchannel footprint area. As a result, the study proposed straightforward guidelines for designing the inlet and outlet plenum, as well as port orientations, to mitigate instabilities in two-phase microchannel heat sinks, especially at high heat fluxes and under unfavourable orientations.

In [4], upward flow boiling heat transfer of HFE-7000 in a vertical tube under a high-frequency alternating-current electric field was investigated. The test section was coated with a 600 nm transparent indium tin oxide layer, enabling visual access to boiling dynamics within the tube while simultaneously serving as an electrical heater element for heat transfer. The experiments were carried out under constant mass flux and inlet subcooling, varying heat flux, voltages, and at three frequencies (100 Hz, 1 000 Hz, and 10 000 Hz). At 100 Hz frequency, the study observed a heat and mass transfer phenomenon, resulting in a more than two-fold enhancement in heat transfer at low heat fluxes.

In [5], the influence of minichannel geometrical configuration on flow structures, hydrodynamics, and heat transfer behaviour in a FC-72 cooling system with high heat flux during subcooled flow boiling was presented. Two-dimensional numerical simulations were conducted for two different configurations (straight and periodic constriction-expansion) of a minichannel mounted vertically, maintaining constant mass and input heat flux, and varying three inlet temperatures. The results in both configurations showed that with an increase in the inlet temperature, the heat transfer coefficient also increased. The periodic constriction-expansion configuration exhibited the greatest enhancement in heat transfer (21.77–36.9%) for an inlet temperature range from 285.35 K to 325.35 K.

Experimental research on flow boiling bubble motion under an ultrasonic field in a vertical minichannel, utilizing a bubble tracking algorithm, was presented in [6]. The central component of the experimental system was the minichannel section with a heat sink. The heat sink featured 14 rectangular minichannels with a length of 220 mm, width of 2 mm, and height of 2 mm, using R141b fluid as the working fluid. It was observed that the use of ultrasound significantly increased the detachment frequency, speed, and bubble travel distance, leading to an extremely unstable two-phase gas-liquid flow. Numerical simulations were employed to quantitatively investigate the movement mechanism of bubbles in microchannels under the influence of

an ultrasonic field.

In [7], a thorough investigation was conducted into the thermo-hydrodynamic effects of the minichannel configuration on the thermal performance of subcooled flow boiling. The study focused on cooling using FC-72 at high heat flux values in various vertical minichannel shapes. Particular attention was given to developing a numerical approach to predict highly subcooled flow. The computational results were validated through experimental measurements, revealing notable agreements that highlighted the effectiveness of the numerical model. The results demonstrated a decrease in the heat transfer coefficient with increasing mass flux, and the design with expanding shapes improved thermal efficiency by up to 24.68% and 10.45% compared to straight and expanding shapes, respectively.

The investigation of flow boiling heat transfer in FC-72 fluid within a vertical rectangular narrow minichannel was presented in [8]. The studies were focused on two-phase flow patterns and a local void fraction. The dimensions of the minichannel were 0.5–1.5 mm in depth, 20 mm in width and 360 mm in length. The results indicated that the local heat transfer coefficient increased with increasing pressure within the channel and this effect was observed under varying mass flux conditions.

In the study [9], flow boiling heat transfer of R1233zd(E) was investigated in a 3 mm vertical circular minichannel at moderate and high saturation temperatures. In particular, all heat transfer trends initially decreased with increasing vapour quality but later stabilised or even increased because of convective boiling effects. The experimental data were compared with predictions from an in-house model and established two-phase flow correlations known from the literature. It was underlined that the in-house model demonstrated the highest accuracy, with a mean absolute percentage error of 23.17% for R1233zd(E) and 19.23% for R245fa.

In [10], the authors investigated boiling heat transfer during R134a flow in a single horizontal circular tube with a diameter of 5 mm. Key findings include that the heat transfer coefficient decreases as the vapour quality increases, sensitivity to heat flux is observed, but is insensitive to mass flux, and sensitivity to vapour quality at low values. Furthermore, nucleate boiling dominates in regions with low vapour quality. Additionally, the study mentions new environmentally friendly low-pressure refrigerants based on fluorocarbons.

Several new environmentally friendly low-pressure refrigerants from fluorocarbon and hydrofluoroether (HFE) groups used in investigations of heat transfer during flow in minichannels were presented in [11]. The authors present the most important properties and applications of refrigerants of these groups and review the literature on their use. In the results, HFE refrigerants show better thermal properties than the Fluorinert FC-72.

In [12], saturated flow boiling in a one-sided heated rectangular microchannel was examined. The working fluid used was deionised water. The primary focus of the investigation was on local heat transfer coefficients, pressure drop and flow patterns for surfaces with various wettability characteristics. The bottom surface was a hydrophilic bare silicon wafer with a contact angle of 65°. In contrast, a superhydrophilic surface was created by depositing a 100 nm thick silicon dioxide film, resulting in a contact angle of less than 5°. The experiments involved a range of mass fluxes from 120–360 kg/(m^2s) and inlet vapour qualities between 0.03 and 0.1. Flow visualisation revealed local dry out on the untreated hydrophilic surface at high heat fluxes and low mass fluxes, leading to a decrease in heat transfer performance. However, this phenomenon was not observed on the superhydrophilic surface under the same conditions. The hydrophilic surface experienced significant heat transfer deterioration with increasing inlet vapour quality, while the heat transfer coefficient of the superhydrophilic surface remained relatively constant. A similar investigation was described in [13]. The authors concluded that the superhydrophilic surface maintained relatively constant heat transfer performance because of the continuous and uniform distribution of the thin liquid film on the heated surface during annular flow dominance. This delayed the onset of partial dryout, resulting in superior performance compared to the untreated hydrophilic surface, without any additional pressure drop penalty.

Authors of [14], discussed a method for studying two-phase heat transfer in mini and microtubes. The focus was on the evaporation of a thin liquid film. The study used the Tikhonov regularisation method to solve the inverse heat conduction problem in the tube wall, providing a way to estimate local convective wall heat flux and heat transfer coefficients. The temperature distributions on the outer surface of the channel, measured by an infrared camera, were taken as input data to solve this inverse problem. The results confirm existing correlations in the average values.

Conducting heat transfer calculations for flow boiling in minichannels was a main topic reported in [15]. The experimental setup was the same as was applied in this article, consisting of five parallel mini-channels, sharing a common heated wall. Temperature measurements were taken using K-type thermoelements and an infrared camera in selected mini-channels to estimate temperature uncertainty. The results from the Monte Carlo simulation method were compared with those from the uncertainty propagation method. The main experiment was conducted to investigate heat transfer in the subcooled boiling region. Local heat transfer coefficients at the interface between the working fluid and the heated wall were calculated using the Robin boundary condition. The mathematical model, described by the heat equation in the mini-channel wall and the Fourier-Kirchhoff equation in the flowing fluid, led to an inverse heat transfer problem. This problem was solved using the Finite Element Method with Trefftz-type basis functions. The final results of the heat transfer coefficient included the estimation of temperature uncertainty measurements from the Monte Carlo method.

Numerous publications have explored research on the pool boiling process involving various working fluids and using developed heated surfaces. References [16–18] and [19] cover various aspects of this topic. In [16] a study was presented on pool boiling heat transfer of water and ethanol using two types of structures prepared on the samples by laser treatment. Research on pool boiling of FC-72 on open surfaces with parallel microchannels made of copper was reported in [17]. Furthermore in [18] explores pool boiling heat transfer process of FC-72 on

open surfaces with microchannels while [19] investigates the same issue related to enhanced heated wall surfaces with mesh structures and microfins.

In general, the authors' previous work focused on boiling heat transfer during flow in a single minichannel at various inclinations relative to the horizontal plane, including 0º, 45º, 90º, 135º, and 180º, using FC-72 as a working fluid [20]. Experiments carried out in a vertical and horizontal minichannel with FC-72, HFE-649, HFE-7000, or HFE-7100 circulated in the main loop were discussed in [21]. Additionally, the results of experiments involving seven inclinations of the test section with a minichannel (0°, 30°, 60°, 90°, 120°, 150°, and 180°) and three refrigerants as working fluids, namely FC-72, HFE-7100, and HFE-7000, were analysed in [22]. The main findings included intensification of heat transfer during flow in minichannels and observation of flow patterns. The novelty of the presented work lies in the assessment of the intensity of flow boiling heat transfer during the flow of Fluorinert FC-770 in a group of five asymmetrically heated minichannels. Another goal is to compare the results of temperature and heat transfer coefficient as the flow direction changes within the orientation range from 0° to 180° with a 15° increment. This helps identify positions that ensure a high intensity of heat transfer processes.

2. Experimental setup

2.1. Research rig

The experiments were carried out using a research rig comprising the main circulation loop with FC-770, the data and image acquisition system equipped with the lighting system, and the power supply and control system, as shown in Fig. 1.

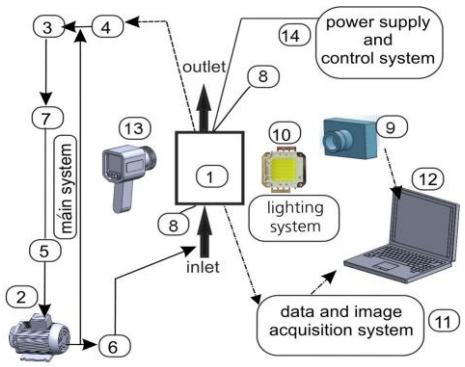


Fig. 1. A schematic diagram of the main systems on the research rig: 1 – a test section; 2 – a gear pump, 3 – a pressure regulator, 4 – a heat exchanger, 5 – a filter, 6 – a Coriolis mass flowmeter, 7 – an air separator, 8 – a pressure meter, 9 – a high-speed camera, 10 – LED lighting system, 11 – the data and image acquisition system, 12 – a PC, 13 – an infrared camera, 14 – the power supply and control system with heat source.

The flow loop consists of: a test section with a group of five minichannels (1), a gear pump (2), a pressure regulator (3), a heat exchanger (4), a filter (5), a Coriolis mass flowmeter (6), an air separator (7), pressure meters (8), a high-speed camera (9) and an infrared camera (13). Detailed information on all elements of the research rig is provided in [23].

2.2. Test section and its spatial orientation

The test section, which features a group of five asymmetrically parallel and rectangular heated minichannels, is a crucial component of the setup, as shown in Fig. 2. Each minichannel has a cross-section of 1 mm x 6 mm, sharing a common heated wall approximately 0.1 mm thick, made of Haynes-230 alloy. The working fluid was FC-770 (Fluorinert™ FC-770, 3M). Table 1 provides the main thermal and flow properties of the Fluorinert FC-770. The experimental series were conducted under stationary conditions with a constant mass flow rate and a slight overpressure.

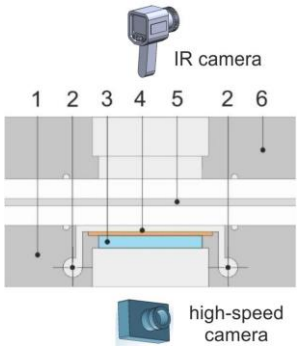


Fig. 2. Schematic of the test section (longitudinal section): 1 – channel body, 2 – inlet/outlet chamber, 3 – glass plate, 4 – minichannel, 5 – heated wall, 6 – top cover.

Table 1. Main properties of Fluorinert™ Electronic Liquid FC-770.

Main properties (units)	Values
Boiling point (K)	368
Heat of vaporization (J/kg)	85.9×10^3
Liquid density (kg/m³)	1793
Vapour pressure (Pa)	6.568×10^3
Thermal conductivity (W/(m·K))	0.063
Kinematic viscosity (m²/s)	0.79×10^3
Coefficient of expansion (1/K)	0.00148
Molecular weight (kg/kmol)	399
Surface tension (N/m)	0.0148

The exterior surface of the heated wall of the minichannels was coated with black paint to achieve an emissivity of 0.83. The temperature of this heated wall surface was measured using an A655SC infrared camera (manufactured by FLIR). The axially symmetric part of the central minichannel was considered for temperature measurements. A high-speed video camera, SP-5000M-CXP2 (manufactured by JAI), recorded the two-phase flow structures through the glass wall of the minichannels, illuminated by high-power LEDs. The temperature (measured with K-type thermocouples) and pressure (measured with pressure metres) of the working fluid were recorded in the inlet and outlet manifolds of the test section. Furthermore, the electrical parameters of the resistance heated wall were captured.

The spatial orientation of the test section and the direction of the fluid flow in the minichannels varied from 0° to 180°, with an increment of 15°, as schematically illustrated in Fig. 3. The

research considered 13 different positions of the test section in relation to the horizontal plane: one vertical with upward flow of the fluid (90°), two horizontal (the position named 0° while the fluid flows above the heated wall, and the other position named 180° while the heated wall was above the fluid), and ten other positions between them. It should be emphasised that the test section is asymmetrically heated.

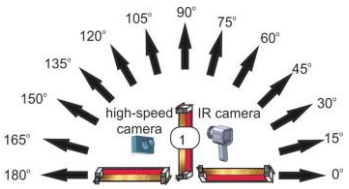


Fig. 3. A scheme of spatial orientation of the test section showing the direction of the fluid flow in minichannels, 1 – the test section with minichannels.

2.3. Experimental methodology, thermal and flow parameters

Fluorinert FC-770 was circulated in the flow loop. During each experiment, the mass flux was stabilised at the constant value, low overpressure was established, and test section was spatially oriented according to the research schedule.

The main experimental thermal and flow parameters of the experimental sets selected for the analyses are listed in Table 2.

Table 2. Main thermal and flow parameters of the experimental sets.

Main thermal or flow parameters	Values / Ranges of values
Heat flux, q_w (kW/m²)	33.3-63.9
Mass flux, G (kg/(m²·s))	145
Inlet pressure, p_{in} (kPa)	103-183
Inlet liquid subcooling, ΔT_{sub} (K)	79.3-101.6

Throughout each series of tests, the subcooled liquid enters the minichannels and heats up as it flows towards the outlet along the heated wall. The heat flux supplied to the heated wall of the minichannels is gradually increased. The heat transfer process converts from single-phase forced convection to subcooled boiling, finally achieving saturated boiling. At the outlet, a two-phase liquid-vapour mixture emerges, directed subsequently to the additional heat exchanger, the condenser.

3. Determination of the heat transfer coefficient and mean relative error

3.1. The heat transfer coefficient

The heat transfer coefficient calculations were performed using a simple 1D calculation method applied to the central channel of the group of five. In this method, only one direction of heat flow was considered, taking into account the primary direction of heat flow perpendicular to the direction of the fluid flow in the channel [23].

Local values of the heat transfer coefficient were calculated using Newton's law:

$$\alpha(x) = \frac{q_w}{T_w(x,\delta_w) - T_f(x)}, \tag{1}$$

where q_w is the heat flux transferred from the heated wall to the fluid, x – distance from the minichannel inlet, along the direction of flow, $T_w(x,\delta_w)$ – the temperature at the heated wall – fluid interface, δ_w – thickness of the minichannel heated wall, T_f – the temperature of the fluid, calculated locally based on measured temperatures at the inlet and the outlet of the minichannel (with the assumption of a linear dependence of the fluid temperature from the inlet to the outlet).

The heat transferred to the fluid in the minichannel was assumed to be equal to the difference between the heat generated by the heated wall and the heat loss to the surroundings:

$$q_w = \frac{I\Delta U}{A_w} - q_{w,loss}, \tag{2}$$

where I – current supplied to the heated wall, ΔU – voltage drop across the heated wall, A_w – surface area of the heated wall, $q_{w,loss}$ – heat loss to the surroundings.

The heat loss to the surroundings was calculated similarly as in previous work [22], according to the following dependence:

$$q_{w,loss} = \alpha_s \cdot [\max T_w(x) - T_s], \tag{3}$$

where α_s – the heat transfer coefficient at the interface between the heated wall and the surroundings, T_w – temperature of the outer surface of the minichannel heated wall registered by an infrared camera, T_s – ambient temperature.

The temperature at the heated wall–fluid interface was calculated as follows:

$$T_w(x,\delta_w) = T_w(x) - q_w \frac{\delta_w}{\lambda_w}, \tag{4}$$

where λ_w – thermal conductivity of the minichannel heated wall.

Finally, local values of the heat transfer coefficient at the subcooled flow boiling region were determined from the following formula:

$$\alpha(x) = \frac{\frac{I\Delta U}{A_w} - q_{w,loss}}{T_w(x) - T_f(x) - \left(\frac{I\Delta U}{A_w} - q_{w,loss}\right)\cdot\frac{\delta_w}{\lambda_w}}. \tag{5}$$

3.2. The mean relative error of the heat transfer coefficient

The mean relative error of the heat transfer coefficient MRE_α was estimated from the following formula:

$$MRE_\alpha = \frac{\sqrt{\left(\frac{\partial\alpha(x)}{\partial T_w(x)}\Delta T_w(x)\right)^2 + \left(\frac{\partial\alpha(x)}{\partial T_f(x)}\Delta T_f(x)\right)^2 + \left(\frac{\partial\alpha(x)}{\partial\lambda_w}\Delta\lambda_w\right)^2 + \left(\frac{\partial\alpha(x)}{\partial\delta_w}\Delta\delta_w\right)^2 + \left(\frac{\partial\alpha(x)}{\partial q_w}\Delta q_w\right)^2}}{\alpha(x)} \tag{6}$$

The absolute errors of components, needed to calculate MRE_α according to the dependence (6) are listed in Table 3.

Table 3. The absolute errors of components of the dependence (6) for determining of MRE_α.

Components in Eq. (6) for determining of MRE_α	Absolute errors
Thermal conductivity of the minichannel heated wall	$\Delta\lambda_w$ = 0.1 W/(m·K)
Thickness of minichannel heated wall	$\Delta\delta_w = 5\times10^{-5}$ m
Temperature of the outer surface of the minichannel heated wall registered by an infrared camera	$\Delta T_w(x)$ = 2.0 K
Heated wall area	$\Delta A_w = 2.8\times10^{-5}$ m^2
Current intensity supplied to the minichannel heated wall	ΔI = 0.18 A
Voltage drop across the minichannel heated wall	$\Delta(\Delta U)$ = 0.02 V
Fluid temperature difference between the temperatures measured by thermocouples at the minichannel inlet and outlet	$\Delta T_f(x)$ = 0.34 K [24]

It should be underlined that each of the two K-type thermocouples (one installed at the inlet and the other at outlet of the minichannels) was additionally calibrated with the use of a temperature calibrator, which was described in detail in [24].

The absolute error of the heat flux Δq_w was determined for the lowest value of the heat flux supplied to the heated wall of the minichannels (q_w = 33.3 kW/m^2). The absolute error of the heat flux was found to be 0.83%. The procedure for calculating the absolute error and the relative error of the heat flux was similar to that reported in [22].

The mean relative errors of the heat transfer coefficient MRE_α, obtained for various flow orientations of the test section, are shown in Table 4.

Table 4. The mean relative error of the heat transfer coefficient MRE_α for various flow orientation.

Spatial orientation of the test section (°)	The mean relative error of the heat transfer coefficient MRE_α (%)
0	3.28
15	3.28
30	3.36
45	3.42
60	2.90
75	3.23
90	3.32
105	3.24
120	3.24
135	3.23
150	3.35
165	3.30
180	3.50

When analysing the values of the mean relative errors of the heat transfer coefficient (MRE_α), listed in Table 4, it was observed that in the subcooled boiling region, they are low, ranging from 2.90% to 3.50%. The lowest MRE_α was achieved for the 60° position, while the highest values were observed for the 180° position. These results are consistent with findings from previous studies, as presented, for example, in [21,22].

4. Results

4.1. Main description

The results are presented in Figs. 4–9 in the form of:

- dependencies of the minichannel heated wall temperature (measured by an infrared camera) as a function of distance from the inlet, for two heat fluxes – Fig. 4;
- dependencies of the heat transfer coefficient as a function of distance from the inlet, for two heat fluxes – Fig. 5;
- dependencies of the heat transfer coefficient as a function of flow orientation of the minichannel at two distances from the inlet, for two heat fluxes – Fig. 6;
- images of two-phase flow patterns characteristic for analysed flow orientations – Fig. 7;
- boiling curves, based on the data collected during the experiments carried out for various flow orientations, for two distances from the inlet – Fig. 8,
- dependencies of the void fraction as a function of heat flux, prepared on the basis of recorded two-phase flow images during experiments at various flow orientations, for one distance from the inlet – Fig. 9.

In Fig. 4 the results for two values of the heat flux supplied to the heated wall in the subcooled boiling region (q_w = 46 kW/m^2 and q_w = 64 kW/m^2) were shown as local temperatures of the outer surface of the heated wall, obtained from measurements due to infrared thermography.

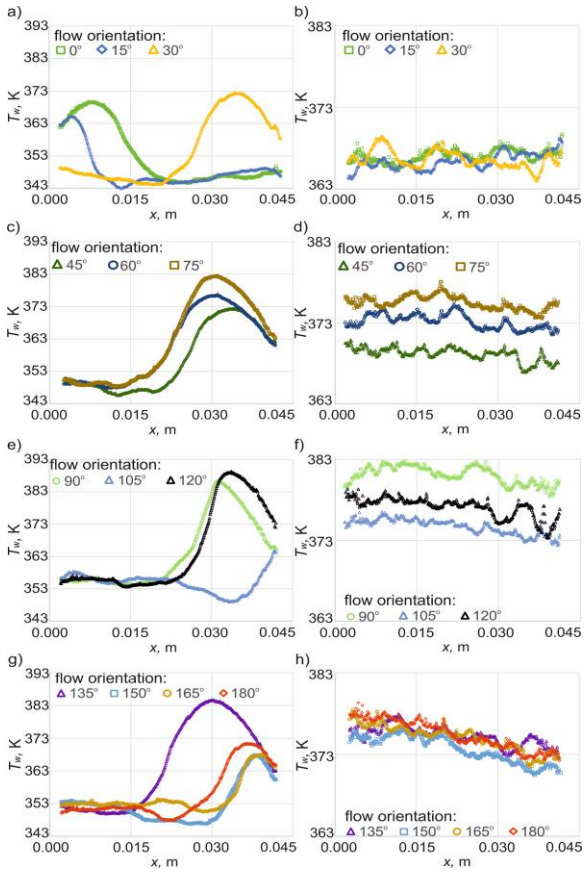


Fig. 4. Dependencies of the minichannel heated wall temperature measured by an infrared camera (T_w) as a function of distance from the inlet (x) for analysed flow orientations, at two heat fluxes (q_w): 46 kW/m^2 (a, c, e, g) and 64 kW/m^2 (b, d, f, h).

The local heat transfer coefficients corresponding to these temperature data are illustrated in Fig. 5. Both dependences are given as functions of the distance from the minichannel inlet.

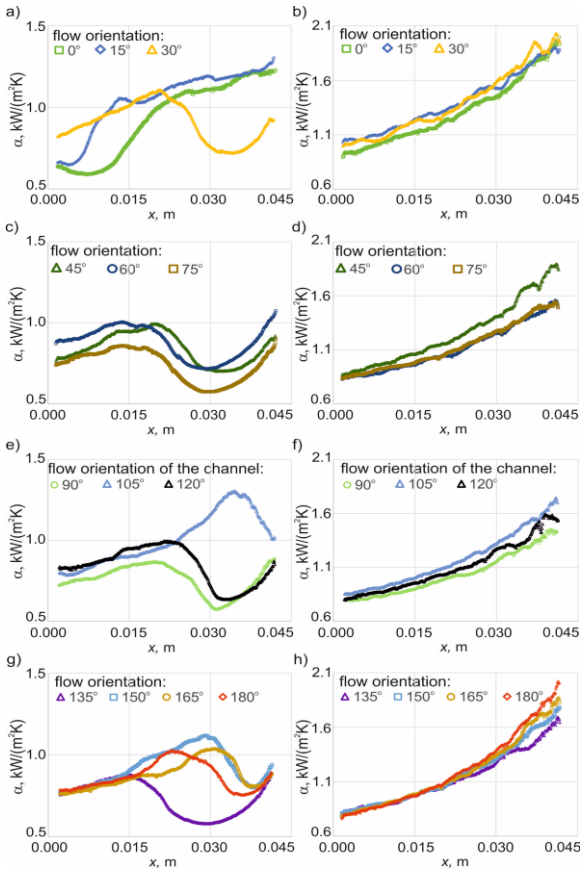


Fig. 5. Dependencies of the heat transfer coefficient (α) as a function of distance from the inlet (x) for the analysed flow orientations, at two heat fluxes (q_w): 46 kW/m^2 (a, c, e, g) and 64 kW/m^2 (b, d, f, h).

Furthermore, the dependence of the heat transfer coefficient and the flow orientation of the minichannel are presented in Fig. 6, at two locations: one-third distance and two-thirds distance, from the inlet, as the results of the calculations for two heat fluxes.

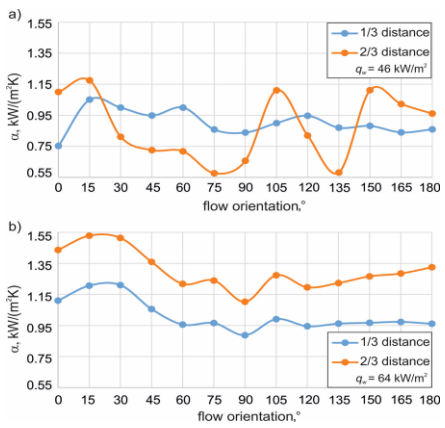


Fig. 6. Dependencies of the heat transfer coefficient (α) as a function of flow orientation, constructed at locations: one-third distance and two-thirds distance from the inlet, for two heat fluxes (q_w): a) 46 kW/m^2 and b) 64 kW/m^2.

For general view, the two-phase flow are shown in Fig. 7 as images of two-phase flow patterns, characteristic for various flow orientations.

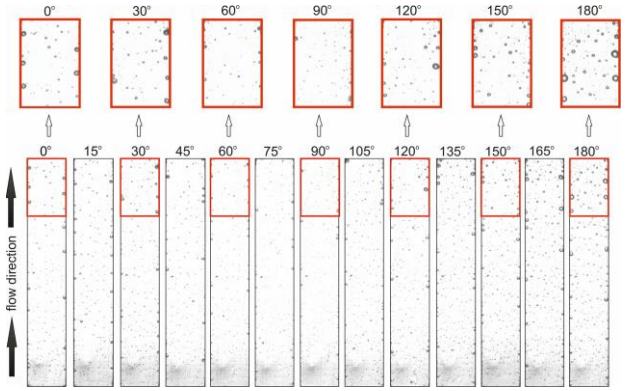


Fig. 7. Images of the characteristic two-phase flow patterns for each of the analysed flow orientations, with enlarged fragments of the outlet area for selected minichannel positions.

The boiling curves are illustrated in Fig. 8, constructed for two distances from the inlet, for all tested spatial orientations of the minichannel.

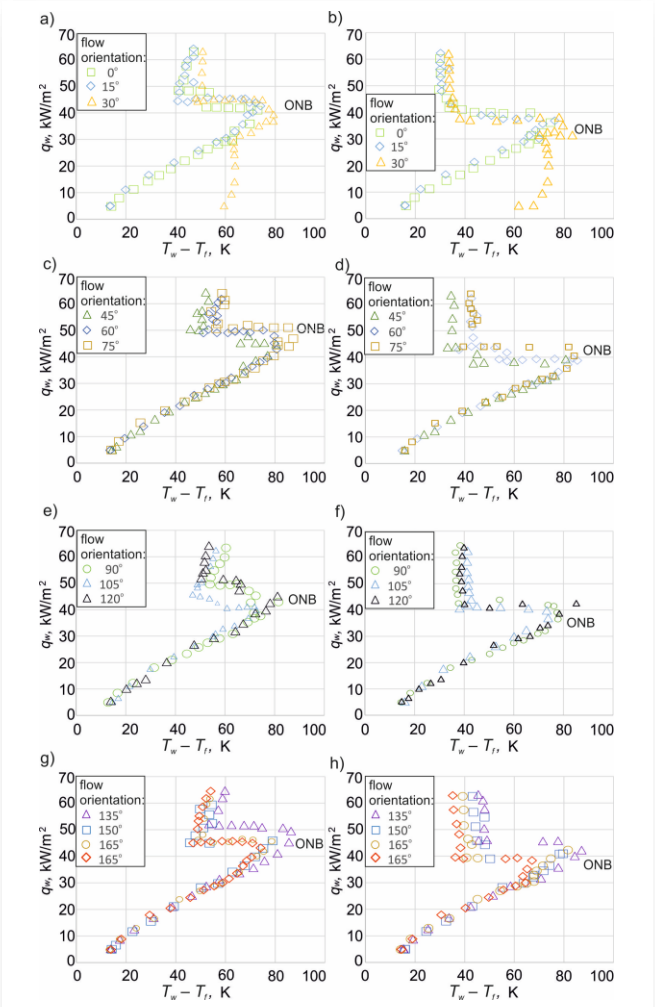


Fig. 8. Boiling curves, based on the data collected during experiments carried out for analysed flow orientations, constructed at locations: one-third distance (a, c, e ,g) and two-thirds distance (b, d, f, h) from the inlet, ONB - onset of nucleate boiling.

In Fig. 9, the relationship between void fraction and heat flux is depicted at a location of two-thirds distance from the inlet.

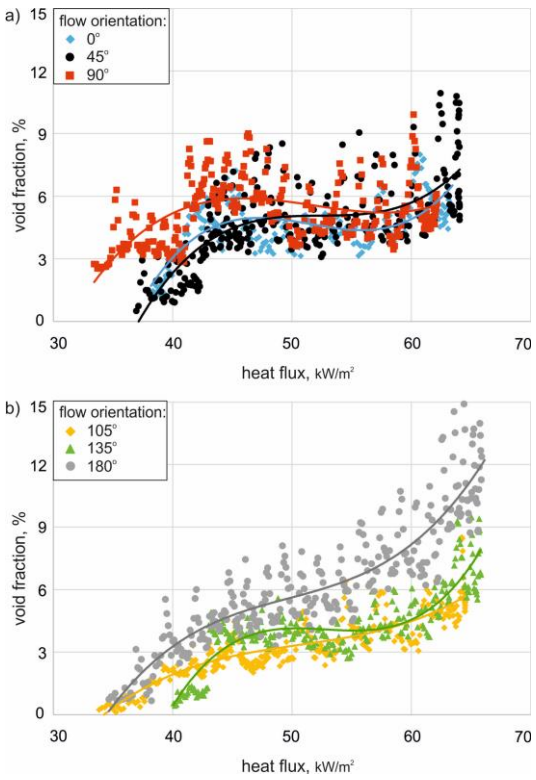


Fig. 9. Void fraction versus heat flux, based on data collected during experiments carried out for selected flow orientations: a) 0°, 45°, 90 °, and b) 105°, 135°, 180°, constructed at a location of two-thirds of the distance from the inlet.

The study described in [25] provides a detailed explanation for determining the procedure for the void fraction. When defining the volumetric void fraction, we consider the proportion of the channel volume filled by the gas phase. Furthermore, for the minichannel, we assume that the two-dimensional area of the vapour is fully occupied by vapour, accounting for the very small third dimension (according to the minichannel depth). Therefore, we provide a cross-sectional void fraction, where the fraction of the channel is assumed to be occupied by the gas phase. Two-phase flow images were performed using a specialist software environment based on LabVIEW functions. Each digital photo was loaded and analysed as a binarized image. To determine the cross-sectional void fraction, the number of pixels corresponding to the gas phase was counted and divided by the total number of pixels in the selected area. For the areas partially filled with vapour, the procedure of closing the bubbles was performed. In the literature on boiling heat transfer, it is common to present thermodynamic vapour quality on the basis of theoretical considerations. However, in this article, the results obtained from the experiments are shown as void fractions, based on the data from the recorded two-phase flow images.

4.2. Observations and analyses

When analysing the temperature distribution on the heated wall surface (Fig. 4), the following observations can be made:

- At a lower heat flux:
  1) The temperature of the heated wall in the outlet part of the minichannel shows a very slight decrease with increasing distance from the inlet (from the inlet up to 1/3 minichannel length), despite the positions of 0° and 15°, for which the diminishing of temperature proceeds much more abruptly;
  2) The temperature of the heated wall increases with distance at the range from 1/3 up to 2/3 minichannel length, reaching a maximum in the end of this range; the highest temperature increase was observed for orientations of 75°, 90°, 120° and 135°, reaching above 385 K while the lowest temperature value was obtained for orientations of 105° and 150°, maximally down to 370 K;
  3) At the outlet part of the minichannel, a diminishing of temperature is noted (despite the position of 105°);

- At a higher heat flux:
  1) The temperature fluctuated very slightly, in comparison with the results obtained for lower heat flux;
  2) The highest values of the heated wall temperature occurred for positions of 90° and 120°;
  3) The lowest temperatures were observed for positions of 0°, 15° and 30°.

When examining the heat transfer coefficient results presented in Fig. 5, several observations can be noted:

- At a lower heat flux:
  1) An increase in the heat transfer coefficient is observed with the distance from the inlet, followed by a decrease in the part of the channel where the highest temperature values were recorded (see Fig. 4), and then a further increase towards the channel outlet;
  2) The heat transfer coefficient values range from 0.5 to 1.4 kW/(m^2·K);
  3) The highest values of the heat transfer coefficient (maximum) are observed for orientations of 0°, 15° and 105°;
  4) The lowest values the heat transfer coefficient (minimum) are seen for orientations of 75°, 90°, 120° and 135°;

- At a higher heat flux:
  1) A clear increase in the heat transfer coefficient is observed along the entire channel length with increasing distance from the inlet;
  2) The values of the heat transfer coefficient are higher in comparison to achieved for lower heat flux, ranging from 0.7 to 2.0 kW/(m^2·K);
  3) The highest values of the heat transfer coefficient are observed for positions of 0°, 15°, 30°, 165° and 180°, reaching a maximum approx. 2.0 kW/(m^2·K);

4) The lowest values of the heat transfer coefficient are obtained for positions of 60°, 75°, and 90° with a maximum of 1.6 kW/(m^2·K).

Upon analysing the results shown in Fig. 6, it is evident that the heat transfer coefficient varies with flow orientation as follows:

- At a lower heat flux (Fig. 6a):
  1) In general, the values of heat transfer coefficients are lower compared to those obtained at higher heat flux, and they are characterised by higher scatter, mainly observed in the results collected at 2/3 distance from the inlet;
  2) The highest values of the heat transfer coefficient at 1/3 distance from the inlet are observed for a position of 15°, while the lowest values are achieved for a position of 0°;
  3) At 2/3 distance from the inlet, the highest values of the heat transfer coefficient are observed also for the position of 15°, while high values are also noted for orientations of 0°, 105°, and 150°; the lowest values are observed for positions of 75° and 135°;
- At a higher heat flux (Fig. 6b):
  1) For both selected distances from the inlet (1/3 and 2/3 distances), similar relationships are obtained, but lower values are noticed at 1/3 distance (it is seen moving down the dependence on the chart by a constant value);
  2) The highest values of the heat transfer coefficient are gained for orientations 15° and 30°;
  3) The lowest values of the heat transfer coefficient are noted for the position of 90° but generally low values are seen in the orientation range 60°–180°.

Describing the two-phase flow patterns illustrated in Fig. 7 for each of the analysed flow orientations, it is emphasized that only a bubbly flow is observed for each channel position. The images show only tiny vapour bubbles, small and uniformly spherical. Larger bubbles can be noticed near the sides of the channels. Moreover, larger spherical bubbles are seen for spatial orientations close to horizontal, where the fluid flows below the heated wall, in the orientation range of 135°–180°.

Boiling curves shown in Fig. 8 are based on the data collected during experiments carried out for analysed flow orientations. The curves were constructed at two selected distances from the inlet (1/3 and 2/3 distances from the inlet), while increasing the heat flux supplied to the heated wall, while heat flux density depends on temperature difference T_w-T_f. The typical shape of the boiling curves is observed. As the heat flux density increases, heat transfer between the heated wall and subcooled liquid flowing in the minichannel occurs through the single-phase forced convection process. The increase in heat flux density activates vapour nuclei on the channel's heated surface. The bubbles formed as a result act as internal heat absorbers, absorbing substantial amounts of energy transferred to the liquid. Spontaneous nucleation causes a drop in the heating surface temperature, while the heat flux density remains nearly constant. This point is marked in the curve course as ONB (onset of nucleate boiling). Further increases in heat flux density lead to developed nucleate boiling [21].

When analysing the courses of the boiling curves presented in Fig. 8, the following observations can be made:

- The boiling curves exhibit a similar course, except for the curve corresponding to 30° in the single-phase forced convection section (Fig. 8a and Fig. 8b);
- The onset of nucleate boiling (ONB) appears at a higher heat flux for the boiling curves generated at the shorter distance from the inlet (1/3 distance) compared to the longer one (2/3 distance), regardless of the flow orientation under consideration;
- The smallest temperature differences are achieved for positions of 0° and 15° (Fig. 8a and Fig. 8b), and for the orientation ranges of 45°–75° and 135°–180°, the highest temperature differences (T_w–T_f) at ONB are observed (Fig. 8c, Fig. 8d and Fig. 8g, Fig. 8h);
- In general, as the angle of flow orientation increases, a higher temperature difference (T_w–T_f) corresponding to ONB occurs for both distances from the inlet;
- For the orientation range of 135°–180°, ONB appears with the highest heat flux compared to other spatial orientations of the test section.

Based on the graphs illustrated in Fig. 9, it was observed that the void fraction increased with rising heat fluxes, as expected. Additionally, it also increased with the increasing angle of inclination of the minichannel to the horizontal plane. The lowest values of void fraction were observed for 0° flow orientation, while the highest values were found for 180° flow orientation (up to 15%).

5. Conclusions

The study investigates boiling heat transfer during the flow of FC-770 in a configuration of five minichannels featuring a shared heated wall. The orientation of the flow was systematically varied from 0º to 180º relative to horizontal plane, with a increment of 15°. Throughout the experiments, an infrared camera monitored the temperature of the outer heated wall, while a high-speed camera captured flow patterns through a glass plate opposite the heated wall. Local heat transfer coefficients on the contact surface between the working fluid and the heated surface in the central minichannel were computed using a simplified 1D calculation method. The results obtained, including the dependencies of the heated wall temperature and the heat transfer coefficient with respect to the distance from the channel inlet for 13 flow orientations, were comprehensively analysed. Additionally, typical boiling curves and two-phase flow patterns were presented and subjected to a thorough discussion. Furthermore, the dependence of the void fraction as a function of heat flux was illustrated for various angles of minichannel inclination to the horizontal plane.

The most important findings cover:

- At a lower heat flux, the temperature of the heated wall reaches a maximum at the outlet part of the channel, and for a higher heat flux, it changes slightly;

- At the lower heat flux, the values of heat transfer coefficients are lower compared to those obtained at higher heat flux, and they are characterised by higher scatter;
- The highest values of the heat transfer coefficient are observed for orientations of 0°, 15° and 105° (at lower heat flux), 0°, 15°, 30°, 165° and 180° (at higher heat flux);
- Analysing the image of flow pattern, the presence of spherical vapour bubbles was observed, with the largest sizes occurring in the orientation range of 135°–180°;
- The initiation of boiling was accompanied by the occurrence of nucleation hysteresis. The typical shape of the boiling curves was observed. The highest temperature difference observed for the orientation ranges of 45°–75° and 135°–180°, and the lowest are achieved for positions of 0° and 15°;
- Void fraction increased with heat flux and also with the increasing angle of minichannel inclination to the horizontal plane, reaching the highest values for 180° flow orientation.

It is crucial to emphasize that boiling processes allow for high heat fluxes with small temperature differences between the heated surface and the working fluid, resulting in high efficiency over a small heat transfer area. Identifying conditions that lead to the most intense flow boiling heat transfer is of paramount importance. The heat transfer coefficient is influenced by various factors, such as thermal and flow parameters, surface roughness, channel geometry, spatial orientation, and properties of the boiling liquid. However, the existing literature on heat transfer in minichannels during flow boiling presents inconsistent results. This underscores the importance of continued research in this field.

Acknowledgments

The research reported herein was supported in part by a grant from Poland's Minister of Education and Science through the Poland's Metrology Programme [Polska Metrologia]. Grant Number: PM/SP/0031/2021/1; Funding: 750 000.00 PLN; Programme budget: 848 200.00 PLN.

References

[1] Widyatama, A., Venter, M., Orejon, D., & Sefiane, K. (2023). Experimental investigation of bubble dynamics and flow patterns during flow boiling in high aspect ratio microchannels with the effect of flow orientation. *International Journal of Thermal Sciences*, 189, 108238. doi: 10.1016/j.ijthermalsci.2023.10823

[2] Vermaak, M., Orejon, D., Dirker, J., Sefiane, K., & Meyer, J.P. (2023). Pressure and Thermal Characterisation of Dynamic Instabilities During Flow Boiling in Micro/Mini-channels at Different Azimuth Orientations. *Applied Thermal Engineering*, 218, 119292. doi: 10.1016/j.applthermaleng.2022.119292

[3] Hedau, G., Qadeer, M., Gulhane, N.P., Raj, R., & Saha, S.K. (2023). On the importance of fluidic manifold design and orientation on flow boiling instability in microchannel heat sinks. *International Journal of Heat and Mass Transfer*, 209, 124120. doi: 10.1016/j.ijheatmasstransfer.2023.124120

[4] Ahmadi, S., Hanafizadeh, P., Eraghubi, M., & Robinson, A.J. (2021). Upward flow boiling of HFE-7000 in high frequency AC electric fields. *International Journal of Thermofluids*, 10, 100076. doi: 10.1016/j.ijft.2021.100076

[5] Igaadi, A., El Amraoui, R., & El Mghari, H. (2023). CFD investigation on heat transfer improvement of subcooled flow boiling in a vertical upflow minichannel with straight and enhanced geometrical structure. *e-Prime - Advances in Electrical Engineering, Electronics and Energy*, 5, 100231. doi: 10.1016/j.prime.2023.100231

[6] Xiao, J., & Zhang, J. (2023). Experimental investigation on flow boiling bubble motion under ultrasonic field in vertical minichannel by using bubble tracking algorithm. *Ultrasonics Sonochemistry*, 95, 106365. doi: 10.1016/j.ultsonch.2023.106365

[7] Igaadi, A., El Amraoui, R., & El Mghari, H. (2024). Thermo-hydrodynamic investigation into the effects of minichannel configuration on the thermal performance of subcooled flow boiling. *Nuclear Engineering and Technology*, 56(1), 265–274. doi: 10.1016/j.net.2023.09.034

[8] Kaniowski, R., & Poniewski, M. (2013). Measurements of two-phase flow patterns and local void fraction in vertical rectangular minichannel. *Archives of Thermodynamics*, 34, 3–21. doi: 10.2478/aoter-2013-0007

[9] Pysz, M., & Mikielewicz, D. (2023). Flow boiling of R1233zd(E) in a 3 mm vertical tube at moderate and high reduced pressures. *Experimental Thermal and Fluid Science*, 147, 110964. doi: 10.1016/j.expthermflusci.2023.110964

[10] Bediako, E.G., Dančová, P., & Vít, T. (2022). Experimental Study of Horizontal Flow Boiling Heat Transfer Coefficient and Pressure Drop of R134a from Subcooled Liquid Region to Superheated Vapor Region. *Energies*, 15, 0681. doi: 10.3390/en15030681

[11] Sikora, M., & Bohdal, T. (2023). New environmentally friendly low-pressure refrigerants mini-channel. *Archives of Thermodynamics*, 44, 89–104. doi: 10.24425/ather.2023.145878

[12] Zhou, K., Coyle, C., Li, J., Buongiorno, J., & Li, W. (2017). Flow boiling in vertical narrow microchannels of different surface wettability characteristics. *International Journal of Heat and Mass Transfer*, 109, 103–114. doi: 10.1016/j.ijheatmasstransfer.2017.01.111

[13] Li, W., Zhou, K., Li, J., Feng, Z., & Zhu, H. (2018). Effects of heat flux, mass flux and two-phase inlet quality on flow boiling in a vertical superhydrophilic microchannel. *International Journal of Heat and Mass Transfer*, 119, 601–613. doi: 10.1016/j.ijheatmasstransfer.2017.11.145

[14] Cattani, L., Bozzoli, F., Ayel, V., Romestant, C., & Bertin, Y. (2023). Experimental estimation of the local heat transfer coefficient for thin liquid film evaporation in a capillary tube. *Applied Thermal Engineering*, 219, 119482. doi: 10.1016/j.applthermaleng.2022.119482

[15] Piasecka, M., Maciejewska, B., & Piasecki, A. (2023). Heat Transfer Calculations during Flow in Mini-Channels with Estimation of Temperature Uncertainty Measurements. *Energies*, 16, 1222. doi: 10.3390/en16031222

[16] Orman, Ł.J., Radek, N., Pietraszek, J., Wojtkowiak, J., & Szczepaniak, M. (2023). Laser Treatment of Surfaces for Pool Boiling Heat Transfer Enhancement. *Materials*, 16(4), 1365. doi: 10.3390/ma16041365

[17] Kaniowski, R., & Pastuszko, R. (2021). Boiling of FC-72 on surfaces with open copper microchannel. *Energies*, 14, 7283. doi: 10.3390/en14217283

[18] Bialek, A., Kargul ,M., & Stokowiec, K. (2023). Boiling heat transfer on porous single layer brass meshes. *Journal of Physics: Conference Series*, 2454, 012004. doi: 10.1088/1742-6596/2454/1/012004

[19] Bialek, A., & Stokowiec, K. (2023). Comparison of boiling heat transfer on heaters with mesh structure and microfins. *Journal of Physics: Conference Series*, 2454, 012005. doi. 10.1088/1742-6596/2454/1/012005

[20] Piasecka, M., & Maciejewska, B. (2015). Heat transfer coefficient during flow boiling in a minichannel at variable spatial orientation. *Experimental Thermal and Fluid Science*, 68, 459–467. doi. 10.1016/j.expthermflusci.2015.05.005

[21] Piasecka, M., Strąk, K., & Maciejewska, B. (2021). Heat transfer characteristics during flow along horizontal and vertical minichannels. *International Journal of Multiphase Flow*, 137, 103559. doi. 10.1016/j.ijmultiphaseflow.2021.103559

[22] Strąk, K., Piasecka, M., & Maciejewska, B. (2018). Spatial Orientation as a Factor in Flow Boiling Heat Transfer of Cooling Liquids in Enhanced Surface Minichannels. *International Journal of Heat and Mass Transfer*, 117, 375–387, doi: 10.1016/ j.ijheatmasstransfer.2017.10.019

[23] Piasecka, M., & Strąk, K. (2022). Boiling Heat Transfer during Flow in Vertical Mini-Channels with a Modified Heated Surface. *Energies*, 15, 7050. doi. 10.3390/en15197050

[24] Piasecka, M., Maciejewska, B., Michalski, D., Dadas, N., & Piasecki, A. (2024). Investigations of Flow Boiling in Mini-Channels: Heat Transfer Calculations with Temperature Uncertainty Analyses. *Energies*, 17, 791. doi. 10.3390/ en17040791

[25] Piasecka, M., Hożejowska, S., Maciejewska, B., & Pawińska, A. (2021). Time-dependent heat transfer calculations with Trefftz and Picard methods for flow boiling in a mini-channel heat sink. *Energies*, 14, 1832. doi. 10.3390/en14071832

Co-published by
Institute of Fluid-Flow Machinery
Polish Academy of Sciences
Committee on Thermodynamics and Combustion
Polish Academy of Sciences

Copyright©2024 by the Authors under licence CC BY 4.0

http://www.imp.gda.pl/archives-of-thermodynamics/

Pool boiling for water on surfaces with inclined microchannel

Robert Mikołaj Kaniowski[a*]

[a]Kielce University of Technology, Faculty of Mechatronics and Mechanical Engineering,
al. Tysiąclecia Państwa Polskiego 7, 25-314 Kielce, Poland
*Corresponding author email: kaniowski@tu.kielce.pl

Received: 19.12.2023; revised: 12.03.2024; accepted:09.05.2024

Abstract

The heat transfer measurements were conducted during pool boiling of water on surfaces with microchannels. Parallel grooves were made on a copper surface with widths ranging from 0.2 mm to 0.5 mm at intervals of 0.1 mm. The inclination angle of the grooves to the horizontal was set at 30° and 60°, and the depth of the microchannel grooves was 0.3 mm. The achieved heat flux ranged from 25 kW/m² to 1730 kW/m², and the heat transfer coefficients ranged from 12 kW/(m²K) to 475 kW/(m²K). The influence of geometric parameters such as width, inclination angle of the microchannel, surface extension, and Bond number on heat exchange efficiency was examined. A nearly sixfold increase in α (heat transfer coefficient) and a twofold increase in critical heat flux were observed compared to a smooth surface.

Keywords: Pool boiling; Inclined microchannel; Heat transfer coefficient; Critical heat flux

Vol. 45(2024), No. 2, 41–49; doi: 10.24425/ather.2024.150850

Cite this manuscript as: Kaniowski, R.M. (2024). Pool boiling for water on surfaces with inclined microchannel. *Archives of Thermodynamics*, 45(2), 41–49.

1. Introduction

The machinery employed in the power sector is engineered to function within a designated temperature range. To maintain optimal operating temperatures for its components, it is crucial to employ appropriate heat exchangers and heat spreaders. These devices utilize specialized surfaces to enhance both the heat transfer coefficient and the dissipation of heat flux. Leveraging the heat of vaporization during boiling facilitates the efficient removal of substantial heat loads while minimizing the required heat exchange surface. To meet criteria for lightweight design and device compatibility, dual-phase heat exchangers and dissipators are employed for effective heat dispersion [1]. These systems find applications in both industrial equipment and scientific test benches. There is also a growing interest in the development of miniature cooling technologies using passive methods such as boiling in closed devices, such as immersion cooling thermosyphons, pulsating heat pipes, and two-phase heat spreaders, etc. [2]. One of the most efficient and versatile methods of increasing the heat transfer coefficient and critical heat flux during boiling is the use of the appropriate fluid and surface type. Surface modifications can consist of texturing, perforation application, subsurface tunnel formation, porous layer coating, creation of metal foams, mesh, perforation, notching of small ribs or microchannels, etc. The two methods of creating surfaces with microchannels analysed in the publication [3], parallel and cross, demonstrated the influence of configuration on heat

Nomenclature

A – area, m^2
a – width of specimen, m
Bo – Bond number
b – angle, °
c_p – specific heat, J/(kg K)
d – diameter, m
g – gravitational acceleration, m/s^2
h – microchannel depth, m
i – enthalpy, kJ/kg
L – length, m
q – heat flux, W/m^2
p – pitch, m
Ra – roughness, μm
T – temperature, K
U – perimeter, m
u – velocity, m/s
w – width, m

Greek symbols

α – heat transfer coefficient, W/(m^2 K)
Δ – error, uncertainty
ΔT – superheat referred to the microfin base, K
δ – distance, m
φ – surface extension
λ – thermal conductivity, W/(m K)
ρ – density, kg/m^3
σ – surface tension, N/m
υ – kinematic viscosity, m^2/s

Subscripts and Superscripts

bs – base
Cu – copper
cap – capillary
cyl – cylinder
ext – extended
h – hydraulic
l – liquid
max – maximum
sat – saturated
$T1, ..., T8$ – thermocouple number
v – vapour

exchange efficiency. This study also examined the effect of material division and material proportions for the parallel configuration, and the effect of division for the cross configuration. The authors have demonstrated that the heat transfer performance is higher for surfaces with a fin arrangement in a cross-flow configuration compared to a parallel configuration.

One effective way to intensify heat transfer in boiling is to increase the number of nucleation sites and ensure their continuous operation [4]. Metals are suitable for this purpose, especially those with a high heat transfer coefficient and at a relatively low price [5]. Another way to improve the heat transfer coefficient is to use other coolants, i.e. water with added nanoparticles, water – Al_2O_3 or water – Cu, and to increase operating pressure [6]. Also being developed are enhanced industrial surfaces GEWA-B5, GEWA-KS, and EHPII coated with nanostructures, which have been described and examined in the work of Dickson et al. [7]. The studies [8,9] also examined how the spatial orientation of minichannels affects the boiling process when FC-72 coolant flows. The tested surfaces were made of Haynes-230 alloy. The following methods were used to develop the heat exchange surface: electro-machining texturing (erosion), laser surface texturing (laser), porous surface produced by soldering iron powder (porous), produced with the use of emery papers of varying roughness.

The subject of the research in the [10] paper by Khalaf-Allah et al. was water at atmospheric pressure on surfaces fabricated by multi-passive techniques. Experiments were conducted in a saturated pool boiling state for heat fluxes ranging from 50 to 580 kW/m^2. The results showed that a maximum improvement of 51–92% could be achieved with the composite surface compared to the smooth surface. Orman et al. [11] examined pool boiling on surfaces featuring microchannels created with lasers. They conducted experiments using water and ethanol under atmospheric pressure. The most effective results were observed on surfaces with microchannels characterized by greater depth and narrower dimensions. Zhang et al. in [12] conducted a heat transfer study on finned surfaces coated with a porous structure consisting of ball-shaped powder with a diameter of 380–550 μm. The boiling medium was water. The heat transfer coefficient decreased with the increase in microporous plate diameter, while it increased with the increase in thickness of the porous copper plate. The paper by Liang and Mudawar [13] presents the results of an experimental study of passive cooling for different types of heating surface modification techniques. One of the techniques used is the production of micro fins and microchannels. These areas have great potential due to the significant increase in CHF (critical heat flux) and the increase in the number of nucleation sites.

Surfaces subjected to micro-processing significantly improve the heat transfer efficiency during pool boiling. Liu et. al. [14] investigated the performance on five micro/nanostructured surfaces. For all structural surfaces, the results show an increase in the heat transfer coefficient. The critical heat flux and the heat transfer coefficient were increased to 60% and 331%, respectively. The authors in [15] experimentally investigated bistructural surfaces based on micro-pin-finned ribbing methods. Compared to smooth surfaces, dual-textured surfaces increased critical heat flow by more than 120%.

Gheitaghy et al. [16] investigated the boiling process of distilled water under atmospheric pressure. The study explores the impact of surface structuring using vertical, inclined, and orthogonal minichannels on pool boiling. The dimensions of inclined minichannels, varying from 0.5 mm to 1.4 mm, were systematically altered. In addition to augmenting the surface area, improvements in boiling performance were achieved by increasing minichannel depth and reducing pitch. Practical surface structuring of inclined minichannels was accomplished through the EDM (electrical discharge machining) method. The study

revealed a 2.7-fold increase in the heat transfer coefficient compared to a smooth surface and a 65% enhancement in critical heat flux.

The paper provides a concise summary of experimental results concerning heat exchange under pool boiling of water. The study aimed to identify the most favorable microchannel geometry to achieve the highest heat transfer coefficients and critical heat flux values.

2. Materials and methods

The experimental setup described in reference [17], as illustrated in Fig. 1, enabled the determination of boiling curves under increasing heat flux conditions. The research involved experimental investigations into heat transfer on inclined microchannels, covering the range from the onset of nucleate boiling (ONB) to the initial boiling crisis in pool boiling. All tests were conducted under atmospheric pressure.

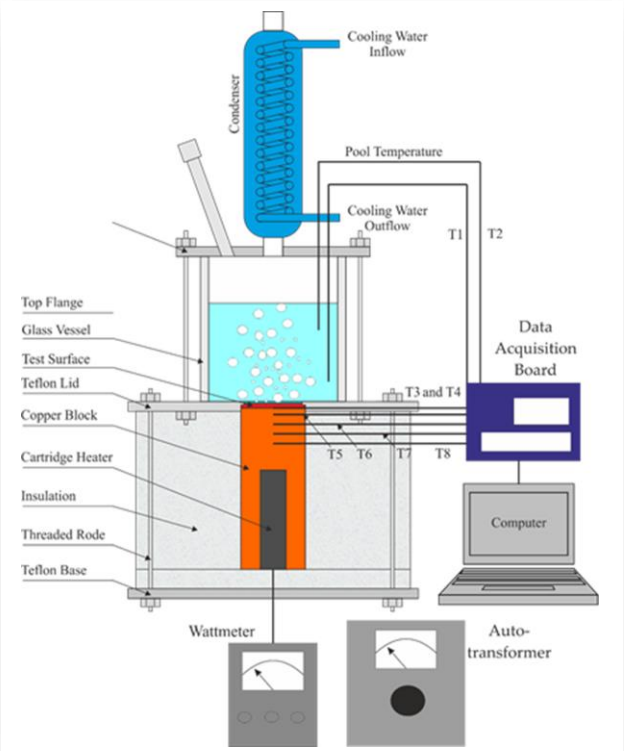


Fig. 1. Test stand diagram.

The measurement process commenced by initiating the water cooler to generate condensate from vaporized boiling water. Subsequently, the heating circuit was activated, and the fluid was heated until it reached the saturation state. This condition was maintained for the following 10 minutes (water degassing). Sequentially, the suitable electric voltages were applied to the autotransformer (simulating the desired heat flow value), and a waiting period of approximately 15 minutes ensued until the system achieved thermal equilibrium (temperature readings remained constant for the subsequent 5 minutes).

Data registration was carried out on the Fluke Hydra Series II 2635A data acquisition station (temperatures on the copper heating rod T3 to T8, liquid saturation temperatures T1 and T2). K-type thermocouples with a protective sheath and a diameter of 0.5 mm were employed for temperature measurements. Before conducting the measurements, calibration of the thermocouples was performed using an Altek 422 calibrator. The sensors underwent testing within the temperature range of 90°C to 300°C at intervals of 5°C. The absolute error of the thermocouple did not surpass 0.1 K.

In order to maintain consistency in experimental investigations and reduce errors associated with the determination of heat flow and heat transfer coefficient, the equation for one-dimensional heat conduction was utilized. The heating cylinder was insulated with a substantial layer, effectively preventing lateral heat transfer. Consequently, the calculations for heat flux adhere to the principles of Fourier's law:

$$q = \lambda_{\mathrm{Cu}} \frac{T_{T8}+T_{T5}}{\delta_{T8-T5}} \frac{\pi d_{cyl}^2}{4a^2}. \tag{1}$$

The distance between the thermocouples, as shown in Fig. 2, is $\delta_{T8\text{-}T5}$ = 35mm, the diameter of the copper cylinder d_{cyl} = 45 mm and the active side of the sample a = 37 mm. Thermal conductivity of copper adopted is 380 W/(m K).

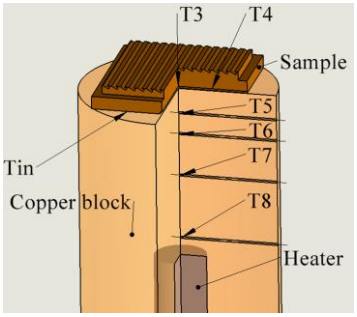


Fig. 2. Distribution of temperature sensors along the heating cylinder.

The heat transfer coefficient α between the surface with incised inclined microchannels and the fluid was determined from the relationship

$$\alpha = \frac{q}{\Delta T} \tag{2}$$

with the temperature difference determined, according to Figs. 1 and 2, as

$$\Delta T = \frac{T_{T3}+T_{T4}}{2} - q \frac{\delta_{bs}}{\lambda_{Cu}} \frac{T_{T1}+T_{T2}}{2}. \tag{3}$$

The distance between the base of the sample and the bottom of the microchannel δ_{bs} for each sample was different and was determined as shown in Fig. 3. It also shows the characteristic dimensions of the developed area.

Water provides the highest heat transfer coefficients and the highest critical heat fluxes. However, its saturation temperature, at atmospheric pressure, is high and cannot be used to directly cool certain components, e.g. microprocessors. This fluid can be used in demineralized form because otherwise there could be

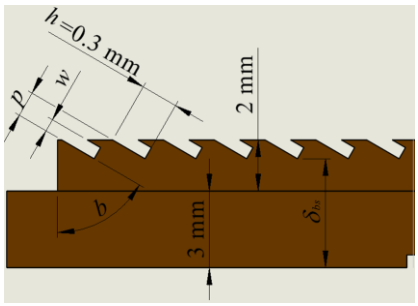


Fig. 3. Characteristic dimensions of the unfolded surface.

a likelihood of channel blockage by sediments. Physical properties of water in a saturated state, necessary for calculations, are presented in Table 1.

Table 1. Water properties.

Parameters under normal pressure	
T_{sat}, °C	100
ρ_l, kg/m³	959
ρ_v, kg/m³	0.597
i_{lv}, kJ/kg	2257
λ_l, W/(m·K)	0.68
σ_l, N/m	0.0589
μ_l, Pa·s	0.00028
c_{pl}, J/(kg K)	4220

The surfaces subjected to testing were constructed from copper, possessing a thermal conductivity of 380 W/(m K). The test specimens (Fig. 4) were surfaces with incised inclined microchannels and a reference smooth surface with a roughness of Ra = 0.12 µm. Incisions on the specimens were made with disc cutters with a width of w = 0.5 mm to 0.2 mm in 0.1 mm increments, to a depth of h = 0.3 mm (as shown in Fig. 3) and an angle to the vertical of b = 30° and 60°. Unfortunately, the technological process of producing the [18] surface results in slight deficiencies on the surface related to surface roughness and the fabrication of microchannels. All specimens were made with a similar face roughness of approximately 0.2 µm. Table 2 presents codes and specifications for the specimens.

Table 2. Specimen codes and specifications.

Specimen code	w, mm	h, mm	p, mm	b,°
M2.3-30	0.20	0.30	0.40	30
M3.3-30	0.30	0.30	0.60	30
M4.3-30	0.40	0.30	0.80	30
M5.3-30	0.50	0.30	1.00	30
M2.3-60	0.20	0.30	0.40	60
M3.3-60	0.30	0.30	0.60	60
M4.3-60	0.40	0.30	0.80	60
M5.3-60	0.50	0.30	1.00	60

Using a complete differential error, the uncertainty of the heat flux measurement was determined:

$$\Delta q = (A^2 + B^2 + C^2 + D^2 + E^2)^{0.5}, \tag{4}$$

whereas the individual components are equal to:

$$A = \frac{\partial q}{\partial \lambda}\Delta\lambda, \tag{4a}$$

$$B = \frac{\partial q}{\partial \Delta T_{T5-T8}}\Delta\left(\Delta T_{T5-T8}\right), \tag{4b}$$

$$C = \frac{\partial q}{\partial \Delta \delta_{T5-T8}}\Delta\delta_{T5-T8}, \tag{4c}$$

$$D = \frac{\partial q}{\partial d_{cyl}}\Delta d_{cyl}, \tag{4d}$$

$$E = \frac{\partial q}{\partial a}\Delta a. \tag{4e}$$

Here the thermal conductivity coefficient $\Delta\lambda$ = 1 W/(m K), the temperature difference in the heating cylinder and the wall superheat error are assumed to be 0.2 K, and length and diameter measurements $\Delta\delta_{T5\text{-}T8} = \Delta d_{cyl} = \Delta a = 2.5\times10^{-4}$ m (calipers for precision).

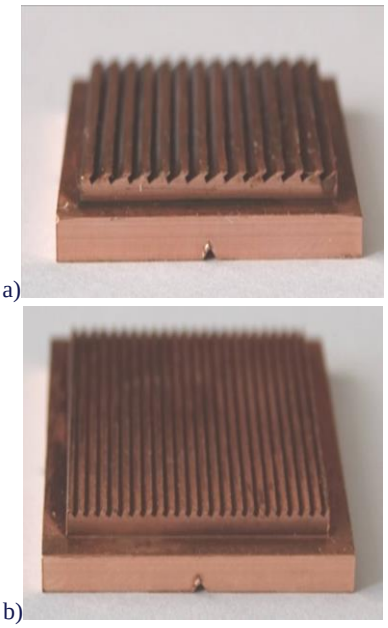


Fig. 4. Example surface images: a) M5.3-60, b) M5.3-30.

The relative error in the measurement of heat flux density between 25 kW/m² and 1730 kW/m² took values between 11.5% and 2.3%. In the analytical considerations, the thickness of the tin and the error associated with its conductivity have been ignored, due to the fact that their values are very small and do not affect the overall result. The largest measurement errors occur at low heat fluxes due to the gradient method of determining the heat flux density used, i.e. a significant absolute error in temperature measurement is generated at low superheats.

The absolute current of the heat transfer coefficient $\Delta\alpha$ was determined using the relationship

$$\Delta\alpha = \left[\left(\frac{\partial\alpha}{\partial q}\Delta q\right)^2 + \left(\frac{\partial\alpha}{\partial\Delta T}\Delta(\Delta T)\right)^2\right]^{0.5} \quad (5)$$

with the absolute error of overheating determined by the formula

$$\Delta(\Delta T) = \left[\left(\frac{\partial\Delta(\Delta T)}{\partial q}\Delta q\right)^2 + \left(\frac{\partial\Delta(\Delta T)}{\partial\Delta T_{sat}}\Delta(\Delta T_{sat})\right)^2 + \right.$$
$$\left. + \left(\frac{\partial\Delta(\Delta T)}{\partial\lambda}\Delta\lambda\right)^2 + \left(\frac{\partial\Delta(\Delta T)}{\partial\delta_{bs}}\Delta\delta_{bs}\right)^2\right]^{0.5}. \quad (6)$$

The outcomes and the procedure for identifying errors align with those outlined in Jaikumar and Kandlikar [19] as well as Kaniowski and Pastuszko [20]. The assessment involved estimating the relative error in determining the heat transfer coefficient, as influenced by the heat flux and superheat (refer to Eq. (5)). The relative error in determining the heat transfer coefficient, spanning from 12 kW/(m^2 K) to 475 kW/(m^2 K), varied between 5.4% and 36.2%.

3. Results and discussion

Experimental heat transfer studies were carried out for deionized water during bubble boiling on a smooth, flat surface and on surfaces with inclined microchannels at atmospheric pressure. Experiments were performed with increasing heat flux density. Heat transfer as a complex phenomenon during boiling in a large volume involves the following basic mechanisms: evaporation of the liquid microlayer, forced convection and heat conduction [21]. Figure 5 shows the boiling curves for all the surfaces analysed. An almost twofold increase in critical heat flux is evident for almost every surface. Only for a surface with a microchannel width of 0.2 mm is the critical heat flux higher by approx. 67% and for sample MC5.3-30 by approx. 44%.

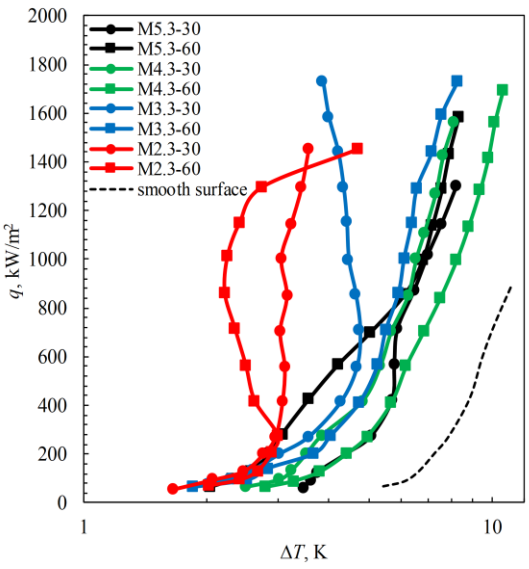


Fig. 5. Boiling curves for the analyzed surfaces.

The impact of the micro-groove's inclination angle relative to the vertical on the heat transfer process was examined. The most favorable outcomes were observed for surfaces with microchannels inclined at 60°, designated as M2.3-60. The heat transfer coefficient reached 475 kW/m^{2}K with a heat flux of 1146 kW/m^2 and a superheat of $\Delta T \approx 2.4$ K, as illustrated in Fig. 5. A notable 5.9-fold increase in the heat transfer coefficient was achieved compared to the smooth sample, as shown in Fig. 6. As the width of the microchannel increases, there is a discernible downward trend in the efficiency of heat transfer. The enhancement of the heat transfer mechanism for surfaces with microchannels occurs when the number of nucleation sites in the channels increases with a small temperature difference (overheating).

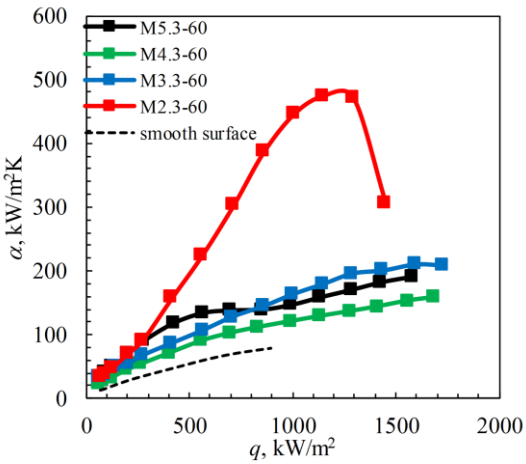


Fig. 6. Heat transfer coefficient vs. heat flux, b = 60°.

Among the various surfaces, those with microchannels featuring a width of 0.2 mm and an inclination angle of 60° demonstrated the highest efficiency. This could be attributed to the enlarged heat transfer surface area and the filling of microchannels by the boiling medium. It's worth noting that, in contrast, Gheitaghy et al. [16] achieved notably superior results for surfaces with channels inclined at 45° in their study. The heat transfer coefficient initially rises and then falls with the temperature difference, reaching a maximum corresponding to a change in slope in the boiling curve. This peak is a common occurrence in pool boiling with finned surfaces. This phenomenon is associated with the transition between two regimes of pool boiling. At low wall superheat, bubble columns form at specific nucleation sites, and their dynamics are independent of neighboring columns. Following the increase in wall temperature, the entire heated surface becomes involved in nucleation, leading to an increase in interaction between the bubble columns. Consequently, the likelihood of fresh fluid flowing to the heated finned surface decreases, resulting in a decrease in heat transfer [21,22].

The surfaces that have been examined combine various methods of enhancing heat transfer. One of the methods involves macroconvection during the flow of liquid and vapor through the microchannel. This leads to enhancements in critical

heat flux and heat transfer coefficients. Additionally, the surfaces feature finned walls that increase surface area, thereby intensifying liquid convection. This, in turn, enhances liquid evaporation and reduces wall overheating, ultimately facilitating improved heat transfer.

Microchannels with a width of 0.3 mm exhibit the highest critical heat flux values, approximately 93% greater than those of the smooth surface. However, their heat transfer coefficients vary significantly depending on the angle of the microchannels relative to the vertical.

From the 0.5 mm and 0.4 mm wide microsurfaces analysed experimentally, it is clear that the inclination of the microchannels does not matter, as the results of the heat transfer coefficients are almost identical. Only in the initial phase of the heat flux increase for a width of 0.5 mm, up to 700 kW/m^2, there is a 60% decrease in heat transfer coefficient to the detriment of a surface with a 30° inclination of the microchannels, Fig. 7.

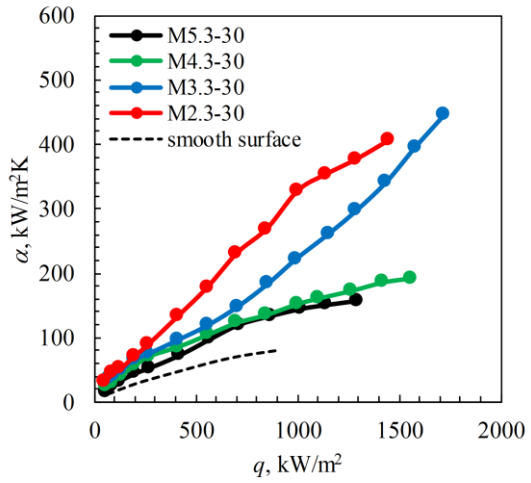


Fig. 7. Heat transfer coefficient vs. heat flux, b = 30°.

More boiling nucleation sites and a larger heat transfer surface area result in an increase in heat transfer coefficient and critical heat flux [23]. One of the parameters describing the surface is the surface extension:

$$\varphi = \frac{A_{\text{ext}}}{A_{\text{smooth}}} = \frac{2h+w\left[1-\tan(b)+\frac{1}{\cos(b)}\right]}{p}. \tag{7}$$

Another parameter is the Bond number, which involves a comparison between two forces: gravity and forces associated with surface tension. A high Bond number indicates the dominance of gravitational forces, while a low Bond number signifies the prevalence of surface tension forces. Below is the relationship for the Bond number [24]:

$$\text{Bo} = \frac{g\rho d_h^2}{\sigma} = \left(\frac{d_h}{L_{cap}}\right)^2, \tag{8}$$

where the hydraulic diameter is specified as

$$d_h = \frac{4A}{U} = \frac{2w[2h-w\tan(b)]}{2h+w\left[1-\tan(b)+\frac{1}{\cos(b)}\right]}, \tag{9}$$

while the capillary length is

$$L_{cap} = \sqrt{\frac{\sigma}{g(\rho_l-\rho_v)}}. \tag{10}$$

Table 3 shows the results of the surface extension, hydraulic diameter, and Bond number calculations. The geometric parameters in Table 1 were used to determine the hydraulic diameter. These values vary from 0.27 mm to 1.26 mm.

Table 3. Calculated values of surface and fluid properties.

Specimen code	φ	d_h, mm	Bo
M2.3-30	2.29	1.26	0.504
M3.3-30	1.79	1.02	0.408
M4.3-30	1.54	0.82	0.330
M5.3-30	1.39	0.66	0.262
M2.3-60	2.13	1.24	0.497
M3.3-60	1.63	0.91	0.362
M4.3-60	1.38	0.58	0.233
M5.3-60	1.23	0.27	0.108

Utilizing the outcomes of surface extension and Bond number computations, the features of critical heat flux and maximum heat transfer coefficients were established, as depicted in Figs. 8 and 9. In both microchannel angles, an initial rise in critical flux with an increase in surface area and Bond number, respectively, is evident, followed by a subsequent decline. This is not in line with the research carried out in [25]. In contrast, the effect of φ and Bo$^{0.5}$ on the heat transfer coefficient is consistent, Fig. 9. The capillary pressure in the space between the fins increases with increasing surface area, resulting in significant resistance to fluid flow in the microchannel and a reduction in critical heat flux. This affects the drying out of the spaces in the microchannel. The width and spacing of the microgrooves can also have a significant effect on heat transfer efficiency, as increasing the channel width affects the coalescence of vapour bubbles. The narrower the channel, the greater the potential for blister bonding at high heat flux [26].

The Reynolds number was determined because the boiling of the fluid causes it to be in motion in a confined space, which is the microchannel. This figure provides an estimate of the ratio of inertial to viscous forces occurring during fluid movement:

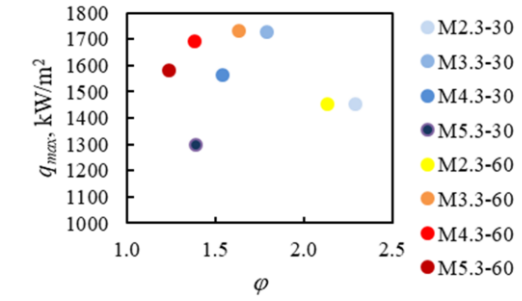
$$\text{Re} = \frac{uL_{cap}}{\upsilon_l}. \tag{11}$$

Assuming that all of the heat is dissipated by the latent heat of vaporization, the vapor velocity is

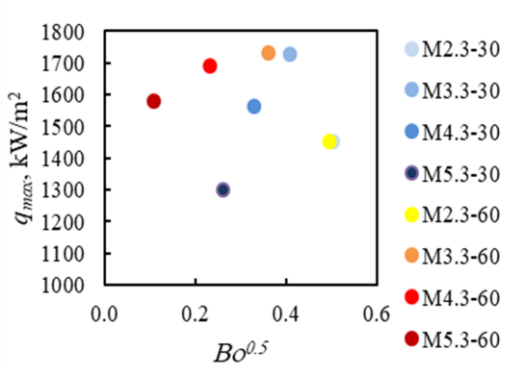
$$u = \frac{q}{i_{lv}\rho_v}. \tag{12}$$

Combining Eqs. (11)–(12) yields an expression for Re:

$$\text{Re} = \frac{qL_{cap}}{i_{lv}\rho_v\upsilon_l}. \tag{13}$$

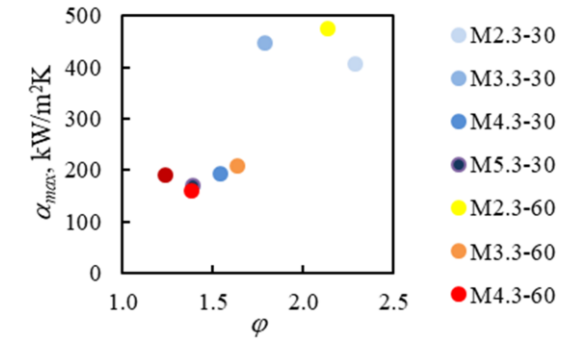


a)

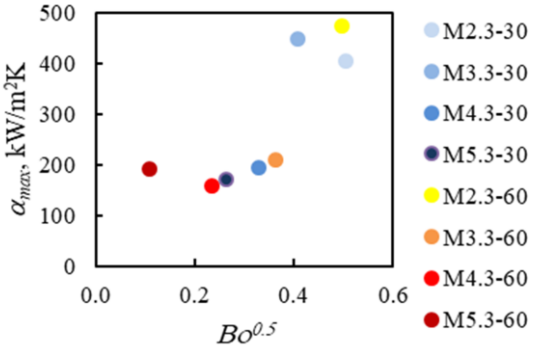


b)

Fig. 8. Variation of critical heat flux with
a) surface extension coefficient, b) $Bo^{0.5}$ for microchannel.



a)



b)

Fig. 9. Variation of heat transfer coefficient with
a) surface extension coefficient, b) $Bo^{0.5}$ for microchannel.

The effect of the Reynolds number on the maximum heat transfer coefficient is shown in Fig. 10. The fluid flows through the microchannels are not large, 8200 < Re < 11000, so the friction factor is large. This has implications for the effective flooding of the microchannel.

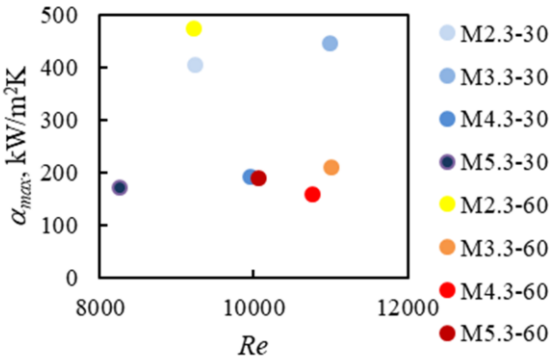


Fig. 10. Variation of heat transfer coefficient
with Reynolds number.

In order to obtain a benchmark for the heat transfer efficiency of the surfaces produced, a comparison is made with experimental studies reported in the literature for saturated pool boiling of water at atmospheric pressure. Figure 11 shows the boiling curves of other authors Gheiaghty et al. [16], Gouda et al. [26], Jaikumar and Kandlikar [19], Walunj and Sathyabhama [27], Zhang et al. [12], and the curve with the best heat transfer efficiency – surface M#2.3-60. The maximum heat flux results, especially for Jaikumar and Kandlikar [19], have almost twice the critical heat flux value, while the superheat values are significantly higher, which is unfavourable. This may be due to the specific and significant development of the surface (skewed microchannels, expansion of the surface).

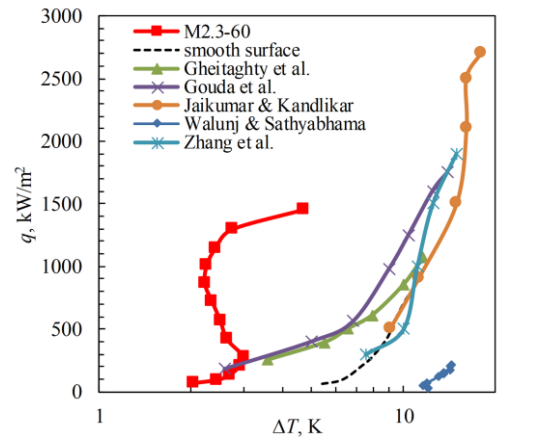


Fig. 11. Boiling curve comparison for other structures in literature.

6. Conclusions

Surfaces with microchannels provide higher heat transfer coefficients compared to smooth surfaces and are easy to produce consistently through subtractive manufacturing processes. The samples tested with microchannels exhibited a notable increase in heat transfer with the heat transfer coefficient dependent on both the angle of inclination to the horizontal and the width of the microchannel. The maximum observed heat flux reached 1730 kW/m^2, while the heat transfer coefficient was 475 kW/(m^2 K). In comparison to a smooth surface, the maximum heat flux nearly doubled, and the heat transfer coefficient was 5.9 times higher.

The largest heat transfer coefficients were achieved with the largest extensions of microchannel surfaces, specifically those with the narrowest microchannel widths. This characteristic contributed to the creation of a substantial number of active nucleation sites at the bottom and lateral surfaces of the microchannels. Comparing boiling curves highlighted the influence of microchannel width and angle on the boiling process.

Understanding the heat transfer coefficient and critical heat flow parameters is crucial in the development of heat spreaders, underscoring the importance of creating new surfaces and heat-receiving fluids.

Acknowledgements

The research reported in this article was partially supported by a grant from Poland's Minister of Education and Science through the Poland's Metrology Program [Polska Metrologia]. Grant Number: PM/SP/0031/2021/1.

References

[1] Liang, G., & Mudawar, I. (2018). Pool boiling critical heat flux (CHF) – Part 1: Review of mechanisms, models, and correlations. *International Journal of Heat and Mass Transfer*, 117, 1352–1367. doi: 10.1016/ j.ijheatmasstransfer.2017.09.134

[2] Moon, J.H., Fadda, D., Shin, D.H., Kim, J.S., Lee, J., & You, S.M. (2021). Boiling-driven, wickless, and orientation-independent thermal ground plane. *International Journal of Heat and Mass Transfer*, 167, 120817. doi: 10.1016/j.ijheatmasstransfer.2020.120817

[3] Chen, Z., Xie, T., & Utaka, Y. (2023). Enhanced critical heat flux in pool boiling applying the method of different-mode-interacting boiling for water. *International Journal of Heat and Mass Transfer*, 201, 123578. doi: 10.1016/j.ijheatmasstransfer.2022.123578

[4] Chuang, T.J., Chang, Y.H., & Ferng, Y.,M. (2019). Investigating effects of heating orientations on nucleate boiling heat transfer, bubble dynamics, and wall heat flux partition boiling model for pool boiling. *Applied Thermal Engineering*, 163, 114358. doi: 10.1016/j.applthermaleng.2019.114358

[5] Qu, Z.G., Xu, Z.G., Zhao, C., Y., & Tao, W.Q. (2012). Experimental Study of pool boiling heat transfer on horizontal metallic foam surface with crossing and single-directional V-shaped groove in saturated water. *International Journal of Multiphase Flow*, 41, 44–55. doi: 10.1016/j.ijmultiphaseflow.2011.12.007

[6] Cieśliński, J., & Kaczmarczyk, T. (2014). Pool boiling of nanofluids on rough and porous coated tubes: experimental and correlation. *Archives of Thermodynamics*, 35, 3–20. doi: 10.2478/aoter-2014-0010

[7] Dickson, D., Bock, B.D., & Thome, J.R. (2024). Heat transfer of uncoated and nanostructure coated commercially micro-enhanced refrigeration tubes under pool boiling conditions. *Applied Thermal Engineering*, 236, 121757. doi: 10.1016/j.applthermaleng.2023.121757

[8] Piasecka, M., Strąk, K., & Maciejewska, B. (2021). Heat transfer characteristics during flow along horizontal and vertical minichannels. *International Journal of Multiphase Flow*, 137, 103559. doi: 10.1016/j.ijmultiphaseflow.2021.103559

[9] Piasecka, M., & Strąk, K. (2022). Boiling heat transfer during flow in vertical mini-channels with a modified heated surface. *Energies*, 15, 7050. doi: 10.3390/en15197050

[10] Khalaf-Allah, R.A., Mohamed, S.M., Saeed, E., & Tolan, M. (2023). Augmentation of water pool boiling heat transfer using heating surfaces fabricated by multi passive techniques. *Applied Thermal Engineering*, 219, 119693. doi: 10.1016/j.applthermaleng.2022.119693

[11] Orman, Ł.J., Radek, N., Pietraszek, J., & Szczepaniak, M. (2020). Analysis of enhanced pool boiling heat transfer on laser-textured surfaces. *Energies*, 13, 1–19. doi: 10.3390/en13112700

[12] Zhang, K., Bai, L., Lin, G., Jin, H., & Wen, D. (2019). Experimental study on pool boiling in a porous artery structure. *Applied Thermal Engineering*, 149, 377–384. doi: 10.1016/j.applthermaleng.2018.12.089

[13] Liang, G., & Mudawar, I. (2019). Review of pool boiling enhance-ment by surface modification. *International Journal of Heat and Mass Transfer*, 128, 892–933. doi: 10.1016/j.ijheatmasstransfer.2018.09.026

[14] Liu, B., Cao, Z., Zhang, Y., Wu, Z., Pham, A., Wang, W., Yan, Z., Wei, J., & Sundén, B. (2018). Pool boiling heat transfer of N-pentane on micro/nanostructured surfaces. *International Journal of Thermal Sciences*, 130, 386–394. doi: 10.1016/j.ijthermalsci.2018.05.012

[15] Kong, X., Zhang, Y., & Wei, J. (2018) Experimental study of pool boiling heat transfer on novel bistructured surfaces based on micro-pin-finned structure. *Experimental Thermal and Fluid Science*, 91, 9–19. doi: 10.1016/j.expthermflusci.2017.09.021

[16] Gheitaghy, A.M., Samimi, A., & Saffari, H. (2017). Surface structuring with inclined minichannels for pool boiling improvement. *Applied Thermal Engineering*, 126, 892–902. doi: 10.1016/j.applthermaleng. 2017.07.200

[17] Kaniowski, R., & Pastuszko, R. (2023). Pool boiling experiment with Novec-649 in microchannels for heat flux prediction. *Experimental Thermal and Fluid Science*, 141, 110802. doi: 10.1016/j.expthermflusci. 2022.110802

[18] Skrzyniarz, M., Nowakowski, L., Miko, E., & Borkowski, K. (2021). Influence of relative displacement on surface roughness in longitudinal turning of X37CrMoV5-1 steel. *Materials*, 14, 1317. doi: 10.3390/ma14051317

[19] Jaikumar, A., & Kandlikar, S.G. (2016). Ultra-high pool boiling performance and effect of channel width with selectively coated open microchannels. *International Journal of Heat and Mass Transfer*, 95, 795–805. doi: 10.1016/j.ijheatmasstransfer.2015.12.061

[20] Kaniowski, R., & Pastuszko, R. (2021). Pool boiling of water on surfaces with open microchannels. *Energies*, 14, 3062. doi: 10.3390/en14113062

[21] Misale, M., & Bocanegra, J.A. (2023). Experiments and qualitative analysis by artificial neural network approach on pool boiling of FC-72 on finned surfaces confined by an unheated horizontal wall. *International Journal of Thermal Sciences*, 187, 108105. doi: 10.1016/j.ijthermalsci.2022.108105

[22] Rainey, K.N., & You, S.M. (2000). Pool boiling heat transfer from plain and microporous, square pin-finned surfaces in saturated FC-72. *Journal of Heat Transfer*, 122(3), 509–516. doi: 10.1115/1.1288708

[23] Kumar, U., Suresh, S., Thansekhar, M.R., & Babu, D. (2017). Effect of diameter of metal nanowires on pool boiling heat

transfer with FC-72. *Applied Surface Science*, 423, 509–520. doi: 10.1016/j.apsusc.2017.06.135

[24] Yu, C.K., & Lu, D.C. (2007). Pool boiling heat transfer on horizontal rectangular fin array in saturated FC-72. *International Journal of Heat and Mass Transfer*, 50, 3624–3637. doi: 10.1016/j.ijheatmasstransfer.2007.02. 003

[25] Cooke, D., & Kandlikar, S.G. (2012). Effect of open microchannel geometry on pool boiling enhancement. *International Journal of Heat and Mass Transfer*, 55, 1004–1013. doi: 10.1016/j.ijheatmasstransfer.2011.10. 010

[26] Gouda, R.K., Pathak, M., Khan, & Mohd., K. (2018). Pool boiling heat transfer enhancement with segmented finned microchannels structured surface. *International Journal of Heat and Mass Transfer*, 127, 39–50. doi: 10.1016/j.ijheatmasstransfer.2018.06.115

[27] Walunj, A., & Sathyabhama, A. (2018). Comparative study of pool boiling heat transfer from various microchannel geometries. *Applied Thermal Engineering*, 128, 672–683. doi: 10.1016/j.applthermaleng.2017.08.157

Co-published by
Institute of Fluid-Flow Machinery
Polish Academy of Sciences
Committee on Thermodynamics and Combustion
Polish Academy of Sciences

Copyright©2024 by the Authors under licence CC BY 4.0

http://www.imp.gda.pl/archives-of-thermodynamics/

Influence of thermodynamics on the development of technology and science

Jarosław Mikielewicz[a], Dariusz Mikielewicz[b*]

[a]Institute of Fluid Flow Machinery, Polish Academy of Sciences, 80-231 Gdańsk, ul. Fiszera 14
[b]Gdańsk University of Technology, 80-233 Gdańsk, ul. Narutowicza 11/12
*Corresponding author email: dmikiele@pg.gda.pl

Received: 26.11.2023; revised: 22.04.2024; accepted: 02.05.2024

Abstract

Understanding thermodynamics can be challenging due to its dealing with abstract concepts such as entropy and energy transfer. This paper outlines six principles of thermodynamics, whose application necessitates a coherent overarching philosophy. The problems studied often entail complex mathematical equations, relying on a strong foundation in physics and mathematics. Moreover, comprehending thermodynamics requires a shift in thinking, focusing on macroscopic properties of matter rather than microscopic interactions, as in other branches of physics. Thermodynamics also introduces a new philosophy in science – the concept of irreversible phenomena, rooted in the heat flow theory, which is currently being extrapolated to other scientific domains. Notably, this involves extending the concept of work to systems performing various types of work beyond volume change.

Keywords: Thermodynamics; Civilization; Energy; Entropy; Technology; Science

Vol. 45(2024), No. 2, 51–61; doi: 10.24425/ather.2024.150851

Cite this manuscript as: Mikielewicz, D., & Mikielewicz, J. (2024). Influence of thermodynamics on the development of technology and science. *Archives of Thermodynamics*, 45(2), 51–61.

1. Introduction

Thermodynamics, as a physical science, accounts for the transformations of energy in the form of thermal energy (heat) into mechanical energy and its equivalent forms (work, other forms of energy, and self-organization of complex systems) and vice versa.

The advancement of civilization is closely tied to the escalating demand for energy. The industrial revolution in England at the close of the 18th century was catalyzed, in part, by Watt's invention of the steam engine, leading to a rapid progression in technology and engineering. This invention facilitated the conversion of chemical energy from fuels into mechanical work, enabling the mass production of goods. Steam locomotives and ships revolutionized transportation, while steam turbines emerged in power plants, followed by gas turbines, facilitating convenient electricity production for various applications.

About half a century after the steam engine's inception, French scientist Sadi Carnot (1796-1832) [1] formulated the Second Law of Thermodynamics (II LT) in his theory of thermal machines. In 1859, French engineer Étienne Lenoir (1822–1900) [2] developed the first internal combustion engine, later improved by Nicolaus Otto in Germany. This development significantly contributed to the understanding of combustion and detonation theories. The rise of transportation driven by internal combustion engines, followed by aircraft engines, led to

Nomenclature

a – generalized displacement, m
e – unit total energy, J/kg
G – mass velocity, kg/(m^2 s)
G – Gibbs function, J
h – enthalpy, J/kg
H – total enthalpy, J
I – irreversibility, J
l – work, J
L – Onsager coefficients, total work, -, J
$\dot{L}$ – power, J/s
$\dot{m}$ – mass flux, kg/s
N – number of particles
p – pressure, probability of microstate, Pa, -
q – unit heat, J/kg
$\dot{q}$ – heat flux, W/m^2
Q – heat, J
$\dot{Q}$ – heat rate, J/s
R – individual gas constant, J/(kg K)
s – specific entropy, J/(kg K)
S – total entropy, J/K
$\dot{S}$ – rate of entropy, J/(s K)
T – temperature, K
u – internal energy, J/kg
v – specific volume, kg/m^3
V – volume, m^3
X – generalised force, N

Greek symbols

α – excitation
β – excitation
Δ – difference
ε – Casimir generalisation coefficients
η – thermal efficiency

Subscripts and Superscripts

C – Carnot cycle
e – change in entropy due to the import of matter from the environment
i – irreversibility of transformations in the system
in – heat input to the system
$isol$ – isolated system
k – kinetic energy
max – maximum
o – reversible process
p – potential energy
ref – reference state
1 – heat introduced to the system
2 – heat removed from the system

Abbreviations and Acronyms

I LT – First Law of Thermodynamics
II LT – Second Law of Thermodynamics

the migration of affluent individuals from urban centres to suburban areas.

The field of thermodynamics, which deals with the conversion of energy into work and heat, was born. Despite its name, it has little to do with dynamics. James Joule [3] was pivotal in establishing the equivalence of work and heat as forms of energy conversion and formulating the principle of energy conservation – the First Law of Thermodynamics (I LT), often referred to as Joule's principle.

This paper aims to introduce an expansion of the concept of work to include systems performing work beyond volume change, and the utilization of thermodynamic principles by modern science, particularly regarding the concept of irreversible states. Presented herein are examples from biology, information technology, and statistics, yet these examples still do not fully explore the capabilities of the tools developed in thermodynamics.

2. Classical thermodynamics in physics

Modern thermodynamics transcends being merely a theory of heat machines; it represents a new philosophical paradigm in physics. During the Renaissance era, phenomena were perceived as lacking a temporal direction, with physical laws assumed to be reversible. Pioneers like Galileo Galilei and Isaac Newton did not account for the asymmetry of process changes. Newtonian physics primarily focused on optics, mechanics, and electrostatics. However, by the late 18th and 19th centuries, the theory of heat gained prominence within physics, highlighting the interplay between thermal and mechanical energy. This gave rise to the field of thermodynamics [4-6], which primarily concerns the conversion of energy into work and heat.

Scientists soon realized that not all thermal energy could be entirely converted into mechanical energy, while the reverse conversion was relatively straightforward. Carnot, in his pursuit of maximizing thermal-to-mechanical energy conversion, identified a limit, later formulated by Clausius [7] as the Second Law of Thermodynamics (II LT). This law underscores the qualitative nature of energy, where although the total energy remains constant, its ability to perform work depends on energy parameters. Clausius introduced the concept of 'entropy,' defining it as the quotient of heat and temperature on an absolute scale. The increase in entropy within the universe delineates the direction of time's arrow, with heat and work serving as components of energy balance.

Classical physics and chemistry predominantly deal with closed systems (see Fig. 1), with equilibrium states being a key consideration. Equilibrium, characterized by uniform parameters across the system, is essential for thermodynamic analysis. A system, separated from the rest of the universe by a boundary, contains matter, while the surrounding environment comprises the rest of the universe.

Equilibrium processes, although idealized, do not naturally occur in nature, as systems tend to lose equilibrium during state transitions. However, for practical purposes, it suffices for states to reach equilibrium faster than the system transitions between states, ensuring a relaxation time shorter than the phenomenon's duration. Equations of state, distinguishing between thermal and caloric equations, relate extensive parameters such as specific volume to intensive parameters like pressure and temperature:

$$f(p, v, T) = 0. \tag{1}$$

The similar holds for the caloric equation of state. It can be represented as:

$$e(v,T) = 0, \tag{2}$$

or, using Eq. (1), in alternative forms:

$$e(p,T) = e(p,v) = 0, \tag{3}$$

where the total energy per kilogram substance reads as $e = E/m$ [kJ/kg], and specific volume $v = V/m$ [m^3/kg]. The parameters p, v, T are fundamental, easily measurable parameters.

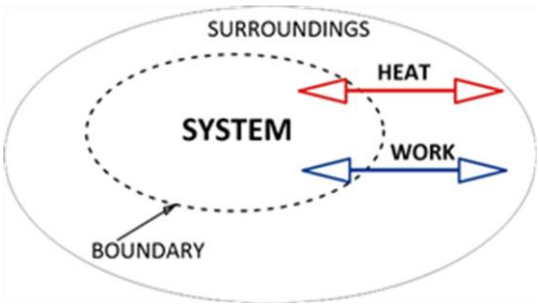


Fig. 1. The concept of a thermodynamic closed system.

Instead of the thermal and energy equations of state, a fundamental equation can be formulated, which contains all the information that the thermal and energy equations of state contain. The parameters of the fundamental equation are the natural equations resulting from the I LT. Let us analyse the internal energy function in intensive coordinates $u(s,v)$, for a simple compressible substance

$$e(p,T) = e(p,v) = 0. \tag{4}$$

From the differentiated version of Eq. (4), the thermal and caloric equation for the substance under consideration can be obtained

$$du = \left(\frac{\partial u}{\partial s}\right)_v ds + \left(\frac{\partial u}{\partial v}\right)_s dv\,. \tag{5}$$

In Eq. (5), comparing the first term on the right with the I LT notation gives the definition of temperature and the second term on the right has the dimension of pressure:

$$T = \left(\frac{\partial u}{\partial s}\right)_v = f_1(s,v), \tag{6}$$

$$p = -\left(\frac{\partial u}{\partial v}\right)_s = f_2(s,v)\,. \tag{7}$$

Eliminating the entropy s from the above relationships, one obtains the thermal equation of state $f(p,v,T) = 0$. Conversely, substituting into Eq. (4) the entropy value from either function f_1, eq. (6), or f_2 eq. (7), one obtains the caloric equation of state. The thermal and caloric equations of state can be encapsulated in a fundamental equation, which encompasses all pertinent information from these individual equations. This fundamental equation, often represented by the internal energy function $u(s,v)$ for a simple compressible substance, provides insights into both thermal and caloric equations of state. Additionally, it facilitates the derivation of other thermodynamic functions through Legendre transformations.

For a simple system, the equilibrium states, depicted in Fig. 2, are characterized by nodes on the state surface. These equilibrium transitions give rise to various processes, such as isochoric, isobaric, and isothermal processes, forming a thermodynamic cycle.

The laws governing thermodynamics are written as its principles. The I LT is the principle that formulates the energy balance valid for both reversible and irreversible transformations of parameters of the system (Accountant's Principle). The change in energy of a closed system is due to the work done and the heat transferred. For closed systems for which external energy changes during the transformation can be neglected, the I LT can be written in the form:

$$\delta q = du + \delta l, \tag{8}$$

where $\delta l = pdv$.

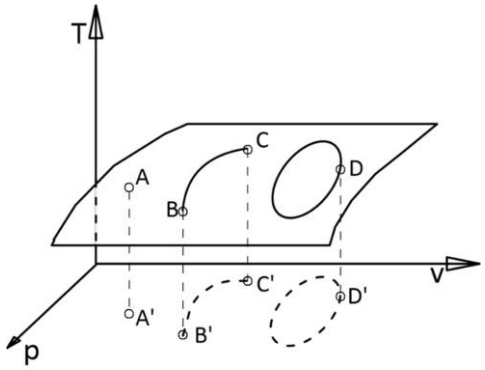


Fig. 2. Equilibrium surface of the state equation with state A, transformation B-C and cycle D-D marked on the surface.

I LT is sometimes referred to as the energy principle because it formulates the internal energy. In order to simplify thermodynamic calculations of thermal devices, another thermodynamic function, the enthalpy h, is introduced. This function was first introduced by Gibbs and reads:

$$h = u + pv. \tag{9}$$

Enthalpy is a function of state, similar as internal energy as well as the product pv. For an insulated system not interacting through heat and work with surroundings the balance of energy is constant. Such a system is called an isolated system with surroundings and would require insulation of the surroundings in Fig. 1. Such system is called an isolated system with surroundings and would require insulation of the surroundings in Fig.1. An isolated system, not being in equilibrium, always strives towards a state of equilibrium. This type of process is called a spontaneous process. The reversal of a spontaneous phenomenon is impossible. This is the most general formulation of the II LT (Principle of the Director), taking into account the existence of a privileged direction of transformation in nature, written mathematically using the entropy function.

Based on the First Law of Thermodynamics, it is always possible to convert work into heat. However, there are limitations

when converting heat into work. If this was not the case, we could build a heat machine that, by taking heat from the environment, would work while simultaneously cooling the environment. We do not observe such phenomena, and a heat machine that would carry out such a process is called a "perpetual motion machine of the first kind". A machine that uses one heat source - is a "perpetual motion machine of the second kind", which is also an unrealistic machine and its operation contradicts, as we shall show, the Second Law of Thermodynamics. A real machine is the one that uses two heat sources. All these machines are schematically illustrated in the p–v diagram in Fig. 3. According to the I LT, any transformation in which the energy principle is conserved can exist. As reality shows, such transformations cannot always be realized. The above example will suffice. There are very many such examples in life. There are unknown cases of people getting younger, for example, or of heat going spontaneously from a lower temperature to a higher one. In nature, there is a privileged direction in which transformations occur. For their analysis, the simple balance provided by the I LT is not sufficient. Such a balance is insensitive to the direction of occurrence of processes and balances even unreal processes.

Assume that the function we are looking for should increase as the spontaneous transformation in an isolated system approaches equilibrium, and for a reversible process, the attained state should reach a maximum. Such a system is the system together with its surroundings. There are no out-of-environment interactions and such a system is called isolated. The function sought, let us call it the function S, has the property that:

$$dS_{isol} \geq 0. \tag{10}$$

This function should be a thermodynamic potential, i.e. it should not depend on the type of transformation, but on the state. Such a function was found in 1850 by Clausius and he called it entropy. It is defined as:

$$dS \overset{\text{def}}{=\!\geq} \frac{\delta Q^o}{T}. \tag{11}$$

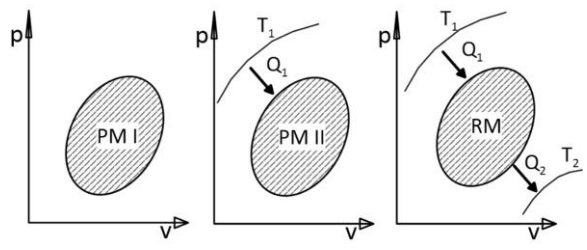


Fig. 3. a) Perpetual motion machine of the first type PMI, without heat source; b) Perpetual motion machine of the second type PMII, one heat source; (c) Real machine RM (two heat sources).

As is well known, δQ^o, the heat transferred by equilibrium transformation, is not a complete differential, whereas dS is already a complete differential, as can be demonstrated by thermodynamic analysis – the Carnot cycle, or by mathematical analysis – the search for an integrating factor for δQ^o (Carathéodory [8]). Entropy changes near zero temperature on the Kelvin scale are described by the Third Law of Thermodynamics.

For all isothermal transformations between two equilibrium states, the entropy changes tend towards zero as the temperature of the transformation goes to zero. It is convenient, but not necessary, to assume that the entropies of all components of the system are equal to zero, with the absolute temperature going to zero. This suggestion normalizes the entropies for $T = 0$, which was postulated by Planck (1911) [9]. It leads to a simple way of presenting entropy in thermodynamic tables.

Planck's Third Law of Thermodynamics (III LT) [10] ($s \to 0$ when $T \to 0$) leads to the conclusion that the dependent parameters, for example $x = x(T, s)$ behave as in Fig. 4. The figure shows that when $\Delta S \to 0$ and $T \to 0$, the process 1–2 from temperature T goes to 1'–2' at temperature T'. As shown earlier, there are relationships between the partial derivatives of the thermodynamic parameters. The III LT obviously affects the values of these derivatives.

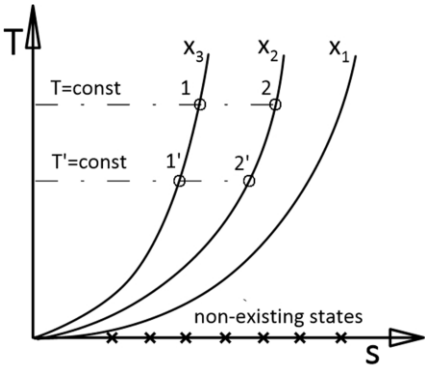


Fig. 4. The dependence of the parameters $x = x(T, s)$ near absolute zero.

Non-equilibrium processes close to equilibrium states are described by the thermodynamics of non-equilibrium processes, where the Onsager Principle is often regarded as the Fourth Law of Thermodynamics [11,12]. Onsager in 1931 [13] reported that for homogeneously linear independent excitations and homogeneously independent flows, the matrix of phenomenological coefficients is symmetric:

$$L_{ik} = L_{ki}. \tag{12}$$

Onsager's relation about the symmetry of the phenomenological coefficient matrix is a new fundamental assumption of the thermodynamics of irreversible processes and does not follow from previous assumptions of thermodynamics. Generalizations of the Onsager relation were given by Casimir [14]:

$$L_{ik} = \varepsilon_i \varepsilon_k L_{ki}, \tag{13}$$

where:

$\varepsilon_i = +1$ – for α type excitations,

$\varepsilon_i = -1$ – for β type excitations.

Parameters of type: α that determine the state of the adiabatic system are even functions of particle velocity, e.g. energy and

concentration, while parameters of type: β are odd functions of particle velocity, e.g. momentum density. Ultimately, therefore:

$$L_{ik} = L_{ki}, \quad \text{when } X_i \text{ and } X_k \text{ are at the same time of } \alpha \text{ or } \beta \text{ type,}$$
$$L_{ik} = -L_{ki}, \quad \text{when } X_i \text{ and } X_k \text{ are of different sign.} \tag{14}$$

Thermodynamics is not limited only to compressible systems such as fluids, which can do the work of volume change. It also applies to other systems such as simple magnetic substances, electrostatic substances, surface membranes, elastic systems (solids), etc. Systems that perform several types of work are called complex systems. Complex systems are described by more parameters than simple systems, namely at least three. The number of parameters describing complex systems is determined by the Principle of State often referred to in the Anglo-Saxon literature as the Minus First Law of Thermodynamics (–I LT).

In general, for a complex substance, it can be written:

$$du = \delta q - \sum_1^k X_k a_k, \tag{15}$$

where: δq – unit heat, X_k – general forces, a_k – generalized displacement, k – number of ways in which work is performed.

The state description of the system requires (k+l) intensive parameters. This follows from the following reasoning: k ways of performing work require k "forces" – intensive parameters, in addition, since $\delta q = Tds$ the intensive parameter is temperature. Thus, (k+1) intensive parameters are needed to describe one extensive quantity.

3. Application of the thermodynamics principles to technology

The principles of thermodynamics allow many technical problems to be solved. Classical thermodynamics does not use a coordinate system, as it deals with equilibrium states in which the intensive parameters (temperature field, pressure field, concentration field) are equalized throughout the volume. Additionally, time does not feature in thermodynamics, due to the fact that it deals with states that have reached equilibrium and is not interested in how long it took for this equilibrium to occur. An important element of thermodynamic analysis is the choice of a system. The classical system is a closed system – associated with a constant and the same number of molecules. For it, the fundamental laws of nature are formulated that energy is constant and entropy changes for irreversible processes are greater than zero. The concept of a closed system is extended in engineering thermodynamics to that of an open system. In an open system, there is a flow of matter causing changes in energy and entropy, Fig. 5.

In thermal power plants, there is a chain of energy conversion: from chemical energy through heat, mechanical energy to electrical energy. The efficiency of a particular process is the ratio of the desired type of energy at the output to the energy at the input. It depends on the physical and chemical laws governing the process.

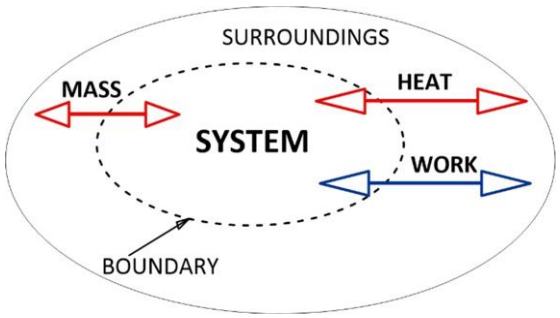


Fig. 5. The open system (control volume).

Since the formulation of the reversible Carnot cycle, many other reversible cycles have been proposed which are modifications of the ideal Carnot cycle that cannot be realized in practice. The Carnot cycle in a T-s system can be represented by two isothermal processes with constant temperatures T_1 and T_2 and two adiabatic processes with constant entropies S_1 and S_2, Fig. 6. The heat extracted from source one is:

$$Q_1 = T_1(S_2 - S_1). \tag{16}$$

On the other hand, rejecting heat to the second heat source yields

$$Q_2 = T_2(S_2 - S_1). \tag{17}$$

Work done during the cycle

$$L = Q_1 - Q_2 = (T_1 - T_2)(S_2 - S_1) \tag{18}$$

is equal to the shaded area in Fig. 6. Defining the cycle efficiency as:

$$\eta = \frac{Q_1 - Q_2}{Q_1} = \frac{L}{Q_1}, \tag{19}$$

we obtain

$$\eta_C = \frac{T_1 - T_2}{T_1}. \tag{20}$$

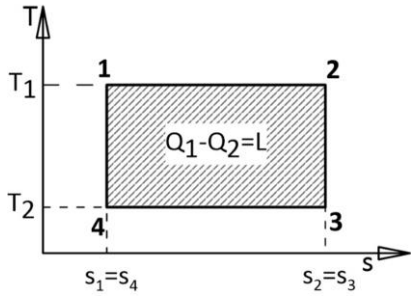


Fig. 6. Carnot cycle in a T-s diagram.

The Carnot cycle is a reversible cycle and therefore has the highest efficiency in a given temperature range. The efficiency of the Carnot cycle does not depend on the properties of the working fluid, but on the temperatures of the heat sources. It can serve as a thermometer. By defining a reference temperature, for example the triple point of water T_2=273.16 K, the temperature

T_1 can be measured by measuring the heat, as stems from Eq. (19). In practice, no such measuring instruments are built, hence the temperature defined by the Carnot cycle is called thermodynamic. Any reversible cycle can be thought of as a composition of infinitely many elementary Carnot cycles, as shown in Fig. 7. Such a cycle can be realized with an infinite number of heat sources at different temperatures. Many of these are so-called comparative cycles, i.e. sets of transformations that replicate the actual processes in thermal machines. Determining the efficiency of a device in which energy is converted requires the application of not only the first, but also the second law of thermodynamics, since the conversion of any kind of energy always leads to the conversion of part of it into heat, resulting in a consequent change in the entropy of the system.

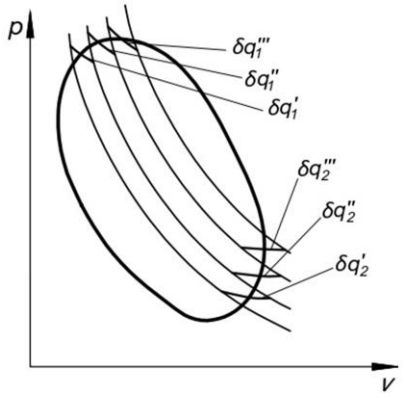


Fig. 7. The cycle decomposed into elementary Carnot cycles.

The ability to do work is a measure of the quality of energy. The reference level of this measure is the environment, whose capacity to do the work is zero. A measure of energy quality based on the entropy function has been called exergy assuming $\dot{m}_{in}= \dot{m}_{out}= \dot{m}$ (steady-state) and $e= h+e_k+e_p$:

$$\dot{L} = \dot{Q}_{in} - \dot{Q}_{out} + \dot{m}(e_{in} - e_{out}). \tag{21}$$

The second law of thermodynamics (II LT) related to the environment can be written in the following form:

$$\dot{S} = \frac{dS}{d\tau} = \frac{\dot{Q}_{out}}{T_{ref}} - \frac{\dot{Q}_{in}}{T} + \dot{m}(s_{out} - s_{in}) \geq 0, \tag{22}$$

or eliminating $\dot{Q}_{out}$ by means of relation (21) as:

$$\begin{gathered}\dot{S}T_{ref} = \dot{Q}_{in}\left(1 - \frac{T_{ref}}{T}\right) + \\ +\dot{m}\left[(e_{in} - e_{out}) - T_{ref}(s_{in} - s_{out})\right] - \dot{L} \geq 0.\end{gathered} \tag{23}$$

Formula (23) gives the expression for the maximum work of the system equal to:

$$\begin{gathered}\dot{L}_{max} = \dot{Q}_{in}\left(1 - \frac{T_{ref}}{T}\right) + \\ +\dot{m}\left[(e_{in} - e_{out}) - T_{ref}(s_{in} - s_{out})\right].\end{gathered} \tag{24}$$

In the case of a closed system ($\dot{m} = 0$), $\dot{L}_{max}$ yields:

$$\dot{L}_{max} = \dot{Q}_{in}\left(1 - \frac{T_{ref}}{T}\right), \tag{25}$$

which is the same as work obtained in the Carnot cycle, as $\eta_c = 1 - \frac{T_{ref}}{T}$. When heat is converted into work in a system, the formula for the efficiency of such a process (defined using I LT) is of the form:

$$\eta^{I\,LT} = \frac{\dot{L}}{\dot{Q}_{in}+\dot{m}e_{in}}. \tag{26}$$

For the closed system, i.e. when $\dot{m} = 0$, the efficiency yields:

$$\eta^{I\,LT} = \frac{\dot{L}}{\dot{Q}_{in}}, \tag{27}$$

where:

$$\dot{L} = \dot{Q}_{in} - \dot{Q}_{out}. \tag{28}$$

Another definition of efficiency, which takes into account the "quality" of energy, is derived from II LT. This approach also takes into account entropy changes, i.e. the irreversibility of the process, which results in work $\dot{L}$ instead of work $\dot{L}_{max}$ being obtained in the cycle. The efficiency calculated in this way is:

$$\eta^{II\,LT} = \frac{\dot{L}}{\dot{L}_{max}}, \tag{29}$$

where $\dot{L}$ is given by Eq. (21), whereas $\dot{L}_{max}$ by Eq. (24). The difference

$$\dot{L}_{max} - \dot{L} = \dot{S}T_{ref} = \dot{I} \tag{30}$$

is the work loss $\dot{I}$ resulting from the irreversibility of the process. In the case $\dot{m} = 0$, Eq. (26) assumes a form:

$$\eta^{II\,LT} = \frac{\dot{Q}_{in}-\dot{Q}_{out}}{\dot{Q}_{in}\left(1-\frac{T_{ref}}{T}\right)} = \frac{\eta}{\eta_c}, \tag{31}$$

where η_c denotes the Carnot efficiency, that is a maximum attainable value.

Heat engines, the subject of interest in engineering thermodynamics, convert thermal energy resulting from the conversion of the chemical energy of fuels such as coal, oil, gas (combustion) into mechanical work. Fissile materials such as uranium in a nuclear reactor are also used as fuel to produce thermal energy, which in turn is used in thermal machines to produce work (electricity). The efficient use of fossil fuels is necessary and has recently been curtailed due to their limited resources and harmful emissions during combustion. Hence, there has been a recent preference to use 'clean' energy sources, i.e. wind, solar, water and geothermal deposits, as much as possible. These are so-called renewable sources.

A consequence of II LT is that heat goes from a body with a higher temperature to a body with a lower temperature. The greater the difference, the more intensively the heat is transported, but in turn, the efficiency of the conversion of heat energy into work in the case of a thermodynamic cycle decreases. The problem of heat transfer between systems is dealt with by a branch of engineering thermodynamics called heat transfer. Thermodynamics does not analyse the rate of heat energy transfer. That is what heat transfer deals with. In technology, there are processes in which the heat transfer process must be intensified, in order to obtain small heat exchange surfaces, which in turn lead to small dimensions of the heat exchange devices exe-

cuting a thermodynamic cycle. There are also processes that require the reduction or isolation of the heat exchange process, e.g. the insulation of district heating pipelines or the thermal insulation of residential buildings. These two types of processes require knowledge of heat transfer theory. The science of heat transfer is developing on the basis of various industries. One can mention power engineering (heat-to-work conversion problems), chemical engineering, refrigeration, etc. Today, it is difficult to identify processes or phenomena in which heat transfer problems do not occur. The development of the field of heat exchange has been dictated by the development of the leading technologies of civilization. Hence, heat exchange initially developed on the basis of power engineering, and more recently it has developed on the basis of nuclear power and electronics. The cooling of electronic microelements is a challenge for modern heat exchange. Current science and technology is interested in open systems. Apart from technology, open systems are found in biology, medicine, economics, sociology, history, etc. in a closed system, entropy can increase and the system possibly reaches equilibrium. In an open system, the system can reach a steady state with a continuous flow of entropy. An open system is, for example, a living organism, where entropy decreases due to the import of matter along with energy from the environment. The total entropy of living organisms is decreasing, but this does not imply incompatibility with II LT, in light of the above comments.

4. Role of thermodynamics in modern science

Currently, science and technology are interested in the analysis of open systems, which, apart from technology, are found in biology, medicine, economics, sociology, history, etc.

In a closed system, entropy can increase until the system possibly reaches equilibrium. In an open system, on the other hand, the system may reach a steady state with continuous entropy production. A broader definition of energy is "the ability to drive a system transformation", which clearly includes all kinds of physical and biological processes.

For systems close to equilibrium, entropy strives to reach a minimum of entropy production. Far-from-equilibrium states undergo an evolution to organize a new order. The environment cannot control such transformations. Systems far from equilibrium are strongly non-linear and seek to minimize free energy and maximize entropy. They amplify the amplitude of disturbances and evolve towards new states [15–17].

The II LT for an open system was formulated by Prigogine (1972) [18]. An example of an open system is, for example, a living organism. In living organisms, entropy decreases due to the import of matter together with energy from the environment.

Biological, sociological and economic systems are complex systems and are subject to evolution in a certain direction just like physical systems, they are characterized by the direction of change determined by II LT [19–22]. The complexity of these systems increases with time. Matter flowing through these systems leads to their self-organization and increase in complexity, which confirms that we are dealing with dissipative systems because, in addition to the import of matter and energy, their entropy is generated and dissipated internally.

Statistical entropy is a measure of disorder. Information is a negative entropy and reduces the total entropy in these systems. An irreversible process is the process of changing a microscopic state from a less probable to a more probable state. It does not follow from the statistical formulation of II LT that perpetual motion machines of the second kind do not exist, they are simply unlikely. Systems consume negative entropy or information, but not energy. Generating entropy means consuming negative entropy. This corresponds to the destruction of information or micro-information, which is related to macro-information in communication theory. In science, three different aspects of the entropy concept introduced in the 19th century by Carnot and Clausius can be distinguished:

- the phenomenological aspect with its thermal nature;
- the statistical aspect as a measure of disorder according to Boltzmann, which is a kind of molecular thermal theory of heat; and
- the informational aspect concerning information content according to Shannon, which is part of communication theory.

Many researchers believe that these three formulations are equivalent. This conclusion was first reached by L.M. Brillouin [23] and more recently by J. Peters [24]. This opens up new possibilities for applications of thermodynamics in the areas of medicine, history, social processes, etc.

The first thermal aspect of entropy has already been presented. Let us consider the next ones.

4.1. Statistical entropy

Boltzmann gives entropy as a measure of the disorder of the molecules that make up a system, which can be written as:

$$S = k \sum_i p_i \ln(p_i), \tag{32}$$

where k is the Boltzmann constant of 1.38×10^{-23} J/K, which is an entropy dimension. The symbol p_i denotes the probability of a microstate. A microstate of the system is a description of the positions and momenta of all its particles. The large number of particles of the gas provides an infinite number of possible microstates for the sample, but collectively they exhibit a well-defined average of configuration, which is exhibited as the macrostate of the system, to which each individual microstate contribution is negligibly small. For the entropy of the system, the contribution of all degrees of freedom is summed. The total energy of the degrees of freedom is equal to $E=kT$ and acts as a constraint on the probability p_i. At low temperatures, some degrees of freedom are frozen and do not contribute to the energy. At zero temperature on the absolute scale, all degrees of freedom have probabilities equal to one or zero and then the entropy value $S=0$ is obtained, according to the third law of thermodynamics.

The distinction between the microstate of a molecule and the degrees of freedom of a system is important from the point of view of information theory. One can then speak of the entropy of the individual degrees of freedom.

4.2. Theory of information

Information, according to Shannon, is the message content of a signal [25]. Each signal occupies a position in the message and can take several discrete values, each with probability p_i, where p_i takes values from 1 to m. The information transported by a given signal i is equal to $\log_2 p_i$. The logarithm at base two is chosen because it gives a unit of information called a bite with 50% probability. The average proportion of information in a message is equal to $p_i \log_2 p_i$. A message is the sum of all possible information:

$$S = -\sum_{i=1}^{m} p_i \log_2(p_i). \tag{33}$$

In binary symbolism $m = 2$ and $p = p_1$ or $p = 1 - p_1$.

Statistical entropy refers to disorder and information reduces it by introducing order. Let us distinguish between micro-information and macro-information. Microinformation corresponds to the individual degrees of freedom of a system, while macroinformation corresponds to macroscopic signals, each consisting of many molecules and their degrees of freedom. Hence, macroinformation is equal to statistical entropy because it distinguishes the values of each degree of freedom.

The information transmitted is defined as the difference between the sum of all possible signals before and after the information is received. Suppose an item's memory has 1024 responses with equal probability p_i=1/1024 for each response before the message. Then the information before the message is equal to 10. After the information is received, only one signal is certain and the others have a probability equal to zero. Then, the message received is 10-bit.

4.3. Equivalence of information, statistical and thermal entropy

The relations (32) and (33) differ only in sign and in the constant k ln2 resulting from the substitution of the logarithm base. As mentioned earlier, statistical entropy is a measure of 'disorder' and information entropy reduces this 'disorder'. The flow of information about the complexity of a system is therefore a flow of negative entropy. The equivalence of thermal and statistical entropy can also be demonstrated based on the perfect gas model.

Consider the irreversible process of expansion of a perfect gas into a vacuum. Because the environment is a vacuum, the system does not work (no back pressure). The system as a whole is insulated, so it does not change energy or temperature.

For an isothermal transformation, there is

$$\Delta L = p\Delta V = \Delta Q, \tag{34}$$

and therefore the entropy change is

$$\Delta S = \frac{\Delta Q}{T} = \frac{p\,\Delta V}{T}. \tag{35}$$

Using the equation of state for a perfect gas, one obtains:

$$\Delta S = R\frac{\Delta V}{V}. \tag{36}$$

Let us consider the same transformation from the microscopic side. The probability of finding a molecule in the original volume equal to V_1 is:

$$p = \frac{V_1}{V_2}, \tag{37}$$

where: V_2 is the final volume of the transformation. The probability of finding N particles in the original volume V_1 is even smaller and, due to the independence of events, is:

$$p_N = \left(\frac{V_1}{V_2}\right)^N. \tag{38}$$

Let us logarithmise this relationship:

$$\ln p_N = N \ln \frac{V_1}{V_2}. \tag{39}$$

Assume that V_2 is a little different from V_1, i.e. that V_2=V_1+ΔV, then:

$$\frac{V_1}{V_2} = 1 - \frac{\Delta V}{V_2}. \tag{40}$$

When the logarithm is expanded into a series, the result is:

$$\ln \frac{V_1}{V_2} = \ln\left(1 - \frac{\Delta V}{V}\right) \approx -\frac{\Delta V}{V}, \tag{41}$$

and then

$$\ln p_N = -N\frac{\Delta V}{V}. \tag{42}$$

Comparing with the entropy change relationship (35), one obtains:

$$\Delta S = -\frac{R}{N} \ln p_N\,. \tag{43}$$

Thus, there is a relationship between thermal entropy and the probability of a particular state of the molecules occurring. An irreversible process is a transition from a less probable microscopic state to a more probable one. It does not follow from the statistical formulation of II LT that a perpetual motion machine of the second kind is impossible. It is only very unlikely. It is unlikely that the gas will concentrate back into the original volume, and it is even less likely that the process will repeat itself cyclically.

Classical physics and chemistry consider closed systems. Current science and technology is interested in open systems. As mentioned earlier, such open systems outside of technology are found in biology, medicine, economics, sociology, history, etc. In a closed system, entropy can increase and the system possibly reaches equilibrium. In an open system, the system may reach a steady state with a continuous flow of energy. The change in entropy, in an open system, is expressed by the relation:

$$\Delta S = \Delta S_i + \Delta S_e. \tag{44}$$

In Eq. (44), ΔS_e is the change in entropy due to the import of energy in the form of a matter from the environment, and ΔS_i – the increase in entropy due to the irreversibility of the transformations taking place in the system. ΔS_i is always posi-

tive, while ΔS_e can be both positive or negative. Hence, it follows that the entropy of a system can decrease. In living organisms, entropy decreases due to the import of matter along with energy from the environment in the form of food. Although in living organisms the total entropy is decreasing, this does not mean, in the light of the above remarks, that this is incompatible with II LT.

The classical idea of thermodynamics (Second Law of Thermodynamics) assumes an increasing disorder in an isolated system and is in opposition to evolution (self-organization). This applies to closed systems. Biological systems are open systems. They are capable of building complex structures while being fed with "negative entropy" – information. Energy from one form is transformed into another form. Plants transform light into chemical energy. In the muscles of animals and humans, chemical energy is converted into mechanical energy. None of these conversions takes place without loss. Some energy is lost as heat. All biological and chemical processes are accompanied by a dispersion of energy in the form of heat. Heat is associated with a decrease in 'order' in the system. The measure of 'order' in a system is entropy. Higher entropy means greater 'disorder' in the system. As already mentioned in an isolated or isolated system, an increase in entropy is assumed to yield the Second Principle of Thermodynamics.

Irreversible processes that exist in any mechanical system, biological system, economic system, etc. depend on the nature of the sources and sinks of energy. These cause an increase in entropy in the system. For an open system, there is also the exchange of entropy with the environment. Any flow of energy from a source at temperature T_1 to a sink at temperature T_2 is constrained by the Carnot relation for irreversible processes:

$$\frac{Q_2}{T_2} - \frac{Q_1}{T_1} \geq 0, \tag{45}$$

where Q_1 is the heat entering the system and Q_2 is the heat leaving the system. The heat flow through the system must be caused by a temperature gradient. Inserting (45) into (44) we get:

$$\Delta S = \Delta S_i + \frac{Q_1}{T_1} - \frac{Q_2}{T_2}. \tag{46}$$

According to Eq. (45), the difference in heats in (46) is negative.

Relationship (45) satisfies the necessary condition for the self-organization of a system associated with evolution, as it shows that a system can reduce its entropy through energy flow. If the system does work (living organisms – fauna) then:

$$L = Q_1 - Q_2, \tag{47}$$

and the resultant change in entropy yields:

$$\Delta S = \Delta S_i + \frac{Q_1}{T_1} - \frac{Q_2}{T_2} + \frac{L}{T_2} = \Delta S_i + \frac{L}{T_2} - Q_1 \frac{T_1 - T_2}{T_1 T_2}. \tag{48}$$

The last term in Eq. (48) is negative which causes the entropy to decrease by energy flow. The same is true if the system only builds up its chemical potential through energy flow (flora). In that case:

$$\Delta H = Q_1 - Q_2, \tag{49}$$

$$\Delta S = \Delta S_i + \frac{\Delta H}{T_2} - Q_1 \frac{T_1 - T_2}{T_1 T_2}. \tag{50}$$

The useful energy potential for biological systems is the Gibbs free energy potential:

$$\Delta G = \Delta H - T\Delta S \tag{49}$$

or

$$\Delta H = \Delta G + T\Delta S. \tag{50}$$

The flow of energy and the associated flow of information through open systems such as biological systems is the thermodynamic explanation for the generation of their complexity and evolution. Evolution in biology is characterised by a concentration of thermodynamic potential and a race between energy dispersion and information flow.

Classical thermodynamics operates with systems at or near equilibrium. A new category of complex systems is in non-equilibrium states. Classical systems tend towards equilibrium, i.e. towards disordered states of matter, while complex systems evolve towards order. For systems close to equilibrium, entropy production tends towards a minimum. States far from equilibrium undergo evolution by organizing a new order. The environment is unable to control such transformations. Systems far from equilibrium are strongly non-linear and tend towards a free energy minimization and entropy maximum. They amplify the amplitude of disturbances and evolve towards new states.

Biological, sociological economic systems are complex and evolve in a specific direction. It can be thought that, as in physical systems, there is a time arrow in them defined by the Second Principle of Thermodynamics. Over time, the complexity of these systems increases. Matter passing through these systems leads to 'self-organization' and an increase in the complexity of the system. Often such systems are called 'dissipative' because, in addition to the import of matter and energy, entropy is generated and dissipated within the system. Static entropy is disorder, while information is negative entropy or negative entropy.

Consumed by a complex system is not energy, but rather negative entropy or information. The generation of entropy means the consumption of negative entropy. This corresponds to the destruction of information.

Information plays an important role not only in physics and technology, but also in biology and economics, e.g. the cost of making a detail depends on its complexity. The arrival of a new technology for making a workpiece changes the cost relationship of making a workpiece. The result of human work is the flow of information. Good workmanship needs more information, etc.

Information and thermodynamics are important in the interaction and self-regulation of complex systems.

Living organisms as well as other complex systems are driven by information and organized by dissipative processes. The basis for the instability of dissipative systems is the nonlinear interaction between the micro-elements of a system that is far from equilibrium. This interaction leads to the organization of the macroscopic state and various bifurcations of the states of the system. The system then moves away from thermodynamic equilibrium to more likely structures at the point of bifurcation. Dissipative systems evolve using feedback in the form of an information loop.

Biological information includes genetic DNA codes. Biological systems are dissipative and self-organizing systems and re-

duce entropy. Life is a process of entropy reduction. The thermodynamics of open systems applies to it. By studying populations of living organisms, one can conclude that they are dissipative structures.

In dissipative biological structures, the memory of the past is a conservative element and danger and threat cause the organisms to move away from a state of equilibrium and self-organization. This is the learning capacity of organisms.

Classical cybernetics uses analyses based on the Shannon information. Some developments in artificial intelligence are related to the thermodynamics of open systems. It should be noted that many artificial intelligence concepts are based on the Shannonian approach. The development of artificial intelligence has enriched psychology and neurophysics.

The development of culture is manifested in the development of language, music, literature, technological knowledge and science. The theory of these fields is based on the theory of complex entropic systems.

More recently, socio-economic and cultural aspects have been analyzed using entropy and self-organizing dissipative structures. Thermodynamics is a new tool for analyzing socio-economic processes. Economics is determined by the development of technology. Technological innovation is an important element in the evolution of economics.

The development of history is controlled by an entropic process. History is a series of bifurcations in a social system far from equilibrium states. The course of history is determined by socio-economic and cultural changes. When there is no innovation and there is socio-cultural stability then there is stagnation and no change. Changes in the socio-technological set-up can lead to revolutionary change through positive feedback. From the point of view of dissipative structures, catastrophe (revolution) arises from internal perturbations reinforced by the environment. The catastrophe leads to a point of bifurcation and to a new level of stability. The new state of the community is more complex after this transition.

5. Conclusions

As has been attempted to show, the thermodynamic principles given are general and can apply to different physical objects. The method of analysis is the same. First, the state of the system is determined, so the thermal and caloric equations are given, then the energy balance (ILT) is used and the reality of the transformation and direction is investigated using II LT. Usually, for the determination of the parameters, systems will behave in a particular way that can be described by simple analytical relations. This behaviour of a substance is considered in thermodynamics as a model. Thus, a real gas is modelled as a perfect gas, a model of a simple magnetic substance is a substance described by the Curie equation of state, a model of an elastic substance is a substance described by Hook's law, and so on.

Classical thermodynamics serves as the analytical tool for determining work, energy, or thermodynamic effects related to heat and temperature, focusing solely on equilibrium states without predicting process rates due to the absence of explicit time representation, although II LT inherently relates to the time axis. In highly dilute systems where statistical laws are inapplicable, phenomenological thermodynamics based on the observation of highly probable phenomena also does not apply, as II LT fundamentally relies on the probability of phenomena occurring, particularly for microscopic phenomena, on a high probability basis.

The thermodynamics of irreversible processes employs the second law of thermodynamics, defining stationary states similar to equilibrium states delineated by II LT in classical thermodynamics. Linear thermodynamics of non-equilibrium processes near equilibrium states has been developed, with non-linear thermodynamics introduced for stationary states far from equilibrium. The thermodynamics of non-equilibrium processes addresses problems involving irreversibility caused by multiple 'thermodynamic forces', each leading to specific branches of thermodynamics, such as heat exchange, mass exchange, and momentum exchange, governed by differential equations and their boundary conditions.

The Laws of Thermodynamics attempt to describe and quantify complexity growth, information storage, distance from thermodynamic equilibrium across different hierarchical levels, and ecosystem development strategies. Equilibrium thermodynamics is more easily described mathematically compared to non-equilibrium thermodynamics due to the non-deterministic nature of self-organizing complex systems. Simplifying models for formal statements of self-organization may limit applicability to real systems and overlook their complexity, although tentative fourth laws aim to establish clear links between thermodynamics, ecology, and evolution.

Thermodynamics has evolved into a comprehensive knowledge system encompassing almost all life sciences branches [26]. Virtually every aspect of reality can be described in thermodynamic terms, reflecting its universal applicability. Despite the complexity within living systems, thermodynamics can be defined as the general science of energy, not only explaining energy transformations in human-dominated devices but also encompassing energy and matter transformations across all systems in the biosphere and beyond.

References

[1] Carnot, S. (1824). *Réflexions sur la puissance motrice du feu et sur les machines propres à développer cette puissance*. Paris: Bachelier.

[2] Lenoir, E.J.J. (1886). *Gas Engine*. US patent 345596, issued 13 July.

[3] Joule, J. P. (1845). On the existence of an equivalent relation between heat and the ordinary forms of mechanical power. *Philosophical Magazine*, 27(3), 205–207.

[4] Mikielewicz, J., Bieliński, H., & Mikielewicz D. (1996). *Thermodynamics in outline*. IMP PAN Publishers, Gdańsk (in Polish).

[5] Wiśniewski, S., Staniszewski, B., & Szymanik, R. (1973). *Thermodynamics of non-equilibrium processes*. PWN, Warszawa (in Polish).

[6] Gumiński, J. (1983). *Thermodynamics of irreversible processes*. PWN, Warszawa (in Polish).

[7] Clausius, R.G. (1850). Uber die bewegende Kraft der Warme. *Annal. Physik Chemie*, 79, 368–397, 500–524. [Translated and excerpted in: Magie, W.F.A. (1935). *Source Book in Physics*. McGraw-Hill, New York].

[8] Carathéodory, C. (Translated by Delphinich, D. H.). (1909). Untersuchungen uber die Grundlagen der Thermodynamik. *Mathematische Annalen*. 67(3), 355–386.

[9] Planck, M. (1911). *Thermodynamik*. 3rd Edn., De Gruyter.
[10] Nernst, W. (1906). Uber die Berechnung chemischer Gleichgewichte aus thermischen Messungen. *Nachrichten von der Gesellschaft der Wissenschaften zu Göttingen, Mathematisch-Physikalische Klasse*, 1, 1–40.
[11] Kestin, J. (1966). *A course in thermodynamics*, Blaisdell, Boston.
[12] Hatsopoulos, G., & Keenan, J. (1965). *Principles of general thermodynamics*, Wiley, New York.
[13] Onsager, L. (1931). Reciprocal relations in irreversible processes, *Physical Review*, 37, 405–427.
[14] Casimir, H.B.G. (1945). On Onsager's principle of microscopic reversibility, *Review of Modern Physics*, 17(2–3), 343–350, doi: 1945.10.1103/RevModPhys.17.343
[15] Bilicki, Z., Mikielewicz, J., & Sieniutycz, S. (2001). *Modern trends in thermodynamics*, IFFM Publishers, Gdańsk (in Polish).
[16] Mikielewicz, J. (2004). Role of thermodynamics in science and engineering. *Archives of Thermodynamics*, 25(2), 3–19.
[17] Collins, M., Stąsiek, J., & Mikielewicz, J. (2007). The laws of thermodynamics: entropy, free energy, information and complexity. *Design and Information in Biology: From Molecules to Systems*, 2, 127-177. doi: 10.2495/978-1-85312-853-0/05
[18] Prigogine, I. (1978). Time, structure, and fluctuations. *Science*, 201, 777–785.
[19] Odum, H.T. (1988). Self-organization, transformity, and information, *Science*, 242, 1132–1139.
[20] Odum, H.T. (1966). *Environmental Accounting: Emergy and Environmental Decision Making*. Wiley, New York.
[21] Kafri, O., (2007). *The second law and informatics*. Cornell University. doi: 10.48550/arXiv.cs/0701016
[22] Rojdestvenski, I., & Cottman, M.C. (2000), Mapping of statistical physics into information theory with application to biological systems. *Journal of Theoretical Biology*, 202(1), 43–54, doi: 10.1006/jtbi.1999.1042.
[23] Brillouin, L. (1949). Life, thermodynamics and cybernetics. *American Scientist*, 37(4), 554–568.
[24] Peters, J. (1967). *Einfiihrung in die allgemeine Informationstheorie*. Springer Verlag, Berlin.
[25] Shannon, C.E., & Weaver W. (1949). *The mathematical theory of communication*. University of Illinois Press.
[26] Ulgiati, S., & Bianciardi, C. (2004). Laws of Thermodynamics, In: *Encyclopedia of Energy*, 6, 1–117. Elsevier Inc. doi: 10.1016/B0-12-176480-X/00086-3

Co-published by
Institute of Fluid-Flow Machinery
Polish Academy of Sciences
Committee on Thermodynamics and Combustion
Polish Academy of Sciences

Copyright©2024 by the Authors under licence CC BY 4.0

http://www.imp.gda.pl/archives-of-thermodynamics/

Experimental and statistical determination of thermal characteristics of the special design minichannel heat exchanger

Maria Karolina Tychanicz-Kwiecień[a*], Witold Rajmund Rybiński[b]

[a]Rzeszow University of Technology, al. Powstańców Warszawy 12, 35-959 Rzeszów, Poland
[b]Institute of Fluid Flow Machinery, Polish Academy of Science, ul. Fiszera 14, 80-231 Gdańsk, Poland
*Corresponding author email: mtychanicz@prz.edu.pl

Received: 28.12.2023; revised: 28.02.2024; accepted: 25.03.2024

Abstract

The paper presents the results of experimental investigation and the new statistical method for the determination of preliminary thermal characteristics of a prototype compact minichannel heat exchanger with laminar flows and significant heat transfer in the manifolds. The exemplary heat exchanger consists of 9 straight, parallel, square-shaped channels and two rectangular-shaped manifolds milled on both sides of the single aluminium plate. The design of the investigated heat exchanger is quite particular, as the heat transfer area of both pairs of manifolds provides almost 1/3 of the total heat transfer area. In the new statistical method presented in this paper, the manifolds' and channels' heat flows are considered separately. The heat exchanger's thermal characteristic was obtained statistically on the basis of the experimental results and is presented in the form of the overall heat transfer rate. The developed thermal characteristic model accounts for two effects, among many others, which may affect heat transfer in the exchanger, i.e. the heat loss to the ambient and the significant heat transfer in the manifolds. It is proved that the heat transfer to the surroundings was negligible due to the suitable thermal insulation. In order to demonstrate that the heat transfer in the manifolds is significant, two calculation variants are presented. The relative differences (residuals) between the experimental and statistically corrected heat transfer rates and the coefficient of determination R^2 are determined in both variants. In the first variant the heat transfer in the manifold pairs is neglected and in the second model it is included. It was observed that the lack of consideration of the heat transfer in the manifold pairs provides drastic dispersion between the experimental and statistical results. In turn, in the second model, where the manifolds are accounted for, a significant enhancement in the consistency of the results is noticed. The relative residuals are much lower, and the corresponding coefficient R^2 is improved from $R^2 = 0.8827$ in the first variant to $R^2 = 0.9335$ in the second one, respectively.

Keywords: Minichannel heat exchanger; Statistical analysis; Thermal characteristics; Laminar flows; Wilson plot

Vol. 45(2024), No. 2, 63–71; doi: 10.24425/ather.2024.150852

Cite this manuscript as: Tychanicz-Kwiecień, M.K., & Rybiński, W.R. (2024). Experimental and statistical determination of thermal characteristics of the special design minichannel heat exchanger. *Archives of Thermodynamics*, 45(2), 63–71.

1. Introduction

For the last decades the revolutionary development of compact miniature systems and installations, particularly for heating and cooling applications and increasing demands in terms of rational thermal energy management, have led to the decrease in size of heat transfer equipment. Heat exchangers of small hydraulic diameter, also called minichannel heat exchangers have received much attention so far due to meeting the requirement of transferring high heat flux rates in small volume and providing thermal performance augmentation. In the view of compact design

Nomenclature

A – heat transfer area, m^2
a – channels or manifolds width, m
b – channels or manifolds height, m
c – correction coefficient
c_p – specific heat capacity at constant pressure, J/(kg·K)
d – wall thickness, m
d_h – hydraulic diameter, m
h – specific enthalpy, J/kg
k – overall heat transfer coefficient, W/(m^2·K)
L – channels or manifolds length, m
N – number of measurements
n – number of channels
Nu – Nusselt number
Pr – Prandtl number
p – pressure, Pa
$\dot{Q}$ – heat flow rate, W
Re – Reynolds number
r_{ba} – normalized aspect ratio
res_{rel} – relative residual
S – cross-sectional area, m^2
T – temperature, K
$\dot{V}$ – volumetric flow rate, m^3/s
W – heat capacity rate, W/K

Greek symbols

α – heat transfer coefficient, W/(m^2·K)
ΔT_{log} – logarithmic mean temperature difference, K
λ – thermal conductivity, W/(m·K)
μ – dynamic viscosity, Pa·s
ρ – density, kg/m^3
φ – sum of squares, $1/W^2$

Subscripts and Superscripts

3 – 3-sided channel
4 – 4-sided channel
A – manifold pair A
B – manifold pair B
c – cold
h – hot
chn – channel
mf – manifold
exp – experimental
pred – predicted
corr – corrected
fd – fully developed flow
in – inlet
out – outlet
lam– laminar
turb– turbulent
rel – relative

and accompanying size reduction of minichannel heat exchangers, the analysis of heat transfer and fluid flow have gained particular attention and became a developing research area.

Accurate thermal and flow performance characterization for prescribed mini- and microchannel system require the consideration of scaling effects [1, 2], design concerns, like the shape and geometry of channels and manifolds [3] as well as flow development and boundary conditions.

In minichannel heat exchangers with two single-phase fluid flows, the determination of thermal characteristics is rather complex as heat transfer generally covers not only the channel region, but often also the inlet and outlet manifolds and additional effects are more feasible to occur. A common approach to estimate thermal characteristics for a given minichannel system is to use simplified analytical heat transfer prediction models and literature correlations appropriate for conventional-size channels. However, it is frequently observed that results obtained are questionable and sometimes inconsistent with theoretical predictions as the fact that assumed boundary conditions are not exactly fulfilled or additional phenomena may occur that were not accounted in the simplified model [4, 5]. The literature survey concerning mini- and microchannel heat exchangers revealed that the studies are rather focused on their practical applications with the aim of presenting overall thermal and hydraulic performance evaluation and effectiveness of the entire heat exchanger, what was reported in following exemplary papers [6–14]. The authors also investigated the optimization of mini- and microchannel heat exchangers design in terms of thermal and hydraulic performance improvement [15]. The consistency of obtained experimental thermal characteristics of mini- and microchannel heat exchangers with fundamental theories of heat transfer and fluid flow in ducts was studied as well [16].

Experimental determination of heat transfer coefficient for particular minichannel heat exchanger requires careful determination of the surface temperature and surrounding fluid. However, accurate experimental measurements of the temperature inside mini-heat exchanger channels in particular are extremely difficult or are even impossible in practice. In order to overcome the temperature measurement impediments, statistical determination of thermal characteristics for minichannel heat exchangers can be considered. Statistical methods, based on the Wilson plot method, use external experimental measurements of heat exchanger's parameters and enable detailed analysis of thermal behavior of investigated heat exchanger [17]. Fernando et al. [18] obtained heat transfer coefficients for shell-and-tube heat exchanger with multiport minichannel tubes with the use of classical version of the Wilson plot method. The comparison of obtained results of Nusselt number and heat transfer coefficients with standard literature correlations reflected partial, but no clear correspondence, especially in the laminar flow regime. In [19] new statistical method was derived for the determination of thermal characteristic of a prototype heat exchanger made of two plates with mini channels. The obtained experimental thermal characteristics of investigated heat exchanger were given in the form of overall thermal resistance. Since the experimental and theoretical thermal resistances are predominantly not equal, corrected thermal resistance was introduced to statistically estimate experimental thermal resistance. The regression function of corrected overall thermal resistance included two experimental lin-

ear coefficients, which corrected the predicted thermal resistance of hot and cold heat exchanger side separately. The relative differences between experimental and corrected overall thermal resistances were in the range of ±5%.

The first version of the new statistical method, developed for the thermal characteristics determination, was introduced in [19] for the minichannel heat exchanger, but without consideration of the manifolds. Unlike in the previous study, the statistical method had to be completely redesigned to take the manifold heat transfer into account. However, the basic idea of the method is preserved: a statistical comparison of the experimental and corrected theoretical values to determine the correction coefficients and the use of the simultaneously varying fluid flow rates at both sides of the heat exchanger. In the presented new statistical method, the heat flow rates are used instead of thermal resistances in the first method [19].

This article presents a new statistical method for the determination of the preliminary thermal characteristics of a prototype minichannel heat exchanger. The thermal characteristic is presented as the total heat transfer rate of the heat exchanger. Experimental measurements were performed for single-phase laminar flows of distilled water in a counter-flow arrangement. The obtained volumetric flowrates are characterized by 12-fold variability, corresponding to the total range of Re = 117 ÷ 2 500. The considered heat exchanger has 9 parallel square channels of 2 × 2 mm cross-section and two rectangular inlet and outlet manifolds milled on both sides of a single aluminium plate. The heat exchanger has an unusual and specific design since the surface area of both manifolds represented about 30% of the total heat transfer surface area. It was predicted that this effect could disturb the thermal behaviour of the heat exchanger and could constitute a significant part of the total heat transfer rate, which was later confirmed. The consideration of the effect of heat transfer in manifold regions for detailed determination of thermal characteristics requires the development of a new method of statistical analysis of experimental measurement results. This new statistical method, based on the Wilson plot approach, enables the assessment of heat transfer in the manifolds region and in the channels region separately. The additional considered effect is heat loss to the ambient, which was found to be negligible afterwards. In order to determine the corrected heat transfer rates, both in the manifolds and channels area, the correction coefficients were obtained using the least squares method. Calculations for the channel region are more precise due to the determination of separate correction coefficients for hot and cold heat exchanger sides, while for the manifold region, one common correction coefficient is determined. The comparison of the experimental and statistically corrected heat transfer rates, expressed in the form of relative differences (residuals), is presented for 2 calculation variants. In the first variant, heat transfer in the manifolds is neglected. In the second variant, the manifolds are included. As a result, an increase in the coefficient of determination R^2 is observed for the second model, which proves the importance of consideration of the heat transfer in the manifolds in the thermal analysis of the investigated minichannel heat exchanger.

2. Description of the experimental investigation

The real view of the experimental test stand for heat exchangers investigations was depicted in Fig. 1 and a detailed characterization of the design, specification of measurement procedure as well as calibration process was presented in [20].



Fig. 1. The picture of the experimental setup: 1 – calibration bath of the cold side, 2 – calibration bath of the hot side, 3 – hot and cold side pressure transducers, 4 – ice point reference, 5 – LabVIEW control program, 6 – Keithley digital multimeter, 7 – investigated minichannel heat exchanger with insulation, 9 – hot and cold side flow meters.

The experimental facility, which operates in a closed loop of circulating hot and cold working fluid, consisted of the investigated minichannel heat exchanger placed in the insulation, the thermocouples, pressure transducers, flowmeters, calibration baths and the measuring control unit. As a reference temperature, the automatic Ice Point Reference unit was used. The entire data registration and acquisition process, as well as the general operation of the test stand, were performed automatically. The Keithley measuring set was used to register the experimental data points and for its further processing, the LabVIEW environment was implemented. The proper measurements have been carried out in steady-state thermal conditions. The following parameters were directly measured: the inlet and outlet fluid temperatures, pressure drops and volumetric flowrates. On the basis of the registered parameters, the thermal power of investigated heat exchanger is obtained with the use of thermal balance method.

The view of investigated minichannel plate with selected manifold pairs is presented in Fig. 2a. The external dimensions of investigated heat exchanger are equal to 150 × 70 mm. The heat exchanger of a modular construction and sandwich form consists of the replaceable aluminum plate with minichannels placed between upper and bottom housing made from plastic. Rubber seals are also inserted on both sides between the aluminum plate and housings. The set of straight, parallel, square-shaped minichannels is milled on both sides of the single aluminum plate, forming symmetric grooves. The channel hydraulic diameter was equal to 2 mm. The plate has its own inlet and outlet manifolds milled on both sides of the plate as well. The working fluids flow through the same core material, therefore a prototype single-plate minichannel heat exchanger is constructed. The detailed geometry specification of channels and

manifolds of the tested heat exchanger is shown in Fig. 2b. The main benefit of this solution is a simplified design with no intermediate plates inside, the reduced amount of heat exchanger components and rapid manufacturing. However, as far as the thermal design of this minichannel configuration is concerned, the channel top surfaces are thermally isolated due to the presence of rubber seals. It follows that only 3 inner sides of a square channel are heated or cooled, thus for accurate description of thermal characteristics of this particular minichannel system, the proper calculation variant for the Nusselt number should be selected. The thickness of the plate layer (intermediate wall),

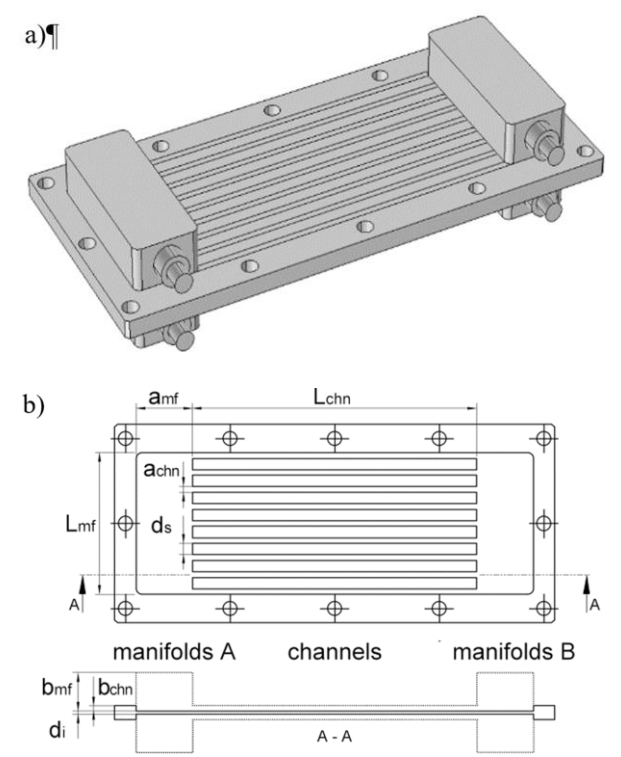


Fig. 2. Schematic view of the minichannel's plate with two pairs of manifolds (a), and sizes of the minichannels and manifolds (b).

which separates the hot and cold fluid is equal to 1 mm. Inlet and outlet plenum has a rectangular shape and both surface area occupy about 30% of the total heat transfer area. The heat exchanger is placed in the thermal insulation made of granulated polystyrene foam.

The experimental measurements were performed for single-phase flows of distilled water in a counterflow arrangement. The only parameter which was varied during measurements was the water flowrate. The inlet temperatures of hot and cold fluids were invariant and adjusted to 70°C and 20°C, respectively. A total of 8 series of measurements with significant variability of the volumetric flowrates were performed. In each series, the flowrate of the cold fluid was adjusted manually, while the flowrate of the hot fluid was maintained constant. Also, the flowrate was reduced from its maximum value (about 1.11 dm^3/min for cold fluid and 1.16 dm^3/min for hot fluid) by approximately 0.15 dm^3/min. Therefore, 8 measurement points were obtained in each series, and the total amount of $N = 64$ measurements were carried out. Due to low flow rates, laminar flows took place.

The thorough determination of experimental measurements uncertainty of individual parameters was presented in [20] and obtained results were collected in Table 1.

Table 1. Results of experimental measurements uncertainty determination.

Measurement	Uncertainty
Pressure	±0.05% of measurement range
Flow rate	±0.35% of measured value
Temperature	±0.25°C

The heat exchanger's dimensions, shown in Fig. 2b, are as follows: channel length $L_{chn} = 100$ mm, channel width $a_{chn} = 2$ mm, channel height $b_{chn} = 2$ mm (aspect ratio 1), manifold length $L_{mf} = 50$ mm, manifold width $a_{mf} = 20$ mm, manifold height $b_{mf} = 14$ mm, intermediate wall thickness $d_i = 1$ mm, side wall thickness $d_s = 4$ mm. The number of channels is $n_{chn} = 9$.

3. Statistical analysis of the measurement data and derivation of the thermal characteristics

Heat flow rates at the hot and cold heat exchanger side are calculated from Eqs. (1) and (2):

$$\dot{Q}_h = \dot{m}_h \cdot \Delta h_h = \dot{m}_h \cdot \left[h\left(T_{h,in}, p_{h,in}\right) - h\left(T_{h,out}, p_{h,out}\right)\right], \quad (1)$$

$$\dot{Q}_c = \dot{m}_c \cdot \Delta h_c = \dot{m}_c \cdot \left[h\left(T_{c,out}, p_{c,out}\right) - h\left(T_{c,in}, p_{c,in}\right)\right], \quad (2)$$

where the mass flow rates are given by:

$$\dot{m}_h = \dot{V}_h \cdot \rho\left(T_{h,out}, p_{h,out}\right), \quad (3)$$

$$\dot{m}_c = \dot{V}_c \cdot \rho\left(T_{c,out}, p_{c,out}\right). \quad (4)$$

For calculation purposes arithmetic mean is used:

$$\dot{Q}_{exp,i} = \left(\dot{Q}_{h,i} + \dot{Q}_{c,i}\right)/2, \quad (5)$$

for $i = 1, 2, ..., N$.

In order to assess heat loss to the ambient, the relative deviation $\delta\dot{Q}_{rel}$ of $\dot{Q}_h$ and $\dot{Q}_c$, relative to $\dot{Q}_{exp}$, is calculated as an average of the half $\left|\dot{Q}_h - \dot{Q}_c\right|/2$ of the distance between $\dot{Q}_h$ and $\dot{Q}_c$ divided by the mean heat flow $\dot{Q}_{exp}$:

$$\delta\dot{Q}_{rel} = \frac{1}{2 \cdot N} \cdot \sum_{i=1}^{N} \frac{\left|\dot{Q}_{h,i} - \dot{Q}_{c,i}\right|}{\dot{Q}_{exp,i}}. \quad (6)$$

It is more pessimistic than the standard deviation.

Due to the sufficient thermal insulation, the relative scattering of $\dot{Q}_{exp}$ amounted only $\pm\delta\dot{Q}_{rel} = \pm 3.1\%$ and therefore heat transfer to the ambient could be acknowledged as negligible.

Figure 3 presents the thermal balance of the heat exchanger in the form of experimentally obtained heat transfer rates of the cold and hot side.

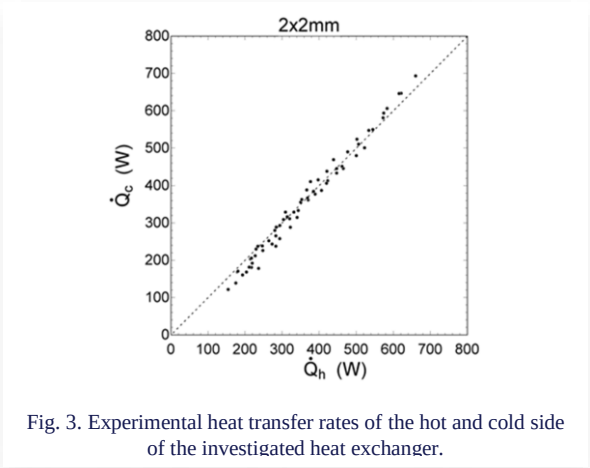


Fig. 3. Experimental heat transfer rates of the hot and cold side of the investigated heat exchanger.

In the developed statistical method the greatest possible variability of both flow rates, $\dot{V}_h$, $\dot{V}_c$ is required.

The Reynolds number Re_h, Re_c in each hot and cold channel or manifold is given by:

$$\mathrm{Re} = \frac{\dot{m}/S \cdot d_h}{\mu}. \tag{7}$$

The fluid's dynamic viscosity μ (and the thermal conductivity λ and the specific heat capacity c_p) in the channels is determined for the mean temperature between the inlet and outlet and in the manifolds for the corresponding inlet or outlet temperature. The hydraulic diameter is calculated from the same formula for the manifolds and channels:

$$d_h = \frac{2 \cdot a \cdot b}{a+b}. \tag{8}$$

The total cross-sectional area S is calculated by:

– for the manifolds:

$$S = a_{mf} \cdot b_{mf}, \tag{9}$$

– for the channels:

$$S = n_{chn} \cdot a_{chn} \cdot b_{chn}. \tag{10}$$

Figures 4a and 4b show the maps of the experimentally obtained volumetric flowrates and of the corresponding Reynolds number, respectively. The numbers show the order of measurements.

In the statistical method developed in this paper, the significant heat transfer area of the manifolds is taken into account. To present the significance of the heat transfer in the manifolds, two variants of the calculation are developed: with the neglected manifolds and with the manifolds taken into account. Figure 5 depicts these two variants of the heat flows.

The manifolds are partly made of metal and plastic, schematically shown in Fig. 2. The heat transfer area in the single pair of manifolds is given by:

$$A_{mf} = L_{mf} \cdot a_{mf} + 2 \cdot \left(L_{mf} + a_{mf}\right) \cdot b_{chn}. \tag{11}$$

The heat transfer area of n_{chn} channels, with only 3 sides exchanging heat, is given by:

$$A_{chn} = n_{chn} \cdot L_{chn} \cdot (a_{chn} + 2 \cdot b_{chn}). \tag{12}$$

Substitution of the numerical values gives $A_{mf} = 0.00128$ m^2 and $A_{chn} = 0.00540$ m^2. Both manifold's heat transfer area is equal to $2A_{mf}/(2A_{mf}+A_{chn}) \approx 32.2\%$ of the total heat transfer area.

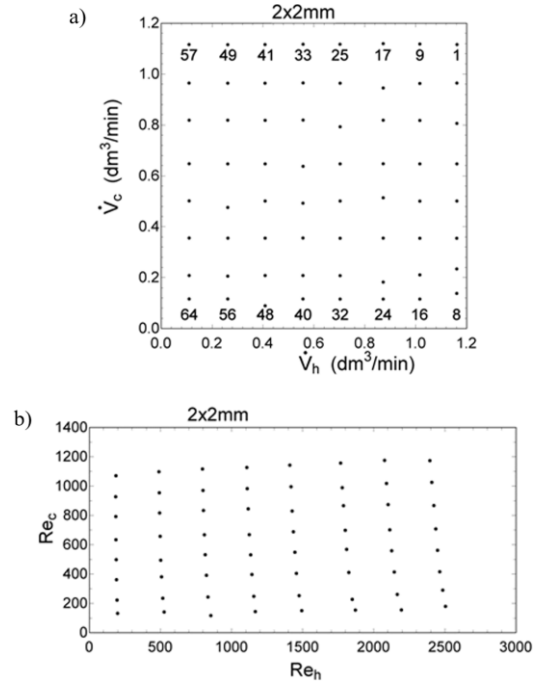


Fig. 4. Maps of the experimental: a) volumetric flowrates with the order of measurements, and b) corresponding Reynolds numbers.

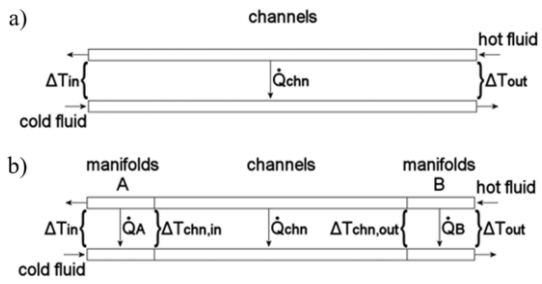


Fig. 5. Heat flows in two variants: a) without manifolds, b) with manifolds.

The theoretical (predicted) values of the heat transfer coefficient α are calculated from the appropriate correlations of the Nusselt number:

$$\alpha_{pred} = \frac{\mathrm{Nu}_{pred} \cdot \lambda}{d_h}. \tag{13}$$

In the manifolds the Nusselt number in this paper is calculated from the Dittus-Boelter correlation [21]:

$$\mathrm{Nu}_{pred} = 0.023 \cdot \mathrm{Re}^{0.8} \cdot \mathrm{Pr}^{0.4}, \tag{14}$$

where the Prandtl number is given by:

$$\mathrm{Pr} = \frac{c_p \cdot \mu}{\lambda}. \tag{15}$$

Although the flows in the manifolds are three dimensional, they are turbulent and the Dittus-Boelter correlation, developed for the flows in pipes, is used as a rough approximation.

In the channels, the way the Nusselt number is calculated depends on the flow type.

For developing laminar flows (Re < 2 300) in a rectangular microchannel the Nusselt number is given by the formula from [22], used for the normalized aspect ratio $0.1 \le r_{ba} \le 1$:

$$\mathrm{Nu}_{pred} = \frac{1}{C_1 \cdot (L^*)^{C_2} + C_3} + C_4. \tag{16}$$

The dimensionless thermal channel's length L^* and the coefficients C_1, ... , C_4 are given by:

$$L^* = \frac{L/d_h}{\mathrm{Re} \cdot \mathrm{Pr}}, \tag{17}$$

$$C_1 = -2.757 \cdot \frac{10^{-3}}{r_{ba}^3} + 3.274 \cdot \frac{10^{-2}}{r_{ba}^2} - 7.464 \cdot \frac{10^{-5}}{r_{ba}} + 4.476, \tag{18}$$

$$C_2 = 0.6391, \tag{19}$$

$$C_3 = 1.604 \cdot \frac{10^{-4}}{r_{ba}^2} - 2.622 \cdot \frac{10^{-3}}{r_{ba}} + 2.568 \cdot 10^{-2}, \tag{20}$$

$$C_4 = -6.094 \cdot r_{ba}^3 + 15.19 \cdot r_{ba}^2 - 13.11 \cdot r_{ba} + 7.301, \tag{21}$$

where the normalized aspect ratio is given by:

$$r_{\mathrm{ba}} = \min(a_{chn}/b_{chn}; b_{chn}/a_{chn}). \tag{22}$$

For $L^* < 0.1$, laminar flows are developed [23].

For fully developed laminar flow, the Nusselt number is given by [24]:

$$\mathrm{Nu}_{fd,pred} = 8.235 \cdot (1 - 2.0421 r_{ba} + 3.0853 r_{ba}^2 + -2.4765 r_{ba}^3 + 1.0578 r_{ba}^4 - 0.1861 r_{ba}^5). \tag{23}$$

The analytical formula for fully developed laminar flows is also derived in [25]. For transitional flows 2 300 < Re < 10 000 the linear interpolation from Gnielinski correlation [26,27] is used. It is based on the values of $\mathrm{Nu}_{lam,2300}$ for the laminar flow of Re = 2 300 (16) and $\mathrm{Nu}_{turb,10000}$ for the turbulent flow of Re = 10 000 (14):

$$\mathrm{Nu}_{pred} = \left(1 - \frac{\mathrm{Re} - 2300}{10000 - 2300}\right) \cdot \mathrm{Nu}_{lam,2300} + + \frac{\mathrm{Re} - 2300}{10000 - 2300} \cdot \mathrm{Nu}_{turb,10000}. \tag{24}$$

For turbulent flows Re > 10 000 the Dittus-Boelter formula (14) is used.

In the investigated heat exchanger only 3 from 4 channels sides are heated or cooled. In this case the approximate formula from [23] is used to calculate the Nusselt number for 3 sides only:

$$\mathrm{Nu}_{pred} = \mathrm{Nu}_{4,pred} \cdot \frac{\mathrm{Nu}_{fd,3}}{\mathrm{Nu}_{fd,4}}, \tag{25}$$

where $\mathrm{Nu}_{4,pred}$ is given by the formulae (14), (16) or (24) in which the subscript 4 is omitted for simplicity. The quotient $\mathrm{Nu}_{fd,3}/\mathrm{Nu}_{fd,4}$ is calculated based on the values of $\mathrm{Nu}_{fd,3}$ and $\mathrm{Nu}_{fd,4}$ for the fully developed flows [24] and is presented in Table 2 for various aspect ratios a/b.

Table 2. Quotients $\mathrm{Nu}_{fd,3}/\mathrm{Nu}_{fd,4}$ for various values of the aspect ratio a/b.

Aspect ratio a/b	$\mathrm{Nu}_{fd,3}$	$\mathrm{Nu}_{fd,4}$	$\mathrm{Nu}_{fd,3}/\mathrm{Nu}_{fd,4}$
0	8.235	8.235	1
0.1	6.939	6.7	1.03567
0.2	6.072	5.704	1.06452
0.3	5.393	4.969	1.08533
0.4	4.885	4.457	1.09603
0.5	4.505	4.111	1.09584
0.7	3.991	3.74	1.06711
1.0	3.556	3.599	0.98805
1.43	3.195	3.74	0.85428
2.0	3.146	4.111	0.76526
2.5	3.169	4.457	0.71102
3.33	3.306	4.969	0.66533
5	3.636	5.704	0.63745
10	4.252	6.7	0.63463
∞	5.385	8.235	0.65392

In the analyzed heat exchanger, three heat flows take place: $\dot{Q}_{\mathrm{A}}$ in the pair of manifolds A, $\dot{Q}_{chn}$ in the channels and $\dot{Q}_{\mathrm{B}}$ in the pair of manifolds B. The predicted values of these flows are calculated from the above-described formulae for the Nusselt number. However, these predicted heat flows should be multiplied by the correction coefficients and the obtained corrected heat flows are statistically compared with the experimental ones. The statistical method of least squares is used to determine these correction coefficients.

Theoretical, predicted heat transfer coefficients are calculated from appropriate Nusselt number correlations. In the manifold pairs the Dittus-Boelter correlation is used and in the channels the correlation (16) in [22] is applied, regarding thermally developing flows in rectangular channels. The corrected overall heat transfer coefficients in two pairs of manifolds and in the channels are calculated using the statistically determined correction coefficients c_h, c_c, c_{AB}, which correct the theoretically predicted heat transfer coefficients:

$$k_{\mathrm{A},corr} = c_{\mathrm{AB}} \cdot k_{\mathrm{A},pred}, \tag{26}$$

$$\frac{1}{k_{chn,corr}} = \frac{1}{c_h \cdot \alpha_{h,chn,pred}} + \frac{1}{c_c \cdot \alpha_{c,chn,pred}}, \tag{27}$$

$$k_{\mathrm{B},corr} = c_{\mathrm{AB}} \cdot k_{\mathrm{B},pred}. \tag{28}$$

The predicted overall heat transfer coefficients $k_{\mathrm{A},pred}$ and $k_{\mathrm{B},pred}$ in the manifolds pairs A and B are calculated using the heat transfer coefficients $\alpha_{h,\mathrm{A},pred}$, $\alpha_{c,\mathrm{A},pred}$, $\alpha_{h,\mathrm{B},pred}$, $\alpha_{c,\mathrm{B},pred}$ from the Dittus-Boelter correlation (14):

$$\frac{1}{k_{\mathrm{A},pred}} = \frac{1}{\alpha_{h,\mathrm{A},pred}} + \frac{1}{\alpha_{c,\mathrm{A},pred}}, \tag{29}$$

$$\frac{1}{k_{\mathrm{B},pred}} = \frac{1}{\alpha_{h,\mathrm{B},pred}} + \frac{1}{\alpha_{c,\mathrm{B},pred}}. \quad (30)$$

Because the main heat flow takes place between hot and cold channels, two separate correction coefficients c_h, c_c are used. For both pairs of manifolds, only one common correction coefficient, c_{AB}, is used. Since there is relatively small number N of the measurements, it is better to statistically determine maximum 3 correction coefficients [19].

The temperature differences of the hot and cold working fluid in the region borders are related by following equations:

$$\Delta T_{chn,in} = \Delta T_{in} \cdot \exp\left(\frac{k_{\mathrm{A}corr} \cdot A_{\mathrm{A}}}{W_{\mathrm{A}}}\right), \quad (31)$$

$$\Delta T_{chn,out} = \Delta T_{chn,in} \cdot \exp\left(\frac{k_{chncorr} \cdot A_{chn}}{W_{chn}}\right), \quad (32)$$

$$\Delta T_{out} = \Delta T_{chn,out} \cdot \exp\left(\frac{k_{\mathrm{B}corr} \cdot A_{\mathrm{B}}}{W_{\mathrm{B}}}\right), \quad (33)$$

where the resultant heat capacity rates for the counter-current flows:

$$\frac{1}{W_{\mathrm{A}}} = \frac{1}{\dot{m}_h \cdot c_{p,\mathrm{A},h}} - \frac{1}{\dot{m}_c \cdot c_{p,\mathrm{A},c}}, \quad (34)$$

$$\frac{1}{W_{chn}} = \frac{1}{\dot{m}_h \cdot c_{p,chn,h}} - \frac{1}{\dot{m}_c \cdot c_{p,chn,c}}, \quad (35)$$

$$\frac{1}{W_{\mathrm{B}}} = \frac{1}{\dot{m}_h \cdot c_{p,\mathrm{B},h}} - \frac{1}{\dot{m}_c \cdot c_{p,\mathrm{B},c}}. \quad (36)$$

The statistically corrected heat transfer rates in the channels and manifolds are described by:

$$\dot{Q}_{\mathrm{A},corr} = k_{\mathrm{A},corr} \cdot A_{\mathrm{A}} \cdot \Delta T_{log,\mathrm{A}}, \quad (37)$$

$$\dot{Q}_{chn,corr} = k_{chn,corr} \cdot A_{chn} \cdot \Delta T_{log,chn}, \quad (38)$$

$$\dot{Q}_{\mathrm{B},corr} = k_{\mathrm{B},corr} \cdot A_{\mathrm{B}} \cdot \Delta T_{log,\mathrm{B}}, \quad (39)$$

where the logarithmic mean temperature differences in the channels and two pairs of manifolds are given by:

$$\Delta T_{log,\mathrm{A}} = \frac{\Delta T_{chn,in} - \Delta T_{in}}{\ln\frac{\Delta T_{chn,in}}{\Delta T_{in}}}, \quad (40)$$

$$\Delta T_{log,chn} = \frac{\Delta T_{chn,out} - \Delta T_{chn,in}}{\ln\frac{\Delta T_{chn,out}}{\Delta T_{chn,in}}}, \quad (41)$$

$$\Delta T_{log,\mathrm{B}} = \frac{\Delta T_{out} - \Delta T_{chn,out}}{\ln\frac{\Delta T_{out}}{\Delta T_{chn,out}}}. \quad (42)$$

The overall and statistically corrected heat transfer rate is a sum of three heat flows:

$$\dot{Q}_{corr} = \dot{Q}_{\mathrm{A},corr} + \dot{Q}_{chn,corr} + \dot{Q}_{\mathrm{B},corr}. \quad (43)$$

This concise formula (43) presents the thermal characteristic of the investigated heat exchanger, in which the right side depends on the flow rates $\dot{V}_h$, $\dot{V}_c$ and contains the statistically determined correction coefficients c_h, c_c, c_{AB}. The first calculation variant (without manifolds) is obtained by the substitution $c_{\mathrm{AB}} = 0$, which indicates that no heat transfer in the manifold region occurs ($\dot{Q}_{\mathrm{A},corr} = \dot{Q}_{\mathrm{B},corr} = 0$).

The correction coefficients c_h, c_c, c_{AB} are determined by statistical fitting the corrected $\dot{Q}_{chn,corr}$ and experimental $\dot{Q}_{chn,exp}$ heat flows in the channels, by the method of least squares.

The corrected heat flow in the channels may be presented with explicitly shown the correction coefficients c_h, c_c:

$$\dot{Q}_{chn,corr} = \left(\frac{1}{c_h \cdot \alpha_{h,chn,pred}} + \frac{1}{c_c \cdot \alpha_{c,chn,pred}}\right)^{-1} \cdot A_{chn} \cdot \Delta T_{log,chn}. \quad (44)$$

The experimental heat flow in the channels $\dot{Q}_{chn,exp}$ is not measured directly, however it is approximated by subtracting the corrected heat transfer rates in the pair of manifold A and B from the measured total heat flow $\dot{Q}_{exp}$:

$$\dot{Q}_{chn,exp} = \dot{Q}_{exp} - \dot{Q}_{\mathrm{A},corr} - \dot{Q}_{\mathrm{B},corr}, \quad (45)$$

or in the form with explicitly shown the correction coefficient c_{AB}:

$$\dot{Q}_{chn,exp} = \dot{Q}_{exp} - c_{\mathrm{AB}} \cdot k_{\mathrm{A},pred} \cdot A_{\mathrm{A}} \cdot \Delta T_{log,\mathrm{A}} - c_{\mathrm{AB}} \cdot k_{\mathrm{B},pred} \cdot A_{\mathrm{B}} \cdot \Delta T_{log,\mathrm{B}}. \quad (46)$$

It is easier to statistically fit the reciprocals $\dot{Q}^{-1}_{chn,corr}$ and $\dot{Q}^{-1}_{chn,exp}$ because the correction coefficients c_h, c_c are determined analytically in this case. The reciprocal $\dot{Q}^{-1}_{chn,corr}$ (44) is written as:

$$\dot{Q}^{-1}_{chn,corr} = \left(\frac{1}{c_h \cdot \alpha_{h,chn,pred}} + \frac{1}{c_c \cdot \alpha_{c,chn,pred}}\right) \cdot \frac{1}{A_{chn} \cdot \Delta T_{log,chn}}, \quad (47)$$

or in the version where the $1/c_h$ and $1/c_c$ are in a linear form:

$$\dot{Q}^{-1}_{chn,corr} = \frac{1}{c_h} \cdot \frac{1}{\alpha_{h,chn,pred} \cdot A_{chn} \cdot \Delta T_{log,chn}} + \frac{1}{c_c} \cdot \frac{1}{\alpha_{c,chn,pred} \cdot A_{chn} \cdot \Delta T_{log,chn}}. \quad (48)$$

The reciprocal of experimental heat transfer rates in the channels is given by:

$$\dot{Q}^{-1}_{chn,exp} = (\dot{Q}_{exp} - c_{\mathrm{AB}} \cdot k_{\mathrm{A},pred} \cdot A_{\mathrm{A}} \cdot \Delta T_{log,\mathrm{A}} - c_{\mathrm{AB}} \cdot k_{\mathrm{B},pred} \cdot A_{\mathrm{B}} \cdot \Delta T_{log,\mathrm{B}})^{-1}. \quad (49)$$

The correction coefficients c_h, c_c, c_{AB} are determined statistically by the use of the least square method [28] by minimizing the sum:

$$\varphi(c_h, c_c, c_{\mathrm{AB}}) = \sum_{i=1}^{N} \left[\dot{Q}^{-1}_{chn,exp,i}(c_{\mathrm{AB}}) - \dot{Q}^{-1}_{chn,corr,i}(c_h, c_c)\right]^2. \quad (50)$$

The short symbols are used for the convenience:

$$y = \dot{Q}^{-1}_{chn,exp}, \qquad x_h = 1/\left(\alpha_{h,chn,pred} \cdot A_{chn} \cdot \Delta T_{log,chn}\right),$$

$$x_c = 1/\left(\alpha_{c,chn,pred} \cdot A_{chn} \cdot \Delta T_{log,chn}\right),$$

$$a_h = 1/c_h, \qquad a_c = 1/c_c.$$

Using these symbols, the reciprocal $\dot{Q}^{-1}_{chn,corr}$ in Eq. (48) has the clear form of a linear function of two variables x_h, x_c:

$$\dot{Q}^{-1}_{chn,corr} = a_h \cdot x_h + a_c \cdot x_c. \tag{51}$$

Minimization of the function (50) for c_h, c_c gives the linear system of equation with two unknowns a_h, a_c, similar to the system in [19]:

$$\begin{cases} a_h \cdot \sum_{i=1}^{N} x_{h,i}^2 & + a_c \cdot \sum_{i=1}^{N} x_{h,i} x_{c,i} & = \sum_{i=1}^{N} x_{h,i} y_i \\ a_h \cdot \sum_{i=1}^{N} x_{h,i} x_{c,i} & + a_c \cdot \sum_{i=1}^{N} x_{c,i}^2 & = \sum_{i=1}^{N} x_{c,i} y_i \end{cases}. \tag{52}$$

The linear coefficients a_h, a_c are calculated analytically by the use of the Cramer's rule:

$$a_h = \frac{\sum_{i=1}^{N} x_{c,i}^2 \cdot \sum_{i=1}^{N} x_{h,i} y_i - \sum_{i=1}^{N} x_{h,i} x_{c,i} \cdot \sum_{i=1}^{N} x_{c,i} y_i}{\sum_{i=1}^{N} x_{h,i}^2 \cdot \sum_{i=1}^{N} x_{c,i}^2 - \left(\sum_{i=1}^{N} x_{h,i} x_{c,i}\right)^2}, \tag{53}$$

$$a_c = \frac{\sum_{i=1}^{N} x_{h,i}^2 \cdot \sum_{i=1}^{N} x_{c,i} y_i - \sum_{i=1}^{N} x_{h,i} x_{c,i} \cdot \sum_{i=1}^{N} x_{h,i} y_i}{\sum_{i=1}^{N} x_{h,i}^2 \cdot \sum_{i=1}^{N} x_{c,i}^2 - \left(\sum_{i=1}^{N} x_{h,i} x_{c,i}\right)^2}. \tag{54}$$

The correction coefficients c_h, c_c are calculated from:

$$c_h = \frac{1}{a_h}, \qquad c_c = \frac{1}{a_c}. \tag{55}$$

The correction coefficient c_{AB} is calculated numerically, the Golden Section method is used to find the minimum of the function (50) for c_{AB}. In every iteration of this method the coefficients c_h, c_c are calculated analytically from (55). This decomposition of the calculation into the linear and nonlinear part reduces the calculation time and gives better accuracy of the values of the coefficients c_h, c_c, c_{AB}.

The coefficient of determination is given by [28]:

$$R^2 = 1 - \frac{\sum_{i=1}^{N} \left(\dot{Q}_{exp,i} - \dot{Q}_{corr,i}\right)^2}{\sum_{i=1}^{N} \left(\dot{Q}_{exp,i} - 1/N \cdot \sum_{j=1}^{N} \dot{Q}_{exp,j}\right)^2}. \tag{56}$$

The relative residuals between the experimental and statistically corrected heat flow in the heat exchanger are calculated as:

$$res_{rel,i} = \frac{\dot{Q}_{exp,i} - \dot{Q}_{corr,i}}{\dot{Q}_{corr,i}}, \tag{57}$$

for i = 1, 2, ..., N.

The computer program was developed in the Engineering Equation Solver (EES) environment to calculate the results.

Figure 6 presents the relative residuals of the experimental and statistically corrected heat transfer rates for the heat exchanger, compiled for two calculation models. Figure 6a corresponds to the model, where the heat transfer in the manifolds was neglected (0-mf symbol), while Fig. 6b denotes the model, where the heat transfer in the manifolds is included.

Each measurement was done after 20–25 minutes of the temperatures stabilization, to reach the steady state, which means the measurements are statistically independent. However there are regularities in Fig. 6, but they are caused by the regular changes of the flowrates, measured in the order shown in Fig. 4a. The regularities also exist in Fig. 6b, where the heat flows in the manifolds are taken into account, but the residuals are significantly lower and are more random.

The highest residuals occur in the primary measurements, what corresponds to the highest flow rates and Reynolds numbers, Fig. 4a. The residuals in Fig. 6b are much lower than in Fig. 6a, which means that the consideration of heat flows in the manifolds is important. Calculation results of the correction coefficients and the coefficients of determination R^2 are presented in Table 3.

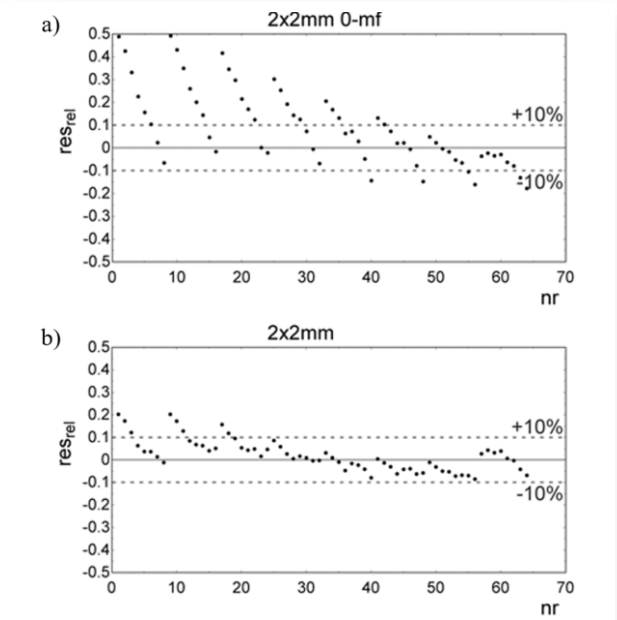


Fig. 6. Relative residuals of the experimental and statistically corrected heat transfer rates in the heat exchanger. Variants: a) without manifolds (0-mf), b) with manifolds.

Table 3. Calculation results for the variants 1 and 2.

Variant	c_{AB}	c_h	c_c	R^2
1 – without manifolds (0-mf)	0	1.529	2.009	0.8827
2 – with manifolds	7.751	1.081	1.549	0.9335

The statistically determined correction coefficients c_{AB}, c_h, c_c in the variant 2 are used in the heat exchanger's thermal characteristics (43).

4. Conclusions

- The use of the proper thermal insulation enables neglecting the heat transfer to the ambient. The experimental difference of ±3.1% between the heat flow supplied and removed from the heat exchanger is slight and therefore the heat flow to the environment may be omitted.
- The statistical method for the determination of preliminary thermal characteristic of minichannel heat exchangers with significant manifolds dimensions was developed.
- The consideration of significant heat transfer in the manifold region improves the fit accuracy (coefficient of determination R^2) with respect to the model, where mani-

folds were not considered. The relative differences between the experimental and statistically corrected heat flows are much decreased.

- In order to describe precisely thermal behavior of investigated minichannel heat exchanger and to obtain exact thermal characteristics, further extended analysis is required.

References

[1] Rosa, P., Karayiannis, T.G., & Collins, M.W. (2009). Single-phase heat transfer in microchannels: The importance of scaling effects. *Applied Thermal Engineering*, 29(17–18), 3447–3468. doi: 10.1016/j.applthermaleng.2009.05.015

[2] Morini, G.L. (2004). Single-phase convective heat transfer in microchannels: A review of experimental results. *International Journal of Thermal Sciences*, 43(7), 631–651. doi: 10.1016/j.ijthermalsci.2004.01.003

[3] Hasan, M.I., Rageb, A.A., Yaghoubi, M., & Homayoni, H. (2009). Influence of channel geometry on the performance of a counter flow microchannel heat exchanger. *International Journal of Thermal Sciences*, 48(8), 1607–1618. doi: 10.1016/j.ijthermalsci.2009.01.004

[4] Steinke, M.E., & Kandlikar, S.G. (2005). Single-phase liquid heat transfer in microchannels. In *Proceedings of ICMM2005, ASME 3rd International Conference on Nanochannels, Microchannels, and* Minichannels, 41855, (pp. 667–678), 13−15 June, Toronto, Ontario, Canada. doi:10.1115/ICMM2005-75114

[5] Dixit, T., & Ghosh, I. (2015). Review of micro-and mini-channel heat sinks and heat exchangers for single phase fluids. *Renewable and Sustainable Energy Reviews*, 41, 1298–1311. doi: 10.1016/j.rser.2014.09.024

[6] Foli, K., Okabe, T., Olhofer, M., Jin, Y., & Sendhoff, B. (2006). Optimization of micro heat exchanger: CFD, analytical approach and multi-objective evolutionary algorithms. *International Journal of Heat and Mass Transfer*, 49(5–6), 1090–1099. doi: 10.1016/j.ijheatmasstransfer.2005.08.032

[7] Kee, R.J., Almand, B.B., Blasi, J.M., Rosen, B.L., Hartmann, M., Sullivan, N.P., & Martin, J.L. (2011). The design, fabrication, and evaluation of a ceramic counter-flow microchannel heat exchanger. *Applied Thermal Engineering*, 31(11–12), 2004–2012. doi: 10.1016/j.applthermaleng.2011.03.009

[8] García-Hernando, N., Acosta-Iborra, A., Ruiz-Rivas, U., & Izquierdo, M. (2009). Experimental investigation of fluid flow and heat transfer in a single-phase liquid flow micro-heat exchanger. *International Journal of Heat and Mass Transfer*, 52(23–24), 5433–5446. doi: 10.1016/j.ijheatmasstransfer.2009.06.034

[9] Cao, H., Chen, G., & Yuan, Q. (2009). Testing and design of a microchannel heat exchanger with multiple plates. *Industrial & Engineering Chemistry Research*, 48(9), 4535–4541. doi: 10.1021/ie801419r

[10] Koyama, K., & Asako, Y. (2010). Experimental investigation on heat transfer characteristics of a gas-to-gas counterflow microchannel heat exchanger. *Experimental Heat Transfer*, 23(2), 130−143. doi: 10.1080/08916150903402799

[11] Alm, B., Imke, U., Knitter, R., Schygulla, U., & Zimmermann, S. (2008). Testing and simulation of ceramic micro heat exchangers. *Chemical Engineering Journal*, 135, S179−S184. doi: 10.1016/j.cej.2007.07.005

[12] Al-Nimr, M.A., Maqableh, M., Khadrawi, A.F., & Ammourah, S.A. (2009). Fully developed thermal behaviors for parallel flow microchannel heat exchanger. *International Communications in Heat and Mass Transfer*, 36(4), 385−390. doi: 10.1016/j.icheatmasstransfer.2009.01.010

[13] Wajs, J., Mikielewicz, D., & Fornalik-Wajs, E. (2016). Thermal performance of a prototype plate heat exchanger with minichannels under boiling conditions. In *Proc. of 7th European Thermal-Sciences Conference (Eurotherm2016)*. *Journal of Physics: Conference Series*, 745(3), 032063. doi: 10.1088/1742-6596/745/3/032063

[14] Mikielewicz, D., & Wajs, J. (2017). Possibilities of heat transfer augmentation in heat exchangers with minichannels for marine applications. *Polish Maritime Research Special Issue*, 24, 133−140. doi: 10.1515/pomr-2017-0031

[15] Yang, Y., Brandner, J.J., & Morini, G.L. (2012). Hydraulic and thermal design of a gas microchannel heat exchanger. In *Journal of Physics: Conference Series*, 362(1), 012023. doi: 10.1088/1742-6596/362/1/012023

[16] Dang, T., Teng, J.T., & Chu, J C. (2010). A study on the simulation and experiment of a microchannel counter-flow heat exchanger. *Applied Thermal Engineering*, 30(14−15), 2163−2172. doi: 10.1016/j.applthermaleng.2010.05.029

[17] Tychanicz-Kwiecień, M. (2022). The application of the Wilson plot method to convective heat transfer-discussion. *Advances in Mechanical and Materials Engineering*, 39(94), 77−89. doi: 10.7862/rm.2022.6

[18] Fernando, P., Palm, B., Ameel, T., Lundqvist, P., & Granryd, E. (2008). A minichannel aluminium tube heat exchanger– Part I: Evaluation of single-phase heat transfer coefficients by the Wilson plot method. *International Journal of Refrigeration*, 31(4), 669−680. doi: 10.1016/j.ijrefrig.2008.02.011

[19] Rybiński, W., & Mikielewicz, J. (2018). Statistical method for the determination of the minichannel heat exchanger's thermal characteristics. *Energy*, 158, 139−147. doi: 10.1016/j.energy.2018.05.175

[20] Tychanicz-Kwiecień, M., Smusz, R., & Gil, P. (2019). The design of experimental set-up for testing of heat exchangers. In *Contemporary issues of heat and mass transfer*, 2 (pp. 901−918). Publishing House of the Koszalin University of Technology.

[21] Mobedi, M., & Gediz Illis G. (2023). *Fundamentals of Heat Transfer: An Interdisciplinary Analytical Approach*. Springer Nature Singapore. doi:10.1007/978-981-99-0957-5

[22] Lee, P.S., & Garimella, S.V. (2006). Thermally developing flow and heat transfer in rectangular microchannels of different aspect ratios. *International Journal of Heat and Mass Transfer*, 49, 3060−3067. doi: 10.1016/j.ijheatmasstransfer.2006.02.011

[23] Kandlikar, S.G., Garimella, S., Li, D., Colin, S., & King, M.R. (2006). *Heat transfer and fluid flow in minichannels and microchannels*. Elsevier Ltd., Oxford.

[24] Shah, R.K., & London, A.L. (1978). *Laminar flow forced convection in ducts*. Academic Press, New York.

[25] Rybiński, W., & Mikielewicz, J. (2014). Analytical solutions of heat transfer for laminar flow in rectangular channels. *Archives of Thermodynamics*, 35(4), 29−42. doi: 10.2478/aoter-2014-0031

[26] Morini, G.L., Lorenzini, M., Salvigni, S., & Celata, G.P. (2010). Experimental analysis of microconvective heat transfer in the laminar and transitional regions. *Experimental Heat Transfer*, 23, 73−93. doi: 10.1080/08916150903402757

[27] Wilk, J. (2013). *Investigation of heat transfer in short minichannels*. Publishing House of the Rzeszów University of Technology.

[28] Brandt, S. (2014). *Data analysis. Statistical and computational methods for scientists and engineers* (4th Edn.). Springer.

Co-published by
Institute of Fluid-Flow Machinery
Polish Academy of Sciences
Committee on Thermodynamics and Combustion
Polish Academy of Sciences

Copyright©2024 by the Authors under licence CC BY 4.0

http://www.imp.gda.pl/archives-of-thermodynamics/

Complexity of two-phase flow dynamics using the recurrence and high speed video analysis

Romuald Mosdorf[a*], Gabriela Rafałko[a], Iwona Zaborowska[a], Paweł Dzienis[a], Hubert Grzybowski[a]

[a]Bialystok University of Technology, Faculty of Mechanical Engineering, Wiejska 45C, Bialystok 15-351, Poland
*Corresponding author email: r.mosdorf@pb.edu.pl

Received: 20.12.2023; revised: 15.03.2024; accepted: 15.04.2024

Abstract

During flow boiling in a system with small (mini/micro) channels, several instabilities may occur at the same time, which overlap each other – such a phenomenon complicates the analysis of boiling dynamics. The above mentioned processes cause that the fluctuation of recorded signals occur on various time scales. Although many criteria for the stability of two-phase flows are available, their practical application is limited (they need many recorded parameter of two phase flow). Methods which we are looking for should allow flow pattern identification based on a small number (or single) recorded signals. The paper presents a new approach to the recurrence plot method combined with Principal Component Analysis and Self-Organizing Map analysis. The single signal of pressure drop oscillations has been analyzed and used for flow pattern identification. New method of correlation analysis of flow patterns on video frames has been presented and used for flow pattern identification. The obtained results show that pressure drop oscillations and high speed video contain enough information about flow pattern for flow pattern identification.

Keywords: Instabilities; Two-phase flow; Recurrence analysis; Image analysis

Vol. 45(2024), No. 2, 73–81; doi: 10.24425/ather.2024.150853

Cite this manuscript as: Mosdorf, R., Rafałko, G., Zaborowska, I., Dzienis, P., & Grzybowski, H. (2024). Complexity of two-phase flow dynamics using the recurrence and high speed video analysis. *Archives of Thermodynamics*, 45(2), 73−81.

1. Introduction

Flow instability in the heated small (mini/micro) channel develops for high heat flux, which are the main factor determining the two-phase flow patterns in channels. The flow instabilities are related to the following processes: phase changes, heat flow, liquid and vapor flow as well as processes occurring in the heat exchanger's supply system with liquid and heat. With high heat flux supplied to the system, a small deviation from equilibrium leads to an exponential increase in the phase distribution [1]. Instabilities in two-phase flows accompanying boiling in small channels cause oscillations in the pressure drop, liquid and vapor flow rates, and channel wall temperatures.

Instabilities have been studied by Kennedy et al. [2], Kandlikar [3,4], Qu and Mudawar [5], Brutin et al. [6], Hetsroni et al. [7], and Bergles et al. [8], Tadrist [9], found that several types of instabilities observed in small channels are similar to those found in conventional channels. These include: Ledinegg instability, pressure drop oscillations and instability caused by changes in the mass flow density. During the experimental studies described in [10,11], oscillations in the pressure drop and

Nomenclature

DET − RQA coefficient, %
G − water flow rate, kg/(m^{2}s)
I − light intensity, scale from 0 to 255
k − percentage of the energy of light falling on the surface that was reflected
L − length, samples
L_{max} − RQA coefficient, samples
m − space dimensional
p − probability
P − histogram of probability, pressure, kPa
R − correlation coefficient
RPDE − RQA coefficient (entropy of points on diagonal lines)
S − $R_{max} - R_{avg}$
SD − standard deviation
T^1 − vertical distance in RP, samples
T^2 − vertical distance in RP, samples
V − volume, cm^3
V_v − coefficient
x − coordinate
Y − pixel brightness
z − channel number
|| || − norm

Greek symbols

α − angle between the vector normal to the surface and the direction of the observer, rad
$\Delta\alpha$ − the transparent diaphragm
$\Delta\beta$ − roughness of the channel bottom
$\Delta\delta$ − roughness of the mirror
ε − diameter of the sphere inside which the distance of two points is measured, samples
Θ − Heaviside step function
τ − delay time, samples

Subscripts and Superscripts

avg − average value
a − ambient light intensity
d − light source intensity
max − maximum
k − frame number

Abbreviations and Acronyms

PCA − Principal Component Analysis
RP − Recurrence Plot
SOM − Self-Organizing Map
RQA − Recurrence Quantification Analysis

temperature of the channel wall were noticed and videos were recorded showing periodic reverse flow in mini channels. This vapor flow heading into the inlet chamber is caused by the operation of the exchanger at critical values of the heat flux, which leads to mixing of the steam with the incoming subcooled liquid. In mini-channel systems, the influence of the channel wall temperature on heat transfer is much greater than in conventional systems. In channels with much smaller hydraulic diameter than the channel length, surface tension has a significant impact on the flow dynamics and stability of the system [12]. Fogg and Goodson in [13] investigated the influence of acoustic waves generated by rapidly nucleating bubbles during boiling in the flow in microchannels. It has also been shown that the negative pressure created by propagating pressure pulses can cause other bubbles to grow at lower channel wall temperatures.

The most commonly used classification, introduced by Bouré et al. [14], divides the instabilities of two-phase flow into static and dynamic. Static instabilities are considered to be momentary disturbances in which new operating conditions of the system tend to asymptotically change the state of the system - such a process is usually accompanied by high-frequency oscillations of pressure and temperature. On the other hand, dynamic instabilities are those in which a system cannot achieve a new equilibrium state, but only oscillates around a new equilibrium state. During dynamic instability, the system constantly changes its state between various unstable states - such a process is also accompanied by high-frequency oscillations of pressure and temperature. The occurrence of a number of instabilities causes the heat and mass transfer process in small channels to be non-stationary, therefore the analysis of boiling requires the use of methods that allow to characterize the non-stationary nature of the system. An important issue in the study of the boiling process in small channels is the identification of two-phase flow patterns in unsteady heat and mass transfer processes. Knowledge about the nature of non-stationary processes will allow the creation of more accurate models predicting heat and mass transfer in mini- and micro-channel systems.

Although many criteria for the stability of two-phase flows are available, their practical application for the analysis of heat transfer in real systems is limited [15]. This is because in real systems it is difficult to control all the flow parameters on the basis of which the nature of the two-phase flow is determined. Therefore, methods which we are looking for should allow flow identification based on a small number (or single) of recorded signals. In work [15] pressure drop oscillations and their impact on heat flux transferred through the exchanger were studied. It was shown that the time-averaged surface temperature and critical heat flux were insensitive to the occurrence of flow instability. Flow patterns identification was possible by taking into account high-frequency pressure oscillations and high-speed visualization.

In the paper [16] a method for indirect recognition of flow patterns was proposed, based on time-frequency analysis and neural networks. In order to examine flow patterns in a narrow rectangular channel, a pressure signal was used. The work [17] classified and summarized various methods of suppressing the instability of two-phase flows. The authors of the work concluded that more investigations should be done to identify instability under different operating conditions in different microchannel systems to avoid and suppress instability. In the paper [18], the authors showed that the use of machine learning becomes effective when the algorithms take into account the physical aspects of processes. Such solutions allow for the analysis of transition areas between boiling regimes.

When examining boiling in two-phase flow in channels on a mini- and micro-scale, a number of experimental data are rec-

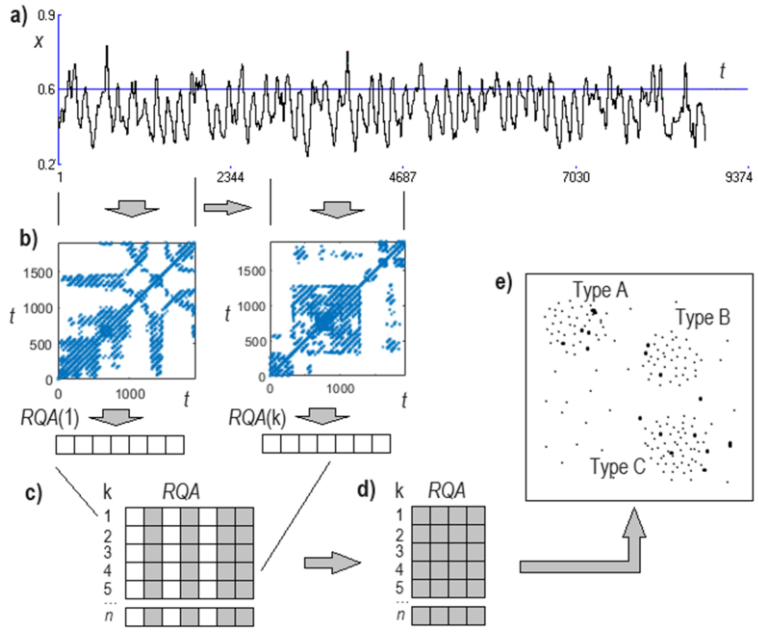


Fig. 1. Scheme of the algorithm for identifying two-phase flow patterns based on pressure fluctuations: a) an example of registered signal, b) the results of RQA analysis, c) a matrix of RQA coefficients determined in subsequent time intervals, d) selection of RQA coefficients, e) PCA or SOM analysis.

orded which contain information about the nature of the phenomenon. Experimental data includes, among others, measurement of pressure changes, liquid temperature changes, channel wall temperature changes and video data recorded by high-speed cameras. Pressure oscillations occurring in two-phase flow contain a lot of noise resulting from the changes in the two-phase flow patterns, therefore, they are difficult to analyze. At the same time, pressure oscillations have an irregular, chaotic character. One of the basic features of a chaotic systems is recurrence, which can be used in the analysis of pressure oscillations.

In this paper the recurrent patterns in the pressure oscillation signal are applied to identify changes in two-phase flow structures. Selected methods for analyzing the dynamics of two-phase flow patterns based on video analysis are also presented.

2. Application of recurrent analysis to study pressure fluctuations

2.1. Algorithm

In Fig. 1a, a diagram of the algorithm for identifying two-phase flow patterns based on pressure fluctuations is shown [19]. Figure 1a shows an example of the registered signal - pressure fluctuations. Figure 1b schematically shows two stages of RQA analysis. In the first stage, the attractor is reconstructed in the multidimensional phase space. Then recurrence plots are created – this process is schematically shown in Fig. 1b. A recurrence plot is a two-dimensional (square) matrix containing zeros and ones. The matrix dimension defines the number of analyzed samples (schematically marked by the black lines in Fig. 1a). RQA analysis involves determining a series of coefficients characterizing the arrangement of ones in the matrix. In the considered method the RQA coefficients are determined for subsequent time intervals [19]. The result of calculation of the RQA coefficient is shown schematically in Fig. 1c as the matrix. A statistical analysis of the changes in the values of RQA coefficients allows the selection of coefficients that best describe the diversity of the two phase flow pattern changes. This analysis creates the matrix shown in Fig. 1d. The visualization of the data in the matrix shown in Fig. 1e can be performed using PCA or neural networks (SOM) methods.

From the formal point of view the recurrence plot is defined as follows [20]:

$$RP_{i,j} = \Theta\left(\varepsilon - \left\|x_i - x_j\right\|\right), \qquad i,j = 1,\dots,N, \tag{1}$$

where $\Theta(\cdot)$ – Heaviside step function, ε – diameter of the sphere inside which the distance of two points is measured, $\|\ \|$ – norm in m-dimensional space.

The *DET* coefficient determines the percentage of recurrence states occurring on diagonal lines to all recurrence states of the system [20]:

$$DET = \frac{\sum_{l=l_{min}}^{N} lP(l)}{\sum_{l=1}^{N} lP(l)}, \tag{2}$$

where $P(l) = P(\varepsilon, l)$ is the histogram of diagonal lines of length l in the neighborhood of ε.

The L coefficient determines the average length of the diagonal lines in a recurrence plot. The L coefficient is described by the following relation [20]:

$$L = \frac{\sum_{l=l_{min}}^{N} lP(l)}{\sum_{l=l_{min}}^{N} P(l)}. \tag{3}$$

The L_{max} coefficient determines the maximum length of diagonal lines.

The *RPDE* coefficient is a measure of the entropy of points on diagonal lines. The *RPDE* coefficient is described by the following relation [20]:

$$RPDE = -\sum_{l=lmin}^{N} p(l)\ln p(l), \quad (4)$$

where $p(l)$ is the probability of finding a diagonal line of length l: $p(l) = \frac{P^{\varepsilon}(l)}{\sum_{l=lmin}^{N} P^{\varepsilon}(l)}$.

Entropy is a measure of uncertainty – an increase in the *RPDE* coefficient means that the system becomes more chaotic.

Gao [21] defines the recurrence time of the first type T^1 and the second time T^2. The recurrence time is calculated as the distance between points belonging to the vertical lines in *RP*. In the case of recurrence time of the first type T^1, all points of *RP* are considered. Such value of T^1 depends on the trajectory density and value of ε. In case of recurrence time of the second type T^2 the vertical distances between the pairs "white" pixel/"black" pixel in the columns are measured [22]. Then, in this case for the periodic motion, T^2 accurately estimates the period of the motion.

2.2. Application

The paper presents the results of the method (Fig. 1) application for analyzing pressure fluctuations in a single mini-channel and in an exchanger consisting of many parallel mini-channels [19,23]. Figure 2a shows a diagram of the measurement stand and Fig. 2b shows example pressure drop fluctuations. The pressure fluctuation amplitudes shown in Fig. 2b increase when vapor bubbles appear in the heated channel, blocking the flow (at the beginning of the cycle the channel is filled with water). When the slug flow begins, the amplitude of pressure fluctuations reaches its maximum values (90 seconds after the beginning of the cycle).

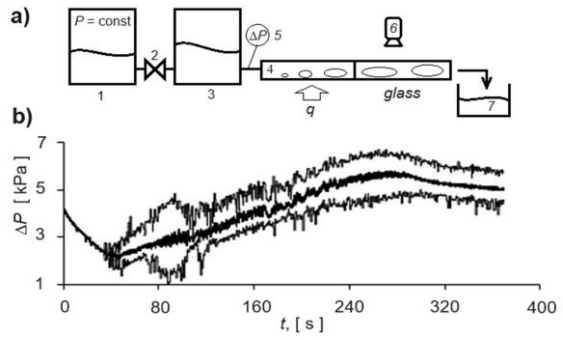


Fig. 2. a) the scheme of the experimental stand: single-channel exchanger, 1 – supply tank; 2 – ball valve; 3 – compressible volume; 4 – heat exchanger; 5 – pressure sensor, 6 – Phantom camera, 7 – output tank; b) pressure drop fluctuations, the chart showing the minimum, maximum and average value of water pressure oscillations at the inlet to the channel; channel diameter – 1 mm, water flow rate, G = 159 kg/(m^{2}s), electric power 57.2 W [19].

The moving window in the windowed RQA analysis contained 5000 samples of pressure oscillations (5s), and the window shift was equal to 1000 samples of pressure oscillations (1s) – 181 windows were analyzed. The RQA coefficient values were calculated using the CRP package [23] in MATLAB. The length of the time window in the RQA analysis was determined by pressure oscillations caused by flowing long slug, which generate pressure changes that occur at low frequency. The assumed interval of 5 s corresponds to the flow of approximately 5 long slugs. In the RQA window analysis, the parameters of the immersion dimension (m), delay time (τ) and threshold distance (ε) were determined separately for each window. The dimension m was estimated using the false nearest neighbours method [23]. The value of τ was selected using the mutual information function [24], while the value of ε was defined as 10% of the maximum attractor diameter. Figure 3 shows the changes in coefficients (*DET*, 1/*L*, T^2, 1/*RPDE*). The values of these coefficients were used to build the SOM map shown in Fig. 4.

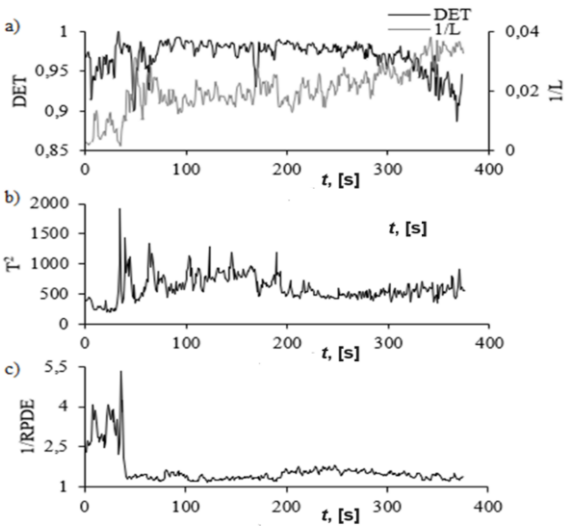


Fig. 3. The changes in the RQA coefficients obtained for water pressure oscillations at the inlet to the mini-channel at G = 159 kg/(m^{2}s), electric power equal to 57.2 W: a) *DET*, 1/*L*, b) T^2, c) 1/*RPDE*; calculations were performed using the RP package [23] in Matlab.

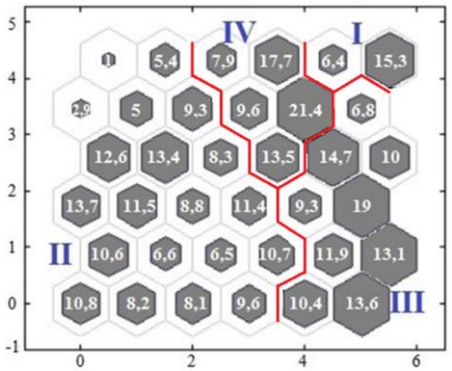
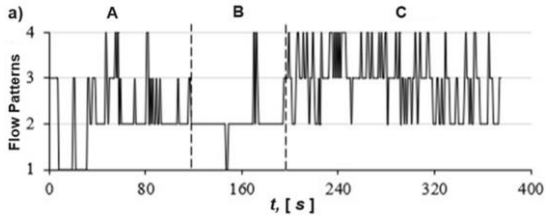


Fig. 4. Average hit histograms obtained from RQA coefficients calculated for inlet water pressure oscillations at: G = 159 kg/(m^{2}s), electric power equal to 57.2 W [25].

The changes in the *DET* coefficient presented in Fig. 3a show that changes in the character of pressure fluctuations occur rapidly in the initial phase of boiling - in bubble flow and in the initial phase of slug flow. Such behaviour appear also at the end of the cycle - when the increasing average pressure value leads to boiling disappearance. The average length of the diagonal line shown in Fig. 3a determines the average duration of a given flow

pattern in the channel – it is the smallest at the end of the cycle (boiling disappearance) and the largest at the beginning of the cycle when the boiling begins. Fluctuations in the T^2 coefficient reflect changes in the characteristic frequencies of pressure fluctuations. The nature of the changes is most rapid in the initial phase of boiling and in slug flow. The entropy values shown in Fig. 3c show the chaotic character of pressure fluctuations during the boiling in the channel.

In Fig. 4, four local maxima can be distinguished, which identify four different two-phase flow patterns.



	Two-phase flow patterns			
	1	2	3	4
A	19%	52%	26%	3%
B	2%	89%	6%	3%
C	0%	27%	54%	19%

Fig. 5. Results of the RQA and SOM analysis obtained for inlet pressure, G = 159 kg/(m^{2}s) and electric power equal to 57.2 W: a) distinguished two-phase flow patterns (vertical axis) - result of training the SOM network (number of local maximum) and they accuracy in time; b) the percentage of the two-phase flow patterns present in the boiling flow. 1 – water flow with small bubbles, 2 – bubble flow, 3 – slug flow, 4 – long slug flow [25].

The analysis of changes in time these patterns, performed on the basis of data collected in the SOM algorithm, allows the identification of the flow patterns, these were: 1 – water flow with small bubbles, 2 – bubble flow, 3 – slug flow, 4 – long slug flow. The ranges of occurrence of flow patterns are shown in Fig. 5.The result of SOM algorithm (distinguished two-phase flow patterns - vertical axis and they accuracy in time are presented in Fig. 5a. The percentage of the two-phase flow patterns presents in the boiling flow is presented in Fig. 5b.

3. Analysis of the dynamics of phase change based on videos

3.1. Algorithm

The validation of the results presented in the previous chapter were performed using the recorded videos of two-phase flow. The videos contain information about processes that are not visible in the pressure fluctuations. Therefore, selected methods for analyzing the dynamics of two-phase flow patterns based on image (video) analysis are presented below. The analysis of characteristic flow features was carried out on the basis of pixel brightness changes. The similarity and complexity of phase distribution were analyzed.

The presented method for examining the similarity of the phase distribution uses the Pearson correlation coefficient. The initial step of the analysis is to divide the recorded videos into frames. The example of the frames set is schematically shown in Fig. 6a.

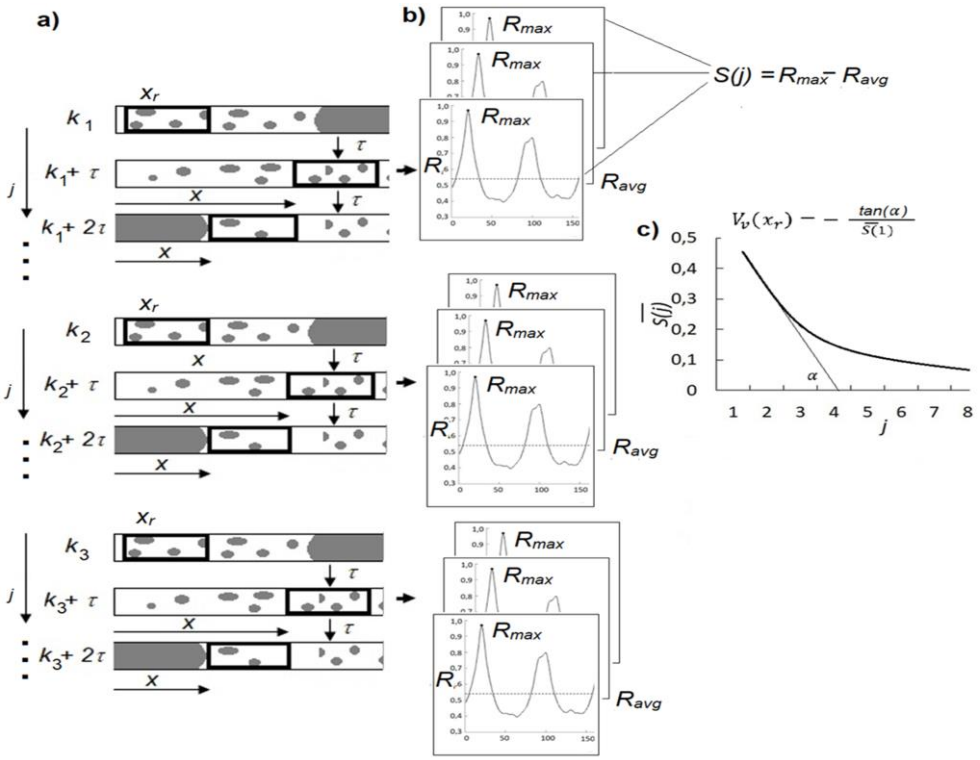


Fig. 6. Two-phase flow video analysis scheme: a) subsequent video frames, reference frames (k) and reference gates (x_r – position of the reference gate), test frames ($k + \tau$ – test frame number), τ – time between subsequent test frames, x – position of the moving gate; arrows indicate the flow direction; b) correlation between the reference gate and the test gates; c) plot of the average values ($R_{max} - R_{avg}$) for subsequent test gates [25].

In the set of frames (Fig. 6a), reference frames (k) and reference gates (x_r - position of the reference gate) are defined. On test frames $k + \tau$, test gates are moved, the position of which is denoted with x. In this way, for each reference gate, a set of graphs is created which describe correlation between reference gate and test gates moving on subsequent test frames. A set of graphs obtained in this way is schematically shown in Fig. 6b. The following value is determined for each graph:

$$S(j) = R_{max} - R_{avg} \tag{5}$$

The $S(j)$ is averaged for subsequent (all) test gates, finally the graph shown in Fig. 6.c is created. The graph is used to determine the value of the V_v coefficient in accordance with the following relation:

$$V_v = -\frac{\tan(\propto)}{\bar{S}(1)}. \tag{6}$$

The algorithm was used to identify flow patterns [25,26]. The analysis of the flow of a mixture of water, glycerin and air showed that the V_v coefficient reaches the lowest values for slug flows and the highest in the case of mini-bubble flows. The slug flow is characterized by smaller changes in phase distribution than mini-bubble flow, which results in a lower value of the V_v coefficient. The obtained result confirms that the value of the V_v coefficient characterizing the "speed" of phase distribution changes in channel.

3.2. Application

The algorithm presented in the previous chapter (Fig. 6) was used to determine the position of the boiling front in an exchanger with parallel mini channels [25,27]. It was assumed that the change in phase distribution occurs most rapidly in the place where the boiling front is formed in parallel microchannels. Therefore in the previous algorithm (Fig. 6), additionally, the movement of the reference gate position was taken into account. Finally, in order to identify the channel fragments with the most rapid phase distribution changes, the position of the reference gate was searched for at which the V_v coefficient reaches its maximum value.

The scheme of the experimental stand is shown in Fig. 7.

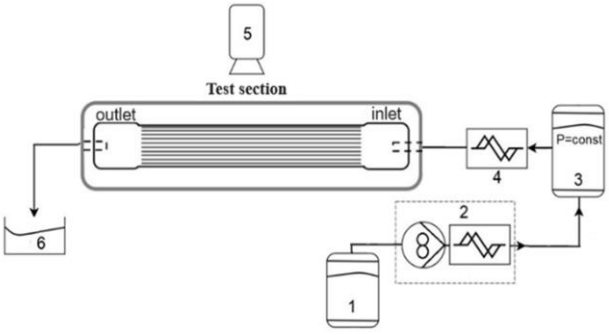


Fig. 7. Experimental stand with microchannels: 1 - feed tank with distilled water, 2 – gear pump with flowmeter (Bronkhorst Cori-Tech M13 with pump), 3 – compressible volume (V = 222.8 cm^3), 4 – flowmeter (Bronkhorst mini CORI-FLOW M13, accuracy ± 0.2% of flow rate), 5 – high-speed camera (Phantom v1610), 6 – outlet tank.

The working medium (distilled water) - see Fig. 7, was supplied from the supply tank (1) by a gear pump (2) connected to a flowmeter (Bronkhorst Cori-Tech M13 with pump, accuracy 2% of the measured value) to the compressible volume (3). The flow rate of water supplied to the inlet space was monitored by a mass flow meter (4) (Bronkhorst Cori-Tech M13 based on the Coriolis measuring principle) installed between the compressible volume and the exchanger (microchannels exchanger consisting of 11 copper microchannels: depth × width × length = 0.13 × 0.25 × 32 mm). Pressure sensors (MPX50DP, range: 0−50 kPa, sensitivity: 1.2 mV/kPa, response time: 0.001 s, accuracy: 1.25 kPa) and thermocouples (type K, diameter 0.081 mm, accuracy: ± 0.8 K, response time: 0.025 s) were installed. After passing through the channels, the water headed to the outlet tank (6). The flow of the medium through the channels was recorded using a high-speed camera - Phantom v1610 (5) through a transparent plexiglass and a mirror. The heat flux supplied to the channels was measured by three thermocouples (type K, diameter 0.081 mm, accuracy: ± 0.8 K, response time: 0.025 s) located in a copper pin. Heat was supplied to the system using eight electric heaters with a maximum power of 50 W. During the experiment, the electrical power supplied to the system was constant, while the liquid flow rate varied. Two measurement data acquisition systems were used (DAQ Data Translation DT9804, Data Translation DT9805) and collected data at a frequency of 1 kHz.

3.3. Measurement error analysis

In this work, the analyzed physical quantity is the pixel brightness (Y) recorded by the Phantom v1610 camera. The level of pixel brightness recorded by the camera is a function of the light intensity reaching the camera lens , and is determined by the relationship [28]:

$$Y = I_a + I_d k \cos\alpha, \tag{7}$$

where: I_a – ambient light intensity, I_d – point light intensity of the light source, k – percentage of the energy of light falling on the surface that was reflected, α – angle between the vector normal to the surface and the direction of the observer.

To determine the absolute maximum uncertainty of pixel brightness resulting from the intensity of light reaching the camera (Y), the complete differential method was used. It was determined on the basis of the uncertainty of individual arguments: roughness of the transparent diaphragm ($\Delta\alpha$), roughness of the channel bottom ($\Delta\beta$) and roughness of the mirror ($\Delta\delta$):

$$Y = \cos\left(\left|\frac{\partial f(\alpha,\beta,\delta)}{\partial\alpha}\right|\Delta\alpha + \left|\frac{\partial f(\alpha,\beta,\delta)}{\partial\beta}\right|\Delta\beta + \left|\frac{\partial f(\delta\alpha,\beta,\delta)}{\partial\delta}\right|\Delta\delta\right). \tag{8}$$

The analysis of the roughness of the channel bottom surface was performed using a VHX-7000 optical microscope (Keyence) at x700 magnification. The pixel brightness error was ±0.13 on a scale from 0 to 255. This allows us to conclude that the proposed image analysis method has a small error.

Figure 8a shows the V_v coefficient obtained for single microchannel which is shown in Fig. 8b. The value of the V_v coefficient identifies the position of the reference gate (x_r) where the "speed" of phase distribution changes reach the maximum.

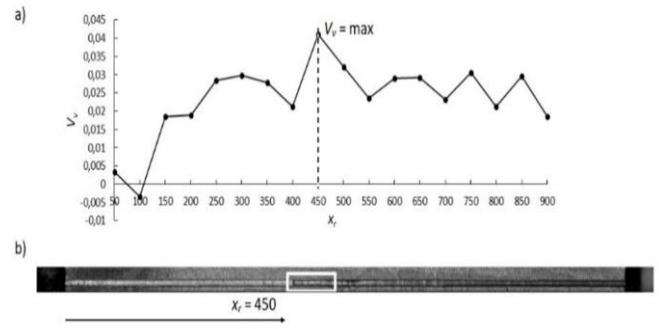


Fig. 8. Determining the channel fragments with the most rapid phase distribution changes: a) V_v coefficient as a function of the position of the reference gate (x_r – number of pixels); b) single frame of video with channel, the position of the maximum value of V_v coefficient was marked by a rectangle [25].

The location of the most rapid phase distribution changes determined for the entire exchanger is shown in Fig. 9. Figure 9 shows the positions of the reference gates (in the form of a point) in subsequent microchannels at which the V_v coefficient reaches its maximum. Fig. 9b shows an example video frame with the marked positions of the reference gates indicating the location of the most significant phase distribution changes.

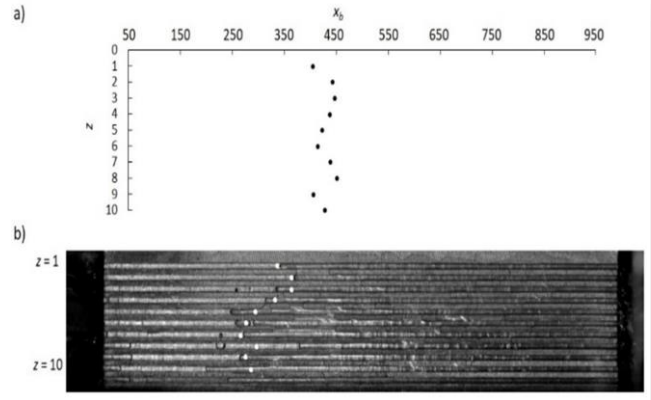


Fig. 9. The location of the most rapid phase distribution changes: a) chart showing the location of the most rapid phase distribution changes (black points); b) an example video frame with the marked positions of the reference gates indicating the location of the most significant phase distribution changes, (x_b – number of pixels from the inlet, z – channel number) [25].

An analysis of the repeatability of the results obtained using the phase distribution similarity method for assessing the dynamics of phase change was carried out. The aim of the repeatability analysis was to determine the size of the dispersion of the boiling front positions in the considered flow fragments. The multiple calculations of the reference gate positions at which the V_v coefficient reached its maximum were carried out for various fragments of recorded videos. The results of calculation for 10 microchannels have been shown in Table 1.

Table 1. The results of the repeatability analysis. z − microchannel number, 1−6 − considered fragments of the film, x_r − position of the boiling front, *avr* − average value of x_r in each microchannel, *SD* – standard deviation of the position of x_r, [25].

z (-)	Considered fragments of the film				*avr* (mm)	*SD* (mm)
	1	2	...	6		
	x_b (mm)	x_b (mm)		x_b (mm)		
1	10.00	11.25		7.50	9.58	1.91
2	8.75	12.50		7.50	9.58	2.60
3	8.75	8.75		11.25	9.58	1.44
4	8.75	6.25		8.75	7.92	1.44
5	10.00	7.50		8.75	8.75	1.25
6	7.50	10.00		8.75	8.75	1.25
7	10.00	10.00		7.50	9.17	1.44
8	7.50	6.25		6.25	6.67	0.72
9	6.25	8.75		10.00	8.33	1.91
10	10.00	7.50		11.25	9.58	1.91

The obtained results show that the proposed analysis method is repeatable and determines the location of the boiling front with an error equal about 20%.

4. Conclusions

The research carried out is consistent with the current research direction in published works which involves the identification of flow patterns based on high-frequency changes in single parameters of two-phase flows. The current work analyzed high-frequency pressure oscillations and high-frequency changes in pixel brightness in high-speed video frames. The paper presents a new approach to flow boiling pattern identification using recurrence plot method combined with PCA and SOM analysis. The new method of correlation analysis of flow patterns on video frames has been presented and used for flow pattern identification.

The obtained results show that pressure drop oscillations and high speed video contain enough information about flow pattern for flow pattern identification. It has been shown that the methods of analyzing boiling pressure fluctuations in small channels using recurrence analysis enable the identification of two-phase flow patterns in boiling. Moreover, the information contained in the pixels brightness changes in the videos directly recorded during two-phase flows in small channels allows identifying flow patterns and studying processes occurring in boiling.

The use of the methods proposed in this paper to identify flow patterns based on selected measurement data is effective, but their application to other measurement data requires a preliminary analysis of the measurement data. An important parameter is the sampling frequency - it cannot be too high because then the signal will be noisy - which will prevent the extraction of important flow features. In this case, signal filtering can be used, but such manipulation of measurement data may affect the result of identifying flow patterns. The sampling frequency cannot be too low because the signal will not contain enough information about important characteristics of the flow patterns. In

the case under consideration in the paper, both sampling frequency of pressure changes and the speed of film frames registration were sufficient to identify the flow of individual bubble, increasing the water flow rate would require increasing the sampling frequency. Research on selecting an appropriate sampling frequency should be continued for different cases.

The new data analysis methods presented in the paper was tested on data collected in experiments performed by the authors of the work. During our measurements the appropriate data recording parameters were set. The analysis methods proposed in this work were also applied to other types of measurement data in order to determine their suitability for identifying selected features of time series. In these cases medical data [30], tribological data [31] and the process of air bubbles departure from nozzles [29] were analyzed. The obtained results confirm the high effectiveness of the analysis methods presented in the paper.

Acknowledgements

The research was funded by the National Science Center grant UMO-2017/27/B/ST8/02905.

References

[1] Ruspini, L.C., Marcel, C.P., & Clausse, A. (2014). Two-Phase Flow Instabilities: A Review. *International Journal of Heat and Mass Transfer*, 71, 521–548. doi: 10.1016/j.ijheatmasstransfer. 2013.12.047

[2] Kennedy, J.E., Roach, G.M., Dowling, M.F., Abdel-Khalik, S.I., Ghiaasiaan, S.M., Jeter, S.M., & Quershi, Z.H. (2000). The Onset of Flow Instability in Uniformly Heated Horizontal Microchannels. *J. Heat Transfer*, 122, 118–125. doi: 10.1115/1.521442

[3] Kandlikar, S.G. (2002). Fundamental Issues Related to Flow Boiling in Mini channels and Microchannels. *Experimental Thermal and Fluid Science*, 26, 389–407. doi: 10.1016/s0894-1777(02) 00150-4

[4] Kandlikar, S., Steinke, M., Tian, S., & Campbell, L. (2001). High-Speed Photographic Observation of Flow Boiling of Water in Parallel Mini-Channels. *Proceedings of NHTC'01 35th National Heat Transfer Conference*, Anaheim, California

[5] Qu, W., & Mudawar, I. (2003). Measurement and Prediction of Pressure Drop in Two-Phase Micro-Channel Heat Sinks. *International Journal of Heat and Mass Transfer*, 46, 2737–2753. doi: 10.1016/S0017-9310 (03)00044-9

[6] Brutin, D., Topin, F., & Tadrist, L. (2003). Experimental Study of Unsteady Convective Boiling in Heated Minichannels. *J. Heat Transfer*, 46, 2957–2965. doi:10.1016/S0017-9310(03)00093-0

[7] Hetsroni, G., Mosyak, A., Segal, Z., & Pogrebnyak, E. (2003). Two-Phase Flow Patterns in Parallel Micro-Channels. International Journal of Multiphase Flow, 29, 341–360. doi: 10.1016/ S0301-9322(03)00002-8

[8] Bergles, A.E., Lienhard V. J.H., Kendall, G.E., & Griffith, P. (2003). Boiling and Evaporation in Small Diameter Channels. *Heat Transfer Engineering*, 24, 18–40. doi: 10.1080/01457630304041

[9] Tadrist, L. (2007). Review on Two-Phase Flow Instabilities in Narrow Spaces. *International Journal of Heat and Fluid Flow*, 28, 54−62. doi: 10.1016/j.ijheatfluidflow.2006.06.004

[10] Grzybowski, H., & Mosdorf, R. (2018). Dynamics of Pressure Drop Oscillations during Flow Boiling inside Minichannel. *International Communications in Heat and Mass Transfer*, 95, 25–32. doi:10.1016/j.icheatmasstransfer.2018.03.025

[11] Rafałko, G., Zaborowska, I., Grzybowski, H., & Mosdorf, R. (2020). Boiling Synchronization in Two Parallel Mini channels - Image Analysis. *Energies*, 13, 1409. doi: 10.3390/en13061409

[12] Yarin, L.P., Mosyak, A., & Hetsroni, G. (2009) Fluid Flow, Heat Transfer and Boiling in Micro-Channels; *Heat and Mass Transfer*; Springer-Verlag: Berlin Heidelberg, doi:10.1007/978-3-540-78755-6

[13] Fogg, D., & Goodson, K. (2009). Bubble-Induced Water Hammer and Cavitation in Microchannel Flow Boiling. *J. Heat Transfer*, 131, 1–12. doi:10.1115/1.3216381

[14] Boure, J.A., Bergles, A.E., & Tong, L.S. (1973). Review of Two-Phase Flow Instability. *Nuclear Engineering and Design*, 25, 165−192. doi: 10.1016/0029-5493 (73)90043-5

[15] Clark, M.D., Weibel, J.A., & Garimella S.V. (2023), Impact of pressure drop oscillations and parallel channel instabilities on microchannel flow boiling and critical heat flux. *International Journal of Multiphase Flow*, 161, 104380. doi: 10.1016/j.ijmultiphaseflow.2023.104380

[16] Chu, A.W., Liu, B.Y., Pan, C.L., Zhu, D.H., & Yang, E.X. (2022). Identification of boiling flow pattern in narrow rectangular channel based on TFA-CNN combined method. *Flow Measurement and Instrumentation*, 83, 102086. doi: 10.1016/j.flowmeasinst.2021. 102086

[17] Wang, B., Hu, T., He, Y., Rodionov, N., & Zhu, J. (2022). Dynamic instabilities of flow boiling in micro-channels: A review. *Applied Thermal Engineering*, 214, 118773. doi: 10.1016/j.applthermaleng .2022.118773

[18] Zhu, L., Ooi, Z.J., Zhang, T., Brooks, C.S., & Pan, L. (2023). Identification of flow regimes in boiling flow with clustering algorithms: An interpretable machine-learning perspective. *Applied Thermal Engineering*, 228, 120493. doi: 10.1016 /j.applthermaleng.2023.120493

[19] Zaborowska, I. (2023). *Experimental studies and numerical identification of the dynamics of two-phase flow patterns in boiling in mini- and micro-channels*. PhD thesis, Bialystok University of Technology.

[20] Zbilut, J.P., & Webber, C.L. (1992). Embeddings and Delays as Derived from Quantification of Recurrence Plots. *Physical Letters A*, 171, 199–203. doi: 10.1016/0375-96 01(92)90426-M

[21] Gao, Z.-K., Jin, N.-D., & Wang, W.-X. (2014). *Nonlinear analysis of gas-water/oil-water two-phase flow complex networks*. Springer: Berlin, Heidelberg. doi: 10.1007/978-3-642-38373-1_1

[22] Gao, Z.-K., Zhang, X.-W., Jin, N.-D., Donner, R.V., Marwan, N., & Kurths, J. (2013). Recurrence Networks from Multivariate Signals for Uncovering Dynamic Transitions of Horizontal Oil-Water Stratified Flows. *Europhysics Letters*, 103(5), 50004. doi: 10.1209/ 0295-5075/103/50004

[23] Zaborowska, I., Grzybowski, H., Rafałko, G., & Mosdorf, R. (2021). Boiling dynamics in parallel minichannel system with different inlet solutions, *International Journal of Heat and Mass Transfer*, 165, 1–10. doi: 10.1016/j.ijheatmasstransfer.2020. 120655

[24] Marwan, N. *Cross Recurrence Plot Toolbox for MATLAB®, Ver. 5.22*. http://Tocsy.Pik-Potsdam.de/ CRPtoolbox/ [accessed 08 Feb. 2024].

[25] Rafałko, G. (2023). *Application of image analysis to identify and investigate the dynamics of two-phase flow patterns.* PhD thesis, Bialystok University of Technology.

[26] Rafałko, G., Mosdorf, R., & Górski, G. (2020). Two-phase flow pattern identification in mini channels using image correlation analysis, *International Communications in Heat and Mass Transfer*, 113, 1–9. doi: j.icheatmasstransfer.2020.104508

[27] Rafałko, G., Grzybowski, H., & Mosdorf, R. (2022). An image analysis method of liquid phase distribution during boiling in parallel mini channels, *International Communications in Heat and Mass Transfer*, 139, 1–10. doi: 10.1016/j.icheatmasstransfer.2022.106453

[28] Lu, R. (2017). Light Scattering Technology for Food Property, *Quality and Safety Assessment*. CRC Press. doi: 10.1201/b20220

[29] Dzienis, P., Zaborowska, I., & Mosdorf, R. (2022). JRP analysis of synchronization loss between signals recording during bubble departures. *Nonlinear Dynamics*, 108, 433–444. doi: 10.1007/s11071-022-07217-9

[30] Gruszczyńska, I., Mosdorf, R., Sobaniec, P., Żochowska-Sobaniec, M., & Borowska, M. (2019). Epilepsy identification based on EEG signal using RQA method, *Advances in Medical Sciences*, 64(1), 58–64. doi:10.1016/j.advms.2018.08.003

[31] Łępicka, M., Grądzka-Dahlke, M., Zaborowska, I., Górski, G., & Mosdorf, R. (2022). Recurrence analysis of coefficient of friction oscillations in DLC-coated and non-coated Ti6Al4V titanium alloy. *Tribology International*, 165, 107342. doi: 10.1016/j.triboint.2021. 107342

Co-published by
Institute of Fluid-Flow Machinery
Polish Academy of Sciences
Committee on Thermodynamics and Combustion
Polish Academy of Sciences

Copyright©2024 by the Authors under licence CC BY 4.0

http://www.imp.gda.pl/archives-of-thermodynamics/

Multiscale entropy applications for complexity analysis of two-phase flow

Gabriela Rafałko[a*], Romuald Mosdorf[a], Hubert Grzybowski[a], Paweł Dzienis[a], Grzegorz Górski[a]

[a]Bialystok University of Technology, Faculty of Mechanical Engineering, Wiejska 45A, Bialystok 15-351, Poland
*Corresponding author email: gabriela.rafalko@pb.edu.pl

Received: 29.12.2023; revised: 15.03.2024; accepted: 20.04.2024

Abstract

Two-phase flow in channels of small dimensions is often a non-stationary process, the nature of such flow is oscillatory. Due to small channel dimensions, high heat flux, parallel channels interactions, pressure and temperature oscillations, the character of the phenomena occurring during boiling is complex. The changes of the measured signals are observed in different time scales. In order to examine in detail two-phase flow parameters changes, many acquisition devices are often installed. This solution becomes challenging concerning mini and microchannel heat-exchangers due to space limitation and modifications of an experimental setup. This paper presents a novel application of multiscale entropies for spatial and temporal analysis of two-phase flow based on only one registered parameter. This analysis is performed based on pixel brightness changes in photo frames registered by a high speed camera during two-phase flow. The spatial changes of pixel brightness are observed on single frames and temporal changes are examined using a set of frames (in time). The Composite Multiscale Sample Entropy is applied to identify two-phase flow patterns and to analyze the complexity of phase distribution. Using Multivariate Multiscale Sample Entropy the most rapid changes of phase distribution in a multichannel heat exchanger are determined.

Keywords: Multiscale entropy; Spatial and temporal image analysis; Two-phase flow; High-speed video

Vol. 45(2024), No. 2, 83–90; doi: 10.24425/ather.2024.150854

Cite this manuscript as: Rafałko, G., Mosdorf, R., Grzybowski, H., Dzienis, P., & Górski, G. (2024). Multiscale entropy applications for complexity analysis of two-phase flow. *Archives of Thermodynamics*, 45(2), 83−90.

1. Introduction

The patterns observed during two-phase flow vary in shape, velocity, size and spatial location. The slug flow is characterized with rather long-term changes, on the other hand, during bubbly flow rapid changes occur which are related to bubble location or coalescence. During annular flow the width of a liquid film flowing near the channel wall and liquid droplets in the flow core change in time. Therefore, signals recorded during two-phase flow, such as fluctuations in pressure, temperature, heat flow and changes in the spatial location of pixels recorded during videos, occur in different time scales [1−3]. Non-linear measures, such as multiscale entropies, are used in current papers to study two-phase flow patterns.

In the paper [4], Rescaled Range Permutation Entropy (*RSPE*) was used for analysis of two-phase flow in plexiglass pipe with the diameter of 20 mm based on data collected by conductivity probes. The authors have observed alternations in flow patterns caused abrupt changes in entropy signals. Four typical multivariate multi-scale entropies were applied to exami-

Nomenclature

m – embedding dimension in *CMSE* algorithm
M – embedding dimension in *MMSE* algorithm
r – distance norm
q – liquid/air flow rate, kg/s

Greek symbols

ε – scale factor
τ – scale factor in *CMSE* algorithm
σ – standard deviation

Subscripts and Superscripts

g – gas
w – liquid

Abbreviations and Acronyms

CMSE – Composite Multiscale Sample Entropy
MMSE – Multivariate Multiscale Sample Entropy
RSPE – Rescaled Range Permutation Entropy
MWMPE – Multivariate Multiscale Weighted Permutation Entropy

ne evolution instability of the data registered with electrical field conductance sensor during oil-water two-phase flow in 20 mm testing pipe [5]. The Multivariate Multiscale Weighted Permutation Entropy (*MWMPE*) presented largest variation range with scale and the best anti-noise ability. The authors of the paper [5] have observed that in the case of very small droplets in the flow, there were weaker fluctuations in sensor signals.

The *CMSE* algorithm has been applied for analysing complex time series including, among others, gait's dynamics [6], river flows [7] or car traffic [8]. A method of analysis for examining the complexity of high-dimensional data within and between individual data series is Multivariate Multiscale Sample Entropy (*MMSE*). This algorithm allows for simultaneous analysis of multi-channel data, enables the examination of linear and non-linear correlations as well as various degrees of synchronization within a given data series and between series [9]. In the paper [2], authors examined horizontal, oil-water two-phase flow data using *MMSE* and concave electrodes. The authors have stated that *MMSE* enables a quantitative analysis of two-phase flow patterns and gives insight into dynamic flow behaviour.

In many of the afore mentioned papers entropy algorithms were applied for spatial (local) analysis of two-phase flow. The installed acquisition devices registered flow parameters only in those parts of the channel where they were placed. In order to gather spatial (local) and temporal changes (in time) of two-phase flow, more acquisition devices have to be mounted. For instance, in the paper [10], authors have observed that an averaged channel surface temperature and critical heat flux were generally insensitive to the flow configurations, thus an additional analysis of two other acquisition parameters (high-frequency pressure, high speed video) was needed. The research direction based on extracting characteristic features from single measurement parameter and using advanced, non-linear tools for its analysis is desirable, especially in the case of industry applications [11].

This paper presents a novel application of multiscale entropy for spatial and temporal analysis of two-phase flow based on only one registered parameter (high speed video). This analysis is performed based on pixel brightness changes in photo frames registered during two-phase flow by a high speed camera. The changes of the pixel brightness in photo frames reflect spatial changes and changes in very short period of time (on the length of the channel). The temporal changes are analysed based on pixel brightness changes in a set of frames. The experimental setup and data characteristics is presented in Section 2. Section 3 shows the application of *CMSE* for flow pattern identification and inlet phenomena complexity analysis. In Section 3 the application of *MMSE* algorithm for identifying the location of the most rapid changes of phase distribution in a multichannel heat exchanger is described. Section 4 presents conclusions.

2. Experimental setup and data characteristics

The scheme of the experimental stand is shown in Fig. 1. Two-phase flow of water mixed with glycerol (solution's concentration (weight): 45%) and air was analyzed.

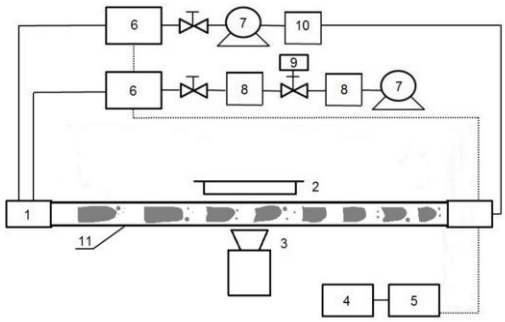


Fig. 1. Scheme of the experimental setup: 1 – minibubbles generator, 2 – light, 3 – high speed camera (Phantom v1610), 4 – PC, 5 – data acquisition station (DT9800, accuracy: 1 mV for voltages od -10V do 10V), 6 – flow meter (Bronkhorst mini CORI-FLOW M13, accuracy ±0,2% flow velocity), 7 – hydraulic pump (Dunkermotoren, BG45x30SI), 8 – air tank, 9 – pressure regulator (Metal Work Regtronic, accuracy: 1 kPa), 10 – liquid tank, 11 – minichannel [12].

The flow through a circular minichannel (11) – see Fig. 1, of a diameter equal to 3 mm and 60 mm long. The rates of water-glycerol and air were constant for each analyzed recording. The special micro-bubbles generator (1) was used to obtain the small bubbles size. The pump (7) generated compressed air which passed through an air tank (8) and a valve (9). Next it was directed to a constant pressure air tank (8), flow meter (6) and special micro – bubbles generator (1). The air rate was controlled by a flow meter (6). The liquid phase was supplied to the tank (10) using the pump (7) and finally heading into minichannel (11). The data acquisition station DT9800 (5) and the PC (4) were connected to the pressure sensors and flow meters. The videos were recorded with a high speed camera with the fre-

quency of 5000 frames per second (3). A light system was installed in the stand (2).

An image analysis of the experimental data was performed based on 56 videos recorded during two-phase flow of water-glycerol and air. The recordings were obtained for a set value of liquid and air flow rates. The flows had a stationary character, their recording began after the system reached a steady state. Bubbles, minibubbles and slugs were observed in the channel.

In Fig. 2 the experimental setup for two-phase flow of distilled water and air was presented. The heat-exchanger with three parallel minichannels was heated using electric power. A vertical row of three thermocouples was installed under minichannels in the copper block (Fig. 2 – T_1, T_2, T_3).

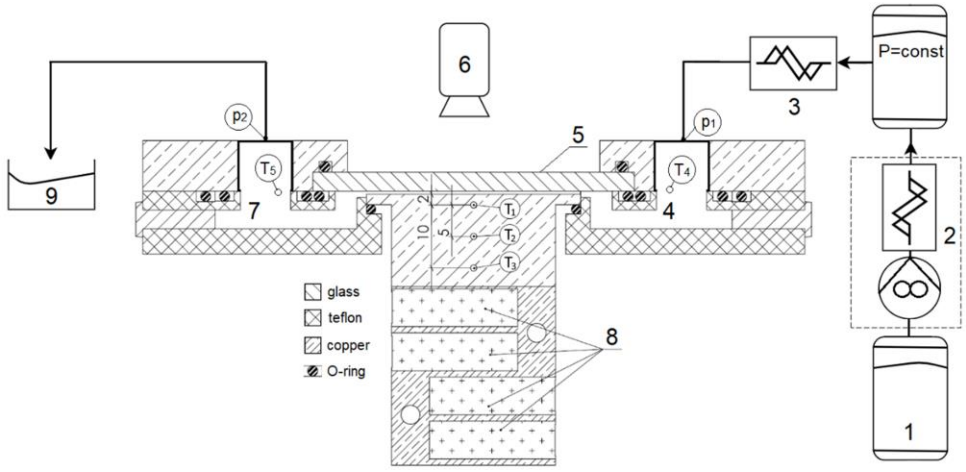


Fig. 2. The experimental setup: 1 – supply tank with distilled water, 2 – gear pump (Tuthill model DGS.11), 3 – compressible volume (V = 222,8 cm^3), 4 – flow meter (Bronkhorst mini CORI-FLOW M13, accuracy ± 0,2% of flow velocity), 5 – inlet, 6 – plexiglass, 7 – high speed camera (Phantom v1610), 8 – outlet, 9 – outlet tank, 10 – electric heaters (24V 50 W), p_1, p_2 – pressure sensors (MPX5050DP, time response: 1 ms), T_1, T_2, T_3, T_4, T_5 – K-type thermocouples (diameter: 0,081 mm, accuracy: ± 0,8 K, time response: 0,025 s) [13].

The dimensions of minichannels were equal to (width × depth × length) 0.25 × 0.50 × 32 mm (the wall between the channels: 0.25 mm wide). The minichannels were covered with a plexi cover which allowed observations of flow boiling inside minichannels. A high speed camera (7) – see Fig. 2, was used to record flow patterns inside minichannels with the speed of 2000 fps. The working liquid was distilled water. A gear pump (1) pumped the water to the compressible volume tank (2). A Coriolis mass flow meter (3) was used to measure the water mass flow rate. The liquid was flowing into a common inlet area, through three parallel minichannel (5) and headed to an outlet tank (9). The thermocouples (T_4, T_5) measured temperature in the water inlet and outlet common area. The pressure sensors were used to measure the pressure in inlet and outlet common area (p_1, p_2). The acquisition systems recorded pressure and temperature signals with a frequency of 1 kHz. The registration of signals and films was synchronized. In this experimental setup two types of multichannel heat-exchanger were examined: 1) three parallel channel system with the following dimensions (width × depth): 0.25 × 0.50 mm, 2) eleven parallel channel system with the following dimensions (width × depth): 0.25 × 0.13 mm. The length of the channels was equal to 34 mm and the wall between channels was 0.25 mm wide. The calculations based on the registered data were peformed in Matlab R2022.

3. Multiscale entropy

3.1. Composite multiscale entropy

Composite Multiscale Sample Entropy (ang. *CMSE*) allows an analysis of the complexity of data series in different time scales. The first step of this algorithm requires forming a coarse-grained series, ($y_n^{(\tau)}$), from original time series (x) [8]:

$$y_{k,n}^{(\tau)} = \frac{1}{\tau}\sum_{i=(n-1)*\tau+k}^{n*\tau+k-1} x_i, \qquad (1)$$

where: $1 \le n \le \frac{N}{\tau}, 1 \le k \le \tau$, x – the original time series, N – the length of each examined time series x, τ – scale factor, n – the length of each coarse-grained time series, k - number of the coarse-grained series for each τ. The length of each coarse-grained time series is equal to N/τ.

When $\tau = 1$, then the coarse-grained series is the original time series. The transformed series, $y_{k,n}^{(\tau)}$, are related to the time scale τ, where the elements of each series are averages of τ consecutive neighbors in the original time series. The composite procedure takes into account various choices of neighbors (the averaging windows are overlapping). In the coarse-grained time series short-term oscillations are the less noticeable, the higher time scale t is.

The next step of the algorithm is calculating SampEn (Sample Entropy) of each coarse-grained time series. The SampEn is a measure of time series regularity – its high value corresponds to high complexity of an analyzed series [14,15] while its low value corresponds to periodic character of the series.

To calculate SampEn of each new reconstructed signal, $y^{(\tau)}$, following steps are required [8]:

(1) forming $N/(\tau - m + 1)$ vectors:

$$y_m^{(\tau)}(i) = \left[y^{(\tau)}(i), \ldots, y^{(\tau)}(i+m-1)\right], \qquad i = 1, \qquad (2)$$

where m is the length of the compared sequences.

(2) computing the maximum norm:

$$d_m[y_m^{(\tau)}(i), y_m^{(\tau)}(j)] = \max[|\, y_m^{(\tau)}(i+k) - y_m^{(\tau)}(j+k)\,|],\ 0 \le k \le m-1, \quad (3)$$

(3) calculating the sequences with the length m – $B^m{}_i(r)$ and sequences with the length $m+1$ – $A^m{}_i(r)$ which are accepted (within the tolerance r):

$$B_i^m(r) = \frac{1}{\frac{N}{\tau}-m+1} c^m(i), \quad i = 1, \dots, \frac{N}{\tau} - m + 1, \quad (4)$$

$$A_i^m(r) = \frac{1}{\frac{N}{\tau}-m+1} c'^{m+1}(i), \quad i = 1, \dots, \frac{N}{\tau} - m + 1, \quad (5)$$

where: $c^m(i)$ is the number of sequences fulfilling the relation $d_m[y_m^{(\tau)}(i), y_m^{(\tau)}(j)] \le r$, $i \ne j$, $c'^{m+1}(i)$ is the number of sequences fulfilling the relation $d_{m+1}[y_{m+1}^{(\tau)}(i), y_{m+1}^{(\tau)}(j)] \le r$, $i \ne j$,

(4) calculating the probability of matching points:

$$B^m(r) = \frac{1}{\frac{N}{\tau}-m+1} \sum_{i=1}^{\frac{N}{\tau}-m+1} B_i^m(r), \quad (6)$$

$$A^m(r) = \frac{1}{\frac{N}{\tau}-m} \sum_{i=1}^{\frac{N}{\tau}-m} A_i^m(r), \quad (7)$$

(5) estimating the sample entropy of data points of finite length:

$$SampEn(m, r, N) = -\ln\left[\frac{A^m(r)}{B^m(r)}\right]. \quad (8)$$

(6) calculating the *CMSE* as the averaged value for N elements in the function of τ:

$$CMSE(x, \tau, m, r) = \frac{1}{\tau}\sum_{n=1}^{\tau} SampEn(y_n^{(\tau)}, m, r) \quad (9)$$

where: x – the original time series, τ – scale factor, $y_n^{(\tau)}$ – coarse-grained time series with the length of n, m – the length of the compared sequences in the coarse-grained time series, r – distance tolerance within compared sequences.

3.1.1. Two-phase flow pattern identification

The *CMSE* was applied to identify two-phase flow patterns on each of the 56 registered photo frames (1 frame out of each recorded video) in the experimental stand presented in Fig. 1 [16]. From each frame with the dimensions of 64 × 1280 pixels, the central fragment of a mini-channel with dimensions of 24 × 800 pixels was extracted. Next, the pixel brightness of the extracted region was summed in each column, this way the original time series, x, was obtained. Figure 3 shows a video frame and the region of interest marked with a yellow rectangle.

In the next step, coarse-grained time series were calculated according to the Eq. (1). The examples of coarse-grained time series for different photo frames were shown in Fig. 4.



Fig. 3. A photo frame and the analysed area (rectangle) of water-glycerol and air flow: liquid flow rate (q_w) and air flow rate (q_g): q_w = 43,44 kg/h, q_g = 0,328 l/min [13].

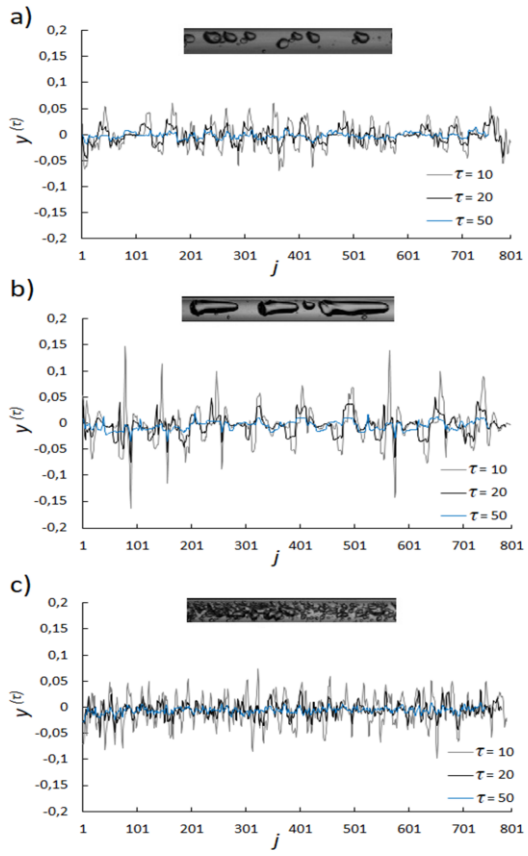


Fig. 4. The coarse-grained time series $y^{(\tau)}$ for τ = {10,20,50} obtained based on the photo frames presenting: a) bubble flow, b) slug flow, c) minibubble flow (dispersed flow).

The parameters of *CMSE* function were set to the following values: m = 2 – the length of the compared sequences, the standard deviation, σ_τ, of each coarse-grained time series was calculated, $r = 0.20*\sigma_\tau$ – the distance tolerance. The *CMSE* functions were calculated. In the last step, the *Complexity Index* (*CI*), which is the integral of *CMSE* function was estimated. The values of the *Complexity Index* for particular data (averaged for 10 subsequent photo frames from one recording) were presented in Table 1.

Table 1. The values of the *Complexity Index* (*CI*) for the analysed *CMSE* functions.

Two-phase flow pattern	*CI* ± SD	q_w (kg/h)	q_g (l/min)
slugs	4,24 ± 0,45	10,76	0,285
	6,14 ± 0,26	16,15	0,156
	7,57 ± 0,07	16,15	0,242
bubbles and cap bubbles	10,18 ± 0,07	16,15	0,070
	10,48 ± 0,47	26,99	0,328
	11,69 ± 0,10	32,61	0,113
bubbles and minibubbles	13,36 ± 0,26	32,55	0,156
	12,34 ± 0,32	21,69	0,027
	13,46 ± 0,36	43,54	0,070
minibubbles	15,33 ± 0,13	38,15	0,070
	14,60 ± 0,33	43,52	0,113
	14,49 ± 0,16	38,00	0,328

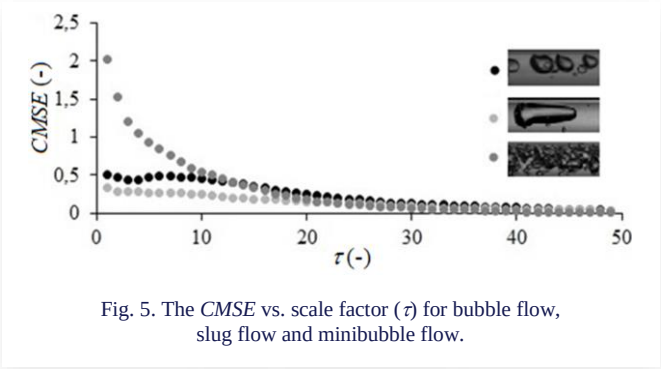


Fig. 5. The *CMSE* vs. scale factor (τ) for bubble flow, slug flow and minibubble flow.

The character of *CMSE* functions for three analysed photo frames was shown in Fig. 5. A hyperbolic shape of *CMSE* is observed for minibubble flow, this data is related to white noise stochastic distribution of small bubbles. For a photo frame representing bubbles, the *CMSE* function has its minimum for $t = 3$, in this case the value of minimum indicates the formation of more correlated (periodic) flow of larger bubbles separated by liquid phase. For a slug flow, more flat distribution of *CMSE* functions is observed informing about the presence of flow correlations but absence of characteristic distance between analysed pixel brightness time series.

3.1.2. Inlet flow complexity analysis

The CMSE algorithm was applied to analyze the complexity of pixel brightness changes in photo frames in time recorded with the speed of 2000 fps by a high speed camera. The time between subsequent photo frames corresponded to a formation of a vapour bubble. The length of the time series was equal to 10 s (20 000 data points). An example photo frame and the region of interest (S_{in}) in the common inlet of three minichannels were marked in Fig. 6.



Fig. 6. A photo frame of flow boiling in three parallel minichannels; the region of analysis was marked with a rectangle.

The analysed time series of pixel brightness sums were extracted from photo frames with following dimensions: 1.1 × 1.4 mm. The example three times series for two-phase flow recorded at following mass flow rates: 210 g/h, 383 g/h and 570 g/h were shown in Fig. 7.

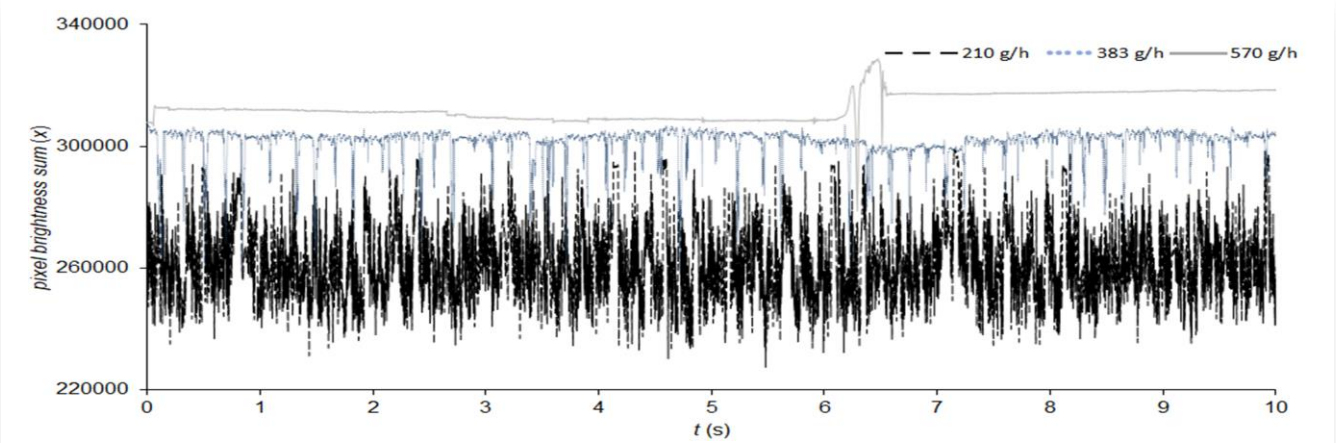


Fig. 7. The sums of pixel brightness in the inlet common area calculated from photo frames recorded during flow boiling for three mass flow rates: 210 g/h, 383 g/h, 570 g/h.

The calculated *CMSE* functions based on the pixel brightness sums in photo frames presenting common inlet of three parallel minichannels were shown in Fig. 8. A hyperbolic-like shape of *CMSE* functions was observed for data registered during flow boiling at lower mass flow rates (175−246 g/h), this corresponds to a stochastic character of phase distribution in the common inlet.

Based on the analyses performed for this experimental data in another paper [17] a high complexity of the inlet flows is related to very intense boiling process, reverse flow, high heat flux, unsynchronized work of minichannels and stochastic changes of pixel brightness. A rather flat distribution of *CMSE* functions was observed for flows with higher water flow rate which informs about a less complex character of pixel brightness changes in the common inlet.

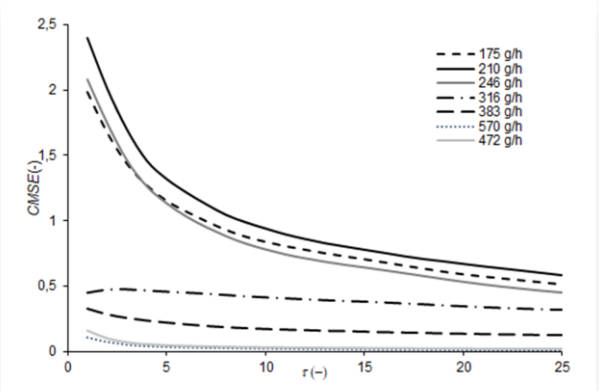


Fig. 8. The CMSE for analysed flows in the function of time scales (τ).

3.2. Multiscale multivariate sample entropy

Multivariate Multiscale Sample Entropy, *MMSE*, is used to simultaneously study the complexity of many series, for example to analyze wind velocities from different directions, car traffic on several streets. This algorithm enables the examination of linear and non-linear correlations as well as degrees of synchronization within and between data series. The algorithm takes into account the number of channels (variables) from which the time series comes. The first step is to construct a multivariate coarse-grained time series according to the following formula [8]:

$$y_{k,n}^{(\tau)} = \frac{1}{\tau}\sum_{i=(n-1)*\tau+1}^{n*\tau} x_{k,i}, \tag{10}$$

where: $k = 1,2, \ldots, p$, $1 \le k \le p$, $1 \le i \le N$, $1 \le n \le N/\tau$.

The following steps of the *MMSE* algorithm were presented in Fig. 9 [8]: constructing coarse-grained time series, forming composite delay vectors, defining the maximum distance norm and calculating MSample Entropy.

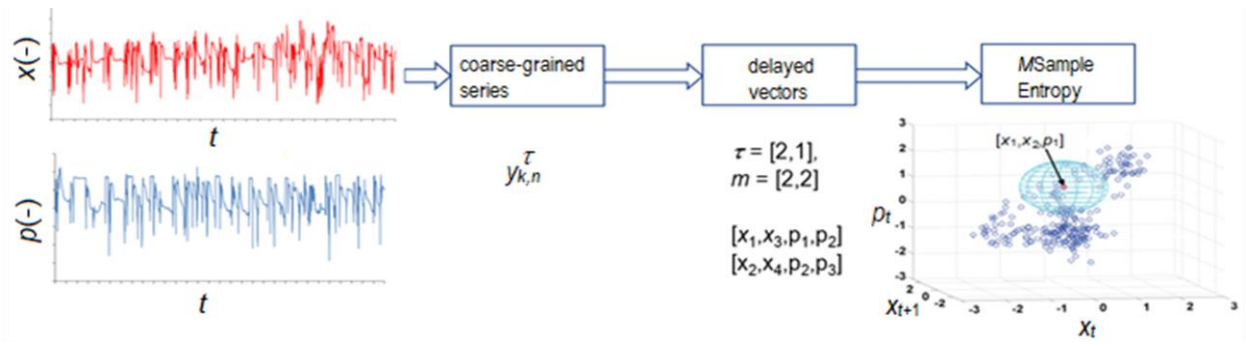


Fig. 9. The steps of *MMSE* algorithm.

3.2.1. Phase distribution complexity analysis

During boiling in mini and micro channels, the rate of the phase distribution changes varies depending on the distance from the inlet, the occurring flow pattern, the delivered heat and mass rate. An analysis of the dynamics of phase distribution changes makes it possible to determine the areas with the most rapid changes. In order to increase the heat dissipation surface, multi-channel systems are used. In this case, separate analyses for each channel are often conducted [18,19]. Such analyses do not take into account interactions between channels in multi-channel heat exchangers which role increases in heat-exchangers with small dimensions channel.

The *MMSE* algorithm described in the section 3.2 was applied to analyse the complexity of the phase distribution in eleven parallel microchannels based on the data registered during flow boiling. Two-phase flow in microchannels was registered with the speed of 3000 fps, the length of each time series was equal to 0.5s (3000 data points), 12 time series were analyzed. The time between subsequent frames (0.0002 s) corresponded to a growth of very small bubble into a bubble with a diameter equal to the channel's width. The analysis of pixel brightness in the photo frames presenting two-phase flow was carried out in the distance ranging from 0 to 660 pixels (from 0 mm to 16.5 mm) from the inlet to the microchannels, as it was shown in Fig. 10.

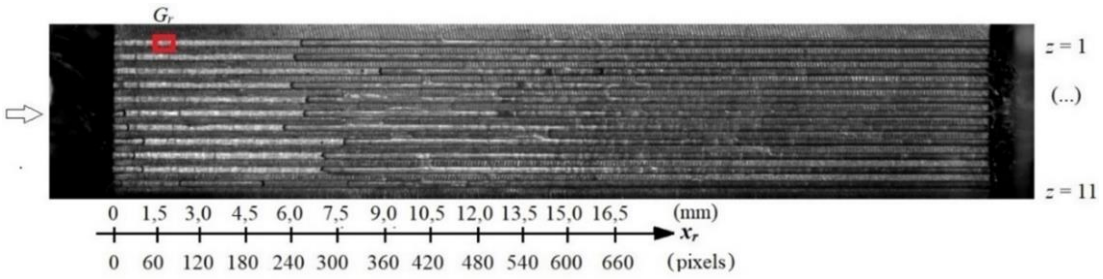


Fig. 10. The example photo frame of flow boiling in eleven parallel microchannels: z – microchannel number, x_r – the locations of the gate G_r (rectangle); the arrow indicates flow's direction [13].

Figure 10 shows the common inlet (on the left) and outlet of the exchanger (on the right) and parallel microchannels (z) with the following dimensions (depth × width × length): 0.13 × 0.25 × 32 mm. Below the figure, the X-axis is placed, marking the considered positions of the region of interest called the gate, G_r, shifted every 1.5 mm (i.e. 60 pixels). The gate's length (L = 20 pixels) corresponded to the length of a short slug or to a pair of bubbles. The brightness of pixels in the image in the case of water flow was higher than in the case of air flow (Fig. 10).

The *MMSE* algorithm was conducted on the data sets containing sums of pixels brightness in gates G_r in each of its positions in time, simultaneously in eleven microchannels. This way the input data matrix had following dimensions: pixel brightness in the gate's location x time x channel number. In the analysis, five scale factors (ε) were considered. The algorithm was calcul-

ated based on the data for subsequent locations of the gate separately. The result of one run of the algorithm is shown in Fig. 11.

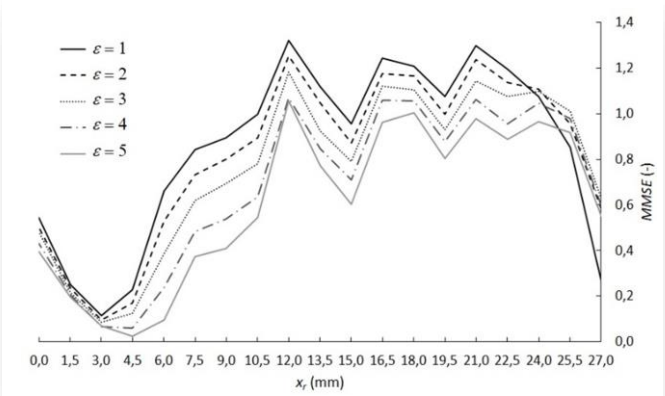


Fig. 11. The *MMSE* vs. position of the gate (x_r) for time scales (ε) [13].

As one can notice, the *MMSE* functions reach their maximum for one, particular position of the gate – in this case in the distance of 12 mm from the inlet. Based on the recorded videos and changes in *MMSE* function, it can be concluded that the maximum value of *MMSE* indicates the position in the heat exchanger where the most rapid changes of phase distribution occur. Based on the analyses presented in the paper [13], the location of the most rapid changes of phase distribution is related to a point from which water and air are heading only to the outlet of the exchanger. Between the inlet and the mentioned point, boiling front movement is continuously observed.

In order to verify the repeatability of the algorithm, the calculations were performed for three sets of parameters (1: $M = \{3,1\}$, $\tau = \{1\}$, $r = \{0.05\ \sigma_\tau\}$; 2: $M = \{2\}$, $\tau = \{2,3\}$, $r = \{0.05\ \sigma_\tau\}$; 3: $M = \{2\}$, $\tau = \{1\}$, $r = \{0.03\ \sigma_\tau, 0.07\ \sigma_\tau\}$) and scale factors $\varepsilon = \{1,2,3\}$. In all the runs of the algorithm, the maximum of the *MMSE* was obtained for $x_r = 12.0$ mm which underlines the high applicability of the algorithm regardless of slight changes in the input parameters. This point indicates the maximum position of the boiling front in the heat exchanger.

4. Results

In the paper, the *CMSE* algorithm enabled the identification of four different two-phase flow patterns based on high speed photo frames of water-glycerol and air two-phase flow in a minichannel. The *CMSE* algorithm was also used to analyze the complexity of inlet flow during flow boiling in three, parallel minichannels. The level of complexity identified using the *CMSE* algorithm is related to the intensity of boiling process, the synchronization/lack of synchronization between processes in minichannels and the character of changes of pixel brightness in photo frames.

The *MMSE* algorithm was applied for identifying the location of the most rapid changes of phase distribution simultaneously in 11 parallel microchannels. The location of the most rapid changes of phase distribution determines the area of the heat-exchanger where boiling front is continuously moving and heat transfer is the highest. Despite slight changes in parameters of *MMSE* algorithms, the determined location of the most rapid changes of phase distribution was the same. This proves a high applicability of the proposed algorithm.

5. Conclusions

This current work presents novel application of multiscale entropies for spatial and temporal analysis of two-phase flow based on one measurement parameter (high speed videos). In the paper, spatial (on a single photo frame) and temporal changes (in a set of subsequent frames) of pixel brightness were analyzed. In the cases under consideration, the sampling frequency of high speed video frames was high enough to later extract characteristic features of two-phase flow based on only one measurement parameter.

It has been shown that multiscale entropies algorithms combined with preliminary analysis of measurement data form an effective tool for identifying two-phase flow patterns and studying their complexity and dynamics. The presented, novel approach to two-phase flow analysis based on only one registered parameter is in an agreement with current research directions, concerning especially industry applications possibilities. The methodology of this paper can be applied, for instance, in dynamical monitoring of oilfields/two-phase flow in small channels due to the non-invasive acquisition method (high speed videos) and the possibilities of complexity and dynamics analyses using multiscale entropies.

Acknowledgement

The research was funded by the National Science Center grant UMO-2017/27/B/ST8/02905.

References

[1] Fabila-Carrasco, J.S., Tan, C., & Escudero, J. (2022). *A noise-robust Multivariate Multiscale Permutation Entropy for two-phase flow characterisation*. The University of Edinburgh. Edinburg Research Explorer. doi: 10.48550/arxiv.2210.09030

[2] Gao, Z.-K., Ding, M.-S., Geng, H., & Jin, N.-D. (2015). Multivariate multiscale entropy analysis of horizontal oil–water two-phase flow. *Physica A*, 417, 7–17. doi: 10.1016/j.physa.2014.09.017

[3] Górski, G., Litak, G., Mosdorf, R., & Rysak, A. (2019). Periodic Trends in Two-Phase Flow Through a Vertical Minichannel: Wavelet and Multiscale Entropy Analyses Based on Digital Camera Data. *Acta Mechanica et Automatica*, 13(1), 51–56. doi: 10.2478/ama-2019-0008

[4] Ren, W., Zhang, J., & Jin, N. (2021). Rescaled range permutation entropy: A method for quantifying the dynamical complexity of gas–liquid two-phase slug flow. *Nonlinear Dynamics*, 104(4), 4035–4043. doi: 10.1007/s11071-021-06468-2

[5] Han, Y.-F., Jin, N.-D., Zhai, L.-S., Ren, Y.-Y., & He, Y.-S. (2019). An investigation of oil–water two-phase flow instability using multivariate multi-scale weighted permutation entropy. *Physica A: Statistical Mechanics and Its Applications*, 518, 131–144. doi: 10.1016/j.physa.2018.11.053

[6] Costa, M., Peng, C.-K., L. Goldberger, A., & Hausdorff, J.M. (2003). Multiscale entropy analysis of human gait dynamics.

Physica A: Statistical Mechanics and Its Applications, 330(1), 53–60. doi: 10.1016/j.physa.2003.08.022

[7] Li, Z., & Zhang, Y.-K. (2008). Multi-scale entropy analysis of Mississippi River flow. *Stochastic Environmental Research and Risk Assessment*, 22(4), 507–512. doi: 10.1007/s00477-007-0161-y

[8] Zhang, N., Lin, A., Ma, H., Shang, P., & Yang, P. (2018). Weighted multivariate composite multiscale sample entropy analysis for the complexity of nonlinear times series. *Physica A: Statistical Mechanics and Its Applications*, 508, 595–607. doi: 10.1016/ j.physa. 2018.05.085

[9] Ahmed, M.U., & Mandic, D.P. (2012). Multivariate Multiscale Entropy Analysis. *IEEE Signal Processing Letters*, 19(2), 91–94. doi: 10.1109/LSP.2011.2180713

[10] Clark, M.D., Weibel, J.A., & Garimella, S.V. (2023). Impact of pressure drop oscillations and parallel channel instabilities on microchannel flow boiling and critical heat flux. *International Journal of Multiphase Flow*, 161, 104380. doi: 10.1016/j.ijmultiphaseflow.2023.104380

[11] Zhu, L., Jhia Ooi, Z., Zhang, T., Brooks, C.S., & Pan, L. (2023). Identification of flow regimes in boiling flow with clustering algorithms: An interpretable machine-learning perspective. *Applied Thermal Engineering*, 228, 120493. doi: 10.1016/j.applthermaleng.2023.120493

[12] Rafałko, G., Mosdorf, R., & Górski, G. (2020). Two-phase flow pattern identification in minichannels using image correlation analysis. *International Communications in Heat and Mass Transfer*, 113,104508. doi: 10.1016/j.icheatmasstransfer.2020.104508

[13] Rafałko, G.S. (2023). *Application of image analysis to identify and investigate the dynamics of two-phase flow patterns*: PhD thesis, Bialystok University of Technology. https://biblioteka.pb.edu.pl/spisy/2023/206140.djvu [accessed 09 Feb. 2024].

[14] Costa, M., Goldberger, A.L., & Peng, C.K. (2005). Multiscale entropy analysis of biological signals. *Physical Review E*, 71(2), 021906. doi: 10.1103/PhysRevE.71.021906

[15] Richman, J.S., & Moorman, J.R. (2000). Physiological time-series analysis using approximate entropy and sample entropy. *American Journal of Physiology-Heart and Circulatory Physiology*, 278(6), H2039–H2049. doi: 10.1152/ajpheart.2000.278.6.H2039

[16] Rafałko, G., Mosdorf, R., Litak, G., & Górski, G. (2020). Complexity of phase distribution in two-phase flow using composite multiscale entropy. *European Physical Journal Plus*, 135(8). doi: 10.1140/epjp/s13360-020-00686-0

[17] Rafałko, G., Grzybowski, H., Dzienis, P., Mosdorf, R., & Adamowicz, A. (2021). Image Analysis of Flow Maldistribution during Boiling in Parallel Minichannels. *Chemical Engineering and Technology*,44(11), 1978–1985. doi: 10.1002/ceat.202100246

[18] Dario, E.R., Tadrist, L., & Passos, J.C. (2013). Review on two-phase flow distribution in parallel channels with macro and micro hydraulic diameters: Main results, analyses, trends. *Applied Thermal Engineering*, 59(1), 316–335. doi: 10.1016/j.applthermaleng.2013.04.060

[19] Ha, M.Y., Kim, C.H., Jung, Y.W., & Heo, S.G. (2006). Two-Phase Flow Analysis in Multi-Channel. *Journal of Mechanical Science and Technology*, 20(6), 840–848. doi: 10.1007/ BF02915947

Co-published by
Institute of Fluid-Flow Machinery
Polish Academy of Sciences
Committee on Thermodynamics and Combustion
Polish Academy of Sciences

Copyright©2024 by the Authors under licence CC BY 4.0

http://www.imp.gda.pl/archives-of-thermodynamics/

Investigations of the specific heat capacity of selected heterogeneous materials

Rafał Gałek[a], Joanna Wilk[a*]

[a]Department of Thermodynamics, Rzeeszów University of Technology, Al.Powstańców Warszawy 12, 35-959 Rzeszów, Poland
*Corresponding author email: joanwilk@prz.edu.pl

Received: 28.12.2023; revised: 19.02.2024; accepted: 18.03.2024

Abstract

This paper presents the results of experimental investigations of the basic thermal property – the specific heat capacity of selected heterogeneous materials – graphene oxide rubber composites. The value of specific heat capacity was measured with a PerkinElmer DSC 8000 differential scanning calorimeter using modulated temperature mode of operation. The heterogeneous material under investigation was the graphene oxide/rubber composite, which is used in the production of roller bearing seals. Two types of rubber have been used as the basic matrix of composites: the hydrogenated acrylonitrile butadiene rubber and the fluoroelastomer. Graphene oxide reduced with sodium hypophosphite was applied as a composite filler. The main goals of the work was to expand the database of thermophysical properties of materials and to investigate the influence of material heterogeneity on the results of specific heat capacity measurements obtained with small-sized test samples.

Keywords: Specific heat capacity; Heterogeneous material; Rubber composite; Modulated temperature; StepScan mode

Vol. 45(2024), No. 2, 91–98; doi: 10.24425/ather.2024.150855

Cite this manuscript as: Gałek, R., & Wilk, J. (2024). Investigations of the specific heat capacity of selected heterogeneous materials. *Archives of Thermodynamics*, 45(2), 91−98.

1. Introduction

Nowadays, materials with a heterogeneous structure are becoming more and more important in technology. One class of such materials encompasses the rubber-based composites filled with nanoparticles in a form of various allotropes of carbon. Both the synthetic and natural rubber are used as a basic matrix in such composite materials. Graphene oxide (GO) may be used as a filling material [1−3], since it improves the mechanical properties and also changes thermal characteristics of the composite. One of the applications of rubber-based composites is the production of the roller bearing seals. The operating temperature of the bearing largely determines the type of the base rubber of composite material. Improving thermal properties of composites with the use of the reduced graphene oxide (rGO) as a filling results in more intensive dissipation of heat generated in the bearing. Thus, the knowledge about physical properties of graphene oxide/rubber composites with heterogeneous structure gains in importance. Thermal conductivity, thermal diffusivity and specific heat capacity are the main important thermophysical properties describing the phenomena of heat transport in materials. For composites with heterogeneous structure it may be difficult to clearly determine these parameters due to the formation of agglomerates and clusters of the filler material.

Nomenclature

A – thermal diffusivity, m^2/s
c_p – specific heat capacity, J/(kg·K)
k – thermal conductivity, W/(m·K)
m – mass, kg
Q – heat, J
$\dot{Q}$ – thermal power, W
t – time, s
T – temperature, °C, K
u – uncertainty
w – weight concentration, %

Greek symbols
δ – correction
ρ – density, kg/m^3
σ – deviation

Abbreviations and Acronyms
DSC − differential scanning calorimetry
FKM − fluoroelastomer
HNBR − hydrogenated acrylonitrile butadiene rubber
HR − heating rate
MT − modulated temperature
rGO − reduced graphene oxide
SEM − scanning electron microscope

Investigations of thermophysical properties of the composites are conducted using both commercial equipment and other unconventional research methods. In some cases the research methods need small samples of investigated materials, thus the heterogeneity can greatly influence test results. Thermal conductivity may be measured directly with the guarded hot plate method [4] or indirectly from the thermal diffusivity measured with a laser flash method [5], either with commercial equipment [6] or unconventional transient techniques [7−9]. The calculation of the value of thermal conductivity uses the basic formula defining the thermal diffusivity in the equation of transient heat conduction. Hence, the thermal conductivity k is equal to the product:

$$k = a \cdot \rho \cdot c_p, \tag{1}$$

where: a – thermal diffusivity, c_p – specific heat capacity, ρ – density.

As can be seen, determination of the thermal conductivity also requires measurements of the specific heat capacity. Heat capacity c_p is one of the basic thermophysical properties of the material. Determining the specific heat capacity is crucial in heat transfer problems, since c_p is an important thermophysical property in predicting heat transfer efficiency. Specific heat capacity is often measured with differential scanning calorimetry method (DSC). In the case of heterogeneous materials like graphene oxide/rubber composites, the use of DSC method causes difficulties in analyzing the measurement results as they may be affected by the small size of the test samples. Therefore, the knowledge about the impact of the material heterogeneity on the investigation results is advisable.

The main goals of the present work are to expand the database of thermophysical properties of the selected graphene oxide/rubber composites with the specific heat capacity values and to investigate the influence of material heterogeneity on the results of DSC measurements. Two different types of rubber: hydrogenated acrylonitrile butadiene rubber and fluoroelastomer were used as the basic matrices of the tested composites. The graphene oxide reduced with sodium hypophosphite acted as a filling material. Specific heat capacity was measured with differential scanning calorimetry method in modulated temperature regime.

2. Materials and methods

2.1. Characteristic of the investigated materials

In the present study the selected graphene oxide/rubber composites, that are used for the production of the roller bearing seals, were investigated experimentally. Two types of rubber were used as the basic matrix of the composites: hydrogenated acrylonitrile butadiene rubber (HNBR) and fluoroelastomer (FKM). Graphene oxide reduced with sodium hypophosphite (rGO) was used as a composite filler. The rGO has an appearance of grey powder, bulk density of $0.019 g/cm^3$ and specific surface area of $266 m^2/g$ [4]. The specific heat capacity and thermal conductivity of GO are approximately 700 J/(kg K) [10] and from several to over two thousands W/(m K) respectively, depending on the form of graphene oxide used [11,12].

The example of the scanning electron microscope (SEM) image of the rGO nanoparticles is presented in Fig. 1.

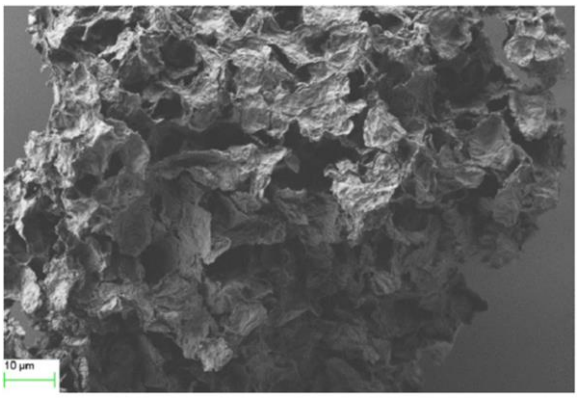


Fig. 1. SEM image (magnification ×1000) of the reduced graphene oxide nanoparticles applied as a filler in tested composites [4].

A conventional method was used to prepare the composite materials: a precisely measured amount of rGO was directly dispersed in the basic rubber matrix during the rolling process [4]. After the process, the weight and the density of rGO/rubber composites were determined using the basic volumetric weighing method. An accuracy of density determination was

±0.003 g/cm^3. The weight concentration of rGO was calculated from the equation:

$$w = \frac{m_{\mathrm{rGO}}}{m_{\mathrm{BM}}+m_{\mathrm{rGO}}}, \tag{2}$$

where m_{BM} is a mass of the composite base matrix.

Figure 2 presents a sample scanning electron microscope (SEM) image of the cross-sectional area of the HNBR composite with a weight concentration of rGO equal to 2.5%.

The basic characteristics of investigated materials including weight concentration of rGO, density and thermal conductivity are presented in Table 1.

Thermal conductivity of the investigated composites was measured with the guarded hot plate method [4]. Thermal diffusivity was obtained using less common methods: thermal regular regime method and the step-heating technique [9].

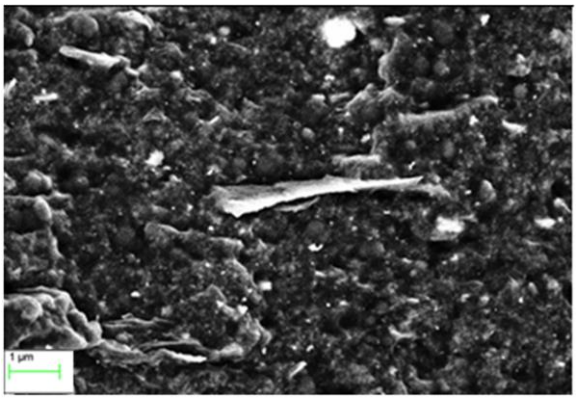


Fig. 2. SEM image (magnification ×10000) of the cross-sectional area of rGO/HNBR composite (H1) [4].

Table 1. Basic properties of investigated composites.

Material	Matrix	Weight concentration of rGO w [%]	Density ρ [kg/m^3]	Thermal conductivity [4] k [W/(m·K)]	Thermal diffusivity a [mm^2/s] (average values [9])
H0	HNBR	0	1 199	0.37	0.160
H1	HNBR	2.5	1 207	0.37	0.162
F1	FKM	1.5	1 885	0.24	0.064
F2	FKM	2.5	1 885	0.25	0.072

2.2. Measuring procedure

Specific heat capacity measurements were carried out using a differential scanning calorimetry (DSC) method, which is a well-established measuring technique in various research areas [13−15]. The main feature of this method is the ability to quickly determine, among others, the specific heat capacity, in a broad temperature range using small amounts of the tested substances. Differential scanning calorimetry involves measuring the change of the difference in the heat flow rate supplied to the sample of the tested material and to a reference sample during the operation of a program that varies the temperature over time. In the classical DSC method the operation mode of the program changing the temperature is characterized by a constant heating rate. It is important that the term "heating rate" is understood in DSC as a rate of temperature change – not to be confused with the heat flow rate (or thermal power), which is in fact a main measured variable in this method. A digital scanning calorimeter may also be operated in variable heating rate regime – techniques utilizing such a mode are collectively known as modulated temperature (MT) methods. In the case of variable heating rate a special modulation term is added to the usual linear change of temperature with time. Modulated-temperature DSC technique may also be applied for the measurements of the specific heat capacity c_p. [13,16,17]. There are several variants of this method [18], one of them being the StepScan mode – a proprietary technique of PerkinElmer - characterized by the temperature vs time function in the form presented in Fig. 3.

In the present study a DSC 8000 calorimeter from PerkinElmer was used for the measurements of specific heat capacity in the StepScan mode. The method involves repeatedly heating

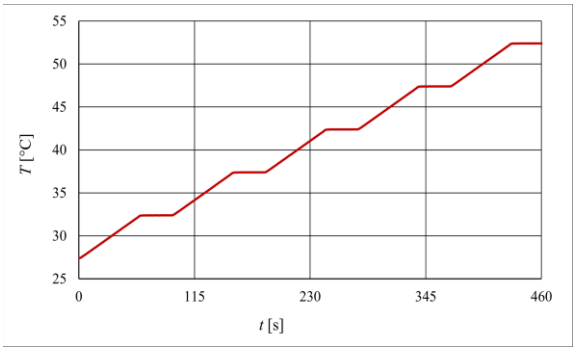


Fig. 3. Variation of the temperature with time in the StepScan mode.

the sample and then maintaining it in isothermal conditions for several dozen seconds. During heating periods, the value of the supplied thermal power depends on the specific heat of the material and on possible phase changes, while in isothermal periods - only on kinetic phenomena. As a variant of temperature-modulated differential scanning calorimetry, the StepScan method is typically used in situations where phase transitions or chemical reactions are expected within the temperature range being investigated. In the present study, the use of the StepScan mode was motivated by the fact that in this method the value of the integral of the recorded relationship between thermal power $\dot{Q}$ and the time t is used to determine the c_p [18] instead of the instantaneous values of $\dot{Q}$ utilized in classic DSC experiment. Hence:

$$c_p = \frac{Q}{m\Delta T}, \tag{3}$$

where: Q – heat supplied to the test sample during the single heating period (integral of $\dot{Q}(t)$), m – sample mass, ΔT – temperature increase during the single heating period.

Calculation of the specific heat capacity from the integral of $\dot{Q}(t)$ for small temperature changes in a short time makes this method practically insensitive to one of the most significant problems of differential scanning calorimetry – the drift of the calorimeter baseline. The baseline is the reaction of the DSC system with both crucibles empty for the prescribed heating rate program in the classical DSC. In standard DSC method of specific heat capacity measurement, where c_p is determined from the value of the thermal power $\dot{Q}$ supplied to the material sample at a given moment and at a specific temperature, the drift of the baseline may significantly affect the measurement results, especially when a single experiment covers a wide temperature range, i.e. it lasts longer. In the StepScan method, the influence of the drift practically does not occur, because the value used in the calculation is the area under the curve $\dot{Q}(t)$ based at the level of neighbouring isotherms. Since the temperature change in a single heating period is small, the isotherms bounding that period are so close in time that significant baseline drift could not have appeared between them. Thus, due to the very short times required for each measuring step, the specific heat capacity value obtained with the StepScan method is not sensitive to baseline drifts, even at higher temperatures.

In the present work the parameters of the StepScan method included a heating rate (HR) of 5 K/min and a temperature increase of 5 K for each heating period. The temperature interval ΔT was selected in such a way that the values of the thermal energy Q for the tested samples were close to the values observed during the caloric calibration of the apparatus using sapphire samples. Such a choice aimed to keep the actual measurement conditions close to the conditions of the calibration, which, in theory, should positively affect the accuracy of measurement of Q. The selection of the heating rate value was based on the rationale derived from the form of the $\dot{Q}(t)$ relationship recorded on the graph. The heating rate was selected low enough so that the $\dot{Q}(t)$ dependence within one step was not dominated by transient state, i.e. so that after the increase of $\dot{Q}$ there was relative stabilization period of at least about 30s. At the same time the HR value was chosen to be high enough so that the maximum of each step was above the value of $\dot{Q}$ = 1 mW, since at lower values it would be expected that the relative accuracy of the calorimeter signal measurement would be decreased.

Sample graphs of the thermal power supplied to the tested sample as a function of temperature and time in StepScan method are shown in Fig. 4. The data presented in the graphs in Fig. 4. are consistent with the temperature vs time dependence from Fig. 3.

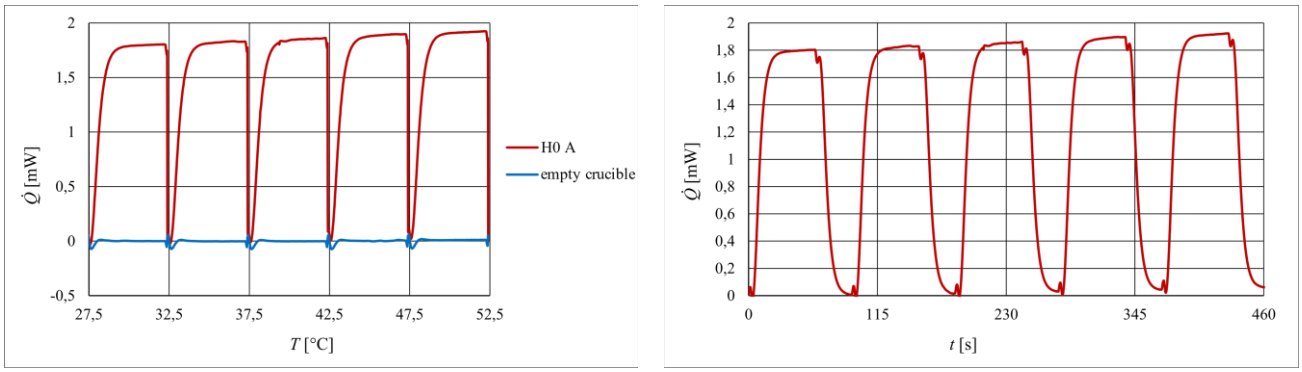


Fig. 4. Thermal power supplied to the test sample in the StepScan mode vs. temperature and time.

2.3. Uncertainty analysis

The uncertainty of the specific heat capacity measurement with StepScan differential scanning calorimetry is affected by the uncertainties of the measurements of temperature, thermal energy and the sample mass. Before the measurements, the temperature calibration and the caloric calibration had been performed for the apparatus used in present work. The melting points of indium and zinc had been used as a temperature standards for the calibration of the temperature measuring subsystem. The thermal power measurement subsystem of the calorimeter had been calibrated using the specific heat capacity of the sapphire standard sample. The mass of the investigated samples was in the range of 13–19 mg. The samples were weighed with a RADWAG XA 210/Y analytical balance with a resolution of 0.01 mg.

The uncertainty of the temperature measurement depends on the uncertainty of the temperature calibration, uncertainty of the certified melting point of the material used in temperature calibration, uncertainty of the thermal lag measurement and the uncertainty caused by linear interpolation of the temperature sensor characteristic [19].

In the StepScan method the temperature measurement takes place in isothermal conditions, before and after each heating step. Therefore, the dynamic correction accounting for thermal lag does not apply here and there is no need to take its uncertainty into account. The manufacturer of the DSC system provides the information that the temperature sensor embedded into calorimeter is a platinum resistance thermometer, however data about the polynomial used in the software for the interpolation of its characteristic are not disclosed. Therefore, the only possible assumption is that general good practices and international standards have been observed regarding application of the temperature sensor. Since both IEC 60751 and ASTM E1137 rec-

ommend using at least second order polynomial for the interpolation of the characteristic of resistance thermometers, the correction due to the linear interpolation is not applicable and its uncertainty is not taken into account. Thus, the standard uncertainty of the temperature measurement takes a form:

$$u(T) = \sqrt{u^2(\delta T_{\text{calib}}) + u^2(\delta T_{\text{mat}})}, \quad (4)$$

where: $u(\delta T_{\text{calib}})$ – uncertainty of the temperature calibration; $u(\delta T_{\text{mat}})$ – uncertainty of the certified melting point of the material used for calibration.

According to [18], the standard uncertainty of the calibration correction $u(\delta T_{\text{calib}})$ may be determined by repeated measurements of the melting temperature of the calibration standard material, i.e. as the standard uncertainty type A [20]. In turn, the uncertainty $u(\delta T_{\text{mat}})$ should be based on the uncertainty of the phase transition temperature of the material used for calibration. In the StepScan method, the c_p value is determined from Eq. (3), where the energy Q is the integral of thermal power $\dot{Q}$ with respect to time. It can be assumed that the main sources of measurement uncertainty of thermal energy Q are analogous to the sources of measurement uncertainty of thermal power $\dot{Q}$. The standard uncertainty of the thermal energy supplied to the tested sample during the measurement may be written as:

$$u(Q) = \sqrt{u^2(Q_s) + u^2(\delta Q_{\text{cal}}) + u^2(\delta Q_{\text{mat}})}, \quad (5)$$

where: $u(Q_s)$ – uncertainty of the determination of thermal energy supplied to the sample during actual measurement (type A), $u(\delta Q_{\text{cal}})$ – uncertainty of the calibration correction, $u(\delta Q_{\text{mat}})$ – uncertainty of the correction resulting from the uncertainty of the calibration material specific heat capacity value.

Uncertainties $u(Q_s)$ and $u(\delta Q_{\text{cal}})$ may be obtained by repeated measurements of the heat supplied to the test sample and the calibration sample, respectively. The value of $u(\delta Q_{\text{mat}})$ is determined as a combined uncertainty of zero-valued correction δQ_{mat} reflecting the conditions during caloric calibration procedure. It is assumed that the certified specific heat capacity value of the calibration material is exact, i.e. $\delta c_p = 0$ and the standard uncertainty of this assumption simplifies to:

$$u(\delta Q_{\text{mat}}) = \sqrt{\left(u(\delta c_{p,\text{cal}}) m_{\text{cal}} \Delta T_{\text{cal}}\right)^2} = \left|u(\delta c_{p,\text{cal}}) m_{\text{cal}} \Delta T_{\text{cal}}\right|, \quad (6)$$

where m_{cal} and ΔT_{cal} are the mass of the calibration sample and the temperature interval of the single heating period during calibration, respectively; $u(\delta c_{p,\text{cal}})$ is the standard uncertainty of the $c_{p,\text{cal}}$ value.

According to [21], the uncertainty of the mass measurement with an analytical balance depends on the repeatability, reproducibility, non-linearity, the standard uncertainty of the calibration and the difference between calibration temperature and measurement temperature. The latter component is neglected in present work, since the temperature in the lab was precisely maintained at the same value during calibration and the actual measurements. The uncertainty of the mass measurement may, therefore, be expressed as [16]:

$$u(m) = \sqrt{S_{\text{r}}^2 + S_{\text{env}}^2 + \frac{a_{\text{L}}^2}{3} + u^2{}_{\text{cal}}}, \quad (7)$$

where: S_{r} and S_{env} are the repeatability and reproducibility, respectively, determined on the basis of the statistical analysis; a_{L} – maximum deviation due to non-linearity as stated by the balance manufacturer; u_{cal} – calibration uncertainty depending on the standard uncertainty of the mass reading and the mass standard used for calibration.

The standard uncertainty of the specific heat capacity measurement with the StepScan mode of MT-DSC method is given by the formula:

$$u(c_p) = \sqrt{\left(\frac{\partial c_p}{\partial Q} u(Q)\right)^2 + \left(\frac{\partial c_p}{\partial m} u(m)\right)^2 + 2\left(\frac{\partial c_p}{\partial T} u(T)\right)^2}, \quad (8)$$

where the partial derivatives (sensitivity coefficients): $\frac{\partial c_p}{\partial Q}$, $\frac{\partial c_p}{\partial m}$, $\frac{\partial c_p}{\partial T}$ are determined on the basis of Eq. (3).

3. Results and discussion

Measurements were performed for five distinct samples of each investigated material with an exception of expectedly the most homogeneous one – H0, for which only 3 samples were tested. The samples were extracted from different locations of a larger piece of composite material. As a final result of the investigation the values of specific heat capacity in the temperature range 10−110°C were obtained. Results of the measurements for materials H0, H1 and F1, F2 are presented in Fig. 5 and Fig 6. The chart in Fig.5 includes the values of c_p for three samples of the base matrix material HNBR (H0) and for five samples of the rGO/HNBR (H1) composite with the weight concentration of rGO equal to 2.5%. In turn, Fig.6 presents the results of five measurements for the rGO/FKM composite also characterized by weight concentration of w = 2.5% (F2) and w = 1.5% (F1). It may be seen, that the dispersion of the c_p values for different samples of a given material is very low.

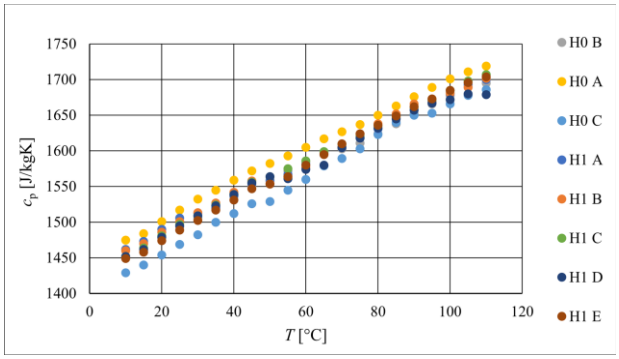


Fig. 5. Specific heat capacity of composites based on HNBR matrix. A, B, C, D, E – results for different samples of the tested material.

As follows from the Eq. (3), the StepScan method basically determines the average value of specific heat capacity in a single heating period, therefore, for ΔT = 5 K, the presented values of c_p for a given temperature should in fact be understood as aver-

age values within the range of ±2.5 K in relation to that temperature.

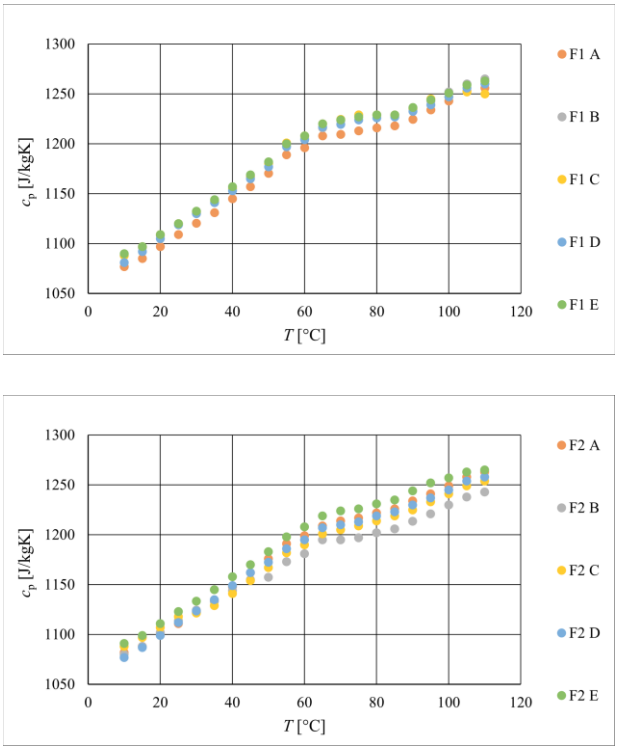


Fig. 6. Specific heat capacity of composites based on FKM matrix. A, B, C, D, E – results for different samples of the tested material.

Based on the analysis presented in Section 2.3, the standard uncertainties of each measurand affecting the uncertainty of c_p measurement were determined. An example of the uncertainty budget for the H0 material at 40°C is presented in Table 2.

Table 2. Uncertainty budget of the specific heat measurement of H0 material at 40°C.

Quantity X_i	Standard uncertainty $u(X_i)$	Sensitivity coefficient $\frac{\partial c_p}{\partial X_i}$
Q	$1.08 \cdot 10^{-3}$ [J]	14.25 [1/(g K)]
m	$6.01 \cdot 10^{-5}$ [g]	-108.5 [J/(g^2 K)]
T	0.1 [K]	0.3 [J/(g K^2)]
c_p	0.046 [J/(g K)]	–––––

The standard uncertainty of the c_p value for the sample estimation presented in Table 2 is $u(c_p)$ = 0.046 J/(g K), which corresponds to relative standard uncertainty of 3%. Assuming the coverage factor of 2 resulting in the level of confidence of approximately 95%, the expanded uncertainty of c_p measurement is 0.092 J/(g K) and the relative expanded uncertainty is 6%.

As a measure of dispersion of the results for a single material, the relative standard deviation σ_{rel} was calculated according to the formula:

$$\sigma_{rel} = \frac{1}{c_{p,m}} \sqrt{\frac{1}{5} \sum_{i=1}^{5} \left(c_{p,i} - c_{p,m}\right)^2}, \qquad (9)$$

where: $c_{p,m}$ - the average value of specific heat capacity calculated from all samples of given material, $c_{p,i}$ - specific heat capacity of the i-th sample.

Sample results of the average specific heat capacity and relative standard deviation obtained for the material F2 at five temperatures are presented in Table 3.

Table 3. Specific heat for rGO/FKM composite with w=2.5% (F2).

T [°C]	$c_{p,m}$ [J/(kgK)]	σ_{rel} [%]
10	1083.6	0.48
25	1115.6	0.40
60	1194.6	0.75
90	1229.3	0.82
110	1256.6	0.62

The calculated relative standard deviation for rGO/FKM composite F2 is below 1% over the entire temperature range considered. Similar results were observed for samples taken from other composites.

Since the dispersion of the results is well below the measurement uncertainty, it may be concluded that for the investigated materials the heterogeneity of the composite does not affect the c_p value in the extent that may be detected with applied experimental method.

The average values of the specific heat capacity for H0, H1, F1 and F2 are presented in Fig. 7 as a function of temperature.

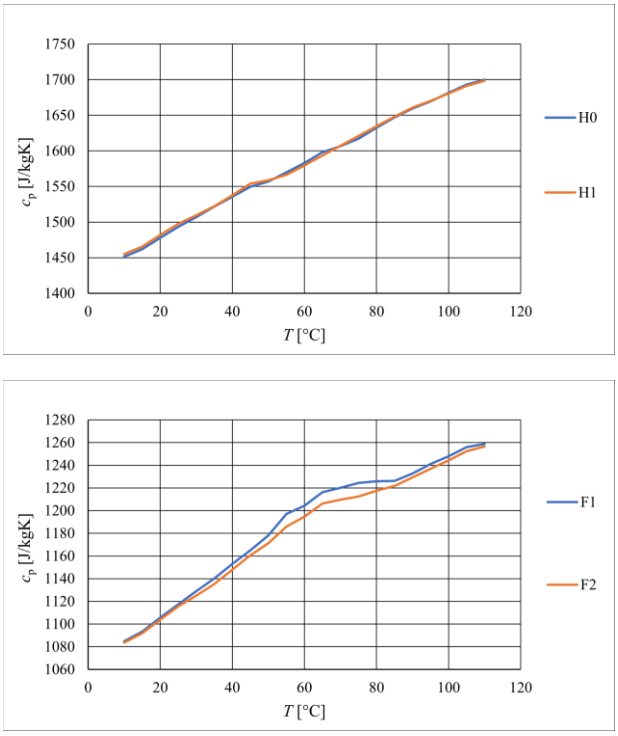


Fig. 7. Specific heat capacity vs. temperature for HNBR and FKM-based GO/rubber composites.

As may be seen, in the case of H0 and H1 materials, the values of specific heat capacity basically coincide in whole temperature range. For FKM-based composites there is a slight deviation in c_p value between F1 and F2 materials in the temperature range 50−80°C, however the value of the observed difference is much lower than the measurement uncertainty, therefore it cannot be considered an evidence of actual disparity between these materials in terms of c_p value. Nonetheless, decreasing specific heat value with increasing rGO content would be explainable [17], since the specific heat capacity of graphene oxide (approximately 700 J/(kg K) [10]) is lower than c_p of fluoroelastomer.

4. Conclusions

In the present study the results of the specific heat capacity measurements performed for reduced graphene oxide/rubber composites are reported. The FKM and HNBR rubbers were used as matrices of tested materials while graphene oxide reduced with sodium hypophosphite was used as a filler material. Specific heat capacity was measured with StepScan method being a variant of the modulated temperature differential scanning calorimetry. Due to the heterogeneity of the composites tested, several samples of each material were investigated. The study includes an estimation of the measurement uncertainty of the applied method.

The following conclusions may be formulated on the basis of performed investigation and the obtained results:

- the StepScan mode of DSC method enabled the measurement of the specific heat capacity of rGO/rubber composites with reasonable accuracy;
- a clear increase in c_p of tested materials with temperature was found;
- due to the heterogeneity of the investigated composites and small size of the test samples, the differences in c_p results obtained from distinct material samples were expected, however, the observed differences turned out to lay well within the measurement uncertainty.

References

[1] Wen, Y., Yin, Q., Jia, H., Yin, B., Zhang X., Liu, P., Wang, J., Ji Q., & Xu, Z. (2017). Tailoring rubber-filler interaction and multifunctional rubber nanocomposites by usage of graphene oxide different oxidation degrees. *Composites Part B: Engineering*, 124, 250−259. doi: 10.1016/j.compositesb.2017.05.006

[2] Lim, L.P., Juan, J.C., Huang, N.M., Goh, L.K., Leng, F.P., & Loh, Y.Y. (2019). Enhanced tensile strength and thermal conductivity of natural rubber graphene composite properties via rubber-graphene interaction. *Materials Science and Engineering B*, 246, 112−119. doi: 10.1016/j.mseb.2019.06.004

[3] Zheng, L., Jerrams, S., Xu, Z., Zhang, L., , L., & Wen, S. (2020). Enhanced gas barrier properties of graphene oxide/rubber composites with strong interfaces constructed by graphene oxide and sulfur. *Chemical Engineering Journal*, 383, 123100. doi: 10.1016/j.cej.2019.123100

[4] Wilk, J., Smusz, R., Filip, R., Chmie,l G., & Bednarczyk, T. (2020). Experimental investigations on graphene oxide/rubber composite thermal conductivity. *Scientific Reports*, 10, 15533. doi: 10.1038/s41598-020-72633-z

[5] Parker, W.J., Jenkins, R.J., Butler, C.P., & Abbott, G.L. (1961). Flash Method of Determining Thermal Diffusivity, Heat Capacity, and Thermal Conductivity. *Journal of Applied Physics*, 32(9), 1679−1684. doi: 10.1063/1.1728417

[6] Bocchini, G.F., Bovesecchi, G., Coppa, P., Corasaniti, S., Montanari, R., & Varone, A. (2016). Thermal Diffusivity of Sintered Steels with Flash Method at Ambient Temperature. *International Journal of Thermophysics*, 37(4), 1−14. doi: 10.1007/s10765-016-2050-4

[7] Kruczek, T., Adamczyk, W.P., & Białecki, R.A. (2013). In Situ Measurement of Thermal Diffusivity in Anisotropic Media. *International Journal of Thermophysics*, 34, 467−485. doi: 10.1007/s10765-013-1413-3

[8] Adamczyk, W., Białecki, R., Orlande, H.R.B., & Ostrowski, Z. (2020). Nondestructive, real time technique for in-plane heat diffusivity measurements. *International Journal of Heat and Mass Transfer*, 154(3), 119659. doi: 10.1016/j.ijheatmasstransfer.2020.119659

[9] Wilk, J., Smusz, R., & Filip, R. (2023). Experimental investigations on thermal diffusivity of heterogeneous materials. *Experimental Thermal and Fluid Science*, 144(9), 110868. doi: 10.1016/j.expthermflusci.2023.110868

[10] Al-Douri, Y. (2022). *Graphene, Nanotubes and Quantum Dots-Based Nanotechnology. Fundamentals and Applications*. (1st Edn.). Woodhead Publishing, Elsevier, Kidlington.

[11] Mahanta, N.K., & Abramson, A.R. (2012). Thermal conductivity of graphene and graphene oxide nanoplatelets. *13th IEEE ITHERM Conference*, 30 May – 01 June, San Diego, USA. doi: 10.1109/ITHERM.2012.6231405

[12] Meng ,Q. L., Liu, H., Huang, Z., Kong, S., Jiang, P., & Bao, X. (2018). Tailoring thermal conductivity of bulk graphene oxide by tuning the oxidation degree. *Chinese Chemical Letters*, 29(5), 711−715. doi: 10.1016/J.CCLET.2017.10.028

[13] McHugh, J., Fideu, P., Herrmann, A., & Stark, W. (2010). Determination and review of specific heat capacity measurements during isothermal cure of an epoxy using TM-DSC and standard DSC techniques. *Polymer Testing*, 29(6), 759–765. doi: 10.1016/j.polymertesting.2010.04.004

[14] Bernardes, C.E.S., Joseph, A., & Minas da Piedade, M.E. (2020). Some practical aspects of heat capacity determination by differential scanning calorimetry. *Thermochimica Acta*, 687, 178574. doi: 10.1016/j.tca.2020.178574

[15] Jiao, Y., Liu, C.F., Cui, X.P., Zhang, J., Huang, L.J., & Geng, L. (2022). A new approach for measurement of the low-temperature specific heat capacity. *Measurement*, 203, 111892. doi: 10.1016/j.measurement.2022.111892

[16] Gill, P.S., Sauerbrunn, S.R., & Reading, M. (2014). Modulated differential scanning calormetry, *Journal of Thermal Analysis*, 40, 931−939. doi: 10.1007/BF02546852

[17] Riviere, L., Causse, N., Lonjon, A., Dantras, E., & Lacabanne, C. (2016). Specific heat capacity and thermal conductivity of PEEK/Ag nanoparticles composites determined by Modulated-Temperature Differential Scanning Calorymetry. *Polymer Degradation and Stability*, 127, 98−104. doi: 10.1016/j.polymdegradstab.2015.11.015.

[18] Höhne, G.W.H., Hemminger, W.F., & Flammersheim, H.J. (2003). *Differential Scanning Calorimetry* (2nd Edn.), Springer-Verlag, Berlin Heidelberg.

[19] Rudtsch, S. (2002). Uncertainty of heat capacity measurements with differential scanning calorimeters. *Thermochimica Acta*, 382 (1−2), 17–25. doi: 10.1016/S0040-6031(01)00730-4

[20] BIPM, IEC, IFCC, ILAC, ISO, IUPAC, IUPAP, OIML (2008). *Evaluation of measurement data - Guide to the expression of uncertainty in measurement* (1st Edn.) Joint Committee for Guides in Metrology, JCGM 100.

[21] González, A.G., & Herrador, M.Á. (2007). The assessment of electronic balances for accuracy of mass measurements in the analytical laboratory. *Accreditation and Quality Assurance*, 12(1), 21−29. doi: 10.1007/s00769-006-0214-9

Co-published by
Institute of Fluid-Flow Machinery
Polish Academy of Sciences
Committee on Thermodynamics and Combustion
Polish Academy of Sciences

Copyright©2024 by the Authors under licence CC BY 4.0

http://www.imp.gda.pl/archives-of-thermodynamics/

Repowering strategies: Analysis of gas turbine integration with steam cycle for enhanced power plant performance

Krzysztof Badyda[a], Artur Harutyunyan[a*], Marcin Wołowicz[a]

[a]Institute of Heat Engineering, Faculty of Power and Aeronautical Engineering, Warsaw University of Technology, Nowowiejska 21/25, 00-665 Warsaw, Poland
*Corresponding author email: arturharutyunyan1983@gmail.com

Received: 30.12.2023; revised: 20.03.2024; accepted:05.05.2024

Abstract

In this paper, various repowering methods commonly employed in practice today are discussed. A particular emphasis is put on the hot wind-box repowering method, which is examined in greater detail. This method stands out for its simpler solution and lower investment costs compared to other repowering methods. Most research and analyses on repowering, taking into account the ecological problems and the possibilities of repowering existing old steam cycle power plants, have focused on the effect of repowering on thermodynamic parameters and emission reduction. However, there are still many important questions that remain open and unexplored when it comes to analyze the selection of the right technology of the repowering and the right gas turbine for such a combined cycle power plant. For that purpose, based on the oxygen fraction in the gas turbine exhaust gases, nine different gas turbine models were tested for a 200 MW steam cycle power plant model. Calculations were carried out using the GateCycle modelling program. As a result of investigations, a GE Energy Oil & Gas MS9001E SC (GTW 2009 – with 123 MW power) gas turbine was selected as the best one for such a combination, in which case the increase of total net power output by 97.69% and the improvement of efficiency by 6.67% were registered, compared to the results before repowering, while carbon dioxide emissions were decreased by 0.29% per megawatt electrical power generated. The conducted research underscores the importance of selecting the right gas turbine for such a gas-steam system.

Keywords: Modeling of thermodynamic properties; Repowering; Gas turbine; Gas-steam system

Vol. 45(2024), No. 2, 99–106; doi: 10.24425/ather.2024.150856

Cite this manuscript as: Badyda K., Harutyunyan A., & Wołowicz M. (2024). Repowering strategies: analysis of gas turbine integration with steam cycle for enhanced power plant performance. *Archives of Thermodynamics*, 45(2), 99–106.

1. Introduction

Due to the challenging circumstances prevalent in today's world, particularly marked by a significant increase in global electricity consumption in developing countries, driven by population growth and industrialization, as well as the continued reliance on fossil fuels leading to environmental pollution, global warming, and the depletion of non-renewable resources, coupled with the substantial presence of outdated steam cycle power plants worldwide, there is a pressing need to analyse methods for enhancing the power generation efficiency using fossil fuels and reducing pollutant emissions from such power plants.

Nomenclature

$GT_{power\ ratio}$ – gas turbine power ratio, %
N_{GT} – gas turbine power, MW
$N_{SCPP\ BR}$ – steam cycle power output before repowering, MW
P_{AR} – power output of combined cycle power plant after repowering, MW
P_{BR} – power output of steam cycle power plant before repowering, MW
P_{el} – combined cycle power output, MW
$P_{el\ GT}$ – gas turbine power output, MW
$Q_{in\ AR}$ – heat supplied to the cycle after repowering, MW
$Q_{in\ BR}$ – heat supplied to the cycle before repowering, MW

Greek symbols

η_{RP} – repowering efficiency, %
λ_{GT} – gas turbine leverage

According to the International Energy Agency (IEA), worldwide electricity consumption has approximately doubled since 1990, rising from 11 000 TWh to 28 000 TWh in 2022. Worldwide carbon dioxide (CO_2) emissions from human activity have increased from insignificant levels two centuries ago to annual emissions of more than 36.8 billion metric tons today (2022) with nearly 45% from coal use – mainly for power generation [1]. In Poland's energy infrastructure, coal-fired steam power plant blocks remain the dominant energy sources. And because there is significant international pressure to move away from coal-based electricity generation the share of renewable sources in the primary energy mix of the power industry is growing rapidly, especially those characterized by dynamic changes in generation capacity.

According to data published on the website of Poland's Electric Energy Distribution Network (Polskie Sieci Elektroenergetyczne), in 2022, the total share of energy generated by wind and photovoltaic farms reached an average annual level of 16.4% of national consumption. The maximum average hourly power of these sources reached 10 610 MW, while the minimum was 33.7 MW. Such significant variability in renewable energy generation underscores the need for compensating the workload with controllable sources in the energy industry. Moreover, coal-fired units have limited flexibility in load changes, whereas installations equipped with gas turbines perform much better in this regard.

Besides that, many existing thermal power plants around the world, especially in the EU, have to face their advanced age and deteriorated efficiency [2] both due to legislation [3] and rising carbon prices [4,5]. Although one of the radical and quick solutions is the rapid shutdown of coal-fired power plants, such an option is associated with huge costs [6]. In contrast to such a solution, rehabilitation and repowering of the existing units to prolong their service, increase their efficiency and reduce pollutant emissions seems more feasible [7,8]. In that case, there is a growing focus on building gas-steam systems, meaning that one of the most suitable solving methods is repowering which could improve the above presented situation and decrease the emissions and fossil fuel consumption. For example, in this context, Poland is investing in new units of this category, while also considering the repowering of existing units, which can be a slightly cheaper alternative to building new installations.

So, in general, repowering could be defined as the process of adding or replacing existing power plant equipment while retaining permitted serviceable components. This aims to enhance generation economics [9], extend equipment lifespan [10], improve environmental performance [11,12], enhance operability and maintainability [13,14], and optimize the utilization of existing sites, as mentioned above [15].

Repowering is ideal for plants in which the steam turbine, after many years of operation, still has a considerable service life expectancy, but the boilers are ready for replacement. The boilers are normally replaced or supplemented with gas turbines and heat recovery steam generators (HRSGs). Steam turbine units in older power stations generally can easily be adapted for use in a combined cycle. Repowering to a combined cycle can improve the efficiency of an existing plant to a level relatively close to that of new combined-cycle plants [16]. In this direction, the power production sector and the associated renovation activities receive a lot of attention both from governments and researchers [17,18].

2. Repowering concepts

In practice, four basic concepts of repowering steam power plant blocks into a gas-steam system are implemented: complete repowering (CR), repowering with feed water heating (FWHR – feed water heating repowering), 'hot wind-box' repowering (HWBR – hot wind-box repowering) and installation of a supplementary boiler (SBR – supplementary boiler repowering).

The first concept is sometimes used in the case of old steam units at the end of their service life. Complete repowering means replacing the boiler with a combination of one or more gas turbines (GT) and a heat recovery steam generator. Typically, repowering projects also include the modification of the steam turbine set by adapting its production capabilities to the efficiency and configuration (including multi-pressure configuration) of the recovery boiler and the modernization of instrumentation and control equipment. It is also possible to use the method of post-combustion after heat recovery steam generator (maximum supplementary firing). This method of repowering (without post-combustion) is currently being considered for 200 MW class units at the Kozienice Power Plant. The first gas turbine unit for power generation installed in Poland in the year 1999 was implemented in such a kind of repowering.

The second concept was often used in the past when superstructures of steam units were used to adapt them to cover peak loads. This solution, also known as a parallel system, involves adding a gas turbine to an existing steam unit. The coupling takes place on the side of the steam regeneration system, where the exhaust gases leaving the gas turbine are directed to heat the feed water [19,20]. This method was considered from the balance side in [19] for the superstructure of an 800 MW class lignite-fired unit at the Bełchatów Power Plant.

In the 'hot wind-box' system, exhaust gases from the gas turbine are directed instead of combustion air in the existing boiler. This method of coupling is also known as a system with exhaust gases discharged into the boiler or a series system. Its use requires modification of the boiler's heating surfaces due to the introduction of hot, but still oxygen-rich exhaust gases from the gas turbine instead of the fresh air from the surroundings. This type of modification of the national 200 MW class block was the subject of consideration in [21,22].

In comparison to simple combined-cycle installations, hot wind-box repowering has some advantages and disadvantages. As an advantage, it should be noted that in this variant of solution, a different type of fuel can be burned in the steam generator, also this type of plant has a very high efficiency in part-loads. At the same time, these units have lower efficiency in nominal loads, higher investment costs and more complex installations, and are more difficult to operate and maintain, especially if the steam generator is solid fuel fired [23].

In the last of the indicated concepts, we are dealing with the addition of a gas turbine to an existing steam power plant block, where a heat recovery steam generator powered by exhaust gases from this turbine constitutes an additional source of steam for the steam part. In this system, the waste heat steam generator is a source of additional steam under peak load conditions, and it is possible to supply it to the steam turbine at more than one pressure level [24].

The methods of connecting the steam and gas parts corresponding to the discussed repowering concepts are presented in a simplified manner according to [31] in Fig. 1. More details about the above mentioned methods were presented in the following works [19,21,25].

In Table 1, there are shown general characteristics of power plants after repowering using three different methods [26–31]. It is obvious from the table that the highest capacity and efficiency are available in the complete repowering method (CR). But in hot wind-box repowering (HWBR) and feed water heating repowering (FWHR) methods, the improvement of characteristics is almost similar.

In general, higher thermodynamic characteristics can be achieved in the complete repowering method without maximum supplementary firing (without post-combustion) compared to the method with maximum supplementary firing. However, as shown in the book by Badyda and Miller [20] (Fig. 11.21 in that book), this fact does not apply to all cases. At temperatures at the gas turbine inlet not higher than about 1100°C and at temperatures at the boiler inlet not higher than about 700°C, the opposite situation is observed, i.e. maximum supplementary firing (post-combustion) leads to improvement of the thermodynamic parameters of gas-steam combined cycle.

Repowering may lead to the conversion of the fuel used, for example from coal to natural gas, or a dual-fuel system (for example gas and coal in a modified installation). Due to fuel availability limits and the current situation in the energy market, electrical energy consumption and environmental limitations, in developed countries, especially in Europe, the main emphasis is on the efficiency of the system. The mentioned fuel conversion from coal to natural gas can be helpful for the reduction of unitary CO_2 emissions. Complete repowering and repowering with feed water heating are the most frequently chosen concepts.

In developing countries, post-Soviet countries, and the Middle East, including Iran, where there are huge reserves of natural gas and at the same time there are very weak environmental restrictions, the main emphasis is on capacity – increasing the available power. Existing installations are usually modified while minimizing investment costs. The most frequently chosen concepts in these regions are hot wind-box repowering and complete repowering with supplementary firing. On the other hand, in developed countries, especially in Europe, due to fuel availability limits and the current situation in the energy market, electrical energy consumption and environmental limitations, the main emphasis is on the efficiency of the system. Complete repowering and repowering with feed water heating are the most frequently chosen concepts [25].

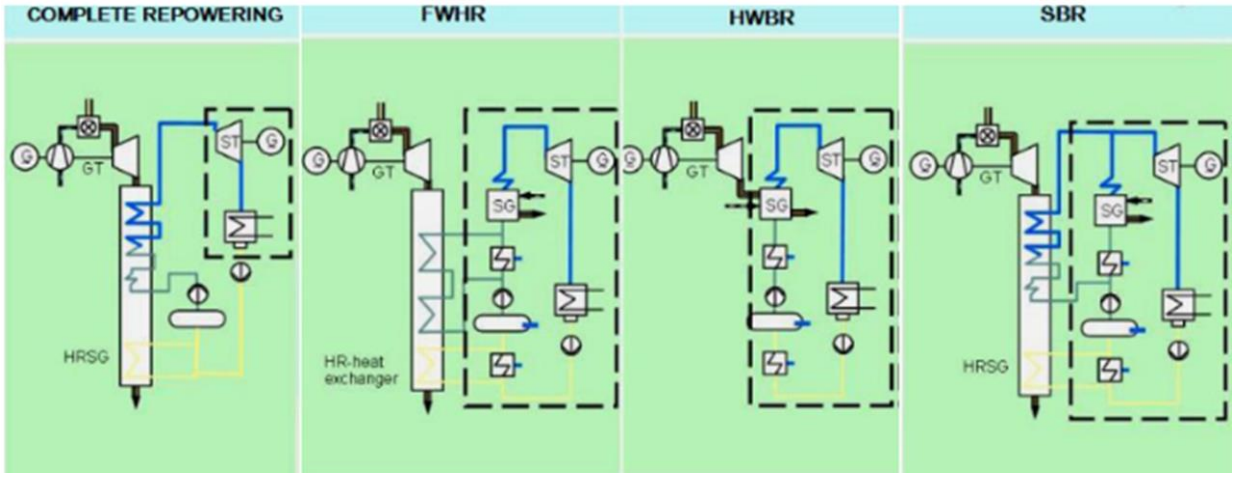


Fig. 1. Simplified diagrams of the repowering concept: G – generator, GT – gas turbine, HRSG – heat recovery steam generator, SG – steam generator, ST – steam turbine.

Table 1. Repowering options specifications [26–31].

	CR	FWHR	HWBR
Capacity increase (%)	160–200	10–30	15–30
Efficiency improvement (%)	Up to 12	2–5	3–6
NO_x decrease (%)	50–80	10–20	50–80
Limitation factor (s)	Existing condenser and steam turbine (s)	Steam turbine (s)	Existing boiler
Special advantage	Heat rate improvement up to 30–40%	Heat rate improvement 5–10%	Heat rate improvement up to 10–15%
Outage time	12–18	2	8
Gas turbine capacity	160-200% of existing steam turbine capacity	Up to 20% of existing steam turbine capacity	Up to 30% of existing steam turbine capacity

3. Analysis of thermodynamic parameters and performance on the example of the hot wind-box system

In general, the complex of analyses involved in preparing the repowering project includes a variety of technical, financial and environmental aspects, taking into account local conditions. In the initial stage of evaluating a repowering project for a generation system, the process involves determining the system's goals, encompassing factors such as assessing additional power consumption, setting targets for emission reductions, analyzing fuel availability and associated costs, evaluating transmission requirements and constraints, forecasting generation load schedules, establishing target electricity market prices and addressing other pertinent requirements and goals. Then, the existing plant is evaluated, which can be repowered to meet the above mentioned generation goals. The next step is to identify a repowering technology. If hot wind-box repowering has been selected as the main technology of a repowering project, then the right gas turbine should be selected for the existing plant. However, a critical prerequisite in selecting a gas turbine is ensuring that the oxygen content in the exhaust gases matches the required oxygen content for combustion in the existing boiler. This match should not limit the nominal load of the boiler, thus preventing the loss of its existing capacity. This alignment helps avoid additional costs associated with supplying fresh air to the boiler. It's important to note that this condition applies only if the chosen gas turbine fits within the targeted capacity limits of the steam-gas combined system intended for repowering.

In recent years, the majority of research and studies on repowering, considering ecological concerns and the repowering potential of existing old steam cycle power plants, have primarily concentrated on thermodynamic analyses and emission reduction strategies. Nevertheless, numerous significant questions remain open and unresolved, particularly regarding the selection of the most suitable repowering technologies and gas turbines for combined cycle power plants. For this purpose, the paper investigates the hot wind-box repowering method using a 200 MW steam cycle power plant as an example, with a particular emphasis on selecting the most suitable gas turbines for integration into this plant.

The commercial GateCycle software was chosen as the calculation tool, enabling the selection of system parameters using libraries containing the characteristics of gas turbines and analysis of the cooperation of the gas and steam parts in nominal conditions and in part loads (off-design). Therefore, based on the fraction of oxygen within gas turbine exhaust gases, a pool of possible gas turbine models was considered, for which the direct use of the exhaust gases leaving them in the steam boiler was assumed (without diluting the exhaust gases with additional fresh air), alternatively with their dilution with fresh air.

The subject of analyses was 9 models of gas turbines, of which the variant with dilution of exhaust gases with fresh air was adopted for five of them. This version assumes that the gas turbine exhaust gases can be diluted with fresh air to lower the exhaust gas temperature and increase the oxygen (O_2) content in the gas stream. For other gas turbine models, the oxygen content in the exhaust gases is sufficient for supplementary firing (post-combustion) in the boiler. The analysed turbines are listed below (the selected gas turbines are marked A to I in Figs. 3–5 and in Table 2):

1. Centrax Gas Turbine Trent 60 DLE SC (GTW 2009) – A,
2. Alstom GT8C2 50Hz SC (GTW 2009) – B,
3. Hitachi PG6101(FA) SC (GTW 2009) – C,
4. Ansaldo Energia V64.3A SC (GTW 2009) – D,
5. GE Energy Heavy Duty PG7121 (EA) SC (GTW 2009) – E,
6. Westinghouse 401 (97 GT World) – F,
7. Siemens V84.2-98 Vendor Data – G,
8. Mitsubishi M501DA SC (GTW 2009) – H,
9. GE Energy Oil&Gas MS9001E SC (GTW 2009) – I.

Ambient parameters for all models of gas turbines are the same, the inlet pressure and temperature are 1.0132 bar and 15°C, respectively, in a 60% relative humidity. The fuel used here is 100% methane with a 50 000 kJ/kg lower heating value (LHV).

In Table 2, the performance parameters of these gas turbines are shown, where: N_{el} – net electrical power, E_{ff} – gas turbine efficiency, CPR – compressor pressure ratio, COT – combustor outlet temperature, G_{exh} – mass flow of exhaust gases after turbine, TAT – temperature of exhaust gases after turbine, O_2 *m.fr.* – oxygen mole fraction in exhaust gases.

The model diagram of the analyzed system illustrated in the GateCycle user interface is shown in Fig. 2.

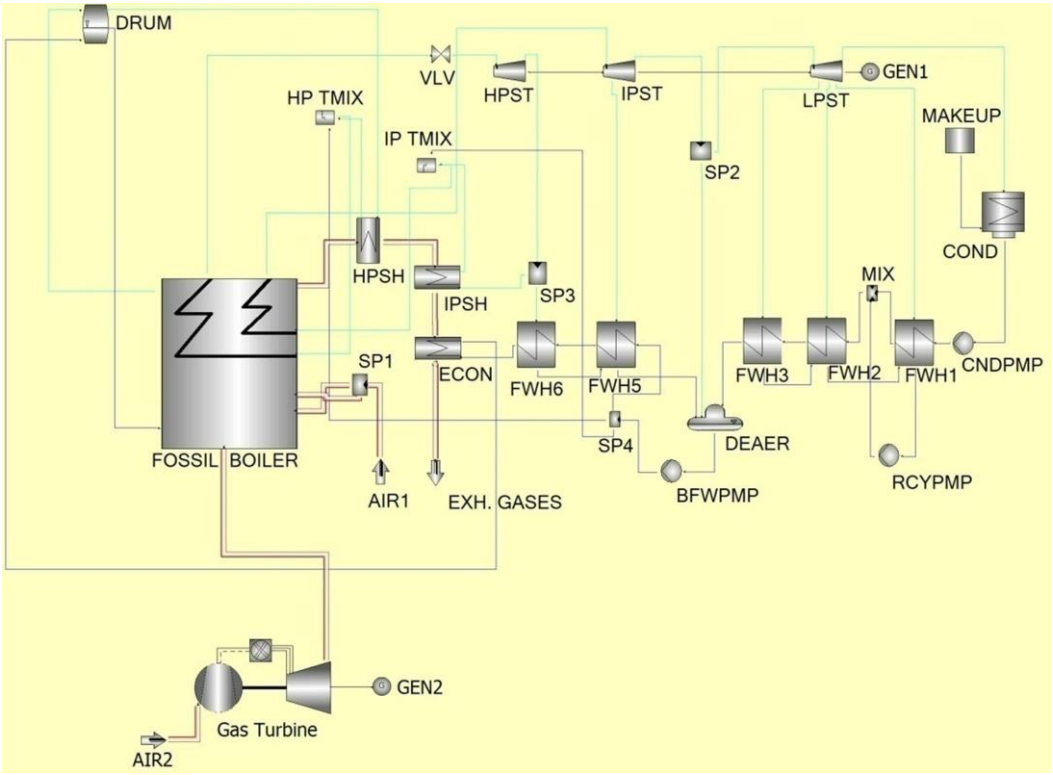


Fig. 2. The analysed model diagram of the considered 200 MW class unit after repowering with a gas turbine: HPST – high pressure steam turbine, IPST – intermediate pressure steam turbine, LPST – low pressure steam turbine, COND – condenser, CNDPMP – condensate pump, RCYPMP – recirculation pump, MIX1–3 – mixers No. 1–3, FWH1–6 – feed water heaters No. 1–6, DEAER – deaerator, BFWPMP – boiler feed water pump, SP1–4 – splitters No. 1–4, ECON – economizer, HPSH – high pressure super heater, IPSH – intermediate pressure super heater, HP TMIX – temperature control mixer in high pressure part, IP TMIX – temperature control mixer in intermediate pressure part, GEN1 – steam turbine generator, GEN2 – gas turbine generator, AIR – ambient air, EXH. GASES – exhaust gases.

Table 2. Performance parameters for gas turbines.

GT	N_{el}	E_{ff}	CPR	COT	G_{exh}	TAT	O_2 *m.fr.*
	MW	%	–	°C	kg/s	°C	%
A	50.5	38.7	35.9	1321.6	150.4	447.3	14.4
B	55.1	33.4	17.5	1211.3	195.4	511.4	14.1
C	69.9	34.1	14.9	1322.3	205.2	593.7	12.9
D	75.5	35.5	17.0	1352.7	211.6	590.1	12.9
E	82.8	32.1	12.6	1190.2	296.7	541.5	13.9
F	89.6	37.8	19.0	1366.7	227.2	582.3	12.6
G	107.7	33.6	10.9	1176.1	357.7	550.6	13.7
H	113.5	34.8	13.9	1249.5	345.6	543.6	13.3
I	122.9	33.2	12.5	1210.9	413.9	547.2	13.7

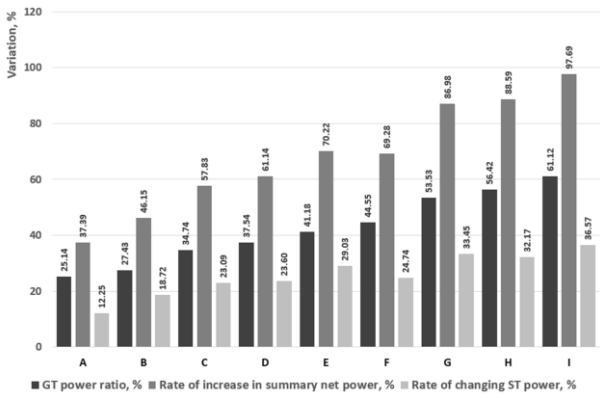


Fig. 3. Variation of GT power ratio, rate of increase of ST and CCPP power after repowering.

Figure 3 shows values of gas turbine (GT) power ratio (%), rate of increase in steam turbine (ST) power (%) and increase in summary net power of the combined cycle power plant (CCPP) (%) after repowering for nine different gas turbine models.

The gas turbine power ratio can be defined as the power value of the added gas turbine for repowering to the power value of the existed steam cycle power plant before repowering:

$$\mathrm{GT}_{\text{power ratio}} = \frac{N_{GT}}{N_{SCPPBR}} \times 100\%. \quad (1)$$

The subscripts SCPP and BR symbolize steam cycle power plant, before repowering, respectively.

The rate of increase in ST power and the rate of increase in summary net power of CCPP can be defined as the power values of ST and of the whole power plant before repowering to the corresponding values after repowering.

The charts illustrated in Fig. 3 show that, after repowering in nine different cases, the GT power ratio changed from 25.14% to 61.12% and that GE Energy Oil & Gas MS9001E SC (GTW 2009) gas turbine (123 MW) had the highest values of GT power ratio and rate of increase in ST and CCPP power. They were 61.12%, 36.57% and 97.69%, accordingly.

Repowering has the effect of increasing the heat energy provided to the steam turbine, because it increases the amount of heat energy provided to the steam boiler from the gas turbine side. This effect can be used in two ways:

1) Keeping the fuel mass flow to the steam boiler stable and modernising the steam boiler and steam turbine equipment. This means for example enlarging the heat exchange surface and changing the installation of a steam turbine electrical generator. These actions result in increasing the power of the steam turbine and increasing in turn the power of the combined cycle too.

2) Reducing the fuel provided to the steam boiler until the power of the steam turbine reaches the level it was at before repowering. This improves the fuel economy of the steam boiler and increases the efficiency of the combined cycle power plant.

The analyses are considered from the point of view of the first case. The relative improvement in efficiency as a result of repowering – repowering efficiency, defined in accordance with Eq. (2), obtained for the considered turbine models is shown in Fig. 4. Additionally, based on performance calculations, this figure illustrates the relative increase in gas turbine power – GT leverage, defined in accordance with Eq. (3).

$$\eta_{RP} = \frac{P_{AR} - P_{BR}}{Q_{inAR} - Q_{inBR}}, \tag{2}$$

$$\lambda_{GT} = \frac{\Delta P_{el}}{P_{elGT}} = \frac{P_{AR} - P_{BR}}{P_{elGT}}, \tag{3}$$

where P means power at the generator terminals; Q_{in} - heat supplied to the cycle; *AR* and *BR* indexes refer to the performance before and after repowering, respectively.

The highest relative efficiency improvement (0.62) as a result of repowering was obtained for the case marked with index A in Fig. 4 (Trent 60 DLE - 50.6 MW), the lowest (0.53) for the case marked with index I – MS9001E turbine (123 MW). The highest relative increase in gas turbine power – GT leverage (1.70) was obtained in the pool under consideration for the case marked with index E (Westinghouse 401 – older generation machines 82.8 MW). The above results are important, but not the only necessary result of the analyses. A broader set of results for the indicated case can be found in [1,3].

According to the results of the analyses, gas turbine models can be divided into two groups: gas turbines with indexes from A to D and gas turbine with index F were entered into the group of hot wind-box repowering with fresh air dilution, whereas the gas turbine with index E and gas turbines with indexes from G to I were entered into the group of direct (without fresh air dilution) hot wind-box repowering.

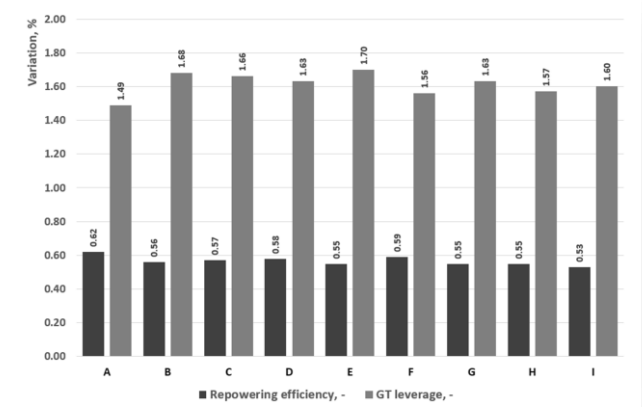


Fig. 4. Repowering efficiency and GT leverage in nine different cases.

The results of analyses, illustrated in Fig. 5 show that although the fraction of CO_2 was increased by 13.10% to 40.12% after repowering, CO_2 emissions in boiler exhaust gases per megawatt power were decreased by 0.18% to 0.29%. This finding may indicate that it is possible to increase the installed capacity while reducing pollutant emissions by hot wind-box repowering of thermal power plants.

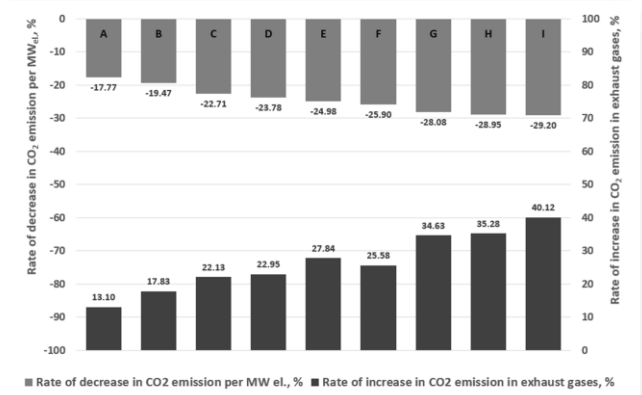


Fig. 5. Rate of increase in CO_2 emission in exhaust gases and decrease in CO_2 emission per MW electrical power.

4. Conclusions

To sum up, it is evident that the concept of repowering gains an increased significance because of the following factors:

- worldwide energy crises with the combination of environmental tight regulations;
- substantial fluctuations within the electrical grid due to the rapid expansion of renewable energy;
- the limitation of flexibility of coal-fired systems;
- the challenge of prolonging the life of existing old power plants.

Based on the past findings of both investigation and practical application, four basic concepts of repowering were defined:

- complete repowering,
- repowering with feed water heating,
- hot wind-box repowering,
- supplementary boiler repowering.

In these concepts, the following facts were registered:

- The complete repowering method without post-combustion (i.e., without maximum supplementary firing) achieves higher thermodynamic characteristics compared to the method with the maximum supplementary firing. While in some cases, the maximum supplementary firing (post-combustion) can lead to an improvement in the thermodynamic parameters of a gas-steam combined cycle.
- Significant improvements have also been observed in the thermodynamic performance of the hot wind-box repowering and feed water heating repowering concepts.
- For the hot wind-box repowering concept it is very important to select the right gas turbine based on the oxygen content in the exhaust gases to match the oxygen content required for combustion in the boiler, which allows to avoid additional costs associated with supplying fresh air to the boiler.

Depending on the objectives, evaluating a repowering concept requires consideration of a wide range of business aspects. This includes determining the additional power consumption and its value, assessing emission reductions, analysing fuel availability and costs, considering transmission requirements and limitations, examining forecasted generation load schedules, evaluating target electricity market prices, and addressing other requirements and goals.

References

[1] https://www.iea.org/ [accessed 7 June 2023].

[2] Monjardino, J., Dias, L., Fortes, P., Tente, H., Ferreira, F., & Seixas, J. (2021). Carbon neutrality pathways effects on air pollutant emissions: The Portuguese case. *Atmosphere*, 12(3), 324. doi: 10.3390/atmos12030324

[3] Țibulcă, I. (2021). Reducing air pollution: Are environmental taxes enough to help the EU member states reach climate neutrality by 2050. *Polish Journal of Environmental Studies*, 30(5), 4205–4218. doi: 10.15244/pjoes/132621

[4] Ciesielska-Maciągowska, D., Klimczak, D., & Skrzek-Lubasińska, M. (2021). Central and Eastern European CO_2 market – Challenges of emissions trading for energy companies. *Energies*, 14(4), 1051. doi: 10.3390/en14041051

[5] Jiang, C., & Yue, Y. (2021). Sensitivity analysis of key factors influencing carbon prices under the EU ETS. *Polish Journal of Environmental Studies*, 30(4), 3645–3658. doi: 10.15244/pjoes/131083

[6] Kefford, B. M., Ballinger, B., Schmeda-Lopez, D. R., Greig, C., & Smart, S. (2018). The early retirement challenge for fossil fuel power plants in deep decarbonisation scenarios. *Energy Policy*, 119, 294–306. doi: 10.1016/j.enpol.2018.04.018

[7] Koch, K., & Alt, B. M. (2020). Dynamic Modeling of a Decarbonized District Heating System with CHP Plants in Electricity-Based Mode of Operation. *Energies*, 13(16), 4134. doi: 10.3390/en13164134

[8] Hamels, S. (2021). CO_2 intensities and primary energy factors in the future European electricity system. *Energies*, 14(8), 2165. doi: 10.3390/en14082165

[9] Günther, M., Greller, M., & Fallahnejad, M. (2014). Evaluation of long-term scenarios for power generation and district heating at Stadtwerke München. *Informatik Spektrum*, 38(2), 97–102. doi: 10.1007/s00287-014-0852-y

[10] Skoczkowski, T., Bielecki, S., Węglarz, A., Włodarczak, M., & Gutowski, P. (2018). Impact assessment of climate policy on Poland's power sector. *Mitigation and Adaptation Strategies for Global Change*, 23(8), 1303–1349. doi: 10.1007/s11027-018-9786-z

[11] Ravina, M., Panepinto, D., Zanetti, M., & Genon, G. (2017). Environmental analysis of a potential district heating network powered by a large-scale cogeneration plant. *Environmental Science and Pollution Research*, 24(15), 13424–13436 doi: 10.1007/s11356-017-8863-2.

[12] Křůmal, K., Mikuška, P., Horák, J., Hopan, F., & Krpec, K. (2019). Comparison of emissions of gaseous and particulate pollutants from the combustion of biomass and coal in modern and old-type boilers used for residential heating in the Czech Republic, Central Europe. *Chemosphere*, 229, 51–59. doi: 10.1016/j.chemosphere.2019.04.137

[13] Rokni, M. (2016). Performance comparison on repowering of a steam power plant with gas turbines and solid oxide fuel cells. *Energies*, 9(6), 399. doi: 10.3390/en9060399

[14] Wang, J., You, S., Zong, Y., Træholt, C., Dong, Z.Y., & Zhou, Y. (2019). Flexibility of combined heat and power plants: A review of technologies and operation strategies. *Applied Energy*, 252, 113445. doi: 10.1016/j.apenergy.2019.113445

[15] Stoll, H.G., Smith, R.W., & Tomlinson, L.O. (1996). *Performance and Economic Considerations of Repowering Steam Power Plants*. Schenectady, New York.

[16] Kehlhofer, R., Rukes, B., Hannemann, F., & Stirnimann, F. (2009). *Combined-Cycle Gas & Steam Turbine Power Plants* (3rd Edn.). Pennwell Corp., Tulsa, Oklahoma.

[17] Kondrateva, O.E., Roslyakov, P.V., Skobelev, D.O., Guseva, T.V., Loktionov, O.A., & Åke, M. (2019). Developing the cost-estimation technique when switching to best available power technologies. *Thermal Engineering*, 66(7), 513–520.

[18] Wang, W., Li, Z., Lyu, J., Zhang, H., Yue, G., & Ni, W. (2019). An overview of the development history and technical progress of China's coal-fired power industry. *Frontiers in Energy*, 13(3), 417–426. doi: 10.1007/s11708-019-0614-2

[19] Wołowicz, M., Milewski, J., & Badyda, K. (2012). Feedwater repowering of 800 MW supercritical power plant. *Journal of Power Technologies*, 2, 127–134.

[20] Badyda, K., & Miller, A. (2014). *Energy gas turbines and systems utilizing them.* Kaprint, Lublin (in Polish).

[21] Harutyunyan, A., Badyda, K., Wołowicz, M., & Milewski, J. (2019). Gas turbine selection for hot windbox repowering on 200 MW fossil fuel power plant. *Journal of Power Technologies*, 99(2), 142–151.

[22] Yilmazoglu, M.Z., & Durmaz, A. (2013). Hot windbox repowering of coal-fired thermal power plants. *Turkish Journal of Engineering and Environmental Sciences*, 37, 33–41. doi: 10.3906/muh-1203-3

[23] Kehlhofer, R. (1997). *Combined-Cycle Gas and Steam Turbine Power Plants*. Tulsa, Oklahoma.

[24] Fränkle, M. (2006). *SRS : The standardized repowering solution for 300MW steam power plants in Russia*. Siemens Power Generation (PG).

[25] Harutyunyan, A. (2021). *Analyses of Thermodynamic Parameters of Gas Turbines and Combined Cycle Power Plants after Repowering Working High Above Sea Level*. PhD thesis, Warsaw University of Technology.

[26] Stenzel, C., Sopocy Dale, M., & Stanley Pace, E. (1999). *Repowering Existing Fossil Steam Plants*. SEPRIL – General Power Solutions. http://www.coal2nuclear.com/MSR%20-%20Repowering%20Existing%20Fossil%20Steam%20Plants%20-%20SEPRIL%20.pdf [accessed 7 June 2023].

[27] Ploumen, P.J., & Veenema, J.J. (1996). Dutch experience with hot windbox repowering. *International Gas Turbine and Aeroengine Congress and Exhibition*, 10–13 June, Birmingham, Birmingham, UK. ASME, GT-250. CorpusID:110395957

[28] Kudlu, N. (1989). *Major options and considerations for repowering with gas turbines: Final report.* EPRI-GS-6156.

[29] Moore, T. (1995). Repowering as a competitive strategy. *EPRI Journal*, 20, 6–13. CorpusID:111903600

[30] Walters, A.B. (1995). Power plant topping cycle repowering. *Energy Engineering*, 92(5), 49–71. CorpusID:107521592

[31] Pace, S., & Walters, A. (1996). Repowering fossil steam power plants with combustion turbine-based technologies. *International Gas Turbine and Aeroengine Congress and Exhibition*, 10–13 June, Birmingham, Birmingham, UK. doi: 10.1115/96-GT-020

Co-published by
Institute of Fluid-Flow Machinery
Polish Academy of Sciences
Committee on Thermodynamics and Combustion
Polish Academy of Sciences

Copyright©2024 by the Authors under licence CC BY 4.0

http://www.imp.gda.pl/archives-of-thermodynamics/

Repowering a coal-fired power plant according to the coal-to-nuclear pathway - analysis of nuclear unit development from the perspective of cooling water availability

Jakub Ochmann[a*], Henryk Łukowicz[a], Sebastian Lepszy[a], Łukasz Bartela[a]

[a]Silesian University of Technology, Department of Power Engineering and Turbomachinery, Konarskiego 18, 44-100, Gliwice, Poland
*Corresponding author email: jakub.ochmann@polsl.pl

Received: 21.12.2023; revised: 13.02.2024; accepted: 23.03.2024

Abstract

Changes in energy fuel markets, the rise of renewables and the aging of existing coal-fired units are leading to increased popularization of research on potential pathways for restructuring power systems. One proposed concept is the Coal-to-Nuclear path, which involves the partial use of existing coal-fired power plant infrastructure in favor of the construction of nuclear units, which can reduce investment costs. An additional benefit is the ability to manage the workforce competencies identified within the coal-fired power unit, and which are also required for the effective operation of the nuclear unit. The article considers the possibility of repowering the Kozienice power plant in Poland from the perspective of the availability of water used to cool the power units. Three different nuclear reactor technologies that are potentially being considered for the construction of the first nuclear units in Poland were analyzed. The study showed that the lowest water flows in the Vistula river recorded in 2022, equal to 146 m^3/s, make it impossible to simultaneously cool the nuclear units and ensure sufficiently low water temperatures from an environmental perspective. Nuclear units were shown to require about 1.55−1.67 times more water for cooling than typical coal-fired units.

Keywords: Coal-to-nuclear; Nuclear power plant performance; Repowering; Cooling water; Efficiency/power output

Vol. 45(2024), No. 2, 107–115; doi: 10.24425/ather.2024.150857

Cite this manuscript as: Ochmann, J., Łukowicz, H., Lepszy, S., & Bartela, Ł. (2024). Repowering a coal-fired power plant according to the coal-to-nuclear pathway - analysis of nuclear unit development from the perspective of cooling water availability, *Archives of Thermodynamics*, 45(2), 107−115.

1. Introduction

The shift in the global hydrocarbon trade market, particularly due to the sanctioning of Russian exports, has resulted in increased public awareness of the effects of fossil fuel shortages and increased support for investment in renewable energy sources, and a renewed interest in nuclear energy. In Poland, which is the largest hard coal producer in Europe, the number of people employed in the mining industry between 2009 and 2017 fell from 183 000 employees to 138 000, respectively. Between 2020 and 2021 there was a 2.2% decrease in employment [1]. The country's coal production fell from 144 million tons to 100 million tons (hard and lignite) between 2012 and 2020 [2]. Although China, which is the world's largest coal producer, reported a decline in production in those years from 3 945 to 3 902 million tons, the trend shows a significant increase in coal production relative to the lowest point in 2016 when China produced 3 410 million tons of coal. According to a report pub

Nomenclature

$c_{p,cond}$ – water heat capacity at constant pressure, kJ/(kg·K)
h – steam enthalpy, kJ/kg
h_s – steam enthalpy for ideal expansion, kJ/kg
$\dot{m}_1$ – steam mass flow in condenser, kg/s
$\dot{m}_{cond}$ – cooling water flow in the condenser, kg/s
N_{el} – net electric power of power plant, W
$N_{el\ b}$ – gross electric power of power plant, W
p – steam pressure, Pa
$\dot{Q}_{cond}$ – heat flux in the condenser, W
$\dot{Q}_{SG}$ – heat flux in the steam generator, W
T_{cond1} – cooling water inlet temperature, K
T_{cond} – cooling water temperature, K

Greek symbols

β – cooling water requirements for installed megawatt installed, kg/(s·MW)
Δ – difference
η_g – gross power plant electric efficiency
η_i – isentropic efficiency of steam turbine
$\eta_{i,k}$ – isentropic efficiency of each k-stage group of steam turbine

Subscripts and Superscripts

$cond$ – condensate
el – net electric
$el\ b$ – gross electric
k – k-stage
s – isentropic
SG – steam generator

Abbreviations and Acronyms

FEM – finite element method
LCOE – levelized cost of energy
SMR – small and medium reactors / small modular reactor
TES – thermal energy storage

lished by the International Energy Agency [3], in 2019 China added approximately 60 GW of renewable energy capacity, half of which was solar PV. In 2021, there was an increase of nearly 130 GW of capacity, with more than 50 GW coming from PV, 40 GW from wind sources, and 30 GW from hydropower. In addition, in 2023, China had 22 nuclear reactors under construction with a total capacity of 22.72 GW_e. However, a similar trend of nuclear power development is not observed in Europe. In 2023, there were two nuclear units under construction in Ukraine, two in the UK and one in France. Figure 1 presents the structure of energy production in European Union countries in (a) 2019 and (b) 2023 [4].

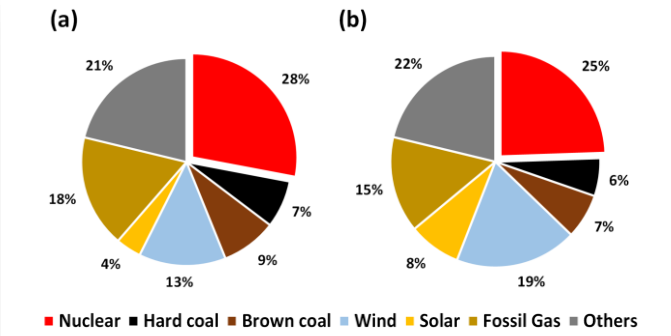


Fig. 1. Share of energy sources in total electricity production in the European Union countries in the years: (a) 2019, (b) 2023 [4].

In 2019, total electricity production in the European Union countries was 2 606 TWh, and in 2023 – 2 408 TWh. During this period, the share of nuclear power in total electricity production fell from 28% to 25%. This decline is mainly due to the implementation of Germany's plan to move away from this energy source, which resulted in the shutdown of 4 nuclear power units with a total electrical capacity of 5.46 GW. In addition, a 907 MW nuclear unit was permanently shut down in Sweden in 2019 and an 881 MW unit in 2020, as well as in Belgium, where a 1 006 MW unit ceased operation in 2022. No new nuclear unit commissioning was reported in the European Union countries during the period under review. Only in 2023 was one 440 MW nuclear unit launched at the Mochovce power plant in Slovakia [5].

Nuclear power, due to the restrictive safety conditions that must be ensured by a series of construction and safety barriers, requires significant financial investment. Figure 2 summarizes the financial expenditures for various power generation technologies [6].

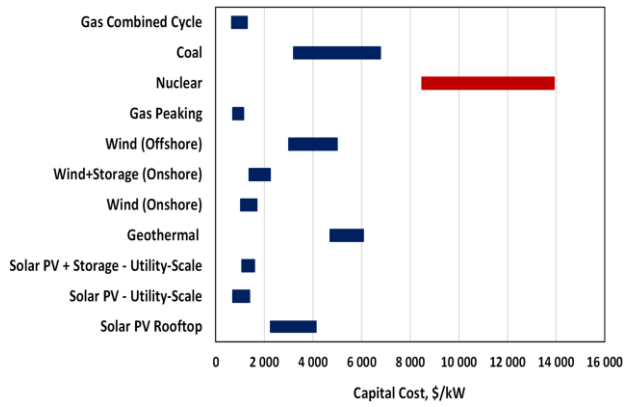


Fig. 2. Financial outlay for different types of energy producers.

Financial expenditures for the construction of a nuclear power plant range from 8 475 $/kW to 13 925 $/kW, which significantly exceeds the expenditures required to build coal and geothermal units. Considering the Levelized Cost of Energy (LCOE) index, since 2009 the value of nuclear power has increased from 1 230 $/MWh to 1 290 $/MWh. The biggest changes have been for photovoltaic power plants, for which the value of the LCOE index has dropped from 359 $/MWh to 60 $/MWh. On the other hand, according to Noland et al. [7] nuclear power has the highest value of energy generated relative to the area occupied 6 703 TWh/km^2. This compares with a value of 3 280 TWh/km^2 for gas-fired power plants and 0.087 TWh/km^2 for solar photovoltaic (PV) plants, which corresponds with studies by Smil [8] and Van Zalk and Bahrens [9].

One of the potential ways to reduce financial outlays for the implementation of investments in nuclear sources is the coal-to-

nuclear path [10]. It assumes at least partial use of the existing infrastructure used in the operation of coal-fired units [11]. Generation IV nuclear reactor technology opens up the possibility of using the existing turbine island due to the similar parameters of live steam obtained from the primary circuit steam generator to the reference parameters of the turbines [12]. In recent years, small and medium reactors (or small modular reactor (SMR)) technologies developed in the group of Generation IV reactors (including those with fully passive safety systems and increased gross efficiency) have become particularly popular, especially in countries with medium or small electricity systems [13,14]. In these countries, the construction of high-power units is problematic, as the possible failure of a large generating unit causes a significant loss of power in the system [15]. Research is also being carried out to increase the flexibility of nuclear units while maintaining a uniform pattern of change in nuclear reactor thermal power. One concept involves the use of high-temperature Thermal Energy Storage (TES) using molten salts [16]. The construction of heat storage tanks allows for short-term storage of heat and its use in a steam generator during periods of higher electricity demand [17]. This concept is also proposed as part of classic coal-fired circuits [18].

This study analyzed a selected location of a coal-fired power plant in Poland in terms of its feasibility as a site for the potential construction of a high-power Generation III nuclear unit. The actual operating parameters of nuclear reactors from three different suppliers were also taken into account.

2. Methods

The analysis of the repowering potential of selected coal- and lignite-fired power plants included the evaluation and ranking of individual units according to six defined categories, which were identified as key from the perspective of restrictive techno-economic requirements for the implementation of nuclear units. These categories were defined as:

1) the area of power units with their supporting infrastructure, their operating parameters and technical considerations for the installation of nuclear reactors, in particular, the CO_2 emissions of the replaced power plant,
2) the area of electricity infrastructure, including power derivation and the technical condition and capacity of electricity transmission networks,
3) the area of associated infrastructure, for example, railroads and roads, in terms of the modernization under consideration and the necessary engineering work associated with the investment process,
4) the area of availability of cooling water and the possibility of building additional water reservoirs,
5) the area of availability of the land required for the development of energy systems and the organization of investment works because of the dates provided for the retirement of coal units,
6) the area of the demand for district heating in the analyzed locations and the possibility of heating the modernized power units.

A separate evaluation criterion is the nuclear safety criterion, which takes into account factors that are not necessarily relevant to the possibility of building a coal-fired power plant at a given location. Certain factors in this category, such as proximity to an airport, proximity to a mine, seismic activity, may be those that would exclude a particular location from the aspect of including it in a nuclear investment. Evaluation of locations according to the security criterion is subject of analyses in this article.

Based on the evaluation conducted according to the mentioned six techno-economic categories, the Kozienice Power Plant located in Świerże Górne, Poland, was selected for further analysis [19]. The power plant is located in the middle part of the Vistula River and consists of 11 coal-fired units – 8 with a capacity of 230 MW, 2 with a capacity of 560 MW, and 1 with a capacity of 1 112 MW. The lower-capacity coal units have an open cooling system using water drawn from the river. The 1 112 MW unit has a closed cooling system equipped with a cooling tower. According to plans, the first 4 (230 MW) units are to be decommissioned in 2025 and the remaining units in 2027. The 560 MW units have been scheduled for operation until 2041 and 2042. The last 1 112 MW unit of the power plant is to be disconnected from the power grid in 2048. Coal supplies to the power plant are carried out entirely by rail transport. In 2022, total CO_2 emissions from Kozienice Power Plant amounted to 15.85 Mt and 7 499 t of SO_2.

Due to Poland's location in the temperate climate zone, cyclical changes in temperature and water flow in rivers are observed due to changes in air temperature levels, as well as the intensity of precipitation. Figure 3 shows the average, minimum, and maximum water temperatures obtained at the Dęblin measuring station in 2022, located 15 km above the water intake for the cooling needs of the Kozienice power plant [20].

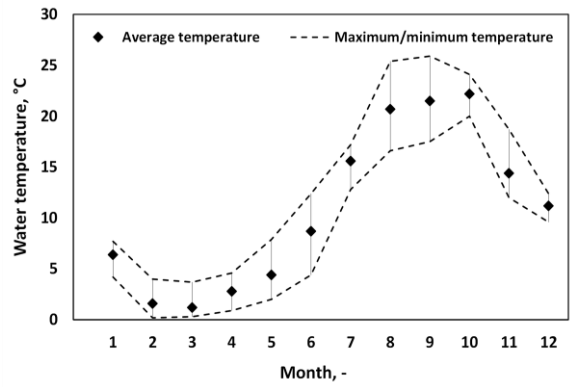


Fig. 3. Water temperature in the Vistula river in 2022.

According to the data presented in Fig. 3, the highest average water temperature was recorded in the month of October and was 22.2°C. The highest water temperature before the water intake for the cooling of the Kozienice power plant was recorded in September and was 25.9°C. The lowest water temperature was recorded in February and was 0.2°C. The lowest average monthly water temperature was recorded in March and was 1.2°C. Cooling water temperature is crucial from the perspective of Kozienice power plant operation also due to environmental and economic aspects. Environmental law in Poland precisely

regulates monetary rates for water withdrawal for power plant cooling depending on the temperature of water emitted into the river. The currently applicable rates are presented in Table 1.

Table 1. Water withdrawal fee depending on the temperature of the discharge water.

Water temperature, °C	Mandatory payment, $/1000 m³ [21]
26 – 32	0.17
32 – 35	0.35
>35	1.08

As indicated in Table 1, exceeding the threshold of 35°C of the temperature used to cool the power plant results in a three-fold increase in the fee relative to the lower temperature level of the water. The 2019 study indicated that the temperature of the water discharged from the power plant was 10.7°C higher than the temperature of the water taken from the river [22]. A measurement taken 1 km downstream of the water discharge indicated an increase of 3.2°C in the river water temperature. The temperature of the mixed water at each measurement section is also affected by the flow of water in the river. Figure 4 shows the average, minimum, and maximum water flow in the Vistula river monitored at the same measuring station.

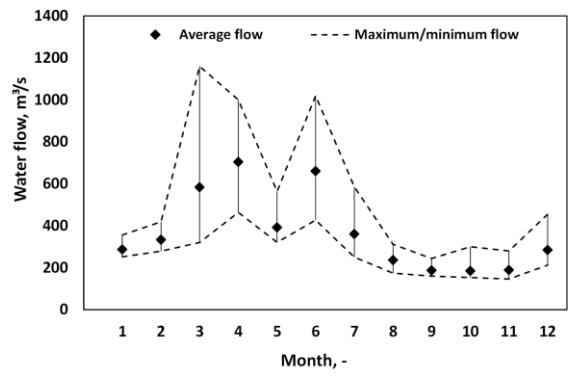


Fig. 4. Water flow in the Vistula river in 2022 [20].

As shown in Fig. 4, the lowest average water flow in 2022 was recorded in October and was 184 m^3/s. The Kozienice power plant uses an average of about 52 m^3/s, which is about 30% of the locally flowing water. The lowest average monthly water flow also corresponds with the maximum average water temperature, which may result in an increased negative impact of discharge water on the environment [23−25].

Pressurized Water Reactor (PWR) high-power (Generation III) technology was selected for thermodynamic analysis [26]. PWR technology is widely used in the world nuclear power industry [27]. As of 2023, 303 reactors of this type, with a total net capacity of 289 GWe, were operating or under temporary suspension of operation. In addition, 49 PWR reactors with a total net capacity of 53 GWe were under construction. In comparison, the second most popular nuclear reactor technology is the Pressurized Heavy-Water Moderated and Cooled Reactor (PHWR) with 46 operating or suspended reactors [5]. The following technologies were selected for analysis [5,28]:

Westinghouse Advanced Passive PWR (AP-1000) - reactor technology based on the earlier AP-600 type. The unit has a gross electrical output of 1 250 MW_e and a thermal output of 3 600 MW_{th}, with both moderator and coolant being light water. The operating pressure of the reactor is 15 513 MPa. The inlet temperature of the reactor coolant is 279.4°C and its temperature rise is 45.2°C. The coolant directed to the two steam generators is used to produce live steam at a rate of 1 889 kg/s with a pressure of 5.76 MPa and a temperature of 272.8°C. The planned lifetime of the reactor is 60 years, assuming operational availability above 93% of the time and a fuel cycle length of 18 months. The reactor requires enrichment of the nuclear fuel to between 2.35% and 4.8% U235 level. A distinctive feature of the AP-1000 reactor is the design of the external safety shield, which uses the natural stack draft to act as one of the passive cooling systems of the internal safety shield. In addition, the roof section of the outer containment has gravity water reservoirs, which can also be used if the need for passive reactor cooling arises.

KEPCO's Advanced Power Reactor 1 400 MWe (APR-1400) - a technology based on the experience developed with OPR1000 technology, which was the first PWR unit in South Korea. The unit has a gross electrical output of 1455 MW_e and a thermal output of 3 983 MW_{th}, with both moderator and coolant being light water. The operating pressure of the reactor is 15.5 MPa. The inlet temperature of the reactor coolant is 290.6°C and its temperature rise is 34.66°C. The coolant directed to the two steam generators is used to produce live steam at a rate of 1 889 kg/s with a pressure of 6.84 MPa and a temperature of 284.3°C. The planned lifetime of the reactor is 60 years, assuming operational availability above 90% of the time and a fuel cycle length of 18 months. The APR-1400 reactor has a passive system to limit the hydrogen concentration to 10% in the reactor building in the event of an accident resulting in damage to the reactor core.

EDF's The Evolutionary Power Reactor (EPR-1600), a technology being developed through Franco-German cooperation. The unit has a gross electrical output of 1 720 MW_e and a thermal output of 4 530 MW_{th}, with both moderator and coolant being light water. The operating pressure of the reactor is 15.5 MPa. The inlet temperature of the reactor coolant is 295.2°C and its temperature rise is 34.8°C. The coolant directed to the four steam generators is used to produce live steam at a rate of 2 443 kg/s with a pressure of 7.8 MPa and a temperature of 284.3°C. The planned lifetime of the reactor is 60 years, assuming operational availability above 92% of the time and a fuel cycle length of 24 months. The reactor requires nuclear fuel enrichment to 5% U235 content. The EPR-1600 nuclear unit can be continuously operated in the range of 25−100% of rated power.

Basic information on the nuclear reactors analysed along with the steam parts is summarized in Table 2 and Table 3.

Figure 5 presents a simplified circuit diagram of the nuclear unit. Saturated steam from the steam generator flows to the high-pressure part of the turbine after which it is directed to the moisture separator and the two-section steam superheater. The first section is fed with steam from the turbine bleed, while the sec-

Table 2. Characteristic data of the studied reactors [5].

Provider	Designation	Reactor type	Electrical power gross/net, MW	Gross efficiency, %
Westinghouse (USA)	AP-1000	PWR	1250/1150	34
KEPCO (South Korea)	APR-1400	PWR	1420/1350	36
EDF (France)	EPR-1600	PWR	1720/1600	38

Table 3. Characteristic parameters of the studied reactors [5].

Parameter	Unit	AP-1000	APR-1400	EPR-1600
Steam pressure at outlet of the steam generator	MPa	5.76	6.84	7.8
Steam temperature/humidity at outlet of the steam generator	°C/%	272.8/2.5	284.3/2.5	293
Steam mass flow at outlet of the steam generator	kg/s	1889	2261	2443
Supply water temperature at inlet of the steam generator	°C	226.7	232	230

ond section is fed with live steam from the steam generator. The condensate from the condensers is heated in a condensate cooler and four low-pressure heaters then flows to a deaerator and is routed via a feedwater pump through two high-pressure heaters to the steam generator.

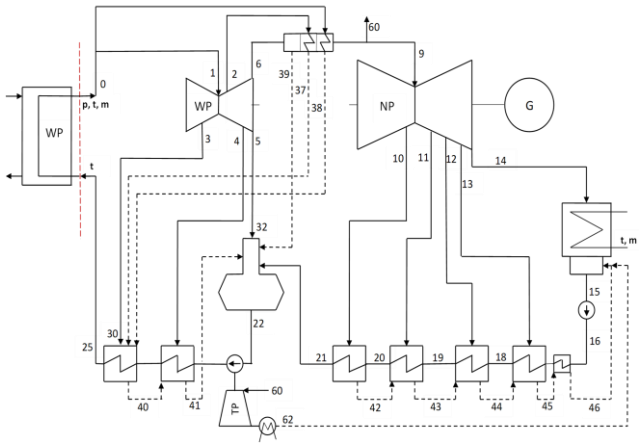


Fig. 5. Diagram of the nuclear system under analysis.

The feedwater pump can be driven by electric motors or an auxiliary steam turbine. For simplicity, only one low-pressure NP part is shown in the diagram, while all low-pressure parts are included in the calculations. In the analysis of the circuit with the APR-1400 reactor, a turbine drive of the feedwater pump was assumed, while with the AP-1000 and EPR-1600 reactor, an electric motor drive was assumed.

The calculations in the mathematical model are carried out iteratively: successive machines and equipment that make up the thermal circuit are modeled until the desired convergence is obtained. The thermodynamic calculations used the mass-energy balance method on the individual elements of the thermodynamic system, and used sets of equations describing the thermodynamic transformations occurring in the machines and equipment that make up the thermal cycle. The characteristic parameters at given points in the system were defined on the basis of the available documentation for each of the reactors studied [5]. The parameters of the working medium at the inlets and outlets are the connections between the objects. The simulation module uses thermodynamic quantities (enthalpy, entropy) comply with the international standard of the International Association for the Properties of Water and Steam (IAPWS).

The isentropic efficiency η_i of a selected group of steam turbine stages is defined as the ratio of the actual steam enthalpy drop in the stage (Δh) to the enthalpy drop for ideal expansion (at constant entropy – Δh_s):

$$\eta_i = \frac{\Delta h}{\Delta h_s}. \tag{1}$$

The isentropic efficiency of the stage groups $\eta_{i,k}$ varies with the load. The study considers a characteristic that relates the efficiency of each k-stage group to the steam flow $\dot{m}_k$ through that group:

$$\eta_{i,k} = f(\dot{m}_k). \tag{2}$$

The isentropic efficiency η_i calculated according to equation 1 is simple to determine for turbine parts operating in the superheated steam region. Measurements of the steam parameters in the pipelines located upstream and downstream of the stage group make it possible to determine the enthalpy and entropy of the steam unambiguously. The difficulty in determining the efficiency characteristics arises for low-pressure turbine parts. The expansion process in the last stage groups occurs in the wet steam region. In this situation, the measurement of temperature and pressure is not sufficient to clearly determine the thermodynamic properties of the steam. The solution to the problem is the simultaneous balancing of the entire thermal cycle and the determination of the enthalpy of the steam in the updrafts through heat exchanger balances. This approach was used in the conducted research.

The condenser is the component of the power unit whose operation remains the most sensitive to ambient conditions. The operation of the condenser, the vacuum that can be created, directly affects the efficiency of power generation in a condensing steam unit. The pressure in the condenser depends on two factors:

- the temperature of the condenser cooling water,
- the steam load of the condenser.

The minimum temperature of the condenser cooling water is determined by the design and operation of the cooling system. Possible solutions, such as cooling towers or the use of natural water reservoirs, vary depending on the location of the power unit. In the framework of the study, to create a universal system for evaluating the degradation of characteristics, the power unit was closed with a control volume that separates the condenser from the cooling system. For this reason, the characteristics of the condenser were used in the analyses in the form of a relationship:

$$p_1 = p_1 = f(T_{cond1}, \dot{m}_1). \quad (3)$$

It was assumed that the wet vapor pressure at the condenser inlet and the condensate pressure at the bottom of the condenser are equal. This assumption makes sense in view of the limited number of measurement sensors installed in condensers. For a circuit with a given reactor, parallel and series connections of turbine condensers were analyzed. The diagram of condenser connections is presented in Fig. 6.

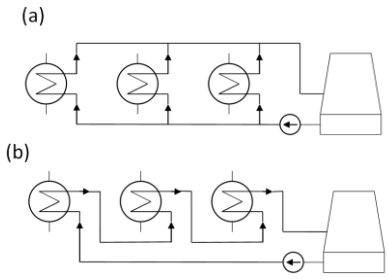


Fig. 6. Diagram of condenser connections: (a) parallel; (b) series.

For a series connection of condensers, a constant cooling water temperature rise in each condenser of 4.65°C was assumed, while for a parallel connection it is 9°C.

To evaluate nuclear technology, the gross electrical efficiency of a nuclear power plant η_g was defined as:

$$\eta_g = \frac{N_{el\,b}}{\dot{Q}_{SG}}, \quad (4)$$

where $N_{el\,b}$ is the gross electric power of power plant and $\dot{Q}_{SG}$ is heat flux in steam generator.

In addition, it was assumed that the net electrical efficiency is due to the use of part of the generated energy for the power plant's own needs. Gross electric power $N_{el\,b}$ was also used to assess the cooling water requirements for each megawatt of power plant installed β according to the equation:

$$\beta = \frac{\dot{m}_{cond}}{N_{el\,b}}, \quad (5)$$

where $\dot{m}_{cond}$ is cooling water mass flow.

The heat flux $\dot{Q}_{cond}$ taken up by the cooling water in the condenser is proportional to the amount of cooling water $\dot{m}_{cond}$ and the increase in its temperature ΔT_{cond} in the condenser:

$$\dot{Q}_{cond} = \dot{m}_{cond} \cdot \Delta T_{cond} \cdot c_{p,cond} \quad (6)$$

3. Results

The thermodynamic model was used to determine the fluxes of water supplied to the condenser depending on the condenser connection variant. Table 4 presents the results obtained for an assumed cooling water temperature of 10.9°C, which is the average annual water temperature from the Vistula River in 2022 above the water intake for the Kozienice power plant.

As shown in Table 4, the parallel connection of the condensers in each variant exceeds the current water intake for the cooling of the active units of the Kozienice power plant, which in the case of the EPR-1600 reactor on an annual basis would indicate the need to increase water intake by 512 460 000 m^3. It should also be noted that the calculations were carried out for relatively low intake water temperatures. During summer periods, as indicated in Fig. 3, the water temperature in the river reaches as high as 26°C, which, in the case of an assumed increase in water temperature of 9°C, would put one on the verge of having to significantly increase the cost of water intake (Table 1). In the case of a series connection, a decrease in the amount of water required was noted in every variant considered. Therefore, the turbine island variant with a series connection of condensers was selected for further analysis. Figure 7 presents the necessary flow of cooling water taken from the river depending on the temperature of this water.

Table 4. Cooling water flow depending on the type of reactor and connection method.

Nuclear reactor	Parallel connection	Series connection
	Cooling water flow, m^3/s	Cooling water flow, m^3/s
EPR-1600	68.25	43.94
APR-1400	66.42	41.74
AP-1000	55.40	35.80

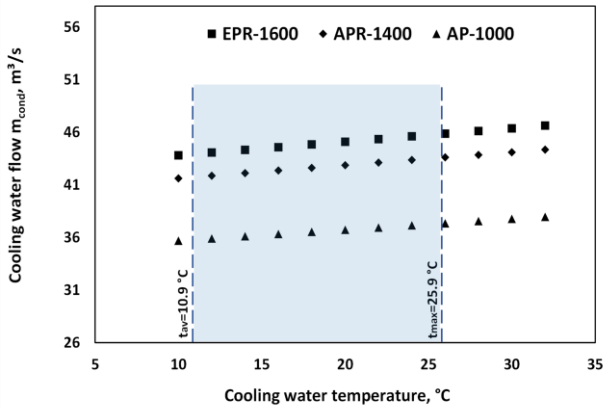
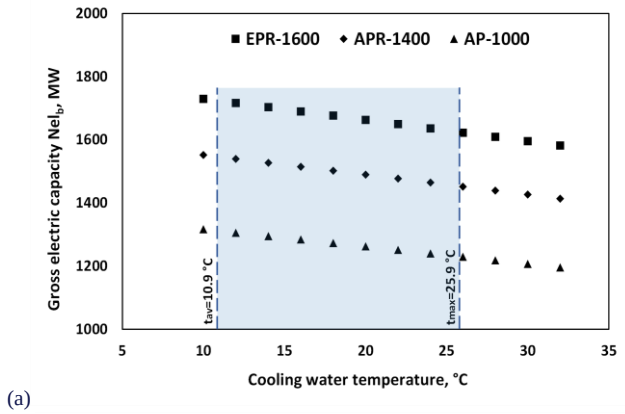


Fig. 7. Cooling water flow depending on its temperature.

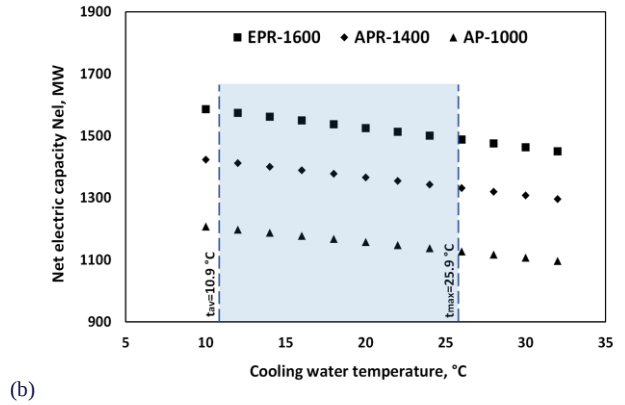
Figure 7 indicates the area of average and maximum annual water temperature in the year 2022. It should be noted that the assumed water temperature increment of 4.65°C at each of the three condensers connected in series will result in the maximum allowable temperature of water taken from the river, which could be 21.05°C, in the event of a desire to avoid significant financial outlays for taking water to cool the nuclear power plant. The data presented in Fig. 3 suggest that situations of potentially reaching the limit temperature of river discharge water may occur during the months of August through October, i.e. during periods of higher air temperature and reduced precipitation. Figure 8a shows the gross electrical power of the nuclear units under consideration as a function of the temperature of the condenser cooling water. Figure 8b shows the net electrical power of the considered nuclear units depending on the temperature of the condensers' cooling water. Figure 8c shows the gross

efficiency of the nuclear power plants under consideration as a function of the cooling water temperature.

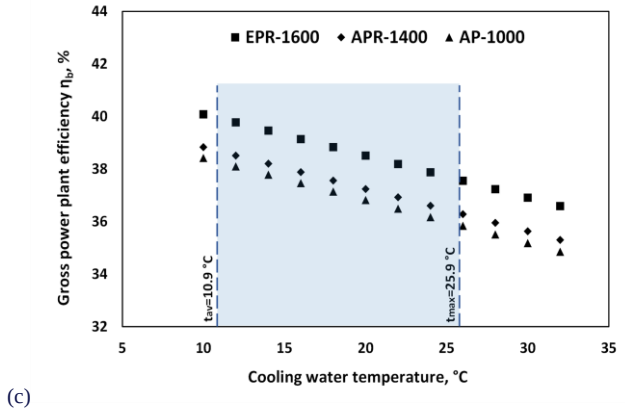
From the perspective of nuclear unit operation, the fact that electrical power changes due to cooling water temperature is crucial. Figures 8a and 8b include the gross and net electrical power of the selected units, respectively. As the study showed, the electrical power for all analyzed units was reduced to about 94% of the power obtained at a nominal average cooling water temperature of about 11°C. It should also be noted that during periods of reduced water flow in the river and a simultaneous increase in its temperature to about 26°C, it may be impossible from the perspective of the environmental impact of the power plant to use the full available power.



(a)



(b)



(c)

Fig. 8. Dependence: (a) gross electrical capacity of nuclear units; (b) net electrical capacity of nuclear units; (c) gross power plant efficiency on the temperature of the cooling water.

According to the 2 022 data, almost three months are characterized by an increased probability of a forced reduction in generated power due to exceeding the allowable maximum discharge water temperature. This is an additional factor that, in addition to increasing the steam expansion pressure, affects the generated power and, consequently, the reimbursement of the costs incurred for the construction of the nuclear power plant.

The data shown in Fig. 8c directly depicts the decrease in gross efficiency of the nuclear unit resulting from changes in condenser pressure and possible steam expansion in the low-pressure part of the turbine. For the most efficient EPR-1600 unit, there was a decrease from 39.95% for a cooling water temperature of 10.9°C to 37.56% for a water temperature of 25.9°C.

The purpose of the retrofit of a coal-fired power plant using nuclear reactors is also to fill the gap in available capacity after the coal units are extinguished. In the case of the retrofitting of the Kozienice power plant, due to the age of the units and their planned retirement, all units (8×230 MW, 2×560 MW) using river cooling water were considered. The total capacity loss of 2 960 MW would require the construction of more than one nuclear unit at this location. Table 5 presents the water demand per nominal 1 MW installed.

Table 5. Cooling water demand.

Unit	Cooling water demand, m³/(s·MW)
Kozienice Power Plant	0.0175
EPR-1600	0.0273
APR-1400	0.0290
AP-1000	0.0293

As shown in Table 5 for nuclear units, the required cooling water flux per MW of installed capacity is 1.55–1.67 times higher than for coal units. Installing two EPR-1600 units covering the replaced installed capacity would result in a required river water intake flux of about 90.5 m^3/s. The minimum recorded water flux in the Vistula River in 2020 was 146 m^3/s, so the withdrawn water flux would be more than 60% of this value. This could therefore result in a significant increase in the temperature of mixed water, and consequently disrupt the local ecosystem. The installation of two AP-1000-type nuclear units, despite the incomplete coverage of the gap after the coal units are shut down, would result in keeping the river water intake at 73.5 m^3/s, which would be about half of the minimum river water flow.

4. Discussion

The study considered the retrofit of the Kozienice power plant (Poland) through the construction of a nuclear unit. The analyses included the three most popular third-generation PWR reactor technologies – EPR-1600, APR-1400, and AP-1000. The main objective of the work was to analyze the availability of water and hydrological conditions at the considered location and to study the possibility of a possible increase in the stream of water withdrawn for the cooling of future nuclear units. Based on the work carried out, the following conclusions were made:

1) The 230 MW and 560 MW class coal-fired units of the Kozienice power plant meet the defined criteria for evaluating recommendations for repowering using nuclear techniques due to the level of emissions, planned shutdown time and adequate transport facilities.
2) Nuclear power is the most expensive source of energy from the perspective of financial outlays for the construction of generating units while having the most favorable density of energy produced per unit area occupied by the unit. The Coal-to-Nuclear path potentially allows for a reduction in the financial outlay for the construction of a nuclear power plant due to the potential use of some of the existing components of coal units.
3) The Vistula river in the area of water intake for the cooling of the Kozienice power plant is characterized by significant variability in flow rate and temperature. The average water temperature in 2022 was 10.9°C, and the maximum in the months of August, September, and October was about 26°C. Restrictive laws in Poland regarding the maximum temperature of discharge water force the temperature of discharge water to be kept below 35°C.
4) Nuclear units have an average of 1.55 to 1.67 times the cooling water flux per MW installed compared to coal units. This therefore makes it impossible to maintain water intake at current levels while covering the units' replaced installed capacity.

Future research work should focus on assessing the potential for using the existing power derivation infrastructure at the plant site. In addition, the ongoing work should include an economic analysis qualifying the costs incurred during the construction of the nuclear unit and at the retrofit stage. Possible modifications to nuclear units to make them more compatible with existing coal unit infrastructure should also be recognized.

Acknowledgement

The paper was created as a result of the project: "Plan of decarbonisation of the domestic power industry through modernization with the use of nuclear reactors", financed by the National Center for Research and Development under the Program "Social and economic development of Poland in conditions of globalizing markets" GOSPOSTRATEG (Contract No.: Gospostrateg VI/0032/2021-00 dated 15.03.2022).

References

[1] Statistics Poland. Average employment in mining and extraction (in Polish). https://stat.gov.pl/ [accessed 20 Feb. 2024].
[2] CEIC Data. Poland Coal Production. https://www.ceicdata.com/ [accessed 20 Feb. 2024].
[3] International Energy Agency. (2022). *Renewable Energy Market Update - May 2022: Outlook for 2022 and 2023 [Full Report]*. https://www.iea.org/reports/renewable-energy-market-update-may-2022 [accessed 20 Feb. 2024].
[4] European Network of Transmission System Operators for Electricity. https://www.entsoe.eu/ [accessed 20 Feb. 2024].
[5] International Atomic Energy Agency. https://www.iaea.org/ [accessed 20 Fe. 2024].
[6] Lazard. (2023). *Lazard's Levelized Cost of Energy Analysis*. https://www.lazard.com/media/typdgxmm/lazards-lcoeplus-april-2023.pdf [accessed 20 Feb. 2024].
[7] Noland, J.K., Auxepaules, J., Rousset, A., Perney, B., & Falletti, G. (2022). Spatial energy density of large-scale electricity generation from power sources worldwide. *Scientific Reports*, 12(1), 21280. doi: 0.1038/s41598-022-25341-9
[8] Smil, V. (2016). *Power Density: A key to understanding energy sources and uses*. MIT Press.
[9] Van Zalk, J., & Behrens, P. (2018). The spatial extent of renewable and non-renewable power generation: A review and meta-analysis of power densities and their application in the US. *Energy Policy*, 123, 83-91. doi: 10.1016/j.enpol.2018.08.023
[10] Bartela, Ł., Gładysz, P., Andreades, C., Qvist, S., & Zdeb, J. (2021). Tech-no-Economic Assessment of Coal-Fired Power Unit Decarbonization Retrofit with KP-FHR Small Modular Reactors. *Energies*, 14, 2557. doi: 10.3390/en14092557
[11] Qvist, S., Gładysz, P., Bartela, Ł., & Sowiżdżał, A. (2021). Retrofit Decarbonization of Coal Power Plants-A Case Study for Poland. *Energies*, 14(1). doi: 10.3390/en14010120 Łukowicz, H., Bartela, Ł., Gładysz, P., & Qvist, S. (2023). Repowering a Coal Power Plant Steam Cycle Using Modular Light-Water Reactor Technology. *Energies*, 16, 3083. doi: 10.3390/ en16073083
[13] Miśkiewicz, A., Chmielewska-Śmietanko, D., & Smoliński, T. (2023). Decarbonization of coal-based energy production in Poland by application of modular nuclear reactors. *Bezpieczeństwo Jądrowe i Ochrona Radiologiczna: Biuletyn Informacyjny Państwowej Agencji Atomistyki*, 1(127), 47–55 (in Polish).
[14] Chmielewska-Śmietanko, D., Miśkiewicz, A., & Smoliński, T. (2023). Dynamic development of small modular reactors (SMR) – situation in the world and in Poland. *Bezpieczeństwo Jądrowe i Ochrona Radiologiczna: Biuletyn Informacyjny Państwowej Agencji Atomistyki*, 3(129), 10–20 (in Polish).
[15] Haneklaus, N., Qvist, S., Gładysz, P., & Bartela, Ł. (2023). Why coal-fired power plants should get nuclear-ready. *Energy*, 280, 128169. doi: 10.1016/j.energy.2023.128169
[16] Bartela, Ł., Gładysz, P., Ochmann, J., Qvist, S., & Martinez Sancho, L. (2022). Repowering a Coal Power Unit with Small Modular Reactors and Thermal Energy Storage. *Energies*, 16(5830). doi: 10.3390/en15165830
[17] Ochmann, J., Rusin, K., & Bartela, Ł. (2023). Comprehensive analytical model of energy and exergy performance of the thermal energy storage. *Energy*, 283, 128783. doi: 10.1016/j.energy.2023.128783
[18] Kosman, W., & Rusin, A. (2020). The Application of Molten Salt Energy Storage to Advance the Transition from Coal to Green Energy Power Systems. *Energies*, 9, 2222. doi: 10.3390/ en13092222
[19] Enea. (2019). *Consolidated Annual Report for 2019* (in Polish). https://ir.enea.pl/ [accessed 20 Feb. 2024].
[20] Institute of Meteorology and Water Management. https://www.imgw.pl/ [accessed 20 Feb. 2024].
[21] Dziennik Ustaw. (2017). Act of *20 July 2017 - Water law act*. https://isap.sejm.gov.pl/ (in Polish) [accessed 20 Feb. 2024].
[22] Cebula, M., Ciężak, K., Mikołajczyk, Ł., Mikołajczyk, T., Nowak, M., Skowronek, D., Wawręty, R., & Żurek, R. (2021). *The impact of the discharge of hot cooling water from power plants into rivers.* Stowarzyszenie Pracownia na Rzecz Wszystkich Istot, Towarzystwo na Rzecz Ziemi, Oświęcim (in Polish).
[23] Latif, S., Souaissi, Z., Ouarda, T., & St-Hilaire, A. (2023). Copula-based joint modelling of extreme river temperature and low flow characteristics in the risk assessment of aquatic life. *Weather and Climate Extremes*, 41, 100586. doi: 10.1016/j.wace.2023.100586

[24] Hannah, D., Webb, B., & Nobilis, F. (2008). River and stream temperature: dynamics, processes, models and implications. *Hydrological Processes*, 22(7), 899-901. doi: 10.1002/hyp.6997

[25] Ficklin, D., Stewart, I., & Maurer, E. (2013). Effects of climate change on stream temperature, dissolved oxygen, and sediment concentration in the Sierra Nevada in California. *Water Resources Research*, 49(5), 2765-2782. doi: 10.1002/wrcr.20248

[26] Laskowski, R., Smyk, A., Jurkowski, R., Ance, J., Wołowicz, M., & Uzunow, N. (2022). Selected aspects of the choice of live steam pressure in PWR nuclear power plant. *Archives of Thermodynamics*, 43(3), 85-109. doi: 10.24425/ather.2022.143173

[27] Dudek, M., Jaszczur, M., & Kolenda, Z. (2019). Thermodynamic analysis of modular high-temperature nuclear reactor coupled with the steam cycle for power generation. *Archives of Thermodynamics*, 40(4), 49-66. doi: 10.24425/ather.2019.130007

[28] Leverenz, R., & Gerhard, L. (2004). The European Pressurized Water Reactor: A Safe and Competitive Solution for Future Energy Needs. In *International Conference Nuclear Energy for New Europe*. September 6−9, Portoroz, Slovenia.

Co-published by
Institute of Fluid-Flow Machinery
Polish Academy of Sciences
Committee on Thermodynamics and Combustion
Polish Academy of Sciences

Copyright©2024 by the Authors under licence CC BY 4.0

http://www.imp.gda.pl/archives-of-thermodynamics/

Coal-plastic waste blendings. Experimental research and prediction of the thermal process

Agnieszka Kijo-Kleczkowska[a*], Adam Gnatowski[a],Marcin Gajek[b], Jaroslaw Krzywanski[c], Magdalena Szumera[b], Krzysztof Knaś[a], Dariusz Kwiatkowski[a]

[a]Czestochowa University of Technology, Faculty of Mechanical Engineering and Computer Science, Dabrowskiego 69, 42-201 Czestochowa, Poland
[b]AGH University of Krakow, Faculty of Materials Science and Ceramics, Mickiewicza 30, Krakow, Poland
[c]Jan Dlugosz University in Czestochowa, Faculty of Science and Technology, Armii Krajowej 13/15, 42-200 Czestochowa, Poland
*Corresponding author email: a.kijo-kleczkowska@pcz.pl

Received: 20.12.2023; revised: 20.03.2024; accepted: 05.05.2024

Abstract

The topic of waste incineration/co-incineration is critical, given the increasingly stringent regulations on environmental aspects. The widespread use of polymeric materials generates significant waste, posing an ecological problem. Current regulations mandate a reduction in the landfilling of plastic waste, which should be replaced by recycling, with the possibility of exploiting the energy potential due to its high calorific value. The electricity generation in Poland is mainly based on coal, so using polymers as alternative fuels is an important research issue. The research results presented in this paper make it possible to compare the properties of selected waste plastics and coal and their behavior during thermal processes, considering the quality of the gases released. Based on the thermal analyses, a FuzzyTherm model was introduced based on one of the fuzzy logic methods, one of the main artificial intelligence modeling approaches. The model predicts the temperatures corresponding to endothermic and exothermic reactions. The model achieved good accuracy. The maximum relative error between measured and calculated data is lower than 11%. These aspects constitute an innovative element of this paper.

Keywords: Polymer waste; Coal; Thermal analysis; TG/DTG/DSC/EGA; Artificial intelligence

Vol. 45(2024), No. 2, 117–128; doi: 10.24425/ather.2024.150858

Cite this manuscript as: Kijo-Kleczkowska, A., Gnatowski, A., Gajek, M., Krzywanski, J., Szumera, M., Knaś, K., & Kwiatkowski, D. (2024). Coal-plastic waste blendings. Experimental research and prediction of the thermal process. *Archives of Thermodynamics*, 45(2), 117-128.

1. Introduction

The issue of fuel combustion is a current topic of scientific work [1]. Still, due to increasingly stringent environmental conditions, the use of renewable energy sources [2] and the thermal disposal of various types of waste, including coal waste [3,4] and polymer waste [5–24], with the possibility of energy recovery, are of great interest. For example, in 2020 (in the EU27+3), about 1/3 of plastic waste was sent for recycling, 40% – for energy recovery, and more than 23% went to landfills [6].

Polymeric materials manufacturing technologies increasingly use modern engineering polymers with a wide range of applications at much higher temperatures of continuous use than typical thermoplastic polymers. This is due to the limited possibility of recycling waste plastics, which cannot be repeatedly processed technologically and in terms of achieved strength parameters.

Nomenclature

FC – fixed carbon
I – ionic current
LHV – low heating value
m – mass number
m/z – mass spectrum
o – crisp, real output value after defuzzification
T_{melt} – temperature corresponding to endothermic (melting) of exothermic reactions, K
T_{max} – temperatures corresponding to maximum temperature of exothermic reactions, K
z – charge number of the ion

Greek symbols

μ – membership value (between 0 and 1)
$\bar{o}$ – centroid of each membership function

Subscripts and Superscripts

exp – measure

Abbreviations and Acronyms

AI – artificial intelligence
DSC – differential scanning calorimetry
DTG – derivative thermogravimetry
EGA – evolved gas analysis
FL – fuzzy logic
FTIR – Fourier transform infrared spectroscopy
GPC – gel permeation chromatography
MS – mass spectrometry
PEEK – polyether ether ketone
POM – polyoxymethylene
PTFE – polytetrafluoroethylene
QMS – quadrupole mass spectrometer
TG – thermogravimetry

There is a problem with the disposal of such materials. Thermal analysis of waste materials and the possibility of utilization in the form of mixtures is essential in energy recovery processes. According to the literature, thermal processes associated with modifying polymeric waste indicate its possible energy recovery.

Thermal analysis (thermogravimetry/differential scanning calorimetry – TG/DSC) with simultaneous detection of released gases (evolved gas analysis – EGA) makes it possible to record the mass change of a sample and obtain information on which temperature ranges these changes occur and which compounds are released into the atmosphere during high-temperature processes. According to the literature, the energy properties of polymer wastes make it possible to recover energy from them. Using fillers such as carbon black, fly ash, and carbon-based materials in polymer composites, on the other hand, improves the thermomechanical properties, and energy recovery of such materials is economically justified, considering the ecological aspects of waste reduction.

In the paper [7], the author presented numerical results of polyoxymethylene combustion in a reactor. Several combustion reactor configurations were introduced to obtain optimal parameters for the polymer combustion process. The mathematical model developed by the author solves the basic features of the combustion process, such as multicomponent reaction gas flow, heat and mass transfer, radiation heat transfer, polymer combustion, and pyrolysis. The paper presents the distribution of hydrodynamic and thermal parameters in the combustion chamber, characterized by a distinct two-dimensional combustion process. It is shown that the combustion of the polymer in the reactor proceeds in a diffusion mode. The paper [8] addresses the recovery of energy and chemical compounds formed during POM combustion. Measurements were carried out using a specially designed burner. The solid fuel's combustion surface temperature and mass burning rates were determined. The chemical structure of the flame was studied by mass spectrometry using a microprobe. The composition of the gas sample was analyzed by spectrometry. The following gas components: CH_2O, CO, CO_2, H_2O, O_2, and N_2 were identified, and their concentration profiles were measured. Mass spectrometry and thermogravimetric analysis determined POM thermal degradation's product composition and kinetic parameters. The authors in [9] presented the effect of reprocessing and thermo-oxidative aging on the degradation behavior of polyoxymethylene. The study used thermogravimetric analysis (TG) in a nitrogen and air atmosphere. Tests were carried out with a five-fold heating process to evaluate the activation energy at several conversion steps. TG measurements were carried out with simultaneous monitoring of the evolved gases using a mass spectrometer (MS) connected to the outlet of the TG furnace. The mass spectra showed that the main decomposition product was formaldehyde and that further water formation could be detected in the air. In nitrogen, samples aged in the atmosphere emitted small amounts of carbon dioxide at the onset of mass loss. The activation energy for low conversion rates (5%) increased in air and nitrogen as a function of conversion. A difference appeared for higher conversions as degradation progressed: the activation energy decreased continuously in air, while no significant changes were obtained in the nitrogen atmosphere. The paper [10] presents a process for energy recycling of polyoxymethylene in a fluidized bed formed from cenospheres (hollow, spherical particles). Air, N_2, and CO_2 were used in the combustion process. The composition of the process products in the flue gases as a function of fluidized bed temperature for each fluidization gas is presented and discussed. Fourier transform infrared spectroscopy FTIR analysis of the flue gases and spectra of multicomponent gas samples were used to quantitatively monitor POM thermal degradation products. POM was thermally recycled at 400°C in an air or CO_2 atmosphere to recover the monomer, and nearly 90% formaldehyde formation efficiency was achieved. At temperatures above 600°C, the air or N_2 use led to energy or CO-rich gas recovery, respectively. CO-rich gas was obtained during POM pyrolysis when CO_2 was the liquefying agent. The amount of CO in the flue gas was almost twice as much as the amount of carbon introduced into the process in the polymer material. This means

that carbon was converted to CO from the fluidization environment, thus recycling POM into a CO-rich feedstock with negative CO_2. The authors of papers [11,12] investigated the effects of processing and physical aging on the degradation behavior of thermally stabilized polyoxymethylene homo- and copolymers using thermogravimetric analysis. To this end, the samples were processed by injection molding, followed by six reprocessings, temperature aging in an oven for up to eight weeks, and ultraviolet (UV) light exposure in a xenon tester. TG points to the accidental rupture of the main chain as the initiating mechanism for degradation. The subsequent process depends on the condition of the material and the degradation treatment – thermal, loading, or UV radiation. As observed by gel permeation chromatography (GPC), repeated processing did not affect the molecular weight distribution of the materials. TG/MS (thermogravimetry /mass spectrometry) studies showed the formation of formaldehyde and stabilizer wear as the main processes during aging procedures, which in some cases result in a strong reduction of POM thermal stability.

The authors of the paper [13], while conducting thermal degradation studies of polyoxymethylene using thermogravimetry-Fourier transform infrared spectroscopy (TG-FTIR), also found that POM tends to separate formaldehyde, starting from the unstable ends of the chain, random chain rupture occurs at elevated temperatures, and several related reactions probably take place during the degradation process. The results show that formaldehyde is the dominant product during degradation. Among engineering plastics used at much higher service temperatures, PEEK and PTFE plastics and their composites are important. The paper [14] points out the possibilities of using and modifying PEEK plastic but considering the material's thermal stability. According to the author, PEEK derivatives have significant commercial applications as plastics, especially molded products, and as composites with glass, carbon, and Kevlar fibers with various structural applications, including but not limited to aerospace and engineering. In [15], the authors performed thermogravimetric analyses for three different modes of non-isothermal heating in an inert atmosphere and observed the reactions for carbon-PEEK at 500–700°C and for carbon-phenol, whose pyrolysis begins at around 200°C. The activation energy was determined using the integral (Starink) and differential (Friedman) isoconversion methods as a function of the degree of conversion responsible for the identified reaction compartments. For carbon- polyether ether ketone under inert conditions for Starink, the average value was estimated at 207.71 kJ/mol, while for Friedman, it was 213.88 kJ/mol. The difficulty of estimating the activation energy of polymeric materials favors using different methods, allowing the identification of a range of activation energies for materials for which no data exists in the literature. The so-called compensation effect method was used to evaluate the decomposition model and the one-step approach proposed by Friedman. An evaluation of possible decomposition was obtained for carbon- polyether ether ketone under inert conditions. Investigations during combustion and thermogravimetric analysis for PEEK are presented in the paper [16], indicating the products of combustion and the reactions taking place. Polyether ether ketone carbon-fiber filled (CA) and glass-fiber filled (GL) samples at 30% were used for the study. TG tests were conducted, and it was determined that the decomposition process of PEEK in an oxidizing environment took place in two separate stages. The first stage of decomposition is attributed to the randomness of the disruption of the ether and ketone bond chain, while the second stage is attributed to the oxidation and carbon charring resulting from the first stage of decomposition [17]. Based on the analysis of the phenomena taking place, the paper [18] proposed mechanisms that attempt to explain the products formed at each stage of PEEK decomposition and identify the intermediates that should be formed at each stage. The authors conducted studies of the thermal and fire properties of the high-temperature polymer material polyether ether ketone using advanced measurement methods [19]. The paper analyzed TG plots of PEEK at different oxygen concentrations, showing that the initial thermal decomposition stage does not depend much on the oxygen level. Several methods were used to understand the mechanism of thermal decomposition of PEEK, including pyrolysis - gas chromatography - mass spectrometry (Py-GC-MS), thermogravimetric analysis (TG) combined with Fourier transform infrared spectrometer.

It was observed that the initial stage of material decomposition could lead to the release of non-flammable gases and the formation of a material with a highly cross-linked carbon structure resembling graphite. During the calorimetric test, PEEK showed excellent char and fire resistance with a heat flux of 50 kW/m^2. Based on the identification of pyrolytic gases formed during PEEK decomposition, the enhanced fire resistance of PEEK was attributed to the dilution of combustible decomposition gases and the formation of a protective carbonized graphite-like structure during decomposition. The paper [20] addresses the study of energy recovery from PTFE polymer and thermal degradation. Thermal degradation of PTFE was carried out in a horizontal tubular reactor [20]. The effects of temperature and atmosphere on the reaction and the degradation products formed were studied. Various processes were carried out, including pyrolysis. The studies were conducted in the range of 750–1050°C. In pyrolysis cycles, C_2F_4 and C_3F_6 were found as perfluorocarbon compounds. Under oxidizing conditions, C_2F_4, C_3F_6 and CF_4 were found. In the paper [21], thermal characterization of PTFE material was carried out using thermal analysis methods and thermophysical property testing techniques, including differential scanning calorimetry to determine the transformation energy and specific heat. The comparison of different physical properties allowed analysis of thermal property changes during phase transitions. Studies related to the thermal processes of modified PTFE were conducted by the authors of the paper [22], analyzing the thermal pyrolysis process of mold-pressed Al/PTFE composites. XRD (X-ray diffraction) studied the composites' energy properties and the composition of the pyrolysis residue. The authors showed that the PTFE content of the composites determined the energy release from the material and the composition of their combustion residue. Analysis of the composition of the combustion residue indicated the formation of AlF_3, Al_2O_3, Al_4C_3, and amorphous carbon.

Analysis of the thermal processes of engineering polymers such as POM, high-temperature PEEK, and PTFE and their modification with fillers indicates the possibility of utilization and energy recovery of this type of material, taking into account the energy values of the fillers. It also shows the potential of thermal utilization of carbon in this material. In [23], the authors studied the combustion characteristics of various coal samples using differential scanning calorimetry (DSC) and thermos-gravimetry (TG-DTG) at different heating rates (5, 10 and 15°C/min). The thermographic and thermogravimetry (TG-DTG) curves indicated two main reaction areas at each heating rate tested. The reaction areas, maximum temperatures, mass loss, and heat of the reaction of the samples were determined. The kinetic parameters of the coal samples were also determined using various methods, and it was found that the activation energy values of the coal samples were in the range of 27.2–76.2 kJ/mol. The paper [24] pointed out the properties of polymer-carbon composites and the possibilities of applications, which also involve thermal processes and the utilization of such materials.

The purpose of this paper is to comparatively analyze selected waste plastics (POM, PTFE, PEEK) and bituminous coal in terms of the potential use of their wastes in thermal research, blending of waste plastics, and energy recovery from them. The authors compared the thermal testing results of polymer waste in mixtures with coal. TG/DTG/DSC/EGA thermal analysis methods made it possible to identify the energy properties of the studied engineering polymers, including high-temperature ones, both in the environmental aspect of waste utilization and in combination with coal blends. Thermal analysis of the base materials (polymer waste, carbon) will allow future clarification of the behavior of the materials, also in the form of composites under high-temperature conditions. Base materials differ in composition and calorific value, which significantly impacts waste plastics' process, conditions, and possibilities for energy recovery.

Finally, since predicting the thermal properties of fuels and fuels/plastic wastes, covering endothermic, with melting processes and maximum exothermic mechanisms, is essential from a practical point of view when considering, e.g., smooth transport in feeding installations of energy objects, we developed a fuzzy logic based FuzzyTherm model to predict the thermal behavior of the considered waste fuels. The model used Fuzzy Logic methods, constituting one of the main artificial intelligence (AI) methods, besides artificial neural networks [25–28] and other modelling techniques [29–31].

2. Methodology

Technical and ultimate analysis of the fuels/wastes under consideration was carried out using apparatus of Częstochowa University of Technology, Poland: CHNS elemental analyzer of the FlashSmart series [32], LECO AC600 calorimeter [33], a laboratory dryer (determination of moisture content), according to Polish standard PN-80/G-04511, a muffle furnace (determination of ash content), according to Polish standard PN-80/G-04512, a muffle furnace (determination of volatiles content), according to Polish standard PN-81/G-04516.

Thermal analysis (TG/DSC) of the samples was performed using the STA 449 F3 Jupiter (Netzsch) coupled to the quadruple mass spectrometer QMS Aëolos [34]. The measurements were carried out on samples weighing 7 mg in platinum crucibles in an atmosphere of synthetic air and argon (flow 20 ml/min of each gas). Samples were heated from ambient temperature up to 700°C at a heating rate of 10°C/min.

An interesting element of the work was determining the changes in the shapes of samples of the tested polymers during heating using a Misura HSM (hot stage microscopy) high-temperature microscope [35]. For this purpose, cylinder-shaped test specimens (ϕ = 2 mm, h = 3 mm) were manually pressed and heated at 10°C/min. The thermal testing apparatus used in the study is located at the AGH University of Krakow, Faculty of Materials Science and Ceramic, Poland.

Since the temperature of endothermic reactions, expressing plastic-based waste melting processes T_{melt}, as well as the temperature of the maximum energy yield during the exothermic reactions in the fuels T_{max}, are the two critical characteristic effects recorded during thermal DSC tests, their accurate prediction is beneficial when choosing the proper operating parameters of the auxiliary equipment of industrial boiler, including, e.g., feed and fuel belt conveyors and fuel hoppers. A FuzzyTherm system, based on the fuzzy logic (FL) methods, is developed in this paper, allowing us to determine both T_{melt} and T_{max} for coal and plastic wastes.

The fuzzy logic-based modelling approach belongs to the so-called soft-computing methods introduced by Lofti Zadeh, which defined it as a precise logic of imprecision and approximate reasoning This approach allows the development of knowledge-based systems for solving complex problems. The method uses fuzzy sets and linguistic variables to deal with imprecise, vague, and uncertain information and employs qualitative judgment to parameters quantitative in nature to describe the behavior of processes or objects. An essential feature of the method is that it allows an empirical problem to be formalized using experience rather than the process's strict knowledge. Therefore, due to complex mechanisms corresponding to the studied processes, applying a fuzzy logic-based approach is justified because it allows the building of a model in cases where the experience of an expert is more easily accessible than a strict knowledge of the system's behavior. Owing to the intricate mechanisms inherent in the investigated processes, the employment of methods grounded in fuzzy logic is warranted by the capacity of these methods to facilitate the construction of a model in scenarios where expert experiential knowledge is more readily available than a precise understanding of the system's dynamics [36,37]. Bituminous coal as a parent fuel and PTFE, PEEK, and POM as plastic wastes are considered in the study. Moreover, the mixtures of coal and plastic wastes as additives with a mass fraction of each additive equal to 20% are included in the developed model.

Table 1. Proximate and ultimate analyses of the considered fuels.

Fuel/waste	Nitrogen content N^a	Carbon content C^a	Hydrogen content H^a	Sulfur content S^a	Moisture content M^a	Ash content A^a	Volatile matter content V^a	FC^{calc}	FR^{calc}	LHV
	[%]	[%]	[%]	[%]	[%]	[%]	[%]	[%]	[–]	[%]
PTFE	0.34	27.01	0.00	0.00	0.06	0.00	97.68	2.26	0.02	4272
PEEK	0.13	72.47	4.64	0.00	0.32	0.00	49.82	49.86	1.00	24402
POM	0.18	42.60	6.90	0.11	0.23	0.00	99.36	0.41	0.01	12960
Bituminous coal	0.85	59.00	4.12	0.92	5.67	17.23	27.74	49.36	1.78	18245

FC = 100-($M^a + V^a + A^a$), FR = FC/V^a, (a – analytical state), calc – calculated.

3. Results

Table 1 shows the results of the proximate and ultimate analysis of the considered wastes of plastics and hard coal. In the case of plastics, it should be noted that they contain a high content of volatile parts, practically zero sulfur and ash, and varying nitrogen, carbon, and calorific values. A high proportion of nitrogen,carbon, sulfur, ash, and high calorific value characterizes hard coal.

The melting temperature of the polymer (329ºC – PTFE, 279ºC – PEEK, 162ºC – POM) plays a crucial role in the subsequent stages of the thermal process. This information, detailed in Table 2, provides valuable insights for practical applications.

Table 2. The shape of the sample (HSM microscope) at the melting temperature determined by thermal analysis.

Polymer/ melting tempera-ture	PTFE (329°C)	PEEK (279°C)	POM (162°C)
			

Figure 1 shows the methodology for recording the maximum DSC and DTG peaks, corresponding to the maximum heat release and the maximum fuel mass loss rate, during the considered thermal process for a hard coal sample. The figure shows the coincidence of the temperatures of the mentioned peaks.

Figures 2–7 illustrate sample TG/DTG/DSC/EGA thermal test results of the fuels/wastes considered, along with the analysis (the type of gas emitted was determined according to the *m*/*z* value [38].

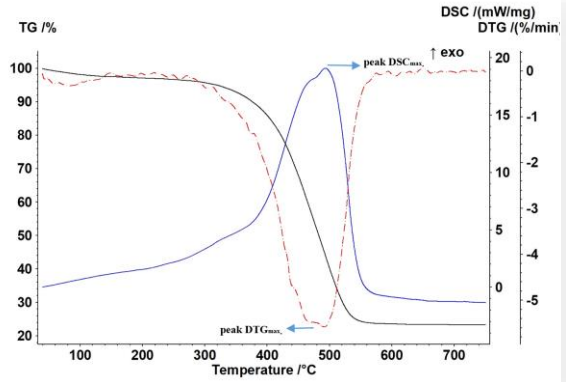


Fig. 1. TG/DTG and DSC profiles for bituminous coal.

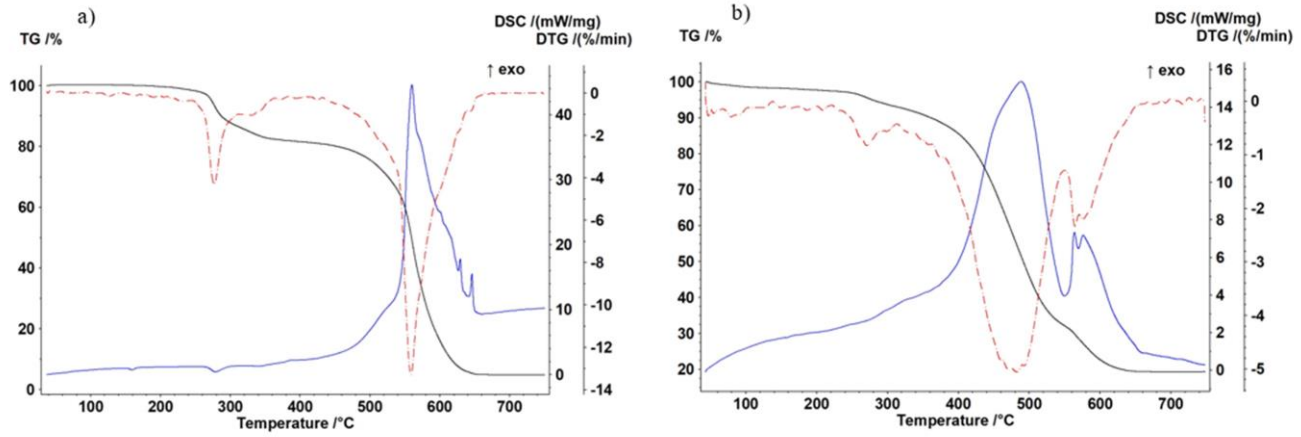


Fig. 2. TG/DTG and DSC profiles of samples: a) PEEK, b) bituminous coal 80%/PEEK 20%.

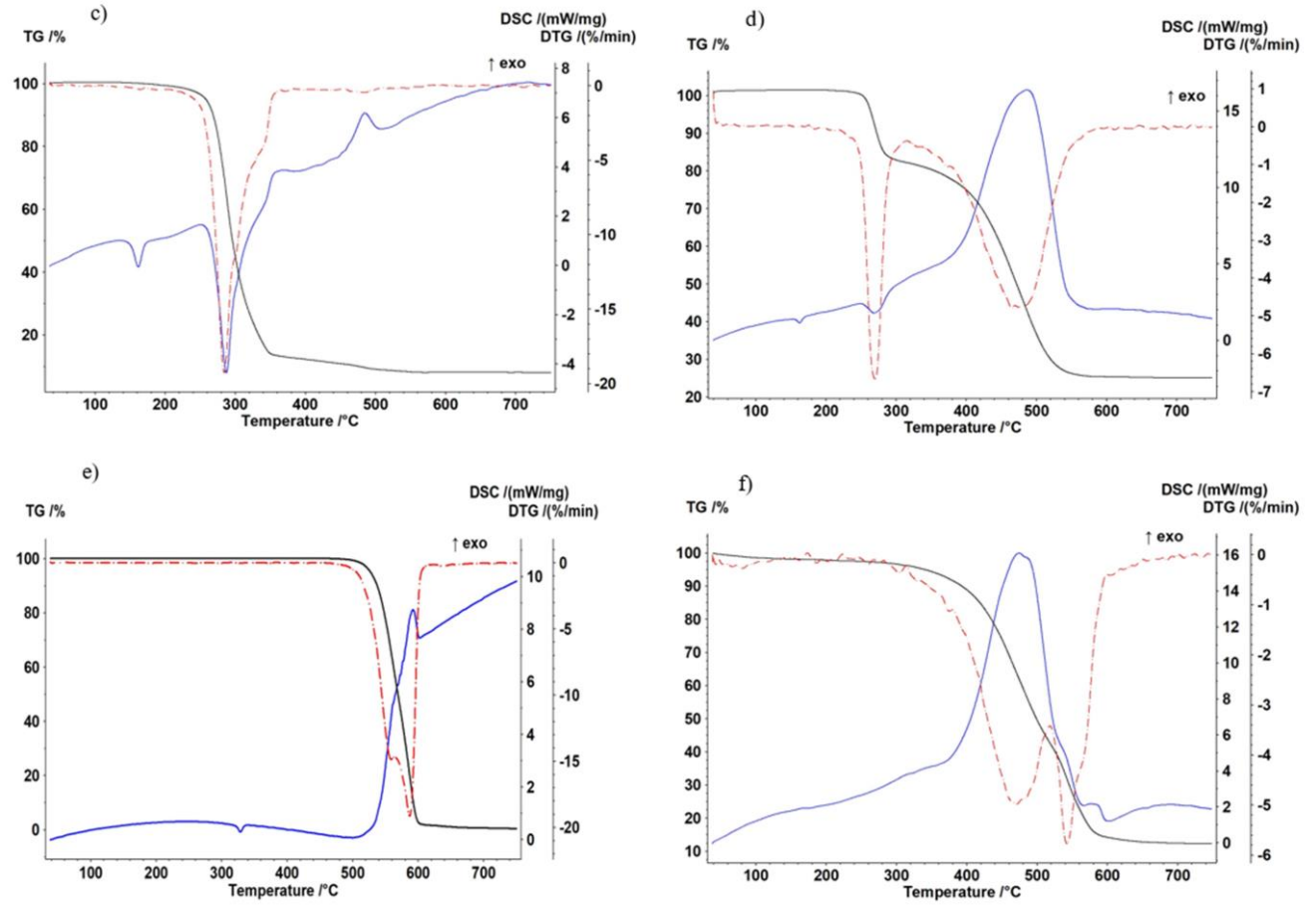


Fig. 2. TG/DTG and DSC profiles of samples: c) POM, d), bituminous coal 80%/POM 20%, e) PTFE f) bituminous coal 80%/PTFE 20%.

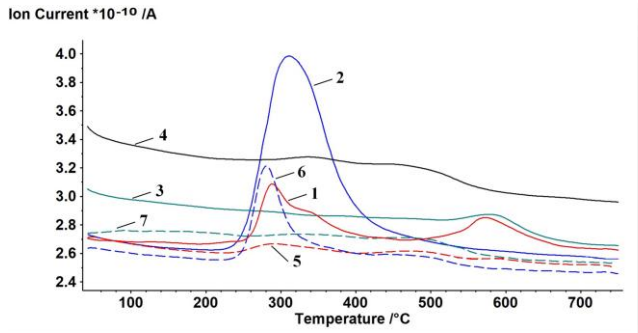


Fig. 3. Results of profiles of evolved gases of m/z = 2 (H_2) samples: 1 – PEEK, 2 – POM, 3 – PTFE, 4 – bituminous coal, 5 – bituminous coal 80%/PEEK 20%, 6 – bituminous coal 80%/POM 20%, 7 – bituminous coal.

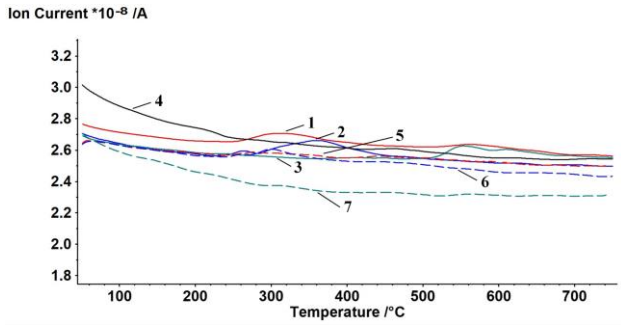


Fig. 4. Results of profiles of evolved gases of m/z = 28 (CO) samples: 1 – PEEK, 2 – POM, 3 – PTFE, 4 – bituminous coal, 5 – bituminous coal 80%/PEEK 20%, 6 – bituminous coal 80%/POM 20%, 7 – bituminous coal 80%/PTFE 20%.

In the EGA method, recording ionic currents I, as a function of temperature, allows qualitative determination of gases emitted during thermal processes. The composition of fuels/wastes significantly affects their behavior during thermal processes and the emission of gases into the atmosphere. The values of FC and FR, and the elemental content of carbon and volatile matter in the fuel, as well as nitrogen, hydrogen, and sulfur, are reflected in the values m/z = 44, m/z = 28, m/z = 46, m/z = 2 and m/z = 64, respectively, which correspond to the emissions of carbon dioxide, carbon monoxide, nitrogen oxides, hydrogen, and sulfur dioxide. The addition of plastic waste to hard coal adequately changes the value of the I_{total} ionic current for these compounds (lowering emissions of CO_2, NO_x, SO_2, and H_2 except for POM, which has a high hydrogen content among plastic waste, and an increase in CO), relative to coal alone (Table 3).

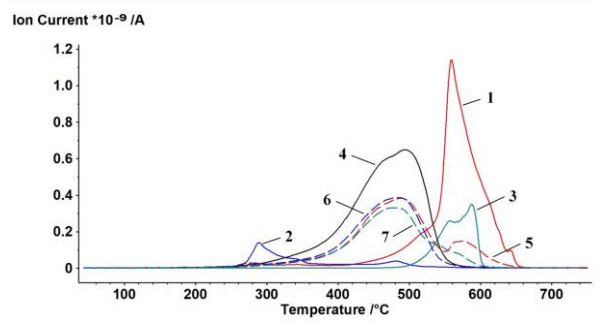


Fig. 5. Results of profiles of evolved gases of m/z = 44 (CO_2) samples: 1 – PEEK, 2 – POM, 3 – PTFE, 4 – bituminous coal, 5 – bituminous coal 80%/PEEK 20%, 6 – bituminous coal 80%/POM 20%, 7 – bituminous coal 80%/PTFE 20%.

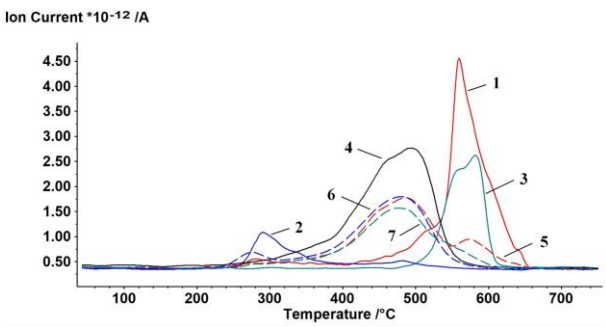


Fig. 6. Results of profiles of evolved gases of m/z = 46 (NOx) samples: 1 – PEEK, 2 – POM, 3 – PTFE, 4 – bituminous coal, 5 – bituminous coal 80%/PEEK 20%, 6 – bituminous coal 80%/POM 20%, 7 – bituminous coal 80%/PTFE 20%.

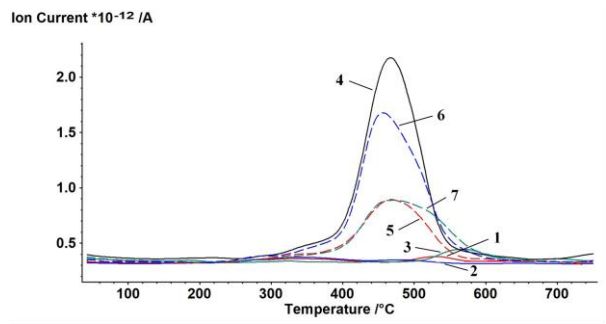


Fig. 7. Results of profiles of evolved gases of m/z = 64 (SO_2) samples: 1 – PEEK, 2 – POM, 3 – PTFE, 4 – bituminous coal, 5 – bituminous coal 80%/PEEK 20%, 6 – bituminous coal 80%/POM 20%, 7 – bituminous coal 80%/PTFE 20%.

Predicting the thermal properties of fuels and fuels/plastic wastes, covering endothermic, with melting processes and maximum exothermic peaks, which are essential from a practical point of view when considering, e.g., smooth transport in feeding installations of energy objects. Therefore, for this paper, we developed a FuzzyTherm model based on fuzzy-logic methods, allowing to predict:

- T_{melt} for PTFE, PEEK, POM, and mixtures of coal with plastic wastes
- T_{max} for bituminous coal, PTFE, PEEK, POM, and mixtures of coal with plastic wastes,

and T_{melt} and T_{max} are the model outputs.

The input section of the FuzzyTherm model has two inputs, i.e.:

- Coal/PlasticWaste/Mixture, as the type of material, including bituminous coal, plastic waste, or their mixture,
- D32 as the particles Sauter mean diameter of the considered materials.

The inputs and outputs are described in Table 4.

The fuzzifier, i.e., the first of the main blocks in the data processing procedure of a typical fuzzy model, maps crisp inputs to fuzzy functions and employs triangular fuzzy sets, assigning each crisp value of an input to a membership value μ of a fuzzy set [39] (see Fig. 8). The selection of triangular fuzzy sets results from simplifying the model, as they belong to the essential fuzzy functions [40].

A knowledge base of the IF-THEN fuzzy rule base allows the transfer of expert knowledge into the developed FuzzyTherm system [41]. The fuzzy rule base for the model is given in Table 5.

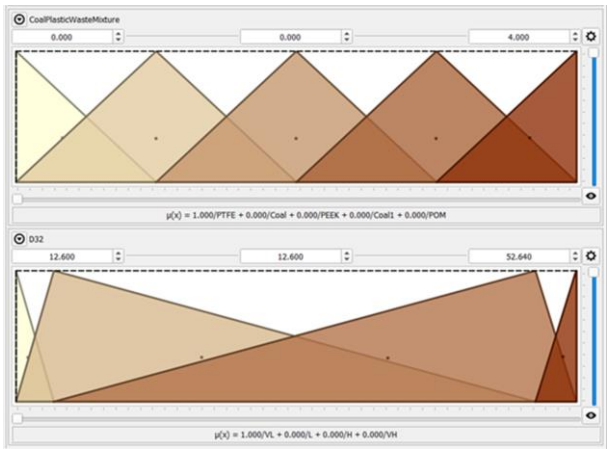


Fig. 8. Inputs of the FuzzyTherm system.

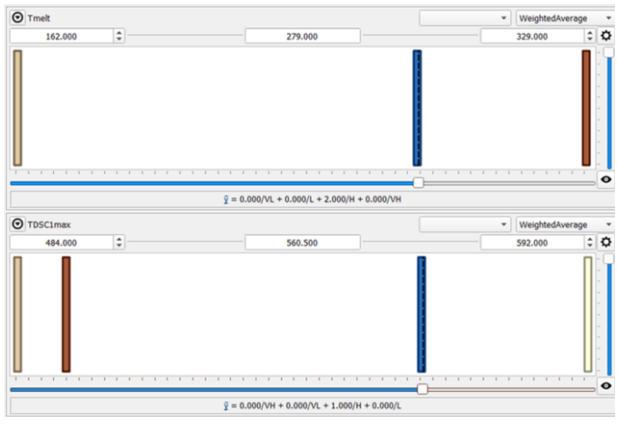


Fig. 9. Outputs of the FuzzyTherm system.

Table 3. Analysis of experimental research results.

Fuel	Characteristic peak DSC	Characteristic peak DTG	Max change in fuel weight	Ionic current I for given m/z (temperature of the characteristic peak of I_{peak}, the total emission of a given gas I_{total}, I_{total} – area under curve of I)	
PTFE	0.29 mW/mg (329°C) endothermic peak – melting 8.74 mW/mg (592°C) maximum exothermic peak	19.13%/min	97.19% (400–600°C)	$I_{max.\ peak\ m/z=2}$ t=587°C $I_{max.\ peak\ m/z=28}$ t=550°C $I_{peak\ m/z=28}$ t=607°C $I_{max.\ peak\ m/z=44}$ t=587°C $I_{max\ peak\ m/z=46}$ t=585°C $I_{peak\ m/z=64}$ t=567°C	$I_{total\ m/z=2}$ = 4.49 10^{-9}A·s $I_{total\ m/z=28}$ = 133.91 10^{-9}A·s $I_{total\ m/z=28}$ = 50.33 10^{-9}A·s $I_{total\ m/z=44}$ = 109.63 10^{-9}A·s $I_{total\ m/z=46}$ =0.77 10^{-9}A·s $I_{total\ m/z=64}$=0.07 10^{-9}A·s
PEEK	.49 mW/mg (279°C) endothermic peak – melting 20.25 mW/mg (561°C) maximum exothermic peak	13.30%/min	65.27% (400–600°C)	$I_{max.\ peak\ m/z=2}$ t=287°C $I_{peak\ m/z=2}$ t=572°C $I_{max.\ peak\ m/z=28}$ t=283°C $I_{peak\ m/z=28}$ t=558°C $I_{max.\ peak\ m/z=44}$ t=557°C $I_{max\ peak\ m/z=46}$ t=559°C $I_{peak\ m/z=46}$ t=282°C $I_{max.\ peak\ m/z=64}$ t=524°C $I_{peak\ m/z=64}$ t=325°C $I_{peak\ m/z=64}$ t=795°C	$I_{total\ m/z=2}$ = 16.03·10^{-9}A·s $I_{total\ m/z=2}$ = 7.80·10^{-9}A·s $I_{total\ m/z=28}$ = 302.28·10^{-9}A·s $I_{total\ m/z=28}$ = 149.15·10^{-9}A·s $I_{total\ m/z=44}$ = 368.69·10^{-9}A·s $I_{total\ m/z=46}$ = 1.33·10^{-9}A·s $I_{total\ m/z=46}$ = 0.03·10^{-9}A·s $I_{total\ m/z=64}$ = 0.01·10^{-9}A·s $I_{total\ m/z=64}$ = 0.01·10^{-9}A·s $I_{total\ m/z=64}$ = 0.01·10^{-9}A·s
POM	0.85 mW/mg (162°C) endothermic peak – melting 5.52 mW/mg (284°C) maximum endothermic peak 2.78 mW/mg (484°C) maximum exothermic peak	19.24%/min.	87.20% (200–400 C)	$I_{max.\ peak\ m/z=2}$ t=307°C $I_{max.\ peak\ m/z=28}$ t=360°C $I_{peak\ m/z=28}$ t=264°C $I_{max.\ peak\ m/z=44}$ t= 288°C $I_{peak\ m/z=44}$ t=481°C $I_{max\ peak\ m/z=46}$ t=291°C $I_{peak\ m/z=46}$ t=482°C $I_{peak\ m/z=46}$ t=668°C $I_{max.\ peak\ m/z=64}$ t=343°C $I_{peak\ m/z=64}$ t=479°C	$I_{total\ m/z=2}$ = 76.65·10^{-9}A·s $I_{total\ m/z=28}$ = 48.94·10^{-9}A·s $I_{total\ m/z=28}$ = 471.97·10^{-9}A·s $I_{total\ m/z=44}$ = 34.19·10^{-9}A·s $I_{total\ m/z=44}$ = 4.41·10^{-9}A·s $I_{total\ m/z=46}$ = 0.22·10^{-9}A·s $I_{total\ m/z=46}$ = 0.02·10^{-9}A·s $I_{total\ m/z=46}$ = 0.006·10^{-9}A·s $I_{total\ m/z=64}$ = 0.02·10^{-9}A·s $I_{total\ m/z=64}$ = 0.008·10^{-9}A·s
Bituminous coal	19.08 mW/mg (493°C) maximum exothermic peak	5.58%/min	62.35% (400–600°C)	$I_{max.\ peak\ m/z=2}$ t= 336°C $I_{peak\ m/z=2}$ t=460°C $I_{max.\ peak\ m/z=28}$ t= 466°C $I_{max.\ peak\ m/z=44}$ t=493°C $I_{max\ peak\ m/z=46}$ t=493°C $I_{peak\ m/z=46}$ t=468°C $I_{max.\ peak\ m/z=64}$ t=468°C	$I_{total\ m/z=2}$ = 1.72·10^{-9}A·s $I_{total\ m/z=2}$ = 1.61·10^{-9}A·s $I_{total\ m/z=28}$ = 20.02·10^{-9}A·s $I_{total\ m/z=44}$ = 470.55·10^{-9}A·s $I_{total\ m/z=46}$ = 1.85·10^{-9}A·s $I_{total\ m/z=46}$ = 1.85·10^{-9}A·s $I_{total\ m/z=64}$ = 0.99·10^{-9}A·s
Bituminous coal 80%/ PTFE 20%	3.92 mW/mg (311°C) endothermic peak – melting 16.08 mW/mg (475°C) maximum exothermic peak	4.88%/min	74.39% (400–600°C)	$I_{max.\ peak\ m/z=2}$ t=329°C $I_{peak\ m/z=2}$ t=465°C $I_{max.\ peak\ m/z=28}$ t=435°C $I_{peak\ m/z=28}$ t=567°C $I_{max.\ peak\ m/z=44}$ t=478°C $I_{max\ peak\ m/z=46}$ t=47°C $I_{max.\ peak\ m/z=64}$ t=470°C	$I_{total\ m/z=2}$ = 0.67·10^{-9}A·s $I_{total\ m/z=2}$ = 0.27·10^{-9}A·s $I_{total\ m/z=28}$ = 25.81·10^{-9}A·s $I_{total\ m/z=28}$ = 15.20·10^{-9}A·s $I_{total\ m/z=44}$ = 228.44·10^{-9}A·s $I_{total\ m/z=46}$ = 0.82·10^{-9}A·s $I_{total\ m/z=64}$ = 0.41·10^{-9}A·s
Bituminous coal 80%/ PEEK 20%	3.09 mW/mg (294°C) endothermic peak – melting 15.1 mW/mg (485°C) maximum exothermic peak	2.70%/min.	63.18% (400–600°C)	$I_{max.\ peak\ m/z=2}$ t=288°C $I_{peak\ m/z=2}$ t=472°C $I_{peak\ m/z=2}$ t=588°C $I_{max.\ peak\ m/z=28}$ t=297°C $I_{max.\ peak\ m/z=44}$ t=487°C $I_{max.\ peak\ m/z=44}$ t=575°C $I_{max\ peak\ m/z=46}$ t= 85°C $I_{peak\ m/z=46}$ t=572°C $I_{max.\ peak\ m/z=64}$ t=467°C	$I_{total\ m/z=2}$ = 3.01·10^{-9}A·s $I_{total\ m/z=2}$ = 1.58·10^{-9}A·s $I_{total\ m/z=2}$ = 0.25·10^{-9}A·s $I_{total\ m/z=28}$ = 32.50·10^{-9}A·s $I_{total\ m/z=44}$ = 168.11·10^{-9}A·s $I_{total\ m/z=44}$ = 9.92·10^{-9}A·s $I_{total\ m/z=46}$ = 0.54·10^{-9}A·s $I_{total\ m/z=46}$ = 0.02·10^{-9}A·s $I_{total\ m/z=64}$ = 0.30·10^{-9}A·s
Bituminous coal 80%/ POM 20%	1.97 mW/mg (268°C) endothermic peak – melting 16.23 mW/mg (484°C) maximum exothermic peak	4.78%/min	49.71% (400–600°C)	$I_{max.\ peak\ m/z=2}$ t=281°C $I_{max.\ peak\ m/z=28}$ t=301°C $I_{max.\ peak\ m/z=44}$ t=485°C $I_{peak\ m/z=44}$ t=275°C $I_{max\ peak\ m/z=46}$ t=486°C $I_{peak\ m/z=46}$ t=274°C $I_{max.\ peak\ m/z=64}$ t=456°C $I_{peak\ m/z=64}$ t=892°C	$I_{total\ m/z=2}$ = 17.54·10^{-9}A·s $I_{total\ m/z=28}$ = 195.49·10^{-9}A·s $I_{total\ m/z=44}$ = 231.09·10^{-9}A·s $I_{total\ m/z=44}$ = 1.85·10^{-9}A·s $I_{total\ m/z=46}$ = 0.91·10^{-9}A·s $I_{total\ m/z=46}$ = 0.05·10^{-9}A·s $I_{total\ m/z=64}$ = 0.78·10^{-9}A·s $I_{total\ m/z=64}$ = 0.05·10^{-9}A·s

Table 4. Parameters of the FuzzyTherm of the model.

Parameter	Values
Inputs	
Coal/PlasticWaste/Mixture, - D32, µm	PTFE, PEEK, POM, Coal 15.3, 52.6
Outputs	
T_{melt}, °C	162–329
Tmax, °C	484–592

Table 5. The knowledge base of the FuzzyTherm model.

ID	Fuzzy rule
1.	If Coal/PlasticWaste/Mixture is PTFE then T_{melt} is VH*
2.	If Coal/PlasticWaste/Mixture is PEEK then T_{melt} is H
3.	If Coal/PlasticWaste/Mixture is POM then T_{melt} is L
4.	If D32 is VH then T_{melt} is L
5.	If D32 is H then T_{melt} is VH
6.	If D32 is VL then T_{melt} is H
7.	If Coal/PlasticWaste/Mixture is PTFE then T_{max} is VH
8.	If Coal/PlasticWaste/Mixture is PEEK then T_{max} is H
9.	If Coal/PlasticWaste/Mixture is POM then T_{max} is VL
10.	If Coal/PlasticWaste/Mixture is Coal then T_{max} is L
11.	If D32 is H then T_{max} is VH
12.	If D32 is H then T_{max} is VH

H – high, L – low, VH – very high.

During the inference step, the fuzzy output is generated. Due to its flexibility, the developed FuzzyTherm model uses the Takagi-Sugeno engine (TSK or Takagi, Sugeno, and Kang model) [42,43]. According to the TSK approach, outputs are polynomial functions of the inputs. In the case considered in this paper, we employed constant functions to define outputs, as shown in Fig. 9.

Finally, the weighted average inference method was applied to determine a crisp value of each output o, generated by the FuzzyThem model, according to the following formula [44,45]:

$$o = \frac{\sum \mu(\bar{o}) \cdot \bar{o}}{\sum \mu(\bar{o})}, \quad (3)$$

where o is the crisp, real output value after defuzzification, μ is the membership value (between 0 and 1), and $\bar{o}$ is the centroid of each membership function. Such a performed FuzzyTerm knowledge-based system allows the simulation of the thermal DSC processes and predicts temperatures T_{melt} and T_{max}, i.e., temperatures corresponding to the endothermic (melting) maximum temperature of exothermic reactions.

The model was built upon data corresponding to pure materials, i.e., coal, PTFE, PEEK, and POM. Its validation was carried out based on coal and plastic waste mixture data. Figure 10 compares trained and validation data calculated and obtained from the experiment.

The FuzzyTherm model achieves good accuracy, close to 99%, for trained data (Fig. 10a). The model's accuracy for the validation data corresponding to mixtures is worse but still acceptable. The maximum relative error between calculated and

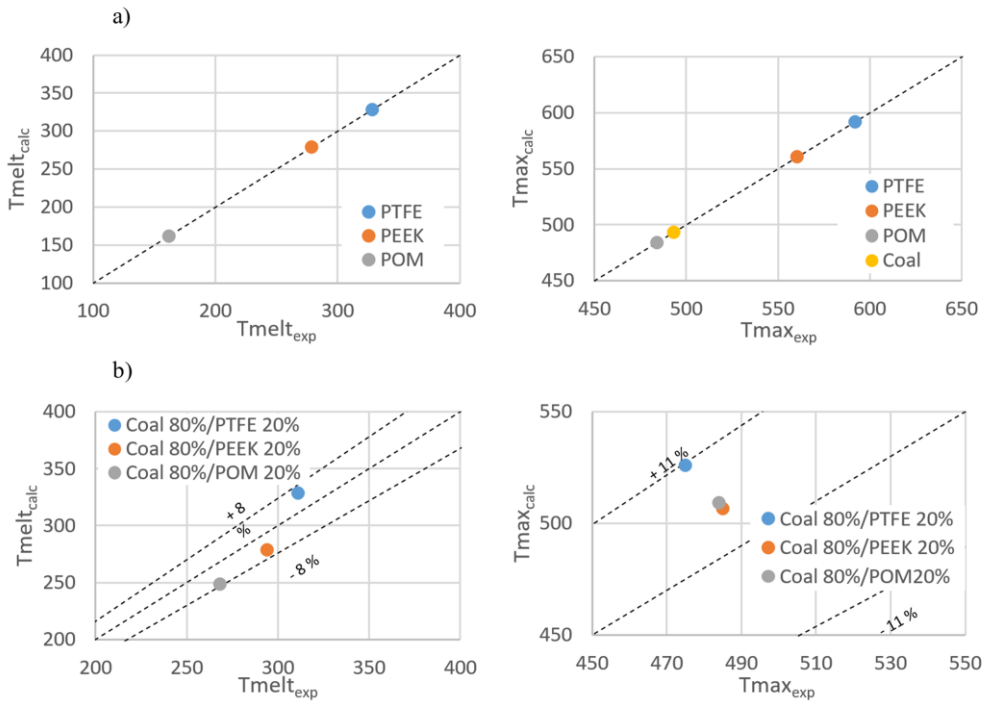


Fig. 10. The comparison of trained a) and validation data b) calculated and obtained from DSC the experiments.

measured data was lower than 11% (Fig. 10b). Based on the reported metrics, the developed FuzzyTherm model can predict Tmelt and Tmax. The presented approach can also be applied to predicting other peaks in TG/DTG/DSC or MS profiles of the evolved gases, which will be the objective of the subsequent papers.

The initial analysis of waste behavior, as outlined in the presented results, marks a significant step in understanding the dynamics of waste management. For a more comprehensive understanding, future studies should delve into the valuation of polymer waste. This should focus on pioneering methods for either repurposing or recycling polymer materials. The emergence of new technologies in managing polymer waste is expected to have far-reaching implications, particularly in sectors such as biofuel production. These advancements are pivotal in enhancing the efficiency and sustainability of waste-to-energy conversion processes [46].

The broader context of energy strategies integrated within the circular economy principles warrants further discussion. This comprehensive framework encompasses energy efficiency and sustainability and emphasizes resource reutilization and recycling to create a more sustainable and resilient energy ecosystem [47,48].

It is imperative to underscore the importance of environmental considerations in waste management and energy engineering. This emphasis is due to the intricate interplay between ecological impacts and economic factors. Furthermore, the profitability of sustainable technologies should not be overlooked. From an investor's perspective, comprehending the motivations behind and trends in funding sustainable technologies is essential. The financial viability of these technologies is a crucial determinant of their long-term sustainability and success [49,50].

The industrial perspective and advanced technologies in modern manufacturing are crucial, especially process optimization and automation in decision-making [51–53]. It is also essential to acknowledge that energy self-sufficiency frequently plays a significant role in national sovereignty. This aspect underscores the strategic importance of a country's ability to independently meet its energy needs, thereby enhancing its autonomy and security on the global stage [54,55].

5. Conclusions

The authors have drawn several key conclusions:

1. The calorific value and composition of the materials directly influence the peak heat generation and emissions of pollutants.
2. Compared to coal, plastic waste has a high content of volatile parts and a negligible share of sulfur.
3. Polyether ether ketone has the highest energy potential of the polymers due to its highest calorific value.
4. The temperatures of maximum gas emissions (I_{peak}) and accompanying thermal processes coincide with DSC and DTG peaks for a given fuel/waste.
5. The developed model, based on fuzzy logic, can predict the maximum heat output from the tested waste materials during the specified thermal processes.
6. Given the environmental considerations, particularly concerning pollutant emissions, the results serve as a foundational benchmark for further refinement of the fuzzy logic-based model beyond just thermal process analysis.

In the context of the discussed study, the authors established two primary research hypotheses: The calorific value and composition of materials are directly correlated with the peak values of heat generation and pollutant emissions.

The model developed utilizing fuzzy logic can predict the maximum heat release from the studied waste materials during the thermal processes under analysis.

The findings shown in the article represent the initial research stages. They offer a comparative analysis of the combustion process of various waste types, employing thermal analysis techniques. The authors plan to extend this research to include co-incineration and energy recovery from these wastes. The exploration into thermal analysis of waste materials as potential fuel sources marks a significant step towards implementing net-zero emission strategies, adhering to sustainable development policies, and enhancing energy efficiency.

Acknowledgements

The paper was carried out under BS/PB-1-100-301/2024/P (Czestochowa University of Technology, Faculty of Mechanical Engineering and Computer Science).

Thermal studies were performed within the framework of funding for statutory activities of AGH University of Krakow, Faculty of Materials Science and Ceramics (16.16.160.557).

The paper was also prepared under SBR/WNSPT/ZZMO/24/2023 (Jan Dlugosz University in Czestochowa).

References

[1] Ongar, B., Beloev, H., Georgiev, A., Iliev, I., & Kijo-Kleczkowska, A. (2023). Optimization of the design and operating characteristics of a boiler based on three-dimensional mathematical modeling. *Bulgarian Chemical Communications,* 55(2), 153–159. doi: 10.34049/bcc.55.2.AESMT22-54

[2] Kijo-Kleczkowska, A., Bruś, P., & Więciorkowski, G. (2022). Profitability analysis of a photovoltaic installation – A case study. *Energy,* 261, 125310. doi: 10.1016/j.energy.2022.125310

[3] Kijo-Kleczkowska, A. (2011). Analysis of cyclic combustion of the coal-water suspension. *Archives of Thermodynamics,* 32(1), 45–75. doi: 10.2478/v10173-011-0003-7

[4] Kijo-Kleczkowska, A. (2010). Research on destruction mechanism of drops and evolution of coal-water suspension in combustion process. *Archives of Mining Sciences,* 55(4), 923–946.

[5] Żukowski, W., Jankowski, D., Wrona, J., & Berkowicz-Płatek, G. (2023). Combustion behavior and pollutant emission characteristics of polymers and biomass in a bubbling fluidized bed reactor. *Energy,* 253, 125953. doi: 10.1016/j.energy.2022.125953

[6] Kijo-Kleczkowska, A., & Gnatowski, A. (2022). Recycling of plastic waste, with particular emphasis on thermal methods—review. *Energies,* 15(6), 15062114. doi:10.3390/en15062114

[7] Shaklein, A.A. (2021). Numerical study of polyoxymethylene burning in a combustion reactor. *Case Studies in Thermal Engineering,* 26, 101114. doi: 10.1016/j.csite.2021.101114

[8] Glaznev, R.K., Karpov, A.I., Korobeinichev, O.P., Bolkisev, A.A., Shaklein, A.A., Shmakov, A.G., & Kumar, A. (2019). Experimental and numerical study of polyoxymethylene (Aldrich)

combustion in counterflow. *Combustion and Flame*, 205, 358–367. doi: 10.1016/j.combustflame.2019.04.032

[9] Luftl, S., Archodoulaki, V.M., & Seidler, S. (2006). Thermal-oxidative induced degradation behaviour of polyoxymethylene (POM) copolymer detected by TGA/MS. *Polymer Degradation and Stability*, 91(3), 464–471. doi: 10.1016/j.polymdegradstab.2005.04.029

[10] Berkowicz, G., Majka, T. M., & Żukowski, W. (2020). The pyrolysis and combustion of polyoxymethylene in a fluidised bed with the possibility of incorporating CO_2. *Energy Conversion and Management*, 214, 112888. doi: 10.1016/j.enconman.2020.112888

[11] Archodoulaki, V.-M., Luftl, S., & Seidler, S. (2004). Thermal degradation behaviour of poly(oxymethylene): 1. Degradation and stabilizer consumption. *Polymer Degradation and Stability*, 86(1), 75–83. doi: 10.1016/j.polymdegradstab.2004.03.011

[12] Archodoulaki, V.-M., Luftl, S., Koch, T., & Seidler, S. (2007). Property changes in polyoxymethylene (POM) resulting from processing, ageing and recycling. *Polymer Degradation and Stability*, 92(12), 2181–2189. doi: 10.1016/j.polymdegradstab.2007.02.024

[13] Duan, Y., Li, H., Ye, L., & Xiaolong Liu. (2006). Study on the thermal degradation of polyoxymethylene by thermogravimetry–Fourier transform infrared spectroscopy (TG-FTIR). *Journal of Applied Polymer Science*, 99(6), 3085–3092. doi: 10.1002/app.22913

[14] Fink, J. K. (2014). *High Performance Polymers Plastics Design Library* (pp. 153–175). William Andrew Publishing.

[15] Tadini, P., Grange, N., Chetehouna, K., Gascoin, N., Senave, S., & Reynaud, I. (2017). Thermal degradation analysis of innovative PEKK-based carbon composites for high-temperature aeronautical components. *Aerospace Science and Technology*, 65, 106–116. doi: 10.1016/j.ast.2017.02.011

[16] Patel, P. (2011). *Investigation of the Fire Behaviour of PEEK-based Polymers and Compounds*. University of Central Lancashire.

[17] Tsai, C.J., Perng, L.H., & Ling, Y.C. (1997). A study of thermal degradation of poly(aryl-ether-ether-ketone) using step-wise pyrolysis/gas chromatography/mass spectrometry. *Rapid Communications in Mass Spectrometry*, 11(19), 1987–1995. doi: 10.1002/(SICI)1097-0231(19971030)11:19<1987::AID-RCM138>3.0.CO;2-Q

[18] Patel, P., Hull, R.T., McCabe, R.W., Flath, D., Grasmeder, J., & Percy, M. (2010). Mechanism of thermal decomposition of poly(ether ether ketone) (PEEK) from a review of decomposition studies. *Polymer Degradation and Stability*, 95(5), 709–718. doi: 10.1016/j.polymdegradstab.2010.01.024

[19] Ramgobin, A., Fontaine, G., & Bourbigot, S. (2020). A case study of polyether ether ketone (I): Investigating the thermal and fire behavior of a high-performance material. *Polymers*, 12(8), 1789. doi: 10.3390/polym12081789

[20] García, A.N., Viciano, N., & Font, R. (2007). Products obtained in the fuel-rich combustion of PTFE at high temperature. *Journal of Analytical and Applied Pyrolysis*, 80(1), 85–91. doi: 10.1016/j.jaap.2007.01.004

[21] Blumm, J., Lindemann, A., Meyer, M., & Strasser, C. (2010). Characterization of PTFE using advanced thermal analysis techniques. *International Journal of Thermophysics*, 31(10), 1919–1927. doi: 10.1007/s10765-008-0512-z

[22] Zhou, X., Xiao, F., Yang, R., Huang, F., & Li, J. (2020). Investigation of the ignition and combustion of compressed aluminum/polytetrafluoroethylene bulk composites. *Journal of Thermal Analysis and Calorimetry*, 139(6), 3013–3021. doi: 10.1007/s10973-019-08662-2

[23] Kok, M.V. (2012). Simultaneous thermogravimetry–calorimetry study on the combustion of coal samples: Effect of heating rate. *Energy Conversion and Management*, 53(1), 40–44. doi: 10.1016/j.enconman.2011.08.005

[24] Eterigho-Ikelegbe, O., Yoro, K.O., & Bada, S. (2021). Coal as a filler in polymer composites: A review. *Resources, Conservation and Recycling*, 174, 105756. doi: 10.1016/j.resconrec.2021.105756

[25] Amjad, A., Ashraf, W.M., Uddin, G.M., & Krzywanski, J. (2023). Artificial intelligence model of fuel blendings as a step toward the zero emissions optimization of a 660 MWe supercritical power plant performance. *Energy Science & Engineering*, 11(8), 2899–911. doi: 10.1002/ese3.1499

[26] Krzywanski, J., Blaszczuk, A., Czakiert, T., Rajczyk, R., & Nowak, W. (2014). Artificial intelligence treatment of NOX emissions from CFBC in air and oxy-fuel conditions. In *CFB-11: Proceedings of the 11th International Conference on Fluidized Bed Technology* (pp. 619–24).

[27] Krzywanski, J., Sztekler, K., Bugaj, M., Kalawa, W., Grabowska, K., Chaja, P.R., et al. (2021). Adsorption chiller in a combined heating and cooling system: Simulation and optimization by neural networks. *Bulletin of the Polish Academy of Sciences: Technical Sciences*, 69(3), 137054. doi: 10.24425/bpasts.2021.137054

[28] Stanek, W., & Rusinowski, H. (2008). Application of empirical modelling for construction of auxiliary models of steam boiler. *Archives of Thermodynamics*, 29(4), 165–176.

[29] Krzywanski, J., Czakiert, T., Muskala, W., Sekret, R., & Nowak, W. (2010). Modeling of solid fuel combustion in oxygen-enriched atmosphere in circulating fluidized bed boiler. Part 2. Numerical simulations of heat transfer and gaseous pollutant emissions associated with coal combustion in O_2/CO_2 and O_2/N_2 atmospheres enriched with oxygen under circulating fluidized bed conditions. *Fuel Processing Technology*, 91(3), 364–368. doi: 10.1016/j.fuproc.2009.11.008

[30] Krzywanski, J., Grabowska, K., Sosnowski, M., Zyłka, A., Sztekler, K., Kalawa, W., et al. (2018). Modeling of a re-heat two-stage adsorption chiller by AI approach. *MATEC Web of Conferences*, 240, 05014. doi: 10.1051/matecconf/ 201824005014

[31] Ashraf, W.M., Uddin, G.M., Kamal, A.H., Khan, M.H., Khan, A.A., Ahmad, H.A., Ahmed, F., Hafeez, N., Sami, R.M.Z., Arafat, S.M., Niazi, S.G., Rafique, M.W., Amjad, A., Hussain, J., Jamil, H., Kathia, M.S., & Krzywanski, J. (2020). Optimization of a 660 MW_e supercritical power plant performance – A case of industry 4.0 in the data-driven operational management, Part 2. power generation. *Energies*, 13(21), 5619, doi: 10.3390/en13215619

[32] ThermoFisher Scientific. (n.d.). Catalog number: 11206100. https://www.thermofisher.com/order/catalog/product/11206100 [accessed 17 Jan. 2023].

[33] Leco Empowering Results. (n.d.). https://pl.leco.com/product/ac600 [accessed 17 Jan. 2023].

[34] Netzsch Proven Excellence. (n.d.). https://analyzing-testing.netzsch.com/en/products/simultaneous-thermogravimetrydifferential-scanning-calorimetry-sta-tg-dsc/sta-449-f3-jupiter [accessed 17 Jan. 2023].

[35] Labcompare. (n.d.). https://www.labcompare.com/471-Dilatometer-Dilatometry-DIL/9818927-Heating-Microscope-Misura-3-HSM-HSML [accessed 17 Jan. 2023].

[36] Krzywanski, J., Wesolowska, M., Blaszczuk, A., Majchrzak, A., Komorowski, M., & Nowak, W. (2018). Fuzzy logic and bed-to-wall heat transfer in a large-scale CFBC. *International Journal of Numerical Methods for Heat & Fluid Flow*, 28(1), 254–266. doi: 10.1108/hff-09-2017-0357

[37] Kijo-Kleczkowska, A., Gnatowski, A., Krzywanski, J., Gajek, M., Szumera, M., Tora, B., Kogut K., & Knaś, K. (2024). Experimental research and prediction of heat generation during plastics, coal and biomass waste combustion using thermal analysis methods. *Energy*, 290, 130168, doi: 10.1016/j.energy.2023.130168

[38] NIST Chemistry WebBook. (2023). *NIST Standard Reference Database Number 69*. doi: 10.18434/T47C7Z

[39] Krzywanski, J. (2019). Heat transfer performance in a superheater of an industrial CFBC using fuzzy logic-based methods. *Entropy*, 21(10), 919. doi: 10.3390/e21100919

[40] Krzywanski, J., Czakiert, T., Zylka, A., Nowak, W., Sosnowski, M., Grabowska, K., et al. (2022). Modelling of SO2 and NOx Emissions from Coal and Biomass Combustion in Air-Firing, Oxyfuel, iG-CLC, and CLOU Conditions by Fuzzy Logic Approach. *Energies*, 15(21), 8095. doi: 10.3390/en15218095

[41] Krzywanski, J., Urbaniak, D., Otwinowski, H., Wylecial, T., & Sosnowski, M. (2020). Fluidized bed jet milling process optimized for mass and particle size with a fuzzy logic approach. *Materials, 13*(15), 3303. doi: 10.3390/ma13153303

[42] Takagi, T., & Sugeno, M. (1985). Fuzzy identification of systems and its applications to modeling and control. *IEEE Transactions on Systems, Man, and Cybernetics*, 15(1), 1399. doi: 10.1109/TSMC.1985.6313399

[43] Krzywanski, J., Czakiert, T., Nowak, W., Shimizu, T., Zylka, A., Idziak, K., Sosnowski, M., & Grabowska, K. (2022). Gaseous emissions from advanced CLC and oxyfuel fluidized bed combustion of coal and biomass in a complex geometry facility: A comprehensive model. *Energy*, 251, 123896. doi: 10.1016/j.energy.2022.123896

[44] Ross, T. J. (2004). *Fuzzy Logic with Engineering Applications*. John Wiley.

[45] Otwinowski, H., Krzywanski, J., Urbaniak, D., Wylecial, T., & Sosnowski, M. (2022). Comprehensive knowledge-driven ai system for air classification process. *Materials*, 15(1), 45. doi: 10.3390/ma15010045

[46] Maroušek, J. (2023). Aluminum nanoparticles from liquid packaging board improve the competitiveness of (bio)diesel. *Clean Technologies and Environmental Policy*, 25(7), 1059–1067. doi: 10.1007/s10098-022-02413-y

[47] Rabe, M., Drożdż, W., Widera, K., Łopatka, A., Leżyński, P., Streimikiene, D., & Bilan, Y. (2022). Assessment of energy storage for energy strategies development on a regional scale. *Acta Montanistica Slovaca*, 27(1), 163–177. doi: 10.46544/AMS.v27i1.12

[48] Razminienė, K., Vinogradova, I., & Tvaronavičienė M. (2021). Clusters in transition to circular economy: Evaluation of relation. *Acta Montanistica Slovaca*, 26(3), 455–465. doi: 10.46544/AMS.v26i3.06

[49] Pavolová, P., Bakalár, T., Kyšeľa, K., Klimek, M., Hajduová, Z., & Zawada, M. (2021). The analysis of investment into industries based on portfolio managers. *Acta Montanistica Slovaca*, 26(1), 161–170. doi: 10.46544/AMS.v26i1.14

[50] Akbari, M., Loganathan, N., Tavokolian, H., Mardani, A., & Streimikiene, D. (2021). The dynamic effect of micro-structural shocks on private investment behavior. *Acta Montanistica Slovaca*, 26(1), 1–17. doi: 10.46544/AMS.v26i1.01

[51] Zvarikova, K., Rowland, M., & Krulicky, T. (2021). Sustainable Industry 4.0 wireless networks, smart factory performance, and cognitive automation in cyber-physical system-based manufacturing. *Journal of Self-Governance and Management Economics*, 9(1), 9–21. doi: 10.22381/jsme9420211

[52] Kovacova, M., & Lăzăroiu, G. (2021). Sustainable organizational performance, cyber-physical production networks, and deep learning-assisted smart process planning in Industry 4.0-based manufacturing systems. *Economics, Management, and Financial Markets*, 16(4), 41–54. doi: 10.22381/emfm16320212

[53] Durana, P., Perkins, N., & Valaskova, K. (2021). Artificial intelligence data-driven internet of things systems, real-time advanced analytics, and cyber-physical production networks in sustainable smart manufacturing. *Economics, Management, and Financial Markets*, 16(1), 20–30. doi: 10.22381/emfm16120212

[54] Skare, M., Porada-Rochon´, M., & Blazevic-Buric, S. (2021). Energy cycles: Nature, turning points and role in England economic growth from 1700 to 2018. *Acta Montanistica Slovaca*, 26(2), 281–302. doi: 10.46544/AMS.v26i2.08

[55] Zheng, Z., Xu, Z., Skare, M., & Porada-Rochon, M. (2021). A comprehensive bibliometric analysis of the energy poverty literature: From 1942 to 2020. *Acta Montanistica Slovaca*, 26(3), 512–533. doi: 10.46544/AMS.v26i3.10

Co-published by
Institute of Fluid-Flow Machinery
Polish Academy of Sciences
Committee on Thermodynamics and Combustion
Polish Academy of Sciences

Copyright©2024 by the Authors under licence CC BY 4.0

http://www.imp.gda.pl/archives-of-thermodynamics/

Effectiveness analysis of a binary ORC power plant with zeotropic organic fluid

Sławomir Wiśniewski[a*], Michał Bańkowski[a]

[a]West Pomeranian University of Technology, Faculty of Mechanical Engineering and Mechatronics, 19 Piastów Avenue, Szczecin
*Corresponding author email: slawomir.wisniewski@zut.edu.pl

Received: 31.12.2023; revised: 04.04.2024; accepted: 06.05.2024

Abstract

A review of the available literature shows that analyses of organic Rankine cycle systems with a zeotropic mixture working medium practically concern single-circuit systems. In these works, it has been shown that the standing of zeotropic mixtures in organic Rankine cycle systems makes it possible to achieve higher power and efficiency compared to organic Rankine cycle systems with pure fluids. In this article, the authors present an analysis of the efficiency of a two-circuit organic Rankine cycle (binary) power plant with a zeotropic mixture in the upper cycle of this power plant. The proposed binary power plant system uses a zeotropic mixture circulating medium in the upper organic Rankine cycle circuit, while the lower circuit uses a homogeneous low-boiling medium. The results of this analysis showed that with properly selected parameters of the binary power plant system, i.e. with appropriate selection of the pressure during the evaporation transformation in the upper and lower circuits, the power obtained in it is higher than for a single-circuit power plant in the same temperature range (for the same heat source and the same condensing temperature). The increase in the power of the binary power plant system was achieved by using the heat contained in the water stream to preheat the medium in the bottom circuit. For example, for the binary organic Rankine cycle power plant with R413A refrigerant in the upper circuit, the generated power is 17.8 kWe, which is 20% higher than for a single-circuit power plant (for the reference power plant, the power is 14.8 kWe).

Keywords: C cycle; Binary power plant; Top cycle; Lower cycle; Zeotropic mixtures

Vol. 45(2024), No. 2, 129–138; doi: 10.24425/ather.2024.150859

Cite this manuscript as: Wiśniewski, S., & Bańkowski, M. (2024). Effectiveness operation analysis of a binary ORC power plant with zeotropic organic fluid. *Archives of Thermodynamics*, 45(2), 129−138.

1. Introduction

The drastic increase in energy prices due to the current geopolitical situation, the costs associated with CO_2 emission rights and the need to protect the environment give a strong impetus to activities directed at the search for new installations allowing electricity to be generated from sources other than fossil fuels. Fuel cells using hydrogen as fuel are an example of this type of installation. Examples of research on improving the efficiency of proton exchange membrane (PEM) type fuel cells can be found in the works [1,2]. During the operation of fuel cells, waste heat is generated, which can be used to power the organic Clausius-Rankine cycle. Power plants of this type allow the management of low- and medium-temperature energy carriers

Nomenclature

h – specific enthalpy of circulating fluid, kJ/kg
$\dot{m}$ – mass flowrate of circulating fluid, kg/s
N – power, kW
$\dot{Q}$ – heat flux, kJ/s
s – entropy, kJ/(kg K)
t, T – temperature, °C, K

Greek symbols
η – efficiency

Subscripts and Superscripts
1, 2*s*, 3, 4*s*, 5, 6 – of the upper cycle
I, II*s*, III, IV*s*, V, VI– of the lower cycle
B – binary cycle
CR – Clausius-Rankine cycle
L – lower cycle
R – reference cycle
U – upper cycle
*w*1, *w*2, *w*3, *w*4 – water supplied from a heat source

(thermal energy), which makes it possible to use waste energy streams to power these systems. Such a solution improves the energy efficiency of individual technological processes, thereby reducing the economy's energy intensity. Due to the low thermal parameters of heat sources in organic Rankine cycle (ORC) power plant systems powered by waste energy streams, low efficiencies are achieved. However, when using waste energy streams, the aim should be to maximise power output. For this reason, the authors in this paper analysed a binary power plant in the sense of a two-cycle power plant, in which the condensation heat from the upper cycle is used to power the lower cycle. This article aims to prove that a binary power plant can obtain greater power than a single-circuit power plant operating in the same temperature range.

In most cases, homogeneous circulating substances are used in ORC power plant cycles, including binary power plants [3]. An important aspect of the use of these substances is its impact on global warming. This impact is determined by the global worming potential (GWP) index. It is worth noting that under current legislation [4], a group of hydrofluorocarbons (HFCs) can be used in part whose GWP index does not exceed the value of 2 500. The use of a fluid with GWP > 2 500 from 2020 is prohibited. The possibility of using a working fluid with very good thermodynamic properties that are safe for use (e.g., non-flammable) but have a GWP index > 2 500 is possible by mixing it with another fluid with a lower GWP so that the resultant mixture index does not exceed the permissible value. For this reason, the analysis included zeotropic mixtures such as R413A, R423A, R426A, R429A, R430A, R435A and R437A. As a result of their analyses, the assumption of an increase in the power obtained in a binary power plant compared to a single-circuit power plant operating in the same temperature range was confirmed. A detailed description of selected zeotropic mixtures is presented in the next section.

1.1. Use of zeotropic mixtures in ORC systems – literature review

Organic Rankine cycle systems have become an area of intensive research as a promising technology for converting low-grade heat into electricity due to the fact that it has a low-cost, simple structure and can utilise various types of heat sources such as solar energy, geothermal energy and waste heat [5].

In the published literature, we find a variety of models to find the best working fluids based on operating conditions [6−8]. In addition, zeotropic mixtures have been proposed as alternative working fluids for ORC systems with homogeneous fluids, as has the use of mixtures in refrigeration systems and heat pumps [9−10].

Compared to homogeneous fluids, zeotropic mixtures are characterised by temperature slippage during the phase transformation process, thus alleviating the temperature profile mismatch in the evaporator and condenser [11]. Chys et al. [12] analysed the use of working fluid mixtures in ORC systems. It has been shown that cycle efficiency can be increased by 16% and power output by almost 20%. Lecompte et al. [13] studied the efficiency of ORCs using different mixtures based on the second law of thermodynamics. They found that the increase in efficiency ranged from 7.1% to 14.2% compared to ORCs using homogeneous working fluids.

It has been shown that the efficiency of the system can be increased by 16%, and power can be improved by nearly 20%. Habka and Ajib [14] performed performance evaluations of several mixtures of zeotropic working fluids for ORC systems. The study proved that mixtures of R438A, R422A and R22M fluids have better performance than homogeneous fluids.

On the other hand, Ochoa et al.[15] conducted an analysis of energy and exergy to evaluate the durability of the overall system and the viability of the zeotropic mixture from an environmental point of view. The results showed that zeotropic mixtures had better performance compared to selected pure fluids in terms of net power and exergy efficiency. Pure fluids had a better energy sustainability index (ESI). Averaging 10%, there is not much difference in this parameter, so the advantages of using zeotropic mixtures as working fluids in this type of system cannot be ignored.

Some work [16] notes the effect of zeotropic fluids on heat transfer through the condenser, indicating that a much larger heat transfer surface area is required for a zeotropic fluid. On the other hand, the work of Blondel et al. [17] points out that it is often pointed out in the literature that there is an increased thermodynamic cycle efficiency in the use of zeotropic mixtures due to improved heat transfer in the hot spring, but the vast majority of these studies are numerical and do not take into account the interactions and system effects occurring in the thermodynamic cycle for zeotropic mixtures (predict biphasic heat transfer coefficients of pure fluids and zeotropic mixtures). The work of Xia et al. [18] indicates that the influence of mixture composition on the performance of the system is different at different positions of the phase transition temperature. In addition, it was found that the use of a zeotropic mixture is not appropriate in all cases.

Analysis of theoretical and practical calculations shows that organic Rankine circulation using zeotropic working fluids has potential for application. However, there are many challenges to be solved in theory and application, such as key design, change of circulating fluid composition, dynamic performance and control strategy, and so on [19].

All the works cited are concerned with the analysis of ORC power plant systems with circulating agents in the form of zeotropic mixtures. The analyses presented in these works have shown that the use of zeotropic mixtures in ORC systems has a positive effect on their operating efficiency. For ORC systems with zeotropic mixtures, power output is increased compared to ORC systems with pure fluids. However, all these analyses concern ORC systems with one cycle (there are no analyses of two-circuit - binary systems). For this reason, this article presents an analysis of a two-circuit ORC power plant - a binary ORC power plant. For this powerhouse, it was assumed that in the upper circuit the working substance is a zeotropic mixture. The operating efficiency of the binary power plant was compared with that of the single-circuit power plant, maintaining the same temperature ranges for both systems. The purpose of the analysis is to demonstrate the impact of replacing a single-circuit ORC power plant with a binary power plant using zeotropic mixtures.

2. Description of the binary power plant system

The paper presents an analysis of the operating efficiency of a binary ORC power plant with a zeotropic low-boiling medium. For the binary ORC power plant, the assumption was made that the upper cycle used a zeotropic organic medium mixture, and the lower cycle used an organic medium from the dry medium group. The upper cycle was thermally coupled to the lower cycle by means of an HE2 (see Fig. 1) condenser-evaporator type exchanger. This coupling allows the condensation heat from the upper cycle to be used to heat, evaporate and superheat the medium in the lower cycle [3]. Due to the use of a circulating medium in the lower cycle from the dry medium group, two variants of the binary power plant were included in the analysis. The first variant of the binary power plant with lower circulation without the use of heat regeneration is shown in Fig. 1.

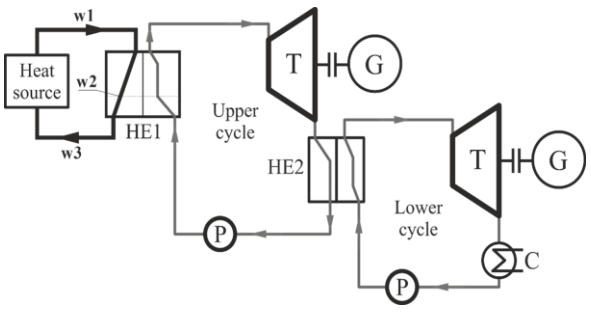


Fig. 1. Schematic of a binary power plant (two-cycle power plant).

The second variant of the binary power plant with a heat exchanger that allows heat recovery from the steam leaving the lower-cycle turbine is shown in Fig. 2. The use of this HE3 exchanger is possible due to the fact that for a dry medium, the steam after expansion in the turbine is still superheated steam with a temperature higher than the condensing temperature in the lower cycle [20,21].

Figure 3 shows a diagram of thermodynamic transformations for the individual cycles of a binary power plant operating according to the scheme shown in Fig. 1 or Fig. 2. In this case, energy from the heat source is transferred to the binary power plant system only in the HE1 exchanger.

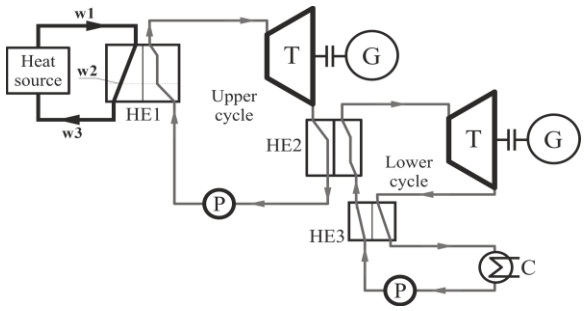


Fig. 2. The scheme of the binary power plant with the applied internal heat exchange in the lower cycle.

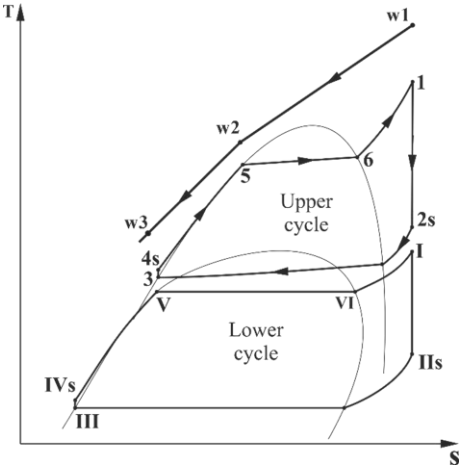


Fig. 3. Thermodynamic transformation diagram for a binary power plant

Analysis of the binary power plant layouts shown in Figs. 1 and 2 revealed that the achievable capacities of these power plants are lower than for the reference power plant (single-cycle power plant) [22,23]. In addition, it was noted that the temperature of the water returning to the heat source, i.e. the temperature of the water downstream of the HE1 heat exchanger, is high at about 90°C. Therefore, the stream of water leaving the HE1 exchanger was used to preheat the working fluid in the lower cycle of the binary power plant. Water from the HE1 exchanger is directed to the HE4 exchanger, where the working medium of the lower cycle is heated up to the saturation state (point V – see Fig. 3). A diagram of the binary power plant operating according to this description is shown in Fig. 4.

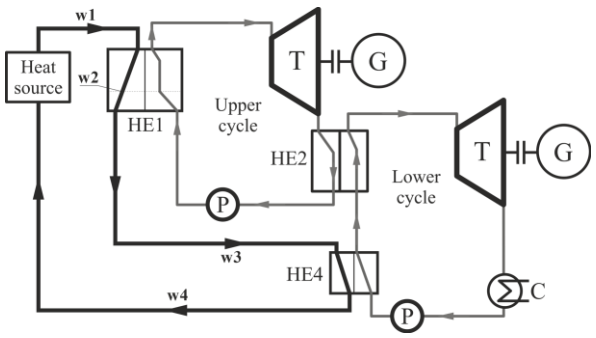


Fig. 4. The scheme of a binary power plant with a pre-heater in the lower cycle.

Figure 5 shows a diagram of thermodynamic transformations for the individual cycles of a binary power plant operating according to the diagram shown in Fig. 4. In this case, energy from the heat source is transferred to the binary power plant system in the HE1 and HE4 exchangers.

Based on previous analyses [24,25], it was assumed that a selection of zeotropic mixture from the 400 series, such as R413A, RTe 423A, R426A, R429A, R435A and R437A, would be analysed in the upper cycle. The basic properties of these zeotropic mixtures are shown in Table 1.

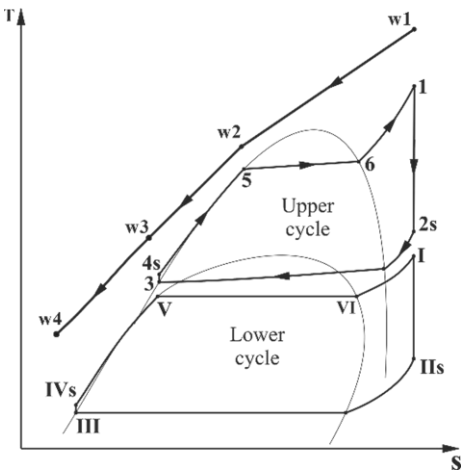


Fig. 5. Thermodynamic transformation diagram for a binary power plant with a pre-heater in the lower cycle.

Table 1. Basic properties for the analyzed zeotropic mixture.

No.	Name of fluid	Type	Composition	Indicator ODP	Indicator GWP_{100}	Density (kg/m^3)	Molecular mass (u)	Critical temperature (°C)	Critical pressure (kPa)	Temp. glide ΔT1 (°C)
1	R-413A	HFC	9±1% C_3F_8 88±2% $C_2H_2F_4$ 3±1% C_4H_{10}	0	2 053	512.53	104	95.335	3 919.8	1.131
2	R-423A	HFC	52.5±1% C_2H_2F 47.5±1% C_3HF_7	0	228	537.18	126	99.136	3 563.0	0.49
3	R-426A	HFC	5.1±1% C_2HF_5 93±1% $C_2H_2F_4$ 1.3±0.2% C_4H_{10} 0.6±0.1% C_5H_{12}	0	1 508	503.13	101.6	98.993	4 018.1	0.48
4	R-429A	HFC	60±1% C_2H_6O 10±1% $C_2H_4F_2$ 30±1% C_4H_{10}	0	139	266.79	50.8	121.95	4 730.0	0.94
5	R-435A	HFC	80±1% C_2H_6O 20±1% $C_2H_4F_2$	0	256	292.02	49	123.06	5 191.2	0.224
6	R-437A	HFC	19.5±0.5% C_2HF_5 78.5±1.5% C_2H_2F 1.4±1% C_4H_{10} 0.6±0.2% C_5H_{12}	0	1 805	517.32	103.7	95.502	4 024.5	1.631

ODP - ozone depletion potential

The use of a zeotropic medium causes evaporation and condensation transformations in the upper cycle to take place with temperature slippage. An example diagram of the thermodynamic transformations taking place in the cycles of the binary power plant and the temperature distribution for the heat carrier is shown in Fig. 3 or Fig. 5.

In the lower cycle of the binary power plant analysed, it was assumed that the evaporation of the low-boiling medium takes place in the near-critical region, which means that the temperature of this transformation is several K lower than the temperature at the critical point. Previous work has shown that such a solution is advantageous from the point of view of ORC system efficiency [26].

Due to the assumption that the heat source is of a waste energy nature, the authors considered the power of the system as the basic parameter determining its operating efficiency.

In order to evaluate the efficiency of operation of the analyzed binary power plant systems, the obtained calculation results were compared with the power obtained in a reference power plant (single-cycle power plant). In this power plant, the same temperatures of evaporation and superheating of the working medium were assumed for the upper cycle of the binary power plant. However, the condensation temperature of the working medium in the single-cycle power plant is equal to the condensation temperature of the working medium in the lower

cycle of the binary power plant. A diagram of the reference (single-cycle) power plant is shown in Fig. 6 (a – the simple ORC system, b – the ORC system with internal heat regeneration).

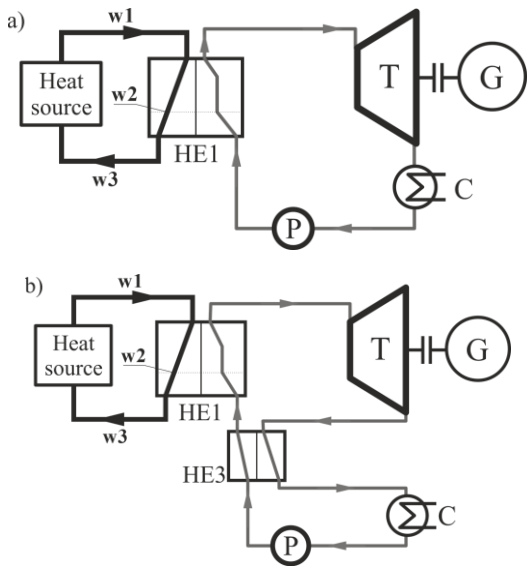


Fig. 6. Single-cycle reference power plant: a) the simple ORC system, b) the ORC system with internal heat regeneration

Figure 7 shows the shape of the saturation curves for the analyzed working fluids in the T–s coordinate system (Temperature–Entropy).

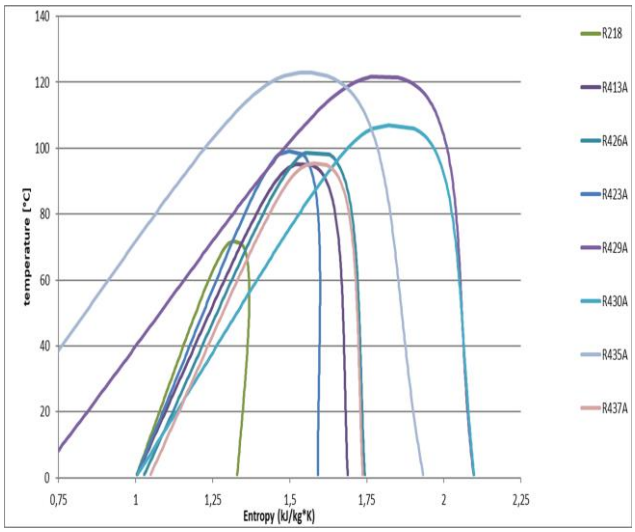


Fig. 7. The shape of the saturation curves for the analyzed working fluids in the T–s coordinate system

3. Methodology of calculations

The detailed methodology for calculating binary power plants can be found, among others, in the works [3,5], and all thermal and caloric parameters of the circulating media and water as the heat carrier were determined using the RefProp 9.1 database of low-boiling media [27]. Selected relationships used in the calculations are presented below.

3.1. Upper cycle

The energy balance equation, ignoring heat losses, for the HE1 exchanger for the superheater and evaporator parts takes the following form:

$$\dot{m}_w c_w (t_{w1} - t_{w2}) = \dot{m}_u (h_1 - h_5), \quad (1a)$$

$$\dot{m}_w (h_{w1} - h_{w2}) = \dot{m}_u (h_1 - h_5). \quad (1b)$$

The mass flow of the working medium in the upper cycle $\dot{m}_u$ was determined by transforming equation (1b):

$$\dot{m}_u = \frac{\dot{m}_w (h_{w1} - h_{w2})}{h_1 - h_5}. \quad (2)$$

The energy balance equation for the HE1 exchanger takes the following form:

$$\dot{Q}_{HE1} = \dot{m}_w c_w (t_{w1} - t_{w3}) = \dot{m}_u (h_1 - h_{4s}). \quad (3)$$

The temperature of the water leaving the HE1 heat exchanger was determined from the transformed relationship (3) as follows:

$$t_{w3} = t_{w1} - \frac{\dot{m}_u (h_1 - h_{4s})}{\dot{m}_w c_w}. \quad (4)$$

3.2. Lower cycle

The energy balance for the HE2 condenser-evaporator exchanger for the binary power plant system shown in Fig. 2 takes the form:

$$\dot{Q}_{HE2} = \dot{m}_U (h_{2s} - h_3) = \dot{m}_L (h_{\mathrm{I}} - h_{\mathrm{IVs}}). \quad (5)$$

The mass flow of the working medium in the lower cycle $\dot{m}_{\mathrm{L}}$ was determined from the above equation:

$$\dot{m}_L = \frac{\dot{m}_U (h_{2s} - h_3)}{h_{\mathrm{I}} - h_{\mathrm{IVs}}}. \quad (6)$$

In the case of the binary power plant system shown in Fig. 4, the energy balance equation for the HE2 condenser-evaporator exchanger takes the form:

$$\dot{Q}_{HE2} = \dot{m}_U (h_{2s} - h_3) = \dot{m}_L (h_{\mathrm{I}} - h_{\mathrm{V}}). \quad (7)$$

The mass flow of the working medium in the lower cycle was determined from the above equation $\dot{m}_L$:

$$\dot{m}_L = \frac{\dot{m}_U (h_{2s} - h_3)}{h_{\mathrm{I}} - h_{\mathrm{V}}}. \quad (8)$$

The medium is heated in the lower cycle for the binary power plant shown in Fig. 4 in the HE4 exchanger using water supplied from the HE1 exchanger.

The temperature of water returning to the heat source was determined from the energy balance equation for the HE4 exchanger:

$$\dot{Q}_{HE4} = \dot{m}_w c_w (t_{w3} - t_{w4}) = \dot{m}_L (h_{\mathrm{V}} - h_{\mathrm{IVs}}), \quad (9a)$$

$$t_{w4} = t_{w3} - \frac{\dot{m}_L(h_V - h_{IVs})}{\dot{m}_w c_w}. \quad (9b)$$

3.3. Upper cycle of binary power plant

Below are the methods for determining unit values (referred to 1 kg of circulating medium) characterizing the Clausius-Rankine cycle.

The specific isentropic work of the pump (for pumping the low-boiling medium in the upper cycle) is the difference between the specific enthalpies of the medium at the pump outlet and at the pump inlet:

$$l_{U\,com} = h_{4s} - h_3. \quad (10)$$

Taking into account the internal efficiency of the pump η_{ip} = 0.80 and the mechanical efficiency of the pump η_{mp} = 0.99, the unit work required to drive the circulating pump l_{Up} was determined as follows:

$$l_{Up} = \frac{l_{U\,com}}{\eta_{ip}\,\eta_{mp}} = \frac{h_{4s} - h_3}{\eta_{ip}\,\eta_{mp}}. \quad (11)$$

The specific isentropic expansion work for the upper cycle was determined as the difference in specific enthalpy before and after the turbine:

$$l_{Uexp} = h_1 - h_{2s}. \quad (12)$$

Taking into account the internal efficiency of the turbine η_{it} = 0.75 and the mechanical efficiency of the turbine η_{mt} = 0.99, the mechanical unit work of the turbine l_{Ut} was determined as follows:

$$l_{Ut} = \eta_{it}\,\eta_{mt}\,l_{Uexp} = \eta_{it}\,\eta_{mt}(h_1 - h_{2s}). \quad (13)$$

The mechanical power of the upper cycle N_U, taking into account pomp work, was determined as follows:

$$N_U = \dot{m}_U\left(l_{Ut} - l_{Up}\right). \quad (14)$$

The electrical power generated in the upper cycle $N_{el\,U}$ was determined by assuming generator efficiency η_g = 0.99 as follows:

$$N_{el\,U} = \eta_g N_U. \quad (15)$$

The heat flux supplied to the upper cycle was determined as follows:

$$\dot{Q}_U = \dot{m}_U(h_1 - h_{4s}). \quad (16)$$

The electrical efficiency of the upper cycle $\eta_{el\,U}$ can be determined from the relationship:

$$\eta_{el\,U} = \frac{N_{el\,U}}{\dot{Q}_U}. \quad (17)$$

3.4. Lower cycle of binary power plant

The specific isentropic work of the pump (for pumping the low-boiling medium in the lower cycle) is the difference between the specific enthalpies of the medium at the pump outlet and at the pump inlet:

$$l_{L\,com} = h_{IVs} - h_{III}. \quad (18)$$

Taking into account the internal efficiency of the pump η_{ip} = 0.80 and the mechanical efficiency of the pump η_{mp} = 0.99, the unit work required to drive the circulating pump for the lower cycle l_{Lp} was determined as follows:

$$l_{L\,p} = \frac{l_{L\,com}}{\eta_{ip}\,\eta_{mp}} = \frac{h_{IVs} - h_{III}}{\eta_{ip}\,\eta_{mp}}. \quad (19)$$

The specific isentropic expansion work for the lower cycle was determined as the difference in specific enthalpy before and after the turbine:

$$l_{L\,exp} = h_{\mathrm{I}} - h_{\mathrm{IIs}}. \quad (20)$$

Taking into account the internal efficiency of the turbine η_{it} = 0.75 and the mechanical efficiency of the turbine η_{mt} = 0.99, the mechanical unit work of the turbine for the lower cycle l_{Ut} was determined as follows:

$$l_{L\,t} = \eta_{it}\,\eta_{mt}\,l_{L\,exp} = \eta_{it}\,\eta_{mt}(h_{\mathrm{I}} - h_{\mathrm{IIs}}). \quad (21)$$

The mechanical power of the lower cycle N_L, taking into account pomp work, was determined as follows:

$$N_L = \dot{m}_L\left(l_{L\,t} - l_{L\,p}\right). \quad (22)$$

The electrical power generated in the lower cycle $N_{el\,L}$ was determined by assuming generator efficiency η_g = 0.99 as follows:

$$N_{el\,L} = \eta_g N_L. \quad (23)$$

The heat flux supplied to the lower cycle was determined as follows:

$$\dot{Q}_L = \dot{m}_L(h_{\mathrm{I}} - h_{\mathrm{IVs}}). \quad (24)$$

The electrical efficiency of the lower cycle η_{elU} can be determined from the relationship:

$$\eta_{el\,L} = \frac{N_{el\,L}}{\dot{Q}_L}. \quad (25)$$

3.5. Binary power plant

The electrical power of the binary power plant was determined as the sum of the eclectic powers of the upper and the lower cycles from the following relation:

$$N_{el\,B} = N_{el\,U} + N_{el\,L}. \quad (26)$$

The heat flux delivered to the binary power plant was determined from the following equation:

$$\dot{Q}_B = \dot{m}_w(h_{w1} - h_{w4}). \quad (27)$$

The electrical efficiency of the binary power plant was determined from the following equation:

$$\eta_{el\,B} = \frac{N_{el\,B}}{\dot{Q}_B}. \quad (28)$$

The calculations were simplified by eliminating heat losses to the environment when balancing heat exchangers of the binary power plant. The results obtained for the binary power plant

were related to the results obtained for the single-cycle power plant operating in the same temperature range.

4. Results of calculations

The calculations were carried out with the assumption that the mass flux of water supplied from the heat source to the binary or single-cycle power plant is 1 kg/s. This assumption allows the system to be easily recalculated for a different value of the mass flux of water supplied from the heat source. The temperature of the water supplied from the heat source to the binary powerhouse is $t_{w1} = 120°C$.

The other assumptions used in the calculations are as follows. The superheated steam temperature for the working medium in the upper cycle is $t_1 = 110°C$ (the same temperature value was assumed for the single-cycle power plant), and the condensation temperature for the reference power plant and the lower cycle of the binary power plant is $t_{III} = 30°C$, and the upper cycle is $t_3 = 68°C$.

Table 2 shows examples of thermal and caloric parameters at characteristic points of the binary power plant cycle (upper cycle – R413a, lower cycle – R218) and the reference power plant.

Table 3 shows the results of calculations for the electrical power output of the reference (single-cycle) power plant and the binary power plant, which uses R218 refrigerant in the lower cycle. The temperature of the medium at the end of the evaporation process in the upper cycle was $t_6 = 93°C$, while the superheat temperature in the lower cycle was $t_I = 68°C$. Also included is the variation of the evaporation temperature of the refrigerant in the lower cycle $t_V = t_{VI}$ from 58°C to 66°C.

Table 2. Thermal and caloric parameters at characteristic points of the circulation of the analyzed power plants.

Single-cycle power plant - zeotropic mixture R413a											
1		2s		3		4s		5		6	
t [°C]	*h* [kJ/kg]	*t* [°C]	*h* [kJ/kg]	*t* [°C]	*h* [kJ/kg]	*t* [°C]	*h* [kJ/kg]	*t* [°C]	*h* [kJ/kg]	*t* [°C]	*h* [kJ/kg]
110.0	447.9	45.5	418.6	30.0	242.1	31.8	244.5	92.5	356.7	93.0	402.4
Binary upper cycle - zeotropic mixture R413a											
1		2s		3		4s		5		6	
t [°C]	*h* [kJ/kg]	*t* [°C]	*h* [kJ/kg]	*t* [°C]	*h* [kJ/kg]	*t* [°C]	*h* [kJ/kg]	*t* [°C]	*h* [kJ/kg]	*t* [°C]	*h* [kJ/kg]
110.0	447.9	83.9	416.4	68.0	302.5	70.1	304.1	92.5	356.7	93.0	402.4
Binary lower cycle - zeotropic mixture R218											
I		IIs		III		IVs		V		VI	
t [°C]	*h* [kJ/kg]	*t* [°C]	*h* [kJ/kg]	*t* [°C]	*h* [kJ/kg]	*t* [°C]	*h* [kJ/kg]	*t* [°C]	*h* [kJ/kg]	*t* [°C]	*h* [kJ/kg]
68,0	320.7	36.3	306.5	30.0	233.8	31.3	234.9	66.0	283.4	66.0	316.0
68,0	322.6	38.2	306.5	30.0	233.8	31.2	234.8	65.0	281.5	65.0	316.4
68,0	324.1	39.9	306.5	30.0	233.8	31.2	234.8	64.0	279.8	64.0	316.6
68,0	325.5	41.3	306.5	30.0	233.8	31.2	234.7	63.0	278.1	63.0	316.8
68,0	326.6	42.7	306.5	30.0	233.8	31.1	234.7	62.0	276.5	62.0	316.9
68,0	327.7	43.9	306.5	30.0	233.8	31.1	234.7	61.0	274.9	61.0	317.0
68,0	328.7	45.1	306.5	30.0	233.8	31.0	234.6	60.0	273.3	60.0	317.0
68,0	329.6	46.2	306.5	30.0	233.8	31.0	234.6	59.0	271.8	59.0	316.9
68,0	330.4	47.2	306.5	30.0	233.8	30.9	234.6	58.0	270.3	58.0	316.8

Using the presented calculation methodology and the parameters summarized in Table 2, the electrical powers of the various systems were determined:

- the single-cycle power plant – (A),
- the binary power plant (Fig. 1) – (B),
- the binary power plant with internal heat exchange in the lower cycle (Fig. 2) – (C).

In the case of the reference power plant, the use of internal heat regeneration did not increase the electrical power of the system. When internal heat regeneration was used, the use of energy from the heat source decreased. This means that the return water temperature to the source of the ORC system shown in Fig. 6b is higher than that of the ORC system shown in Fig. 6a.

The calculation results shown in Table 3 indicate that for the binary power plants operating according to the schemes shown in Figs. 1 and 2, the electrical power obtained is lower than for the reference power plant. This is due to the fact that the heat flux to the binary power plant is supplied only in the HE1 heat exchanger. This results in less cooling of the water supplied from the heat source.

In binary power plant systems (B), (C), the heat flux to the lower cycle is supplied in the HE2 condenser-steamer exchanger. Thus, the mass flow of the working medium in the lower cycle $\dot{m}_L$ determined from equation (6) is small, which affects the power of the lower cycle.

The calculation results summarized in Table 3 show that the use of internal heat regeneration in the lower cycle of the binary power plant affects a small increase in the power of the system.

Table 4 shows the values of water temperatures at various points in the cycle for the reference power plant (A) and binary power plants (B), (C). From the data presented in Table 4, it is clear that the temperature of the return water to the heat source in the cases of binary power plants is higher than for the reference power plant. For this reason, the system of the binary power plant (D) operating according to the scheme shown in Fig. 4 was also analyzed. In this system, water from the HE1 exchanger of the upper cycle is directed to the HE4 exchanger of the lower

cycle. In the HE4 exchanger, the working fluid of the lower cycle is heated to saturation temperature. This will make the HE2 exchanger use the heat from the upper cycle only to evaporate and superheat the working fluid of the lower cycle. This translates into an increase in the mass flow of the working fluid in the lower cycle (Eq. (8)) and an increase in its power output.

The results of the power calculation of the binary power plant system (D) compared to the single-cycle power plant are shown in Table 5.

Table 3. The electrical power of the single-cycle power plant (A) and the binary power plant (B), (C) for analyzed zeotropic mixture of the upper cycle (t_1 = 110°C, t_6 = 93°C, t_l = 68°C).

t_V [°C]	The electrical power of the power plant [kWe]																	
	R413A			R423A			R426A			R429A			R435A			R437a		
	(A)	(B)	(C)	(A)	(B)	(C)	(A)	(B)	(C)	(A)	(B)	(C)	(A)	(B)	(C)	(A)	(B)	(C)
66.0		10.2	10.6		9.6	10.0		9.6	9.9		8.6	8.9		8.4	8.7		10.2	10.6
65.0		10.1	10.6		9.6	10.1		9.5	10.0		8.6	9.0		8.4	8.8		10.1	10.6
64.0		10.1	10.7		9.5	10.1		9.5	10.0		8.5	9.0		8.3	8.8		10.1	10.7
63.0		10.0	10.7		9.4	10.1		9.4	10.0		8.5	9.0		8.2	8.8		10.0	10.7
62.0	14.8	9.9	10.7	14.1	9.3	10.1	14.0	9.3	10.0	12.1	8.4	9.0	11.7	8.2	8.8	14.9	9.9	10.6
61.0		9.8	10.6		9.2	10.0		9.2	10.0		8.3	9.0		8.1	8.7		9.8	10.6
60.0		9.7	10.5		9.1	10.0		9.1	9.9		8.2	8.9		8.0	8.7		9.6	10.5
59.0		9.5	10.5		9.0	9.9		9.0	9.8		8.1	8.9		7.9	8.6		9.5	10.5
58.0		9.4	10.4		8.9	9.8		8.8	9.7		8.0	8.8		7.8	8.6		9.4	10.4

Table 4. Water temperature at various points in the cycle (working fluid – R413a).

Power plant	Water temperature		
	t_{w1} [°C]	t_{w2} [°C]	t_{w3} [°C]
Reference power plant (A)	120.0	102.5	80.8
Binary power plant (B), (C)	120.0	102.5	92.3

Table 5. The electrical power of the single-cycle power plant (A) and the binary power plant (D) for the analyzed zeotropic mixture of the upper cycle (t_1 = 110°C, t_6 = 93°C, t_l = 68°C).

t_V [°C]	The electrical power [kWe]											
	R413A		R423A		R426A		R429A		R435A		R437a	
	(A)	(D)	(A)	(D)	(A)	(D)	(A)	(D)	(A)	(D)	(A)	(D)
66		17.8		16.8		16.6		14.8		14.3		17.8
65		16.8		15.8		15.6		14.0		13.5		16.8
64		15.9		15.0		14.8		13.3		12.8		15.9
63		15.2		14.3		14.1		12.7		12.2		15.2
62	14.8	14.5	14.1	13.7	14.0	13.5	12.1	12.1	11.7	11.7	14.9	14.5
61		13.9		13.1		13.0		11.6		11.3		13.9
60		13.4		12.6		12.5		11.2		10.9		13.4
59		12.9		12.2		12.0		10.8		10.5		12.9
58		12.4		11.7		11.6		10.4		10.1		12.4

From the calculation results shown in Table 5, it can be seen that for each of the analyzed fluids in the upper cycle in the binary power plant (D), more power was obtained compared to the reference power plant (A).

The highest powers were obtained for the binary power plant (D) with R413a and R437a factors. Analysis of the results for the achieved power for the binary power plant (D) shows that as the evaporation temperature of the refrigerant in the lower cycle increases, the power of the refrigerant increases, causing the power of the entire binary power plant to increase. For evaporation temperatures in the lower cycle lower than about 62°C, the power of the binary power plant is lower than that of the reference power plant.

Analysis of the operation of the binary power plant system (D) showed that it is possible to use the water leaving the HE1 heat exchanger of the upper cycle to carry out the process of heating the medium in the lower cycle to saturation temperature.

This procedure was shown to have a beneficial effect on the power output of the binary power plant.

5. Conclusions

The analysis showed that by properly selecting the parameters of the cycles in a binary power plant, it is possible to obtain more power without changing the heat source than in the case of a single-cycle power plant operating in the same temperature range.

In addition, it was shown that carrying out the process of evaporation of the working medium of the lower cycle in the near-subcritical region causes an increase in the power of the binary power plant.

It follows from the above conclusion that the condensing temperature in the upper cycle should be adjusted to the lower cycle medium in such a way that the condensing temperature in the upper cycle is higher than the critical temperature of the lower cycle medium (this will allow the evaporation temperature in the lower cycle to be adjusted accordingly).

Analysis of the impact of the superheat temperature in the lower cycle showed that an increase in this temperature negatively affects the power output of the binary power plant. For example, for the R413a refrigerant for the superheat temperature in the lower cycle t_1 = 68°C, the electrical power plant's output was 17,8 kWe, and after the temperature increased to t_1 =70°C, the output dropped to 17.1 kWe (a further increase in this temperature caused a further decrease in output).

As shown in Table 5, the use of zeotropic mixtures in a binary power plant for each of the analyzed fluids allowed an increase in the electrical power of the power plant compared to a single-circuit power plant. For example, for the binary ORC power plant with R413A refrigerant in the upper circuit, the generated power is 17.8 kWe, which is 20% higher than for a single-circuit power plant (for the reference power plant, the power is 14.8 kWe).

The increase in the power of the binary power plant system was achieved by using the heat contained in the water stream to preheat the medium in the bottom circuit. Such a solution increases the power of the bottom circuit and allows greater cooling of the water, which consequently increases the degree of utilization of energy from the waste heat source.

The established conclusions are consistent with the work analyzed by the authors and are additionally extended to include the use of zeotropic mixture in binary power plants.

In the next articles, the authors plan to conduct an economic analysis of the proposed solution.

References

[1] Taner, T. (2021). The novel and innovative design with using H_2 fuel of PEM fuel cell: Efficiency of thermodynamic analyze. *Fuel*, 302, 121109. doi: 10.1016/j.fuel.2021.121109

[2] Taner, T. (2017). The micro-scale modeling by experimental study in PEM fuel cell. *Journal of Thermal Engineering*, (3)6, 331755. doi: 10.18186/journal-of-thermal-engineering.331755

[3] Stachel, A.A., & Wiśniewski, S. (2015). Influence of the type of working fluid in the lower cycle and superheated steam parameters in the upper cycle on effectiveness of operation of binary power plant. *Archives of Thermodynamics*, 36(1), 111–123. doi: 10.1515/aoter-2015-0008

[4] EU. (2024). *Regulation (EU) 2024/573 of the European Parliament and of the Council of 7 February 2024 on fluorinated greenhouse gases, amending Directive (EU) 2019/1937 and repealing Regulation (EU) no 517/2014*. https://eur-lex.europa.eu/legal-content/EN/TXT/?uri= CELEX%3A32024R0573 [accessed 29 April 2024].

[5] Landelle, A., Tauveron, N., Haberschill, P., Revellin, R., & Colasson, S. (2017). Organic Rankine cycle design and performance comparison based on experimental database. *Applied Energy*, 204, 1172–1187. doi: 10.1016/j.apenergy.2017.04.012

[6] Su, W., Zhao, L., & Deng, S. (2017). Developing a performance evaluation model of Organic Rankine Cycle for working fluids based on the group contribution method. *Energy Conversion and Management*, 132, 307–315. doi: 10.1016/j.enconman.2016.11.040

[7] Su, W., Zhao, L., & Deng, S. (2017). Simultaneous working fluids design and cycle optimization for Organic Rankine cycle using group contribution model. *Applied Energy*, 202, 618–627. doi: 10.1016/j.apenergy.2017.03.133

[8] Brown, J.S., Brignoli, R., & Daubman, S. (2014). Methodology for estimating thermodynamic parameters and performance of working fluids for organic Rankine cycles. *Energy*, 73, 818–828. doi: 10.1016/j.energy.2014.06.088

[9] Modi, A., & Haglind, F. (2017). A review of recent research on the use of zeo-tropic mixtures in power generation systems. *Energy Converssion and Management*, 138, 603–626. doi: 10.1016/j.enconman.2017.02.032

[10] Bamorovat Abadi, G., & Kim, K.C. (2017). Investigation of organic Rankine cycles with zeotropic mixtures as a working fluid: Advantages and issues. *Renewable and Sustainable Energy Reviews*, 73C, 1000–1013. doi: 10.1016/j.rser.2017.02.020

[11] Wu, W., Zhao, L., & Ho, T. (2012). Experimental investigation on pinch points and maximum temperature differences in a horizontal tube-in-tube evaporator using zeotropic refrigerants. *Energy Conversion and Management*, 56, 22–31. doi: 10.1016/j.enconman.2011.11.009

[12] Chys, M., Van Den Broek, M., Vanslambrouck, B., & Paepe, D. (2012). Potential of zeotropic mixtures as working fluids in organic Rankine cycles. *Energy*, 44(1), 623–632. doi: 10.1016/j.energy.2012.05.030

[13] Lecompte, S., Ameel, B., Ziviani, D., van den Broek, M., & De Paepe, M. (2014). Exergy analysis of zeotropic mixtures as working fluids in Organic Rankine Cycles. *Energy Conversion and Management*, 85, 727–739. doi: 10.1016/j.enconman.2014.02.028

[14] Habka, M., & Ajib, S. (2015). Evaluation of mixtures performances in Organic Rankine Cycle when utilizing the geothermal water with and without cogeneration. Applied Energy, 154, 567−576. doi: 10.1016/j.apenergy.2015.05.046

[15] Ochoa, G.V., Caballero, A.P., & Castilla, D.V. (2023). Assessing sustainable operational conditions of a bottoming organic Rankine cycle using zeotropic mixtures: An energy-emergy approach, *Heliyon*, 9(1). doi: 10.1016/j.heliyon.2022.e12521

[16] Zheng, Z., Cao, J., Wu, W., & Leung, M.K.H. (2022). Parallel and in-series arrangements of zeotropic dual-pressure Organic Rankine Cycle (ORC) for low-grade waste heat recovery. *Energy Reports*, 8, 2630–2645. doi: 10.1016/j.egyr.2022.01.057

[17] Blondel, Q., Tauveron, N., Lhermet, G., & Caney, N. (2023). Zeotropic mixtures study in plate heat exchangers and ORC systems. *Applied Thermal Engineering*, 219, 119418. doi: 10.1016/j.applthermaleng.2022.119418

[18] Xia, X., Sun, T., Wang, Z., Zhang, H., Yang, C., & Wang, K. (2023). Thermodynamic, economic and environmental assessment of a novel organic Rankine cycle-vapor compression refrigeration system using zeotropic mixture. *Energy and Buildings*, 301(3). doi: 10.1016/j.enbuild.2023.113736

[19] Xu, W., Zhao, R., Deng, S., Zhao, L., & Mao, S.S. (2021). Is zeotropic working fluid a promising option for organic Rankine cycle: A quantitative evaluation based on literature data. *Renewable and Sustainable Energy Reviews*, 148, 111267. doi: 10.1016/j.rser.2021.111267

[20] Szargut, J. (2007). *Exergy. Calculation and application guide*. Wydawnictwo Politechniki Śląskiej. Gliwice (in Polish).

[21] Szargut, J. (2009). *Technical thermodynamics*. PWN. Kraków (in Polish).

[22] Nowak, W., Borsukiewicz-Gozdur, A., & Wiśniewski, S. (2012). Influence of working fluid evaporation temperature in the near-critical point region on the effectiveness of ORC Power plant operations. *Archives of Thermodynamics*, 33(3), 77–88. doi: 10.2478/v10173-012-0019-7

[23] Lewandowski, W.M., Ryms, M., Kołoła, R., Kubski, P., Klugmann-Radziemska, E., & Ostrowski, P. (2010). Improving the efficiency of ORC systems and trigeneration systems by using various thermo-dynamic variants of their operation. *Nafta-Gaz*, 9, 794–799 (in Polish).

[24] Bańkowski, M., & Borsukiewicz-Gozdur, A. (2017). Analysis of selected thermodynamic parameters of zeotropic substances in terms of their use as working fluids in ORC systems, In *Współczesne problemy energetyki IV* (pp. 217−228). Politechnika Śląska, Gliwice (in Polish).

[25] Borsukiewicz-Gozdur, A., Wiśniewski, S., Mocarski, S., & Bańkowski, M. (2014). ORC power plant for electricity production from forest and agriculture biomass. *Energy Conversion and Management*, 87, 1180–1185. doi: 10.1016/j.enconman.2014.04.098

[26] Nowak, W., Borsukiewicz-Gozdur, A., & Wiśniewski, S. (2012). Influence of working fluid evaporation temperature in the near-critical point region on the effectiveness of ORC power plant operation. *Archives of Thermodynamics*, 33(3), 73–83. doi: 10.2478/v10173-012-0019-7

[27] Lemmon, E., Huber, M., & McLinden, M. (2010). *NIST Standard Reference Database 23, Version 9.0, 2010, Reference Fluid Therodynamic and Transport Properties* (9.0), Gaithersburg.

Co-published by
Institute of Fluid-Flow Machinery
Polish Academy of Sciences
Committee on Thermodynamics and Combustion
Polish Academy of Sciences

Copyright©2024 by the Authors under licence CC BY 4.0

http://www.imp.gda.pl/archives-of-thermodynamics/

Fractional order transient free-convection flow in a channel: application of the optimal homotopy asymptotic method

Sadia Irshad[a], Shah Jahan[a], Ahmed Zubair Jan[b*], Krzysztof Kędzia[b], Afraz Hussain Majeed[c], Fiza Khan[d]

[a]Institute of Mathematics, Khawaja Fareed University of Engineering and Information Technology, Rahim Yar Khan, Punjab 64200, Pakistan
[b]Faculty of Mechanical Engineering, Wroclaw University of Science and Technology, 50-370 Wroclaw, Poland
[c]School of Energy and Power Engineering, Jiangsu University, Zhenjiang 212013, China
[d]Department of Mathematics, Air University, PAF Complex E-9, Islamabad 44000, Pakistan
*Corresponding author email: ahmed.jan@pwr.edu.pl

Received: 30.07.2023; revised: 21.10.2023; accepted: 19.04.2024

Abstract

In this study, a new physical model has been created to look into the behaviour of transient incompressible unsteady flow between two infinite parallel plates exposed to high temperatures. The model takes into consideration thermal radiation flux, chemical reaction, and mass diffusion at the boundaries. To handle non-integer behaviour, the model incorporates the Caputo notion of time fractional derivative. To solve this complex physical fractional order fluid model, a novel optimal homotopy asymptotic method and semi-analytical methodology is extended and utilized successfully. This method provides a third-order highly approximate solution, offering valuable insights into the behaviour within the system. The study comprehensively examines the effects of varied flow characteristics and fractional order on the dynamics of the system. The results are visually presented through graphs, offering a clear understanding of the system's response under different conditions. The effectiveness and ease of use of the optimal homotopy asymptotic method make it a valuable tool for solving boundary value fractional order problems encountered in scientific fields. The developed physical model and its fractional extension contribute significantly to the understanding of unsteady flow phenomena with thermal and chemical effects, advancing knowledge in this area of research.

Keywords: Parallel plates; Flow; Fractional model; Caputo derivative; Optimal homotopy asymptotic method

Vol. 45(2024), No. 2, 139–144; doi: 10.24425/ather.2024.150860

Cite this manuscript as: Irshad, S., Jahan, S., Jan, A.Z., Kędzia, K., Majeed, A.H., & Khan, F. (2024). Fractional order transient free-convection flow in a channel: application of the optimal homotopy asymptotic method. *Archives of Thermodynamics*, 45(2), 139–144.

1. Introduction

In the natural world, various processes entail the simultaneous transport of mass and heat. These occurrences arise not only due to temperature gradients but also from concentration differences or a combination of both factors. Over the past few decades, scientists have extensively studied buoyancy-driven flows influenced by mass and thermal diffusion working together. These investigations have found significant applications in diverse technological and engineering fields, including nuclear fuel

Nomenclature

$^{C}D^{\alpha}_{0,t}$ – Caputo derivative
C_1, C_2, C_3 – constants
c_i – convergence control parameters
c_p – specific heat at constant pressure, J/(kg K)
D – coefficient of molecular diffusivity
g – acceleration due to gravity, m/s^2
H – nonlinear operator – Caputo fractional derivative operator (denotes space of functions)
k – thermal conductivity, W/(m K)
k^* – mean value of heat absorption parameter
Kr – chemical reaction parameter
L – Caputo fractional derivative operator
n – order of approximation
N_r – particles per unit volume, 1/m^3
Pr – Prandtl number
q_{ry} – radiative heat flux, W/m^2
R – Caputo fractional derivative operator (denotes space of functions that are Lebesgue integrable)
s – parameter (that represents the convergence rate)
Sc – Schmidt number
t – time, s
u – velocity, m/s

Greek symbols

α – fractional order
β – volume expansion coefficient for the heat transfer
β^* – volume expansion coefficient for the mass transfer
Γ – gamma function
θ – fluid temperature, K
θ_d – far field temperature, K
θ_w – temperature of the wall, K
ν – kinematic viscosity, m^2/s
ρ – density, kg/m^3
σ^* – Stefan-Boltzmann constant, W/(m^2 K^4)
ψ – concentration
ψ_d – far field concentration
ψ_w – wall-based nanoparticle concentration, mol/m^3

Subscripts and Superscripts

eff – effective order of approximation
t – time variable or independent variable
yy – second derivative

Abbreviations and Acronyms

HPM – homotopy perturbation method
HVAC – heating, ventilation and air conditioning
OHAM – optimal homotopy asymptotic method

storage, underground coal gasification, groundwater hydrology, chemical engineering and processor cooling. Consequently, the study of free convective flow in vertical channels has garnered substantial attention because of its profound relevance in applied sciences and engineering [1]. Among the notable research efforts, Harris et al. [2,3] have examined the effects of transient free convective flow along a straight plate embedded in a porous medium that has been exposed to abrupt changes in heat flow and surface temperature. As the fluid flows towards the wall, heat generated through viscous temperature rises as a result of dissipation, resulting in reduced viscosity and significant flow stratification. These changes notably influence the heat transfer rate (HTR) [4,5], rendering this phenomenon practically important in various engineering applications. The study of fractional calculus has gained considerable interest in recent times, becoming a popular subject due to its widespread applications across scientific and engineering disciplines [6]. In this context, Sarwar et al. [7] investigated the behaviour of a fluid of the non-Newtonian fractional Brinkman type using the optimal homotopy asymptotic method (OHAM). OHAM has demonstrated to be a valuable tool for solving complex problems involving fractional calculus effectively implemented to various physical models, demonstrating its efficacy in providing accurate and efficient solutions [8]. Furthermore, references [9–12] delve into the time fractional operator's importance in heat transfer analysis, highlighting its usefulness in comprehending and modelling heat transfer processes involving fractional derivatives. In conclusion, the exploration of flows involving the interaction of mass and heat transport has enriched our understanding of intricate natural phenomena and has opened up numerous applications in engineering and applied sciences. By employing advanced mathematical techniques such as OHAM and studying fractional calculus, researchers have gained valuable insights and offered innovative solutions to challenging problems across various scientific and engineering domains.

Heat transfer analysis in a micro-channel was thoroughly investigated by Ojemeri and Hamza [13], with a focus on the complex interactions of Arrhenius-controlled processes, free convection, hydromagnetic flow and the effects of heat generation and absorption.

Through a microchannel that includes a non-Darcy porous medium, Bhatti et al. (his research team) [14] investigated the dynamics of natural convection in a non-Newtonian electromagnetohydrodynamics (EMHD) dissipative flow. Their research focused on using the homotopy perturbation method (HPM) to do the analysis.

A theoretical investigation on heat transfer in a micro-channel under Arrhenius control was carried out by Hamza et al. (team of experts) [15]. Their main focus was on how an artificial magnetic field affected natural convection.

In a composite channel that was partially filled with a porous material, Ajibade et al. [16] (research collaborators) conducted a thorough analysis of the effects of both viscous and Darcy dissipations on fully developed natural convection flow. They used HPM for analysis as part of their research technique.

In order to account for convective boundary conditions, Ray et al. [17] studied the non-similar solution of fluid flow and heat transfer for Eyring-Powell fluids. In their analysis, they used the homotopy analysis method (HAM).

Many studies [18–20] focus on the optimization of secondary energy sources in hydrostatic drive systems, which is relevant to machinery operating in tight spaces. In these specific operating circumstances, this study emphasizes the benefits of energy efficiency and custom technical solutions. The second collaborative study investigates the effect of blade design on fan efficiency using cutting-edge prototyping methods. These in-

sights have an effect on a number of applications, such as ventilation, HVAC and cooling systems, and can increase the performance of fans. Increasing the maximum speed of underground suspended monorails is an essential part of safe crew mobility in the challenging environment of Polish underground mining. In mining, operational efficiency and safety are crucial, and this research looks into realistic approaches to achieve both. The fourth study evaluates a special energy recovery system created especially for hybrid cars in order to satisfy the pressing need for enhanced energy efficiency and sustainability within the automotive sector. By giving experts and researchers insightful information, these countless study discoveries significantly advance their respective fields.

In this study, we examine temperature and concentration gradient-driven unsteady free convection flow between two parallel plates. To take into consideration non-integer order derivatives in the equations, fractional order Caputo derivatives are introduced. Solving these difficult fractional differential equations and comprehending their ramifications for real-world applications are the main goals of the research. An important part of this inquiry involves validating and interpreting boundary conditions as well as taking into account their restrictions and potential future orientations.

This research introduces a fresh perspective by applying fractional calculus to transient free-convection flow in channels. It stands out due to the innovative use of OHAM, offering an efficient approach to complex fluid dynamics problems. The study's interdisciplinary potential, optimization focus and practical relevance make it a unique and impactful contribution to the field.

2. Materials and methods

Consider a free convective fluid that is incompressible, unstable, and flows between two parallel plates with a temperature gradient and mass diffusion, placed in the *xy*-Cartesian coordinate system. As seen in the image, one of the plates is fixed along the x-axis, while the *y*-axis is normal to the plate. Temperature and concentration variations have resulted in a free convection flow seen in Fig. 1.

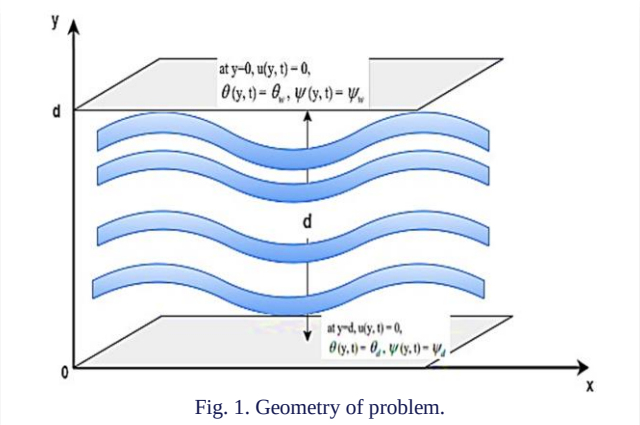


Fig. 1. Geometry of problem.

We make assumptions that at t ≤ 0, the plates as well as the fluid are at ambient concentration of ψ_d and temperature θ_d. At time t > 0, fluid concentration and temperature at $y = 0$ are altered to ψ_w and θ_w, respectively.

The governing equations for unsteady flow are derived from Boussinesq's approximations as:

$$u_t - \nu u_{yy} - g\beta(\theta - \theta_d) - g\beta^*(\psi - \psi_d) = 0; \quad (1)$$

$$\rho c_p \theta_t - k\theta_{yy} + q_{ry} = 0, \ \ y, t > 0, \quad (2)$$

where q_{ry} is radiative heat flux, and the above equation can be rewritten using the Roseland approximation:

$$\theta_t - \frac{k}{\rho c_p}\left(1 + \frac{16\sigma^*\psi_d^3}{3kk^*}\right)\psi_{yy} = 0, \quad (3)$$

where σ^*, ρ, k, k^* and c_p are Stefan-Boltzmann constant, density, thermal conduction, mean value of heat absorption parameter and specific heat with invariant pressure, respectively;

$$\psi_t - D\psi_{yy} + Kr(\psi - \psi_d) = 0, \quad (4)$$

where Kr is the chemical reaction parameter. The appropriate boundary conditions are:

$$t > 0: \ \ u(t,0) = 0, \ \ \theta(t,0) = \theta_w, \ \ \psi(t,0) = \psi_w, \quad (5)$$

$$t > 0: \ \ u(t,d) = 0, \ \ \theta(t,d) = \theta_d, \ \ \psi(t,d) = \psi_d. \quad (6)$$

Equations (1), (3) and (4), after using the appropriate dimensionless variables and parameters, become

$$u_t - u_{yy} - \theta - N_r\psi = 0, \quad (7)$$

$$\theta_t - \frac{1}{\mathrm{Pr}_{eff}}\theta_{yy} = 0, \quad (8)$$

$$\psi_t + \frac{1}{\mathrm{Sc}}\psi_{yy} - \frac{Kr}{\mathrm{Sc}}\psi = 0, \quad (9)$$

with dimensionless boundary conditions:

$$t > 0: \ \ u(t,0) = 0, \ \ \theta(t,0) = 1, \ \ \psi(t,0) = 1, \quad (10)$$

$$t > 0: \ \ u(t,1) = 0, \ \ \theta(t,1) = 0, \ \ \psi(t,1) = 0. \quad (11)$$

In Eqs. (8)–(10), we replace the time derivative terms with the time fractional order Caputo derivative; then we have:

$${}^{C}D_{0,t}^{\alpha}u(t,y) - u_{yy}(t,y) - \theta(t,y) - N_r\psi(t,y) = 0, \quad (12)$$

$${}^{C}D_{0,t}^{\alpha}\theta(t,y) - \frac{1}{\mathrm{Pr}_{eff}}\theta_{yy}(t,y) = 0, \quad (13)$$

$${}^{C}D_{0,t}^{\alpha}\psi(t,y) + \frac{1}{\mathrm{Sc}}\psi_{yy}(t,y) - \frac{Kr}{\mathrm{Sc}}\psi(t,y) = 0, \quad (14)$$

where ${}^{C}D_{0,t}^{\alpha}$ is the Caputo derivative defined as:

$${}^{C}D_{0,t}^{\alpha}f(t) = \frac{1}{\Gamma(n-\alpha)}\int_0^t (t-\tau)f^{(n)}(\tau)d\tau, \ \ 0 < \alpha < 1. \quad (15)$$

3. Implementation of OHAM

Equations (8) and (9) describe the optimal homotopy asymptotic approach (OHAM). To the best of our knowledge, Sarwar et al. [10], Sarwar and Rashidi [11] and Sarwar and Iqbal [12] firstly formulated this approach applicable to fractional order partial

differential equations. The key steps of OHAM for fractional order partial differential equations are as follows (for details we refer to [10–12]):

(a) construct the governing fractional order differential equation as follows (see Eq. (16)):

$$ {}^{C}D^{\alpha}_{0,t}u(r,t) = L\big(u(r,t)\big) + N\big(u(r,t)\big) + f(r,t), 0 < \alpha < 1, \quad , \tag{16}$$

with boundary condition $B(u, u_t) = 0$, where ${}^{C}D^{\alpha}_{0,t}$ denotes the Caputo fractional derivative operator defined in Eq. (15);

(b) construct an optimal homotopy $H(\psi; c_i)$, defined as $\psi(r, t; p): \Omega \times [0, 1] \longrightarrow R$ which satisfies Eq. (17)

$$H(\psi; c_i) = (1-p)\left({}^{C}D^{\alpha}_{0,t}\psi(r,t) - f(r,t)\right) - H(p; c_i)\times$$

$$\left({}^{C}D^{\alpha}_{0,t}\psi(r,t) - (L(\psi(r,t)) + (N(\psi(r,t)) + f(r,t))\right) = 0, \tag{17}$$

where $r \in \Omega$ and $p \in [0, 1]$ is an embedding parameter, c_i are convergence control parameters;

(c) expand $\psi(r, t; p, c)$ in Taylor's series about p, to get approximate solutions;

(d) equate the coefficients of like powers of p, if necessary, zeroth order, first order, second order, and higher order issues can be obtained;

(e) apply the fractional order integral operator on the obtained problems and with the boundary conditions and get the desired outcomes.

4. Numerical example

In this section, we will look for a solution to the problem (12–14) with boundary conditions (10–11). To begin the simulations, the following starting guesses are suggested: $u_0 = y - y^2$, $\theta_0 = 1 - y^2$, $\psi_0 = 1 - y^2$. The solution for the fractional concentration, temperature and velocity can be found in the form as below in Eqs. (18–20). These equations encapsulate the comprehensive understanding of the system's dynamics, offering insights into the interplay between various parameters and phenomena.

Results of Fractional Concentration Field:

$$\psi(t,y) = \frac{t^{\alpha}}{\mathrm{Sc}^3}\left[-\frac{2C_1(C_1^2+C_1+C_2)Kr\mathrm{Sc}t^{\alpha}\left((y^2-1)Kr+4\right)}{\Gamma(2\alpha+1)} + \frac{(C_2+C_1((C_1+1)^2+2C_2)+C_3)\mathrm{Sc}^2\left((y^2-1)Kr+2\right)}{\Gamma(\alpha+1)} + \frac{C_1^3Kr^2t^{2\alpha}\left((y^2-1)Kr+6\right)}{\Gamma(3\alpha+1)}\right]. \tag{18}$$

Results of Fractional Temperature Field:

$$\theta(t,y) = \frac{2(C_1(C_1(C_1+3)+3)-2C_2-C_3)t^{\alpha}}{\Gamma(\alpha+1)\mathrm{Pr}} - y^2 + 1. \tag{19}$$

Results of Fractional Velocity Field:

$$u(t,y) = y - y^2 + \frac{C_1(N_1(y^2-1)+y^2+1)t^{\alpha}}{\alpha\Gamma(\alpha)} + t^{\alpha}\left(\frac{(C_2+C_1((C_1+1)^2+2C_2)+C_3)(N_1(y^2-1)+y^2+1)}{\Gamma(\alpha+1)} - \right.$$

$$\left.\frac{\sqrt{\pi}2^{1-2\alpha}C_1t^{\alpha}\left(2\mathrm{Sc}\left((C_1^2+C_1+C_2)(N_1+1)\mathrm{Pr}+C_1^2+C_1\right)+(C_1^2+C_1+C_2)N_1\mathrm{Pr}\left((y^2-1)Kr+2\right)\right)}{\Gamma\left(\alpha+\frac{1}{2}\right)\Gamma(\alpha+1)\mathrm{ScPr}}\frac{C_1^3N_1Krt^{2\alpha}(2(\mathrm{Sc}+2)+(y^2-1)Kr)}{\Gamma(3\alpha+1)\mathrm{Sc}^2}\right) +$$

$$\frac{t^{\alpha}}{\Gamma(\alpha+1)}\left((C_1^2+C_1+C_2)(N_1(y^2-1)+y^2+1) - \frac{\sqrt{\pi}4^{-\alpha}C_1^2t^{\alpha}\left(N_1\mathrm{Pr}(2(\mathrm{Sc}+1)+(y^2-1)Kr)+2\mathrm{Sc}(\mathrm{Pr}+1)\right)}{\Gamma\left(\alpha+\frac{1}{2}\right)\mathrm{ScPr}}\right). \tag{20}$$

5. Analysis of OHAM

This research delves into the dynamics of transient, viscous, and incompressible flow in the absence of restrictions between two parallel upright plates. This research's main focus is identifying the length component. We consider the consequences of mass dispersion and thoroughly examine the uniform temperature distribution of the system.

We used an analytical strategy and OHAM to solve the resulting model, allowing us to identify the solutions for all boundary and beginning conditions. The research provided important new understandings of the temperature, concentration, and velocity expressions. These results are graphically shown in Chapter 6, allowing us to see and comprehend how these parameters varied over the flow domain. The system's complicated interactions between temperature, concentration, and velocity are made clearer by the graphical representation, which also highlights significant patterns and trends. We are able to fully comprehend the transient, viscous and free convective flow behaviour between the parallel plates by applying the OHAM technique to this particular issue.

This study offers a vital basis for future research and applications in the fields of engineering and science by adding to our understanding of fluid dynamics and convective heat and mass transfer.

6. Results

Figures 2–4 present the velocity, temperature, and concentration field behaviour. Figure 2 is diagrammed for varied effective Pr numbers against y by restricting t = 0.01 and α = 0.9 on the velocity. We can see that by increasing the Pr number, the velocity is decreased. In Fig. 3, as the Pr number increases, the

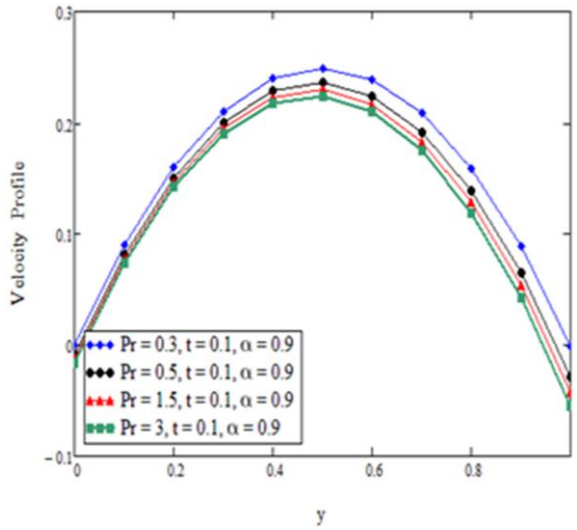


Fig. 2. Velocity profile for Sc = 0.22, N = 0.5, N_r = 1, Kr = 1.5.

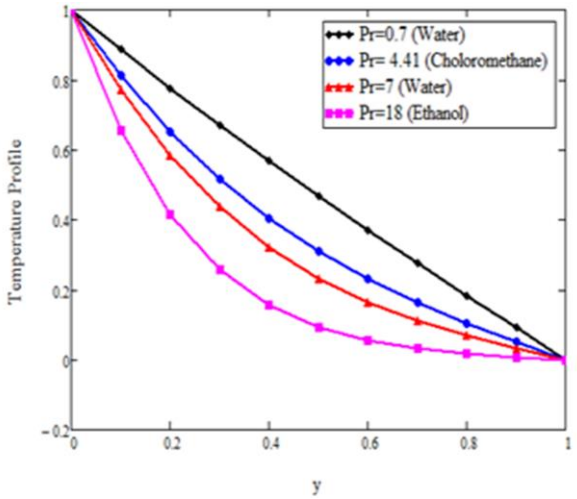


Fig. 3. Temperature profile for Sc = 0.22, N = 0.5, N_r = 1, Kr = 1.5.

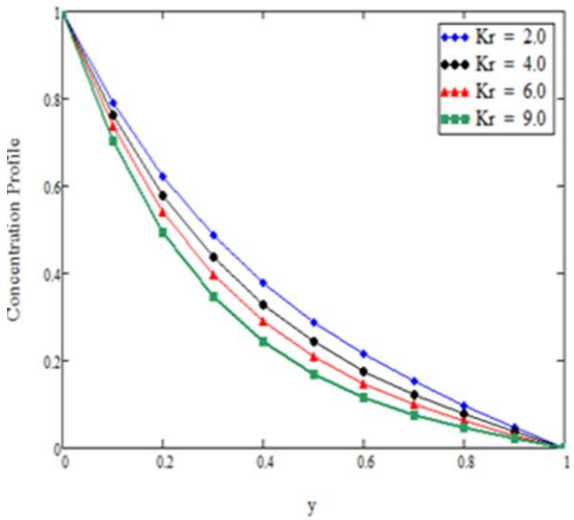


Fig. 4. Concentration profile for Sc = 0.22, N = 0.5, N_r = 1, Pr = 1.5.

Table 1. Values of convergence control parameters for velocity, temperature and concentration field at fractional order α = 0.9.

Parameter	u	θ	ψ
C_1	–1.0026	–2.77074	0.3003
C_2	–0.00001	–1.9757	–0.3247
C_3	–5.65601	–1.60073	–0.0121

liquid temperature decreases. Raising Pr, as expected, shortens thermic conduction and lowers the thickness of the caloric border layer due to its high viscosity. Figure 4 depicts the impact of the chemical reaction parameter *Kr*. It is apparent that as *Kr* increases, the flow concentration diminishes. Table 1 provides values of convergence control parameters.

7. Conclusions

The optimal homotopy asymptotic method (OHAM) is utilised in this paper to solve a new fractional model based on the Caputo derivative. In order to observe the heat and momentum boundary layer concentration thickness, the model includes a fractional-order parameter. The analysis demonstrates that the fluid temperature increases as time values increase and decrease. In contrast, the temperature drops when Pr (probably a related metric) increases in value. These results imply that higher temperatures in the system are caused by lower values and longer time periods. Additionally, the fractional parameter has a substantial impact on the concentration growth and increases noticeably with longer time values. The concentration rise becomes more obvious as the values drop. Along with the decreasing boundary layer thickness, the concentration also decreases with the increasing Schmidt number (Sc) and chemical reaction parameter (*Kr*) values. This implies that narrower boundary layers are produced as a result of suppressing the concentration growth at higher Sc and *Kr* values.

Overall, these research results offer insightful information on how the fractional-order parameter and other significant characteristics, such as fluid temperature, concentration and velocity affect the system's behaviour. These findings greatly advance our knowledge of fractional models and their prospective applications to fluid dynamics and related fields of study.

A fractional model is created using the Caputo derivative, and it is solved by a semi-analytical method OHAM. The concentration thickness of heat and momentum boundary layers is observed by the fractional-order parameter in this model. The fluid temperature falls for larger Pr. The concentration increases with decreasing fractional parameter values and increasing time values. Furthermore, the concentration decreases by increasing Sc and *Kr*, as well as the boundary layer thickness. The velocity increases by increasing the parametric values of N and time t, while it decreases by increasing Pr, *Kr*, and Sc.

Future research should investigate the influence of different fractional orders on transient free convection in channels and determine their practical significance. Additionally, the impact of nanofluids and non-Newtonian fluids on heat and mass trans-

fer should be examined, while optimizing channel designs. Collaborating across disciplines can enhance the practical relevance of the research.

References

[1] Marneni, N. (2008). Transient free convection flow between two long vertical parallel plates with constant temperature and mass diffusion. *Proceedings of the World Congress on Engineering*, II, 2-4 July, London, U.K.

[2] Harris, S.D., Ingham, D.B., & Pop, I. (1996). Transient free convection from a vertical plate subjected to a change in surface heat flux in porous media. *Fluid Dynamic Research*, 18, 313–324. doi: 10.1016/0169-5983(96)00025-1

[3] Harris, S.D., Elliott, L., & Ingham, D.B. (1998). Transient free convection flow past a vertical flat plate subject to a sudden change in surface temperature. *International Journal of Heat and Mass Transfer*, 41, 357–372. doi: 10.1016/S0017-9310(97)00136-1

[4] Sharma, R., & Ishak, A. (2013). Numerical simulation of transient free convection flow and heat transfer in a porous medium. *Mathematical Problems in Engineering*, 2013, 1–9. doi: 10.1155/2013/371971

[5] Sharma, R., Ishak, A., & Pop, I. (2013). Partial slip flow and heat transfer over a stretching sheet in a nanofluid. *Mathematical Problems in Engineering*, 2013, 1–7. doi: 10.1155/2013/724547

[6] Asjad, M.I., Danish Ikram, M., & Akgül, A. (2020). Analysis of MHD viscous fluid flow through porous medium with novel power law fractional differential operator. *Physica Scripta*, 95(11), 115209. doi: 10.1088/1402-4896/abbe4f

[7] Sarwar, S., Aleem, M., Imran, M. A., & Akgül, A. (2024). A comparative study on non-Newtonian fractional-order Brinkman type fluid with two different kernels. *Numerical Methods for Partial Differential Equations*, 40(1). doi: 10.1002/num.22688

[8] Marinca, V., & Herişanu, N. (2008). Application of Optimal Homotopy Asymptotic Method for solving nonlinear equations arising in heat transfer. *International Communications in Heat and Mass Transfer*, 35(6), 710–715. doi: 10.1016/j.icheatmasstransfer.2008.02.010

[9] Marinca, V., & Herişanu, N. (2010). Determination of periodic solutions for the motion of a particle on a rotating parabola by means of the optimal homotopy asymptotic method. *Journal of Sound and Vibration*, 329(9), 1450–1459. doi: 10.1016/j.jsv.2009.11.005

[10] Sarwar, S., Alkhalaf, S., Iqbal, S., & Zahid, M.A. (2015). A note on optimal homotopy asymptotic method for the solutions of fractional order heat- and wave-like partial differential equations. *Computers & Mathematics with Applications*, 70(5), 942–953. doi: 10.1016/j.camwa.2015.06.017.

[11] Sarwar, S., & Rashidi, M.M. (2016). Approximate solution of two-term fractional-order diffusion, wave-diffusion, and telegraph models arising in mathematical physics using optimal homotopy asymptotic method. *Waves in Random and Complex Media*, 26(3), 365–382. doi: 10.1080/17455030.2016.1158436

[12] Sarwar, S., & Iqbal, S. (2018). Stability analysis, dynamical behavior and analytical solutions of nonlinear fractional differential system arising in chemical reaction. *Chinese Journal of Physics*, 56(1), 374–384. doi: 10.1016/j.cjph.2017.11.009

[13] Ojemeri, G., & Hamza, M.M. (2022). Heat transfer analysis of Arrhenius-controlled free convective hydromagnetic flow with heat generation/absorption effect in a micro-channel. *Alexandria Engineering Journal*, 61(12), 12797–12811. doi: 10.1016/j.aej.2022.06.058

[14] Bhatti, M.M., Bég, O.A., Ellahi, R., & Abbas, T. (2022). Natural convection non-Newtonian EMHD dissipative flow through a microchannel containing a non-Darcy porous medium: Homotopy perturbation method study. *Qualitative Theory of Dynamical Systems*, 21(4). doi: 10.1007/s12346-022-00625-7

[15] Hamza, M.M., Ojemeri, G., & Ahmad, S.K.K. (2023). Theoretical study of Arrhenius-controlled heat transfer flow on natural convection affected by an induced magnetic field in a microchannel. *Engineering Reports: Open Access*, 5(8). doi: 10.1002/eng2.12642

[16] Ajibade, A.O., Gambo, J.J., & Jha, B.K. (2023). Effects of viscous and Darcy dissipation on fully developed natural convection flow in a composite channel partially filled with porous material: Homotopy perturbation method (HPM). *Zeitschrift fur Angewandte Mathematik und Mechanik*, 103(6). doi: 10.1002/zamm.202100583

[17] Ray, A.K., Vasu, B., Murthy, P.V.S.N., & Gorla, R.S.R. (2020). Non-similar solution of Eyring–Powell fluid flow and heat transfer with convective boundary condition: Homotopy Analysis Method. *International Journal of Applied and Computational Mathematics*, 6(16), 1-22. doi: 10.1007/s40819-019-0765-1

[18] Kędzia, K. (2022). A method of determining optimal parameters for the secondary energy source of a multisource hydrostatic drive system in machines working in closed spaces. *Energies*, 15(14), 5132. doi: 10.3390/en15145132

[19] Szelka, M., Drwięga, A., Tokarczyk, J., Szyguła, M., Szewerda, K., Banaś, M., Kołodziejczyk, K., & Kędzia, K. (2023). Study of the blade shape impact on the improvement of fan efficiency based on state-of-the-art prototyping methods. *Energies*, 16(1), 542. doi: 10.3390/en16010542

[20] Świder, J., Szewerda, K., Tokarczyk, J., Plewa, F., Grodzicka, A., & Kędzia, K. (2023). An overview of possibilities of increasing the permissible speed of underground suspended monorails for transporting people in the conditions of Polish underground mining. *Energies*, 16(9), 3703. doi: 10.3390/en16093703

Co-published by
Institute of Fluid-Flow Machinery
Polish Academy of Sciences
Committee on Thermodynamics and Combustion
Polish Academy of Sciences

Copyright©2024 by the Authors under licence CC BY 4.0

http://www.imp.gda.pl/archives-of-thermodynamics/

Simulations and techno-economic analysis of solar cooling system

Jacek Kalina[a*], Michał Rabiej[a*], Carlos Santos Silva[b]

[a]Silesian University of Technology, Faculty of Energy and Environmental Engineering, Konarskiego 18, 44-100 Gliwice, Poland
[b]Technical University of Lisbon, Mechanical Engineering Department, Alameda da Universidade, 1649-004 Lisboa, Portugal
*Corresponding author email: jacek.kalina@polsl.pl

Received: 17.10.2023; revised: 26.01.2024; accepted: 12.02.2024

Abstract

In this paper, a solar absorption cooling system with a chilled water storage tank and peak load compression system was considered for cooling the Instituto Superior Tecnico Tower building in Lisbon, Portugal. To fulfill this task, a dynamic simulation of the building was performed using the DesignBuilder software, then a solar collector field was designed. The next step was to build a computational model of the absorption chiller in the Engineering Equation Solver software, which allowed for further simulation of the annual operation of the system supported by the chilled water tank and the backup system with compressed air conditioning. The last stage of the work was the economic analysis of such a system in comparison with conventional compressed air conditioning. The simulation results and economic analysis showed that the solar absorption cooling system could be a beneficial cooling solution for the Instituto Superior Tecnico Tower building. However, it would have to operate with an energy storage system and a peak load compression backup system to be able to cool the building efficiently all year round. Additionally, such a solution could have a significant positive impact on climate through considerable annual savings in electricity consumption. Results revealed that the proposed system meets the cooling demand of the building, mainly by solar-energy-driven absorption chiller. The annual contribution of a backup compression chiller ranges from 20% to 36% depending on the size of chilled water storage tanks. Financial calculations revealed discounted payback periods in the range of 4.5 to 12.5 years depending on the system configuration.

Keywords: Solar cooling; Building simulation; Absorption chillers, Solar thermal collectors; Thermal energy storage

Vol. 45(2024), No. 2, 145–155; doi: 10.24425/ather.2024.150861

Cite this manuscript as: Kalina, J., Rabiej, M, & Silva, C.S. (2024). Simulations and techno-economic analysis of solar cooling system. Archives of Thermodynamics, 45(2), 145−155.

1. Introduction

In times of climate crisis, depletion of fossil energy sources, and global energy transition, in all branches of the global energy system solutions are sought for the reduction of fuel consumption and environmental impacts. The cooling sector is one of the sectors where the integration of renewable energy sources has been constantly increasing over the past several years [1]. Conventional and widely used grid-connected compression cooling systems can be replaced with heat-driven systems using absorption or adsorption chillers, PV-driven compression or thermoelectric technologies, and several other solutions [2]. Considering technology maturity and financial aspects of projects, in practice, absorption technology is usually taken into account as a feasible

Nomenclature

A – total aperture area, m^2
a_1 – first- order loss coefficient
a_2 – second-order loss coefficient
COP – coefficient of performance
G – solar irradiance, W/m^2
h – specific enthalpy, kJ/(kg K)
$\dot{m}$ – mass flow, kg/s
p – pressure, Pa
P – power, kW
$\dot{Q}$ – heat flux, kW
$\dot{Q}_{E,nom}$ – nominal cooling capacity, kW
$\dot{Q}_{G,nom}$ – nominal driving heat flux, kW
x – mass fraction, kg/kg

Greek symbols

η_0 – zero loss efficiency
ΔT_{sol} – temperature difference, K
υ – specific volume, m^3/kg

Subscripts and Superscripts

1, 2, … , 18 – specific points in the plant scheme
ch – cooling
C – condenser
E – evaporator
G – generator
nom – nominal
max – maximum
w – water

Abbreviations and Acronyms

COP – Coefficient of Performance
EES – Engineering Equation Solver
IST – Instituto Superior Tecnico
NPV – Net Present Value
PV – Photovoltaic
SPB – Simple Payback

solution. Although the coefficient of performance (COP) of the absorption cooling devices (typically in the range of 0.7 to 1.2) is significantly lower than in the case of conventional vapour compression chillers (typically above 3.0), the key advantage of absorption technology is much lower electricity consumption and peak power demand. As electric grids become affected more strongly by cooling systems due to hotter weather conditions [1], solar cooling projects can also generate positive external systemic effects. Additionally, as sorption chillers use natural refrigerants only, they can effectively support the fluorinated gases (F-gas) phase-out [1].

The single-effect LiBr absorption chillers require hot fluid at a temperature higher than 70−80ºC, which can be achieved by solar collectors. At this temperature level, commercially available technology solutions can achieve a COP of around 0.7. Higher values of the COP can be reached at higher inlet temperatures of the heat carrier, depending on the configuration of the absorption chiller system. The noticeable disadvantage is however relatively large size of the cooling unit. Although sorption cooling can be implemented starting from 100 kW of cooling capacity [1], typical applications are considerably bigger. Typical places of implementation are skyscrapers, large office buildings, shopping centers, industrial facilities, hospitals, etc. Examples are [3]: Surgery Hospital for children in Soba (Sudan) where a 2 × 615 kW absorption chiller and 12 000 m^2 solar field were installed, the United World College in Singapore with 1 470 kW of cooling capacity absorption system and the 3 900 m^2 field of solar collectors, the METRO Cash Carry in Rome (Italy) with absorption chillers of 700 kW of cooling capacity, or the office building of the bank Caixa Geral de Depositos in Lisbon (Portugal), which is cooled by an absorption system of 585 kW cooling capacity driven by hot water from the 1 592 m^2 rooftop system of 158 solar collectors of 845 kW heating capacity.

Although the technologies and implementation examples are already known, solar cooling is still a relatively rare solution. This is mainly due to the low level of dissemination, and lack of relevant information regarding the long-term effects and bankability of projects. According to Delmastro et al. [1], the number of newly installed solar-driven systems can be estimated for 1 800 small units in 2018. Nowadays broad measures are required for affordable, safe, and reliable cooling systems for the sunbelt regions worldwide, including the development of innovations, adaptation of components and systems, demonstration, assessment tools, and dissemination [4]. According to the definition of the research topic “Solar Cooling Technologies: Challenges, Applications, and improvements” of the Frontiers Open Access Publisher and Open Science Platform [5] it is necessary to recognize the main advantages, challenges, disadvantages, and feasibility of different solar cooling technologies, and the area of interest, among other issues, includes simulation, modelling and techno-economic analysis of solar cooling systems.

Regarding research activities in the field of solar cooling different projects and studies have been reported in the published literature. For example, Assilzadeh et al. [6] proposed a solar cooling system with evacuated tube solar collectors and LiBr absorption unit for a building in Malaysia. The system was optimally sized using the TRNSYS software and the typical meteorological year weather data. The optimal key system design parameters were: 3.5 kW (1 refrigeration ton) chiller, 35 m^2 evacuated tubes solar collector sloped at 20º and 0.8 m^3 hot water storage tank. The results revealed that life cycle savings generated by the system against conventional air conditioning were negative, which was due to the high cost of the solar collectors and the low price of electricity.

Narayanan [7] presented a simulation-based study on absorption solar cooling systems and their application in commercial/office buildings in India. A typical Indian commercial building of 1 156 m^2 floor area and 289 m^2 roof area was simulated using TRNSYS software in order to examine feasibility and operational strategy of the cooling system. The results revealed that the proposed solar absorption cooling system in comparison to a traditional air conditioner unit will achieve full payback time after 15.5 years. According to the author, this period may vary depending on climate and the cooling demand.

However, the author drew attention to the high initial installation costs, which for the system with 105 kW cooling capacity chiller, 20 m^3 heat storage tank, and 42 evacuated tube collectors of 220 m^2 total area was estimated at 81 650 USD.

Similarly, Praene et al. [8] considered the possibility of implementing a single-stage solar absorption system for classroom cooling in Reunion Island, where the yearly average solar radiation and is 5.4 kWh/m^2/day. The system simulation and optimization were performed using TRNSYS to determine the optimum solar energy collector area, storage tank volume and absorption chiller nominal capacity of 60 m^2, 0.8 m^3 and 33 kW, respectively. The author did not provide information on system economics.

Iranmanesh et al. [9] presented results of the optimization of a solar cooling system with a 350 kW (100 t of cooling capacity) double-effect LiBr–H_2O absorption chiller using a combined EES - MATLAB software environment. It was infeasible to operate a solar double-effect absorption chiller without any auxiliary energy source to provide the required energy for the chiller at most hours during the day. Therefore, two objective functions were defined, namely the amount of auxiliary energy consumed and net profit. The input parameters taken into account in the sensitivity analysis are the volume of the storage tank, the area of the evacuated tube collector, and mass flow rates of water passing through the collector and generator. The results revealed very positive financial performance with the investment return period from 1.79 to 2.75 years.

Pinamonti et al. [10] investigated different configurations of solar-assisted heat pump systems in combination with energy storage for a typical single residential dwelling in Italy of 140 m^2 heated floor area and a ratio of heat dispersion area over conditioned volume (S/V) of 0.59. The study was focused on factors influencing energy demand of the system, self-consumption of solar energy, and installation cost. Several configurations of the system were simulated using the TRNSYS software. The proposed solution was compared to a standard air-source heat pump. The results revealed that for a highly insulated building, a maximum reduction of energy consumption at the level of -30% could be achieved in the case of photovoltaic (PV) panels and battery storage. On the other hand, in the case of solar thermal (ST) panels the achievable energy savings are lower (−24%), however, financial benefits are more advantageous over a 20-year period. The solution based on ST panels appeared to be the most profitable solution also for a low-insulated building. The results also revealed that the role of energy storage is essential.

Altun et al. [11] investigated the parameters of a 10 kW solar-powered absorption cooling system using dynamic modelling under the weather conditions of Mugla, Trabzon, Izmir, Konya, Canakkale and Istanbul using the TRNSYS software. In most of the studied cases, the results of the financial analysis revealed the payback periods between 10.7 and 15.0 years.

Drosou et al. [12] proposed the implementation of an integrated solar cooling system using parabolic trough solar collectors and a double-effect chiller is discussed, used to cover the cooling needs of a typical office building in Greece. The results of the study revealed that concentrating solar collectors give significantly higher output temperatures that can enable the use of two-stage absorption chillers with a higher COP. Unfortunately, although the costs of major system components were assessed, the level of project profitability was not determined.

Eicker et al. [13] presented the results of a systematic solar cooling system design study covering most climatic regions worldwide and different cooling technologies. According to the study, single-effect absorption cooling systems easily reach 80% solar cooling fraction for all but very humid climates, and primary energy savings between 30 and 79%, depending on system design and cooling load data. The economic analysis revealed that solar thermal cooling and heating are more viable in hot climates than in moderate European climates, and in order to obtain reasonable payback periods in the range of 10 years significant investment cost reductions are required.

Casals [14] performed a detailed TRNSYS dynamic simulation of some of the first commercial solar heating and cooling installations implemented in Spain. He claims that due to the low fraction of profitable thermal storage capacity in the cooling season, very high storage volumes would be required to significantly decouple the solar field and the absorption chiller. He also concluded that limited effective storage capacity should be compensated as far as possible with appropriate design choices (solar multiple and solar field mass flow), and implementing high inertia air conditioning distribution systems like radiant floors or walls which regularize the cooling load imposed on the solar absorption system.

Ge et al. [15] presented a literature review summarizing the current situation of solar heating and cooling and discussed new achievements in related areas and potential future market penetration. According to the authors, the investment payback period is widely adopted to evaluate economic performance. Results reveal that solar cooling systems can be economically attractive with payback periods varying from 3 to 15 years.

Palomba et al. [16] developed. an advanced hybrid solar cooling system, which consists of a thermal and an electric unit in parallel integrated into a single unit with the dry cooler. They also presented the results of sizing for the same building in three different climates (Athens, Berlin and Ryiad). The configuration of the solar cooling system included a solar field of 40 m^2 in combination with a 1 000-litre hot water tank corresponding to a specific storage ratio of 25 l/m^2. The authors claimed that larger storage volumes do not affect the performance of solar cooling systems significantly. The results revealed annual energy savings in the range from 35% in Riyadh to 89% in Berlin, which well justified replacing traditional cooling systems with solar-powered ones.

The aim of this study is to assess whether an absorption cooling system with solar collectors as a heat source would be an advantageous solution for a university building compared to a typical vapour compression cycle air conditioning system. To examine this, the annual simulations of both the solar absorption cooling system and the vapour compression cooling system were carried out for the Instituto Superior Tecnico (IST) Tower in Lisbon using the DesignBuilder software [17]. In the first

step, the dynamic model of the building was created, which resulted in cooling demand data on hourly basis. In the next step, a field of solar thermal collectors was simulated to determine possible heat output profile. Then a calculation model was prepared which firstly calculated the design parameters of the absorption chiller and later simulated the annual performance of the system. Within the model the chiller correction curves and solar field data of commercially available equipment were used. Subsequently, the energy storage system was modelled and sized for the installation. In the case of the solar cooling system, a backup vapour compression chiller was taken into consideration, which allowed the system to operate in the absence of solar energy or insufficient cooling capacity produced by the absorption chiller. Dimensions and costs of the whole installation were assessed for 2020 energy prices. Finally, the two alternative solutions of the building cooling system were compared using economic indicators, such as net present value (NPV), net present value ratio (NPVR), internal rate of return (IRR), discounted payback period (DPB), and simple payback (SPB), which presented economic justification for the project.

1. The IST Tower building simulation

The IST Tower building is located in Lisbon, Portugal (38º44´N, 9º08´W). This is a 10-story high-rise building of 50 m height. Its facade material is glass. The building is not equipped with external blinds. inside It entered into exploitation in 1994 as a university building. The building is depicted in Fig. 1.



Fig. 1. IST Tower building (Source: Google Earth: https://earth.google.com/web/).

To determine energy demand profiles, the building was modelled using the DesignBuilder software [17]. The software allows creation of complex building models in a user-friendly and intuitive manner. It uses EnergyPlus™ [18] whole building dynamic energy simulation program as calculation engine software and simulates building thermal conditions over a long time. In this work, the annual simulation of the IST Tower building performance was carried out. The building model is depicted in Fig. 2.

The occupied floor area of the designed building was equal to 7 994.5 m^2 and the occupied volume 100 768.5 m^3. Lightweight concrete clad wall was selected as an external walls material. The interior of the building was divided with walls in order to take into account its thermal inertia. Occupancy density was set to 0.111 people/m^2, fresh air flow was 10 dm^3/s per person, and the power density of office equipment was set to 11.77 W/m^2. Light office work was used as the occupation scenario of the building. The cooling setpoint temperature was 24°C and the cooling set back temperature was set to 28°C.

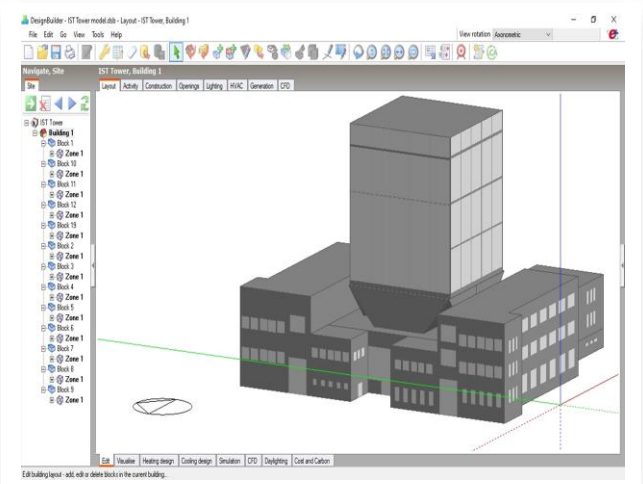


Fig. 2. IST Tower building model in the DesignBuilder.

The weather data for Lisbon in hourly resolution was obtained from a publicly available weather data repository for the typical meteorological year (TMY), which was imported by the weather data import tool of the DesignBuilder software. Figures 3 and 4 depict the annual variability of the ambient temperature and solar irradiation for the site. The analysis of data revealed that the annual values of temperature and solar irradiation are very high and promising for the use of solar technologies to generate energy. The average annual ambient temperature was equal to 16.32°C, while the maximum was 36°C and the temperature did not fall below 4.1°C. As far as irradiation is concerned, the annual average was 397 Wh/m^2 (excluding fully cloudy conditions and nights) or 196.01 Wh/m^2 (taking into account every hour of the year).

As a result of the simulation, the necessary hourly data was obtained for cooling demand and heating demand of the building. The DesignBuilder software also enabled calculation of the demand for electric power for needs for heating system, conventional air conditioning system (vapour compression), and domestic hot water. The annual profile of the cooling demand is depicted in Fig. 5. Figure 6 depicts the annual cooling demand duration curve revealing relatively sort annual time of cooling system operation (in the range of 2500 hours per year).

During the hottest hours cooling demand did not fall below 800 kW and the peak values exceeded 1 550 kW. It was also found that the demand for cooling also occurs during colder months. In January and December, the temperature dropped down to 4°C but sometimes values as high as 17°C registered, and the cooling demand reached at some hours 250 kW. An important factor for the operation of the air conditioning system was that all the spring months (especially May) and early autumn months (especially September) there may occur very high temperatures (up to even 32°C), and at the same time high demands for cooling.

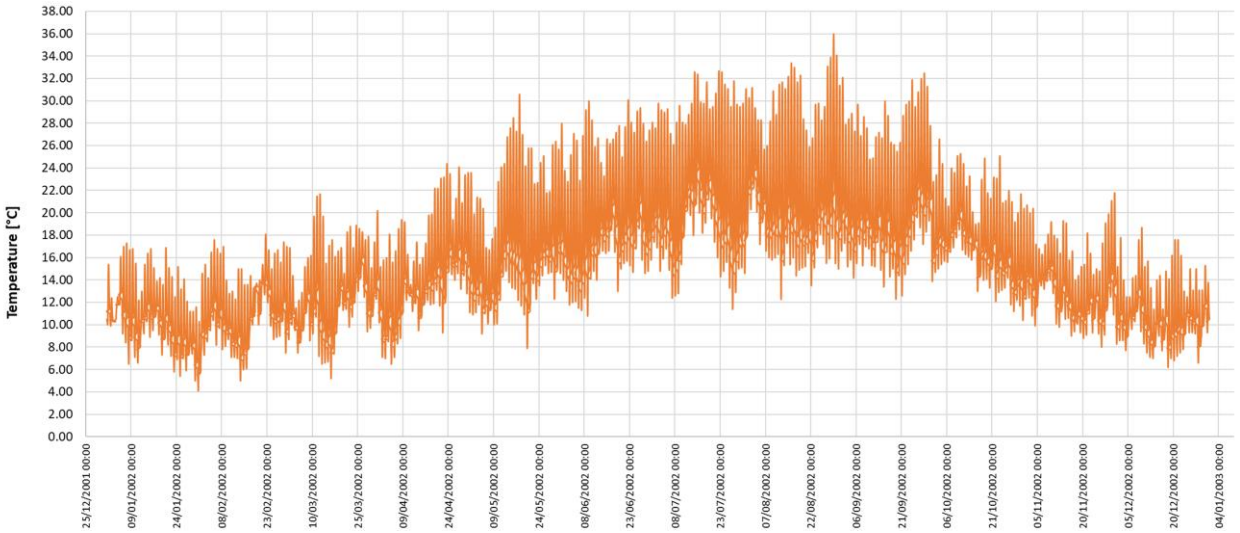


Fig. 3. Annual dry bulb temperature variations in Lisbon.

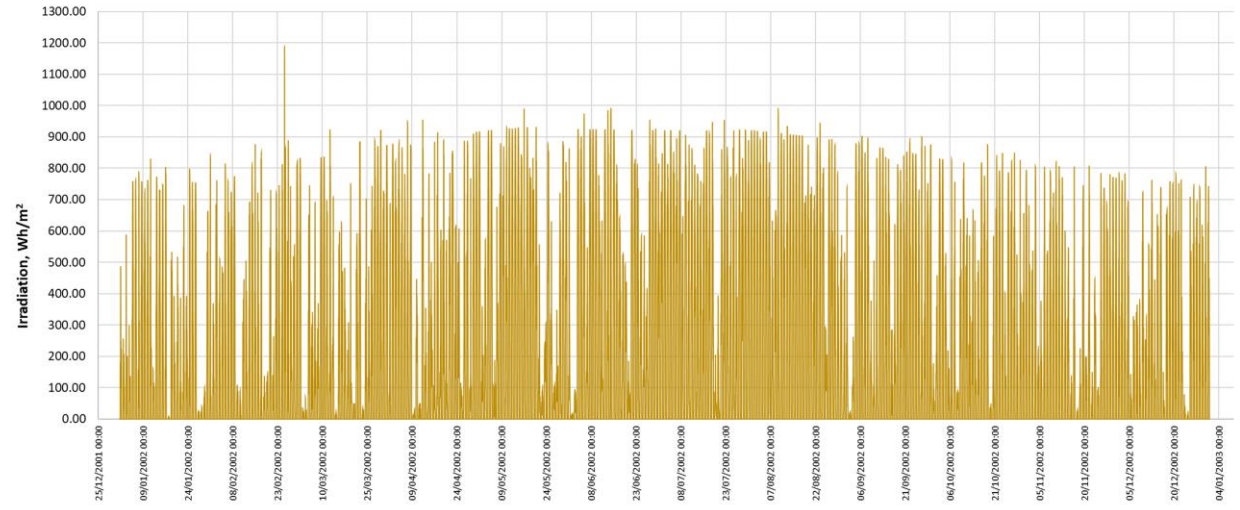


Fig. 4. Annual variations of solar irradiation in Lisbon.

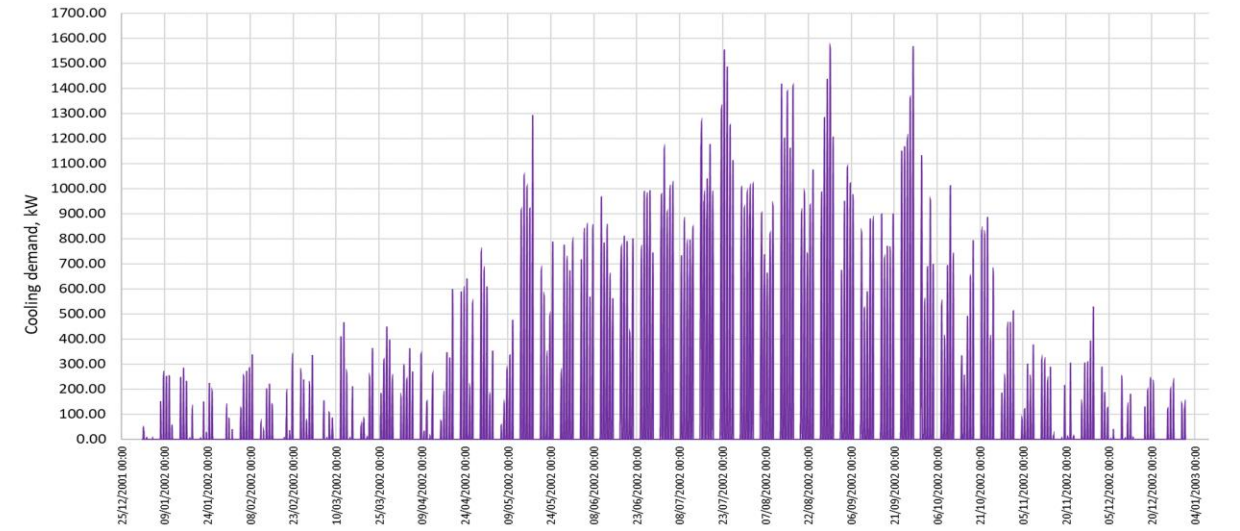


Fig. 5. Annual cooling demand profile.

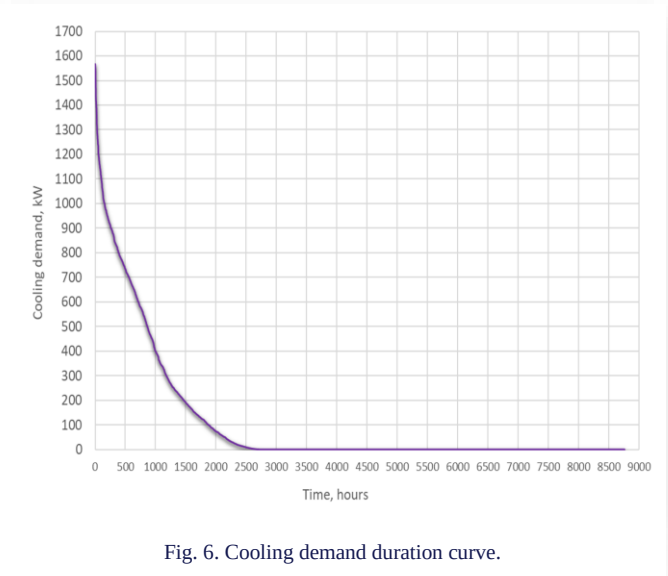


Fig. 6. Cooling demand duration curve.

2. Design and characteristics of solar collectors and solar field

It was assumed that the driving heat for the absorption chiller would be generated by solar collectors. The solar field was designed on the roofs of the IST buildings. The obtained value of the available space for the solar collectors' field was 3 056.8 m^2. For the calculation of the total aperture area, the land use coefficient was assumed to be 2.5. Arcon-Sunmark A/S HT- SolarBoost 35/10 collectors [19] were adopted as the solar collectors for the entire installation. Technical specification of the collector is given in Table 1.

The available roof area allowed for the placement of 225 solar collectors, which gave 3 053.25 m^2 of collector aperture area. The peak power of such a field at solar irradiance G = 1 000 W/m^2 would be around 2 366.8 kW. The heating power of the solar collector was calculated using the formula:

$$\dot{Q} = A \cdot (\eta_0 G - a_1 \Delta T_{\mathrm{sol}} - a_2 \Delta T_{\mathrm{sol}}^2), \quad (1)$$

where: A – total aperture area, η_0 – zero loss efficiency, G – solar irradiance, a_1 – first- order loss coefficient; a_2 – second-order loss coefficient; ΔT_{sol} – temperature difference between the average temperature of the solar fluid and ambient temperature.

Table 1. Parameters of Arcon-Sunmark A/S HT-SolarBoost 35/10 solar collector.

Parameter, unit	Value
Gross area, m^2	13.57
Gross length, m	26
Gross width, m	26
Gross height, m	0.24
Zero-loss efficiency (η_0)	0.773
First order loss coefficient (a_1), W/(m^{2}K)	2.27
Second order loss coefficient (a_2), W/(m^{2}K^2)	0.018
Peak power (at G = 1000 W/m^2), kW.	10.519

Solar collector field simulation was performed in MS Excel to determine the heat flux that can be transferred to the absorption chiller generator. The collector water inlet/outlet temperature was assumed 80/90°C taking into consideration the requirements of the absorption chiller. Results are depicted in Fig. 7. The maximum value of the collector field throughout the year was 2 080.15 kW. The annual average of obtained heat was equal to 240.68 kW (770.87 kW – excluding hours during the night and periods without any thermal energy obtained from solar collectors).

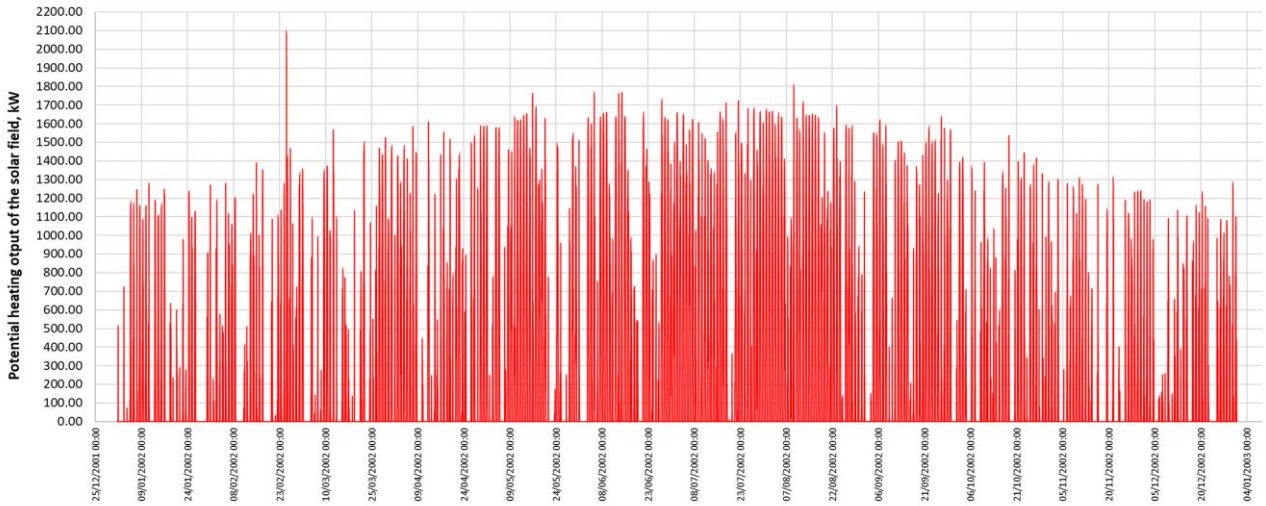


Fig. 7. Results of solar collector field simulation – hourly.

3. Sizing of solar absorption cooling system

The proposed cooling system is depicted in Fig. 8. The main part of the installation is the absorption chiller. A hot water-driven lithium bromide/water (LiBr/ H_2O) system was assumed as a typical solution for air conditioning applications [20]. The chiller is interconnected with the field of solar collectors,

a chilled water cycle with cold storage reservoir and cooling water cycle. For cooling the absorber and condenser of the chiller, a wet cooling tower is taken into consideration. The cooling water temperature for Portugal was set to 31°C [21]. The constant chilled water inlet/outlet temperature of 12.2°C/6.7°C was assumed according to technical specifications [22]. To provide cooling during unfavourable weather conditions and exceptionally high cooling demand, chilled water storage was designed. The reservoir sizing was performed taking into account cooling demand as well as the financial profitability of the project.

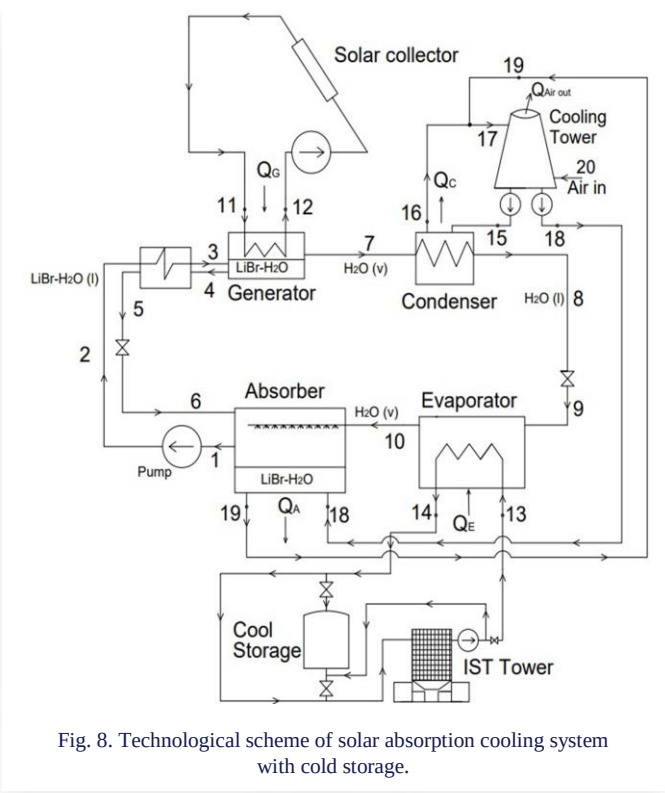


Fig. 8. Technological scheme of solar absorption cooling system with cold storage.

The absorption chiller was modelled using Engineering Equation Solver (EES) software and its built-in LiBr/H_2O thermodynamic properties library. Energy balance for the absorber is:

$$\dot{Q}_A = \dot{m}_{10}h_{10} + \dot{m}_6h_6 - \dot{m}_1h_1. \quad (2)$$

The heat of absorption is removed by cooling water, what gives:

$$\dot{Q}_A = \dot{m}_{19}h_{19} - \dot{m}_{18}h_{18}. \quad (3)$$

The energy balance of generator:

$$\dot{Q}_G = \dot{m}_4h_4 + \dot{m}_7h_7 - \dot{m}_3h_3. \quad (4)$$

In the condenser where the H_2O vapour from generator is cooled down and subjected to the condensation process, energy balance was as follows:

$$\dot{Q}_C = \dot{m}_7h_7 - \dot{m}_8h_8. \quad (5)$$

And from the side of cooling water it is:

$$\dot{Q}_C = \dot{m}_{16}h_{16} - \dot{m}_{15}h_{15}. \quad (6)$$

Energy balance of the evaporator, where cooling effect occurs is:

$$\dot{Q}_E = \dot{m}_{10}h_{10} - \dot{m}_9h_9. \quad (7)$$

Energy balance of the regenerative heat exchanger is:

$$\dot{m}_4h_4 - \dot{m}_5h_5 = \dot{m}_3h_3 - \dot{m}_2h_2. \quad (8)$$

The mass flow of chilled water was calculated from energy balance:

$$\dot{m}_{w,ch} = \frac{\dot{Q}_E}{h_{13}-h_{14}}. \quad (9)$$

The required mass of water from the solar collectors to the generator was calculated as:

$$\dot{m}_{w,G} = \frac{\dot{Q}_G}{h_{11}-h_{12}}. \quad (10)$$

The thermodynamic model also takes into account the operation of the pump in the absorption chiller:

$$P_{\text{pump}} = \dot{m}_1v_1(p_2 - p_1). \quad (11)$$

Moreover, considering steady state energy for expansion and refrigerant valves and mass conservation equations, the following enthalpies relations are:

$$h_5 = h_6, \quad (12)$$

$$h_9 = h_8. \quad (13)$$

LiBr concentration balance for generator is:

$$\dot{m}_3x_3 = \dot{m}_4x_4. \quad (14)$$

Concentration in other points of the system is:

$$x_2 = x_1, \quad (15)$$

$$x_3 = x_1, \quad (16)$$

$$x_5 = x_4\,, \quad (17)$$

$$x_6 = x_4, \quad (18)$$

$$x_8 = x_7, \quad (19)$$

$$x_9 = x_7, \quad (20)$$

$$x_{10} = x_9. \quad (21)$$

Additionally, the following parameters were assumed:

- temperature difference between the cooling water before/after condenser: 6 K,
- pinch temperature difference in the absorber, generator, condenser, and evaporator: 3 K.

The coefficient of performance is defined as:

$$COP = \frac{\dot{Q}_E}{\dot{Q}_G}. \quad (22)$$

From the thermodynamic point of view the definition of COP should also account for the pump work P_{pump}. However, the standard approach used by manufacturers is to present COP

as the ratio of the cooling effect to the heat input, where the work used by the pump is neglected, the same as power used by electronics. This is mainly because relatively low electricity consumption. The EES model results for design parameters of the absorption chiller are presented in Table 2.

Table 2. Key design parameters of the absorption chiller.

Parameter	Symbol	Unit	Value
Nominal cooling capacity	$\dot{Q}_{E,nom}$	kW	622.5
Absorption heat flux	$\dot{Q}_A$	kW	826.1
Condensation heat flux	$\dot{Q}_C$	kW	660.0
Nominal driving heat flux	$\dot{Q}_{G,nom}$	kW	863.7
Pump work	P_{pump}	kW	0.02
Total heat inlet	$\dot{Q}_E$+$\dot{Q}_G$	kW	1 486.0
Total heat outlet	$\dot{Q}_C + \dot{Q}_A$	kW	1 486.0
Design coefficient of performance	COP	–	0.72

An important aspect of the system design is sizing the absorption chiller in relation to the heating output of the solar field. The number of working hours of the chiller results from availability of the driving heat flux and the demand for cooling. It can be observed in Fig. 7 that the maximum heating output of solar collectors occurs in a very short annual time as a peak value. The minimum thermal load of the absorption chiller was set to 55% of nominal heat input. It has to be emphasised that sizing of the absorption chiller was performed assuming that its nominal of heating power input (output from the solar field) is:

$$\dot{Q}_{G,nom} = 0.4\dot{Q}_{max}. \tag{23}$$

This assumption results in 1871 chiller working hours per year. The operation window of the absorption chiller is depicted in Fig. 9. The higher is the nominal capacity of the chiller, the shorter is its annual time of operation. The heat which is not used by the chiller is presented in the results of the study as the unused heat. Actually, the nominal cooling capacity of the chiller should by subject to optimisation, which is foreseen as a future work. The study also reveals the demand for heat management and storage of hot water from the solar field.

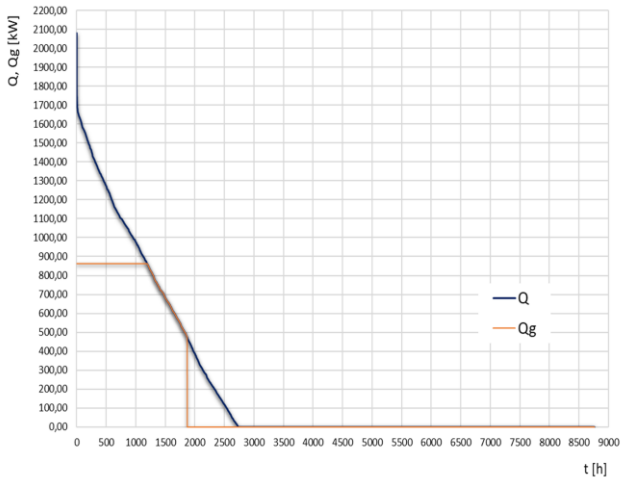


Fig. 9. Duration curves of heat output from the solar field and heat input to the absorption chiller.

In off-design calculations of the absorption chiller correction curves were used. Those were adopted from manufacturer data of the WFC-M100 Yazaki Energy absorption chiller [22]. The cooling capacity of the unit was then:

$$\dot{Q}_E = (0.0048 \cdot \dot{m}_{w,G} + 0.534)\dot{Q}_{E,nom}, \tag{24}$$

where $\dot{m}_{w,G}$ is the actual mas flow of hot water into the generator.

3. Simulation of integrated cooling system

Using design calculations, correction curve and solar collector field simulation, it was possible to perform an annual simulation of the absorption cooling system performance. The key parameters determining the efficiency as well as the legitimacy of using such an installation were the COP values and the generated cooling effect which should meet the building's demand. Sample daily COP values for the absorption system, which result from weather conditions are depicted in Fig. 10.

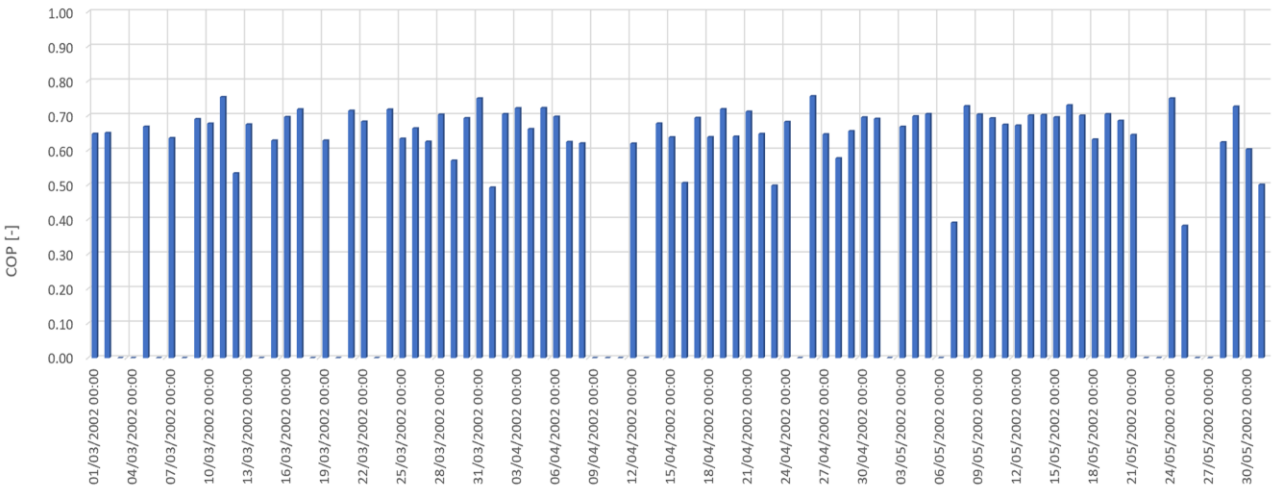


Fig. 10. Achievable values of COP in the spring period (March – May).

It was found that the absorption cooling system with solar collectors as a heat source was not able to provide cooling for the building every hour of the year. To solve this issue heat storage or cold storage system was necessary. In this work, the system with chilled water storage and additional compressor chiller as a backup unit was considered. Three different maximum energy storage tank capacities were considered: 2 500 kWh (392 m^3), 5000 kWh (784 m^3) and 12 500 kWh (1 958 m^3). It must be emphasised that the study does not present an optimization problem but only enables the identification of potential issues related to the operation of the proposed system. Therefore the proposed sizes are just trial values, which enable observation of the trends. The optimisation task has been left for the future work.

As for the principle of operation of the entire solar absorption cooling system with a chilled water storage and backup system of a compressor chiller, the cooling capacity required for the building was the main input to calculate the compressor energy balance. Priority was given to the system of the absorption chiller and chilled water tank, and the compressor chiller balanced the cooling capacity with the cooling capacity required by the building. Results of annual simulation for 5 000 kWh storage tank are depicted in Fig. 11. Summary of annual results for three different systems is given in Fig. 12.

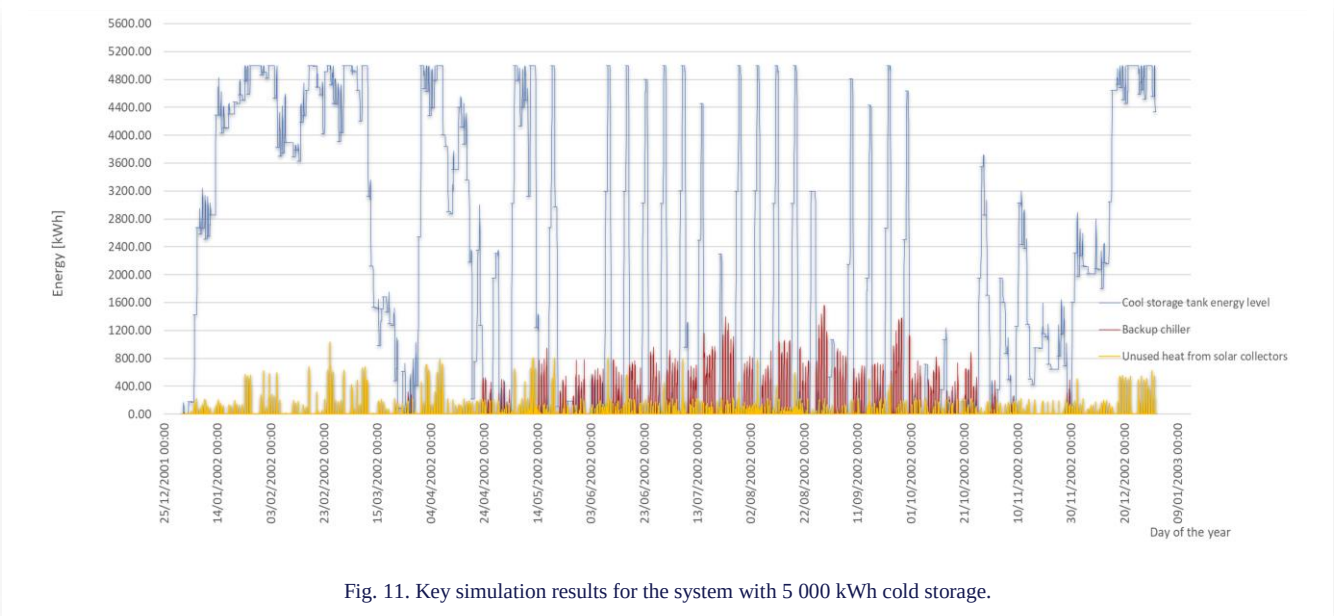


Fig. 11. Key simulation results for the system with 5 000 kWh cold storage.

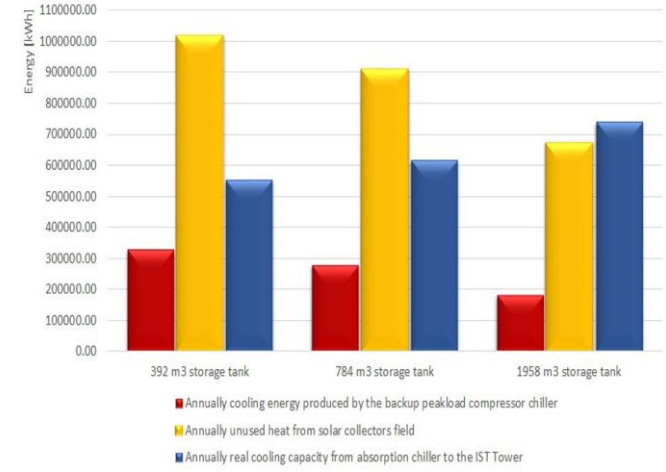


Fig. 12. Summary of key results of annual energy simulation.

In order to limit the unused solar energy throughout the year, a configuration with a smaller collector field (the number of solar collectors has been reduced to 112) and 784 m^3 storage tank was simulated and economic indicators were calculated. This configuration resulted in the reduction of the active field area of the solar collectors to 1 519.84 m^2. The cooling capacity of the absorption chiller was downsized from 622.5 kW to 331.9 kW.

The solution also takes into account the situation in which the conventional air conditioning system has been already installed, so it could be used as backup system, and its initial capital cost would be 0. The key to such a system was to calculate again design parameters of the absorption chiller, which had to be lower than originally assumed due to the operating range of the absorption chiller. Simulation results for this case are presented in Fig. 13.

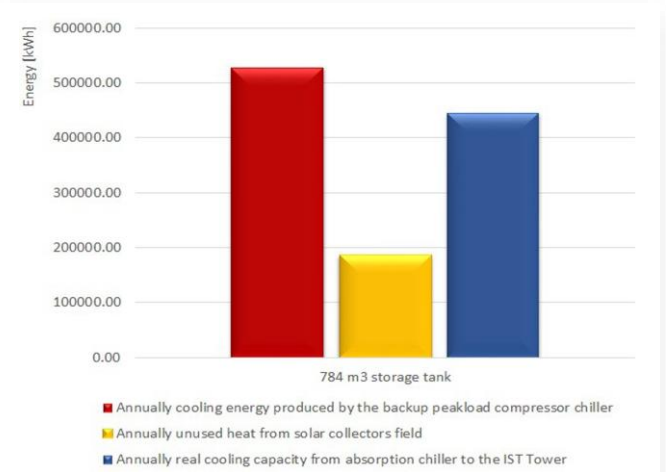


Fig. 13. Summary of key simulation results for downsized solar field.

4. Project profitability assessment

Undoubtedly, the initial capital costs of classic air conditioning system are lower than absorption cooling systems. However, savings in electricity consumption due to the new cooling system could be so significant that, with a long-term investment, the absorption solar cooling system can turn out to be a profitable investment, especially for a large-scale building, such as the IST tower. The economic analysis of the solar absorption cooling system was carried out with reference to the conventional vapour compression cycle air conditioning system. Thus, the annual cash flow was due to the lower operating costs of the system. The considered lifetime of the project was 20 years. The cost of electricity was assumed € 0.147/kWh. The capital costing model was adopted from [23]. The absorption cooling system cost was assessed to be € 159 982.50 and in the case of vapour compression refrigeration units it amounts to € 491 222.88. Additionally, for the absorption cooling system the costs of 784 m^3 chilled water reservoir (€ 98 000.00), cooling tower (€ 99 447.38), solar collectors installation (€ 405 000.00), piping, valves, controllers, pumps (€ 66 298.25) and evaporative condenser installation (€ 47 040.85) were added. Key results of the profitability assessment for the three initial cases are shown in Figs. 14 to 16.

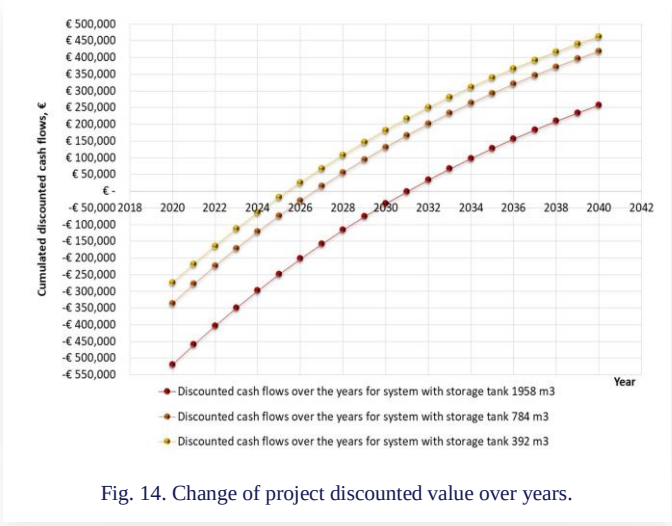


Fig. 14. Change of project discounted value over years.

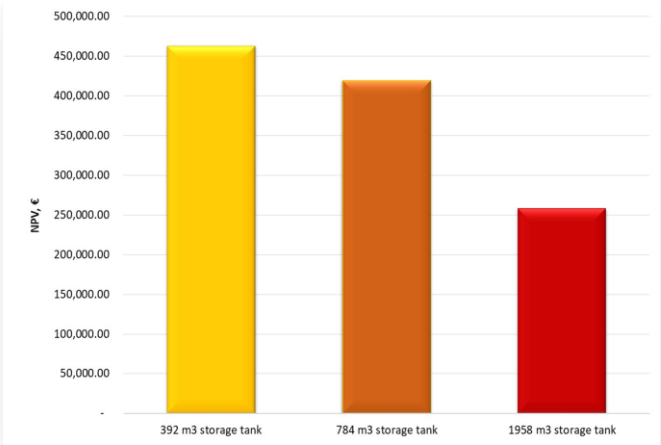


Fig. 15. NPV assessment results.

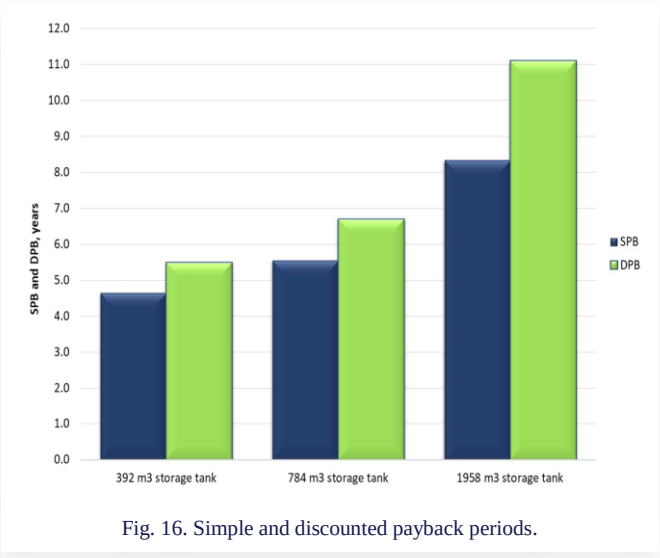


Fig. 16. Simple and discounted payback periods.

The discounted cash flow rate used in the analysis was 5%. In the case of the downsized system the NPV is € 189 770.04, SPB is 9,1 years and DPB is 12.5 years.

Another aspect of the project is that it would have a significant impact on greenhouse gas emissions into the atmosphere as the CO_2 per MWh of electricity indicator for Portugal is equal to approximately 248.57 kg of CO_2 per MWh of electrical energy [24].

4. Conclusions

In this detailed energy simulation and financial analysis were performed for the solar cooling system for the IST Tower in Lisbon, Portugal. Atmospheric and sunlight conditions in Lisbon are ideal for testing this type of solution. After analysing a classic air conditioning compression system, it turned out that such a system would consume approximately 549 238.21 kWh per year. Such amount of electricity consumption could result in really high costs (approximately € 80 738.02 per year).

Results revealed that the proposed system meets the cooling demand of the building, mainly by solar energy-driven absorption chiller. The annual contribution of backup compression chiller ranges from 20% to 36% depending on the size of chilled water storage tanks. Financial calculations revealed discounted payback periods in the range of 4.5 to 12.5 years depending on system configuration. The best solution appeared to be the system with 3 053.25 m^2 of solar collector aperture area, an absorption chiller of 622.5 kW cooling capacity and a relatively small cold water storage tank of 392 m^3. The results of the profitability analysis are very encouraging. As the project has also a considerable impact on the environment, the Life Cycle Assessment (LCA) is considered for future work.

References

[1] Delmastro, C., & Abergel, T. (2020). *Cooling. Tracking report*. International Energy Agency. https://www.iea.org/reports/cooling [accessed 19 Jan. 2024].

[2] Alazazmeh, A.J., & Mokheimer, E.M. (2015). Review of solar cooling technologies. *Journal of Applied Mechanics and Engineering*, 4(05), 1−15. doi: 10.4172/2168-9873.1000180

[3] Chwieduk, D., Grzebielec, A., & Rusowicz, A. (2014). Solar cooling in buildings. *Technical Transactions - Civil Engineering*, 3-B(8), 65−73.

[4] Neyer, D., & Jakob, U. (2020). Solar Cooling for the Sunbelt Regions – a new IEA SHC Task. *ISES and IEA SHC International Conference on Sustainable and Solar Energy for Buildings and Industry*. 26−30 August, Limassol, Cyprus. International Solar Energy Society. EuroSun 2020 Proceedings. doi: 10.18086/eurosun.2020.02.08

[5] Alahmer, A., Wang, X., & Ajib, S. (2021). *Solar cooling technologies: Challenges, applications, and improvements*. Frontiers. https://www.frontiersin.org/research-topics/17585/solar-cooling-technologies-challenges-applications-and-improvements#overview [accessed 19 Jan. 2024].

[6] Assilzadeh, F., Kalogirou, S.A., Ali, Y., & Sopian, K. (2005). Simulation and optimization of a LiBr solar absorption cooling system with evacuated tube collectors. *Renewable Energy*, 30, 1143−1159. doi: 10.1016/j.renene.2004.09.017

[7] Narayanan, M. (2017). Techno-economic analysis of solar absorption cooling for commercial buildings in India. *International Journal of Renewable Energy Development*, 6(3), 253−262. doi: 10.14710/ijred.6.3.253-262

[8] Praene, J.P., Bastide, A., Lucas, F., Garde, F., & Boye, H. (2007, June). Simulation and optimization of a solar absorption cooling system using evacuated tube collectors. *9th REHVA World Congress 'WellBeing Indoors', Clima 2007*, Helsinki, Finland.

[9] Iranmanesh, A., & Mehrabian, M.A. (2014). Optimization of a lithium bromide–water solar absorption cooling system with evacuated tube collectors using the genetic algorithm. *Energy and Buildings*, 85, 427−435. doi: 10.1016/j.enbuild.2014.09.047

[10] Pinamonti, M., & Baggio, P. (2020). Energy and economic optimization of solar-assisted heat pump systems with storage technologies for heating and cooling in residential buildings. *Renewable Energy*, 157, 90−99. doi: 10.1016/j.renene.2020.04.121

[11] Altun, A.F., & Kilic, M. (2020). Economic feasibility analysis with the parametric dynamic simulation of a single effect solar absorption cooling system for various climatic regions in Turkey. *Renewable Energy*, 152, 75−93. doi: 10.1016/j.renene.2020.01.055

[12] Drosou, V., Kosmopoulos, P., & Papadopoulos, A. (2016). Solar cooling system using concentrating collectors for office buildings: A case study for Greece. *Renewable Energy*, 97, 697−708. doi: 10.1016/j.renene.2016.06.027

[13] Eicker, U., Pietruschka, D., Haag, M., & Schmitt, A. (2015). Systematic design and analysis of solar thermal cooling systems in different climates. *Renewable Energy*, 80, 827−836. doi: 10.1016/j.renene.2015.02.019

[14] Casals, X.G. (2006). Solar absorption cooling in Spain: Perspectives and outcomes from the simulation of recent installations. *Renewable Energy*, 31, 1371−1389. doi: 10.1016/j.renene.2005.07.002

[15] Ge, T.S., Wang, R.Z., Xu, Z.Y., Pan, Q.W., Du, S., Chen, X.M., Ma, T., Wu, X.N., Sun, X.L., & Chen, J.F. (2018). Solar heating and cooling: Present and future development. *Renewable Energy*, 126, 1126−1140. doi: 10.1016/j.renene.2017.06.081

[16] Palomba, V., Wittstadt, U., Bonanno, A., Tanne, M., Harborth, N., & Vasta, S. (2019). Components and design guidelines for solar cooling systems: The experience of ZEOSOL. *Renewable Energy*, 141, 678–692. doi: 10.1016/j.renene.2019.04.018

[17] DesignBuilder Software Ltd.. *DesignBuilder software*. https://designbuilder.co.uk/software/product-overview [accessed 19 Jan. 2024].

[18] EnergyPlus. https://energyplus.net/ [accessed 19 Jan. 2024].

[19] Arcon-Sunmark. (2020). *Specification of the Arcon-Sunmark a/s HT-SolarBoost 35/10 collector. Annex to the Solar Keymark Certificate.*

[20] Iranmanesh, A., & Mehrabian, M.A. (2014). Optimization of a lithium bromide–water solar absorption cooling system with evacuated tube collectors using the genetic algorithm. *Energy and Buildings*, 85, 427–435. doi: 10.1016/j.enbuild.2014.09.047

[21] European Commission. (2001). *Integrated pollution prevention and control (IPPC) - reference document on the application of best available techniques to industrial cooling systems*. https://eippcb.jrc.ec.europa.eu/sites/default/files/2019-11/cvs_bref_1201.pdf [accessed 19 Jan. 2024].

[22] Yazaki Energy. (2020). *Wfc-m100 specification*. https://yazakienergy.com/literature.php [accessed 19 Jan. 2024].

[23] Narayanan, M. (2017). Techno-economic analysis of solar absorption cooling for commercial buildings in India. *International Journal of Renewable Energy Development*, 6(3), 253–262. doi: 10.14710/ijred.6.3.253-262

[24] International Energy Agency. (2019). *Energy Transitions Indicators*, IEA, Paris. https://www.iea.org/reports/energy-transitions-indicators, License: CC BY 4.0 [accessed 19 Jan. 2024].

Co-published by
Institute of Fluid-Flow Machinery
Polish Academy of Sciences
Committee on Thermodynamics and Combustion
Polish Academy of Sciences

Copyright©2024 by the Authors under licence CC BY 4.0

http://www.imp.gda.pl/archives-of-thermodynamics/

Determination of the heat capacity of a water-ice reservoir as a lower heat source for heat pump - Numerical analysis

Piotr Tarnawski[a*]

[a]Warsaw University of Technology, Plac Politechniki 1, 00-661 Warsaw, Poland
*Corresponding author email: piotr.tarnawski@pw.edu.pl

Received: 10.10.2023; revised: 20.02.2024; accepted: 09.04.2024

Abstract

The paper presents the design of a heat exchanger immersed in a water-ice reservoir and the determination of its heat capacity as a lower heat source for the heat pump. This is an innovative solution, the first project on this scale in Poland. Heat absorption from the water-ice tank took place in three stages: from water at a temperature range of 20°C to 0°C, from the water-ice phase change at 0°C, and from ice at a temperature range of 0°C to –10°C. The CFD (Computational Fluid Dynamics) analysis of a heat exchanger performance was performed. It required simulation of water natural convection, water-ice phase change, and heat transfer from the ground. The heat flux absorbed in the designed exchanger was calculated based on the current glycol temperature and the implemented COP (Coefficient of Performance) characteristic of the heat pump. This was done via the user-defined function (UDF) available in Ansys FLUENT. The compiled internal software subroutine was defined based on the DEFINE_ADJUST macro. Moreover, the thermal resistance of ice forming on the pipes was included. The numerical analysis indicated that 66097 kWh of heat would be absorbed from the reservoir in 500 hours of exploitation. The volume fraction of water at the end of the simulation was equal to 26.7% and the volume fraction of ice was equal to 73.3%. The CFD simulation confirmed the heat capacity value of the water-ice storage tank which fulfilled the design requirements.

Keywords: Renewable energy; Water-ice tank; Ground reservoir; Heat pump; CFD simulation

Vol. 45(2024), No. 2, 157–163; doi: 10.24425/ather.2024.150862

Cite this manuscript as: Tarnawski, P. (2024). Determination of the heat capacity of a water-ice reservoir as a lower heat source for heat pump – Numerical analysis. *Archives of Thermodynamics*, 45(2), 157–163.

1. Introduction

One way to reduce fossil fuels for energy production is to use stored heat. The huge reservoir of stored heat is in the ground. Its average temperature is about 9 – 10°C [1,2]. This level of temperature makes it useful in the winter season for heating up and for cooling in the summer season. The most obvious way of using it is by heating and cooling ventilation air in an air-ground heat exchanger [3,4]. A more sophisticated approach is the use of the ground as a lower heat source for heat pumps [5,6]. The thermal energy of a tank filled with water as a storage medium gives better results because it has a greater heat capacity [7]. Water has a heat density of 1000 kg/m^3 and a specific heat capacity of 4200 J/(kg K). The ground density is 1750 kg/m^3 and its specific heat capacity is equal to 1200 J/(kg K).

Nomenclature

A – area, m^2
c – specific heat capacity, J/(kg K)
g – gravitational acceleration, m/s^2
h – sensible enthalpy, J/kg
H – enthalpy, J/kg
ΔH – latent heat content, J/kg
k – thermal conductivity, W/(m K)
L – latent heat of material, J/kg
p – pressure, Pa
$\dot{Q}$ – heat flux, W
q – density of heat flux, W/m^2
t – time, s
T – temperature, °C
S – source term (momentum sink), Pa
$\boldsymbol{w}$ – velocity vector, m/s

Greek symbols
β – liquid fraction
ε – momentum sink constant
μ – dynamic viscosity, Pa s
ρ – density, kg/m^3
$\boldsymbol{\tau}$ – stress tensor, Pa

Subscripts and Superscripts
HP – heat pump
mush – mushy zone
p – pull velocity

Abbreviations and Acronyms
2D, 3D – two-dimensional, three-dimensional
CFD – computational fluid dynamics
COP – coefficient of performance
PE – polyethylene
UDF – user-defined function

The water gives even more heat capacity when utilizing its phase changes during freezing and melting [8,9]. The heat of the phase change of water is equal to 333×10^3 kJ/m^3. In contrast, the heat capacity of liquid water is 4200 kJ/(m^3 K). The amount of latent heat accumulated in 1 m^3 of water during a phase change is equal to sensible heat accumulated in liquid water at the temperature of 80°C [10]. Heat absorbing from the water phase exchange proceeds at quite a low temperature which is equal to 0°C. But when it is used as a lower heat source for the heat pump it gives satisfactory results, since the temperature value is higher than external the temperature of the air in winter or the temperature of the ground around the pipes of the ground collector [5, 11]. As regards cooling purposes, a temperature of 0°C seems to be a very convenient temperature.

The paper presents a summary of the project focused on the design of a heat exchanger immersed in a ground water-ice tank and the determination of the thermal capacity of a tank. The water-ice reservoir is designed as an innovative lower-source solution for heat pumps in the system glycol/water. This system is designed to provide heat to public buildings of Science Center Cogiteon located in Cracow, Poland, as well as natural cooling in the summer, using clean and renewable energy sources.

The system consists of a special concrete tank filled with water. The heat pump absorbs energy from the tank using a heat exchanger made of many equally distributed polyethylene (PE) pipe loops. As heat is drawn from the tank, the water temperature drops until the freezing process begins. Additional energy, called phase change energy (latent heat), is released. Then the source (tank) can be regenerated using waste heat gained from the building. After the ice melts and the water temperature in the tank increases, the entire process starts again. This is an innovative solution, the first project on this scale in Poland.

The first chapter of the paper is focused on the tank construction and the design of a heat exchanger made of PE pipe loops. In the second chapter full description of the computational fluid dynamics (CFD) numerical approach is given. Then the most important results are shown and discussed. Finally, the results are concluded.

2. Design of tank heat exchanger

2.1. Aim of the analysis and its assumptions

The first goal of the project was to design a heat exchanger of a lower heat source (water-ice tank). The assumption for the project was that the exchanger should consist of 32×2 mm PE loop pipes. PE material is convenient since it can deform when water is freezing and melting. The length of a single-pipe loop should not exceed 100 m. The sum length of pipes of the heat exchanger shall be at least 7650 m. The working fluid was ethylene-glycol with a concentration of 35%.

The second goal of the project was to confirm by CFD simulation the assumed heat capacity of the water-ice tank. The amount of heat extracted from the tank must be at least 66000 kWh for the working period of 500 h. For purposes of the analysis, the heat pump has to work with a constant power of 200 kW. The heat pump should work with the parameters of the upper heat source as follows: inlet water temperature was equal to 35°C, and outlet water temperature of 45°C (supply temperature). The CFD simulation shall include changing the temperature of glycol in a lower heat source and changing the coefficient of performance (COP) characteristic of a heat pump.

2.2. Water-ice tank construction

The water-ice tank was made of concrete with a wall thickness equal to 0.5 m. It was located 6.7 m under the earth's surface. It had dimensions of 11.325 m×12.8 m×6.1 m according to Fig. 1.

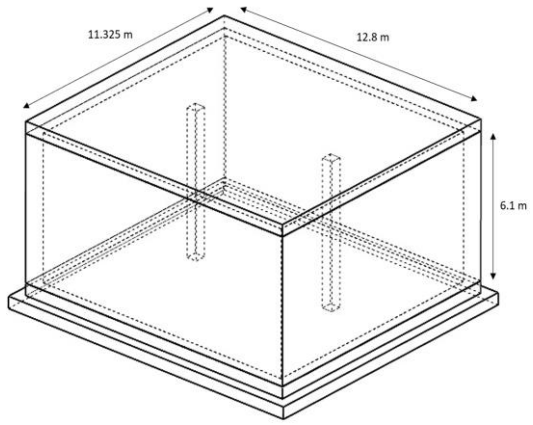


Fig. 1. Water-ice tank dimensions.

2.3. The arrangement of pipe loops in the water-ice tank

The minimum spacing between surrounding pipes should be 31 mm. It was calculated analytically based on that 712 m^3 of water has a latent heat equal to 66×10^3 kWh. To accommodate a heat exchanger with a total length of pipes equal to 7650 m, the pipes must be spaced every 31 mm.

From an operational point of view, the pipe loops should have the smallest possible pressure drop (the smaller the number of elbows the better). Moreover, the loops should have similar pressure drops (the same length and the same number of elbows), since they will be supplied from a common collector. The best solution is when pipe loops do not intersect each other. Figure 2 presents different considered variants of the arrangement of pipe loops. Each variant consists of 18 identical layers of pipe loops. The single layer consists of four pipe loops.

From a technical point of view, the best was VARIANT_4. It provided an equal length of pipe loops and the smallest pressure drop (only 56 elbows). In comparison, the VARIANT_2 had 136 elbows. See a comparison of the parameters of different arrangement variants in Table 1.

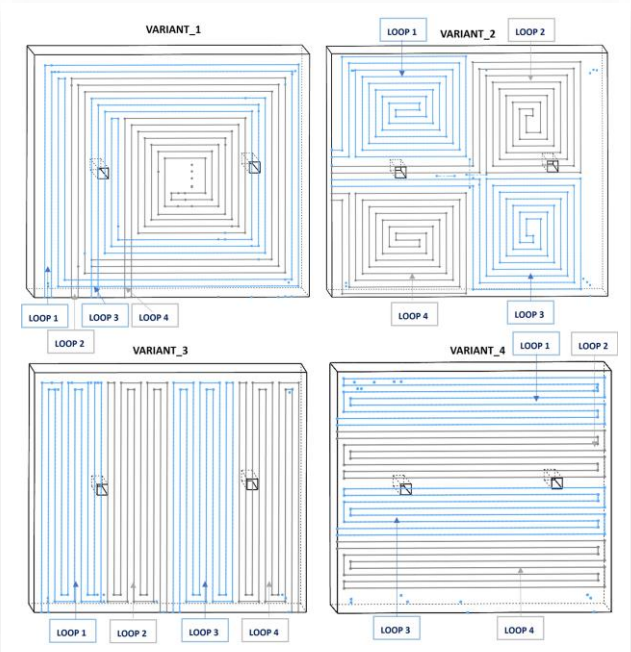


Fig. 2. Different variants of pipe loop arrangements in water-ice tank (single layers).

Table 1. Comparison of different arrangement variants of pipe loops.

VARIANT_1						
Loop	**1**	**2**	**3**	**4**	**Sum/ Layer**	**Sum /Tank**
Length [m]	105.4	108.5	105.4	106.9	426.1	7670
Elbows	10	12	14	28	64	

VARIANT_2						
Loop	**1**	**2**	**3**	**4**	**Sum/ Layer**	**Sum/ Tank**
Length [m]	98.5	105.2	98.5	105.2	407.4	7333
Elbows	34	34	34	28	136	

VARIANT_3						
Loop	**1**	**2**	**3**	**4**	**Sum/ Layer**	**Sum/ Tank**
Length [m]	106.8	106.8	106.8	106.8	427.2	7689
Elbows	18	18	18	18	72	

VARIANT_4						
Loop	**1**	**2**	**3**	**4**	**Sum/ Layer**	**Sum/ Tank**
Length [m]	100.2	100.2	100.2	100.2	400.9	7617
Elbows	14	14	14	14	56	

3. Description of CFD simulation approach

The CFD simulation had to include physics associated with laminar natural convection of water, freezing of water, and heat conduction in ice in transient mode. Moreover, the thermal interaction with the ground should be taken into account. It required resolving the equations of continuity, momentum, and energy, respectively:

$$\frac{\partial \rho}{\partial t} + \nabla \cdot (\rho \boldsymbol{w}) = 0, \tag{1}$$

$$\frac{\partial (\rho \boldsymbol{w})}{\partial t} + \nabla \cdot (\rho \boldsymbol{w}\boldsymbol{w}) = -\nabla p + \nabla \cdot \boldsymbol{\tau} + \rho g + S, \tag{2}$$

$$\frac{\partial (\rho H)}{\partial t} + \nabla \cdot (\rho \boldsymbol{w} H) = \nabla \cdot (k \nabla T), \tag{3}$$

where: ρ – density, t – time, $\boldsymbol{w}$ – velocity vector, p – pressure, $\boldsymbol{\tau}$ – stress tensor, g – gravitational acceleration, H – enthalpy, k – thermal conductivity, T – temperature, S – source term (momentum sink).

An enthalpy-porosity technique is used in Ansys FLUENT for modelling the solidification/melting process, based on the following equations [12]:

$$S = \frac{1-\beta}{\beta^3+\varepsilon} A_{mush}(\boldsymbol{w} - \boldsymbol{w}_p), \quad (4)$$

$$H = h - \Delta H, \quad (5)$$

$$\Delta H = \beta L, \quad (6)$$

where: β – liquid fraction, ε = 0.001 – constant, $A_{mush} = 10^5$ – default constant, h – sensible enthalpy, ΔH – latent heat content, L – latent heat of the material, $\boldsymbol{w}_p = 0$ – pull velocity.

In the enthalpy-porosity technique, the melt interface is not tracked explicitly. Instead, a quantity called the liquid fraction β, which indicates the fraction of the cell volume that is in liquid form, is associated with each cell in the domain. The liquid fraction is computed at each iteration, based on an enthalpy balance. The mushy zone is a region in which the liquid fraction β lies between 0 and 1. The mushy zone is modelled as a "pseudo" porous medium in which the porosity decreases from 1 to 0 as the material solidifies. When the material has fully solidified in a cell, the porosity becomes zero, hence the velocities also drop to zero. If $T < T_{solidus}$, $\beta = 0$; $T > T_{solidus}$, $\beta = 1$ [13,14].

The calculation of freezing is very time-consuming because for obtaining the solution convergence the single time step has to be very small [15,16]. For the assumed computation time step equal to 0.1 s and the required simulation period of 600 h, the two-dimensional (2D) simulation was only the option [17]. It was decided to simulate only a 2D repeating middle section of the tank heat exchanger which is shown in Fig. 4. However, such a 2D section should pretty well represent most of the tank region. The imperfection of the 2D approach was first of all, that it did not take into account the heat flux from the tank walls (only heat flux from the bottom of the tank was taken into account). It was a negligible simplification because as reported in the simulation, the amount of heat from the bottom of the tank was about 1% of the total heat absorbed from the tank. If the 2D model meets the requirements, the three-dimensional (3D) model will even better meet the requirements, because of additional heat from side walls [18]. The second simplification was that the 2D approach assumed a constant temperature of glycol, therefore, only a density of heat flux can be resolved. It is justified since the real temperature of glycol in a single pipe loop changes by only about 2 – 3 K [19]. After appropriate multiplication, the 2D solution can be used for the entire tank heat exchanger.

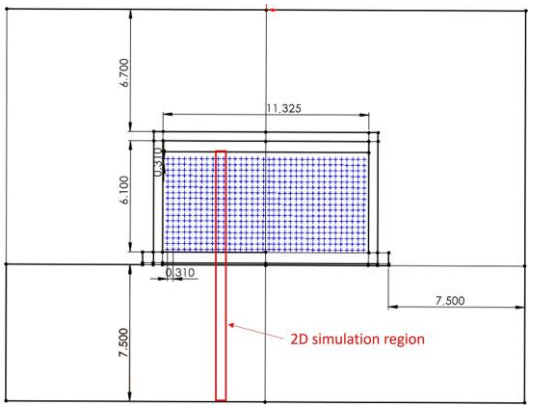


Fig. 3. Cross section of 3D model of the tank with surrounding ground.

The 2D geometry model, boundary condition, and computational mesh are shown in Fig. 3 and Fig. 4. The computational mesh consisted of quadrilateral elements with a total number of 12690. The smallest element in the vicinity of walls has a height equal to 1 mm. The thermal parameters of solids used in the simulation are shown in Table 2. The parameters of water and ice as a function of temperature are presented in Table 3. Changing the thermal parameters of water and ice in simulation allowed the current thermal resistance in the pipes' vicinity to be considered. The heat of the water-ice phase change (latent heat) was equal to L = 333 kJ/kg. The simulation took into account the real amount of water and the required mirror level of water. The analytical calculation included the sum of objects volume in the

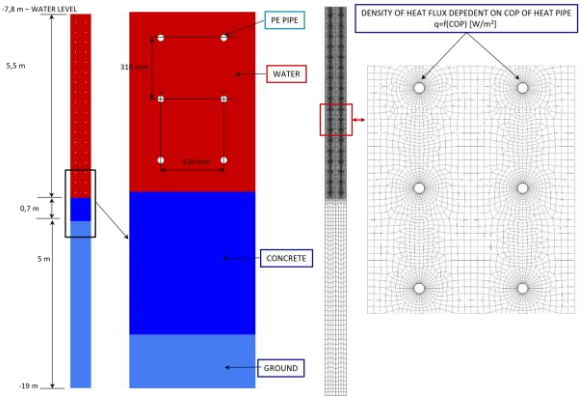


Fig. 4. A 2D simulation model of a tank heat exchanger with boundary conditions.

Table 2. Thermal parameters of solids used in simulation.

Material	Density ρ [kg/m³]	Thermal conductivity k [W/(m K)]	Specific heat capacity c [J/(kg K)]
PE	950	0.4	1750
Concrete	2500	1.7	840
Ground	1750	1.45	1200

Table 3. Parameters of water and ice in the function of temperature.

Temperature T [°C]	Density ρ [kg/m³]	Thermal conductivity k [W/(m K)]	Dynamic viscosity μ [Pa s]	Specific heat capacity c [J/(kg K)]
-20	919.4	2.39	-	1943
-15	919.4	2.34	-	1972
-10	918.9	2.30	-	2000
-5	917.5	2l25	-	2027
-0.05	916.2	2.22	-	2050
0.05	999.9	0.555	0.00175	4216
4.44	1000	0.566	0.00155	4204
10	999.7	0.589	0.0013	4195
15.6	999.2	0.609	0.00113	4187
21.1	998.1	0.625	0.00097 7	4183

tank (concrete poles, heat exchanger pipes, regenerating pipes, steel elements, others) and required free space in the upper part of the tank in a value of 10% of the water volume.

Figure 5 presents the COP change of the heat pump in function of glycol temperature. The supply temperature of water for this function was equal to 45°C. The lowest COP = 2.6 was for the temperature of glycol equal to –12°C. The highest COP = 5.5 was for the temperature of glycol equal to 20°C.

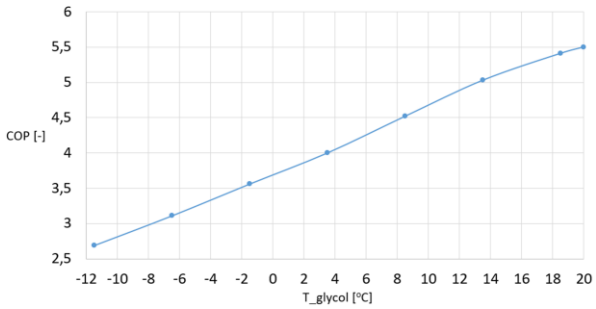


Fig. 5. COP characteristic of heat pump for supply water temperature of 45°C.

Thus, the heat flux absorbed from the water-ice tank should be calculated according to:

$$\dot{Q} = \dot{Q}_{HP} \cdot \frac{\dot{Q}_{HP}}{\mathrm{COP}(t)}, \tag{7}$$

where: $\dot{Q}_{HP}$= 200 kW – heat pump working power, COP(t) – COP function dependent on glycol temperature in pipes. See heat flux as a function of glycol temperature in Fig. 6.

The density of heat flux prescribed to the internal surface of pipes was calculated from:

$$q = \frac{\dot{Q}}{A}, \tag{8}$$

where A is the internal surface of the total pipe loops of the heat exchanger.

The calculation procedure required the use of advanced software UDF (user-defined function) capability. The compiled internal software subroutine was defined by DEFINE_ADJUST macro [17]. Within the subroutine, the temperature of the internal surface of pipe walls was read and averaged in each iteration. Next, using the COP function of the heat pump the new value of

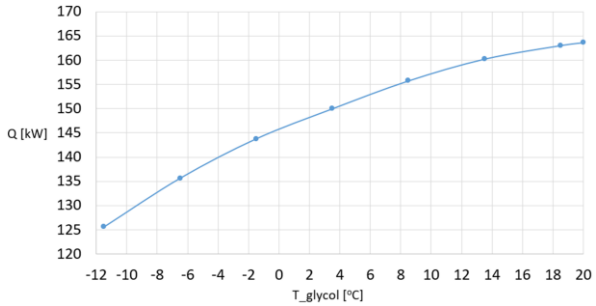


Fig. 6. Heat flux absorbed from the water-ice tank in the function of glycol temperature.

density of the heat source was prescribed to the internal surface of pipe walls. This procedure proceeded automatically over the simulated operating time of the tank heat exchanger. Simplification made in the analysis was that the temperature of glycol was assumed to be equal to the temperature of the inner surface of pipes. This is a reasonable assumption since the gradient temperature was below 0.05°C.

4. CFD simulation results

The initial temperature of the water was set to 20°C and the initial temperature of the ground was set to 8.9°C. While the heat was absorbed from the tank the water temperature dropped. It caused convection movements of water. The colder water was flowing to the lower part of the tank (Fig. 7). Below 4.44°C the flow direction has changed. The colder water was flowing to the upper part of the tank (Fig. 8). The reason for this was an increase in the density of water with a decrease in temperature from 21.1°C to 4.44°C, then a decrease in the density of ester with the change in temperature from 4.44°C to 0°C.

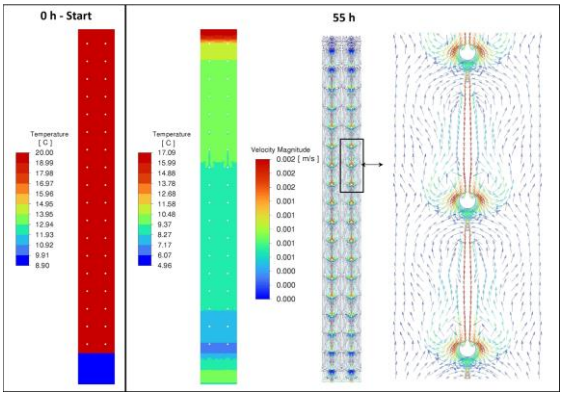


Fig. 7. Temperature and velocity distribution of water at the start and after 55 h of simulation.

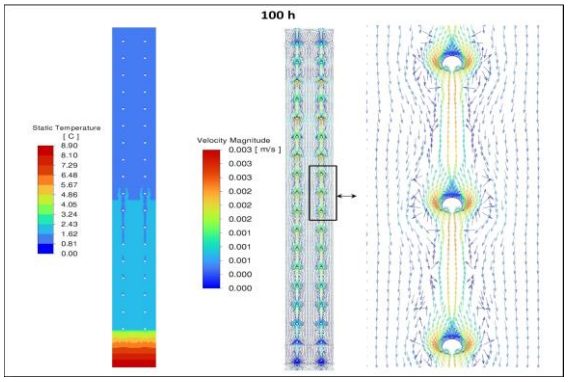


Fig. 8. Temperature and velocity distribution of water after 100 h of simulation.

When the water temperature reached 0°C the convective movements were stopped. The freezing process started firstly on the surfaces of the upper pipes (Fig. 9). The reason for this was

the flow of colder water to the upper part of the tank. The thickness of the ice around the pipes increased with the time of heat absorption (Fig. 10).

The simulation results indicated that 66097 kWh was absorbed in 500 h. After this time, the water volume fraction decreased to 26.7% and thus the volume ice fraction increased to 73.3%. As aforementioned, the simulation model included changes in water thermal properties in temperature function (Fig. 11). It allowed to take into account variable thermal resistance of the heat exchanger. An ice fraction of 98% was reached at 600 h after 86257 kWh of absorbed heat (Fig. 12).

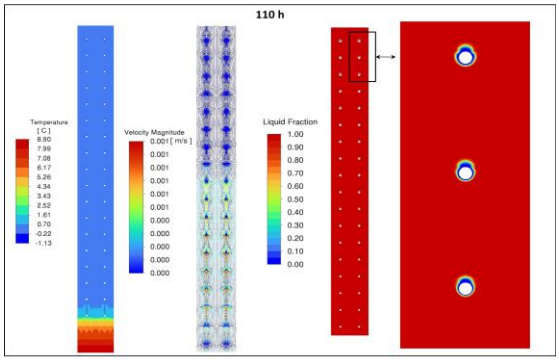


Fig. 9. Temperature, velocity, and liquid fraction distribution after 110 h of simulation.

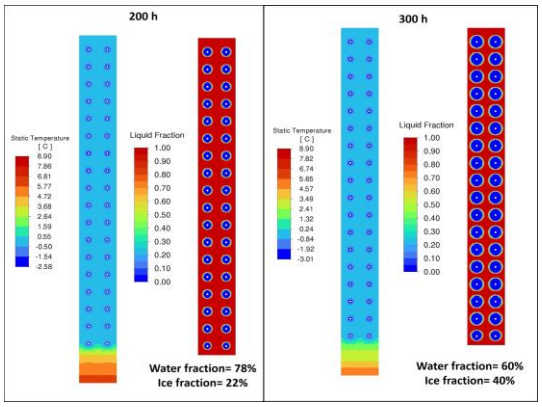


Fig. 10. Temperature and liquid fraction distribution after 200 h and after 300 h of simulation.

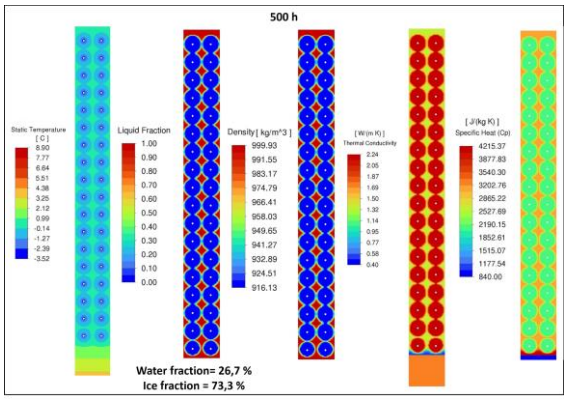


Fig. 11. Temperature, liquid fraction, and material properties distribution after 500 h of simulation.

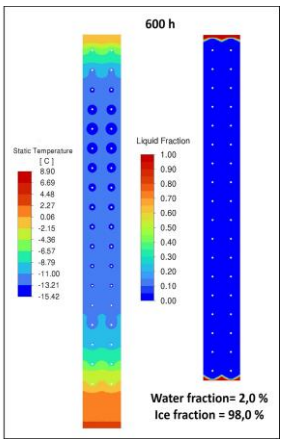


Fig. 12. Temperature and liquid fraction distribution after 600 h of simulation.

The change of glycol temperature throughout the simulation time of 600 h is presented in Fig. 13. As seen from the figure, the temperature decreased from 20°C to –10°C during convection and freezing. After reaching 100% of ice the temperature dropped below values acceptable by the heat pump. The smallest glycol possible working temperature was equal to –10°C.

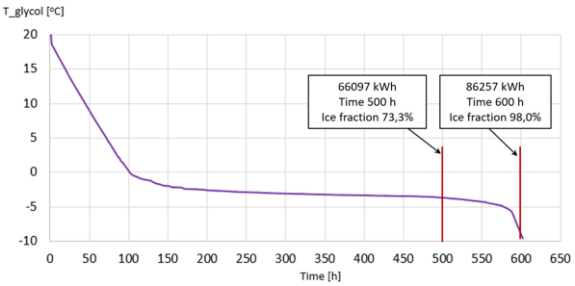


Fig. 13. Change of glycol temperature during heat absorption from water-ice tank.

The predicted heat flux absorbed from the tank changed according to Fig. 14. The maximum value was equal to 165 kW and the minimum value was equal to 130 kW at the end of the simulation.

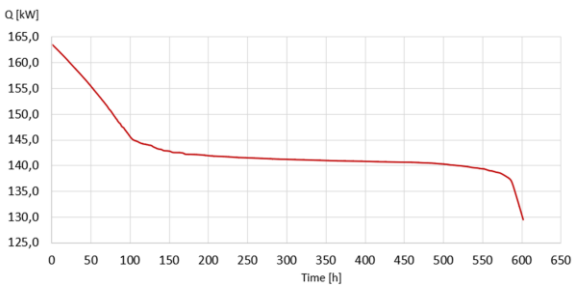


Fig. 14. Change in heat flux absorbed from the water-ice tank.

5. Conclusions

Several variants of pipe loops of the heat exchanger in a water-ice tank were considered and the optimal design was chosen for the CFD analysis. Then the simulation of heat absorption from the water-ice tank for 600 hours was carried out. The COP characteristic of the heat pump was taken into account as a function of the actual glycol temperature. Moreover, the thermal resistance of forming ice on the pipes of the heat exchanger was included. Such a procedure made it possible to take into account the actual amount of heat absorbed from the tank. As a result, the heat flux function absorbed from the tank throughout the entire working period of the heat exchanger was evaluated.

The simulation results showed that 66097 kWh of heat was absorbed from the water-ice tank during 500 hours. After this time the volume fraction of ice in the tank was equal to 73.3%, and the volume fraction of water was equal to 26.7%. This means that there was still a surplus of heat in the tank that could be further absorbed.

Assumptions on the heat capacity of the lower heat source (water-ice tank), as well as the adopted characteristics of the heat pump meet the requirements of the project. In the case of a real tank, the parameters should be better than in the simulation because:

1) The 2D simulation does not take into account the side walls of the tank from which the tank will be additionally heated (only the bottom of the tank is taken into account).

2) A conservative ground temperature of 8.9°C was assumed. When heating the tank to 20°C, the surrounding ground will also heat up, so its temperature will be higher than 8.9°C.

References

[1] Craciun, A. V., Sandu, F., & Pana, G. (2010). Monitoring of a ground source heat pump with horizontal collectors. In *12th International Conference on Optimization of Electrical and Electronic Equipment* (pp. 1–4). Brasov, Romania. doi: 10.1109/ OPTIM.2010.5510546

[2] Condego, P. M., Lorusso, C., De Giorgi, M. G., Marti, R., & D'Agostino, D. (2016). Horizontal air-ground heat exchanger performance and humidity simulation by computational fluid dynamic analysis. *Energies*, 9(11), 930. doi: 10.3390/en9110930

[3] Tarnawski, P. (2015). Analysis of the cooling performance of a tube ground heat exchanger. *Czasopismo Chłodnictwo i Klimatyzacja*, 8. (in Polish) http://www.chlodnictwoiklimatyzacja.pl/component/content/article/248-wydanie-08-2015/3609-analiza-cfd-wydajnosci-chlodzenia-rurowego-gwc.html [accessed: 18 Sep. 2023].

[4] Tarnawski, P. (2015). CFD analysis of ground heat exchanger performance. *Czasopismo Rynek Instalacyjny*, 6. (in Polish) https://www.rynekinstalacyjny.pl/artykul/projektowanie-c-o/20326,analiza-cfd-wydajnosci-rurowego-wymiennika-ciepla [accessed: 18 Sep. 2023].

[5] Hanuszkiewicz-Drapała, M. (2009). Modelling of thermal phenomena in ground heat exchangers of heating pumps, taking into account the flow resistance of the intermediary medium. *Modelowanie Inżynierskie,* 38, 57–68. ISSN 1896-771X (in Polish).

[6] Hanuszkiewicz-Drapała, M., & Bury, T. (2016). Utilization of the horizontal ground heat exchanger in the heating and cooling system of a residential building. *Archives of Thermodynamics*, 37(1), 47–72. doi: 10.1515/aoter-2016-0004

[7] Jastrzębski, P., & Saługa, P. (2018). Innovative methods of heat storage (in Polish). *Zeszyty Naukowe Instytutu Gospodarki Surowcami Mineralnymi i Energią Polskiej Akademii Nauk,* 105, 225–232. doi: 10.24425/124376

[8] Maślankiewicz, P., & Wojciechowski, H. (2017). Heating with freezing water. *Instal*, 4(2017), 19–23.

[9] Mania, T., & Kawa, J. (2015). Heat and cold energy storage systems – practical applications. *Energetyka,* 1 (in Polish).

[10] Jin, W., Suying, W., & Youtao, Z. (2010). Study on ice storage characteristics of a small-scale storage tank filled with ice balls. *Asia-Pacific Power and Energy Engineering Conference*. doi: 10.1109/APPEEC.2010.5448598

[11] Bezrodny, M., Prytula, N., & Tsvietkova, M. (2019). Efficiency of heat pump systems of air conditioning for removing excessive moisture. *Archives of Thermodynamics*, 40(2), 151–165. doi: 10.24425/ather.2019.129546

[12] ANSYS. (2018). *Fluent Theory Guide 19.1, Chapter 18: Solidification and Melting*.

[13] ANSYS® Academic Associate CFD. *ANSYS Fluent User Guide.*

[14] Selvenes, H., Allouche, Y., Sevault, A., & Hafner, A. (2019). CFD modeling of ice formation and melting in horizontally cooled and heated plates. In *Eurotherm Seminar 112: Advances in Thermal Energy Storage*, 15–17 May, Lleida, Spain.

[15] Ramesh, V., Terala, S., Mazumder, S., Matharu, G., Vaishnv, D., & Ali, S. (2021). Development and validation of a model for efficient simulation of freezing of water in large tanks. *Journal of Thermal Science and Engineering Applications*, 13(1), 011008. doi: 10.1115/1.4047166

[16] Ramesh, V., Terala, S., Mazumder, S., Matharu, G., Vaishnv, D., & Ali, S. (2022). Efficient simulation of freezing of water in large tanks including expansion of ice. *Journal of Thermal Science and Engineering Applications*, 14(11), 111006. doi: 10.1115/1.4054513

[17] Michałek, T., & Kowalewski, T. (2003). Simulations of the water freezing process – numerical benchmarks. *Task Quarterly*, 7(3), 389–408.

[18] Muszyński, T., & Kozieł, S. M. (2016). Archives of thermodynamics. *Archives of Thermodynamics*, 37(3), 45–62. doi: 10.1515/aoter-2016-0019

[19] Hanuszkiewicz-Drapała, M., & Składzień, J. (2010). Heating system with vapor compressor heat pump and vertical U-tube ground heat exchanger. *Archives of Thermodynamics*, 31(4), 93–110. doi: 10.2478/v10173-010-0031-8

Co-published by
Institute of Fluid-Flow Machinery
Polish Academy of Sciences
Committee on Thermodynamics and Combustion
Polish Academy of Sciences

Copyright©2024 by the Authors under licence CC BY 4.0

http://www.imp.gda.pl/archives-of-thermodynamics/

Comprehensive parametric and design review for reducing pulsating heat pipes dependence on space orientation

Kishor Vishwanath Mane[a*], Yevhenii Alekseik[b]

[a]Faculty of Mechanical Engineering, Fr. C. Rodrigues Institute of Technology, Vashi, University of Mumbai, India
[b]Educational and Scientific Institute of Atomic and Thermal Energy, National Technical University of Ukraine "Igor Sikorsky Kyiv Polytechnic Institute", Kyiv, Ukraine
*Corresponding author email: manekv555@gmail.com

Received: 17.10.2023; revised: 13.01.2024; accepted: 30.03.2024

Abstract

It has been three decades since pulsating heat pipes were first introduced and garnered more attention due to their uncomplicated structural design and superior heat transfer capabilities. The pulsating heat pipe of the original design is strongly affected by space orientation, which is connected with the influence of gravity. Even though more turns will hold pulsating heat pipe operational in any orientation, more space is needed to handle pulsating heat pipes, limiting its potential in space and the power electronics industry. This paper aims to present a comprehensive review of pulsating heat pipe's progress based on the most recent findings of both experimental and theoretical investigations of parametric influence on pulsating heat pipe thermal performance in horizontal and top heating modes. It aims to identify research gaps in pulsating heat pipe functioning in different orientations. Additionally, a comparative analysis of pulsating heat pipe design features described in the existing literature is conducted to determine the most promising designs for orientation-independent pulsating heat pipe systems. It is concluded that the integration of design attributes, encompassing an uneven-turn design, a channel structure featuring alternating shapes and size of cross-section, and the utilization of nanofluids and binary mixtures as heat carriers are expected to serve as the basic reference for researchers aiming to achieve a stable pulsating heat pipe operation devoid of gravitational influences.

Keywords: Pulsating heat pipe; Inner diameter; Number of turns; Zones lengths; Cross section

Vol. 45(2024), No. 2, 165–182; doi: 10.24425/ather.2024.150863

Cite this manuscript as: Mane, K. V., & Alekseik, Y. (2024). Comprehensive parametric and design review for reducing pulsating heat pipes dependence on space orientation, *Archives of Thermodynamics*, 45(2), 165–182.

1. Introduction

Heat transfer is one of the key processes for functioning of different apparatus such as, for example, steam generators, heat exchangers, solar collectors intended for both heat supplying and water desalination [1–3] cooling and thermal control systems for space and electronic devices and many others in different areas of industry. In most cases efficiency of heat transfer defines overall efficiency of apparatus functioning. That's why increasing of heat transfer efficiency is one of the main problems in power engineering, heat waste recovery, heating, ventilation, and air conditioning (HVAC) systems, energy efficient technologies, electronics cooling etc. Heat pipes were found out as one of the most effective solutions of this problem. Amongst them, pulsating heat pipe (PHP), a novel idea proposed by Akachi [4]

Nomenclature

Bo – Bond number
D – capillary tube diameter, m
D_h – hydraulic diameter, m
D_i – inner diameter of PHP, m
g – acceleration due to gravity, m/s^2
L_{eff} – effective length of PHP, m
R_h – thermal resistance in a horizontal orientation, K/W
R_v – thermal resistance in a vertical orientation, K/W
R_{vb} – thermal resistance in vertical bottom heating mode, K/W
R_{vt} – thermal resistance in vertical top heating mode, K/W

Greek symbols

ρ_g – density of vapour, kg/m^3
ρ_l – density of liquid, kg/m^3
σ – surface tension, N/m

Abbreviations and Acronyms

AB-PHP – additional branch pulsating heat pipe
CEMPHP – closed end micro pulsating heat pipe
CLMPHP – closed loop micro pulsating heat pipe
CLPHP – closed loop pulsating heat pipe
CTPHP – capillary tube pulsating heat pipe
DI – deionized
FPPHP – flat plate pulsating heat pipe
FR – filling ratio
ID – inner diameter
PHP – pulsating heat pipe

in 1990, fulfils all existing cooling requirements. Unlike conventional heat pipes, pulsating heat pipe have simple structure and are completely free from wick, providing an advantage over its manufacturing aspect. PHP is made of capillary tube in form of serpentine with multiple meandering turns. Due to the small inner diameter of the capillary tube, the size of the PHP heat transfer device can be very small too. Key benefits of PHP are quick-thermal response, compact size, and simple construction. PHP is gaining more popularity due to its versatility and significance in advancing thermal engineering solutions across broad industries. In solar energy, PHPs enhance efficiency by minimizing irreversibility during heat transfer in heat waste recovery [5]. It can contribute to sustainability efforts in aerospace thermal management ensuring precise temperature control, and in electronic industry dissipating heat effectively from various devices can solve problem of cooling highly compact and dense electronic gadgets.

PHP should have low temperature difference and thermal resistance, high transferred heat flux to operate effectively as heat transfer device. Achieving of such characteristics when PHP is used in most power engineering applications, such as heat exchangers, solar collectors etc., is relatively simple task because, as a rule, there is a lot of space to place PHP with big number of turns and overall working heat flux is high. Due to combination of these factors PHP can have low thermal resistance and it can be almost insensible to space orientation. The opposite situation is observed in the field of electronics cooling. The evolution of electronic devices, as they become smaller, faster, and more efficient, has set a challenge for the electronic industry, to dissipate high heat flux from electronic chips. One of the significant challenges is fitting devices into smaller spaces, which makes it more difficult to retain them at operating temperatures.

The downside of PHP, however, is that its working philosophy is still needs to be fully established and it is unable to function effectively at all orientations [6,7]. Gravity effects pose a significant threat to this form of cooling technology. Various parameters, such as inner diameter, number of turns, inclination angle, filling ratio (FR), channel geometry, type of working fluid, and heat input, have a significant impact on the heat transfer efficiency of PHP, and numerous studies are performed to investigate the PHP's heat transfer characteristics. The parametric investigation on PHP conducted in the last decade, both experimentally and computationally, has been reviewed and published [8–12]. The influence of geometrical, operational, and working fluid property parameters was reviewed in depth from 2009 till 2017 [8,10]. A complete review is conducted by Nazari et al. [9] to provide researchers with a deeper understanding of how to choose the best working fluid based on the latent heat of vaporization and boiling point, surface tension, thermal conductivity and dynamic viscosity. In recent studies, the combining utilization of hybrid nanofluids and geometrical alterations in heat exchangers has showcased substantial advancement in augmenting heat transfer efficiency [13,14]. Concurrently, active initiatives are also underway to enhance the thermal performance of PHPs through the integration of diverse nanofluids. A thorough literature study of the nanofluids used in PHPs was also carried out. In a recent review, Zhang et al. [11] explored the impact of cross-section, fluid properties, and external field action (i.e., magnetic field, ultrasonic wave, etc.) on PHP start-up characteristics. A flat plate pulsating heat pipe (FPPHP) is a promising design for electronics cooling. An in-depth review of thermohydraulic working principles and thermal attributes of FPPHP was conducted by Ayel et al [15]. A comprehensive critical assessment of the progress made in the theoretical modeling and simulation of PHP to date is provided in a detailed review conducted by Nikolayev [16], and it was concluded that performing PHP simulations in horizontal position and top heating mode is necessary for a better understanding of PHP working mechanisms. Mameli et al. [17], in their review of innovations in PHPs, stated that the development of ideally independent from orientation PHP is one of the future challenges in the fields of FPPHP development and application of non-conventional fluids (binary mixtures, nanofluids) as heat carriers. An insufficient quantity of visualization research on PHP working under horizontal and top heating conditions was noted by Su et al. [18].

As it can be seen, there is plenty of data on the influence of different parameters, including inclination angle, on PHP performance, but on the other hand, many reviewers note the necessity of PHP functioning investigation in horizontal and vertical top heating positions. It is because researchers paid more attention to studying of PHP performance in vertical bottom heating mode or at inclination angles between this mode and horizontal

orientation. To the best of the authors knowledge, limited reviews have been published addressing the critical parameters influencing the thermal performance of pulsating heat pipes with a specific focus on mitigating the impact of gravity. Meanwhile, knowledge about PHP functioning in horizontal and vertical top heating (or so-called anti-gravity) modes has great importance for better understanding of principles of PHP operation, designing of PHP with fully orientation independent performance and practical PHP application. In the present investigation, a comprehensive analysis is undertaken to assess the influence of geometrical parameters - encompassing cross-sectional area, inner diameter, number of turns (Fig. 1), channel design, and zone length (Fig. 1); operational parameters – encompassing orientation and heat input, working fluid parameters – encompassing fluids physical properties, fluid category, and filling ratio (Fig. 2).

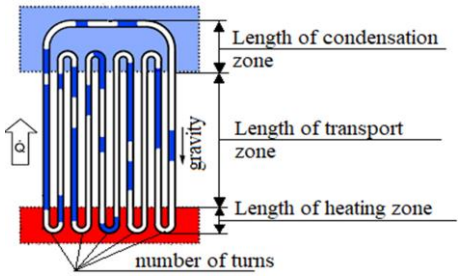


Fig. 1. Some parameters influencing PHP functioning (bottom heating mode is depicted).

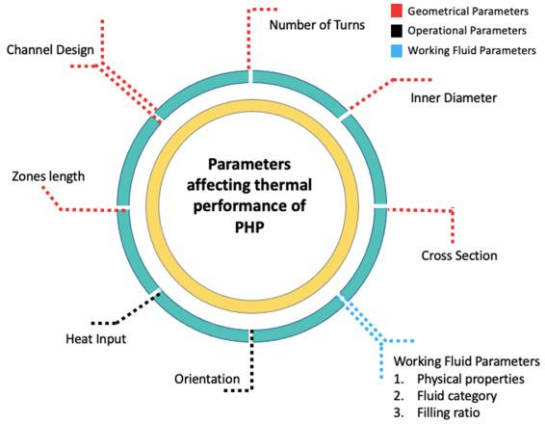


Fig. 2. Parametric review categorization.

The primary objective is to identify and address research gaps associated with PHP functionality, specifically in horizontal and top heating modes. A review of PHP design features described in the literature and their comparison is also made to find the most prospective designs of orientation-independent PHP.

2. Geometrical parameters

2.1. Inner diameter

The PHP's distinctive feature is its ability to produce liquid slugs and vapor bubbles in the channels. When the inner diameter of the channels is less than a critical diameter, surface tension forces overpower gravitational forces and the working fluid spreads across the tube in the form of liquid slugs and vapor plugs [19]. The major design restriction for PHP is the Bond number (Bo) – Eq. (1) [8], which limits the capillary tube diameter and gives the minimum internal diameter required for the capillary tube to operate in its true nature

$$Bo = \sqrt{\frac{g(\rho_l - \rho_g)}{\sigma} D^2}. \quad (1)$$

Very few researchers focused solely on the influence of inner diameter on PHP performance. They focused mainly on the impact of a range of other characteristics combined with an inner diameter on PHP output. The PHP's thermal resistance decreased as the inner diameter grew larger, which was attributed to the fact that a smaller inner diameter gave more friction resistance [20–23]. PHP's ability to manage large heat load is found to be closely related to diameter. In this regard, a larger choice of diameter would be advantageous, as for the same filling ratio, PHP with a 2 mm hydraulic diameter in horizontal mode could withstand a heat input of up to 390 W before its dry-out, whereas 1 mm hydraulic diameter PHP catches dry-out at a heat input of 190 W [22]. The heat transfer performance was also shown to increase with a 3 mm diameter tube compared to a 1.5 mm diameter tube [24]. Likewise, thermal resistance almost dropped to half when the diameter was raised from 1.05 mm to 1.9 mm [25]. Similar results were obtained when closed loop pulsating heat pipe (CLPHP) was experimented with a single turn [26]. Moreover, PHP showed different results when tested at different orientations. In horizontal mode with water as a working fluid, thermal resistance was reduced to nearly 52% with a 2 mm inner diameter compared to 1 mm, but only a marginal change was observed when ethanol was used as a working fluid [20]. The study reported by Rittidech et al. [27] found that thermal performance in horizontal orientation is not just a function of inner diameter but it is greatly affected by the properties of working fluid, as an experimental investigation revealed that heat transfer efficiency for R123 was higher, while ethanol performed poorly at a larger internal diameter. When the PHP was evaluated for a space application with a diameter bigger than the static critical diameter, which was 1.68 mm, the PHP may respond in microgravity like a real oscillating system [28]. Ayel et al. [29] concluded that the effect of gravity is more in a vertical position when experiments are carried out under conditions of hyper and microgravity, whereas the performance of PHP remained undeterred in horizontal positions, largely attributed to higher hydraulic dimeters; results of this paper were compared with experimental work by Mameli et al. [30] in the same working environment. Recently, a theoretical model was also developed to provide the absolute limit of the inner diameter and Bond number, which could allow PHP to work under microgravity conditions [31].

From the above findings, it can be seen that decreasing the PHP inner diameter leads to decreasing of gravity influence on PHP performance. But, on the other hand, the smaller PHP inner diameter the less maximal transferred heat flux. Thus, some optimal value of the inner diameter should be chosen to provide

high PHP thermal characteristics independent from gravity. This precise value of the internal diameter that yields optimum performance is still in doubt, still researchers agree that the physical properties of the working fluid play a significant role in influencing the internal diameter on PHP's thermal performance.

2.2. Number of turns

Since the inception of PHP, researchers have agreed that a large number of turns has several advantages for reducing gravity's influence on PHP operation. When the number of turns approaches 80, the thermal resistance is independent of the orientation but occupies more area, limiting demand [19]. Increasing the number of turns could increase internal pressure disturbances and achieve better results in heat transfer [32]. The necessity of increasing of number of turns to provide of possibility of PHP operation in horizontal position was experimentally shown by Kravets and Alekseik [33]. Among PHPs with 4, 7 and 9 turns, tested by authors, only the latter was able to operate in both positions: vertical with bottom heating and horizontal. Moreover, experimental work carried out on square micro-channels with the number of turns varying from 5–20 (steps of 5) revealed that the dependence of maximum permissible heat flux on the angle of inclination becomes weaker as the number of turns increases and, as the number of turns increases to 20 or more, the PHP device can operate independently of its space orientation [34]. PHP study conducted with 20 turns resulted in successful operation at all inclination angles, and PHP with higher diameter comparatively produced 10% lower thermal resistance in horizontal operation [21]. Meanwhile, to limit the effect of gravity on the PHP output, 16 turns of copper PHP were used [35]. While extensive research on the impact of meandering turn numbers on CLPHP thermal performance has been published in the past, little theoretical study has been done to establish the optimal number of turns for greater heat transmission. Experimental research carried out on both horizontal and vertical CLPHP has successfully established a correlation to predict the optimum meandering turn number of the pulsating heat pipes in the vertical, closed loop, still, the same could not be determined for horizontal closed-loop pulsating heat pipes, as heat flux varies directly with the number of turns [36]. Numerical work has also been carried out to predict the optimum number of turns; in this regard, Noh and Kim [37] obtained a merit-number correlation to determine an optimum number of turns, which could guide the design of the pulsating heat pipe by optimizing the pulsating heat pipe's thermal performance while maximizing its merit number. According to literature data only PHP with 20 or more turns can be operated independent of gravity influence [34,37–39]. Still, such PHPs has large sizes which contradicting modern trend on miniaturizing of electronic components and equipment. So, it is necessary to find out methods which make working of PHP with fewer turns (less than 20) independent of space orientation.

2.3. Cross-section of PHP

PHPs of the same hydraulic diameter but varied cross sections, such as round, square, and triangular, flowed in the channel differently. The sharp angled corners formed due to varied cross section appear to collect more working fluid, resulting in increased capillary action [22]. Besides the commonly used circular cross-section, many researchers attempted to experimentally observe PHP's thermal characteristics by switching it to another cross-section. Khandekar et al. [40] experimentally verified the performance of PHP with rectangular and circular cross-sections for the same hydraulic diameter. The thermal resistance of the rectangular cross-section was observed to be lower than the circular cross-section when experimented with a filling ratio (FR) of less than 10%. However, there was not much difference in the improvement in thermal performance, and thermal resistance observed for both cross-sections in a horizontal mode of operation was more than 4 K/W. Similarly, as demonstrated by Hua et al. [41], using a rectangular section improves start-up characteristics while reducing thermal resistance by 60–70% compared to traditional PHP. A silicon-based micro PHP with trapezoidal channels could increase temperature uniformity in the evaporator section considerably [42]. Likewise, the PHP performance with a triangular cross-section resulted in a lower thermal resistance than a square channel as reported by Li and Jia [43]. A similar trend was also observed in a comparative study between square and circular channel [44,45]. A recent study on FPPHP confirmed that using a dual cross-section ratio (Adjacent channels with different width ratio in condenser and evaporator) between adjoining channels can provide practically orientation independent performance with over 34% less thermal resistance at horizontal orientation over a varying filling ratio and 40 W heat input [46]. However, Takawale et al. [47] conducted a recent study that contradicted previous observations. Comparison of PHPs made of flat plates (FPPHP) and capillary tubes (CTPHP) using ethanol as a working fluid revealed that CTPHP had a total thermal resistance was approximately 48% lower than FPPHP when operating under the same parameters. The researchers attributed this difference to lateral conduction between adjacent channels and brief perturbations in the amplitude of FPPHP. Nevertheless, a comparison of results obtained between Ayel et al. [29] and Mameli et al. [35] in the same conditions which include not only different orientation in space but also changes in gravity level from micro- to hyper-gravity has shown that FPPHP has less sensitivity to gravity influence than CTPHP.

While much work has been done to find out PHP's thermal performance with various cross-sections, there still needs to be clear understanding of which cross-section would result in better thermal efficiency. Past literature indicates a research gap about the cross-section impact of PHP on its thermal efficiency at different orientations. To understand the effect of cross-section on its thermal performance with regard to orientation, experimental research into the combined effect of cross-section and orientation, along with comparative analysis under similar conditions is necessary.

2.4. PHP channel design

Initially, numerical simulations were used to explore the use of uneven capillary forces in order to enhance flow circulation and, ultimately, to improve heat transfer by varying the diameter of the channels [48]. Similar strategies were then experimentally tested by Liu et al. [49] on three closed-loop PHPs with slightly

different channel diameters and have been found to be effective in building and sustaining efficient working fluid circulation. By experimental investigation on vertical top heated PHP, Hathaway et al. [50] noticed a significant decrease in sensitivity to gravity when using coil-type, or what is commonly referred to as three-dimensional (non-planar) PHP systems with uneven turn combinations, such as a 20-turn evaporator and a 14-turn condenser. Pagliarini et al. [51] also manufactured and tested coil-type or three-dimensional PHP but with 13 turns in both evaporator and condensation zones. This PHP successfully operated in all space orientations. However, the functioning of the PHP was not fully independent from orientation. Thus, thermal resistance in the horizontal position was up to approximately 1.4 times higher and at top heating mode – up to 2.6 times higher than at bottom heating mode. Even at high heat loads (more than 120 W) where, according to authors' statement, PHP was independent from gravity, this ratio was 1.05–1.36 for horizontal position and 1.36-2.31 for top heating mode. In addition, it was found that PHP sensitivity to gravity decreases with increasing condenser temperature [51].

The three-dimensional design was also applied by Alekseik and Kravets [52] to make PHP-based cooler for electronic components. However, this was three-dimensional design of another kind than in [50–51]. The authors transformed conventional planar 24-turn PHP into three-dimensional PHP by arranging turns into 8 rows, as it is shown in Fig. 3, to place all turns on copper plate with dimensions 50×50 mm which acted like a thermal interface between PHP and cooled component. This PHP successfully operated at any orientation, including top heating mode, but its characteristics were still under gravity influence. For example, thermal resistance in top heating mode was up to 4.16 times higher than in bottom heating mode at the cooling of condensation zone by natural convection and up to 2.14 times higher

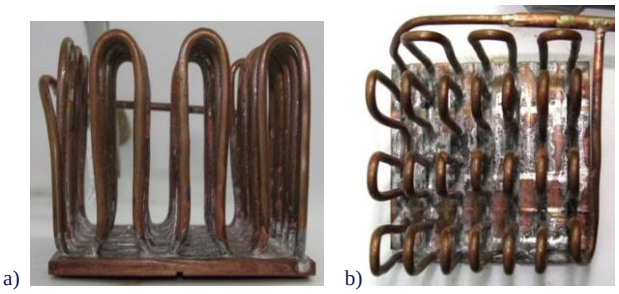


Fig. 3. Multi-row pulsating heat pipe [52]: front view (a), top view (b).

at forced convection. The same ratio for horizontal position was up to 2.06 at natural convection conditions. It should be noted, that in all these three cases, [50–52], PHP functioning at any orientation can be provided not only by three-dimensional design but also by large number of turns.

It was found that the PHP system could function horizontally with square channels of varying sizes. But the system could not operate in a horizontal position with uniformly arranged square channels [53]. Tseng et al. [54] further supported these findings by developing a strategy for operating CLPHP in a horizontal position. They conducted a comparative analysis between uniform and no-uniform PHP designs. Uniform design is a standard PHP design with round channels of an internal diameter 2.4 mm, and in non-uniform design round channels alternate with channels flattened to an oval shape with a minor diameter of 1.5 mm. The study found that when operated horizontally, the PHP with alternate channel design started at a relatively low heat input and produced substantially low thermal resistance, up to 65% compared to the conventional uniform diameter design [54]. Sedighi et al. [55] recently fabricated PHP with an additional branch (AB-PHP; Fig. 4a on Pyrex glass and compared it to standard flat plate PHP (FP-PHP). Due to an additional branch, thermal resistance decreased in the range of 11% to 20% at different FR, and flow circulation improved, resulting in better oscillation starting.

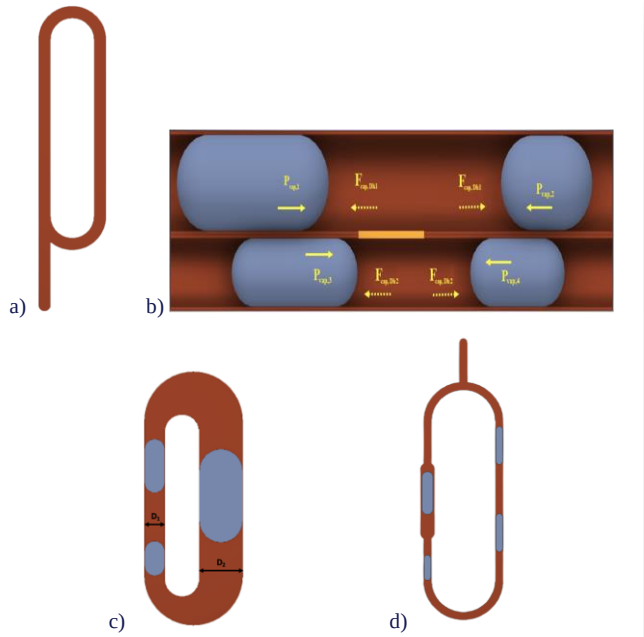


Fig. 4. Different channel design configurations: a) PHP with an additional branch [55], b) alternate double-pipe tube diameters with extra open connections [56], c) asymmetric PHP [57], d) PHP with asymmetric adiabatic channel [58].

Even after using many turns and geometric modifications, the PHP device can operate horizontally but fails to work in top heated position. To refine this problem, Tseng et al. [56] suggested a novel design using a mix of alternate double-pipe tube diameters with extra open connections between the dual pipe, as shown in the Fig. 4b. This novel design could allow PHP to operate in both top and bottom heated positions by adding an "extra unbalanced pressure force" for fluid circulation. The results of this new design were compared with Tseng et al. [54] and found that, due to this new design, thermal resistance decreased to 0.0729 K/W compared to 0.17 K/W with traditional CLPHP. Using of asymmetric PHP [57] like one shown in Fig. 4c showed 45% decrease in thermal resistance compared to symmetric PHP. Although proposed PHP model tested by Kwon and Kim was verified for one turn, but it was confirmed that increasing in the number of turns could allow asymmetric PHP work without gravity influence through this model [57]. A recent experiment

[58] was conducted on an asymmetric adiabatic channel (Fig. 4d), which yielded comparable results to the previous study. The findings indicated that PHP was ineffective when operated horizontally but could function at a lower inclination angle. When subjected to similar operating conditions with a heat input of 25 W, PHP exhibited a 30–33% decreasing in thermal resistance compared to conventional designs [58]. Therefore, it was clearly stated that even in the case of horizontal operation, using of non-uniformity in the channel layout could improve flow circulation. So in order to measure the effect of channel layout on thermal performance, the concept of effective dissimilarity was first introduced recently by Lim and Kim [59] and investigated micro pulsating heat pipe with HFE-7000 as a working fluid (50% FR) at various values of effective dissimilarity. Effective dissimilarity is a ratio between dissimilarities which show difference between current channel layout and both: uniformly arranged channel layout and decreasing channel layout. Due to using of non-uniformity in channel layout the channel with maximum effective dissimilarity reported 32% higher thermal conductance than channel with minimum effective dissimilarity in horizontal operation. Using of alternating channels with width 1.5 mm and 0.5 mm allowed horizontal operation of flexible flat-plate closed loop micro-PHP as it was reported by Jung et al. [60]. However, thermal characteristics of this PHP was still influenced by gravity. For example, its effective thermal conductivity in horizontal position was on 20.4% lower than in bottom heating position. From the other hand, its possibility of working in horizontal position can also be caused by large number of turns which was equal to 15.

Most recently, the influence of the tandem tapered nozzle on three-dimensional glass tube CLPHP was studied both experimentally and numerically [61]. Results revealed that after the modification, the thermal resistance was decreased by 29.5%, and the unidirectional flow was greatly encouraged. In addition, the dry-out condition that existed at 40% FR in the ordinary CLPHP was also removed in the tapered model. Similarly, Jang et al. [62] conducted an experiment on a radial pulsating heat pipe with diverging channels of both uniform and non-uniform sizes under horizontal operation, and discovered that the PHP with non-uniform diverging channels exhibited a thermal resistance that was up to 11.7% less than that of the uniformly designed channels However, the author did not explore how orientation impacts PHP performance [62].

The idea of non-uniform diameter PHP was further developed by Fallahzadeh et al. [63]. They fabricated and tested a single-turn triple-diameter PHP. Inner diameter of the left arm of heating and adiabatic zone was 2.5 mm, right arm of heating and adiabatic zone – 3.5 mm and condensation zone – 4.5 mm. Water was used as working fluid with variable FR from 40% to 70%. PHP was tested at inclination angles from 10° to 90°. Obtained results [63] has shown that using of triple-diameter allows to improve start-up and thermal performance, even at near-horizontal positions (inclination angles 10°–30°), and to decrease thermal resistance in comparison with single- and double-diameter PHP. Thus, applying of triple-diameter can be regarded as one of the prospective ways of decreasing of PHP sensitivity to space orientation but its effect still needs to be investigated on multiturn PHP at horizontal and top heating mode.

It can be seen that applying three-dimensional design and channels with no-uniform diameter or cross-section are prospective methods for decreasing of PHP sensitivity to space orientation. The latter can be implemented in two ways: alternating diameter or cross section of channels in an adiabatic section or making different PHP sections of different diameters. Both are proven to be effective but mostly for single-turn PHP at bottom heating and horizontal operation. It is still necessary to investigate the efficiency of these ways for multi-turn PHP and at top heating mode.

2.5. Zones length

In addition to using asymmetry in channels as one criterion to improve circulation, few authors have attempted to improve PHP performance by incorporating different sizes of evaporator lengths, adiabatic and condenser zones.

The influence of the heating zone length on PHP performance was investigated [20], which stated that the thermal resistance decreased with decrease in evaporator length and maximum performance occurred at 50 mm evaporator length. However, these findings contradict the results of a comprehensive study performed on flat plate solar collectors in combination with pulsating heat pipes [64]. It was observed that the longer the length of the evaporator, the higher the temperature of the outlet. Therefore, an increasing evaporator's length resulted in more heat being added to the tank. However, the heat transfer rate decreased with decrease in inclination, and optimum inclination of 200 for heat transfer to be maximum was observed. Similar findings from a recent study on an ethane-based low-temperature PHP also supported the idea that the PHP's heat transfer characteristics can be enhanced (the evaporator temperature may be stabilized and thermal resistance may be decreased) by lengthening the evaporator [65]. However, these results were obtained only for the vertical mode of operation with bottom heating.

Regarding the influence of adiabatic length, all researchers have come to a common conclusion that the larger the length of the adiabatic region, the greater the thermal resistance [66,67]. It was also recorded that thermal resistance was increased by just 30% by increasing adiabatic zone length by 500%, showing the possible benefits of PHPs to transmit heat over a long distance efficiently [68]. The effect of the adiabatic section length on the start-up and heat transfer efficiency was also evaluated using a two phase flow CFD model [69]. The start-up time of the PHP was reduced as the adiabatic section length increased, but the thermal resistance of the PHP increased too, and the PHP's anti-dry-out capability was weakened.

Kim and Kim [70] tested the effect of condenser length on micro-PHP and confirmed the existence of optimum condenser length for which the evaporator temperature was lowest (condenser temperature being constant). Moreover, the length ratio of the heating section to the cooling section was used as a criterion for assessing the performance of the closed-loop PHP via CFD simulation. It was found that raising the ratio leads to accelerating start-up and decreasing thermal resistance at the same FR and heat input [66]. To improve PHP performance, the effect of PHP zone length was also investigated in terms of its real-life

potential application. Considering the entire length of PHP (evaporator to condenser), it is experimentally established that with increasing PHP length, thermal performance deteriorates [71].

It is evident from previous research that the findings on how each zone length affects PHP's thermal performance are contradictory. Additionally, there needs to be more research conducted on the effect of heating zone lengths less than 50 mm on the thermal performance of PHPs at various inclination angles, despite the fact that such lengths are relevant to modern electronics cooling. It is also noted that the length of the zone and the configuration of the PHP channel have a huge influence on thermal efficiency. In this regard, a novel channel design can take care of PHP working at any orientation and varied zone length can increase thermal efficiency, but there is no research to date on the combined effect of these two factors.

3. Working fluid parameters

3.1. Physical properties of working fluid

A PHP's work and thermal performance depend enormously on the properties of the working fluid. The fluid attributes to be accounted while choosing the working fluid are surface tension, dynamic viscosity, latent heat, specific heat, thermal conductivity, boiling point and, the rate of pressure variance over-temperature under saturated conditions $(dp/dt)_{sat}$. The following section will pay examine all these properties and list their impact on PHP thermal performance.

As specified in Eq. (1), the maximum permissible PHP diameter occurs when the gravitational force roughly equals the capillary force. It is a well-known fact that higher surface tension generates a large capillary force and allows PHP to operate in any orientation, but at the same time, blocks the flow during liquid slug oscillation. In support of these theoretical postulates, numerical and experimental studies were carried out by Bastakoti et al. [72] and Kumar et al. [73], respectively, revealing that lower surface tension was found to increase thermal efficiency. On the other hand, fluid with greater surface tension tends to increase the diameter of the operating tube which due to lower frictional resistance, in effect, decreases the pressure drop. Many researchers have started using surfactant solution to lower the surface tension. PHP thermal efficiency with surfactant aqueous solutions of cetyl trimethyl ammonium bromide (CTAB) in the concentration range of 0.025% to 0.25% has been studied recently [74]. It is noted that it can significantly reduce surface tension and increase wettability by adding a surfactant solution. Due to the addition of surfactant, thermal resistance at heat inputs of 100 W and FR 50% decreased by 48.5% when compared to water. Likewise, several researchers have recently made the same attempt to reduce surface tension with the aid of surfactant solution and have found positive results with regard to PHP thermal performance [75–77].

In line with the fact that a small viscosity value can minimize channel shear stress, experimental research documented by Liu et al. [78] stated that low dynamic viscosity helped boost start-up performance. Whereas in terms of heat transfer performance, lower dynamic viscosity was found to be the dominant property at lower heat input but its effect at higher heat input weakened [79]. A similar trend was observed even in silicon-based micro pulsating heat pipes fabricated with different hydraulic diameters; working fluid with lower dynamic viscosity (FC-72 and R113) could start up PHP operation at low heat input, while fluid with a high value of dynamic viscosity (water and ethanol) failed to start up [80].

Low latent heat fluids exhibit better oscillation and start-up characteristics but are likely to dry out if the heat input continues to increase [79]. In terms of the working fluid, PHP demonstrated comparatively better thermal properties for methanol than all other fluids for both closed and open loops. For open-loop PHP, methanol is considered the best fit working fluid in horizontal operation, pertaining to its high thermal conductance [81]. A circular tube cross-section with 0.9 mm diameter was used in this experiment and performance is compared with water and acetone. Using DI water and methanol, Srikrishna et al. [82] investigated the effect on closed-loop PHP (2.2×2 mm). Better heat transfer results were obtained for methanol than DI water at 70% FR. So, it is recommended to use small latent heat fluids for low heat flux applications and high latent heat fluids for high heat flux.

The thermal conductivity of the fluid and the specific heat are two other parameters that greatly influence on thermal performance, as their higher values are likely to increase heat transfer rate. Another important parameter that was given utmost importance due to its unique characteristic is $(dp/dt)_{sat}$. The larger its value, higher the difference in vapor pressure between evaporator and condenser for small temperature change [7]. Ammonia, which has higher $(dp/dt)_{sat}$ than water, was experimentally tested as a working fluid in a glass PHP with ID = 2 mm [83]. It was found that during horizontal operation, it was easy for PHP to start up at low heat input, but circulation was not that effective. In a recent study, authors [84] also emphasize fluid properties that can provide the least PHP thermal resistance. But when comparing all the working fluids used in these two experimental works [83, 84], it can be found that the fluids with the lowest boiling points provide the least thermal resistance across most of the temperature ranges of the condenser and evaporator.

The literature analysis indicates that high thermal conductivity, specific heat and lower boiling point values provide high thermal performance of PHP. The effect of other fluid properties is controversial. To take advantage of the surface tension property and its influence on capillary force, the fluid must be selected which provides a compromise between the useful and blocking action of capillary force. Low latent heat, low viscosity, and high $(dp/dt)_{sat}$ provoke better start-up of PHP, but at high heat fluxes positive effect of these properties deteriorates. Therefore, a working fluid should be selected with regard to working range of heat fluxes and space orientation of PHP or some new alternative working fluids, such as binary mixtures, nanofluids, etc., should be used.

3.2. Fluid category

The most commonly used working fluids in PHP operation are water, ethanol, methanol, acetone, R123, and FC-72 [79,80,85]. Past studies have shown that one specific working fluid cannot

meet all the requirements mentioned in the above section. Regarding PHP thermal performance, the combination of two different fluids, a binary mixture, has shown improvement. For example, as stated by Zhao et al. [86], using of binary mixtures reduces of PHP thermal resistance by 68.9% when compared to pure liquids.

Vertically placed and bottom-heated PHP with water-acetone mixture as heat carrier was investigated [87], Results have shown that at FR 35%, 45% and mixing ratios 13:1, 1:1, 1:4, 1:13 PHP has better start-up performance and 33.6–68.9% lower thermal resistance when compare with pure liquids. Increasing the fraction of pure water (mixing ratio 13:1) is effective against dry-out and increasing the fraction of pure acetone makes an opposite effect. Improving PHP thermal performance by applying the binary mixture at high FR 62% and 70% is insignificant when compared to pure liquids. A similar study was conducted by Pachghare and Mahalle [88], which used pure water, ethanol, methanol, acetone, and binary mixtures (1:1 by volume) of water-ethanol, water-methanol and water-acetone as heat carriers. It was found that the thermal resistance of PHP with all tested binary mixtures was lower than that with corresponding pure liquids at low heat input, but changes are marginal at higher values of heat input. Among binary mixtures, the best PHP thermal performance was obtained for the water-acetone mixture. In another study [89], it was found that, at higher FR and heat input, the thermal performance of PHP with binary mixtures essentially becomes a function of the energy carrying capacity of fluid which again is a function of latent heat value and specific heat of the fluid. All binary mixtures have shown better anti-dry-out performance at low and medium FR (35–55%) than pure liquids. However, this advantage of binary mixtures was not observed at high FR. At heat input of more than 65 W and large FR (62%) mixing ratio 1:1 can be a good choice but thermal resistance of PHP with binary mixtures at these conditions is higher than that of pure water. The experimental probe by Wang et al. [90] on PHP with acetone-based mixtures (2:1, 4:1, 7:1) of water, methanol, and ethanol reported that at both low and medium FR, acetone-water binary mixture outperformed all other fluid mixtures with regards to its dry out features, but reverse effects were observed at high FR, and pure acetone exhibited better thermal performance.

Recently, the effect of other immiscible binary mixtures such as those not discussed in the above findings, is also tested on PHP. Xu et al. [91] used a combination of deionized water and HFE-7100 at different proportions (4:1, 2:1, 1:1; 1:2, 1:4) and varied inclination angles (30°–90°), whereas FR (50%) was kept constant and heat input was given between 20–250 W. It was found that a binary mixture with a 1:2 proportion performed well at heat input range 130–250 W (inclination 90°). When experimented with different heat inputs, the effect of gravity showed different characteristics at low inclination angle; at low heat inputs such as 20 W, binary mixture with 1:1 ratio performed comparatively well in terms of thermal resistance, whereas binary mixture with 1:4 ratio showed good results at high heat input.

Apart from soluble mixtures like acetone and ethanol in water, a comparative study of insoluble mixtures such as toluene and hexane in water was also carried out by Zamani et al. [92]. The mixing ratio was 3:1, 1:1, and 1:3, FR was 50%, and again acetone-water (3:1), displaying consistent trend, outperformed all other combinations and pure liquids, in terms of overall results. In addition, it was noted that soluble mixtures showed better thermal performance than that of insoluble mixtures. However, authors [86], based on literature analysis, make the opposite conclusion: insoluble mixtures significantly improve PHP thermal performance and can be prospective topic for further investigations.

Partially miscible binary mixtures can be regarded as some intermediate variant between miscible and immiscible ones. Zhou et al. [93] tested a 3-turn closed loop PHP filled with a partially miscible mixture of HFE-7100-ethanol. They found out that PHP had the best start-up characteristics and the lowest thermal resistance at mixing ratios of 3:1 and 3.5:1. Unfortunately, PHP was tested only in bottom heating mode.

The next step in using mixtures as heat carriers in PHP is applying ternary mixtures. The first mention of ternary mixtures applied in PHP was made by Su et al. [94] but they called a mixture of binary fluid (de-ionized water + n-butanol) and nanofluid as ternary mixture. At the same time, the authors do not specify which fluid was used as the base fluid for the nanofluid. If it was one of the binary mixture components then this heat carrier was just a mixture with nanoparticles (graphene oxide) addition, but not ternary mixture. In other case, it can be regarded as ternary mixture. However, using of such so-called “ternary mixture” led to the enhancement of PHP heat transport performance by approximately 15% when compared to de-ionized water at vertical bottom heating mode. Recently, Markal and Varol [95] investigated flat-plate 8-turns PHP with uneven channel width and a ternary mixture of water-methanol-pentane with mixing ratios 1:1:1, 1:2:3 and 1:3:2 at FR 30%, 50%, 70%. They found out that the optimal FR for ternary mixtures is 50% and PHP with such mixtures has better thermal performance than PHP with pure liquids at vertical bottom heating mode. The best thermal performance was achieved with a mixing ratio of 1:2:3 due to low surface tension and low boiling point. In addition, this mixture enhances start-up characteristics because of low viscosity and high $(dp/dt)_{sat}$. Unfortunately, PHPs with ternary mixtures don’t operate better in the horizontal position than PHPs with pure liquids. However, ternary mixtures can still be regarded as prospective heat carriers for PHP because of their potential to enhance thermal performance and presence of rewetting phenomenon that prevents dry-out of the heating zone.

Another way to improve thermal performance of PHP is the application of nanofluids. Adding nanoparticles to the working fluid at an optimal proportion can effectively increase the thermal conductivity of the fluid, and, hence the heat transfer rate. According to [86], applying of nanofluids with non-metallic particles as heat carriers in PHP decreases thermal resistance up to 83.6%.

Initially, many researchers used nanoparticles made primarily of pure materials such as: gold, diamond, silver, and copper [96–100]. All the researchers have come to a common conclusion that using nanofluids in PHP operation can certainly improve its performance due to their better thermal conducting properties. Later, researchers began using oxides as materials for nanoparticles. One such comparative experimental work was

carried out [101], where authors used Al_2O_3 and SiO_2 nanoparticles and found that Al_2O_3 nanoparticles give rise to better thermal performance than SiO_2 particles. However, its effect depends precisely on its concentration. A recent review by Xu et al. [102] described the detailed development of the use of nanofluids in PHP and the workings mechanism and strategies for stability improvement. Authors have concluded that future investigations should be intended to find out the optimal concentration of nanoparticles, which will enhance of PHP heat transfer performance and, at the same time, will not lead to significant increasing in nanofluid viscosity.

When PHP experimented with graphene oxide as a nanofluid in water (in the concentration of 0.25–1.5 grams/liter), it was found that thermal resistance of PHP was reduced to 42 % with 2.5 grams/liter concentration, but the reverse trend was observed with a higher concentration [103]. Moreover, the stability of the working fluid is another factor that affects its performance, as reported by Akbari and Saidi [104]. It is observed that a lower value of thermal resistance was obtained with titania-water (TiO_2) nanofluid than graphene-water nanofluid, as the former had more stability than latter. According to results obtained during the investigation of PHP with a slant angle 24°, a noticeable improvement in the performance is observed upon the introduction of silver nanoparticles in water. However, marginal improvements were seen for a higher filling ratio [105]. In addition, thermal conductivity, which is the root cause of heat transfer enhancement, particularly given the effect of nanofluid, is strongly affected by both the size and shape of the nanoparticles. It is reported that increasing nanoparticle size leads to an increase in the conductivity of a nanofluid [106]. Whereas, out of three shapes (platelet, blade, and brick) of Al_2O_3 nanoparticles which were experimented, brick shape outperformed all other shapes in terms thermal conductivity and stability [107]. On the other side, according to information from review [9], PHP filled with nanofluid made of binary mixture of deionized water and ethylene glycol with addition of aluminum nanoparticles in concentration 0.3% by volume showed the best performance with nanoparticles of cylinder shape at heat inputs lower than 100 W. And at heat input higher than 150 W the best performance was achieved with brick-like nanoparticles. Moreover, optimal concentration is also dependent on nanoparticles shape [9]. Such ambiguous results indicate that the influence of nanoparticles form on PHP performance still needs to be investigated.

While researchers gave much attention to improving thermal performance of PHP in vertical position using nanofluid, experimental research was also carried out to study the impact of gravity on CLPHP with DI-water and CuO nanofluid [108]. However, in horizontal operation, the tested PHP could not perform, suggesting that although nanofluid improves PHP thermal performance, it has little effect on gravity. However, PHP with water-based ferrofluid was able to operate at any orientation in presence of magnetic field as experimented by Mohammadi et al. [109]. Thermal performance was significantly elevated in horizontal operation at a larger filling ratio and heat input. In a parallel investigation, Goshayeshi et al. [110] dispersed Fe_2O_3 nanoparticles into kerosene and studied its effect on closed-loop copper PHP under a magnetic field. Even in horizontal operation, the PHP functioned successfully, although its thermal resistance increased from vertical to horizontal.

All the results mentioned showed that using of binary mixtures enhances PHP's thermal performance in compared with traditional pure working fluids in most cases. However, positive effect of applying binary mixtures takes place at low FR (less than 50%), and at high FR, it deteriorates. Information about optimal mixing ratio and impact of binary mixtures on PHP performance at different orientations is limited, and research work in these ways needs to be done. In addition, a question about the type of binary mixture (soluble or insoluble) that provides better PHP performance is still unsolved. Most researchers concluded that enhancing PHP thermal performance due to application of nanofluids is related to high thermal conductivity of these fluids. However, the optimal concentration of nanoparticles, stability, sizes and form, and thermal performance of PHP with nanofluids at different space orientations still need more attention.

3.3. Filling ratio

Filling ratio (FR) is ratio between volume of liquid heat carrier filled inside PHP and total inner volume of PHP. Past studies have found that for PHP to show its true nature, FR should range between 20% to 80% [7]. However, a critical review by Han et al. [89], showed that the most authors used FR of between 35% and 65% as the optimal value for almost all the working fluids. The properties of working fluid have a significant influence on the optimum FR. Experimental work reported by Han et al. [79] revealed that working fluid with low latent heat value was easier to dry out for the same FR. Results also showed that with regards to low thermal resistance, at low heat flux, FR of approximately 60 % is a fair choice for acetone, whereas, at high heat flux, the optimal filling ratio for methanol and DI water ranges from 60% to 70%.

Similar behavior was observed for acetone, as it displayed a lower thermal resistance value at 60% FR when PHP was tested at FR ranging from 50% to 90% [111]. Ethanol, on the other hand exhibited optimum performance at FR of 50% to 70% [112]. It was 70–80% for ammonia to avoid burn out of evaporator [82]. Besides working fluid properties, PHP performance in terms of FR often varies with PHP system orientation and cross section. When a flat plate aluminum PHP was operated with ethanol as a working fluid, the optimum FR was found to be 50–65% in horizontal and top heated positions, whereas it was between 40–70% with bottom heated mode [22]. At close horizontal orientations, the performance of water as a working fluid is lower than methanol with the same fill ratio, and, methanol displayed less thermal resistance when measured at 40% FR for inclination angles from 90° to 7.5° [82]. In another investigation, DI-water charged PHP with a circular channel showed the lowest thermal resistance at FR of 40% while, rectangular channel showed the lowest thermal resistance at 30% FR [41]. A recent study of liquid metal high-temperature 6-turn PHP filled with sodium-potassium alloy performed by Wu et al. [113] has shown that the best PHP thermal performance was obtained at FR equals to 48%. However, FR did not show a significant influence on PHP sensitivity to inclination

angle: at FR equals to 22% PHP failed to start in horizontal position, but for all other tested FRs (35%, 48%, 64%, 80%) similar trend was observed – decreasing of inclination angle from 90° (bottom heating mode) to 0° (horizontal position) leads to increasing of thermal resistance.

Although FR is a crucial parameter to decide heat transfer characteristics of PHP devices, past studies show that optimum FR of a working fluid varies with a particular experimental design, which again is a function of many other parameters that were discussed. Theoretical studies that could establish the optimum FR for optimizing heat transfer characteristics are rare. One such study was carried out recently by Yin et al. [114], who developed a mathematical model to predict the effect of FR on startup heat flux. The study found that the heat input required to start the oscillation depends on FR, but the upper limit of FR is again considered to be a function of the type of fluid. It is, therefore, imperative that many experimental or computational tests need to be carried out in terms of FR to create a database that will help design future PHP devices at optimum FR.

4. Operational parameters

4.1. Heat input

The heat input to the PHP system relates directly to its operating temperature. About the application of PHP for cooling of electronic devices, the reliability of electronic components is closely linked to the failure factor (failure rate ratio at any temperature to failure rate at 75ºC), which increases exponentially with the system temperature [115]. It is, therefore, of utmost importance to build a PHP that can be operated over a wide range of temperatures and prevent electronic components from raising their temperature beyond its failure threshold.

A study carried out by Spinato et al. [11] on copper CLPHP (ID = 2 mm) using water, ethanol, methanol, and acetone as working fluid showed influence of heat input value on flow patterns inside PHP. Bubbly and slug flow patterns were observed in the upward flow under the impact of gravity after slug boiling at power up to 40 W, and semi-annular and annular flows were found in the downward flow. At high heat flux, the gravity effect showed no impact (70 to 80 W). In particular, it was shown that thin-film evaporation makes the most significant contribution to the overall local heat transfer coefficient for all the conditions studied and can be considered as the prevailing heat transfer process. This research suggested that the collective activity of bubble nucleation, agglomeration, and condensation is responsible for the two-phase flow movement. More recently, similar observations were made when utilizing gravity pulsating heat pipe to intensify the gravity impact of the working fluid for preventing dry-out at heat input range 30–230 W. These observations validated that film boiling heat transfer is the leading driving force behind stable operation [117].

As mentioned before, Spinato et al. [116] did not observe a significant effect of space orientation on PHP performance at high heat fluxes. Similar results were obtained by Torresin et al. [118] on double condenser PHP cooler, which demonstrated close to orientation-free PHP operation at high heat input (higher than 2000 W).

An attempt was also made to find out the liquid and vapor volume fraction within PHP by experimenting with water-based PHP (6 turns) using neutron imaging technique. It was found that the average liquid volume fraction was always less than 25% and more than 80% in the evaporator and condenser, respectively, during the steady-state oscillation within PHP [119]. The thermodynamic state of a vapor plug in the micro pulsating heat pipe (MPHP) was recently experimentally determined by Jun and Kim [120], and it was observed to be depend on the presence of the liquid film covering the vapor plug. The vapor plug becomes saturated when surrounded by a liquid film. On the other side, the vapor plug is superheated when it is in close contact with the dry wall without the liquid film (Fig. 5).

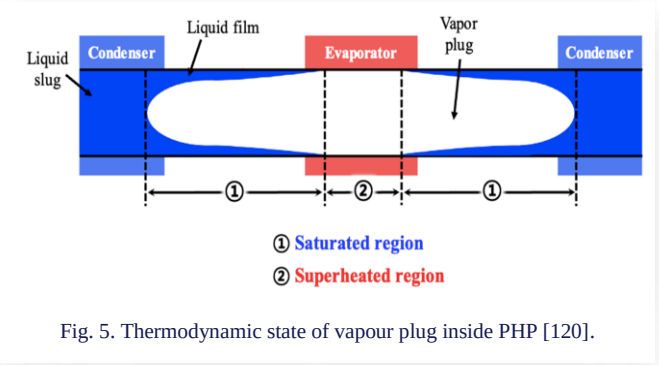


Fig. 5. Thermodynamic state of vapour plug inside PHP [120].

The startup analysis was conducted with binary fluids (acetone, ethanol, methanol) and surfactant solutions (sodium dodecyl sulphate) based on water. It was found that the onset of pulsation remained the same even after using PHP for more than 7 hours, but with a rise in evaporator temperature [121]. Although heat flux is responsible for generating a driving force required to bring PHP into operation, start-up heat flux is different for different working fluids.

Experimental testing of PHP at different orientations from horizontal to vertical has shown that each tilting angle displayed different starting heat input values. Furthermore, the operational range of allowable heat fluxes becomes narrower and closer to lower heat power values as the tilting angle increases [122]. Meanwhile, heating patterns significantly influenced startup process and thermal resistance of PHP as indicated numerically by Jiansheng et al. [123]. The PHP's start-up time was decreased due to the non-uniform heating pattern (heating at one or many turns), which was attributed to the additional imbalance stimulating the device's start-up. However, thermal resistance increased under the same conditions. Experimental analysis with non-uniform heating of 8-turn PHP with HFE-7100 as heat carrier at bottom heating mode carried out by Jang et al. [124] demonstrated findings similar to those of the previous study. A concept of "dimensionless heat difference (ratio of the difference in heat input between two sources to total heat input)" was used and thermal resistance was found to be increased due to early drying out on the higher side of the heat input with an increase in this factor. A recent experimental study on inclination angle influence on thermal performance of 4-turn CLPHP with ethanol and HFE-7100 as heat carriers conducted by Zhang et al. [125] showed decreasing of thermal resistance and PHP sensitivity to space orientation with application of non-uniform

heating pattern when compare it to uniform at inclination angle range 45°–90°. These results contradict the results of previous studies.

However, the heating pattern does not only influence PHP performance. Okazaki et al. [126] experimentally shown that presence of large quantity of alternating heating and condensation zones has vital importance for ensuring of PHP functioning in horizontal position. They compared performance of circular single-turn PHP and serpentine multi turn PHP in horizontal position. Both PHPs had the same overall capillary tube length, quantity of check valves and quantity of alternating heating and condensation zones, both were filled with HFC-134a. Both PHP demonstrated almost similar thermal performance with a thermal resistance of approximately 0.45–1.1 K/W. This means that the presence of large quantity of alternating heating and condensation zones has more importance for ensuring of PHP operation in horizontal position than even large number of turns. Moreover, this result shows that PHP for a horizontal mode of operation can be designed without U-shaped turns at all.

Heat input level strongly affects thermo-fluid dynamics within PHP and, as a result, affects the thermal performance of PHP- Startup and dry-out heat input levels, which are the borders of PHP operational range of heat flux. High heat input levels significantly decrease PHP sensitivity to space orientation, but such levels not always achievable in practical applications. The application of non-uniform heat input patterns could be named as prospective method of improving PHP start-up characteristics. However, the influence of such patterns on PHP heat transfer characteristics needs further and deeper investigation in wide range of inclination angles, including horizontal and vertical top heating mode, because of contradictions in existing results. Furthermore, it is necessary to provide investigations and develop new PHP designs for minimizing of inclination angle influence on an operational range of heat flux.

4.2. Orientation of PHP

Gravity adds to the unequal distribution of pressure in the PHP, which could increase the perturbation of the fluid and the enhanced heat transfer that follows it. Moreover, gravity facilitates the backflow of the liquid phase into the evaporator at low heat flux, which is a significant element in stopping the evaporator from drying out. One of these benefits is missed by PHP in a horizontal position or vertical top heating mode. Therefore, PHP orientation indirectly brings gravity into the picture and plays a vital role in evaluating its thermal performance, which could also be described using Eq. (1). Several attempts have been made in the past, to make PHP work independently of its orientation and weaken the influence of gravity by finding out balance between the capillary and vapor pressure forces using new PHP designs [50,51,53,54,56]. It is observed that PHP's thermal performance becomes independent of the orientation using the number of turns as high as 80 [19]. Attempts have also been made to use a fewer number of turns (to minimize space) and yet be able to weaken the influence of gravity. The first attempt to understand the role of gravity in the operational characteristics of PHP is made by Khandekar and Groll [6], A 'stopover' phenomenon was observed and described as repetitive activity phase occurrence (large amplitude oscillations) and static phase occurrence (very small amplitude oscillations). Liquid plugs oscillate with very small amplitude in the condenser segment during the static phase. This 'stopover' phenomenon is also explained clearly by Jun and Kim (Fig. 6) [127]. Due to this issue, the liquid plugs do not circulate from the condensing to the heating zone, contributing to the evaporator drying out. This 'stopover' phenomenon seldom happens in PHP with large number of turns, because of sustained high amplitude oscillations.

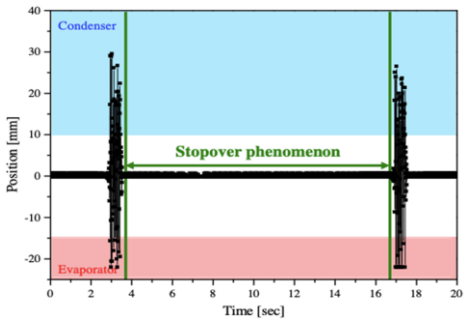


Fig. 6. Stopover phenomenon observed in 10 turn PHP during horizontal operation [127].

Therefore, quite recently, Jun and Kim [128] established a criterion through theoretical and experimental investigation on micro-PHP (10 turns) to prevent this 'stopover' phenomenon and to allow PHP function in horizontal mode. For normal PHP operation in horizontal mode, a figure of merit was introduced. Its analysis has shown that the ratio of the minimum thermal resistance in a vertical orientation to that in a horizontal orientation is proportional to the square of the ratio of the hydraulic diameter to the effective length of PHP [128]:

$$\left(\frac{R_{v,\,\min}}{R_{h,\,\min}}\right) \sim \left(\frac{D_h}{L_{eff}}\right)^2 \tag{2}$$

so as to prevent a 'stopover' defect in horizontal operation. It is also confirmed that the ratio of hydraulic diameter to the effective length of ethanol-filled micro-PHP must be greater than 0.03 for this purpose.

Moreover, simulation findings by Nekrashevych end Nikolayev [129] reveals that the variation in PHP performance is related to the difference in the phase distribution within the PHP evaporator at various orientations. Similar results were observed previously by Khandekar et al. [130] during the experimental study.

Findings from the literature imply that PHP can work at any orientation even without using a significant number of turns. A key to such functioning is balancing forces acting on heat carrier and phase distribution inside PHP. However, further investigations are necessary to discover physical insights and design solutions which provide optimal forces balance and phase distribution, allowing PHP function independently of orientation.

5. Comparison of design features enabling PHP functioning at different space orientation

As can be seen from previous sections, researchers try to apply some design features to make PHP operation at different space orientation possible. Some even call their PHP applicable to all orientations [53] or anti-gravity [71,132]. Moreover, according to published results working of these PHPs at any space orientation, including horizontal or even vertical with top heating is really possible. However, this possibility and full independence of PHP operation from space orientation are not the same. We regard the absence or minimal influence of space orientation on PHP performance in wide range of heat power as the latter. Let us compare different design features in terms of providing PHP operation independence from space orientation. The ratio of PHP thermal resistance at horizontal position (Rh) or at the top heating mode (R_{vt}) to thermal resistance at bottom heating mode (R_{vb}) is used for this purpose. Such an approach, for example, was used by Tseng et al. [132] to evaluate effectiveness of their design solution in comparison with other researchers. Thermal resistance is chosen because it is one of the main and most investigated PHP characteristics. The form of ratio (R_h/R_{vb} and R_{vt}/R_{vb}) is chosen to compare PHP thermal resistance in unfavorable orientations (horizontal and top heating mode) with that one in one of the most favorable orientations (bottom heating mode). If this ratio is equal or close to 1.0, then PHP works equally well in both favorable and unfavorable orientations. If it is higher than 1–1.1, then orientation has significant influence on PHP operation. The results of the comparison are presented in Table 1.

Table 1. Comparative table of design features enabling PHP functioning at different space orientation.

Operational parameter	Features of PHP design	Ratio of PHP thermal resistance at various space orientation		Reference
		R_h/R_{vb}	R_{vt}/R_{vb}	
Inner diameter	FPHP having more hydraulic diameter than critical value	1.56–1.89	N/A	[29]
Number of turns	Number of turns >>20	1.0–1.62	N/A	[34]
	Flat plate closed loop micro-PHP with 20 turns	1.0–2.15	N/A	[127]
	Flat plate closed end micro-PHP with 20 turns	1.0–1.09	N/A	[127]
Channel design	Closed loop FPPHP with square channels 1x1 mm and 2 x 2 mm	1.0–1.22	1.0–1.48	[22]
	FPHP dual cross section (different width ratio of adjacent channels in condenser and evaporator)	1.11–4.0	N/A	[46]
	Coil-type (three-dimensional) PHP with uneven-turn design: 20 turns in heating zone, 14 turns in condensation zone	N/A	1.0–2.31	[51]
	Coil-type (three-dimensional) PHP with 13 turns	0.56–1.36	1.03–2.57	[51]
	Multi-raw PHP	1.61–2.06	1.13–4.16	[52]
	Non uniform square channel	1.1–1.58	N/A	[53]
	Alternate tube diameter	1.19–7.78	N/A	[54]
	Double pipe PHP with alternate tube diameter and extra opening connection	N/A	1.32–15.0	[56]
	Flexible micro-FPPHP with alternating channels with width 1.5 mm and 0.5 mm	1.13–1.43	N/A	[60]
	Double condenser PHP with heat input at middle section	0.85–0.98	1.0–1.06	[118]
	Closed loop micro-FPPHP with D_h/L_{eff} = 0.038	0.91–1.2	1.0–1.93	[128]
	Ring-shaped rectangle PHP with dual cross section (round and oval-shaped)	N/A	1.04–2.06	[132]
Zones length	Coil-type PHP with zones length ratio $L_e : L_a : L_c$ = 1 : 1 : 1	N/A	1.5–4.23	[71]
Physical properties of working fluid	Pure liquids: ammonia	2.4–7.6	N/A	[83]
	Liquid metals: sodium-potassium alloy with the potassium mass fraction of 78%)	1.27–3.11	N/A	[113]
	Binary mixtures: water-HFE (4:1, 2:1, 1:1, 1:2, 1:4)	1.09–2.07*	N/A	[91]
	Ethanol-pentane (1:1, 1:3, 3:1)	0.94–1.68	N/A	[131]
	Ternary mixtures: water-methanol-pentane (1:1:1, 1:2:3, 1:3:2)	1.02–2.04	N/A	[95]
	Nanofluids: water-copper 5% by mass, particle diameter 29 nm	1.15–1.66	1.15–2.09	[99]
	Water-Fe particles (magnetic ferrofluid) 7% by volume+magnetic field	1.55–1.9	N/A	[109]
	Kerosene-Fe_2O_3 (magnetic ferrofluid) 2% by volume, particle diameter 20 nm + magnetic field	1.12–1.25	N/A	[110]

*Ratio between thermal resistances at inclination angle 30° and at vertical bottom heating mode is presented.
N/A – data not available
L_e, L_a, L_c – length of evaporation, adiabatic and condensation zones respectively
HFE-7100 (methoxy-nonafluorobutane) is engineered fluid which was used as a heat carrier in PHP.

Data presented in Table 1 shows that the thermal resistance ratio for all listed design features changes in a wide range (much wider than 1–1.1) which means none of these features can provide PHP operation full independent from space orientation. However, despite this fact, there are some design features, which could be named, as prospective because they ensure the narrowest range of the thermal resistance ratio. Applying uneven-turn design, alternative channel design in form of non-uniform square channels [53] and using binary mixtures [91,131] and nanofluids [99,109,110] are among them. It is important to note that good results in [109] and [110] were achieved due to the application of magnetic field to PHPs filled with magnetic ferrofluids which is possible only in some specific practical applications.

One of the narrowest range thermal resistance ratios at horizontal position was obtained for double condenser PHP proposed by Torresin et al. [118]. Moreover, the values of the ratio are less than 1 (0.85–0.98) which means that PHP performance in horizontal orientation was even better than in vertical. As for the vertical orientation, there was no differences between possible variants of vertical orientation for this PHP in terms of mutual placement of heating and condensation zones because of its design: condensation zones were placed at both ends of the PHP and heating zone – between them in the middle part of the PHP. Thus, at any vertical orientation one of the condensers was always above the heating zone and the other one was below. Thereby, data on the top heating mode presented in table 1 for this PHP are quite conditional, and the difference in condensers channels design can explain insignificant difference of thermal resistance ratio from 1. Two important things should be noted about the results presented in [118]. First, they were obtained for high heat input in the range 500–2500 W, at which even PHPs of classical design have significantly decreased sensitivity to space orientation. Achieving such a result at lower heat power (up to 100–150 W), which is more conventional for electronics cooling, is much harder. Second, the thermal resistance presented in [118] is not the thermal resistance of PHP itself. In fact, it is a sum of PHP thermal resistance and thermal resistance of heat transfer from the outer surface of PHP to the cooling air because it was calculated by difference between maximal temperature in heating zone and temperature of cooling air.

Alternative channel designs such as double pipe PHP with alternate tube diameter and extra opening connection [55] and ring-shaped rectangle PHP with dual cross section [132] can be regarded as prospective because possibility of working of PHPs with these designs at top heating mode was proven experimentally. The relatively narrow range of thermal resistance ratio at top heating mode was obtained by authors [50] (1.0–2.31) and [132] (1.04–2.06). However, these results were also obtained for high heat input of 200–800 W.

The narrow range of thermal resistance ratios for both horizontal (1.0–1.22) and top heating mode (1.0–1.48) was obtained in [22]. However, these results can be explained by a large number of turns (20 and 33) and a high heat input 200–400 W.

It should be noted that in most cases listed in the Table 1, the lower border of the range of thermal resistance ratio is equal to 1–1.1. However, these ratios were obtained only for a few values of heat fluxes and not for whole working range of heat flux. It is also evident from Table 1 that most of the PHPs with design features were not tested at top heating mode.

Results different from those described above were obtained by Jun and Kim [127] on flat plate closed loop micro-PHP (CLMPHP) and closed end micro-PHP (CEMPHP) filled with ethanol at FR equal to 50% and tested at heat input range 2–82 W. 20-turns CLMPHP showed orientation independent performance in terms of thermal resistance (R_h/R_{vb} = 1.0) in the heat input range 42–82 W. The highest value of thermal resistance ratio was obtained at heat input lower than 20 W where PHP start-up takes place. It means that space orientation still influenced the start-up parameters of this PHP. This influence was absent for 15-turns CEMPHP which demonstra-ted full orientation independent performance in whole range of tested heat inputs (R_h/R_{vb} = 1.0–1.09).

These results confirm the possibility of designing of PHP free of space orientation influence. However, on the other hand, thermal resistance of these PHPs in the main working mode is in the range 1–2 K/W which is too high for some practical applications such as, for example, electronic cooling. Therefore, it is necessary to enhance the design of these PHPs to decrease thermal resistance.

The same authors in their subsequent work [128] found a criterion which allows designing of PHP with orientation independent performance. This criterion is the ratio D_h/L_{eff} (see Eq. (2)). They manufactured 10-turns CLMPHP with D_h/L_{eff} = 0.038, and ethanol as heat carrier (FR = 50%) and tested it in the range of heat input 12–44 W. According to the results obtained, thermal resistance ratio of this PHP for both horizontal and vertical top heating mode is equal to 1.0 at heat input range 22–44 W. This is the evidence of full independence of PHP performance from space orientation. However, at heat input lower than 20 W, thermal resistance ratios reach the value of 1.2 for the horizontal position and 1.93 – at vertical top heating mode. This indicates the influence of space orientation on start-up characteristics of PHP. Taking these results into account, proposed criterion can be regarded as one of the key parameters for providing of orientation independent PHP performance, but it needs some improvement and further experimental verification for a few reasons. First, it does not offer orientation independent performance during start-up period. Second, its derivation was based on visualization data obtained for micro-PHP and it was verified on ethanol as heat carrier. It is unknown how it works for PHP of conventional design and for other heat carriers. Third, it does not take into account the surface tension of heat carrier, which plays significant role in liquid slugs formation and movement, and PHP number of turns, which has a significant influence on PHP sensitivity to space orientation. The fourth, it contains effective length. Despite relatively frequently applying this parameter as characteristic length of PHP, in our opinion, it is not correct. This parameter appears in a field of conventional wick heat pipes. It is a sum of length on which mass flow rate of liquid heat carrier through a wick has maximal and constant value (adiabatic zone) and half-sum of lengths on which it linearly changes from zero to maximum (heating zone) and vice versa (condensation zone) [133]. However, PHP does not contain a wick; liquid and vapor phase of a heat carrier are not separated, as it takes place in conventional heat pipes, and flow as single two-phase stream; PHP is multichannel device and mass flow rate of liquid may differ from channel to channel at the same moment of time. Thus, it is necessary to find out the physical justification for applying of effective length to PHP or derivate some alternative characteristic length of PHP.

It can be summarized that applying of uneven-turn design, channel design with alternating shape and size of cross-section, double-condenser design, and using of nanofluids and binary mixtures as heat carriers are some of the most prospective ways of providing independent PHP working from space orientation. However, they still need improvement and additional investi-

gation to decrease the thermal resistance ratio. In addition, it is necessary to investigate the influence of design features on PHP operation at top heating mode.

6. Conclusions

Space orientation has a significant impact on PHP's heat transfer efficiency. Despite several benefits of PHP in various applications involving efficient heat transfer requirements, the commercial aspect of PHP has been presented very narrow in the market. This is because of the fact that the original PHP works better when gravity assists the process. With such high hopes for PHP's future prospects, various challenges linked to reducing PHP space orientation dependence must be resolved, and some recommendations for further study are provided here:

1. In terms of cross-section, state-of-the-art claims that micro-PHP with a non-circular cross-section (such as rectangular, triangular, trapezoidal) has shown better thermal characteristics than these with circular cross section. However, there still needs to be a clear understanding of which cross-section would result in better thermal efficiency for PHP in general. In addition, there are research gaps regarding the combined effect of cross-section and space orientation of PHP on its thermal efficiency. Thus, investigations in this way are necessary.
2. In terms of geometrical parameters, PHP with an ID less than 2 mm can work in any space orientation. However, because decreasing ID increases thermal resistance, it is vital to develop a solution to reduce thermal resistance. There is lack of information about zone lengths influence on thermal performance of PHP. Moreover, information about the influence of this parameter on the possibility of PHP working at any orientation in space is absent. Therefore, this factor needs to be investigated. PHP with a number of turns more than 20 can operate independent to orientation in space. However, the sizes of such PHPs are too large for application in modern electronic devices. Therefore, it is necessary to find ways of making orientation-independent PHP with small number of turns such as from 1 to 10.
3. High thermal conductivity values of the working fluid and the specific heat provide high thermal performance of PHP. The effect of other liquid properties is controversial. Surface tension should have a value that provides a compromise between the useful and blocking action of capillary force. Low latent heat, low viscosity, and high $(dp/dt)_{sat}$ provoke better start-up of PHP, but at high heat fluxes, positive effect of these properties deteriorates. Therefore, a working fluid should be selected with regard to working range of heat fluxes and space orientation of PHP or some new alternative working fluids should be used.
4. Using binary mixtures and nanofluids greatly enhances PHP's thermal performance in compared with traditional pure working fluids in most cases. However, information about optimal mixing ratio of binary mixtures, optimal parameters of nanofluids: concentration, size and form of nanoparticle, stability of fluid and impact of these fluid categories on PHP performance at different orientations (especially horizontal and top heating mode) is limited and research works in these ways need to be done. In addition, a question about type of binary mixture (soluble or insoluble) which provides better PHP performance is still unsolved.
5. Filling ratio (FR) is one of the main parameters affecting thermal performance of PHP. Optimal FR range depends on many factors such as PHP design and physical properties of heat carrier. Many experimental or computational tests need to be carried out to create a database that will help design future PHP devices at optimum FR.
6. Applying three-dimensional design, uneven-turn design, channel design with alternating shape and size of cross section, double-condenser design and using of nanofluids and binary mixtures as heat carriers could be named as one of the prospective ways of providing independent PHP working from space orientation. However, they need to be improved and investigated to further decrease PHP sensitivity to space orientation. In addition, it is necessary to investigate the influence of design features on PHP operation at the top heating mode.

The findings of this study offer a reference for future research intended for stabilization of PHPs thermal performance across varying orientations. This stabilization holds promise for expanding PHP applications in domains where passive heat transfer is a critical requirement. The future scope of PHP researches is connected not only with decreasing of sensitivity to space orientation but also with PHP miniaturization, design modifications, further development of flat-plate PHP, applying of alternative casing materials and heat carriers in order to obtain compact high efficient heat transfer devices and thermal spreaders based on PHP.

References

[1] Gautam, A., & Saini, R.P. (2021). Development of correlations for Nusselt number and friction factor of packed bed solar thermal energy storage system having spheres with pores as packing elements. *Journal of Energy Storage*, 36, 102362. doi: 10.1016/j.est.2021.102362

[2] Gautam, A., Dave, T., & Krishnan, S. (2023). Can solar energy help ZLD technologies to reduce their environmental footprint?- A Review. *Solar Energy Materials and Solar Cells*, 256, 112334. doi: 10.1016/j.solmat.2023.112334

[3] Gautam, A., & Saini, R.P. (2022). Performance analysis and system parameters optimization of a packed bed solar thermal energy storage having spherical packing elements with pores. *Journal of Energy Storage*, 48, 103993. doi: 10.1016/j.est. 2021.103993

[4] Akachi, H. (1990). *Structure of a heat pipe*. US patent 4921041.

[5] Jouhara, H., Almahmoud, S., Chauhan, A., Delpech, B., Bianchi, G., Tassou, S.A., Llera, R., Lago, F., & Arribas, J.J. (2017). Experimental and theoretical investigation of a flat heat pipe heat exchanger for waste heat recovery in the steel industry. *Energy*, 141, 1928–1939. doi: 10.1016/j.energy.2017.10.142

[6] Khandekar, S., & Groll, M. (2004). An insight into thermo-hydrodynamic coupling in closed-loop pulsating heat pipes. *International Journal of Thermal Sciences*, 43(1), 13–20. doi: 10.1016/S1290-0729(03)00100-5

[7] Zhang, Y., & Faghri, A. (2008). Advances and unsolved issues in pulsating heat pipes. *Heat Transfer Engineering*, 29(1), 20–44. doi: 10.1080/01457630701677114

[8] Han, X., Wang, X., Zheng, H., Xu, X., & Chen, G. (2016). Review of the development of pulsating heat pipes for heat dissipation. *Renewable and Sustainable Energy Reviews*, 59, 692–709. doi: 10.1016/j.rser.2015.12.350

[9] Nazari, M.A., Ahmadi, M.H., Ghasempour, R., & Shafii, M.B. (2018). How to improve the thermal performance of pulsating heat pipes: A review on working fluid. *Renewable and Sustainable Energy Reviews*, 91, 630–638. doi: 10.1016/j.rser. 2018.04.042

[10] Bastakoti, D., Zhang, H., Li, D., Cai, W., & Li, F. (2018). An overview on the developing trend of pulsating heat pipe and its performance. *Applied Thermal Engineering*, 141, 305–332. doi: 10.1016/j.applthermaleng.2018.05.121

[11] Zhang, D., He, Z., Jiang, E., Shen, C., & Zhou, J. (2020). A review on start-up characteristics of the pulsating heat pipe. *Heat and Mass Transfer*, 57, 723-735. doi: 10.1007/s00231-020-02998-4

[12] Dave, C., Dandale, P., Shrivastava, K., Dhaygude, D., Rahangdale, K., & More, N. (2021). A review on pulsating heat pipes: latest research, applications and future scope. *Journal of Thermal Engineering*, 7(3), 387–408. doi: 10.18186/thermal. 878983

[13] Olabi, A.G., Wilberforce, T., Sayed, E.T., Elsaid, K., Rahman, S.A., & Abdelkareem, M.A. (2021). Geometrical effect coupled with nanofluid on heat transfer enhancement in heat exchangers. *International Journal of Thermofluids*, 10, 100072. doi: 10.1016/j.ijthermalsci.2020.100072

[14] Bouselsal, M., Mebarek-Oudina, F., Biswas, N., & Ismail, A.A.I. (2023). Heat transfer enhancement using Al_2O_3-MWCNT hybrid-nanofluid inside a Tube/Shell heat exchange with different tube shapes. *Micromachines*, 14(5), 1072. doi: 10.3390/mi14041072

[15] Ayel, V., Slobodeniuk, M., Bertossi, R., Romestant, C., & Bertin, Y. (2021). Flat plate pulsating heat pipes: A review on the thermohydraulic principles, thermal performances and open issues. *Applied Thermal Engineering*, 197, 117200. doi: 10.1016/ j.applthermaleng.2021.117200

[16] Nikolayev, V.S. (2021). Physical principles and state-of-the-art of modeling of the pulsating heat pipe: A review. *Applied Thermal Engineering*, 195, 117111. doi: 10.1016/j.applthermaleng.2021.117111

[17] Mameli, M., Besagni, G., Bansal, P.K., & Markides, C.N. (2022). Innovations in pulsating heat pipes: From origins to future perspective. *Applied Thermal Engineering*, 203, 117921. doi: 10.1016/j.applthermaleng.2021.117921

[18] Su, Y., Hu, Z., Zheng, S., Wu, T., Liu, K., Zhu, M., & Huang, J. (2023). Recent advances in visualization of pulsating heat pipes: A review. *Applied Thermal Engineering*, 221, 119867. doi: 10.1016/j.applthermaleng.2022.119867

[19] Akachi, H., Polasek, F., & Stulc, P. (1996). Pulsating heat pipes. *Proc. 5th International Heat Pipe Symposium*, Melbourne, Australia, 208–217.

[20] Charoensawan, P., & Terdtoon, P. (2008). Thermal performance of horizontal closed-loop oscillating heat pipes. *Applied Thermal Engineering*, 28(5−6), 460–466. doi: 10.1016/j.applthermaleng. 2007.06.027

[21] Yang, H., Khandekar, S., & Groll, M. (2008). Operational limit of closed loop pulsating heat pipes. *Applied Thermal Engineering*, 28(1), 49–59. doi: 10.1016/j.applthermaleng. 2007.01.033

[22] Yang, H., Khandekar, S., & Groll, M. (2009). Performance characteristics of pulsating heat pipes as integral thermal spreaders. *International Journal of Thermal Sciences*, 48(4), 815–824. doi: 10.1016/j.ijthermalsci.2008.05.017

[23] Wang, S., & Nishio, S. (2005). Heat transport characteristics in closed-loop oscillating heat pipes. *Heat Transfer Summer Conference*, 47349, 805–810. doi: 10.1115/HT2005-72273

[24] Shafii, M.B., Faghri, A., & Zhang, Y. (2002). Analysis of heat transfer in unlooped and looped pulsating heat pipes. *International Journal of Numerical Methods for Heat and Fluid Flow*, 12(5), 585–609. doi: 10.1108/09615530210434304

[25] Chu, L., Ji, Y., Liu, Z., Yu, C., Wu, Z., Wang, Z., & Yang, Y. (2022). Structure optimization of a three-dimensional coil oscillating heat pipe. *International Journal of Heat and Mass Transfer*, 183, 122229. doi: 10.1016/j.ijheatmasstransfer.2021. 122229

[26] Sreenivasa Rao, C., Gupta, A., & Rama Narasimha, K. (2016). Parametric characterization on the thermal performance of a closed loop pulsating heat pipe. *Journal of Applied Fluid Mechanics*, 9(2), 615–624. doi: 10.18869/acadpub.jafm. 68.225.24449

[27] Rittidech, S., Terdtoon, P., Murakami, P., Kamonpet, P., & Jompakdee, W. (2003). Correlation to predict heat transfer characteristics of a closed-end oscillating heat pipe at a normal operating condition. *Applied Thermal Engineering*, 23, 497−510. doi: 10.1016/S1359-4311(02)00215-6

[28] Mangini, D., Mameli, M., Georgoulas, A., Araneo, L., Filippeschi, S., & Marengo, M. (2015). A pulsating heat pipe for space applications: Ground and microgravity experiments. *International Journal of Thermal Sciences*, 95, 53–63. doi: 10.1016/j.ijthermalsci.2015.04.001

[29] Ayel, V., Araneo, L., Scalambra, A., Mameli, M., Romestant, C., Piteau, A., Marengo, M., Filippeschi, S., & Bertin, Y. (2015). Experimental study of a closed-loop flat plate pulsating heat pipe under a varying gravity force. *International Journal of Thermal Sciences*, 96, 23–34. doi: 10.1016/j.ijthermalsci. 2015.04.010

[30] Mameli, M., Manno, V., Filippeschi, S., & Marengo, M. (2014). Thermal instability of a closed-loop pulsating heat pipe: Combined effect of orientation and filling ratio. *Experimental Thermal and Fluid Science*, 59, 222–229. doi: 10.1016/ j.expthermflusci.2014.04.009

[31] Qu, J., Wang, Q., & Sun, Q. (2016). Lower limit of internal diameter for oscillating heat pipes: A theoretical model. *International Journal of Thermal Sciences*, 110, 174–185. doi: 10.1016/j.ijthermalsci.2016.07.002

[32] Quan, L., & Jia, L. (2009). Experimental study on heat transfer characteristic of plate pulsating heat pipe. *ASME 2009 Second International Conference on Micro/Nanoscale Heat and Mass Transfer*, December 18–21, Shanghai, China, Vol. 3, 361–366.

[33] Kravets, V.Yu., & Alekseik, Ye.S. (2010). Effect of number of turns on heat-transfer behavior of oscillating heat pipe. *Eastern-European Journal of Enterprise Technologies*, 6(48), 7, 59–63. doi: 10.15587/1729-4061.2010.3370

[34] Lee, J., Joo, Y., & Kim, S. J. (2018). Effects of the number of turns and the inclination angle on the operating limit of micro pulsating heat pipes. *International Journal of Heat and Mass Transfer*, 124, 1172–1180. doi: 10.1016/j.ijheatmasstransfer. 2018.04.054

[35] Mameli, M., Araneo, L., Filippeschi, S., Marelli, L., Testa, R., & Marengo, M. (2014). Thermal response of a closed loop pulsating heat pipe under a varying gravity force. *International Journal of Thermal Sciences*, 80, 11–22. doi: 10.1016/j.ijthermalsci. 2014.01.023

[36] Kammuang-Lue, N., Sakulchangsatjatai, P., Sriwiset, C., & Terdtoon, P. (2018). Investigation and prediction of optimum meandering turn number of vertical and horizontal closed-loop pulsating heat pipes. *Thermal Sciences*, 22(1), 273–284. doi: 10.2298/TSCI180409267K

[37] Noh, H.Y., & Kim, S.J. (2020). Numerical simulation of pulsating heat pipes: Parametric investigation and thermal optimization. *Energy Conversion and Management*, 203, 112237. doi: 10.1016/j.enconman.2019.112237

[38] Charoensawan, P., Khandekar, S., Groll, M., & Terdtoon, P. (2003). Closed loop pulsating heat pipes - Part A: Parametric experimental investigations. *Applied Thermal Engineering*, 23(16), 2009–2020. doi: 10.1016/S1359-4311(03)00159-5

[39] Li, M., Li, L., & Xu, D. (2018). Effect of number of turns and configurations on the heat transfer performance of helium cryogenic pulsating heat pipe. *Cryogenics*, 96, 159–165. doi: 10.1016/j.cryogenics.2018.09.005

[40] Khandekar, S. (2003). Thermofluid dynamic study of flat-plate

closed-loop pulsating heat pipes. *Microscale Thermophysical Engineering*, 6(4), 303–317. doi: 10.1080/10893950290098340

[41] Hua, C., Wang, X., Gao, X., Zheng, H., Han, X., & Chen, G. (2017). Experimental research on the start-up characteristics and heat transfer performance of pulsating heat pipes with rectangular channels. *Applied Thermal Engineering*, 126, 1058–1062. doi: 10.1016/j.applthermaleng.2017.02.106

[42] Qu, J., Wu, H.-Y., & Wang, Q. (2012). Experimental investigation of silicon-based micro-pulsating heat pipe for cooling electronics. *Nanoscale and Microscale Thermophysical Engineering*, 16(1), 37–49. doi: 10.1080/15567265.2011.645999

[43] Li, Z., Jia, L., & Wei, W. B. (2013). Experimental study on natural convection cooling of LED based on plate pulsating heat pipe. *Heat Transfer Research*, 44(1), 133–144. doi: 10.1615/HeatTransRes.2012005690

[44] Lee, J., & Kim, S.J. (2017). Effect of channel geometry on the operating limit of micro pulsating heat pipes. *International Journal of Heat and Mass Transfer*, 107, 204–212. doi: 10.1016/j.ijheatmasstransfer.2016.11.036

[45] Mehta, K., Mehta, N., & Patel, V. (2021). Experimental investigation of the thermal performance of closed loop flat plate oscillating heat pipe. *Experimental Heat Transfer*, 34(1), 85–103. doi: 10.1080/08916152.2020.1718802

[46] Markal, B., Candere, A.C., Avci, M., & Aydin, O. (2021). Effect of double cross sectional ratio on performance characteristics of pulsating heat pipes. *International Communications in Heat and Mass Transfer*, 127, 105583. doi: 10.1016/j.icheatmasstransfer.2021.105583

[47] Takawale, A., Abraham, S., Sielaff, A., Mahapatra, P.S., Pattamatta, A., & Stephan, P. (2019). A comparative study of flow regimes and thermal performance between flat plate pulsating heat pipe and capillary tube pulsating heat pipe. *Applied Thermal Engineering*, 149, 613–624. doi: 10.1016/j.applthermaleng.2018.11.119

[48] Holley, B., & Faghri, A. (2005). Analysis of pulsating heat pipe with capillary wick and varying channel diameter. *International Journal of Heat and Mass Transfer*, 48(13), 2635–2651. doi: 10.1016/j.ijheatmasstransfer.2005.01.013

[49] Liu, S., Li, J., Dong, X., & Chen, H. (2007). Experimental study of flow patterns and improved configurations for pulsating heat pipes. *Journal of Thermophysics and Heat Transfer*, 16, 56–62. doi: 10.1007/s11630-007-0056-8

[50] Hathaway, A.A., Wilson, C.A., & Ma, H.B. (2012). Experimental investigation of uneven-turn water and acetone oscillating heat pipes. *Journal of Thermophysics and Heat Transfer*, 26(1), 115–122. doi: 10.2514/1.56863

[51] Pagliarini, L., Cattani, L., Mameli, M., Filippeschi, S., Bozzoli, F., & Rainieri, S. (2021). Global and local heat transfer behaviour of a three-dimensional pulsating heat pipe: combined effect of the heat load, orientation and condenser temperature. *Applied Thermal Engineering*, 195, 117144. doi: 10.1016/j.applthermaleng.2021.117144

[52] Alekseik, Ye.S., & Kravets, V.Yu. (2013). Oscillating heat pipe cooler for heat-generating elements of electronics. *Tekhnologiya i Konstruirovanie v Elektronnoi Apparature*, 1, 19–24. (in Russian)

[53] Chien, K.H., Lin, Y.T., Chen, Y.R., Yang, K.S., & Wang, C.C. (2012). A novel design of pulsating heat pipe with fewer turns applicable to all orientations. *International Journal of Heat and Mass Transfer*, 55(21-22), 5722–5728. doi: 10.1016/j.ijheatmasstransfer.2012.05.068

[54] Tseng, C.Y., Yang, K.S., Chien, K.H., Jeng, M.S., & Wang, C.-C. (2014). Investigation of the performance of pulsating heat pipe subject to uniform/alternating tube diameters. *Experimental Thermal and Fluid Science, 54*, 85–92. doi: 10.1016/j.expthermflusci.2014.01.019

[55] Sedighi, E., Amarloo, A., & Shafii, B. (2018). Numerical and experimental investigation of flat-plate pulsating heat pipes with extra branches in the evaporator section. *International Journal of Heat and Mass Transfer*, 126, 431–441. doi: 10.1016/j.ijheatmasstransfer.2018.05.047

[56] Tseng, C.Y., Yang, K.S., Chien, K.H., Wu, S.K., & Wang, C.C. (2016). A novel double pipe pulsating heat pipe design to tackle inverted heat source arrangement. *Applied Thermal Engineering*, 106, 697–701. doi: 10.1016/j.applthermaleng.2016.06.034

[57] Kwon, G.H., & Kim, S.J. (2014). Operational characteristics of pulsating heat pipes with a dual-diameter tube. *International Journal of Heat and Mass Transfer*, 75, 184–195. doi: 10.1016/j.ijheatmasstransfer.2014.03.032

[58] Patel, E.D., & Kumar, S. (2023). Thermal performance of a single loop pulsating heat pipe with asymmetric adiabatic channel. *Applied Thermal Engineering*, 219(119541), 119541. doi: 10.1016/j.applthermaleng.2022.119541

[59] Lim, J., & Kim, S.J. (2019). Effect of a channel layout on the thermal performance of a flat plate micro pulsating heat pipe under the local heating condition. *International Journal of Heat and Mass Transfer*, 137, 1232–1240. doi: 10.1016/j.ijheatmasstransfer.2019.03.121

[60] Jung, C., Lim, J., & Kim, S.J. (2020). Fabrication and evaluation of a high-performance flexible pulsating heat pipe hermetically sealed with metal. *International Journal of Heat and Mass Transfer*, 149(119180), 119180. doi: 10.1016/j.ijheatmasstransfer.2019.119180

[61] He, Y., Jiao, D., Pei, G., Hu, X., & He, L. (2020). Experimental study on a three-dimensional pulsating heat pipe with tandem tapered nozzles. *Experimental Thermal and Fluid Science*, 119(110201), 110201. doi: 10.1016/j.expthermflusci.2020.110201

[62] Jang, D.S., Cho, W., Ham, S.H., & Kim, Y. (2022). Thermal spreading characteristics of novel radial pulsating heat pipes with diverging nonuniform channels. *International Journal of Heat and Mass Transfer*, 199, 123488. doi: 10.1016/j.ijheatmasstransfer.2022.123488

[63] Fallahzadeh, R., Aref, L., Bozzoli, F., Cattani, L., & Gholami, H. (2023). A novel triple-diameter pulsating heat pipe: Flow regimes and heat transfer performance. *Thermal Science and Engineering Progress*, 42, 101902. doi: 10.1016/j.tsep.2023.101902

[64] Kargarsharifabad, H., Mamouri, S.J., Shafii, M.B., & Rahni, M.T. (2013). Experimental investigation of the effect of using closed-loop pulsating heat pipe on the performance of a flat plate solar collector. *Journal of Renewable and Sustainable Energy, 5*(1), 013106. doi: 10.1063/1.4780996

[65] Zhan, J., Chen, X., Ji, Y., Zheng, P., & Duan, W. (2023). Experimental study of ethane pulsating heat pipe with varying evaporator lengths based on pulse tube refrigerator. *International Journal of Refrigeration*, 145, 40–49. doi: 10.1016/j.ijrefrig.2022.09.010

[66] Wang, J., Ma, H., & Zhu, Q. (2015). Effects of the evaporator and condenser length on the performance of pulsating heat pipes. *Applied Thermal Engineering*, 91, 1018–1025. doi: 10.1016/j.applthermaleng.2015.08.106

[67] Dilawar, M., & Pattamatta, A. (2013). A parametric study of oscillatory two-phase flows in a single turn Pulsating Heat Pipe using a non-isothermal vapor model. *Applied Thermal Engineering, 51*(1–2), 1328–1338. doi: 10.1016/j.applthermaleng.2012.11.025

[68] Gan, Z., Sun, X., Jiao, B., Han, D., Deng, H., Wang, S., & Pfotenhauer, J. M. (2019). Experimental study on a hydrogen closed loop pulsating heat pipe with different adiabatic lengths. *Heat Transfer Engineering*, 40(3–4), 205–214. doi: 10.1080/01457632.2018.1426223

[69] Li, Q., Wang, C., Wang, Y., Wang, Z., Li, H., & Lian, C. (2020). Study on the effect of the adiabatic section parameters on the performance of pulsating heat pipes. *Applied Thermal Engineering, 180*(115813), 115813. doi: 10.1016/j.applthermaleng.2020.115813

[70] Kim, J., & Kim, S.J. (2018). Experimental investigation on the effect of the condenser length on the thermal performance of a

micro pulsating heat pipe. *Applied Thermal Engineering*, *130*, 439–448. doi: 10.1016/j.applthermaleng.2017.11.009

[71] Deng, Z., Zheng, Y., Liu, X., Zhu, B., & Chen, Y. (2017). Experimental study on thermal performance of an anti-gravity pulsating heat pipe and its application on heat recovery utilization. *Applied Thermal Engineering*, 125, 1368–1378. doi: 10.1016/j.applthermaleng.2017.07.107

[72] Bastakoti, D., Zhang, H., Cai, W., & Li, F. (2018). Numerical analysis of the effects of surface tension and viscosity on a 3-dimensional pulsating heat pipe. *Proceedings of the ASME Fluids Engineering Division Summer Meeting (FEDSM18)*, 1–7. doi: 10.1115/FEDSM2018-83417

[73] Kumar, M., Kant, R., Das, A.K., & Das, P.K. (2019). Effect of surface tension variation of the working fluid on the performance of a closed loop pulsating heat pipe. *Heat Transfer Engineering*, 40(7), 509–523. doi: 10.1080/01457632.2018.1436390

[74] Xing, M., Wang, R., & Xu, R. (2018). Experimental study on thermal performance of a pulsating heat pipe with surfactant aqueous solution. *International Journal of Heat and Mass Transfer*, 127, 903–909. doi: 10.1016/j.ijheatmasstransfer.2018.07.130

[75] Gandomkar, A., Kalan, K., Vandadi, M., Shafii, M.B., & Saidi, M. H. (2020). Investigation and visualization of surfactant effect on flow pattern and performance of pulsating heat pipe. *Journal of Thermal Analysis and Calorimetry*, 139(3), 2099–2107. doi: 10.1007/s10973-019-08649-z

[76] Wang, J., Xie, J., & Liu, X. (2019). Investigation on the performance of closed-loop pulsating heat pipe with surfactant. *Applied Thermal Engineering*, 160(113998), 113998. doi: 10.1016/j.applthermaleng.2019.113998

[77] Bao, K., Wang, X., Fang, Y., Ji, X., Han, X., & Chen, G. (2020). Effects of the surfactant solution on the performance of the pulsating heat pipe. *Applied Thermal Engineering*, 178, 115678. doi: 10.1016/j.applthermaleng.2020.115678

[78] Liu, X., Chen, Y., & Shi, M. (2013). Dynamic performance analysis on start-up of closed-loop pulsating heat pipes (CLPHPs). *International Journal of Thermal Sciences*, 65, 224–233. doi: 10.1016/j.ijthermalsci.2012.10.012

[79] Han, H., Cui, X., Zhu, Y., & Sun, S. (2014). A comparative study of the behavior of working fluids and their properties on the performance of pulsating heat pipes (PHP). *International Journal of Thermal Sciences*, 82, 138–147. doi: 10.1016/j.ijthermalsci.2014.04.003

[80] Qu, J., Wu, H.Y., & Cheng, P. (2012). Start-up, heat transfer and flow characteristics of silicon-based micro pulsating heat pipes. *International Journal of Heat and Mass Transfer*, 55, 6109–6120. doi: 10.1016/j.ijheatmasstransfer.2012.06.024

[81] Saha, M., Feroz, C.M., Ahmed, F., & Mujib, T. (2012). Thermal performance of an open loop closed end pulsating heat pipe. *Heat and Mass Transfer*, 48, 259–265. doi: 10.1007/s00231-011-0882-9

[82] Srikrishna, P., Siddharth, N., Reddy, S.U.M., & Narasimham, G.S.V.L. (2019). Experimental investigation of flat plate closed loop pulsating heat pipe. *Heat and Mass Transfer*, 55(9), 2637–2649. doi: 10.1007/s00231-019-02607-z

[83] Xue, Z., & Qu, W. (2014). Experimental study on effect of inclination angles to ammonia pulsating heat pipe. *Chinese Journal of Aeronautics*, 27(5), 1122–1127. doi: 10.1016/j.cja.2014.08.004

[84] Kim, J., & Kim, S.J. (2020). Experimental investigation on working fluid selection in a micro pulsating heat pipe. *Energy Conversion and Management*, 205, 112462. doi: 10.1016/j.enconman.2019.112462

[85] Khandekar, S., Dollinger, N., & Groll, M. (2003). Understanding operational regimes of closed loop pulsating heat pipes: an experimental study. *Applied Thermal Engineering*, 23(6), 707–719. doi: 10.1016/s1359-4311(02)00237-5

[86] Zhao, X., Su, L., Jiang, J., Deng, W., & Zhao, D. (2023). A Review of Working Fluids and Flow State Effects on Thermal Performance of Micro-Channel Oscillating Heat Pipe for Aerospace Heat Dissipation. *Aerospace*, 10(2), 179. doi: 10.3390/aerospace10020179

[87] Zhu, Y., Cui, X., Han, H., & Sun, S. (2014). The study on the difference of the start-up and heat-transfer performance of the pulsating heat pipe with water-acetone mixtures. *International Journal of Heat and Mass Transfer*, 77, 834–842. doi: 10.1016/j.ijheatmasstransfer.2014.05.042

[88] Pachghare, P.R., & Mahalle, A.M. (2014). Thermo-hydrodynamics of closed loop pulsating heat pipe: An experimental study. *Journal of Mechanical Science and Technology*, 28, 3387–3394. doi: 10.1007/s12206-014-0751-9

[89] Han, H., Cui, X., Zhu, Y., Xu, T., Sui, Y., & Sun, S. (2016). Experimental study on a closed-loop pulsating heat pipe (CLPHP) charged with water-based binary zeotropes and the corresponding pure fluids. *Energy*, 109, 724–736. doi: 10.1016/j.energy.2016.05.061

[90] Wang, W., Cui, X., & Zhu, Y. (2017). Heat transfer performance of a pulsating heat pipe charged with acetone-based mixtures. *Warme- und Stoffubertragung [Heat and Mass Transfer]*, 53(6), 1983–1994. doi: 10.1007/s00231-016-1958-3

[91] Xu, R., Zhang, C., Chen, H., Wu, Q., & Wang, R. (2019). Heat transfer performance of pulsating heat pipe with zeotropic immiscible binary mixtures. *International Journal of Heat and Mass Transfer*, 137, 31–41. doi: 10.1016/j.ijheatmasstransfer.2019.03.070

[92] Zamani, R., Kalan, K., & Shafii, M. B. (2019). Experimental investigation on thermal performance of closed loop pulsating heat pipes with soluble and insoluble binary working fluids and a proposed correlation. *Warme- und Stoffubertragung [Heat and Mass Transfer]*, 55(2), 375–384. doi: 10.1007/s00231-018-2418-z

[93] Zhou, G., Guan, F., Yang, W., Sun, Q., & Qu, J. (2023). Start-up and heat transfer characteristics of oscillating heat pipe charged with binary partially miscible organic fluid mixtures. *Applied Thermal Engineering*, 231(120952), 120952. doi: 10.1016/j.applthermaleng.2023.120952

[94] Su, X., Zhang, M., Han, W., & Guo, X. (2015). Enhancement of heat transport in oscillating heat pipe with ternary fluid. *International Journal of Heat and Mass Transfer*, 87, 258–264. doi: 10.1016/j.ijheatmasstransfer.2015.04.002

[95] Markal, B., & Varol, R. (2021). Experimental investigation and force analysis of flat-plate type pulsating heat pipes having ternary mixtures. *International Communications in Heat and Mass Transfer*, 121(105084), 105084. doi: 10.1016/j.icheatmasstransfer.2020.105084

[96] Tsai, C.Y., Chien, H.T., Ding, P.P., Chan, B., Luh, T.Y., & Chen, P.H. (2004). Effect of structural character of gold nanoparticles in nanofluid on heat pipe thermal performance. *Materials Letters*, 58(9), 1461–1465. doi: 10.1016/j.matlet.2003.10.009

[97] Ma, H.B., Wilson, C., Yu, Q., Park, K., Choi, U.S., & Tirumala, M. (2006). An experimental investigation of heat transport capability in a nanofluid oscillating heat pipe. *Journal of Heat Transfer*, 128(11), 1213–1216. doi: 10.1115/1.2352789

[98] Lin, Y.H., Kang, S.W., & Chen, H.L. (2008). Effect of silver nano-fluid on pulsating heat pipe thermal performance. *Applied Thermal Engineering*, 28(11–12), 1312–1317. doi: 10.1016/j.applthermaleng.2007.10.019

[99] Riehl, R.R., & Santos, N. (2012). Water-copper nanofluid application in an open loop pulsating heat pipe. *Applied Thermal Engineering*, 42, 6–10. doi: 10.1016/j.applthermaleng.2011.01.017

[100] Karthikeyan, V.K., Ramachandran, K., Pillai, B.C., & Brusly Solomon, A. (2014). Effect of nanofluids on thermal performance of closed loop pulsating heat pipe. *Experimental Thermal and Fluid Science*, 54, 171–178. doi: 10.1016/j.expthermflusci.2014.02.007

[101] Qu, J., & Wu, H. (2011). Thermal performance comparison of oscillating heat pipes with SiO_2/water and Al_2O_3/water nanofluids. *International Journal of Thermal Sciences*, 50(10), 1954−1962. doi: 10.1016/j.ijthermalsci.2011.04.004

[102] Xu, Y., Xue, Y., Qi, H., & Cai, W. (2021). An updated review on

working fluids, operation mechanisms, and applications of pulsating heat pipes. *Renewable and Sustainable Energy Reviews*, 144(110995), 110995. doi: 10.1016/j.rser.2021.110995

[103] Nazari, M.A., Ghasempour, R., Ahmadi, M.H., Heydarian, G., & Shafii, M.B. (2018). Experimental investigation of graphene oxide nanofluid on heat transfer enhancement of pulsating heat pipe. *International Communications in Heat and Mass Transfer*, 91, 90–94. doi: 10.1016/j.icheatmasstransfer.2017.12.006

[104] Akbari, A., & Saidi, M.H. (2019). Experimental investigation of nanofluid stability on thermal performance and flow regimes in pulsating heat pipe. *Journal of Thermal Analysis and Calorimetry*, 135, 1835–1847. doi: 10.1007/s10973-018-7388-3

[105] Gonzalez, M., & Kim, Y.J. (2014). Experimental study of a pulsating heat pipe using nanofluid as a working fluid. In *Proceedings of the Fourteenth Intersociety Conference on Thermal and Thermomechanical Phenomena in Electronic Systems* (pp. 541–546). doi: 10.1109/ITHERM.2014.6892328

[106] Ali, F.M., Yunus, W.M.M., & Talib, Z.A. (2013). Study of the effect of particle size and volume fraction concentration on the thermal conductivity and thermal diffusivity of Al2O3 nanofluids. *International Journal of Physical Sciences*, 8(28), 1442–1457. doi: 10.5897/IJPS10.544

[107] Kim, H.J., Lee, S.H., Lee, J.H., & Jang, S.P. (2015). Effect of particle shape on suspension stability and thermal conductivities of water-based bohemite alumina nanofluids. *Energy*, 90, 1290–1297. doi: 10.1016/j.energy.2015.06.084

[108] Karthikeyan, V.K., Ramachandran, K., Pillai, B.C., & Solomon, A.B. (2015). Understanding thermo-fluidic characteristics of a glass tube closed loop pulsating heat pipe: Flow patterns and fluid oscillations. *Heat and Mass Transfer*, 51, 1669–1680. doi: 10.1007/s00231-015-1525-3

[109] Mohammadi, M., Mohammadi, M., & Shafii, M.B. (2012). Experimental investigation of a pulsating heat pipe using ferrofluid (magnetic nanofluid). *Journal of Heat Transfer*, 134(1), 014504. doi: 10.1115/1.4004805

[110] Goshayeshi, H.R., Goodarzi, M., Safaei, M.R., & Dahari, M. (2016). Experimental study on the effect of inclination angle on heat transfer enhancement of a ferrofluid in a closed loop oscillating heat pipe under magnetic field. *Experimental Thermal and Fluid Science*, 74, 265–270. doi: 10.1016/j.expthermflusci.2016.01.003

[111] Babu, E.R., Reddappa, H.N., & Gnanendra Reddy, G.V. (2018). Effect of filling ratio on thermal performance of closed loop pulsating heat pipe. *Materials Today: Proceedings*, *5*(10), 22229–22236. doi: 10.1016/j.matpr.2018.06.588

[112] Rahman, M.L., Chowdhury, M., Islam, N.A., Mufti, S.M., & Ali, M. (2016). Effect of filling ratio and orientation on the thermal performance of closed loop pulsating heat pipe using ethanol. *AIP Conference Proceedings*, 1754(1), 050011. doi: 10.1063/1.4958402

[113] Wu, M., Ji, Y., Feng, Y., Liu, H., & Yang, X. (2023). Experimental study on the effects of filling ratios on heat transfer characteristics of liquid metal high-temperature oscillating heat pipes. *International Journal of Heat and Mass Transfer*, 209, 124153. doi: 10.1016/j.ijheatmasstransfer.2023.124153

[114] Yin, D., Rajab, H., & Ma, H.B. (2014). Theoretical analysis of maximum filling ratio in an oscillating heat pipe. *International Journal of Heat and Mass Transfer*, 74, 353–357. doi: 10.1016/j.ijheatmasstransfer.2014.03.018

[115] Sohel Murshed, S.M., & Nieto de Castro, C.A. (2017). A critical review of traditional and emerging techniques and fluids for electronics cooling. *Renewable and Sustainable Energy Reviews*, 78, 821–833. doi: 10.1016/j.rser.2017.04.112

[116] Spinato, G., Borhani, N., & Thome, J.R. (2016). Operational regimes in a closed loop pulsating heat pipe. *International Journal of Thermal Sciences*, 102, 78–88. doi: 10.1016/j.ijthermalsci.2015.11.006

[117] Xu, R., Li, X., Lei, T., Wu, Q., & Wang, R. (2022). Operation characteristics of a gravity pulsating heat pipe under different heat inputs. *International Journal of Heat and Mass Transfer*, 189, 122731. doi: 10.1016/j.ijheatmasstransfer.2022.122731

[118] Torresin, D., Agostini, F., Mularczyk, A., Agostini, B., & Habert, M. (2017). Double condenser pulsating heat pipe cooler. *Applied Thermal Engineering*, 126, 1051–1057. doi: 10.1016/j.applthermaleng.2017.02.066

[119] Yoon, I., Wilson, C., Borgmeyer, B., Winholtz, R.A., Ma, H.B., Jacobson, D.L., & Hussey, D.S. (2012). Neutron phase volumetry and temperature observations in an oscillating heat pipe. *International Journal of Thermal Sciences*, 60, 52–60. doi: 10.1016/j.ijthermalsci.2012.05.004

[120] Jun, S., & Kim, S.J. (2019). Experimental investigation on the thermodynamic state of vapor plugs in pulsating heat pipes. *International Journal of Heat and Mass Transfer*, 134, 321–328. doi: 10.1016/j.ijheatmasstransfer.2019.01.053

[121] Patel, V.M., & Mehta, H.B. (2017). Influence of working fluids on startup mechanism and thermal performance of a closed loop pulsating heat pipe. *Applied Thermal Engineering*, 110, 1568–1577. doi: 10.1016/j.applthermaleng.2016.09.017

[122] Mameli, M., Marengo, M., & Khandekar, S. (2014). Local heat transfer measurement and thermo-fluid characterization of a pulsating heat pipe. *International Journal of Thermal Sciences*, 75, 140–152. doi: 10.1016/j.ijthermalsci.2013.07.025

[123] Jiansheng, W., Zhenchuan, W., & Meijun, L. (2014). Thermal performance of pulsating heat pipes with different heating patterns. *Applied Thermal Engineering*, *64*(1–2), 209–212. doi: 10.1016/j.applthermaleng.2013.12.004

[124] Jang, D.S., Chung, H.J., Jeon, Y., & Kim, Y. (2018). Thermal performance characteristics of a pulsating heat pipe at various nonuniform heating conditions. *International Journal of Heat and Mass Transfer*, 126, 855–863. doi: 10.1016/j.ijheatmasstransfer.2018.05.160

[125] Zhang, D., Li, H., Wu, J., Li, Q., Xu, B., & An, Z. (2022). Experimental study on the effect of inclination angle on the heat transfer characteristics of pulsating heat pipe under variable heat flux. *Energies*, 15(22), 8252. doi: 10.3390/en15218252

[126] Okazaki, S., Fuke, H., & Ogawa, H. (2021). Performance of circular oscillating heat pipe for highly adaptable heat transfer layout. *Applied Thermal Engineering*, 198, 117497. doi: 10.1016/j.applthermaleng.2021.117497

[127] Jun, S., & Kim, S.J. (2016). Comparison of the thermal performances and flow characteristics between closed-loop and closed-end micropulsating heat pipes. *International Journal of Heat and Mass Transfer*, 95, 890–901. doi: 10.1016/j.ijheatmasstransfer.2015.12.064

[128] Jun, S., & Kim, S.J. (2019). Experimental study on a criterion for normal operation of pulsating heat pipes in a horizontal orientation. *International Journal of Heat and Mass Transfer*, 137, 1064–1075. doi: 10.1016/j.ijheatmasstransfer.2019.03.163

[129] Nekrashevych, I., & Nikolayev, V.S. (2019). Pulsating heat pipe simulations: Impact of PHP orientation. *Microgravity Science and Technology*, 31(3), 241–248. doi: 10.1007/s12217-019-9684-3

[130] Khandekar, S., Gautam, A.P., & Sharma, P.K. (2009). Multiple quasi-steady states in a closed loop pulsating heat pipe. *International Journal of Thermal Sciences*, 48(3), 535–546. doi: 10.1016/j.ijthermalsci.2008.04.004

[131] Markal, B., & Varol, R. (2020). Thermal investigation and flow pattern analysis of a closed-loop pulsating heat pipe with binary mixtures. *Journal of the Brazilian Society of Mechanical Sciences and Engineering*, 42, 1–18. doi: 10.1007/s40430-020-02618-6

[132] Tseng, C.Y., Yang, K.S., & Wang, C.C. (2020). Non-uniform three-dimensional pulsating heat pipe for anti-gravity high-flux applications. *Energies*, 13, 3068. doi: 10.3390/en13123068

[133] Reay, D.A., Kew, P.A., & McGlen, R.J. (2014). *Heat Pipes: Theory, Design and Applications* (6th ed.). Butterworth-Heinemann. doi: 10.1016/C2011-0-08979-2

Co-published by
Institute of Fluid-Flow Machinery
Polish Academy of Sciences
Committee on Thermodynamics and Combustion
Polish Academy of Sciences

Copyright©2024 by the Authors under licence CC BY 4.0

http://www.imp.gda.pl/archives-of-thermodynamics/

Enhancement of adiabatic effectiveness in a combustion chamber liner with effusion cooling through conical and fan shaped holes

Yellu Kumar[a*], Adnan Qayoum[a], Shahid Saleem[a]

[a]Mechanical Engineering Department, National Institute of Technology Srinagar, J&K, 190006, India
*Corresponding author email: yellukumar.rage@gmail.com

Received: 01.11.2023; revised: 15.02.2024; accepted: 20.04.2024

Abstract

The present study involves computational investigation of effusion cooling over a flat plate through the different shaped holes. The interaction between the film jet and the mainstream flow creates a counter-rotating vortex pair, resulting jet detachment from the surface and insufficient film cooling coverage over the surface. To enhance the effusion cooling performance, shaped holes are used in place of standard cylindrical holes to reduce the effects of the counter-rotating vortex pair. Two different shaped holes i.e., conical-shaped and fan-shaped holes are used in the investigation and compared to the cylindrical holes. A commercial finite element method package COMSOL Multiphysics 5.5 is used to simulate and analyse the three-dimensional combustor liners of gas turbine. Data is presented for total 10 rows of effusion holes with injection angles 30° at blowing ratios 0.25, 1.0 and 3.2. The shaped holes provide better cooling effectiveness by increasing the lateral spread of coolant over the surface wall. The results show that both the shaped hole geometries can generate additional anti-counter rotating vortex pairs, which contribute to reducing the strength of the counter-rotating vortex pair. The coolant penetration and strong shear zones at the interaction of coolant jet and main stream in shaped holes are greatly reduced in comparison with cylindrical holes. For a low blowing ratio of 0.25, the conical-shaped holes exhibited adiabatic effectiveness that was 25% and 19% greater than the cylindrical and trapezoidal-shaped holes respectively. On the other hand, fan-shaped holes provide enhanced adiabatic effectiveness at increased blowing ratios. At higher value of blowing ratio 3.2, the adiabatic effectiveness increased by 13% compared to cylindrical holes and 4% compared to conical-shaped holes. In addition, velocity profiles and two-dimensional streamlines have been examined in order to study the flow behavior on the surface.

Keywords: Gas turbine; Combustion chamber liners; Effusion cooling; Adiabatic effectiveness; Conical-shaped holes

Vol. 45(2024), No. 2, 183–193; doi: 10.24425/ather.2024.150864

Cite this manuscript as: Kumar, Y., Qayoum, A., & Saleem, S. (2024). Enhancement of adiabatic effectiveness in a combustion chamber liner with effusion cooling through conical and fan shaped holes. *Archives of Thermodynamics*, 45(2), 183−193.

1. Introduction

Nowadays, aero engines and gas turbines are designed with inlet temperatures ranging from 1 200°C to 1 500°C maintained over extended operational periods to optimize thermal efficiency, which surpasses the metallurgical capacity of their constituent metals [1−4]. As a result, a proficient cooling system becomes essential for elongating the operational lifespan of the high-temperature components within a gas turbine engine such as the combustion chamber liners, turbine blades and nozzles. The secondary fluid/coolant fluid is allowed to pass through discrete holes drilled on the surface of hot components involved in form-

Nomenclature

d – diameter of effusion hole, m
t – thickness of effusion plate, m
S_x/d – streamwise distance between two adjacent holes in x-direction
S_y/d – spanwise distance between two adjacent holes in y-direction
T – temperature, K
U – flow velocity, m/s
X – streamwise coordinate, m
Y – spanwise coordinate, m
Z – normal coordinate, m

Greek symbols

α – injection angle, °
η – adiabatic effectiveness
$\overline{\eta}$ – area-averaged adiabatic effectiveness
ρ – density, kg/m^3

Subscripts and Superscripts

∞ – mainstream flow
c – coolant flow
wt – wall temperature on adiabatic surface of effusion plate

Abbreviations and Acronyms

ACRVP – anti-counter rotating vortices pair
BR – blowing ratio
CRVP – counter rotating vortices pair
DR – density ratio
VR – velocity ratio

ing a thin film layer on the hot surface which acts as a thermal shield between the hot gases and metal components. Film cooling and effusion cooling (full coverage film cooling) are more efficient than other cooling strategies [5]. However, the former cooling method does not provide enough cooling due to the discrete nature of holes. In contrast, in the latter one, many holes are arranged in an array to ensure full coverage protection on the surface. The overall effusion cooling effectiveness is dependent on both geometrical and flow parameters like coolant hole diameter, spacing of holes, coolant injection angle, base material thermal conductivity, density ratio, blowing ratio (BR) and momentum flux ratio, etc. Tests are being carried out using a flat plate designed to resemble an actual combustion chamber liners of gas turbine engine. The purpose of these tests is to enhance our comprehension of the fluid dynamics between the main airflow and the coolant flow.

Andrews et al. [6−8] conducted experiments to examine the effects of geometrical parameters such as the diameter of injection hole, shape of coolant hole, and injection angle on the effusion cooling performance. Kumar et al. [9, 10] studied the effect of blowing ratio and enhancement of adiabatic effectiveness by placing an upstream ramp in front of the effusion holes. The authors [11, 12] investigated both experimentally and numerically to determine the effects of hole spacing in streamwise and spanwise directions and different coolant injection angles and deflection angles, all while measuring the adiabatic film effectiveness at various BRs. Kumar et al. [13] have compiled a comprehensive review of effusion cooling system performance. The study results demonstrated a statistically significant relationship between various parameters and adiabatic efficiency. The above literature studies indicated that the adiabatic effectiveness gradually increases from starting holes to ending holes by the lateral spreading of coolant by the adjacent holes.

Later, researchers have focused their effects on improving the overall efficiency of cooling performance by conducting numerous experimental and numerical methods on shaped holes. A well-known fact is that expanded exits in hole geometries can greatly enhance cooling performance by allowing coolant to spread laterally over the surface. Expanding the exit of the hole leads to a reduction in the velocity of the coolant as it exits. The decrease in velocity helps to minimize lift-off without penetration, allowing the coolant to spread out over a larger area more effectively, allowing the coolant to spread out over a larger area more effectively. This coolant coverage over the optimizes heat transfer efficiency by ensuring greater contact between the cooling fluid and the heated surface thereby enhancing cooling effectiveness. However, the counter-rotating vortices pair (CVRP) generated by the coolant jet with the interaction of mainstream flow, might degrade the cooling efficiency on the surface by causing aerodynamic lift. Due to their rotational direction, these vortices enable the hot mainstream gases to flow beneath the coolant jet, leading to elevated temperatures on the surface. The anti-contour rotating vortex pairs (ACRVPs) are generated when the coolant jet interacts with the high-speed mainstream flow, leading to the formation of vortices that rotate in opposite directions of CRVPs. The formation ACRVPs in effusion cooling systems significantly enhances cooling effectiveness by providing better mixing, increasing surface coverage, disrupting the thermal boundary layer and enhancing convective heat transfer. It is crucial to elevate the lateral expansion of the coolant jets to optimize the cooling effectiveness at an increased distance downstream from the coolant jet outlets. Therefore, in order to attain enhanced cooling performance on the effusion plate, it becomes crucial to alter the flow patterns. Some of the possible ways to alter the flow structures are: 1) to altering the boundary-layer/cooling jet interactions, 2) by modifying the flow upstream of the coolant jet, 3) modifying the shape of hole geometry. Goldstein et al. [14] were the first to introduce the concept of shaped cooling holes to enhance the film cooling process. A comparison was done between the inclined cylindrical holes and 12° laterally expanded exit holes. According to the effectiveness data, the results show that the shaped film holes provide better film cooling protection.

Zing and Zhang [15] conducted numerical simulations to examine the depth of a contoured hole known as a crater, affecting both the downstream flow field and the effectiveness of adiabatic cooling across a range of blowing ratios. Prasanna et al. [16] concluded that the 3D hybrid slot-effusion setup offers significant benefits in enhancing film cooling effectiveness and decreasing cooling nonuniformity. Huang et al. [17] investigated a multi-objective optimization process aimed at refining the shape of the round to slot holes (RTSH). In the process two independent objective functions the discharge coefficient (Cd) and spatially-averaged adiabatic film cooling effectiveness were utilized. Hao et al. [18] examined film cooling performance both experimentally and numerically, revealing that larger compound

angles exacerbate the effects under lateral pressure gradients, in stark contrast to findings observed in zero pressure gradient environments. Park et al. [19] conducted experimental investigations on the film cooling effectiveness concerning three parameters of a fan-shaped hole: the forward expansion angle, lateral expansion angle, and metering length ratio. Their findings indicated that increasing the forward and lateral expansion angles, along with reducing the metering length ratio, led to an overall enhancement in film cooling effectiveness. Li et al. [20] investigated the adiabatic effectiveness of three different arrangements of tangential inlet cooling holes and their respective cooling efficiencies. They observed that the cooling film produced by the tangential jet adopts a divergent "horsetail" shape, closely adhering to the inner wall of the liner. The tight adherence of horsetail increases both the cooling area and effectiveness. The authors [21−23] demonstrated that compound-angle injection has cooling effectiveness over simple-angle injection. The coolant jet ejected from the compound-injection holes provides more lateral spread over the surface than the normal cylindrical holes as the coolant travels downward. Thole et al. [24] demonstrated the turbulence and velocity flow field measurements of cylindrical, forwarded diffused fan-shaped, and laterally diffused fan-shaped holes. The results show that the laterally diffused holes provide better cooling performance by producing less coolant jet penetration, reducing the velocity and turbulence gradients than the round holes. Bell et al [25] measured the adiabatic effectiveness of film cooling and other performance parameters for different shaped holes: (i) cylindrical simple angle holes, (ii) laterally diffused coolant holes, (iii) laterally diffused compound angle holes, (iv) forward diffused simple angle holes, and (v) forward diffused compound angle (FDCA) holes. Their findings demonstrated that the cooling protection provided by laterally diffused compound angle (LDCA) holes is more effective compared to other hole geometries for a wide range of Blowing ratios. Schmidt et al. [26] studied the combined effects of compound angle with expanded exit on the flat plate. They concluded that forward expanded holes with compound angles 60° provide better film cooling than other configurations. From the past literature studies, Researchers have made efforts to improve the overall effusion cooling performance by modifying the flow and geometrical parametric conditions. However, the shaped holes with expanded exits enhanced the film cooling performance.

The objective of this paper is to quantify the downstream adiabatic effectiveness in the streamwise direction of effusion holes. The primary focus of this study is on two types of hole geometries: fan-shaped and a novel conical-shaped hole. The local adiabatic effectiveness and area-averaged adiabatic effectiveness are measured for both the fan-shaped and conical-shaped holes and subsequently compared to the baseline model represented by cylindrical holes. The investigations are carried on 10 rows of effusion holes with injection angle 30° at BRs 0.25, 1.0 and 3.2. The BRs taken are low BR 0.25, intermediate BR 1.0, and high BR 3.2. The velocity profiles and two-dimensional stream lines are investigated just downstream of the first and last row of effusion holes for obtaining a complete physics of the flow behavior over the flat plate under the influence of effusion cooling.

2. Numerical methods

2.1. Geometry

Figures 1 and 2 shows the schematic of computational model and details of effusion plate for cylindrical holes (baseline). The computational domains consist of three segments i.e., mainstream flow, effusion plate and coolant flow. Hot gases are directed to pass over the effusion plate within the mainstream duct, while coolant air is introduced through the effusion holes into the same mainstream duct. The effusion plate consists of 10 rows of holes arranged in a staggered pattern. The diameter of coolant injection holes (d) is 5.7 mm. The spacing of holes in streamwise and spanwise direction $S_x/d = 4.6$ and $S_y/d = 2.4$. The thickness of the effusion plate (t) is 3d and the coolant is injected into the mainstream flow at (α) is 30°. The dimensions of mainstream duct are 130d (x-direction) and 10d (y-direction). The symmetric boundary conditions are applied on either side of the computational domain in the y-direction.

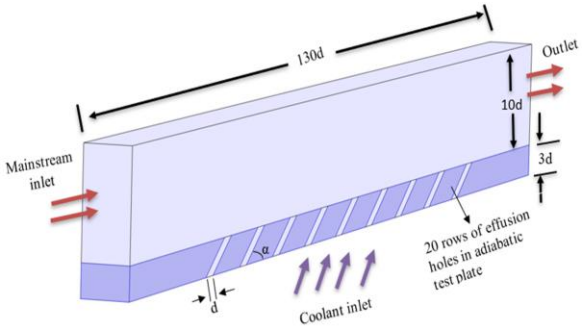


Fig. 1. Isometric view of computational domain and boundary conditions.

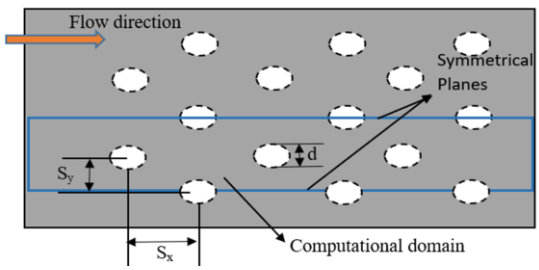


Fig. 2. Top view of computational domain on effusion plate surface (XY plane).

Three different hole geometries (cylindrical, conical, and fan-shaped holes) are used as cooling injection holes as shown in Fig. 3. The conical-shaped holes have an expanded exit of 10° in both x-direction and y-direction. However, the inlets of the conical shaped holes and fan-shaped holes are equal to diameter d same as of cylindrical holes.

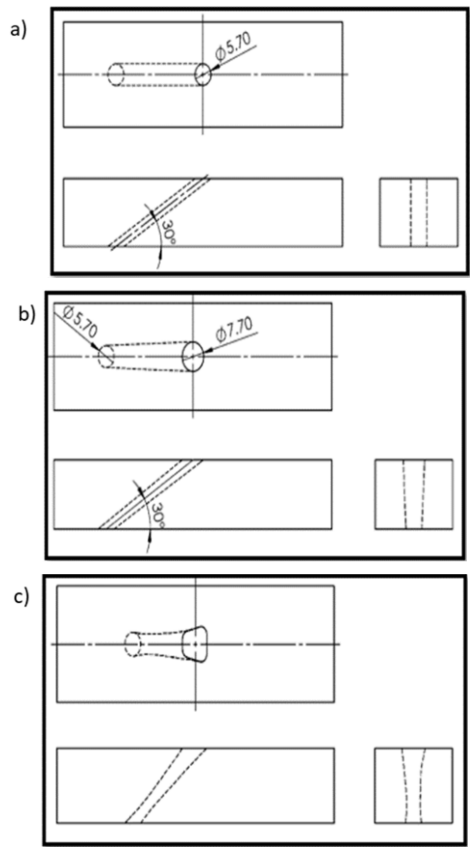


Fig. 3. Sketch map of different hole geometries: (a) cylindrical holes, (b) conical, (c) fan-shaped hole.

2.2. Boundary conditions

Air is used as a working medium for both mainstream and coolant flow. Both the inlets are set as velocity inlets, and the outlet of mainstream flow is set as a static pressure outlet. The velocity of mainstream flow is constant at V_∞= 50 m/s, and the coolant velocities V_c are varied according to the required BR. The inlet temperatures of mainstream flow and coolant flow are uniformly maintained at 350 K and 300 K respectively. The effusion plate was made of urethane foam with a low thermal conductivity k = 0.029 W/(m K) resulting in a maximum conduction loss to allow for adiabatic surface temperature measurements. Consequently, the effusion plate is configured as an adiabatic plate, so conduction and internal cooling in holes are negligible. A complete list of all the combination of the various parameters used in the investigation are tabulated in Table 1.

Table 1. Boundary conditions.

Surface	Boundary conditions
Mainstream inlet	Velocity inlet
Coolant inlet	Velocity inlet
Test plate	Adiabatic wall
Mainstream outlet	Pressure outlet
Sides of mainstream flow	Wall with symmetry
Coolant hole wall	Wall with symmetry

2.3. Measurement and parameter definition

Blowing ratio is the key parameter used to investigate the effect of coolant flow velocity on effusion cooling performance with a constant mainstream flow. The BR is defined as the coolant mass flux to mainstream mass flow:

$$\mathrm{BR} = \frac{\rho_c U_c}{\rho_\infty U_\infty}, \tag{1}$$

where ρ_c and U_c are the density and velocity of coolant flow at effusion hole exit, respectively, and ρ_∞ and U_∞ are the density and velocity of mainstream flow. The BRs used in these studies are 0.25, 1.0, and 3.2.

The effusion cooling performance is measured by the adiabatic effectiveness on the centerline of symmetrical plane and is defined as:

$$\eta = \frac{T_\infty - T_{wt}}{T_\infty - T_c}, \tag{2}$$

where T_{wt} is the adiabatic wall temperature after the exposure of coolant flow on the effusion plate, T_∞ and T_c are the temperatures of mainstream and coolant flow.

The area-averaged adiabatic effectiveness measured in the area between the leading edge of the effusion plate to trailing edge of the plate by considering the local adiabatic effectiveness i.e X_{start} to X in streamwise direction and Y_{start} to Y in spanwise direction:

$$\bar{\eta} = \frac{1}{|x_{start} - x|}\frac{1}{|y_{start} - y|}\int_{x_{start}}^{x}\int_{y_{start}}^{y}\eta\,(x, y)\mathrm{d}x\mathrm{d}y. \tag{3}$$

2.4. Computational details and validation test

The commercial software COMSOL Multiphysics 5.5 is utilized to solve the three-dimensional steady, incompressible, and turbulent flow. Employing an appropriate turbulence model in simulations becomes crucial to achieve precise forecasts of the flow pattern and temperature distribution across the effusion surface. Previous research studies showed that the k-ε model could predict the centerline adiabatic effectiveness and velocity flow [27,28]. In order to determine the adiabatic effectiveness on the effusion surface, a number of validation test runs are carried out before starting the computations for the model.

The present simulation results are validated by comparing with the experimental results of Scrittore et al. [29]. The geometrical and flow parameters were strictly followed to validate the simulation results as in ref [29]. The validation test run was carried for cylindrical holes at high BR 3.2 for 20 rows of effusion holes.

The comparison of experimental and computational results for centerline adiabatic efficiency along the streamwise is shown in Fig. 4. The current findings show a good agreement with the experimental data. However, to reduce the computational run time the holes in the effusion region were reduced to 10 rows of holes for all geometrical models. The small variances between the computational and experimental outcomes in the initial rows might stem from the experimental conditions not being entirely adiabatic.

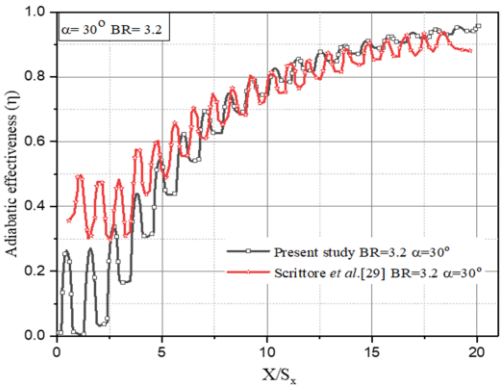


Fig. 4. Comparison of centerline adiabatic effectiveness of computational results with experimental results [29] for BR = 3.2.

2.5. Grid distribution and convergence criteria

A grid independence study was performed to ensure that the results obtained were independent of the mesh size. The grid size has an impact on the accuracy of the results. A user-controlled mesh is applied to the entire domain to obtain the required results. The effusion plate surface is modelled by free triangular mesh with extremely fine grid size, and the remaining domains were modelled with swept mesh. Figure 5 shows the details of computational mesh.

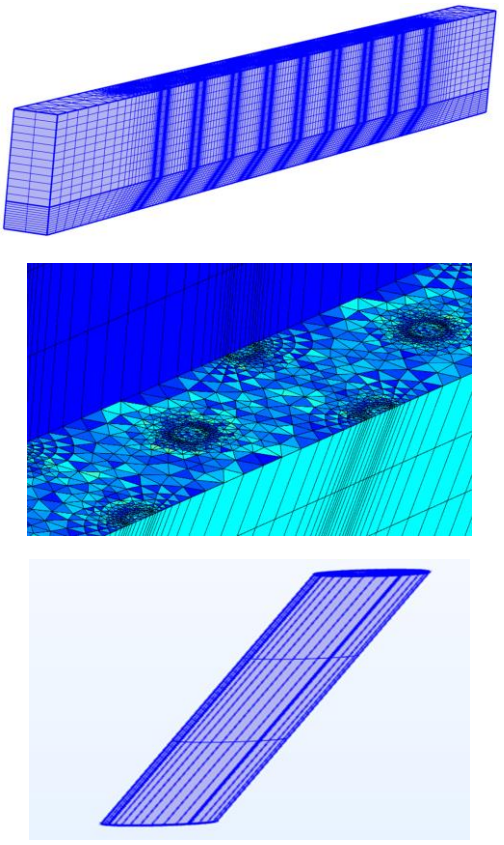


Fig. 5. Computational details: top – entire geometry, middle – effusion plate surface, bottom – effusion hole.

Grid independence study was carried for cylindrical holes with three different grid sizes consisting of 3 631 174, 1 511 096 and 522 762 elements. For proper visualization of temperature counters, better efficiency and computational time economy, a grid size of 1 511 096 elements was chosen for the current simulation. To ensure a mesh of high quality and resolution, the average element quality is maintained at 0.8.

To accurately model the laminar sub-layer and buffer region, the distance of the nearest nodes from the wall is kept at approximately (y^+) = 11.225 for all simulations. To maintain consistency in the modelling approach, a scalable wall function is employed, which adjusts the near-wall mesh to achieve a y^+ value of 11.225. This value corresponds to the beginning of the log-law zone and helps ensure proper representation of near-wall flow dynamics in the simulations This adjustment is necessary due to the differing levels of resolution in the grid and near-wall refinement caused by variations in geometric and velocity scales within the current model. To prevent the excessive resolution of the laminar sublayer, which is not accurately captured by epsilon-based models, the mesh is internally modified using the scalable methodology.

Convergence criteria has been set such that residuals for the continuity, momenta and turbulent transport equations were required to be below 10^{-5}, while the energy equation residuals had to be below 10^{-8}. Furthermore, the average temperature of the bottom wall is monitored to ensure constant convergence.

3. Results and discussion

The primary focus of this paper was on the computational prediction of adiabatic effectiveness for effusion cooling systems. The effect of the shaped holes and BR on effusion cooling performance is discussed and compared between: (a) cylindrical holes, (b) conical holes, and (c) fan-shaped holes at different BRs 0.25, 1.0 and 3.2 for injection angle α = 30°.

3.1. Effect of blowing ratio on adiabatic effectiveness

The centerline adiabatic effectiveness for cylindrical holes at BRs 0.25, 1.0 and 3.2 for injection angle α = 30° is shown in Fig. 6. The figure shows that the BR significantly impacts the adiabatic efficiency of effusion cooling.

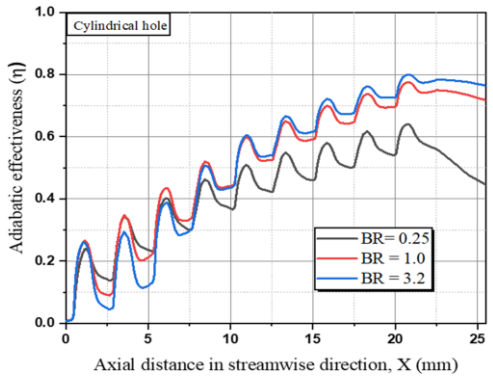


Fig. 6. Comparison of centerline adiabatic effectiveness for cylindrical holes at blowing ratios 0.25, 1.0 and 3.2.

The adiabatic effectiveness peak appears to oscillate increasingly from first row of effusion hole to last row of effusion holes for all blowing ratios. This is due to measurement taken over the effusion plate including coolant holes. The adiabatic effectiveness is high for a low BR until X/d = 7. After that, the values decrease compared to high BRs, and opposite behavior is seen for high BRs. The coolant velocity is lower than the mainstream velocity at low BRs and is higher at high BRs. Note that, for low blowing ratios, low coolant mass flow rate is expected from the injection holes and high coolant mass flow rate at high BR. However, the overall performance for each individual shaped hole increases as the blowing ratio increases.

As a result, the coolant jet remains closer to the surface for low BR without penetrating into the mainstream flow and prevents the hot gases from reaching the surface. For this reason, the initial rows just downstream of the coolant holes (X/d > 5) are more effective than the latter downstream. Further moving downstream, the adiabatic effectiveness decreases compared to the high BR. Because the hot gases dominate the low coolant mass flow, and the high advection of hot gases causes hot air to be drawn closer to the surface. With decreased coolant fluid mass from effusion holes, it is expected a thin coolant air film will form over the surface as seen in Fig. 7a and Fig. 9, which will be unable to protect the surface from hot gases, leading to a drop in adiabatic efficiency.

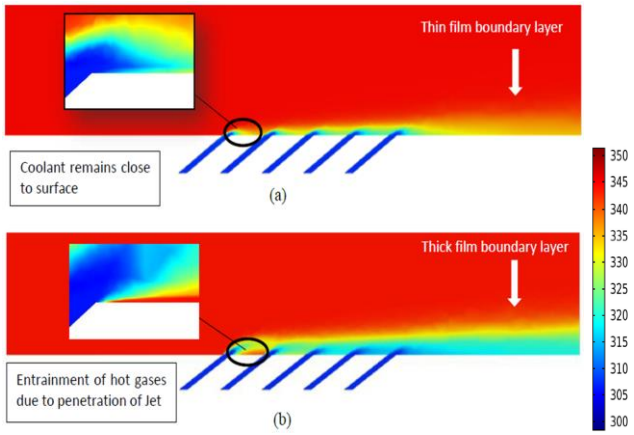


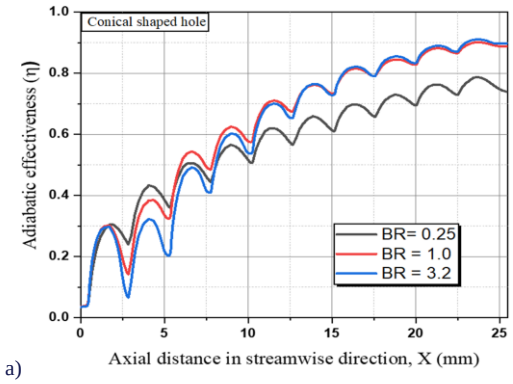
Fig. 7. Penetration of coolant jet in *XZ* plane for:
a – low blowing ratio 0.25, b – high blowing ratio 3.2.

At higher BRs, the coolant jet penetrates into the mainstream flow for the first few holes, which entrains the hot gases closer to the surface. Downstream in the region (after (X/d < 5)), a thick boundary layer of coolant fluid is formed over the surface due to the accumulation of large mass flow rates through effusion holes as seen in from Fig. 7b and Fig. 9. The adiabatic effectiveness is high for high BRs in the downstream region.

3.2. Effect of shaped holes on adiabatic effectiveness

Figure 8 shows the comparison of adiabatic effectiveness at different blowing ratios for conical-shaped and fan-shaped hole. It has been observed that the adiabatic effectiveness of the shaped holes also increases with increased blowing ratios. Because of the differences in conditions, the level of improvement varies as expected. The trend of adiabatic effectiveness is similarly observed to that of cylindrical holes as discussed in section 3.1.

The rise in adiabatic effectiveness by the shaped holes (varied hole geometries) is attributed to enhancements in all three turbulent mixing process effects associated with the lateral spread of the cooling jets in the vicinity of the cooling holes. The processes are: 1) the mixing process that occurs at the coolant jet's interaction with the main crossflow reduces the strong shear zone, 2) the lateral spread of coolant jet on the surface just downstream of the coolant hole, 3) the mixing process that occurs within the coolant jet itself by weakening the counter-rotating vortices inside the jets as it enters the mainstream.



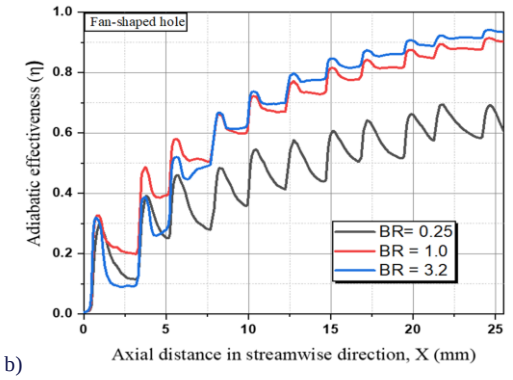


Fig. 8. Comparison of centerline adiabatic effectiveness for blowing ratios 0.25, 1.0 and 3.2: a – conical-shaped holes, b – fan-shaped holes.

Figures 9, 10 and 11 show the temperature contours distribution (cooling effectiveness) on the *XY*-plane. From Fig. 9, it is observed that for low values of blowing ratios, as the coolant remains close to surface, the temperature contours distribution downstream to the exit of hole geometry in streamwise flow is very thick with coolant jets temperature. But for higher values of blowing ratios, the coolants jet moves away from the surface due to coolants jet lift-off, such that the hot gases reach to the surface. such that the wall temperatures near the holes will be very high. Moving downward in streamwise direction, the wall temperatures are gradually decreased by accumulation of coolant mass flow rate by coalescence of upstream and adjacent effusion holes in turn increases the adiabatic effectiveness.

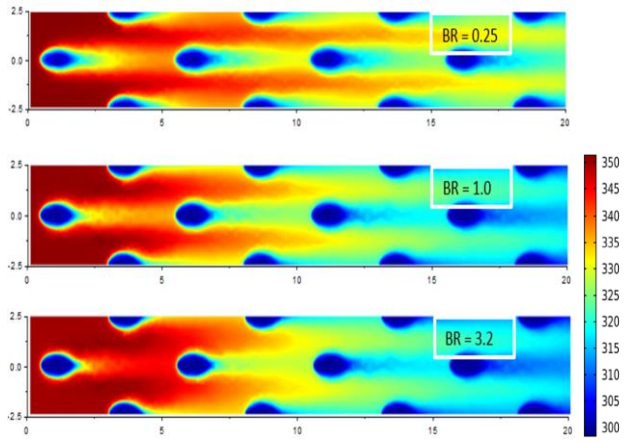


Fig. 9. Surface temperature contours of the effusion plate for cylindrical-shaped hole at different blowing ratios.

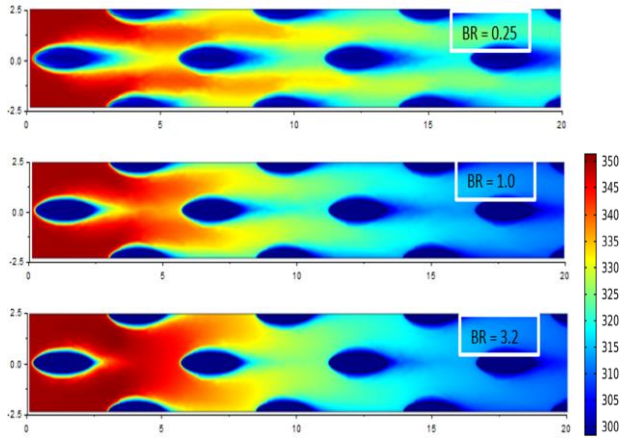


Fig. 10. Surface temperature contours of the effusion plate for conical-shaped hole at different blowing ratios.

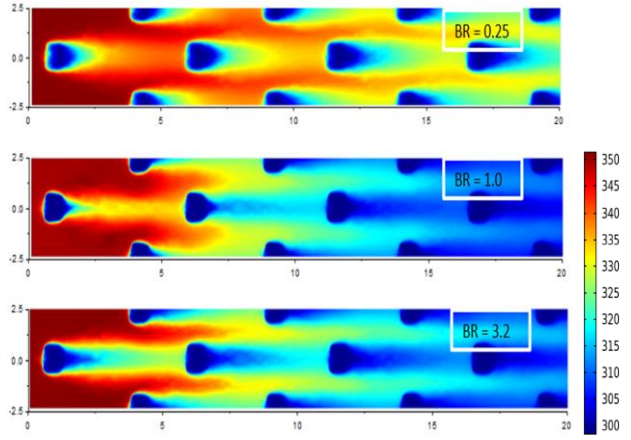


Fig. 11. Surface temperature contours of the effusion plate for fan-shaped hole at different blowing ratios.

From the Fig. 12 for the low values of BR, the conical-shaped holes provide better adiabatic effectiveness than the cylindrical holes and trapezoidal holes. This phenomenon is due to more lateral spread of coolant downstream of injection holes as the central plane of conical-shaped holes is wider compared to the cylindrical and trapezoidal holes. For such type of holes under steady state flow conditions (low BR) their jets generate anti- counter rotating- vortex pair.

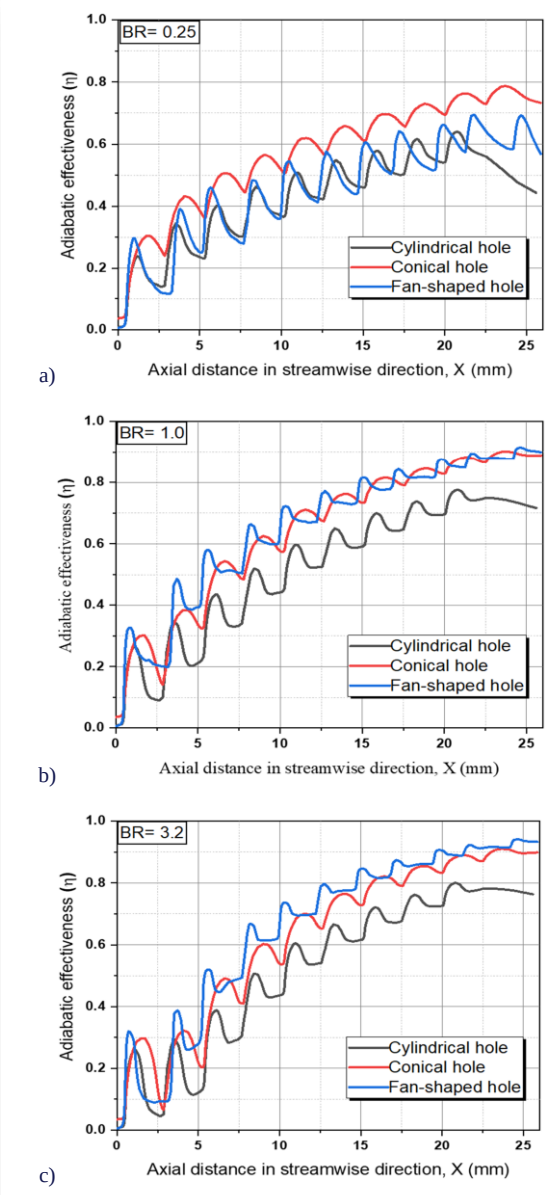


Fig. 12. Comparison of adiabatic effectiveness for different hole geometries at blowing ratios: a) 0.25, b) 1.0 and c) 3.2.

The adiabatic efficiency is increased by the vortex interactions between the jets. For the elevated BR, the fan-shaped shaped holes provide better cooling coverage. When the fan-shaped holes are used, it is expected that mixing at the interface between the coolant jets and the mainstream for a particular coolant flow rate is dramatically reduced near the holes. The decrease in mixing of cross flow and coolant jet is mostly caused by decrease in the jet's velocity as the diffused cross-sectional area at the exit section of fan-shaped holes is more compared to other shaped holes. This slows down coolant jet's lift-off into mainstream flow and remains closer to the surface by enhancing

the adiabatic effectiveness over the surface. In this case, the anti-CRVPs does not exit due to very low velocity caused due to expansion.

3.3. Flow field measurements

The coolant jet flow in conical-shaped hole or the fan-shaped hole expands as it passes through the film cooling hole, which results in the lateral distribution of the jet flow along the spanwise direction. Because of this, the uniformity of coolant jet outflow distribution along spanwise will be greater for the conical hole and fan-shaped hole compared to that of cylindrical hole.

From Fig.13 it is observed that for the cylindrical shaped holes, the two counter rotating vortices formed is much closer to the centerline of the cut plane by generating more strength to CRVPs, and prevent coolant from spreading over the surface. But the vortices generated in shaped holes moves slightly away from the centerline of cut plane which allows the coolant to spread laterally in spanwise direction. In conical shaped holes, the anti-CRVPs are clearly visible. The temperature boundary layer increases as the coolant flows downstream in the streamwise direction by coalescence of the upstream coolant jet. Furthermore, it is observed the film boundary layer of temperature increases eventually as the coolant flows from row 1 to row 5. The differences in temperature boundary layer for row 1 and row 5 can be seen in the Fig. 13 and Fig. 14.

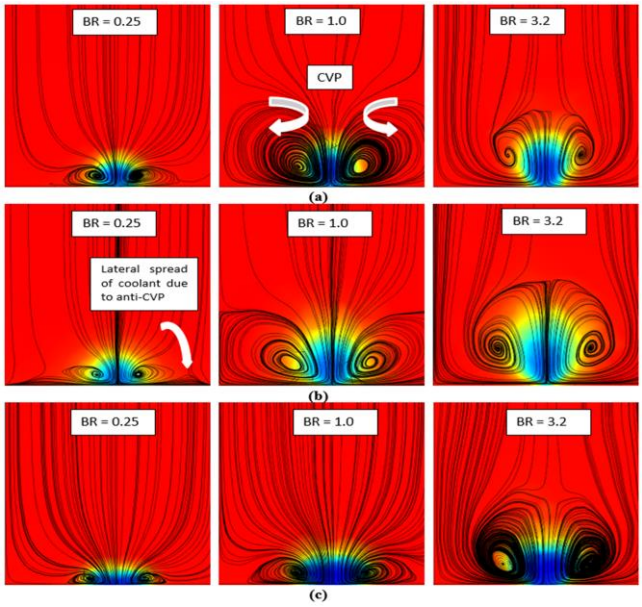


Fig. 13. Streamline-temperature distribution in *YZ* cut plane downstream of row 1.

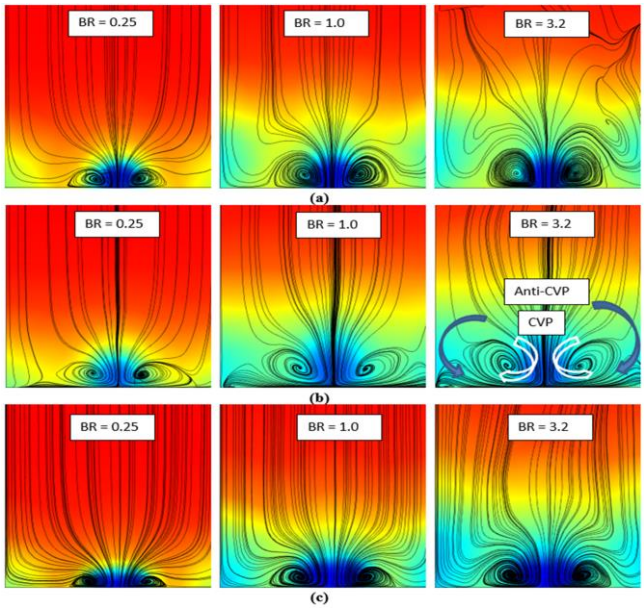


Fig. 14. Streamline-temperature distribution in *YZ* cut plane downstream of row 5.

3.4. Velocity profile

The velocity profiles are evaluated on the effusion surface downstream of effusion hole at rows 1 and row 5 to determine whether the flow is fully developed or not. The velocity profiles are generated just downstream of corresponding hole in streamwise direction at blowing ratio 0.25, 1.0 and 3.2.

Figure 15 shows the mean velocity profiles for row 1 and row 5 for blowing ratio 0.25, 1.0 and 3.2, respectively. There is a gradual drop in coolant jet penetration height, as indicated by the maximum streamwise velocity, as the flow moves from row one to row 5. From Fig. 15(b), for cylindrical holes, the maximum peak for row 1 occurs at 0.15*d* and 0.35*d* for row 5. Another interesting phenomenon is that the continuous ejection of coolant flow causes an increase in the velocity of the outer portion of the flow.

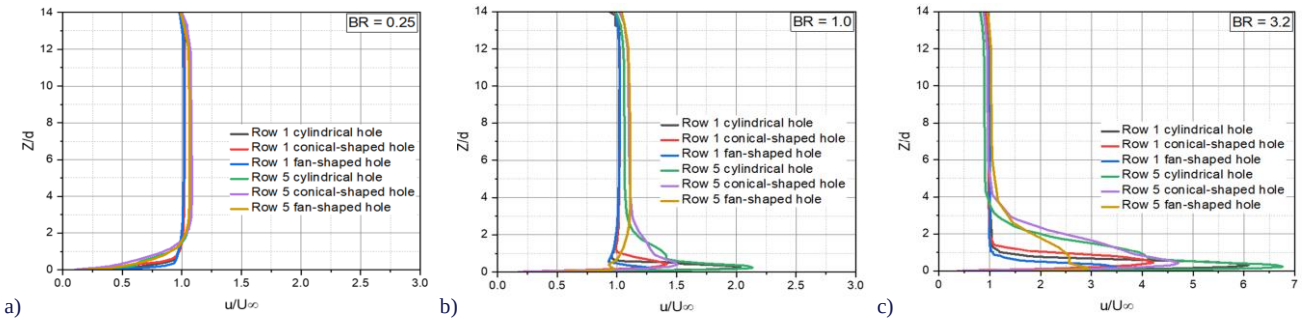


Fig. 15. Stream wise velocity profiles for blowing ratio 0.25, 1.0 and 3.2 just downstream of row 1 and row 5.

As discussed, earlier coolant flow velocity is reduced for shaped holes compared to cylindrical holes. From Fig. 15, the maximum velocity peak in streamwise direction at row 5 for cylindrical holes is 2.2*d*, for conical is 1.5*d* and for fan-shaped hole is 0.9*d*. Theses clearly indicates that the velocity of coolant jet has reduced due to expansion of hole exit and there by the lateral spread of coolant increases in both spanwise and streamwise direction as shown in Fig. 16.

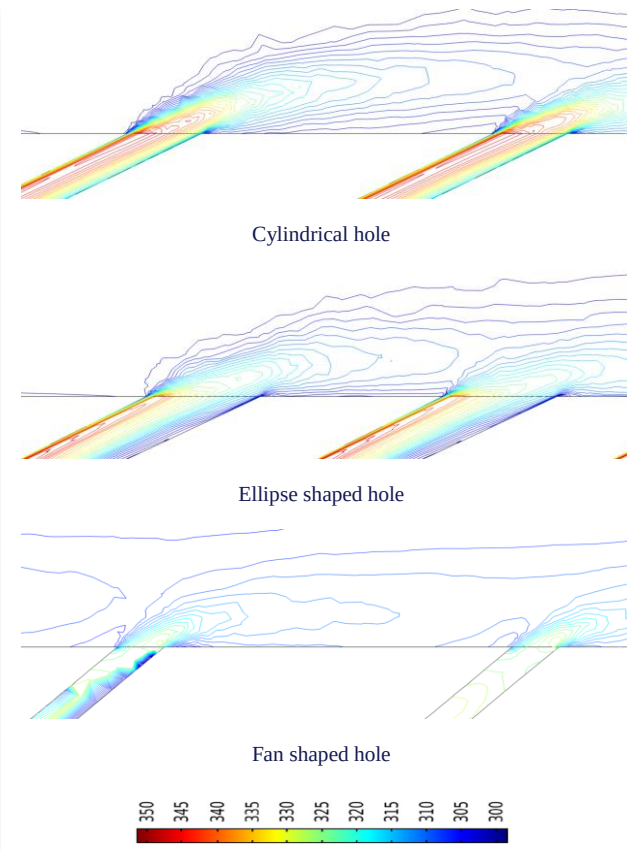


Fig. 16. Velocity distribution and streamlines in the *XZ* plane cross-section at the exit of holes for BR = 3.2.

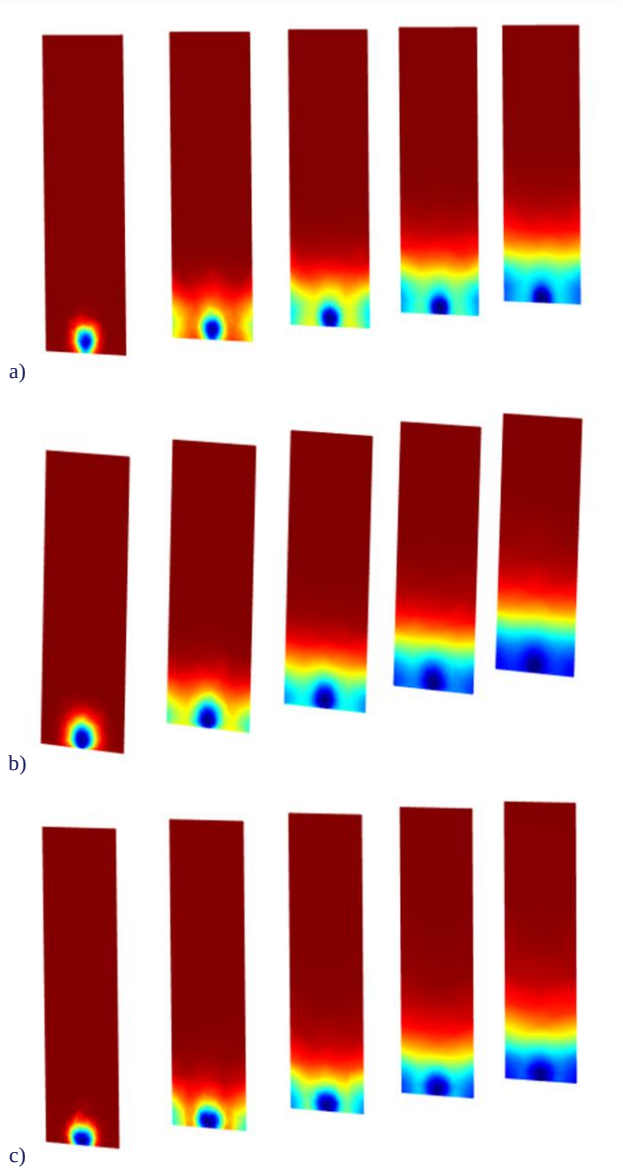


Fig. 17. Temperature contour distribution downstream of film cooling holes in *YZ* plane for: a) cylindrical holes, b) ellipse shaped holes, c) fan shaped holes.

Figure 17 illustrates the temperature contour distribution across five cross-sections on the test surface in *YZ* plane. These cross-sections are positioned downstream of individual injection holes at a distance of 0.5d of the effusion holes. It is observed that the trend of the jet cores gradually rises in the streamwise direction. This trend indicates the penetration of coolant from the neighboring holes, resulting in the accumulation of coolant in the downstream direction. When analysing the vortex generator cases in comparison to the Baseline case, it is evident that as the mainstream flow passes through conical and fan-shaped holes, two extra regions of low speed emerge laterally. These regions subsequently interact with the downstream film jet, resulting in a reduction of the jet core's height. This reduction is attributed to the creation of supplementary coherent vortices in a direction opposite to that of the CRVP phenomenon. This trend enhances the lateral expansion of coolant in lateral direction for the shaped holes.

3.5. Area-averaged adiabatic effectiveness ($\bar{\eta}$)

Figure 18 shows the relation between the blowing ratio and area-averaged adiabatic effectiveness ($\bar{\eta}$). These area-averaged adiabatic effectiveness ($\bar{\eta}$) is represented as overall performance of effusion cooling on the surface. The area-averaged adiabatic effectiveness ($\bar{\eta}$) increases as the blowing ratio increases for all hole geometries. It is clear from Fig.16 that the conical-shaped and fan-shaped holes provide better cooling effectiveness compared to the cylindrical holes at all blowing ratios. At low BR 0.25, the adiabatic effectiveness of conical- shaped holes was 25% and 19% higher than the cylindrical and trapezoidal shaped holes respectively. For intermediate BR 1.0, the trapezoidal holes provided 21% and 10% higher than cylindrical and conical-shaped holes. Further increasing the blowing ratio to 3.2, the effectiveness increased to 13% and 4% respectively compared to cylindrical and conical shaped hole respectively.

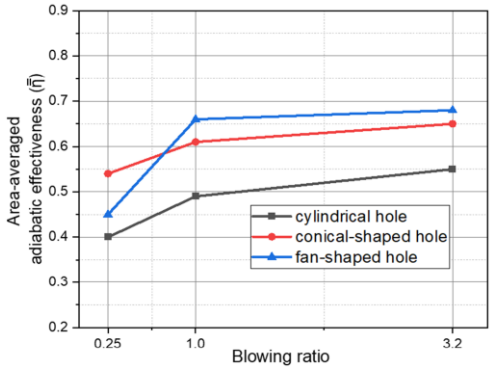


Fig. 18. Area-averaged adiabatic effectiveness ($\bar{\eta}$) vs. BR.

4. Conclusions

The present paper investigates the effect of hole geometries (shaped holes) and coolant jet blowing ratios on effusion cooling performance. The adiabatic effectiveness is measured and compared for three different types of shaped holes (cylindrical hole, conical-shaped hole, and fan-shaped hole) for blowing ratios 0.25, 1.0 and 3.2 at injection angles 30^o over a flat surface. In addition, velocity profiles and streamlines on vertical planes are measured at row 1 and row 5 on the flow field.

1. Compared to the cylindrical holes, the shaped holes provide more adiabatic effectiveness on effusion plate. The overall adiabatic effectiveness increases as the blowing ratio increases from 0.25 to 3.2.
2. At low blowing ratios, the conical-shaped holes are preferable than the cylindrical and fan-shaped holes. The formation of anti-CRVP's at the exit of hole geometry provides more lateral spread of coolant on the surface.
3. At high blowing ratios, the fan-shaped holes are preferable than the other shaped holes. Due to diffused shape at the exit of hole's geometry, the coolant jet velocity is reduced which in turn lowers the mixing between the coolant jet and mainstream. This causes the coolant to remain close to the surface and increases the lateral spread of coolant.

At a low blowing ratio of 0.25, conical-shaped holes exhibit 25% and 19% higher adiabatic effectiveness compared to cylindrical and trapezoidal-shaped holes respectively. For intermediate BR 1.0, the trapezoidal holes provided 21% and 10% of adiabatic effectiveness higher than cylindrical and conical-shaped holes. Further increasing the blowing ratio to 3.2, the effectiveness increased to 13% and 4% respectively compared to cylindrical and conical shaped hole respectively.

References

[1] Yuen, C.H.N., & Martinez-Botas, R.F. (2005). Film cooling characteristics of rows of round holes at various streamwise angles in a crossflow: Part I. Effectiveness. *International Journal of Heat and Mass Transfer*, 48(23−24), 4995−5016. doi: 10.1016/j.ijheatmasstransfer.2005.05.019

[2] Qayoum, A., & Panigrahi, P. (2019). Experimental investigation of heat transfer enhancement in a two-pass square duct by permeable ribs. *Heat Transfer Engineering*, 40(8), 640−651. doi: 10.1080/01457632.2018.1436649

[3] Rasool, A., & Qayoum, A. (2018). Numerical analysis of heat transfer and friction factor in two-pass channels with variable rib shapes. *International Journal of Heat and Technology*, 36(1). doi: 10.18280/ijht.360106

[4] Rasoo, A., & Qayoum, A. (2018). Numerical investigation of fluid flow and heat transfer in a two-pass channel with perforated ribs. *Pertanika Journal of Science and Technology*, 26(4).

[5] Goldstein, R. J. (1971). Film cooling. In *Advances in Heat Transfer*, 7 (pp. 321−379). Elsevier.

[6] Andrews, G.E., Alikhanizadeh, M., Tehrani, F.B., Hussain, C.I., & Azari, M.K. (1988). Small diameter film cooling holes: The influence of hole size and pitch. *International Journal of Turbo and Jet Engines*, 5(1−4), 61−72. doi: 10.1515/tjj.1988.5.1-4.61

[7] Andrews, G.E., Asere, A.A., Gupta, M.L., & Mkpadi, M.C. (1985). Full coverage discrete hole film cooling: The influence of hole size. In *ASME Turbo Expo: Power for Land, Sea, and Air*, 79405, p. V003T09A003 (85-GT-47). doi: 10.1515/TJJ.1985.2.3.213

[8] Andrews, G.E., Gupta, M.L., & Mkpadi, M.C. (1984). Full coverage discrete hole wall cooling: Cooling effectiveness. In *ASME Turbo Expo: Power for Land, Sea, and Air American Society of Mechanical Engineers*, 79498, V004T09A018 (84-GT-212). doi: 10.1515/TJJ.1985.2.3.199

[9] Kumar, K.R.Y., Qayoum, A., Saleem, S., & Mir, F.Q. (2022). Effect of blowing ratio on adiabatic effectiveness for effusion cooling in gas turbine combustor liners. *Research on Engineering Structures and Materials*, 8(3), 431−445. doi: 10.17515/resm2022.359me1028

[10] Kumar, Y., Qayoum, A., Saleem, S., & Mir, F.Q. (2021). Combined effect of upstream ramp and effusion cooling in combustion chamber liners of gas turbines. *Journal of Thermal Engineering*, 9(2), 297–312. doi: 10.18186/thermal.1284759

[11] Lin, Y., Song, B., Li, B., Liu, G., & Wu, Z. (2003). Investigation of film cooling effectiveness of full-coverage inclined multihole walls with different hole arrangements. In *ASME Turbo Expo: Power for Land, Sea, and Air*, 36886 (651−660). doi: 10.1115/GT2003-38881

[12] Zhang, C., Lin, Y., Xu, Q., Liu, G., & Song, B. (2009). Cooling effectiveness of effusion walls with deflection hole angles measured by infrared imaging. *Applied Thermal Engineering*, 29(5−6), 966−972. doi: 10.1016/j.applthermaleng.2008.05.011

[13] Kumar, K.Y., Qayoum, A., Saleem, S., & Qayoum, F. (2020). Effusion cooling in gas turbine combustion chambers − a comprehensive review. In *IOP Conference Series: Materials Science and Engineering*, 804(1), 012003. IOP Publishing. doi: 10.1088/1757-899X/804/1/012003

[14] Goldstein, R.J., Eckert, E.R G., & Burggraf, F. (1974). Effects of hole geometry and density on three-dimensional film cooling. *International Journal of Heat and Mass Transfer*, 17(5), 595−607. doi: 10.1016/0017-9310(74)90007-6

[15] Fu, J.L., Bai, L.C., Zhang, C., & Ju, P.F. (2019). Film cooling performance for cylindrical holes embedded in contoured craters: effect of the crater depth. *Journal of Applied Mechanics and Technical Physics*, 60, 1068−1076. doi: 10.1134/S0021894419060129

[16] Revulagadda, A.P., Adapa, B.R., Balaji, C., & Pattamatta, A. (2024). Performance assessment and optimization of three-dimensional hybrid slot–effusion jet cooling configuration of an annular combustor liner. *Applied Thermal Engineering*, 240, 122198. doi: 10.1016/j.applthermaleng.2023.122198

[17] Huang, Y., Zhang, J.Z., & Wang, C.H. (2020). Multi-objective optimization of round-to-slot film cooling holes on a flat surface. *Aerospace Science and Technology*, 100, 105737. doi: 10.1016/j.ast.2020.105737

[18] Zhang, H., Wang, Q., Chen, Z., Su, X., & Yuan, X. (2020). Effects of compound angle on film cooling effectiveness considering endwall lateral pressure gradient. *Aerospace Science and Technology*, 103, 105923. doi: 10.1016/j.ast.2020.105923

[19] Park, S.H., Kang, Y.J., Seo, H.J., Kwak, J.S., & Kang, Y.S. (2019). Experimental optimization of a fan-shaped film cooling hole with 30 degrees-injection angle and 6-hole length-to-diameter ratio. *International Journal of Heat and Mass Transfer*, 144, 118652. doi: 10.1016/j.ijheatmasstransfer.2019.118652

[20] Li, Z., Xie, P., Zeng, Q., & Chen, X. (2023). Study of tangential effusion cooling of a combustor liner. *Processes*, 11(8), 2433. doi: 10.3390/pr11082433

[21] Schmidt, D.L., Sen, B., & Bogard, D.G. (1996). Film cooling with compound angle holes: adiabatic effectiveness. *Journal of Turbomachinery*, 118(4), 807−813. doi: 10.1115/1.2840938

[22] Sofi, A.Y., & Qayoum, A. (2023). Numerical investigation of thermo-hydraulic performance and irreversibility behaviour in a pulsating turbulent flow ribbed duct. *Arabian Journal for Science and Engineering*, 49(2), 1515−1529. doi: 10.1007/s13369-023-07902-w

[23] Qayoum, A., Gupta, V., Panigrahi, P.K., & Muralidhar, K. (2010). Influence of amplitude and frequency modulation on flow created by a synthetic jet actuator. *Sensors and Actuators A: Physical*, 162(1), 36−50. doi: 10.1016/j.sna.2010.05.008

[24] Thole, K.A., Gritsch, M., Schulz, A., & Wittig, S. (1997). Effect of a crossflow at the entrance to a film-cooling hole. *Journal of Fluids Engineering*, 119(3), 533−540. doi: 10.1115/1.2819277

[25] Bell, C.M., Hamakawa, H., & Ligrani, P.M. (2000). Film cooling from shaped holes. *Journal of Heat Transfer*, 122(2), 224−232. doi: 10.1115/1.521484

[26] Sen, B., Schmidt, D.L., & Bogard, D.G. (1996). Film cooling with compound angle holes: heat transfer. *Journal of Turbomachinery*, 118(4), 800−806. doi: 10.1115/1.2840937

[27] El-Gabry, L.A., & Kaminski, D.A. (2005). Numerical investigation of jet impingement with cross flow − comparison of yang-shih and standard k–ϵ turbulence models. *Numerical Heat Transfer, Part A*, 47(5), 441−469. doi: 10.1080/10407780590891254

[28] Silieti, M., Divo, E., & Kassab, A.J. (2004). Numerical investigation of adiabatic and conjugate film cooling effectiveness on a single cylindrical film-cooling hole. In *ASME International Mechanical Engineering Congress and Exposition*, 4711, 333−343.

[29] Scrittore, J.J., Thole, K.A., & Burd, S.W. (2007). Investigation of velocity profiles for effusion cooling of a combustor liner. *Journal of Turbomachinery*, 129(3), 518-526. doi: 10.1115/1.2720492

Co-published by
Institute of Fluid-Flow Machinery
Polish Academy of Sciences
Committee on Thermodynamics and Combustion
Polish Academy of Sciences

Copyright©2024 by the Authors under licence CC BY 4.0

http://www.imp.gda.pl/archives-of-thermodynamics/

Thermal performance of tubular heat exchangers with the discontinuous swirl-inducing conical baffle with opposite-oriented flow deflectors

Md Atiqur Rahman[a*]

[a] Department of Mechanical Engineering, Birla Institute of Technology, Mesra, Jharkhand 835215, India
*Corresponding author email: rahman.md4u@gmail.com

Received: 10.08.2023; revised: 29.12.2023; accepted: 01.04.2024

Abstract

An experiment was conducted to analyze a tubular heat exchanger's turbulent heat transfer characteristics. The heat exchanger was equipped with a newly designed perforated (rectangular) conical baffle plate consisting of two rectangular opposite-oriented flow deflectors with adjustable tilt angles. The baffle plate was installed at the entrance of the heat exchanger, resulting in a counter-swirling flow pattern downstream. Three baffle plates were installed along the flow direction with different pitch ratios (spacing between baffle plates divided by the diameter of the heat exchanger). The experiment examined the effects of pitch ratio (ranging from 0.6 to 1.2), deflector tilt angle (ranging from 30° to 50°) and Reynolds numbers (ranging from 16 500 to 30 000) on the heat transfer performance. The results showed that the pitch ratio and tilt angle significantly affected the performance of the heat exchanger. In particular, a configuration with a tilt angle of 30° and a pitch ratio of 1 resulted in an average improvement of 26.9% in the heat exchanger's performance compared to a heat exchanger without a conical baffle plate under similar operating conditions.

Keywords: Inclination angle; Recirculation; Rectangular deflector; Flow resistance; Swirl flow; Thermo-fluid performance

Vol. 45(2024), No. 2, 195–204; doi: 10.24425/ather.2024.150865

Cite this manuscript as: Rahman, M.A. (2024). Thermal performance of tubular heat exchangers with the discontinuous swirl-inducing conical baffle with opposite-oriented flow deflectors. *Archives of Thermodynamics*, 45(2), 195–204.

1. Introduction

Heat exchangers play a crucial role in various industries' thermal systems, making the use of heat transfer enhancement techniques essential for energy efficiency. These techniques have been widely implemented in refrigeration, automotive, process, and solar air heater systems to reduce energy consumption and operating costs [1–4]. Turbulators, or vortex/reverse flow devices, are commonly used in HT (heat transfer) engineering to improve heat and momentum transfer. By promoting vortex flow and boundary dissipation, turbulators enhance heat transfer coefficients and increase convection at the tube's surface. This is achieved by reducing the cross-sectional flow area, increasing velocity, and creating a higher temperature difference. These deflectors, when strategically placed in the flow field [5], can generate longitudinal swirl flow and can be referred to as swirl generators/promotors, which may be continuous, e.g. twisted tapes [6], or discontinuous [7]. A few of the literature showing the effect of deflector are discussed below.

Nomenclature

A – duct's cross-sectional area, m^2
A_c – duct area of cross-section, m^2
A_i – total heat transfer surface area, m^2
A_p – copper tube heat transfer surface area, m^2
BR – blockage ratio,
c_p – specific heat of air, kJ/(kg K)
d – outer diameter of copper tube, m
D – test section inner diameter, m
E – area (cross-sectional) of the test section, m^2
f – friction factor
h_m – convective heat transfer coefficient, $W/(m^2 K)$
H – height ratio, $= H_1/H_2$
j – Colburn factor
k_p – thermal conductivity of Plexiglas, W/(m K)
k_t – thermal conductivity of copper tube, W/(m K)
L – duct length, m
Nu – Nusselt number
p – distance between consecutive baffle plates, m
PEC – performance evaluation criterion
Pr – Prandtl number of air
PR – pitch ratio
Q – air side heat transfer rate, W
Re – Reynolds number
t – average temperature, °C
T – temperature, °C
TEF – thermal enhancement factor

Greek symbols

α – tilt angle (angle between the deflector and baffle plane), °
Δp – pressure drop in test section, Pa
Δp_o – pressure drop at orifice plate, Pa
Δt_{lm} – LMTD of test section
λ – thermal conductivity of air, W/(m K)
μ – dynamic viscosity of air, Pa s
v – average velocity, m/s
ρ – density, kg/m^3

Subscripts and Superscripts

a – local
in – inner
out – outer
w – wall

Abbreviations and Acronyms

CDBP– conical deflector baffle plate
HT – heat transfer
HX – heat exchanger
LMTD– logarithmic mean temperature difference
TEF – thermal enhancement factor
VG – vortex generator

Yaningsih et al. [8] conducted an experimental study to investigate the impact of a louvered strip insert's slant angle (α) on HT and f (friction factor). We examined slant angles of 15°, 20° and 25° at Reynolds number (Re) ranging from 5300 to 17 500. We also included a plain tube for comparison purposes. The results revealed that the louvered strip insert significantly enhanced HT and f compared to the plain tube, with increases of up to 77.02% and 3.35 times, respectively. Moreover, the results indicated that HT and f increased as the slant angle increased. The highest slant angle demonstrated the most favourable thermal enhancement factor (TEF) with a value of 1.12.

Bartwal et al. [9] investigated a novel geometric insert called circular rings with wire net inserts as HT enhancement devices. Three wire net grades (G = 4, 9, and 16) and three PRs (pitch ratio – p/D) of 2, 3 and 4 are chosen to investigate their impact on HT, f and TEF. Turbulent airflow with Re between 5 000 to 40 000 is used as the working fluid. The results show significant improvements in HT and pressure drop (Δp) in the test section compared to a smooth tube. Results showed that the highest TEF of approximately 3.35 is achieved for PR = 2 and G = 16. An extreme of 2.84 for TEF is obtained for PR = 3 and G = 9.

Ibrahim et al. [10] performed numerical investigations of the effectiveness of using conical rings as turbulators for enhancing heat transfer. Conical inserts were placed inside a tube, and the performance of three different configurations (convergent, convergent-divergent, and divergent) was analyzed. The study focused on air as the working fluid and Re between 6 000–25 000. Varying diameter ratios and pitch ratios were tested. Results showed that the Nu (Nusselt number) and f rose as the conical ring diameter and pitch ratio declined. Compared to a plain tube, the average Nu values achieved were significantly higher with the convergent, convergent-divergent and divergent ring arrays, with enhancements of 330%, 419% and 765%, respectively. The best overall performance was observed for the divergent ring with a diameter ratio of 0.4 and PR of 2 at the Reynolds number of 6000, achieving an enhancement in tube efficiency of 1.291.

Nalavade et al. [11] conducted experimental and numerical investigations of the effect of unique flow divider-type turbulators on the characteristics of f and HT for airflow inside a heated tube. The tests were conducted with Re between 7 000 and 21 000. The parameters studied included PR (p/D = 0.54, 0.72 and 1.09) and a twist angle 90°. These novel turbulators created additional turbulence near the tube wall, effectively disrupting the thermal boundary layer. Both experimental and numerical results showed that the HT rate, f and TEF increased with decreasing PR of the turbulators. This enhancement is attributed to the fluid displacement from the central core region towards the tube walls caused by the flow divider-type turbulator. Additionally, computational simulations were utilized to examine the impact of varying the twist angle of the turbulator, revealing that the Nusselt number increased by approximately 1.33–1.46 times and 1.43–1.60 times for angles of 45° and 30°, respectively.

Hassan et al. [12] experimentally examined a novel square turbulator tape with three square fins' design in a double-tube heat exchanger (HX). The inner copper tube side had diameters of 0.022 m, while plexiglass shells had diameters of 0.054 m, respectively. It was found that plummeting the width of fins augments the HT rate. The experimental results exhibit that the square-cut turbulator with a width of 0.25 cm resulted in a 271.7% increase in Nu number values, a 117.6% increase in total convective heat transfer coefficient (h_m), and a TEF of 2.9.

Lamlerd et al. [13] studied the impact of circular-ring tabulators on the HT characteristics of a steam generator. The tabulators have a tilt angle (α) of 45° with blockage ratio (BR) of 0.20 mm. The researchers investigated length ratios (LR) between 25% to 100%, PR of 1.0 to 4.0, and water flow rates of 12–36 l/h. Waste lubricating oil was utilized as the heat source to generate steam. The findings demonstrate that HX with circular-ring inserts outperforms a smooth tube in terms of steam rate (6.88–10.35% improvement), vapour quality (x) (0.21– 0.92 improvement), heat transfer (1.27–1.55 times improvement) and thermal efficiency (0.46–0.68 improvement).

Jayranaiwachira et al. [14] experimentally studied a heat exchanger equipped with louvered curved-baffle (LCB) vortex generator (VG). The study measured HT and Δp of air flowing through the tube at different Re ranging from 4760 to 29 300. LCB VGs have an attack angle of 30° arranged in a V-shape on two tape sides. The results showed that the LCB-inserted tube had significantly higher Nu and f compared to the plain tube. Additionally, Nu and f increased as the PR and tilt angle α decreased. LCB VGs increased Nu and f by 4.66 times and 39.37 times, respectively. The highest TEF was observed when the LCB had a PR of 1, $\alpha\ \theta$ of 45° and lower Re.

Promvonge et al. [15] investigated the effectiveness louver-punched V-baffle (LPVB) VG in improving thermal performance in a solar HX duct with air as the working fluid at Re ranging from 5 300 to 23 000. LPVBs with an α = 45° were placed on the heated wall of the duct. The investigation focused on determining the optimal PR and louver angles and exploring the impact of different relative louver sizes. The results showed that the LPVB with louver angles greater than 0° significantly reduced solid-baffle friction loss, although heat transfer was slightly lower. The LPVB with a relative baffle pitch of 1.5 and a louver angle of 45° demonstrated the best performance in the first part of the investigation, while the LPVB with a relative louver size of 0.9 performed the best in the second part.

Promvonge et al. [16] experimentally investigated the HT characteristics of a circular tube equipped with conical nozzles and a swirl generator. The conical nozzles, serving as turbulators and reverse flow generators, were placed in a modelled pipeline where the air was used as the working fluid. Different arrangements of the conical nozzles were tested, with three PR of 2.0, 4.0 and 7.0 in each run. Additionally, a snail design was employed to induce swirling flow at the tube inlet. Results showed significant improvements in heat transfer rate when using either the conical nozzles or the snail, with increases of approximately 278% and 206%, respectively, compared to a plain tube. Combining the conical nozzles with the snail resulted in a maximum HT rate enhancement of 316%.

Samruaisin et al. [17] experimentally investigated the effects of V-shaped delta-wing baffles on TEF of a circular tube. The baffles with different numbers of wings (4, 6 and 8) were compared. Various PR (p/D = 2.0, 2.5 and 3.0) were used to fit the V-shaped delta-wing baffles inside the tube. These baffles created both recirculation/reverse flow behind the solid baffle and longitudinal vortex flow behind the V-shaped wing. The V-shaped winged baffles with 8 wings showed higher HT rates by promoting the development of reverse and vortex flows, allowing for better fluid mixing. The Nu enhancement ranged from 97% to 105.6% for wings number N = 4, 105.8% to 127.8% for N = 6, and 114.8% to 138.9% for N = 8. The V-shaped winged baffles with 8 wings also created additional multi-vortex flows, contributing to fluid mixing and increased heat transfer. Lower pitch ratios increased turbulent intensity and led to a higher HT rate, with a Nusselt number increase of up to 118.26% to 151.3% compared to a tube with a pitch ratio of 2.0. Baffles with 8 wings and a pitch ratio of 3.0 had a maximum aerothermal performance factor (APF) of 1.01, indicating potential energy savings at low Reynolds numbers (Re ≤ 6 000).

Durmuş [18] experimentally investigated a swirl generator in the form of a snail attached at the entrance of a concentric double-pipe HX inner pipe. In the experimental setup, cold air was directed through the inner pipe while hot water flowed through the annulus. The study examined the impact of the snail on HT and Δp in both parallel and counter-flow configurations. The results were presented as a correlation between Nu, Re, Pr and the swirling angle. The highest enhancement, up to 120% in Nu, was observed in the counter-flow configuration with a swirling angle of 45°. Although the snail-induced swirl flow caused a slight increase in Δp, this was irrelevant compared to the improvement in HT efficiency.

Rahman and Dhiman [19,20] developed a novel tubular heat exchanger with axial flow and tested several configurations to enhance its heat transfer efficiency. They employed circular perforated plates with trapezoidal air deflectors at different angles (α) to induce turbulence in the air duct surrounding the hot water tube bundle. The plates, spaced evenly but with varying pressure ratios, were found to significantly improve the thermal and fluid performance of HX when inclined at 50° and with a pressure ratio of 1.4. They further studied the geometric constraint by replacing the trapezoidal deflector with rectangular openings with one deflector [21] or two opposite-oriented flow deflectors [22] on the HT and flow characteristics. It was found that using a single flow deflector resulted in a 41.49% enhancement in TEF while incorporating two flow deflectors with opposing orientations only achieved 0.19 times the thermal effectiveness equated to a HX without a baffle plate. Using opposite-oriented diverters improved heat transfer rates and increased pressure drop (Δp). Rahman [23] further replaced perforated flat circular baffles with flow diverters in an HX to a conical baffle plate (CBP), resulting in a 22% improvement in thermal effectiveness. In another experiment, multiple (sixteen) rectangular deflectors [24] were used as flow deflectors, leading to a 1.17 enhancement in thermal effectiveness for a PR of 1 and an angle (α) of 30°. Furthermore, the use of triangular blinds [25] as flow deflector baffles showed additional improvement in the HT efficiency of HX.

Habet et al. [26] studied the effects of different angles of tilt (0°, 30°, 45° and 60°), and ratios of perforation (ranging from 10% to 40%) were investigated in a rectangular channel with an aspect ratio of 3:1. The upper and lower surfaces of the channel were insulated. They were exposed to a uniform heat flux. The research focused on Reynolds numbers ranging between 12 000 and 42 000. The results showed that the best HT enhancement and significant changes in friction factor occurred when the baffles were tilted at a 0-degree angle and had a perforation ratio of

10%. When the angles of tilt and perforation ratios were lower, the heating surfaces experienced stronger reattachment and recirculating flow, leading to increased HT and a Nu ratio of 2.6. The configuration that yielded the highest TEF of 0.7 was achieved with a 60-degree angle of tilt and a perforation ratio of 10% at the Reynolds number of 12 000.

The aforementioned literature reveals that the implementation of swirl promoters within a heat exchanger yields improved fluid mixing. Consequently, this leads to heightened heat transfer capabilities as the fluid and heat transfer surfaces have more substantial contact, resulting in elevated heat transfer coefficients. Additionally, the incorporation of swirl flow reduces fouling in heat exchangers by preventing the accumulation of deposits on high-temperature surfaces. This is primarily achieved by the continuous agitation of the fluid, which effectively washes the surfaces and facilitates the removal of unwanted elements. These two factors collectively contribute to a higher thermal efficiency within the heat exchanger. The heat exchanger can achieve the desired heat transfer objectives with minimal energy input, resulting in energy savings and an overall increase in system effectiveness. Another advantageous outcome of swirl flow is its capacity to enable the design of more compact HX. The enhanced heat transfer capabilities achieved through the swirling motion allow for smaller heat transfer surfaces or reduced heat exchanger sizes, optimizing space utilization. Furthermore, the implementation of a swirler can also address the issue of stagnation zones within the heat exchanger. By promoting a more uniform distribution of temperature, the swirler helps eliminate areas where fluid movement is limited. This feature is particularly crucial in applications where maintaining a consistent temperature profile, such as thermal processing or heating/cooling systems, is critical.

In recent studies, scientists have been exploring novel methods to improve the transfer of heat and reduce pressure drop in devices that induce rotational movement. These advancements include the utilization of coiled structures [27], twisted strips [28], and perforated cone-shaped rings [29]. Different perforation patterns, such as triangles [25], rectangles [22], circles and trapezoids [19], have been experimentally examined to find the most effective way to enhance heat transfer or reduce pressure variations. Novel baffle plate designs like conical [18], and conical with perforation [23] have been studied. However, the understanding of utilizing multiple flow deflectors [21] on baffle plates and the deflector orientation [24] on thermal-hydraulic performance is limited in the current literature. This study aims to bridge these knowledge gaps by developing and evaluating a unique design for a device that induces discontinuous swirling motion. Our approach involves incorporating opposing flow deflectors on conical baffle plates to induce swirling motion and turbulence in the fluid.

The primary objective of this research is to develop and test a novel perforated conical baffle plate capable of producing a swirl, which aims to manipulate the flow. This device achieves its purpose by utilizing opposite-oriented rectangular deflectors mounted on each conical baffle plate (CDBP) to induce a counter-swirl motion and turbulence. The flow deflectors are strategically positioned at a slant length of 15 mm from the apex of the conical baffle plate. Three successive baffle plates are located within HX at regular intervals to facilitate flow reversal, extending residual air time within HX and disrupting the thermal boundary layer, causing air-side HT augmentation.

The study investigates the influence of two key factors: the ratio of HX diameter to the distance between adjacent baffle plates (PR) and the inclination angle (α) in circular ducts for heat transfer (HT) and friction factor (f). The PR values are considered in the range from 0.6 to 1.2, while the tilt angle varies between 30° and 50°. The experimental analysis maintains consistent conditions, with Reynolds numbers ranging between 15 000 and 30 000. Further performance comparison in terms of TEF is done between HX with and without baffle plate under similar operating parameters.

2. Materials method

2.1. Experimental configuration

The experiment was carried out within an open-loop experimental system, as Rahman and Dhiman extensively described in [19,20]. The loop consisted of a circular duct linking a 4 kW blower to a settling tank, with the inclusion of an orifice flow meter in this pipeline. Following the straightener, a channel was utilized, comprising a calm segment measuring 1.3 m, a test segment measuring 0.6 m, and an exit measuring 0.3 m. The test channel, portrayed in Fig. 1, was constructed using plexiglass material characterized by low thermal conductivity, featuring a channel diameter (D) of 19 cm, a length (L) of 60 cm and a thickness of 0.5 cm.

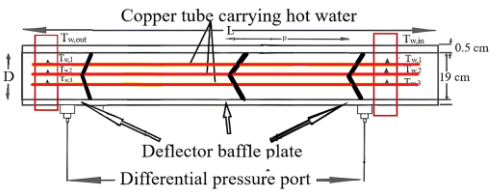


Fig. 1. Test section.

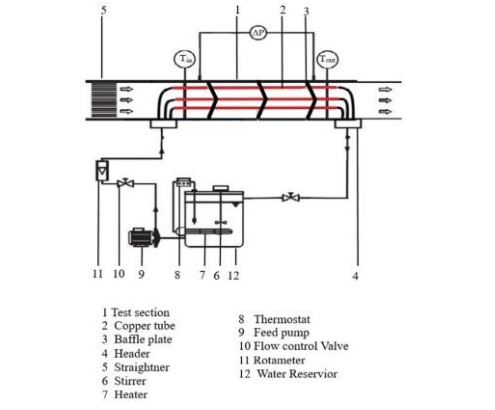


Fig. 2. Hot water loop.

Inside the test section, three conical baffles, each having a thickness of 5 mm and fabricated using 3D printing technology, were placed at equal intervals. Further details regarding these baffles will be elaborated later in this section. A nondimensional parameter, known as pitch ratio (PR = p/D) was investigated at four specific values: 0.6, 0.8, 1 and 1.2. The test section was wrapped with cotton wool to minimize heat loss and covered with 8 mm urethane foam. Further, five copper tubes (DHP 12 200) with an outer diameter (d) of 1 cm and a thickness of 1 mm were arranged in a circular array, with one at the centre and the other four at a circular distance of 5 cm from the centre of the baffle plate. To calculate h_m (Eq. (5)) of air, the tube average surface temperature at the inlet ($T_{w,in}$) and outlet ($T_{w,out}$) is measured using ten J-type thermocouples attached to NI-9213 DAQ card with a resolution of ± 0.02°C with digital readout using LabView software. Two additional thermocouples ($T_{a,in}$ and $T_{a,out}$) are employed at the test section's air inlet and exit. Also, Δp in the test section is measured using silicon microstructure pressure transducers (connected to an analogue-to-digital converter – ADC), board interface and RS 232 serial interface) with digital readout via Lab-View software.

A closed hot water loop was employed to provide heat to the test section, as illustrated in Fig. 2. The water was heated using an electrical heater with a power rating of 4 kW, whose temperature was then regulated by a thermostat in a reservoir. The heated water was circulated at a constant flow rate of 4 LPM (litres per minute) to a distributor using a 0.25 hp (0.18 kW) feed pump, a bypass valve and a rotameter. The temperature of this hot water was measured using PT100 and uniformly distributed to all the copper tubes within the test section.

Table 1. Experimental operating conditions [20].

Air-inlet temperature, °C	32.5 ± 0.5
Air-inlet velocity, m/s	7–13
Water-inlet temperature, °C	55–60
Water mass flow rate, kg/s	0.06

Table 2. The accuracies of the measurements [20].

Parameters	Accuracy
Air temperature-inlet, °C	± 0.5
Pressure drops, Pa	± 0.1
Water temperature-inlet, °C	± 0.5
Water flow rate, kg/s	± 0.003

During experimentation, the cold air from the atmosphere is sucked in using a blower which enters the test section after passing through a straightener. As it travels through the test section, it gains temperature, which is used in calculating h_m. Modifications are made to the airflow rate (constant Re) while maintaining a consistent water flow rate during the experiment to conduct a comparative analysis. The arrangement is then permitted to achieve a state of equilibrium, at which point the air and surface temperatures of the copper pipes in the test section are measured.

Table 1 provides a condensed overview of the testing criteria, while Table 2 demonstrates the determination of instrument precision by utilizing the root mean sum square method. The potential maximum uncertainty associated with the variables Re, v, f and Q is estimated to be ± 3.25, ± 5, ± 5.34 and ± 5%, respectively [30].

2.2. Baffle plate and tube arrangement

The CDBP of fixed height (h = 5 cm) with a geometry angle of 28° as seen in Figs. 3(a)–3(c) comprises five tube configurations. The central configuration is surrounded by four tubes arranged in a circular pattern, positioned 4 cm away from the centre of the conical plate. Four regularly spaced rectangular openings of $7d \times 1.5d$ are integrated into the baffle plate with a distance of $1.5d$ from the centre of the baffle to ensure smooth airflow. Two deflectors of the same dimensions ($3.5d \times 1.5d$) are oppositely oriented to each other and are fixed on each rectangular opening at a tilt angle (α). One deflector named FD1 is directed towards the tube bundle. At the same time, FD2 is directed towards the test section wall. This arrangement generates two counter-swirl flow currents between the baffles, intending to generate counter-rotational airflow within the test section, enhancing mixing and heat transfer and increasing Δp. The turbulent intensity, vortex formation and flow rotation can be manipulated by adjusting the baffle PR (0.6, 0.8, 1 and 1.2) and deflector tilt angles (30°, 40°

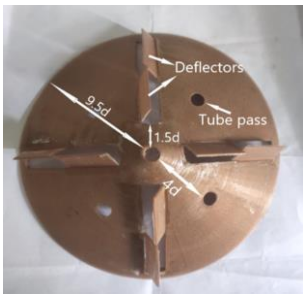


Fig. 3(a). Conical deflector baffle plate.

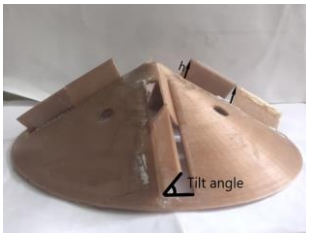


Fig. 3(b). Tilt angle.

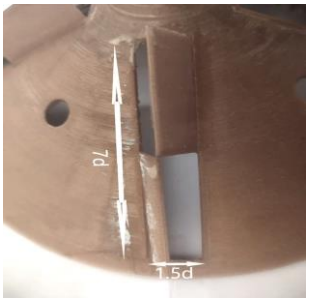


Fig. 3(c). Deflector details.

and 50°). The baffle plate is intentionally placed at the inlet to generate discontinuous swirl flow downstream and support the tube bundle.

2.3. Design parameters

The following design parameters are defined below, the pitch ratio [19,20]:

$$\mathrm{PR} = \frac{p}{D}, \tag{1}$$

and the blockage ratio [21,22]:

$$\mathrm{BR} = \frac{S}{E}, \tag{2}$$

where: $S = E$ – (4 × area of the rectangular perforation), α – deflector tilt angle.

This study focused on investigating the impact of different tilt angles on three specific configurations of counter-directional deflector profiles on CDBP. The tilt angles considered were 30°, 40° and 50°, while the duct maintained a constant blockage ratio of 0.70 and a longitudinal flow. Furthermore, the experiment was replicated by altering the PR between 0.6, 0.8, 1 and 1.2. Comparisons were made between the obtained data to analyze how the PR, α, influenced the relative j and f values, and PEC (defined as PEC = $(j/j_0)/(f/f_0)^{1/3}$).

2.4. Data aggregation

Cao's technique [31] is used to evaluate h_m:

$$h_m = Q/A_p \Delta t_{lm}, \tag{3}$$

where:

$$Q = c_p \rho v A_c \left(T_{a,out} - T_{a,in}\right), \tag{4}$$

$$v = \sqrt{2\Delta p_o/\rho}, \tag{5}$$

and Δt_{lm} is estimated as

$$\Delta t_{lm} = \frac{\left(t_{w,in} - T_{a,in}\right) - \left(t_{w,out} - T_{a,out}\right)}{\ln\left(t_{w,in} - T_{a,in}\right)/\left(t_{w,out} - T_{a,out}\right)}. \tag{6}$$

The average surface temperature of the copper tube wall is calculated by averaging the surface temperature at the inlet ($t_{w,in}$) and the outlet ($t_{w,out}$):

$$t_{w,in} = \left[\frac{\sum_1^5 T_{w,i} A_i}{A_p}\right]_{in}, \qquad t_{w,out} = \left[\frac{\sum_1^5 T_{w,i} A_i}{A_p}\right]_{out}, \tag{7}$$

where i at the inlet refers to the thermocouples 1–5, while i at the exit refers to thermocouples 6–11, A_i is the HT area of an individual tube and T_w represents individual copper tube surface temperature. The average Nu, f and j are described as:

$$\mathrm{Nu} = \frac{h_m D_h}{\lambda}, \tag{8}$$

$$f = \frac{2\Delta p D}{\rho v^2 L}, \tag{9}$$

$$j = \frac{\mathrm{Nu}}{\mathrm{RePr}^{1/3}}. \tag{10}$$

From Eqs. (4) and (6):

$$h_{c,m} = \frac{c_p \rho v A_c \left(T_{a,out} - T_{a,in}\right)}{A_p \Delta t_{lm}}. \tag{11}$$

Dimensionless factors like (j/j_0), (f/f_0) and PEC were used, where f_0 and j_0 serve as benchmarks and represent the test section without CDBP [22,23].

3. Results and discussion

3.1. Heat transfer augmentation

Figure 4 displays the relative Coburns factor (j/j_0) for three different deflector tilt angles (α = 30°, 40° and 50°), investigated at varying Re and pitch ratios (PR). The j/j_0 values for CDBP first reduce with the rise in Re and then increase with the increasing Reynolds number until reaching a peak value, after which they decrease. A similar pattern is observed for all other α. Notably, CDBP with a smaller inclination angle (α = 30°) exhibits the highest relative j/j_0 values among the different inclination angles.

At a smaller inclination angle, the velocity of air entering the duct increases. This increase in velocity corresponds to higher eddy energy, which refers to the energy associated with random fluid motions. The presence of eddies generates convective cells on the tube surfaces, promoting faster heat transportation compared to laminar flow conditions. Moreover, eddies increase the effective surface area near the tube walls, enhancing heat transfer.

The narrowing passage of the airflow caused by the smaller α of the deflectors results in an inclined jet flow and swirl flow upon entering the test section. This swirling motion disrupts the boundary layer formation and improves heat transfer. It also enhances the flushing ability of the fluid on the duct side. However, at higher Reynolds numbers, the increased velocity can reduce residence time near the heat transfer surface, limiting effective heat exchange.

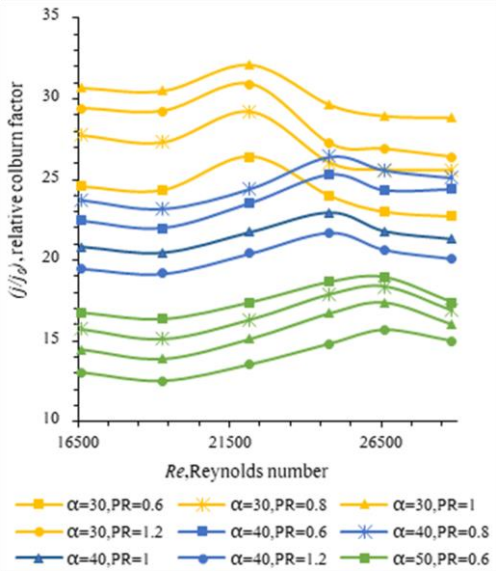


Fig. 4. Fluctuation in j/j_0 with Re.

Additionally, the flow may become highly turbulent, resulting in a thicker inertial sublayer that acts as a thermal resistance. Moreover, flow separation and recirculation zones can occur, creating quasi-stagnant regions that hinder heat transportation and reduce heat transfer performance. While it is generally assumed that higher Reynolds numbers lead to higher heat transfer rates, in these cases, factors such as reduced residence time, turbulence, flow separation and recirculation can actually decrease the heat transfer with the increasing Reynolds number. The optimized Reynolds number and pitch ratio for efficient heat transfer can be found in Fig. 5.

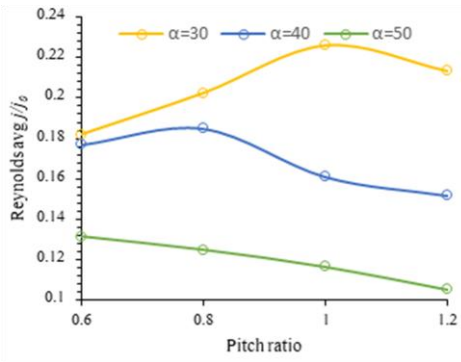


Fig. 5. Reynolds number averaged j/j_0 vs. PR.

The research conducted by Wang et al. [32] emphasized the significance of PR in relation to heat transfer enhancement. The study revealed that the downstream vortex flow increases as the spacing between down-wash baffle plates decreases. However, if the spacing is too small, the interaction between vortex flows becomes strong, resulting in vortex break-up and diminishing the heat transfer enhancement. On the other hand, larger spacing causes rapid separation of vortex flow from the boundary layer, leading to high-pressure losses. Consequently, it is crucial to determine an appropriate PR to optimize the heat transfer.

Figure 4 also demonstrates the relative j/j_0 based on the pitch ratio PR for different Reynolds numbers ranging from 16 600 to 28 800 at tilt angles (α) of 30°, 40° and 60°. The heat transfer performance peaks at a specific PR value for each tilt angle are shifted towards lower PR values as α increases. To further understand the impact of PR and α, the averaged values of relative j/j_0 are plotted in Fig. 6. The plot illustrates that the relative j/j_0 value varies with PR at each α, and the maximum j/j_0 represents the optimum combination of PR and α. Figure 6 guides determining the optimum combination, showing that decreasing α and increasing PR results in a higher heat transfer. Additionally, by referring to Fig. 6, it can be observed that a PR value of 0.6 and α of 50° yield the lowest heat transfer, while a PR value of 1 and α of 30° result in higher heat transfer.

3.2. Friction factor and thermo-fluid performance

The combination of two oppositely oriented deflectors creates counter-swirl flow, which constantly washes the tube bundle and test section wall, creating a larger air-surface interaction area, and hence a higher frictional loss. Figure 7 presents a graphical representation of the friction factor ratio (f/f_o) as a function of Re at different PRs. From a heat transfer perspective, it is evident that higher friction over the surface leads to increased heat transfer. However, this can also result in a rise in pressure drop due to friction. The f/f_o values exhibit a wide range for all PR at various α of the deflector.

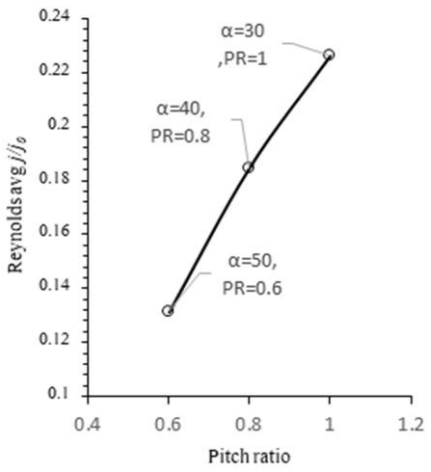


Fig. 6. Maximum Reynolds number averaged j/j_o values for different α.

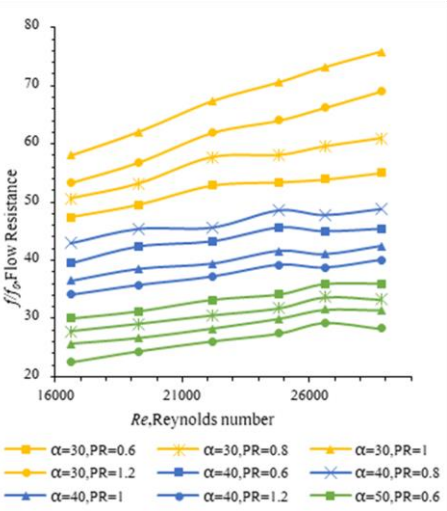


Fig. 7. Effect of Re on flow resistance (f/f_o)

The f/f_o values increase with Re, and the rate of increase remains consistent across all PRs. This indicates that the rise in friction from the entrance to the duct's exit follows a constant trend. The highest f/f_o value is observed at α = 30° but consistently decreases with increasing α.

To provide a more generalized observation, the Reynolds averaged f/f_0 values are plotted against PR for different α in Fig. 8. The trend in the graph is similar to that of Fig. 5, suggesting that a higher heat transfer leads to a higher frictional loss. The lowest recorded relative frictional loss is at PR = 0.6 for α = 30°. The maximum j/j_0 and minimum f/f_0 are tabulated in Table 3. Further, the minimum Reynolds number averaged f/f_o values obtained for different PRs are shown in Fig. 9.

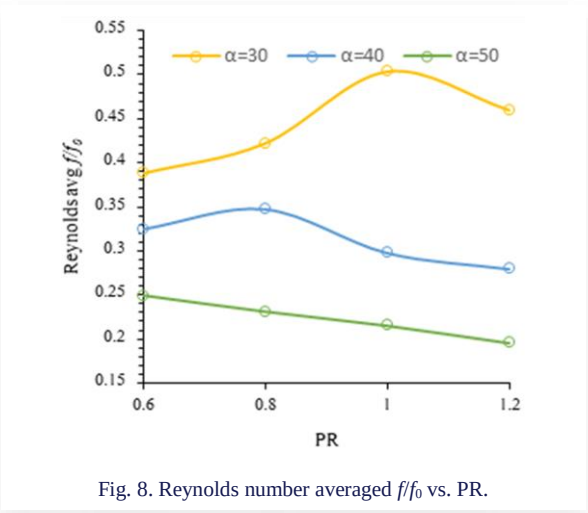


Fig. 8. Reynolds number averaged f/f_0 vs. PR.

Table 3. Maximum and mimimum value of relative j and f.

α	j/j_0		f/f_0	
	PR	Max value	PR	Min value
30°	1	0.503	0.6	0.38
40°	0.8	0.347	1.2	0.27
50°	0.6	0.24	1.2	0.19

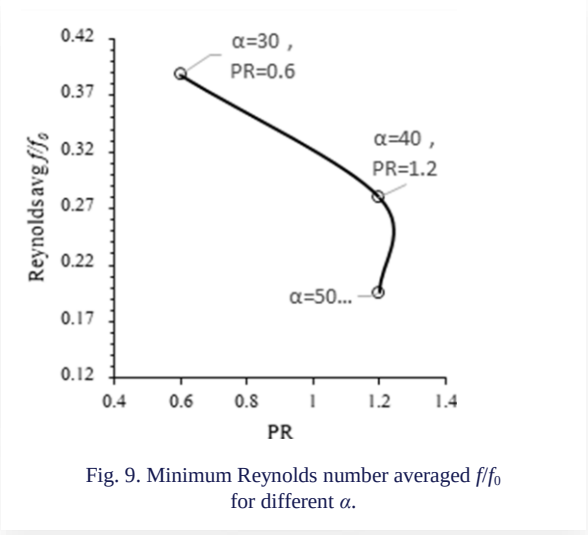


Fig. 9. Minimum Reynolds number averaged f/f_0 for different α.

The pressure drop of air flow between the entrance and exit of the duct is heavily influenced by the arrangement of baffle plates, the deflectors' tilt angle and the baffles' pitch ratios. To provide a visual representation of this relationship, Fig. 10 displays the plotted pressure drop values against different air volume flow rates. The figure clearly demonstrates that as the volume flow rate of air through the duct increases, the pressure drop also increases. Additionally, the slope of the pressure drop curve becomes steeper with higher pitch ratios. The figure also reveals that the slope of the pressure drop is most prominent at higher PRs, and it decreases as α increases. Another noteworthy observation is that the pressure drop is higher at a low inclination angle of the deflector (α = 30°), but it decreases as the inclination of the deflectors increases.

In Fig. 11, for a given Re range, the tilt angle of 30° gives the maximum PEC at PRs larger than 1, compared to larger angles. Smaller angles yield a higher heat transfer ability with comparatively low friction losses at larger PRs. A maximum of a 0.28 times increment in PEC is recorded using CDBP at α = 30° and PR = 1.

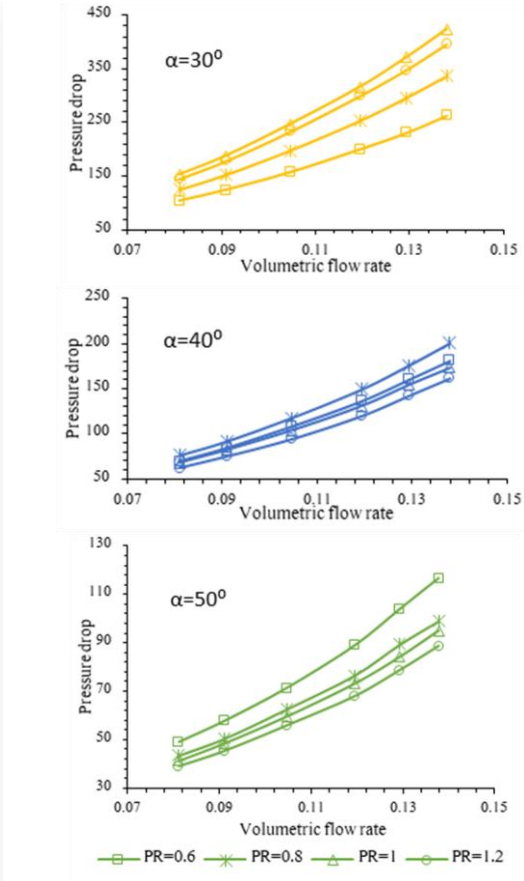


Fig. 10. Pressure drops for different α.

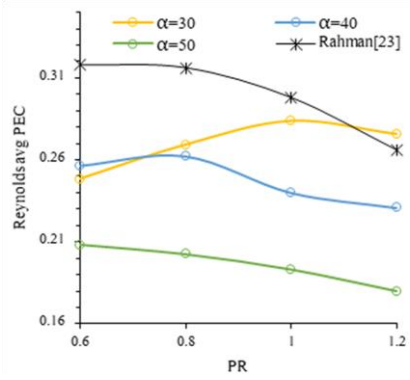


Fig. 11. Averaged PEC-value comparison.

Further comparison with the available literature on CDBP with a single deflector shows that employing an opposite-oriented deflector leads to an average decrement of 10% in PEC due to the relatively higher friction.

4. Conclusions

Upon comparing conical deflector baffle plate (CDBP) samples, it is noted that:

1. For the given Re range, the maximum average relative Colburn factor reduces with an increase in α, with maximum (j/j_0) value obtained at a lower α and then diminishes with the rise in α.
2. Re at which the maximum (j/j_0) is attained increases with an increase in the α value from 22 200 for $\alpha = 30°$ to 26 000 for $\alpha = 50°$.
3. The optimum PR to maximize j reduces with a rise in α from 1 for $\alpha = 30^o$ to 0.6 for $\alpha = 50^o$.
4. The flow resistance increases with an increase in Re.
5. The average PEC value achieves its maximum of 0.28 at $\alpha = 30°$ at PR = 1, and declines with the rise in α.

References

[1] Bergles, A. E., & Webb, R. L. (1985). Guide to the literature on convection heat transfer augmentation. *Advances in Enhanced Heat Transfer*, 43, 81–89.

[2] Shelare, S.D., Aglawe, K.R., & Belkhode, P. . (2022). A review on twisted tape inserts for enhancing the heat transfer. *Materials Today Proceedings*, 54, 560–565. doi: 10.1016/j.matpr.2021.09.012

[3] Poonpakdee, P., Samutpraphut, B., Thianpong, C., Chokphoemphun, S., Eiamsa-ard, S., Maruyama, N., & Hirota, M. (2022). Heat Transfer Intensification in a Heat Exchanger by Means of Twisted Tapes in Rib and Sawtooth Forms. *Energies*, 15, 8855. doi: 10.3390/en15238855

[4] Abed, N., & Afgan, I. (2020). An extensive review of various technologies for enhancing the thermal and optical performances of parabolic trough collectors. *International Journal of Energy Research*, 44, 5117–5164. doi: 10.1002/er.5271

[5] Dong, Z., Liu, P., Xiao, H., Liu, Z., & Liu, W. (2021). A study on heat transfer enhancement for solar air heaters with ripple surface. *Renewable Energy*, 172, 477–487. doi: 10.1016/j.renene.2021.03.042

[6] Barzegar, A., & Vahid, J.D. (2019). Numerical study on heat transfer enhancement and flow characteristics of double pipe heat exchanger fitted with rectangular cut twisted tape. *Heat and Mass Transfer*, 55, 3455–3472. doi: 10.1007/s00231-019-02667-1

[7] Nanan, K., Thianpong, C., Pimsarn, M., Chuwattanakul, V., & Eiamsa-ard, S. (2017). Flow and thermal mechanisms in a heat exchanger tube inserted with twisted cross-baffle turbulators. *Applied Thermal Engineering*, 114, 130–147. doi: 10.1016/j.applthermaleng.2016.11.153

[8] Yaningsih, I., Wijayanta, A. T., Miyazaki, T., & Koyama, S. (2018). Thermal hydraulic characteristics of turbulent single-phase flow in an enhanced tube using louvered strip insert with various slant angles. *International Journal of Thermal Sciences*, 134, 355–362. doi: 10.1016/j.ijthermalsci.2018.08.025

[9] Bartwal, A., Gautam, A., Kumar, M., Mangrulkar, C. K., & Chamoli, S. (2018). Thermal performance intensification of a circular heat exchanger tube integrated with compound circular ring–metal wire net inserts. *Chemical Engineering and Processing: Process Intensification*, 124, 50–70. doi: 10.1016/j.cep.2017.12.002

[10] Ibrahim, M.M., Essa, M.A., & Mostafa, N.H. (2019). A computational study of heat transfer analysis for a circular tube with conical ring turbulators. *International Journal of Thermal Sciences*, 137, 138–160. doi: 10.1016/j.ijthermalsci.2018.10.028

[11] Nalavade, S.P., Prabhune, C.L., & Sane, N.K. (2019). Effect of novel flow divider type turbulators on fluid flow and heat transfer. *Thermal Science and Engineering Progress*, 9, 322–331. doi: 10.1016/j.tsep.2018.12.004

[12] Hassan, J. H., & Hameed, V. M. (2022). Evaluate the hydrothermal behavior in the heat exchanger equipped with an innovative turbulator. *South African Journal of Chemical Engineering*, 41, 182–192. doi: 10.1016/j.sajce.2022.06.003

[13] Lamlerd, B., Bubphachot, B., & Chompookham, T. (2023). Experimental investigation of heat transfer characteristics of steam generator with circular-ring turbulators. *Case Studies in Thermal Engineering*, 41, 102549. doi: 10.1016/j.csite.2022.102549

[14] Jayranaiwachira, N., Promvonge, P., Thianpong, C., Promthaisong, P., & Skullong, S. (2023). Effect of louvered curved-baffles on thermohydraulic performance in heat exchanger tube. *Case Studies in Thermal Engineering*, 42, 102717. doi: 10.1016/j.csite.2023.102717

[15] Promvonge, P., Promthaisong, P., & Skullong, S. (2022). Heat transfer augmentation in solar heat exchanger duct with louver-punched V-baffles. *Solar Energy*, 248, 103–120. doi: 10.1016/j.solener.2022.11.009

[16] Promvonge, P., & Eiamsa-ard, S. (2006). Heat transfer enhancement in a tube with combined conical-nozzle inserts and swirl generator. *Energy Conversion and Management*, 47, 2867–2882. doi: 10.1016/j.enconman.2006.03.034

[17] Samruaisin, P., Rangsan M., Thianpong, C., Chuwattanakul, V., Maruyama, N., Hirota, M., & Eiamsa-ard, S. (2023). Enhanced Heat Transfer of a Heat Exchanger Tube Installed with V-Shaped Delta-Wing Baffle Turbulators. *Energies*, 16(13), 5237. doi: 10.3390/en16135237

[18] Aydın Durmuş, A., Durmuş, A., & Esen, M. (2002). Investigation of heat transfer and pressure drop in a concentric heat exchanger with snail entrance. *Applied Thermal Engineering*, 22(3), 321–332. doi: 10.1016/S1359-4311(01)00078-3

[19] Rahman, M.A., & Dhiman, S.K. (2023). Performance evaluation of turbulent circular heat exchanger with a novel flow deflector-type baffle plate. *Journal of Engineering Research*, 100105. doi: 10.1016/j.jer.2023.100105

[20] Rahman, M.A., & Dhiman, S.K. (2023). Investigations of the turbulent thermo-fluid performance in a circular heat ex-changer with a novel flow deflector-type baffle plate. *Bulletin of the Polish Academy of Sciences Technical Sciences*, 71(4). doi: 10.24425/bpasts.2023.145939

[21] Rahman, M.A. (2024). Effectiveness of a tubular heat exchanger and a novel perforated rectangular flow-deflector type baffle plate with opposing orientation. *World Journal of Engineering*. doi: 10.1108/WJE-06-2023-0233

[22] Rahman, M.A. (2023). Experimental Investigations on Single-Phase Heat Transfer Enhancement in an Air-To-Water Heat Exchanger with Rectangular Perforated Flow Deflector Baffle Plate. *International Journal of Thermodynamics*, 26(4), 31–39. doi: 10.5541/ijot.1285385

[23] Rahman, M.A. (2023). The influence of geometrical and operational parameters on thermofluid performance of discontinuous colonial self-swirl-inducing baffle plate in a tubular heat exchanger. *Heat Transfer*, 53(2), 328-345. doi: 10.1002/htj.22956

[24] Rahman, M.A. (2023). Thermo-fluid performance comparison of an in-line perforated baffle with oppositely oriented rectangular-wing structure in turbulent heat exchanger. *International Journal of Fluid Mechanics Research*, 51(1), 15–30. doi: 10.1615/InterJFluidMechRes.2023051418

[25] Rahman, M.A. (2024). The effect of triangular shutter type flow deflector perforated baffle plate on the thermofluid performance of a heat exchanger. *Heat Transfer*, 53(2), 939–956. doi: 10.1002/htj.22981

[26] Habet, M.A., Ahmed, S.A., & Saleh, M.A. (2022). The effect of using staggered and partially tilted perforated baffles on heat transfer and flow characteristics in a rectangular channel. *International Journal of Thermal Sciences*, 174, 107422. doi: 10.1016/j.ijthermalsci.2021.107422

[27] Kumar, R., & Chandra, P. (2022). Experimental analysis to study the effect of perforated louvered strip-coiled spring insert on heat transfer performance in a double pipe heat exchanger. *Heat Transfer*, 51, 3035–056. doi: 10.1002/htj.22435

[28] Maithani, R., & Kumar, A. (2020). Effect of helical perforated twisted tape parameters on thermal and hydrodynamic performance in heat exchanger circular tube. *Heat and Mass Transfer*, 56, 507–519. doi: 10.1007/s00231-019-02716-9

[29] Veerabhadrappa B.M., Nagaraj, P.B., Lalagi, G., & Rajesh, K. (2023). Effect of triangular perforated flat cone-shaped inserts on performance of double-tube heat exchanger. *Physics of Fluids*, 35(11), 115133. doi: 10.1063/5.0169821

[30] Coleman, H. W., & Steele, W. G. (2018). *Experimentation, Validation, and Uncertainty Analysis for Engineers*. John Wiley & Sons.

[31] Cao, Y.Z. (1998). *Experimental Heat Transfer* (pp. 120–125). National Defence Industry Press, Beijing.

[32] Zhao, H., Wang, F., Wang, C., Chen, W., Yao, Z., Shi, X., & Zhong, Q. (2021). Study on the characteristics of horn-like vortices in an axial flow pump impeller under off-design conditions. *Engineering Applications of Computational Fluid Mechanics*, 15(1), 1613–1628. doi: 10.1080/19942060.2021.1985615

Co-published by
Institute of Fluid-Flow Machinery
Polish Academy of Sciences
Committee on Thermodynamics and Combustion
Polish Academy of Sciences

Copyright©2024 by the Authors under licence CC BY 4.0

http://www.imp.gda.pl/archives-of-thermodynamics/

Comparative experimental analysis of fluid flow in a concentric tube exchanger having semi hollow cylindrical macro inserts with nanofluid and base fluid

Shivasheesh Kaushik[a*], Vikas Singh Mahar[b], Satyendra Singh[c], Rahul Kshetri[d], Bhupendra Kumar[d], Jagdish Singh Mehta[e], Ashwarya Raj Paul[f], Satish Kumar[f], Samriddhi Vashisth[f], Raj Singh Pundir[f], Amit Kumar[g]

[a*]Assistant Professor, Department of Mechanical Engineering, S. C. E. Dehradun, India.
[b]Assistant Professor, Department of Electrical and Electronics Engineering, S. C. E. Dehradun, India.
[c]Professor, Department of Mechanical Engineering, B.T.K.I.T. Dwarahat, India.
[d]Assistant Professor, Department of Mechanical Engineering, Dr. A.P.J.A.K.I.T. Tanakpur, India.
[e]Assistant Professor, Department of Mechanical Engineering, Graphic Era Hill University, Bhimtal, India.
[f]Scholar, Department of Mechanical Engineering, S. C. E. Dehradun, India.
[g]Assistant Professor, Department of Mechanical Engineering, G.B.P.I.E.T., Pauri, India.
*Corresponding author email: skaushik@sce.org.in

Received: 06.07.2023; revised: 25.10.2023; accepted: 14.01.2024

Abstract

Nanofluids represent a novel category of advanced heat transfer fluids composed of nanoparticles within a size range of 1-20 nm dispersed in a base fluid such as water. Contemporary research predominantly focuses on incorporating nanoparticles like Al_2O_3 and ZnO into the water at a 0.1% volume fraction to create nanofluids. Recent investigations aim to optimize thermal performance by introducing nanoparticles into the base fluids and inducing turbulence through various macro-inserts. Key factors influencing heat exchanger efficiency enhancement include geometric parameters, thermal conductivity and volume fraction. This study endeavours to analyse the thermal and fluid flow characteristics of a proposed nanofluid, augmenting thermal transfer through computational simulations and experimental validation, achieving an error margin of 3%-5%. The impact of rectangular micro inserts, with dimensions of 4 cm in height and longitudinal spacings of 5 cm and 11.5 cm, on the heat transfer rate is examined to enhance fluid flow turbulence. Results indicate that among different geometric profiles, the insert with a spacing of 11.5 cm demonstrates superior performance, yielding higher heat transfer rates and Nusselt numbers. This research holds significant implications for various industries including thermal, power, aviation, space and automotive sectors, particularly in the utilization of concentric tube heat exchangers across diverse applications. By exploring novel geometrical and fluid domains within heat exchangers, this study unveils promising avenues for enhancing the heat transfer efficiency compared to conventional methods, highlighting the potential for further investigation into alternative materials and configurations for heat elimination enhancement.

Keywords: Longitudinal spacing; Macro insert; Fin height; Nanofluid; Orientation; Ultrasonication

Vol. 45(2024), No. 2, 205–212; doi: 10.24425/ather.2024.150866

Cite this manuscript as: Kaushik, S., Mahar, V.S., Singh, S., Kshetri, R., Kumar, B., Mehta, J.S., Paul, A.R., Kumar, S., Vashisth, S., Pundir, R.S., & Kumar, A. (2024). Comparative experimental analysis of fluid flow in concentric tube exchanger having semi hollow cylindrical macro inserts with nanofluid and base fluid. *Archives of Thermodynamics*, 45(2), 205–212.

1. Introduction

Nanofluids have admirable physio-chemical, thermal and heat transfer properties [1, 2]. Thermal performance and pressure drop in heat exchangers are examined by many researchers but specifically good thermal performance is achieved for TiO_2–H_2O nanofluids with deionised H_2O as a base fluid. For the nanoparticle concentration of w = 0.1%, 0.3% and 0.5%, the

Nomenclature

A – area of pipe, m^2
C – capacity rate, J/K
C_p – specific heat of fluid, J/(kg K)
D – diameter of pipe, m
h – heat transfer coefficient, W/(m^2 K)
H – heat transfer coefficient, W/(m^2 K)
K – thermal conductivity of fluid, W/(m K)
L – length of pipe, m
m – mass flow rate of fluid, kg/s
ΔP – differential pressure, bar
Q – heat transfer rate of fluid (*htr*), J/s
Q_{ds} – fluid discharge, lps
T – temperature, K
u – fluid velocity, m/s
U – overall heat transfer coefficient, W/(m^2 K)
V – fluid volume, m^3

Greek symbols

η – efficiency
μ – dynamic viscosity, Pa s
ρ – density, kg/m^3

Subscripts and Superscripts

cf – cold fluid
ds – discharge
f – fluid
hf – hot fluid
i, in – inner
o, out – outer
st – smooth tube
s – simulation
thpf – thermal performance factor

Abbreviations and Acronyms

CSTHE – concentric spiral tube heat exchanger
CTAB – cetyl trimethyl ammonium bromide
CTHE – concentric tube heat exchanger
GI – galvanized iron
HCHE – helical coil heat exchanger
HTC – heat transfer coefficient
LMTD – logarithmic mean temperature difference
LS – longitudinal spacing
NTU – number of transfer units
TE – tube exchanger
TPCR – tapered perforated conical ring
TPF – thermal performance factor

heat transfer rate increases by 10.8%, 13.4% and 14.8%, respectively, as compared to H_2O. On the tube side, the pressure drop increases by 51.9%, and on the shell side by 40.7% (both sides operate with nanofluids and are corrugated). Also, the number of transfer units (NTU) and effectiveness is increased [1]. Physical properties of nanofluids have been evaluated previously in the literature, these properties have two parameters (optical and geometrical). In both cases, the working fluid is H_2O; the viscosity and thermal conductivity depend on the temperature. The results predict an improvement in the Nusselt (Nu) number at the shell side by 10%, at the coil side by 0.8%. The heat transfer coefficient decreased when Nu of both sides was increased, Nu of the coil side more than twice that of the shell side Nu number. (temperature of coil 81.49–82.74°C, temperature of shell 66.65–60.95°C, Reynolds (Re) number of coil 1000–27 000, Re of shell 2000–49 000) [3], where the heat transfer performance has been analyzed for a screw pitch and nano particle mass fraction with a spiral tube. The results predicted that the Nu number increases when the screw pitch decreases and the nanoparticle mass fraction increases. The screw pitch of S = 10 cm achieved the smallest heat transfer rate but it can be improved by 49.8–62.0% with the spiral tube rotation angle β = 45° and β = 90° [4]. Experimental investigations have been performed on the heat transfer and pressure drop for Al_2O_3-H_2O nanofluids with small volume fractions such as 0.1%. The Nusselt number increased by 12.24 compared to that of distilled H_2O. While comparing the pressure drop with that of distilled H_2O, then the increasing trend was shown by the pressure drop. For the test set-up made of stainless steel and 2 wire coil inserts with a pitch ratio 2 and 3, the Nusselt number increased by 15.91 and 21.53 as compared to that of distilled H_2O. For Al_2O_3 nano particles of size 43 mm, the optimum Nu number value was 2275 [5].

Some studies focused on the effect of nano particle size on the heat transfer and pressure drop properties for the laminar forced convection in a micro channel subject to a constant heat flux. Here, aqueous nanofluids containing dispersions of Al_2O_3 and TiO_2 have been simulated using a discrete phase model (DPM) for a range of particle size between 20–200 nm. The change in hydrothermal properties of nanofluids with the diameter was better observed at a higher particle concentration. The maximum differences in the heat transfer rates and friction factors of 11% and 20% were observed within the range of particle size 20–200 nm for the particle concentration of 2% [6]. In previous studies, a two step method has been adopted to prepare $NaNO_3$–Al_2O_3 nanofluid, where the neutron activation analysis (NAA) and the modulated differential scanning calorimeter (MDSC) have been used to measure the specific heat. Results predicted that for Al_2O_3 nanoparticles dispersed in $NaNO_3$ with a 60-mole fraction or for Al_2O_3 nanoparticles dispersed in KNO_3 with a 40-mole fraction, the actual value of specific heat changes less than by 2%. The mass fraction of Al_2O_3 was 0.78%. The results conclude that an enhancement of 30.6% in mass fraction of Al_2O_3 nano particles yields an increase in specific heat value of less than 4%. During fabrication, Al_2O_3 nanoparticles lost 20% to 40% of their nominal content and their fraction expanded nominally by up to 41% [7].

The proposed paper analyses the behaviour of convective heat transfer and thermal conductivity of nanofluids (CuO–water, CuO–ethylene glycol (EG)) and (TiO_2–water, CuO–EG) in laminar and turbulent flow and it was clearly reported that the thermal conductivity rises with the concentration of nano particles and a rise in temperature. The main purpose of using nano-

fluids rather than the base fluid is the enhancement of the heat transfer rate [8]. Numerical and experimental investigations have been done to perform the heat transfer analysis of various heat exchangers, like a solar air heater based on the absorber plate [9–11], perforation based tapered hollow conical rings (THCR) [12], shell-tube type heat exchangers based on a helical coil [13–15], with diverse fluids like air, water and nanofluid [12–15], or to analyse the location of fins in LED [16]. Some researchers presented diverse properties of sensible materials [17–18], some worked on diverse sensible materials such as rock, dry clay, nylon and teflon for analysing thermal behaviour in a packed bed (PB) and used air as a medium [19–21], whereas some used flue gas as a medium for thermal storage in a packed bed [22]. Some specific properties are important for further utilization of nanofluids in various applications. A wide range of heat exchangers are used in various engineering applications for heat transfer between two or more fluids for both cooling and heating processes. Some researchers focus their attention on the pipe bend loss effects, for improvement of performance of the concentric tube heat exchanger (CTHE), and some analyse the impact of flow velocity through pipes in a conventional and protruded cyclone separator for segregation of ash from hot air [23,24].

Increasing the concentration of nano particles in the base fluid improves the heat transfer rate as reported in some literature [8,14]. Many researchers work on the performance, keeping an eye on environmental aspects [13–15], while analysing flow and heat transfer parameters of nanofluids in spiral tubes with diverse fluids like water [12–15], diverse bio-oils or bio-fuels and nanofluids [15,25] for power plant applications.

Recently, micro channels attract the researchers' attention because of their tremendous performance in a compact size for a wide range of heat transfer applications, especially for machine automation and mobile equipment. The main objective of micro-channel technology is to increase product longevity with minimum maintenance [26,27]. A recent trend in this scope is to analyse the effects of geometrical domain of the micro channels [28–29], or mini channels [30,31], and the fluid domain like nanofluid, specifically for enhanced thermal behaviour of CTHE [28–31].

The present work is based on diverse gaps in the past literature. A brief analysis of research trends in diverse exchangers, design, materials and fluids is shown in Table 1. The methodology of the present work is based on solving steady state problems of forced convection through CFD, FEM, etc. [32]. The novelty of the present work is to enhance the efficiency and performance of a flat plate collector by two diverse approaches, that is, first the installation of a new geometrical design of the heat pipe having a semi hollow cylindrical macro insert inside the copper tube of the flat plate collector, and second is the flow of a modified hybrid nanofluid.

Table 1. Research trend of tube exchanger (TE).

Author	Set-up details
Qi et.al. (2019) [2]	Researchers used only normal double-tube HE for analyzing the effect of thermal transfer with nanofluid.
Chamsa-ard et.al. (2017) [1]	Corrugated TE has been used to evaluate the impact of nanofluid on thermal behaviour.
Zhai et.al. (2019) [4]	Researchers used spiral TE with diverse geometrical parameters like pitch and orientation angle for analyzing the effect of geometry with nanofluid on thermal characteristic.
Chandrasekar et.al. (2010) [5]	Coil insert has been used to enhance the performance of CTHE and pipe exchanger with nanofluid.
Ambreen et.al. (2018) [6]	Researchers analyzed the effect of nanofluid particle size on thermo-hydraulic performance of micro channel.
Kumar et.al. (2018) [8]	Researchers used bundle TE for analyzing the effect of different nanofluid particle sizes with diverse base fluids on thermal and flow parameters.
Uniyal et.al. (2021) [12]	Auhtors used TPCR TE for enhancement of performance of circular air duct.
Kaushik et.al. (2020) [13]	Authors analyzed the flow and thermal attributes of diverse hybrid nanofluid in a spiral coil for enhancement of performance in CTHE.
Kanojia et.al. (2021) [20]	Packed bed was filled with sensible material pebbles, storing heat energy for space heating.
Shrivastav et.al. (2022) [11]	Wedge shape exchanger was used as an absorber to enhance the performance of air heaters.

2. Materials and methods

The selection of nanofluid material for the proposed research work was completely based on the literature survey [14,15]. Going through multiple research papers, the first point of consideration was what nano particles are being popularly used and why they are so popular. The most popular nano particles in terms of cost and properties were identified as Al_2O_3, ZnO and CuO, as compared to other nano particles, all shown in Table 2.

It could be noted that the CuO nanofluid shows a linear behaviour in its conductivity. While changing the size and concentration of Al_2O_3, the thermal conductivity changes non-linearly [33]. Al_2O_3 and ZnO show more diversity in their properties. The preparation of an Al_2O_3 + ZnO + H_2O nanofluid sample is based on the technique of ultrasonication, where Al_2O_3 and ZnO are mixed in water at a 0.005% volume fraction each with 0.51 ml of CTAB surfactant [14,15] through the mechanical string process. After that, a mechanical string sample is transferred to the ultrasonication tub for 6 hours of ultrasonication. The finally prepared sample is ready for the evaluation of its physio-chemical properties experimentally, through the use of a hydrometer for density measurements, and a calorimeter for thermal conductivity and specific heat measurements as shown in Table 2. The experimental values were further validated with the help of a numerical model [14,15].

In this study, the experiment on a heat pipe with macro inserts is performed in a test set-up as shown in Fig. 1. This picture presents the schematic description of the running procedure of

set-up used during experimental work. the accuracy of the measurements is attained at the level of ±0.5%. The computational analysis is carried out using the ANSYS software. Heat pipes with different spacing and orientation of semi hollow cylindrical macro inserts were used in this study. The spacing was 5.5 cm, or alternatively 11.5 cm, whereas the height of macro inserts was 4 cm. The computational geometry of the heat pipe with macro inserts was prepared using the Solidworks software as shown in Figs. 2 and 3. The temperature and velocity contours obtained during the analysis using the ANSYS software are shown in Figs. 4 and 5.

Table 2. Properties of nano material.

Nano-particles and nanofluid sample	Thermal conductivity, W/(m K)	Specific heat, J/(kg K)	Density, g/m³	Reference
Al_2O_3	40	880	3700	[1,2]
ZnO	29	544	5600	[1,2]
CuO	77	540	6800	[1,2]
SiO_2	1.39	745	2220	[1,2]
TiO_2	11.2	650	3900	[1,2]
Al_2O_3 + ZnO + H_2O	0.80831	2958.44	1370.9	-

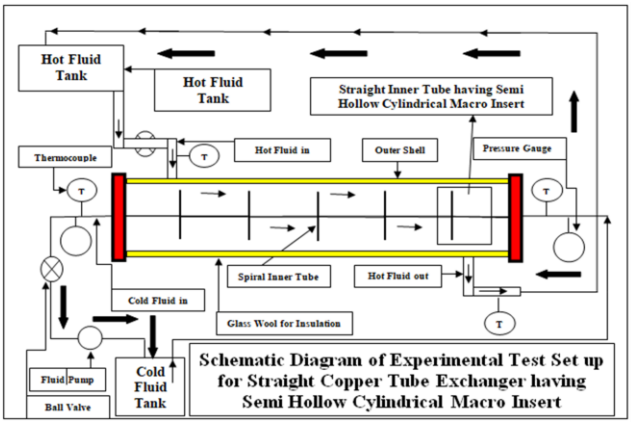


Fig. 1. Line diagram of experimental setup.

3. Grid independence procedure and testing result

Firstly, after completing all processes in the design modeller, the geometry is opened in the mesher. In the first step, a coarse mesh was generated, in subsequent steps the mesh was gradually refined. After the meshing was completed, the meshed geometry was solved in the solver. After the solution was converged, values of the essential parameters as required were obtained. The number of nodes for subsequent meshes, and the obtained corresponding values of the Nusselt number can be seen in Figs. 6 and 7.

Increasing the number of mesh nodes and repeating the computations was carried out until the solved values no longer varied with the mesh refinement. The process of grid independence investigations was terminated if the value of the crucial parameter with respect to that found for the previous mesh was less than one percent.

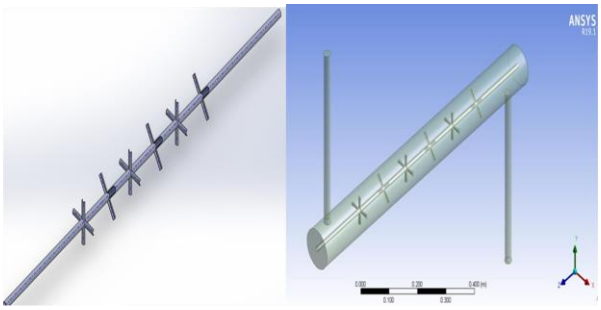


Fig. 2. Macro insert model.

Fig. 3. Computational geometric model.

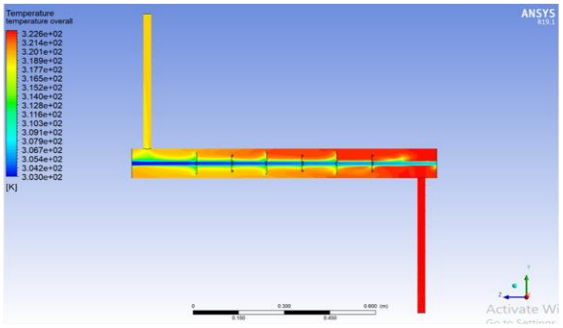


Fig. 4: Temperature distribution.

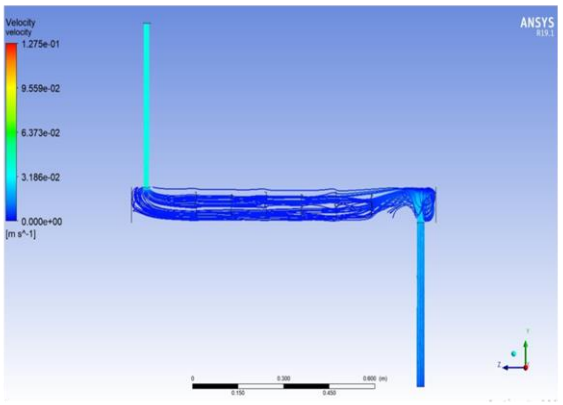


Fig. 5: Velocity contours.

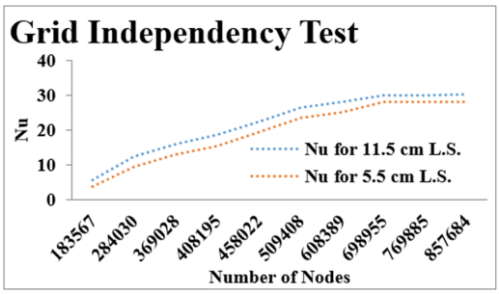


Fig. 6. Grid independence test of computational geometry.

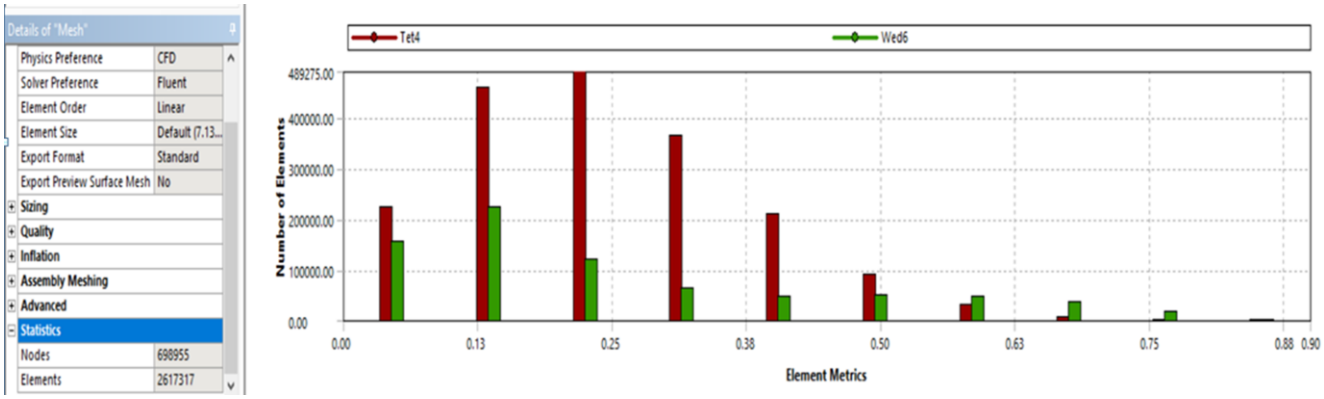


Fig. 7. Grid independence interface.

4. Data reduction

Experiments were carried out for different temperature fluids at diverse flow rates determined by the following equations

$$Q_{ds} = \frac{V}{t} \quad \text{where: } Q_{ds} = Area \cdot u, \tag{1}$$

$$m = \rho\, A\, u\,. \tag{2}$$

The heat transfer rate was obtained by the following equations:

$$Q_{hf} = m_{hf}\, C_{phf}(T_{in} - t_{out}) = Q_{cf} = m_{cf}\, C_{pcf}(T_{out} - t_{in}), \tag{3}$$

where T_{in} – outer GI shell tube inlet temperature, T_{out} – outer GI shell tube outlet temperature, t_{in} – spiral inner tube inlet temperature and t_{out} – spiral inner tube outlet temperature.

The heat transfer coefficient h and overall heat transfer coefficient U were calculated using the Log Mean Temperature Difference (LMTD) method and the equations used are as follows:

$$Q_r = h\, A\, \Delta T, \tag{4}$$

where:

$$\Delta T = \frac{(\Delta T_1 - \Delta T_2)}{\ln\left(\frac{\Delta T_1}{\Delta T_2}\right)},$$

$$\Delta T_1 = (T_{out} - T), \quad \Delta T_2 = (T - T_{out}),$$

$$U = h\, \frac{1}{\left(\frac{1}{h_i} + \frac{1}{h_o}\right)}. \tag{5}$$

Now, fluid properties for cold fluid are calculated by the following formulas:

$$\mathrm{Nu} = \frac{h\,D}{K_{cf}} = 0.023\mathrm{Re}^{0.8}\mathrm{Pr}^{0.4}, \quad \text{where: } Re = \frac{\rho u D}{\mu}, \tag{6}$$

$$f = \frac{\Delta P}{\left(\frac{L}{D}\right)\left(\frac{\rho V^2}{2}\right)}. \tag{7}$$

The performance parameters are further calculated for cold fluid flow:

$$\varepsilon = \frac{Q_{actual}}{Q_{max}}, \tag{8}$$

$$\mathrm{NTU} = \frac{U\, A_s}{(C_p)_{min}}, \tag{9}$$

where:

$$C = \left(mC_p\right)_{min}, \mathrm{NTU}_{\mathrm{counter}} = \frac{1}{c-1}\ln\left(\frac{\varepsilon - 1}{\varepsilon c - 1}\right), \tag{10}$$

$$\eta_{thpf} = \frac{\left(\frac{\mathrm{Nu}}{\mathrm{Nu}_{\mathrm{st}}}\right)}{\left(\frac{f^{0.33}}{f_{st}{}^{0.33}}\right)}, \tag{11}$$

$$\mathrm{Nu}_s = 0.023\mathrm{Re}^{0.8}\mathrm{Pr}^{0.4}, [8], \tag{12}$$

$$f_s = 0.316\mathrm{Re}^{-0.25}\,, [8]. \tag{13}$$

5. Results and discussion

In this research, fluid flow properties were investigated. The effects of nanofluid H_2O + ZnO + Al_2O_3 at 0.1% volume fraction inside a circular tube with macro inserts having LS of 11.5 cm and 5.5 cm are shown in Figs. 8–11 and 12.

Thermal behaviour of fluid was acknowledged for a range of Re number from 999 to 9 995 under counter flow conditions. Fluid flow peculiarities like the f factor and Nu number vary from 0.0992 to 0.0530 (simu. – simulated values), 0.00959 to 0.0529 (exp. – experimental values) and 11.21 to 30.33 (simu.), 10.81 to 29.75 (exp.) for 11.5 cm LS, whereas they change from 0.0998 to 0.0523 (simu.), 0.00932 to 0.0252 (exp.) and 9.86 to 23.65 (simu.), 9.49 to 23.04 (exp.) for 5.5 cm spacing. It has been clearly visible that the simulated results for the f factor show a decreasing trend and those of the Nu number show an increasing trend as the Re number and flow rate increase [14–15]. An enhancement of 3–6% in simulated values was acknowledged compared with experimental values for all profiles as shown in Figs. 8–11 and 12.

On the other hand, thermal performance peculiarities like f/fs and $\mathrm{Nu}/\mathrm{Nu}_s$ show an opposite trend compared with that of f factor and Nu number. Here, the f/f_s factor increases with a decreasing $\mathrm{Nu}/\mathrm{Nu}_s$ [14–15]. These values vary from 0.52 to 1.364 (simu.), 0.050 to 1.362 (exp.) and 0.132 to 0.051 (simu.), 0.133 to 0.421(exp.) for 11.5 cm LS, whereas they vary from 0.171 to 1.09 (simu.), 0.172 to 1.785 (exp.) and from 0.1325 to 0.0512 (simu.), 1.145 to 0.0326 (exp.) for 5.5 cm spacing. It is also

clearly visible that only Q shows an increasing trend, whereas ε, TPF and NTU show a decreasing trend as the Re number increases for 11.5 cm LS [14–15].

The thermal performance peculiarities are higher for 11.5 cm LS than for 5.5 cm spacing, where Q (*htr*) values vary from 171.55 to 269.40 (simu.), 170.59 to 268.40 (exp.) and ε varies from 0.26 to 0.171 (simu.), 0.128 to 0.126 (exp.), TPF obtained

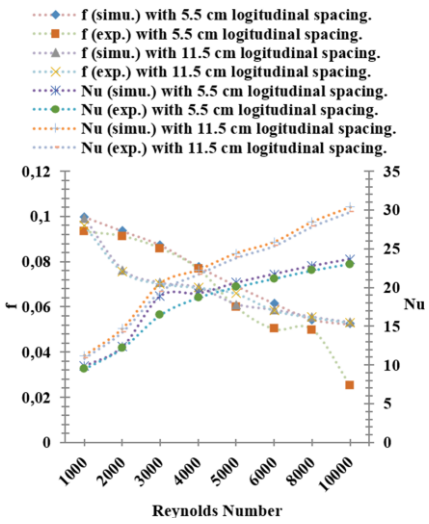


Fig. 8. Dependence of *f* and Nu on Re.

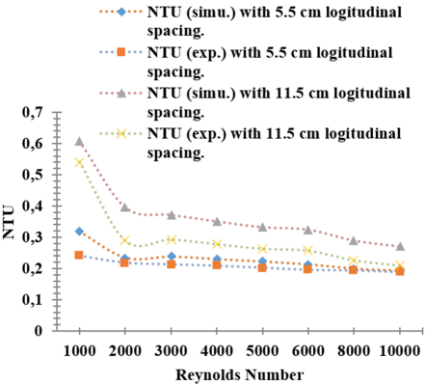


Fig. 9. Dependence of NTU on Re.

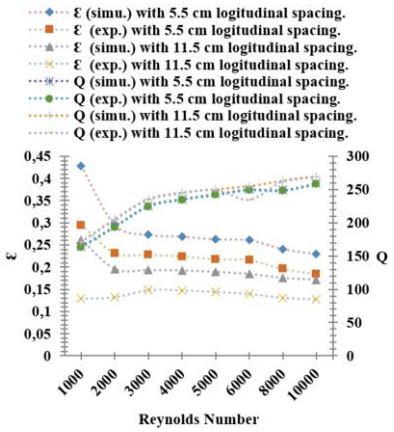


Fig. 10. Dependence of ε and Q (*htr*) on Re.

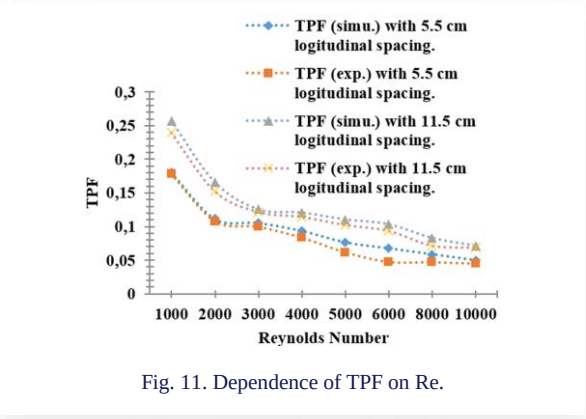


Fig. 11. Dependence of TPF on Re.

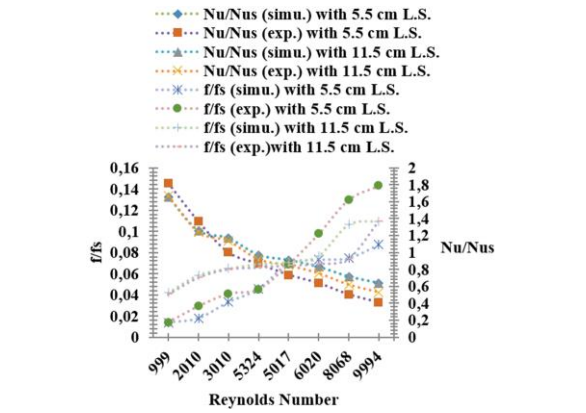


Fig. 12. Dependence of Nu/Nu_s and f/f_s on Re.

0.257 to 0.071 (simu.), 0.239 to 0.068 (exp.) and NTU 0.607 to 0.269 (simu.), 0.54 to 0.209 (exp.) for 11.5 cm spacing. TPF is an important heat exchanger parameter that has been identified to acknowledge the exchanger utilization aspect from Eq. (11). It is the ratio of a real value or a simulated value of the Nu number of the tube with insert to that of the smooth tube divided by the ratio of the f factor of the tube with insert to that of the smooth tube, expressed in a power of 0.33. The TPF values shown in Fig. 11 exhibit a decrease as the Re number rises when comparing smooth and insert-equipped tube performance, Fig.12. is utilized to indicate the performance improvement in the area. It is shown that smooth tubes perform inefficiently low at lower Re numbers and marginally well at higher Re numbers. The insert-equipped tubes exhibit much better results in both Reynolds number regions compared with smooth tubes. However, a decreasing trend of TPF values implies that the Nu ratio and f factor ratio are higher and lower in the low Re range, whereas the Nu ratio and f factor ratio are lower and higher in the high Re range between the smooth tube and insert-equipped tube, that is why TPF decreases with higher value of Re number. It has been discovered that 11.5 cm LS inserts work better than 5.5 cm LS.

6. Conclusions

Geometrical parameters, thermal conductivity and volume fraction play an important role in heat exchanger efficiency. This research focused on the thermal and fluid flow characteristics of

the proposed nanofluid. The effect of rectangular micro inserts was also acknowledged at 4 cm height and diversified longitudinal spacing, i.e. 5 cm and 11.5 cm. The present study was based on experimental and simulation investigations, leading to the following conclusions:

1. The obtained simulation results were validated with the experiment, and were found in a good agreement with experimental results with an error of 3 to 5%.
2. It was observed that semi-hollow cylindrical macro inserts produce more turbulence at 11.5 cm LS and 4 cm height with nanofluid Al_2O_3 + ZnO + H_2O when compared with other profiles. It happens because of the curved shape and extra exposed area of inserts.
3. The flow was maintained turbulent throughout the pipe with the micro inserts. The location and orientation of the micro inserts should be appropriate to get a constant production of turbulence.
4. The thermal performance rate at 11.5 cm LS increased by 20% when compared with 5.5 cm LS.
5. A 30% heat transfer enhancement was observed at 11.5 cm LS when compared with other configurations.
6. It is also concluded that nanofluid with a geometrical profile having macro-inserts at 11.5 cm longitudinal spacing shows better results as compared to other profiles at the optimum operating point, where the flow rate is 0.083 kg/s, Nu is 29.75, *f* factor is 0.052, *htr* is 268.40 J/s and ε is 0.126.

The present work has a wide scope of application in thermal engineering, power, aviation, space and automobile sectors, as these sectors use concentric tube heat exchangers in diverse applications. This work on nanofluids opens a new domain for research and various opportunities that lie in analysing different thermally feasible materials for enhancement of heat transfer. The effect of perforation in inserts will be analyzed in future for economical perspective and lowering material cost of concentric tube heat exchangers.

Acknowledgements

This research project is supported by Kumar Infratrade Pvt. Ltd. and infrastructure is provided by Shivalik College of Engineering, Dehradun.

References

[1] Chamsa-ard, W., Brundavanam, S., Fung, C., Fawcett, D., & Poinern, G. (2017). Nanofluid types their synthesis properties and incorporation in direct solar thermal collectors. A review. *Nano materials (MPDI)*, 7(6), 1–131. doi: 10.3390/nano7060131

[2] Qi, C., Luo, T., Liu, M., Fan, F., & Yan, Y. (2019). Experimental study on the flow and heat transfer characteristics of nanofluids in double-tube heat exchangers based on thermal efficiency assessment. *Energy Conversion and Management*, 197, 11187. doi: 10.1016/j.enconman.2019.111877

[3] Alimoradi, A., & Veysi, F. (2016). Prediction of heat transfer coefficient of shell and coiled tube heat exchanger. *International Journal of Thermal Science*, 107, 196–208. doi: 10.1016/j.ijthermalsci.2016.04.010

[4] Zhai, X., Qi, C., Pan, Y., Luo, Y., & Lian, L. (2019). Effect of screw pitches and rotation angles on flow and heat transfer characteristics of nanofluids in spiral tubes. *International Journal of Heat and Mass Transfer*, 130, 989–1003. doi: 10.1016/j.ijheatmasstransfer.2018.10.131

[5] Chandrasekar, M., Suresh, S., & Bose, A.C. (2010). Experimental Studies on heat transfer & friction factor characteristics of Al_2O_3/H_2O nanofluids in a circular pipe under laminar flow with wire coil insert. *Experimental Thermal and Fluid Science*, 34, 122–130. doi: 10.1016/j.expthermflusci.2009.10.001

[6] Ambreen, T., & Kim, M. (2018). Effect of variable particle sizes on hydrothermal characteristic of nanofluids in a micro channel. *International Journal of Heat and Mass Transfer*, 120, 490–498. doi: 10.1016/j.ijheatmasstransfer.2017.12.067

[7] Schuller, M., Show, Q., & Lalk, T. (2015). Experimental investigation of the specific heat of a nitrate – alumina nanofluid for solar thermal energy storage systems. *International Journal of Thermal Science*, 91, 142–145. doi: 10.1016/j.ijthermalsci.2015.01.012

[8] Kumar, N., Sonawane, S.S., & Sonawane, S.S. (2018). Experimental study of thermal conductivity, heat transfer and friction factor of Al_2O_3 based nanofluid. *International Communications in Heat and Mass Transfer*, 90, 1–10. doi: 10.1016/j.icheatmasstransfer.2017.10.001

[9] Kaushik, S., & Singh, S. (2019). Analysis on heat transmission and fluid flow attributes in solar air accumulator passage with diverse faux jaggedness silhouettes on absorber panel. *International Journal of Engineering and Advanced Technology*, 8, 32–41. doi: 10.35940/ijeat.E1011.0785S319

[10] Kaushik, S., Panwar, K., & Vashisth, S. (2022). Investigating the Thermionic Effect of Broken Perforated Curved Ribs on Solar Preheater through CFD Simulation. *Res Militaris*, 12(5). 1508-1524. https://resmilitaris.net/index.php/resmilitaris/article/view/2286/2139

[11] Abulkhair, H., Alsaiari, A.O., Ahmed, I, Almatrafi, E., Madhukeshwara, N., & Sreenivasa, B.R., (2023). Heat transfer and airflow friction in solar air heaters: A comprehensive computational and experimental investigation with wire-roughened absorber plate, Case Studies in Thermal Engineering, 48, 103148. doi: 10.1016/j.csite.2023.103148

[12] Uniyal, V., Kumar, J., S., Kaushik, S., & Kanojia, N. (2021). CFD Investigation of transfer of the heat and turbulent flow in circular copper tube with perforated conical rings of aluminium material. *Materials Today: Proceeding*, 46(15), 6719–6725. doi: 10.1016/j.matpr.2021.04.217

[13] Kaushik, S., Singh, S., Kanojia, N., Rawat, K., & Panwar, K. (2020). Comparative Study for Thermal and Fluid Flow Peculiarities in Cascading Spiral Inner Tube Heat Exchanger with or without Diverse Inserts over Spiral Tube. *IOP Conference Series: Materials Science and Engineering*, 802. doi: 10.1088/1757-899X/802/1/012009

[14] Kaushik, S., Singh, S., & Panwar, K. (2021). Comparative analysis of thermal and fluid flow behavior of diverse nanofluid using Al2O3, ZnO, CuO nanomaterials in concentric spiral tube heat exchanger. *Materials Today: Proceedings*, 46(15), 6625–6630. doi: 10.1016/j.matpr.2021.04.100

[15] Kaushik, S., Singh, S., & Panwar, K. (2022). Experimental Study of Fluid Flow Properties in Spiral Tube Heat Exchanger with Varying Insert Shape over Spiral Tube Profile. *Materials Today*. Proceeding Elsevier. 80(1), 78–84. doi: 10.1016/j.matpr.2022.10.117

[16] Kaushik, S., Singh, S., Kanojia, N., Naudiyal, R., Kshetri, R., Paul, A.R., Kumari, R., Kumar, A., & Kumar, S. (2021). Effect of introducing a varying number of fins over LED light bulb on

thermal behavior. *Materials Today: Proceeding*, 46(19), 9794–9799. doi: 10.1016/j.matpr.2020.10.876

[17] Kanojia, N., Kaushik, S., Singh, M., & Sha, M.K. (2021). A Comprehensive Review on Packed Bed Thermal Energy Storage System. In *Lecture Notes in Mechanical Engineering*, 1, 165–174. Springer Nature Singapore. doi: 10.1007/978-981-16-0942-8

[18] Yang, X., & Cai, Z., (2019). An analysis of a packed bed thermal energy storage system using sensible heat and phase change materials, International Journal of Heat and Mass Transfer, 144, 118651. doi: 10.1016/j.ijheatmasstransfer.2019.118651

[19] Kaushik, S., Panwar, K., & Karki, S.S. (2022). Comparative Thermal Analysis and Characteristic Optimization of Cram Bed Regenerator for Space Warmth Applications in Mountainous Areas. *Res Militaris* (resmilitaris.net), 12(5), 1525-1539. https://resmilitaris.net/index.php/resmilitaris/article/view/2287/2140

[20] Kanojia, N., Kaushik, S., Panwar, K., Kshetri, K., Uniyal, V., & Singh, M. (2021). Experimental investigation of optimum charging and discharging time on packed bed heat regenerator for space heating and solar drying application. *Materials Today: Proceedings*, 46(15), 6712–6718. doi: 10.1016/j.matpr.2021.04.210

[21] Elouali, A., Kousksou, T., Rhafiki, T., E., Hamdaoui, S., Mahdaoui, M., Allouhi, A., & Zeraouli, Y., (2019). Physical models for packed bed: Sensible heat storage systems, Journal of Energy Storage, 23, 69-78. doi: 10.1016/j.est.2019.03.004

[22] Panwar, K., & Kaushik, S. (2022). Investigation of Thermo-Mechanical Properties of Flue Gases Using CFD in Thermal Regenerator. *Res Militaris* (resmilitaris.net), 12(5), 1366-1376. https://resmilitaris.net/index.php/resmilitaris/article/view/2271/2124

[23] Sati, V., Kaushik, S., Kshetri, R., Panwar, K., & Pandey, R. (2020). Comparison of a Classical Cyclone Separator and Protruding Surface Cyclone Separator using CFD Software. *IOP Conference Series: Materials Science and Engineering*, 802, *2nd International Conference on Futuristic Trends in Materials and Manufacturing 2019*, 8-9th November 2019, Greater Noida, India. doi: 10.1088/ 1757-899X/802/1/012008

[24] Sati, V., Kaushik, S., Singh, S., Kshetri, R., & Pandey, R. (2019). Reduction of Losses in 90 Degree Pipe Bends by Varying Design Parameters using CFD Software, *International Journal of Engineering and Advanced Technology*, 8, 78–87. doi: 10.35940/ijeat.E1022.0785S319

[25] Kaushik, S., Sati, V., Kanojia, N., Mehra, K.S., Malkani, H., Pant, H., Gupta, H., Singh, A.P., Kumar, A., Paul, A.R., & Kumari, R. (2021). Bio-Diesel a Substitution for Conventional Diesel Fuel: A Comprehensive Review. In *Lecture Notes in Mechanical Engineering*, 1, 113–122. Springer Nature Singapore. doi: 10.1007/978-981-16-0942-8

[26] Kaushik, S., Pandey, R., & Singh, A. (2023). Industrial Automation System and its effect on the position of laborers and their consciousness. *Journal for ReAttach Therapy and Developmental Diversities*, 6(2s), 159–163. https://jrtdd.com/index.php/journal/article/view/276/212

[27] Kaushik, S., Singh, A., & Kumar, G. (2022). A Comprehensive Study on the Utilization of the Energy Using Mobile Solutions. *Res Militaris* (resmilitaris.net). 12(5), 1487–1497. https://resmilitaris.net/index.php/resmilitaris/article/view/2284/2137

[28] Kaushik, S., Ali, S., Kanojia, N., Uniyal, V., Verma, A.K., Panwar, S., Uniyal, S., Goswami, S., Kindo, S., Som, D., & Yadav, N.K. (2023). Experimental and CFD analysis of fluid flow in a rectangular strip-based microchannel with nanofluid. *Materials Today: Proceedings*. doi.: 10.1016/j.matpr.2023.05.647

[29] Kaushik, S., Verma, A., K., Singh, S., Kanojia, N., Panwar, S., Uniyal, S., Goswami, S., Kindo, S., Som, D., & Yadav, N.K. (2023). Comparative Analysis of Fluid Flow Attributes in Rectangular Shape Micro Channel having External Rectangular Inserts with Hybrid Al2O3+ZnO+H2O Nano Fluid and (H2O) Base Fluid. *EVERGREEN Joint Journal of Novel Carbon Resource Sciences & Green Asia Strategy*, 10(2), 851–862. doi: 10.5109/6792839

[30] Kaushik, S., Uniyal, V., Ali, S., Kanojia, N., Verma, A.K., Joshi, S., Makhloga, M., Pargai, P., S., Sharma, S.K., Kumar, R., & Pal, S. (2023). Comparative analysis of fluid flow in a mini channel with nanofluids and base fluid. *Materials Today: Proceedings*. doi: 10.1016/j.matpr.2023.05.363

[31] Kaushik, S., Uniyal, V., Verma, A.K., Jha, A.K., Joshi, S., Makhloga, M., Pargai, P., S., Sharma, S.K., Kumar, R., & Pal, S. (2023). Comparative Experimental and CFD Analysis of Fluid Flow Attributes in Mini Channel with Hybrid CuO+ZnO+H2O Nano Fluid and (H2O) Base Fluid. *EVERGREEN Joint Journal of Novel Carbon Resource Sciences & Green Asia Strategy*, 10(1), 182–195. doi: 10.5109/6781069

[32] Mehra, K.S., Kaushik, S., Pant, G., Kandwal, S., & Singh, A.K. (2021). Finite Element Modeling and Parametric Investigation of Friction Stir Welding (FSW). *Advances in Industrial Machines and Mechanisms, Lecture Notes in Mechanical Engineering*, 1, 251–259. doi: 10.1007/978-981-16-1769-0_23

Co-published by
Institute of Fluid-Flow Machinery
Polish Academy of Sciences
Committee on Thermodynamics and Combustion
Polish Academy of Sciences

Copyright©2024 by the Authors under licence CC BY 4.0

http://www.imp.gda.pl/archives-of-thermodynamics/

Possibilities of energy storage in residential photovoltaic installations - Overview

Karol Mzyk[a*]

[a]Cracow University of Technology, Department of Energy, al. Jana Pawła II 37, 31-864 Kraków, Poland
[*]Corresponding author: karol.mzyk@doktorant.pk.edu.pl

Received: 30.05.2023 revised: 16.01.2024; accepted: 31.03.2024

Abstract

World widely, efforts of governments and industry focus on the global sustainability. Facing global warming and rapidly growing electricity demand, it is crucial to develop technologies that will allow humanity use planet resources in the most efficient way, which is possible. Energy storage systems are vast and common concepts nowadays, concerning also small residential energy systems with renewable energy sources like photovoltaic installations. This paper describes different solutions for this issue. Characteristics of mentioned methods include basic features and values, advantages and disadvantages, estimated investing (CAPEX) and operating (OPEX) costs for the investors and issues related with environment like efficiency and emissions. As researched in the document, current technologies base on well-known solutions implemented in residential installations but also there is also possibility to develop new methods and combine few of them to use any possible energy surplus, later when it is needed the most. Description of various energy storage system includes both technical and commercial aspects. As most of storage applications differ from each other, choosing proper energy storage system implies economic and environmental benefits. The review has provided sufficient information to conclude that there is no one-size-fits-all solution to store electricity. Suitable solution should be selected based on size of the installation, geographical conditions as well as economic possibilities. For examined energy storage systems there is still necessity of further research and development but overview of those presented in the article, makes it possible to deduce comparison and conclusion.

Keywords: Energy storage; Residential photovoltaic installations; Technical and commercial aspects

Vol. 45(2024), No. 2, 213–230; doi: 10.24425/ather.2024.150867

Cite this manuscript as: Mzyk, K. (2024). Possibilities of energy storage in residential photovoltaic installations – overview. *Archives of Thermodynamics*, 45(2), 213−230.

1. Introduction

The research field of electricity storage systems has significantly advanced in the last few years. However, there are still research gaps that need to be examined and improved. One of the key issues is an efficiency-cost ratio; while many storage technologies currently coexist, their efficiency and cost-effectiveness still require further development. Additionally, durability and environmental impact of energy storage systems are also aspects under constant research, as it is crucial to deeply understand a long-term durability and environmental footprint (e.g., materials used, recycling of the whole system, etc.). To investigate these topics, further experimental research is required. As the globe transitions towards cleaner energy solutions (e.g., photovoltaics, wind turbines), integration of storage systems with renewable energy installations remains quite a challenge. Nowadays, the electricity grid is filled with renewable energy sources. Most of these installations are launched in households,

creating a new role in the Energy Market – that of a prosumer. In the past, the electricity grid was very straightforward. There were two types of grid users: producers (big energy concerns and companies) and consumers. Due to this simplicity, the energy system used to be stable most of the time. Of course, there were critical situations for some electricity grids, causing blackouts on various dates, like on August 14, 2003. At 04:00 PM (during time of increased energy consumption, discussed in paragraph 3.1.), Northeastern states of the USA (Ohio, Michigan, Pennsylvania) and Southeastern parts of Canada (Ottawa, Montreal, Toronto) faced one of the biggest power grids shut down in the 2 000 s. Power shortage lasted for 2 days for most of the regions, but some of these areas lacked electricity for 4 days until systems were back to normal state. These circumstances contributed to at least 11 deaths [1]. It caused great disturbance in the US stock market and affected an enormous volume of trades and great price losses. This example shows how national energy systems impact the lives of every citizen, as well as national markets.

As mentioned before, modern energy systems are full of renewable energy sources, relying heavily on weather conditions. The higher the percentage of that kind of installation, the more unstable the grid is. In Europe, a trend can be noticed. Most countries must meet the requirement of renewable installation percentage in the whole energetic production system. In the case of Poland, the European Parliament expects that as a part of the European Union, the percentage of renewable energy production will rise to 32% by 2030 [2]. The newest reports show that by 2020 Poland has reached 16.13% [3] of this criterion (energy produced by renewable sources) according to Central Statistical Office. This score is questionable for the European Parliament because of one of the assumptions, which states that wood used to generate heat at households in furnaces and fireplaces counts as a renewable energy source. Discussion about the accuracy of this assumption is not a subject of this paper, but this decision helped to avoid penalties. On the other hand, these requirements forced the government to make progress in terms of a cleaner energy system. It can be accomplished within two independent levels. Macro scale level, which consists of the modernisation of existing power plants (mostly based on coal) by building new turbogenerator units powered by gas or other alternative fuels like RDF (Refuse-Derived Fuel). The micro-scale level is more individual, and it is based on households and small renewable energy installations. This led to many "citizen-friendly" campaigns, which allowed the building of photovoltaic installations or solar thermal collectors in many households. These programs were extremely popular and led to greater awareness of consumers and creating of prosumers – electricity grid users with possibilities to generate and consume electricity in a scale of their own demand.

Photovoltaic installation is one of the most common small systems integrated on a small scale, which is because all the campaigns help investors to fund that kind of power source. Before the law revision planned for the year 2022, refund and terms of billing allowed to achieve SPBT (Simple Payback Time) in the range of 6−7 years [4]. Updated terms of billing extended this value to about 11 years, which means that PV installation working on terms after revision will take 4–5 years more to pay back than before the revision.

These two examples of the USA electricity blackout and the Polish share of renewable energy are the main reasons why energy storage is such a critical issue in modern energy systems. An efficient energy storage system could make national grids more stable (macro-scale) and make small PV installations even more profitable for investors (micro-scale). Discussion about various methods lasts for decades, and this paper brings an analysis of one traditional and two alternative approaches. The conducted review aims to describe, confront and escalate mentioned research gaps with possible solutions, providing insights for researchers, policymakers as well as industry stakeholders. Based on the review, the identification of the best practices and implementation examples will be described. Secondly, the evaluation of opportunities and threats of each solution will be analysed. Lastly, providing some innovative solutions may be a sufficient choice after further research.

2. Review materials and methodology

The rapid growth of intermittent renewable energy sources, such as wind and solar, has led to increased interest in electrical energy storage. The research is based on a literature review of various journal articles, conference publications and chapters of books. All of the mentioned materials referred to electricity storage systems subject.

The methodology of this review includes a collection of available scientific research, articles and reports. The below steps have been taken to proceed with the paper. The first step involved the definition of what aspects of electricity storage need to be investigated in this research. To provide a comprehensive analysis, both technical and economic principles of different applications were described. Next, based on reliable scientific databases, such as Science Direct, Research Gate, and Google Scholar, a suitable bibliography has been selected and analysed. Publications have been selected based on date, subject matter, innovation, and reliability.

The review begins with an indication of electricity consumption data according to databases provided by third parties and also based on personal research data, as well as a description of Photovoltaic installations used in residential systems. With basic values of energy consumption defined, elaboration of chosen energy storage systems has been conducted, including both technical and economic advantages and disadvantages, as well as possibilities of implementation for analysed residential systems.

3. Household energy consumption and systems

Before focusing on energy storage analysis, unified starting conditions and assumptions shall be determined. A semi-detached house domiciled by a family of 4 people, with a standard power connection of 16 kW, has been selected as a basic model for this research. This means that electricity is used to power basic home appliances and induction hob. Households' energy consumption is the main factor which is required for this study. In this research, energy consumption data from several Polish households

has been used to show characteristics and crucial points of higher and lower energy demand.

3.1. Energy consumption characteristics

Figure 1 shows the average electricity demand of the studied sample household throughout the year. The maximum power (around 3 kW) is used for a brief period of time due to simultaneous usage of some of the most energy demand equipment (e.g., induction hub, dryer, electric kettle). Most of the time during the entire year, consumption is lower and caused by devices like lighting and fridges.

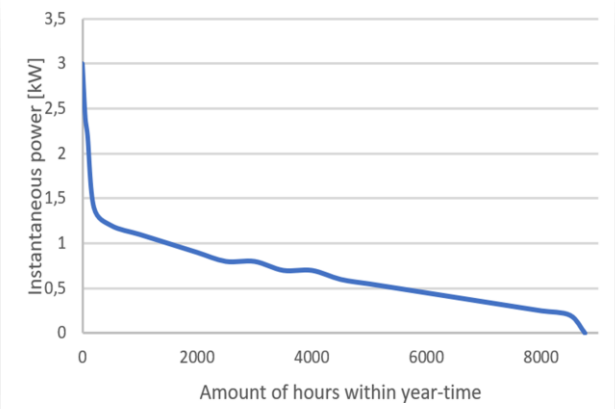


Fig. 1. Number of hours of instantaneous power demand.

Figure 2 represents the average energy daytime consumption. This characteristic is closely related to the activity of residents and their work type.

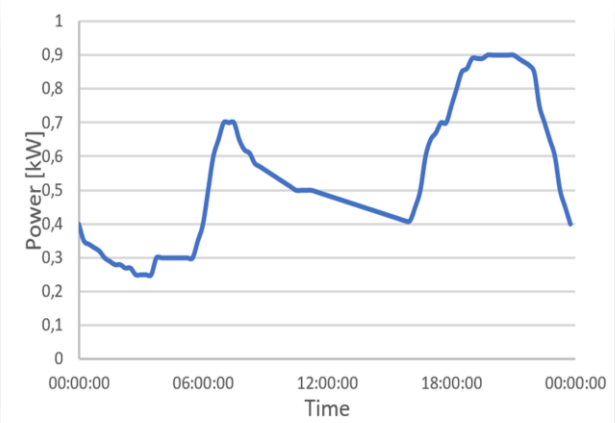


Fig. 2. Instantaneous power demand during daytime.

In the case of our example (and it is the most common example), the Fig. 2 shows us two peak points. At 06:00, energy consumption rises as residents prepare to leave for work, and after 07:30, energy demand signifyingly drops. The next peak is affiliated with work return and evening activity in households. Data from Figs. 1 and 2 allows us to estimate the average annual energy demand, which is equal to 4 500 kWh.

3.2. Photovoltaic installations used in households

This paper focuses on statistics and data from Poland (Central Statistical Office). In November 2020, photovoltaic (PV) installation power in Poland reached 3 954.96 MW [3] (Central Statistical Office, 2022). However, another 1 000.00 MW is assumed as the power of small household micro-installation [5], which indicates the total power of PV systems in Poland at the level of 4 954.96 MW. Energy production from PV installation increased from 710.67 GWh (in 2019) to 1 957.92 GWh, which shows the significant development of this energy source. According to recent studies and simulations [6], if 30% of all households in Poland have independent small PV installations (about 6 kW), analysis shows a significant reduction of maximal hourly energy demand for those households because of demand covered by PV installation, no power grid. In the case of months from April to August, this demand drops accordingly by 50, 23, 85, 68 and 19 MWh. This scenario where 30% of households own small PV installation, reduces the demand by about 50% in May and by 7% in December [6]. Considering the fact that rural households consume about 7% of total energy consumption in Poland, even though the scenario shown above will impact national energy demand, it can result in a sample standard deviation ratio at a level from 13.5% to even 20% (in December).

However, even with this scenario, there is still one major problem, which will be even more significant if the percentage of household PV installations increases above 30%. This problem is energy surplus, as an increasing amount of residential PV installations will lead to excess energy being generated on the national power grid scale. PV installations have similar conditions on vast regions that can cause major grind disturbances. The reason of this excess energy production is a fact that it is impossible to cover all of the PV energy production during the day with consumption, as it is shown in Fig. 2. Figure 3 shows how increasing number of PV installations in households (in percentages) will correspond with energy surplus production ration (energy surplus to energy produced by system).

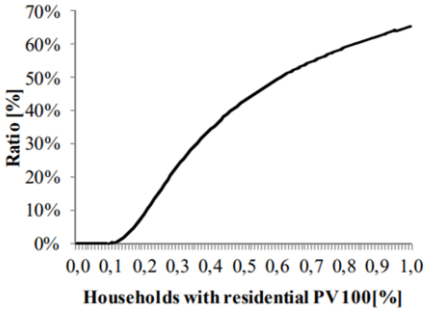


Fig. 3. Energy surplus to generated energy ratio of PV system depending on number of PV installations [7].

Considering the situation where 10% of households use PV installation to generate electricity according to Fig. 3, there is no impact on energy surplus exported to the energy system grid and examined ratio is close to 0. However, above 10% this impact rises greatly and for theoretical conditions where 100% of households use PV, ratio reaches about 70%. Therefore, 70% of

generated energy is exported to grid as a surplus. As PV installations are small and are used by 10% of households' energy surplus can be easily used and controlled by national power grid. The more of these installations are plugged to power grid, the more notable this energy surplus issue become and one of the most promising solutions for this problem seem to be energy storages.

4. Energy storage different technologies and benefits

Every single fossil fuel can be determined as an energy storage, even simple kettle filled with water has a features of energy storage. Wherever there is energy conversion to different type of energy and this energy is not consumed instantly (or where there is a process which consume energy to cover demand or lower the energy consumption at different time or place) – we can speak of energy storage. Several global factors driven interests to this prosses, two of them are: increased energy consumption each year with increasement of energy production from renewable sources of energy and lower cost and greater access to storage technologies like lithium-ion batteries. In most of the countries (also in Poland) pumped hydropower technology is a main form of storage significant amount of energy. In Poland, there are currently six primary pumped-storage power stations: Żarnowiec (716 MW), Porąbka-Żar (500 MW), Solina-Myczkowce (200 MW), Żydowo (167 MW), Niedzica (92 MW), and Dychów (90 MW) power plants. Its role in power grid is really simple and well-known from 1907 (in Switzerland). During production peaks electricity is used to pump water to upper reservoir, usually located hundreds meter above lower reservoir (also supply water source) – e.g. in Żarnowiec, the reservoirs have a level difference of 125−108 meters. During increased demand of electricity this process is reversed and whole facility works as a normal water power plant. Water flow through the pipelines in Żarnowiec during the discharge cycle can reach 700 m^3/s.

Energy storage equipment and applications are increasingly popular topic during scientific conferences and also commercial presentations. In Google Scholar 17 900 articles for phrase "energy storage" has been found in years 2000–2005. In period of 2015-2020 this number of papers changed to 75 600. These solutions play relevant part in power grid optimization by cutting peaks and filling valleys of energy demand. Storages also lowers energy surplus to generated energy ration in almost every renewable energy source (not only PV installations). Increased economic efficiency and also flexibility of small residential energy installation can be also achieved. Implementation of wide range of small, decentralized storages will require also "smart grids" solution where one centralized national power grid is replaced by many deferent smaller power grids in a local scale. Even nowadays, with such cheap costs of lithium-ion batteries (in September 2021, the cost of lithium-ion batteries was approximately in the range of 100 to 200 per kilowatt-hour ($/kWh)) there is still problem to use efficient technical solution too store greater amounts of energy or smaller (residential) amount of energy, simultaneously and without huge value of CAPEX (Capital Expenditures). To consider cost of stored energy, a few parameters need to be described. First of which is cost of maximum power output ($/W) – related with CAPEX and cost of energy produced ($/Wh) – related with OPEX (Operating Expenditures). Along these it is also crucial to consider system lifetime and recharge cycles amount determined by energy losses and material properties. Final factor describing energy storage technology is cost of maintenance and reliability, both of them can determine usage of particular technology to different sectors like national power grid, industrial power grid, residential power grid. Last but not least factor – round-trip efficiency and it is percentage of electricity put into the storage, which is later retrieved, the higher this factor is the less amount of energy is lost within storage process.

A few types of energy storages technologies can be described such as: mechanical energy storage, compressed-air energy storage, thermal energy storage, electrochemical energy storage. One of the large-scale mechanical storages was mentioned before – pumped hydropower plants. In case of this technology cost of maximum power output is estimated by 1 000.00–2 500.00 $/kW, there is no cost of energy being produced as electricity to supply pumps is cheaper than that produced during demand valley. Its round-trip efficiency factor equals 70−85% [8]. This solution has one major limit – geographical location. Such installation requires special shape of landscape to be effective enough – which means there is no place for this technology on small residential scale. Thermal storage requires about 1 250−1 500 $ per every kW of storage installed, cost of energy refund is at level of 20−30 $/kWh. Round-trip efficiency of this technology is one of the lowest – about 33% [8]. The main disadvantage is that only heat can be stored using such technology, there are no geographical requirements and present technology is well developed in that kind of systems and devices, this energy storage technology is widely used in heat water supply installations.

To use the full possibilities of variable renewable energy (VRE) sources it is crucial to develop efficient energy storage technologies. According to performed research in United Kingdom showing that implementation of energy storage system alone itself can reduce annual electrical bills by 25−35% [9], only by benefiting from electricity tariff (low prices on valleys and unaffordable prices on peaks). Moreover, when integrated with PV installation those savings can increase even to 41−74% [9], depending of course on many factors like weather conditions, electricity prices and tariffs policy regulations. The new European Union Renewable Energy Directive (2018/201) are one of the main documents in Europe that focuses on the problem of increasing renewable energy self-consumption, asking member countries to rely on energy storage installations. As electricity prices raising each year, achieving global "all-time heights" (ATH) prices at the turn of 2021 and 2022 a significant rise of energy storage interests occurred. For instance, after electricity prices raised in Germany, about 65 000 home PV-batteries [10] were installed only in 2019. Also declining price of battery systems caused vast impact on this rapid growth. Figure 4 illustrates energy produced by PV systems self-consumption in solar PV system alone and with implementation of electricity storage system based on li-ion batteries.

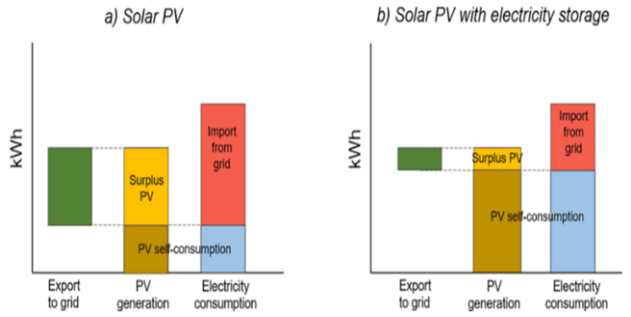


Fig. 4. Illustration of energy storage benefits in terms of PV self-consumption [9].

Also, Fig. 5 shows how different residential energy systems (with PV alone, with energy storage) affect the energy consumption curve/production curve under time of use (ToU).

To summarize all different energy storage systems, Table 1 shows comparison of different energy storage technologies in terms of: CAPEX cost [$/kW], OPEX cost [$/kWh], round-trip efficiency, charge, and discharge rates any other features, that can determine storage technology choice.

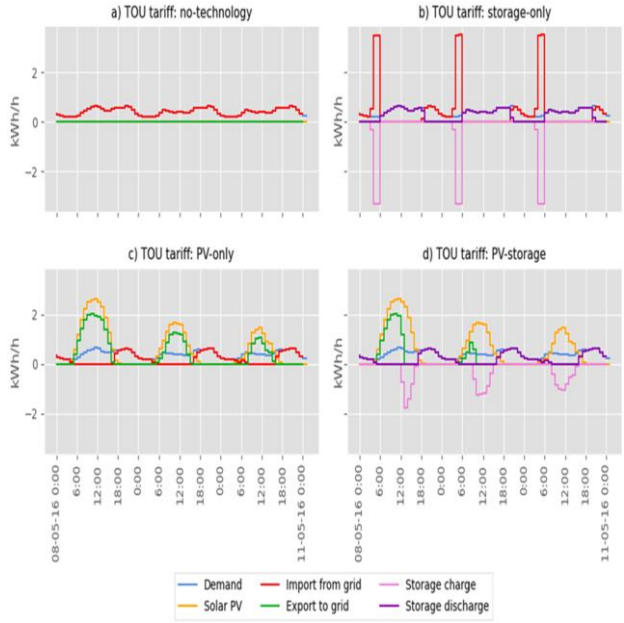


Fig. 5. Energy conversion through the day for different residential energy systems [9].

Table 1. Energy storage technologies and parameters [8].

Technology	Cost [$/kW]	Cost [$/kWh]	Round-trip efficiency [%]	Charge/Discharge rates	Cycles/product lifetime	System size	Key limitations
Pumped hydro	1 000–2 500	–	70–85	Rate specified by maximum rated power: 6–4·10^6 kW	20+ years	6–4·10^6 kW/ 10^2–10^7 kWh	Geographically limited
Compressed air	1 000–2 800	–	With natural gas: Energy ratio: 0,8; <55% efficiency. Adiabatic compression alone: 70-75%	Charging: 0.25–0.65 C Discharging: 0.04–0.5 C	20–30 years	1–110 000 kW/ 2 640 000 kWh	Geographically limited, historically dependent on natural gas
Thermal storage	1 250–1 500	20–30	33	0.05–0.33C	25–40 years	100–280 000 kW/ 1 000–1 100 000 kWh	Typically paired with concentrated solar systems
Flywheel	250–300	1 000–5 000	90–95	10–35C	20+ years	100–250 kW/ 3–25 kWh	High energy costs, self-discharge rate
Lithium-ion batteries	250–500	175–225	80–85	0.03–6C	10–20 years	1–40 000 kW / 10–120 000 kWh	Dependent on minerals
Sodium-ion batteries	250–500	250–300	90–95	0.05–0.8C	20+ years	10–50 000 kW / 20–300 000 kWh	Dependent on minerals, larger ion size (more expansion)
Vanadium flow battery	150–400	125	75–95	0.1–0.66C	20 years	5–5 000 kW/ 40-10 000 kWh	Additional system hardware, high storage material cost
Iron flow battery	150–400	7	≤70	0.16C	20+ years	10kW/60kWh	Additional system hardware, high storage material cost
ZnBr flow battery	150–400	10	65–75	0.16–0.5C	10 years	3–1 000 kW/ 50–6 000 kWh	–
Lead acid	250–500	100–300	81	0.025–2C	5–10 years	2–10 000 kW/ 7–10 500 kWh	Low energy density and specific capacity, battery useful like highly dependent on cycling behavior
Capacitors	25–50	10 000–20 000	75–95	2–720C	20+ years	28–4 000 kW/ 3.5–150 kWh	Excellent power density and cycle life but very low energy density, limit the duration of charging and discharging cycles without extreme cost

For residential usage, consumers savings form electricity storage system highly depends on evolution of the electricity and energy systems. Investor before storage system implementation should not only focus on storage capacity but also how this system fill corresponds with possible renewable energy sources. Regarding domestic circumstances and residential PV installation some of those storage technologies seem to be more suitable. For the purpose of this paper in further analysis and

research of three chosen technologies will be made: battery energy storage, hydrogen fuel cell, compressed air and hydrogen energy storage.

5. Battery energy storage

Regarding coming changes on energy market battery energy storage are more common with every year, in specific batteries based on lithium-ion technology. The main appliances of this technology include emergency power supply (UPS), current and frequency stabilization of power grid, increasing of renewable energy sources self-consumption. In present times battery (lithium-ion) energy storage market is increasing and there is prediction that in 2022 it will rise by 11%, in 2023 by 13% and by 16% in year 2024 [11].

5.1. Battery energy storage specification

Due to electrochemical processes of energy conversion, it is possible to store energy surplus generated by PV residential systems and to raise self-consumption of those installations. Growing popularity of this solutions is based on high energy density (150–500 Wh/dm^3) [11] and high efficiency (round-trip efficiency) reaching even 97% [11]. However, Li-ion batteries have high self-discharge rate at level of 8–31% [12], which results of energy leakage during time. In terms of life cycles lithium-ion batteries can withstand 1 000 to even 10 000 of cycles [11]. Table 2 introduces different batteries and their parameters in terms of energy storage.

Table 2. Battery energy storage examples based on Soltec company solutions [11].

Type and brand	Capacity [kWh]	Mass [kg]	Dimensions [mm]	Modularity
Huawei, Li-ion, LFP	5.00	51.8	670×150×600	up to 3 units
Pylontech, Li-ion, BD	3.552	35.5	296×296×450	up to 4 units (min. 2)
BYD, Li-ion, LFP	2.56	38	585×233×298	up to 15 units (min. 2)
Sofar, Li-ion, BD	2.25	30	515×480×125	up to 10 units (min. 4)

Most of energy battery storages system construction include two elements: physical batteries groups and power conversion system [13]. Group of batteries are installed in waterproof container to protects cells from weather conditions. Depending on storage capacity groups can be organized in bigger modules where each module is configured as an individual cell [14]. Along those modules there is also system that protects those call from variant circumstances like high temperature, high voltage. One of each is BMS (Battery Management System) and other TMS (Thermal Management System). They are responsible for monitoring parameters and protecting from situations mentioned in previous sentence, which can lead to battery performance and efficiency reduction. Moreover, those monitoring systems are responsible for SOC (State of Charging) control. Depending on the application, the power conversion system consist of DC/DC conversion and/or DC/AC conversion (DC - direct current, AC - alternating current). In power converter there are rectifiers and inverters along with output power filters and transformers. Figure 6 represents visual scheme of standard battery energy storage system.

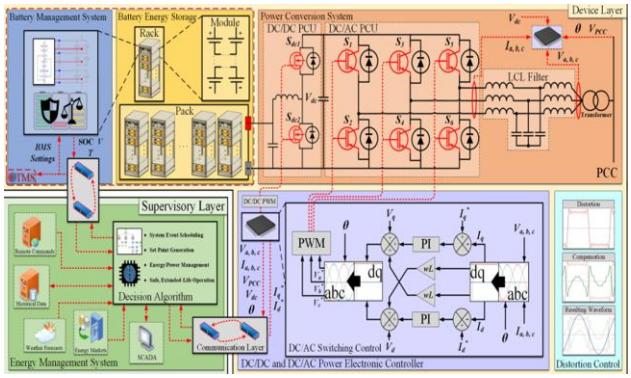


Fig. 6. Battery energy storage system elements [13].

Battery Energy Storage Systems (BESSs) shown in Fig. 6, consist of two main elements: the physical battery pack(s) and the interfacing Power Conversion System (PCS). The battery pack is typically housed in a weather-resistant container and comprises battery racks containing multiple battery modules, each with specific configurations of individual battery cells. Monitoring and protective systems are implemented to ensure battery safety and performance. The PCS includes various components, such as DC/DC and/or DC/AC, Power Conditioning Units (PCUs), DC and/or AC filters, and, for most AC systems, a step-up transformer. The complete system-level architecture of the BESS used in grid-connected Microgrids (MG) is depicted in Fig. 6. At the device layer, the battery pack is configured to achieve a certain voltage and capacity. The Battery Management System (BMS) and Thermal Management System (TMS) continuously monitor and protect the battery racks and cells from voltage, temperature, and SOC fluctuations that could affect battery performance. In the power conversion sublayer, various components like DC/DC converters, DC/AC inverters, passive LCL filters, and step-up/down transformers are employed based on the specific application. A power electronic controller integrated into the PCS handles the switching of the converter and inverter circuitry, utilizing Pulse Width Modulation (PWM) for inversion. The supervisory layer comprises an Energy Management System (EMS) that gathers data from both internal and external sources of the BESS. Internally, the BMS, TMS, and power electronic controller provide readings on temperature, voltage, current, DC link voltage, and measurements at the Point of Common Coupling (PCC). Externally, the EMS may receive information from system operators, historical data, weather forecasts, and energy markets. Based on the collected data, the EMS interprets and makes decisions by setting specific control points for conversion, BMS/TMS/PCS operation, and parameter limits. These decisions aim to optimize system performance and extend battery lifetime. Communication facilitates the exchange of information between the EMS and various components for power flow management, battery protection,

and maintenance. The continuous feedback loop allows for dynamic control during grid-tied and islanded operations, ensuring compliance with operational and performance guidelines.

Along the most popular type of battery – lithium-ion type batteries, there are several diverse types of rechargeable batteries that can be used in battery energy storage system. For instance, sodium-based batteries, flow batteries, nickel-based batteries, lead acid batteries, metal air batteries. Lithium-sulfur (Li-S) battery are lighter than Li-on batteries. Currently development of those batteries showed that they can reach density of 2 800 Wh/dm^3 [15] and this score downgrades Li-on battery in this regard. Another type of lithium iron phosphate (LFP) features in increased safety both for user and environment as they produce no waste. This kind of batteries also show successful life cycle of 2 000 cycles [16]. Lithium-air batteries have possibility to achieve 20 272 Wh/dm^3 [17]. In specific circumstances (if the oxygen supplied is not included in the calculation) this type of storage can provide density of 11 000 Wh/kg [17], which can be competitive with liquid fuels. These batteries can be found in appliances like personal electronics, electric vehicles and large-scale grid storage. Production of sodium-based batteries is cheap due to abundant natural resources of sodium salts. Sodium-sulfur (Na-S) battery features high efficiency and no self-discharge, which meant that there is no energy leakage during charged stance. However, the operating temperature for this batter in at 300°C to maintain the electrolyte in liquid state [18]. This fact crosses out this type of batteries as an energy storage system solution for residential PV installations. Flow batteries technology consists of two separated fluids with the membrane between them. They feature with flexibility in system design, good cost to capacity ratio, high efficiency fast responsiveness, long durability and reliability [19,20]. Among these group vanadium redox and zinc-bromine batteries can be found. Vanadium redox is the most promising technology of these flow batteries, which can be introduced on a commercial scale in the future. It uses same metal ions in both of electrolyte, the electrodes and membrane, this feature determines longer life [21] as cell capacity does not decrease over time. Figure 7 shows how diverse types of batteries are used in different kind of appliances, depending on storage time and power.

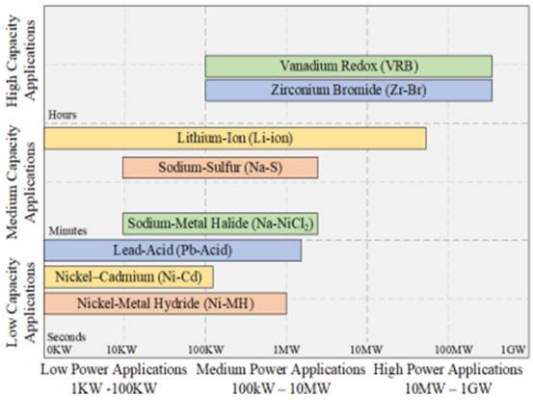


Fig. 7. Different types of batteries regarding storage time and power [13].

5.2. Battery energy storage market and benefits

Across last ten years lithium-ion batteries prices rapidly dropped down. In 2019 cost of this type of batteries was around 175–225 $/kWh [22], which was 13% less than in 2018 and even 80% than in 2012 [13]. As it is showed in this example cost of kWh reduced by almost 100% in 7 years, due to technology development and reducing manufacturing costs. According to predictions in 2025 the total cost of lithium-ion batteries can be established at level of 100 $/kWh. Among one of the most recognizable manufacturers of ESS based on lithium-ion batteries Samsung, BYD, LG, Huawei, Sofar Solar can be listed. Basing on prices of batteries, components, taxes, cost of the whole BESS working with lithium-ion batteries can be estimated and it reaches price of 535−1 095 $/kWh [13] depending on size. According to research conducted in Germany [23], the average installation for home energy storage systems in the country during 2020 consisted of 4 kW of power capacity and 8 kWh of storage capacity. However, due to a reduction in the price of these solutions and increased availability of the technology, the market for home energy storage systems experienced substantial growth. In 2019 alone, around 60 000 new units were installed, resulting in a total of approximately 185 000 units in the country [23]. Overall, these installations yield a total power capacity of 750 MW and a storage capacity of approximately 1 420 MWh. These figures are comparable to those of a medium-sized hydro-pump storage power plant, such as the Żarnowiec plant with a capacity of 716 MW. In 2019, the average price for medium-capacity storage (ranging from 5 kWh to 10 kWh) was estimated to be around 1 100 €/kWh. This cost estimation, which aligns with previous research from other references, e.g. [13], encompasses all expenses related to electronics, taxes, and installation services. We can also observe that 40% of battery home storage systems is coupled with heat pump installation and about 10% with electric car charging station [13]. According to researchers [24], BESS have enormous potential to develop and to help to create secure smart power grids, powered by renewable energy sources. Although significant progress has been made, certain crucial aspects still require improvement in BESS. Among the most vital challenges are enhancing the design of BESS DC-AC converters by incorporating advanced circuit technologies and ensuring reliable support for multiple grid services. Additionally, it is essential to develop accurate and simultaneous battery models to enhance the overall performance of BESS. Enhancing the design of BESS DC-AC converters requires advanced circuit technologies and functionalities to improve efficiency and reliability. A critical challenge is to ensure BESS can reliably provide multiple grid services simultaneously, necessitating sophisticated control strategies and energy resource management. Developing accurate real-time battery models is crucial for optimizing BESS performance, preventing overcharging, and extending battery lifespan. The potential improvements mentioned above will have a significant impact on both the economic and technological performance of battery energy storage systems. While these systems are becoming more widespread each year, certain issues remain that require resolution in order to fully optimize their capabilities.

6. Utilizing hydrogen for energy storage

Hydrogen energy storage systems are emerging as promising solutions for storing energy generated from renewable sources. These systems exhibit exceptional specific energy parameters, enabling them to store a substantial amount of energy per unit mass or volume. The high energy density of hydrogen makes it an attractive option for large-scale energy storage applications. Additionally, hydrogen storage systems boast long life cycles, meaning they can maintain their performance and capacity over an extended period, making them durable and reliable choices for energy storage needs. One of the key considerations for hydrogen energy storage systems is round-trip efficiency, which measures how efficiently the system converts electrical energy to hydrogen during charging and converts the stored hydrogen back to electricity during discharge. A high round-trip efficiency is essential to minimize energy losses and optimize the overall performance of the storage system. The cycle life of hydrogen storage systems is also crucial, as it determines the number of charge and discharge cycles the system can undergo before experiencing significant degradation. A longer cycle life ensures the system's longevity and economic viability. Safety is a paramount concern for hydrogen energy storage systems, given hydrogen's flammable nature. Rigorous safety measures must be in place for handling, storage, and transport to ensure secure operations. Cost considerations play a vital role in the widespread adoption of hydrogen storage.

The cost of production, distribution, and infrastructure for hydrogen can impact the competitiveness of this storage technology compared to other energy storage options. Scalability is an important feature of hydrogen energy storage, allowing it to be adapted to varying energy storage requirements, from small-scale applications in remote areas to large utility-scale installations. Integration with renewable energy sources is another critical parameter, as hydrogen storage can help stabilize intermittent renewable energy grids by providing a reliable energy buffer.

Finally, the environmental impact of hydrogen production and storage is essential in evaluating its sustainability. The overall carbon footprint and greenhouse gas emissions associated with hydrogen generation need to be minimized to ensure that hydrogen energy storage remains an environmentally friendly choice for the transition to cleaner and more sustainable energy systems. With ongoing research and advancements, hydrogen energy storage systems hold great promise as a key component in the future energy landscape, offering grid stability and enhanced renewable energy integration.

However, one of the barriers for customers to implement this technology to residential and industrial energy storage systems is its initial cost (CAPEX). This highly explosive gas (when mixed with oxygen) is widely used in chemical industry but with every year it increases its popularity across energetic sector. One of the types of evidence of growing hydrogen interest is number of scientific papers in Scopus database regarding hydrogen using keywords ”hydrogen energy production and storage”. In 1990 there were only 10 papers related to this issue and over 680 in 2021 [25]. Hydrogen is a common element on planet Earth; it is related to such substances like water and fossil fuels [26].

It has the highest energy density per kg of all the other known elements but has the lowest volumetric energy density among all other commonly used fuels – 0.01079 MJ/dm^3) [27]. Nowadays, over 95% of consumed hydrogen worldwide is obtained from fossil fuels like natural gas by a technique called steam reforming. This process requires the gas-steam mixture to reach a temperature between 700°C–1000°C. The process itself emits 10 kg of CO_2 into the atmosphere for every kilogram of produced H_2 [28]. Although this method makes hydrogen not as environmentally friendly and green as it seems, there are no doubts that this is the most economical way to obtain hydrogen on a larger scale. Even though the cost of the production is estimated at around 1.5 €/kg, which is three times higher than natural gas extraction [29,30].

However, there is one method that allows the receipt of clean, green hydrogen (without the emission of greenhouse gases). This process is called electrolysis, and it requires an energy supply to power the electrolyser. if this power is from renewable energy sources, we can qualify hydrogen as green and environment friendly. For example, if it is powered by a power grid which mostly relies on nuclear power, the hydrogen label is yellow – which means that this way of production is not that environmentally friendly [31] For the purpose of this paper, we will only discuss green-labelled hydrogen produced by residential PV systems.

There are several types of electrolysers mentioned before. The most common ones are: alkaline water electrolyser using an aqueous solution of sulphuric acid (H_2SO_4) [32], solid oxide electrolysers (SOE) operating at temperature above 773 K [33] and polymer electrolyte membrane usually called proton exchange membrane (PEM). This last type – PEM operates in lower temperatures than SOE, about 333–363 K [34]. There are plenty of advantages of PEM electrolyser. Its response time is almost instant, which means that the process of hydrogen production starts immediately after supplying power to the device.

Moreover, the theoretical efficiency of hydrogen production in the PEM system of 80% [35], which is high and provides a solid source of hydrogen when combined with a renewable energy source supply. This means that for every 100 units of electrical energy supplied to the PEM electrolyser, approximately 80 units of (chemical) energy stored within hydrogen gas can be generated, with the remaining energy lost as heat. The lifetime of such a system is also promising and reaches 60 000 hours; it depends mostly on membrane thinning [36]. An innovative electrolyser technology is in the works, aiming to achieve an energy consumption rate of 50 kWh per 1 kg of hydrogen (H_2) produced at the plant level within the next few years. To produce 1 kg of H_2, approximately 10 dm^3 of water is required. Furthermore, during this hydrogen production process, around 8 kg of oxygen (O_2) is generated per kg of hydrogen, along with approximately 10 kWh of potential heat per kg of hydrogen. Thanks to the possible modular design of the PEM system, it can be easily implemented in residential power supply systems. A detailed description of electrolysers can be found in paragraph 6.1.

As hydrogen can be generated from PEM supplied by the energy surplus of PV installations, there is the next step to use this green element as an efficient energy storage system and to

store hydrogen itself. There are several methods to store hydrogen, and it can be in gas or liquid. Every solution differs in volume, pressure, and duration of the stored medium. There are also a few ways to store hydrogen as a gas. It can be achieved using tanks, cylinders, or natural underground caverns. Because the energy density of this gas is low, it is crucial to compress it into pressure above 700 bar.

The process of raising hydrogen pressure also requires vast amounts of energy. To compress hydrogen from 1 bar to 200 bar, there is a need to deliver about 7% of the energetic value of compressed hydrogen itself and even 10% to go up to 700 bar [37,38]. This means that the storage process itself immediately consumes 10% of the energy stored in this gas only during compression. Storing in huge underground caverns (e.g. abandoned mine shafts) allows for a reduction in investment costs (lower CAPEX expenses) and storage of abundant volume under even higher than seven hundred bar pressure.

Until 2016 there were about 672 underground gas storages worldwide, mostly for natural gas, which contain altogether about 424 billion cubic meters of gases [25]. However, an underground storage system has its geological limits. Because of its scale, it cannot be used as a residential solution. Storing hydrogen in cylinders and tanks in a compressed gas state provides a density of the substance at a level of 7–30 kg/m^3 – depending on compression pressure [39]. To increase this density, hydrogen can be stored in a liquid state to achieve a density of 70 kg/m^3. However, to change the state of gas to a liquid, the temperature must drop to –253°C [40], which requires a constant and high amount of energy to be supplied, as well as a high-tech vacuum-insulated tank. This method is not suitable for prolonged periods of storage because of the gradual decrease of the hydrogen volume stored inside the tank due to the boil-off effect [41]. The last of the hydrogen states that can be used in the storage process is the solid state. It can also be a hybrid or material-based method because it creates new substances due to the reaction of hydrogen and metal that results in the creation of metal hydrides [42].

Those substances enable to store hydrogen at high density due to extraordinarily strong bonds between metal and hydrogen atoms. Another advantage is the safety of that method of storage, due to storage in stable substances without the requirement of high pressure or low temperature during the entire process of storage. However, some of the metal hydrides still require these. Those parameters are required only during the phase of joining and splitting metal and hydrogen atoms. So-called reversibility is one of the key factors in choosing the proper metal-hydrogen combination substance, which means how strong bonds between atoms can be achieved and how much energy and time is required to change it back to separate metal and hydrogen, which can be used in further energy production. These days, one of the most promising metals to form metal hydrides is magnesium, which has been proven to have a low cost of usage and high reversibility [46].

Fig. 8 represents different methods of hydrogen storage systems and density.

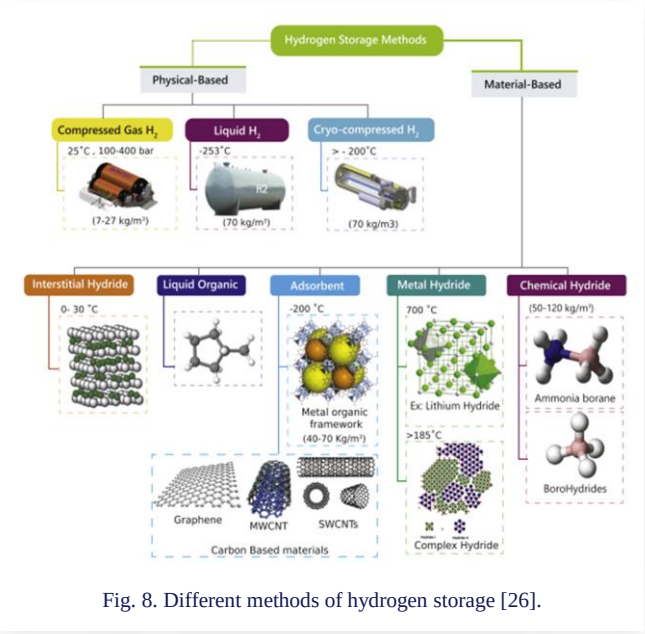


Fig. 8. Different methods of hydrogen storage [26].

6.1. Electrolysers and fuel cells

Hydrogen's energy is 140 MJ/kg, which is much higher than fossil fuels [43] The energy density of fossil fuels is as follows: anthracite coal – about 25–35 MJ/kg, lignite coal – about 10–25 MJ/kg, and natural gas 48−55 (MJ/kg). Many researchers seek the solution for future energetic crisis in this element.

Nowadays, global hydrogen production is estimated at around five hundred billion cubic meters [44]. However, the produced hydrogen is not used in electricity production. It is used especially in industries like the gas and crude oil sector, agriculture fertilizers industry, metal refining industry and others. Only a small amount of that hydrogen is used in fuel cells to generate electricity.

As mentioned before, hydrogen is often described as a green energy source which will replace fossil fuels in the future; however, over 96% of hydrogen is being produced by non-renewable processes, like steam methane reforming (SMR) [45]. In this technique, methane produced from natural gas is used. Gas is heated with steam (and with catalyst), in this mixture of carbon monoxide and hydrogen is produced. To really qualify hydrogen as an eco-friendly fuel (green hydrogen), it must be generated with the use of renewable energy.

These days, special attention has been given to the process of electrochemical splitting of water – electrolysis, powered by renewable energy sources. Taking into consideration residential installations, photovoltaics can be a perfect source of energy for electrolysis. Every decomposition of water in this process can be described by two separate processes (two half-cell reactions) taking place on an electrode with an energy supply. The first reaction is called the hydrogen evolution reaction (HER), and the second is the oxygen evolution reaction (OER). To perform these two reactions, electrocatalysts, made of precious metals like Au, Pt, Ag, etc., must be used in the electrolyser, making this method expensive regarding investment costs (CAPEX). The cost of an alkaline water electrolyser (AWE) is 500−1 000 USD/kW, and the lifetime of the system is 90 000 h. The production cost of a PEM electrolyser is 700–1 400 USD/kW [48]. In the next paragraph, three of the main electrolysis methods will be described in detail.

Alkaline water electrolysis is the most developed electrolysis methos known present days. It was invented in the year 1789 by two scientists, Troostwijk and Diemann [49]. This method can generate hydrogen at an operating temperature of 40−90°C. Substances like NaOH or KOH are used in AWE as electrolytic solutions with concertation range of 20−30% [50].

To separate two electrodes from each other, a special membrane made of asbestos is implemented to prevent the mixing of gas products. Cathodes, as the main elements of the application, are made of nickel material submersed into the electrolytes. At the cathode, surrounding parts of water are broken down into one molecule of hydrogen and two molecules of hydroxyl ions. Next, one of the products – the hydroxyl ion, moves in an anode direction, where four OH-molecules oxidize and produce one molecule of oxygen gas and two molecules of water with 4 free electrons. The primary principle of this reaction is hydrogen gas production on the cathode and oxygen production on the anode side. The main products of this reaction are separated by membrane or diaphragm mentioned before. The scheme of AWE electrolysis is shown in Fig. 9 [47].

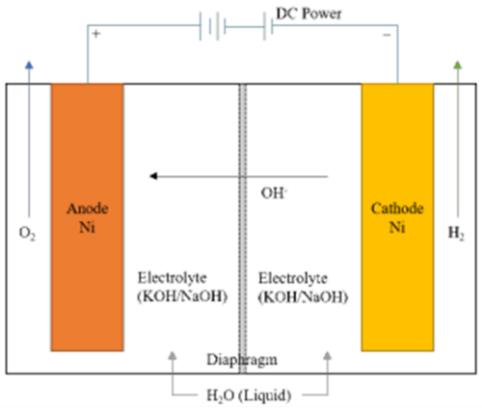


Fig. 9. Alkaline water electrolysis scheme [47].

Despite the fact that this method is one of the most advanced and developed regarding electrolysis, it still has some major disadvantages, as high water consumption - around 20 dm^3 per kg of H_2 produced, according to stoichiometry calculations, only 9 dm^3 of water is required to produce 1 kg of H_2. However, as water electrolysis generates heat, it requires more water as a cooling fluid. Confined current densities and low operating temperature and pressure indicate a low energy efficiency of 70−80%. During this process, corrosion from electrolytes occurs, as well as product (gases) migration throughout the diaphragm. However, it benefits from pure hydrogen and has no requirement for precious metals. Moreover, electrolysers based on the AWE method feature modularity that can increase the volume of production.

Considering the purity of hydrogen, the next method, called Solid-oxide electrolysis (SOE), can generate hydrogen with an even higher level of purity than AWE, with greater efficiency. This technology was implemented by Doniz and Erdle in 1980, and it is not as advanced and developed. There is still much of research ongoing at present times [51]. In SOE technology, instead of liquid NaOH electrolyte, solid ceramic electrolyte is used to increase its responsivity. This method operates at temperatures of 500−1 000°C and can withstand pressure up to 3 MPa; with those values, this technology is not yet commercialized for residential usage. The basic principle of SOE is based on the reduction of molecules of water into two molecules of H_2 and molecules of O_2 – ions, which move throughout the ceramic electrolyte to the anode side and oxidize, producing molecules of oxygen. SOE scheme is shown in Fig. 10 [47].

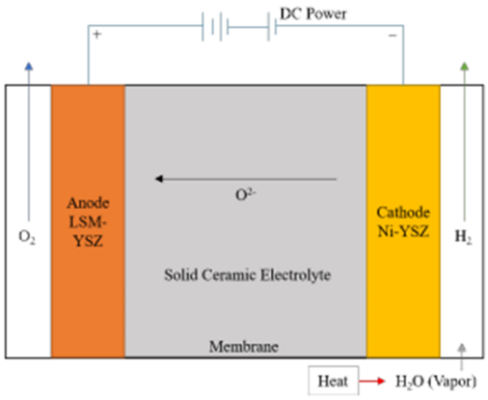


Fig. 10. Solid-oxide electrolysis cell scheme [47].

Among the most used materials for cathode nickel-zirconia and strontium, doped lanthanum magnetite can be found, and for the anode, zirconia is commonly used [52]. As main advantages, high efficiency (90−100%) and high output must be mentioned. Electrode degradation and usage of the ceramic electrolytes at a temperature of 1 000°C can be considered a disadvantage. As this technology is still in the development phase, there is still much research to perform.

Proton exchange membrane electrolysis (PEME) is the last method of electrolysis taken into consideration in this paper. PEME was discovered in 1966 as a replacement for alkaline water electrolysis. To prevent mixing of liquid special polymer electrolyte is used. This type of electrolyser operates in temperature range of 20−100°C [49]. Devices based on PEME usually operate at high pressure - about 40 MPa), allowing the reduction of the energetic demand of the whole process due to compression. The PEME process scheme is shown in Fig. 11 [47].

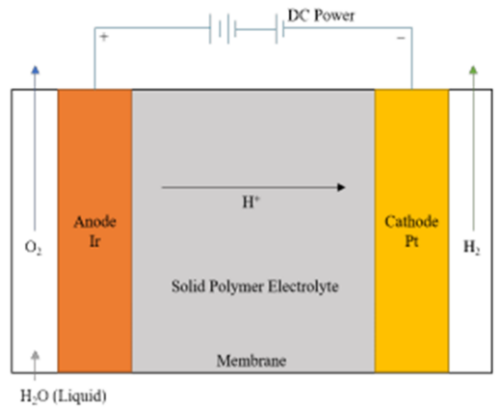


Fig. 11. Proton exchange membrane electrolysis scheme [47].

The main difference in this method is the principle, where it is an H^+ particle, which is moving throughout the membrane, not

OH^-. At the side of the anode, two particles of water H_2O oxidize to produce oxygen gas O_2 and four ions of hydrogen H^+, which move through the membrane. Next, two hydrogen (H^+) molecules are reduced on the cathode side to produce one molecule of hydrogen gas – H_2. For PEME cathode usually precious metals like Pt are used. However, for anode non-precious material like Ir can be used [53].

Electrochemical electrolysis is one of the fastest-advancing technologies nowadays. Scientists assume that it will be the main source of pure hydrogen in the next years. For now, PEME technology is the one that researchers are focusing on the most on implementing solutions that will allow the use of this technology commercially, while SOE technology is still in the experimental phase. Despite technology, one of the main challenges regarding electrolysis is the replacement of precious metals, which are rare, planned and expensive. Several techniques are currently under investigation where metal compounds and oxides such as Fe, Ni, Co and Mn based were used to replace precious metals for HER and OER electrodes half-cell reactions. Along with fuel cells, electrolysis is considered one of the main energy sources in the future, which will help to manage the surplus of energy from renewable energies and provide clean fuel for transportation.

In the global energy production transformation, there is also one type of device which will take a significant role, as a next step from electrolysis – fuel cells. Those devices, as mentioned before, convert hydrogen, generated by electrolysis, into electricity, which can be used to supply households' industry, etc. Energy conversion that takes place in fuel cell is one of a few where chemical energy stored in fuel I converted into electrical energy without any kind of concomitant emission of gases like CO_2, SO_2, NOx. This concept of fuel cell was invented by William R. Grove in 1839, electrochemist and layer [54, 55]. Grove used two electrodes made of platinum dipped into electrolyte. One of which hydrogen catalytic reaction occurred: $2H_2 \rightarrow 4H$ (ads) $\rightarrow 4H^+ + 4e-$. On the other electrode he noticed $O_2 + 4H^+ + 4e- \rightarrow 2H_2O$ reaction. Despite of reactions there is also electron movement throughout external circuit, which generated electricity. Term "fuel cell" was used in 1889 by Ludwig Mond who researched Grove's invention and improved electro-chemical oxidation of hydrogen [56]. First practical hydro-oxygen fuel cell, which could be used commercially, was developed by Thomas Bacon in 1930. All Bacon's patents regarding fuel cell were licensed by company Pratt & Whitney and were used during Apollo 11 moon mission in 1969 to provide electrical power. Through all these years since first invention of fuel cell, today we can list several different types of fuel cells, among which Polymer Electrolyte Membrane Fuel Cell (PEMFC), Solid Oxide Fuel Cell (SOFC), Molten Carbonate Fuel Cell (MCFC), Alkaline Fuel Cell (AFC), Phosphoric Fuel Cell (PFC), Reversible Fuel Cell (RFC), Direct Carbon Fuel Cell (DCFC) and Direct Methanol Fuel Cell (DMFC) can be listed.

Polymer electrolyte membrane fuel cell (or PEM) is one of the most accessible among fuel cells, although it has a lot of advantages: fast start-up and shut-down times, high power density, low noise pollution and low operating temperature – around 80°C. Researches predicts that this type of will be one of the main power sources for transportation in the future [57]. Due to not complex design PEM fuel cell can be used in simple installations and it requires minimal maintenance. Moreover, PEM fuel cell does not emit any kind of toxic gases during operation. Efficiency of PEM fuel cell can highly exceed efficiency of traditional heat engine. The electrical efficiency of PEM fuel cell can reach 40−60%, depending on purity of hydrogen. Fuel cell itself requires hydrogen-rich fuels and most of fuels like methane, methanol, gasoline, etc. which contain hydrogen, are not suitable for PEMFC operation [58]. This type of fuel cell has two key issues during operation, first issue relates to water management and second to heat management. The polymer barrier required specific hydration level to provide efficient work. However, when hydration level reaches higher value than required, water floods holes of both catalyst and gas diffusion layer of membrane and it causes disturbances in mass transportation – Fig. 12 [59]. So, it is crucial to balance hydration level of PEM fuel cell and eliminate process of fuel cell degradation. Heat management is related with resistance and losses of mass transport which can cause deviation of operating voltage from the nominal voltage and as a result fuel cell releases heat to environment and generate even more losses.

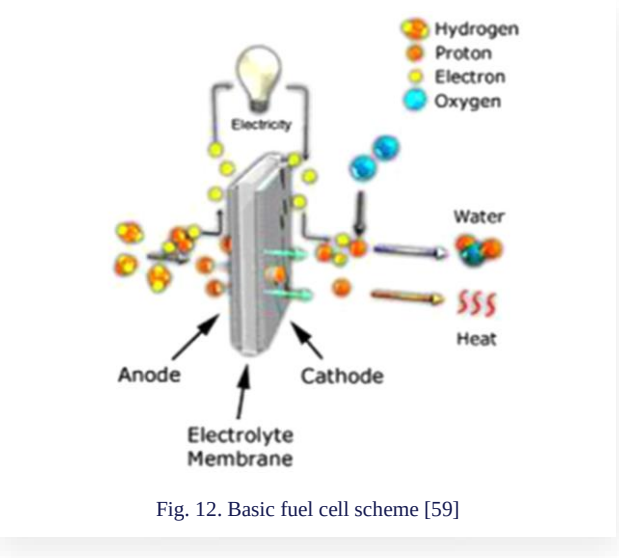


Fig. 12. Basic fuel cell scheme [59]

Solid oxide fuel cells are usually used in bigger installations such as cement plants and other industrial facilities. SOFC uses hard, non-porous ceramic alloy as electrolyte element, placed between electrodes. The shape of electrolyte can vary depending on application. SO fuel cell operates at much higher temperature ranges than PEM fuel cell, around 1 000°C (the same conditions as for SO electrolysis method). Electricity conversion process efficiency reached 50−60% [60]. SOFCs are considered high-performance hydrogen-driven solutions without air pollution. One of the biggest advances of ceramic electrolytes is their solid state. Due to that, electrolyte losses are not a significant concern [61]. One of the main disadvantages of this technology is the high-temperature requirement, resulting in personnel thermal protection and heat resistant materials. Due to these facts, start-up and shut-down times are longer than in the PEMFC solution. However, SOFC operating at lower temperature (800°C) are under development, reducing temperature impact.

Molten carbonate fuel cell can be fuelled with both natural gas and coal, so why is it compared with fuel cells that are associated with "green" hydrogen electricity production? As mentioned before, all fuel cells have higher theoretical efficiency when compared with heat engines. The MCFC electricity production process can achieve 75% efficiency. This is due to the

fact that they do not operate according to Carnot or Rankine cycles. MCFC has the potential to be integrated into applications like industrial electricity generation and military applications. It operates in the temperature range of 450°C to 650°C. This temperature allows the use of non-precious metal on both anode and cathode. A ceramic matrix with carbonate-salt impregnation is used as an electrolyte. Moreover, MCFCs are not vulnerable to CO and CO2 fuel cell poisoning, which allows them to fuel with gases produced from coal. However, MCFC technology is only suitable when large-scale continuous duty is required (with big hydrogen storage), which makes the technology perform better in industrial areas rather than residential systems.

An AFC features higher efficiency due to increased oxygen flow, which improves the electricity generation process. This type of fuel cell can be used with applications where higher current densities with lesser voltage losses are needed. The OPEX cost is relatively low, as most of the AFC parts are made out of low-cost materials. Alkaline fuel cell also has a long lifetime due to minor corrosion issues. To increase performance and reach an operating point with the highest efficiency possible, a catalyst in the electrolyte is required [62]. Carbon dioxide pollution is one of the main threats to this type of fuel cell. It must operate in a no CO_2 environment. After contact with carbon dioxide, carbonates are created, which can stop electrodes and result in electricity production failure. For this reason, fuel needs to be purified before application to remove all particles of CO_2. This type of cells were widely used by NASA during the Apollo mission in the 1960s.

The last type of fuel cell taken into consideration in this paper is Phosphoric Acid Fuel Cell (PAFC). In this solution, liquid phosphoric acid (H_3PO_4) is saturated into a matrix made out of silicon carbide. PAFC operates at a temperature range of 150−210°C. This type of electrolyte and temperature reduces the impact of carbon oxide and dioxide pollution, and fuel cells can be supplied with air instead of pure oxygen. Due to high-temperature, waste heat is produced, which can be used to heat and electricity cogeneration, resulting in up to 80% efficiency. Moreover, PAFC can operate in atmospheric and also high-pressure conditions. During the operation of every fuel cell type, water is produced and it is a significant concern in PAFC. Excess water must be removed to prevent electrolyte form being dissolved. Water removal is usually performed by air passing through the cathode and transporting water as vapour. When starting and during normal operation heat must be also removed but it can be later used to increase efficiency [63]. Based on the previous description of different fuel cell types, it can be concluded that the use of specific solutions is mostly related to the type of application. Table 3 lists several types of fuel cells with suitable applications where those can be used and also summarizes their advantages and disadvantages.

Table 3. Types of fuel cell divided by application type.

Fuel cell technology	PEMFC	SOFC	MCFC	AFC	PAFC
Power range	1 W–100 kW	0.5–400 kW	0.5–400 kW	0.5–400 kW	0.5–400 kW
Application	Portable, Stationary, Transportation	Stationary	Stationary	Stationary	Stationary
Examples	•Military systems •Stationary systems •UPS •e-Mobility	•Stationary systems combined with heat regeneration. •UPS	•Stationary systems combined with heat regeneration. •UPS	•Stationary systems combined with heat regeneration. •UPS	•Stationary systems combined with heat regeneration. •UPS
Advantages	•High power density in pressurized cell stack. •Operates easily with pressurized system due to mechanical properties of solid polymer electrolyte. •Low operating temperature (80°C) allows for cost-effective materials in cell stack.	•Highest efficiency (up to 80%). •No need for expensive materials. •Potential for long operative life cycle (to be demonstrated). •Simple cell structure streamlines production lines. •Very low emissions with hydro-carbon fuels. •Low noise production system.	•MCFCs achieve up to 45% efficiency. •Combined heat systems boost efficiency to 50%-60%. •Use hydrogen-rich fuels, no need for external reformer. •Low-cost materials.	•Simple cell structure •Fast start-up •Competitive construction costs •High electrical efficiency (65%)	•65,000+ hours operating life cycle (150ºC to 220ºC). •Electric efficiency up to 40%, can reach 60% with combined heat systems. •Partial immunity to carbon monoxide poisoning (low gas concentration). •Uses less pure hydrogen fuels.
Disadvantages	•PEMFC catalysts susceptible to CO poisoning (low operating temp.). •CO concentration must be reduced below 10 ppm with CO removal when using reformate from hydrocarbons or alcohols as fuel for PEMFC. •Effective water management is crucial for maintaining sufficient ionic conductivity and optimizing cell performance.	•High operating temperatures (above 600°C) with longer start-up times and material costs. •Vulnerable to thermal stresses and mechanical issues. •Sensitive to fuel impurities, leading to catalyst poisoning. •Limited durability and degradation at high temperatures. •Lower efficiency at partial loads.	•Short operative life cycle (corrosion, electrolyte loss, cathode dissolution). •Slow starting times (required temperature: 650°C). •No restart capability after shutdown.	•Requires pure hydrogen as fuel, limiting fuel source options. •Sensitive to carbon dioxide in the fuel, leading to performance issues. •Shorter lifespan and durability compared to some other fuel cell technologies. •Typically, bulky and heavy, making them less suitable for certain applications.	•Slower start-up times due to the phosphoric acid electrolyte characteristics. •Limited commercial availability and research compared to more established fuel cell types. •Higher cost and complexity of system components. •Bulkier and heavier, making them less suitable for certain applications.

6.2. Fuel cell energy storage

As described in previous paragraphs. Electricity can be generated from stored hydrogen using fuel cells, which can be divided into four main groups considering the type of electrolyte and temperature of work: MCFC, AFC, SOFC and most common one PEMFC [64]. Most the fuel cells operate at a temperature lower than 200°C [65]; regarding fuel cell type, its electrical ef-

ficiency can reach 45% and even 90% of efficiency can be reached with heat recovery, as the process performed by the fuel cell is highly exothermic [66]. However, the mentioned efficiency is related only to the discharging process of ESS (Energy Storage System) and does not cover electrolyser efficiency, energy needed to compress hydrogen and also hydrogen losses throughout the storage phase. When those factors are taken into consideration, the efficiency of the whole ESS itself can be estimated at around 25%-30%. Table 4 below illustrates a techno-economic comparison between PEM fuel cells and various sources of energy.

Table 4. Technoeconomic comparison of PEM fuel cell and different energy sources [67].

Transportation propulsion technology	Power level [kW]	Efficiency [%]	Specific power [kW/kg]	Power density [kW/l]	Vehicle range [km]	Capital cost [$/kW]
Proton exchange membrane fuel cell (on-board fuel processing)	10–300	40–45	400–1 000	600–2 000	350–500	100
Proton exchange membrane fuel cell (off-board hydrogen)	10–300	50–55	400–1 000	600–2 000	200–300	100
Gasoline engine	10–300	15–25	>1 000	>1 000	600	20–50
Diesel engine	10–200	30–35	>1 000	>1 000	800	20–50
Diesel engine/battery hybrid	50–100	45	>1 000	>1 000	>800	50–80
Gasoline engine/battery hybrid	10–100	40–50	>1 000	>1 000	>800	50–80
Lead-acid or nickel metal hydride battery	10–100	65	100–400	250–750	100–300	>100

Fuel cells, in most cases, include three main elements: an oxidant electrode (cathode), a fuel electrode (anode) and finally, an electrolyte placed between them. The electrodes are made of porous material covered with catalyst material (often platinum). Stored hydrogen is delivered as a gas-flow stream to the anode, where it reacts. The H_2 oxidizes to generate hydrogen ions and also electrons. Those ions migrate through the electrolyte. Meanwhile, electrons are forced to find their way through an external electrical circuit – generating electricity. Finally, on the cathode, electrons and hydrogen ions react with oxygen from air and form water as a waste product.

Fuel cells as an energy source have several unique features like no harmful emissions, high efficiency, modularity, static nature, and a vast range of applications. In terms of no harmful emission, the products of the reaction held inside the cell are only water, DC electricity and heat. However, in the case of fuel cells and their emissions, it is crucial to also consider their fuel – hydrogen, and the method of obtaining it. Regarding this description as hydrogen produced in electrolyser supplied by surplus form PV system, no-emission cells can be considered as real. Moreover, when hydrogen is produced by grid-supplied devices and the grid system itself relies on conventional fossil fuel power plants, then electricity produced by the fuel cells is more harmful to the environment than the production of the same amount of energy in a conventional way. According to research performed by Argonne National Laboratory [68] 3 000 000–3 500 000 BTUs (British Thermal Units) of energy from fossil fuels is required to produce 1 000 000 BTUs of energy in a fuel cell (using hydrogen from "non-green labelled" source), which is comparable or even less than conventional production of energy in coal power plants. However, the cost of fuel cell-based plants is incomparably higher than that of traditional coal-fired power plants. The high efficiency of the cell, compared to the heat engine, which is limited by the ideal Carnot Cycle, reaches higher values. It is because of the fact that the fuel cell as an electrochemical device is not limited by the cycle mentioned before, and it mostly depends on chemical energy content bound with the provided fuel. The modularity feature is possible due to the simple construction of the fuel cell. System power output can be easily controlled by changing a number of cells in the stack or changing the number of stacks in the complete system. It is also worth noticing that stacking and increasing the power output of cells does not affect the efficiency of the entire system, and this fact gives this solution enormous potential in terms of energy storage systems. Due to its nature, fuel cells as electrochemical devices can feature very static workflow. There are almost no dynamic parts that could cause vibrations or major faulty damage, which is why this source of energy is very reliable and also safe. However, as presented in Table 4, fuel cells are undoubtedly much more expensive than conventional sources of energy. The high price is determined by the usage of exceedingly rare materials as catalysts (mostly platinum), and delicate membrane manufacturing techniques. Experts estimate that the cost per one kW with a fuel cell must drop by 10 times [69] to successfully appear on the residual energy market. There is potential to lower the price as with every year, fuel cells are more likely to be "mass-produced". Another issue is the durability of the cells as power-generating devices. It is assumed that for sustaining the power supply device, the durability of the fuel cell needs to be increased more than 5 times (of current durability) to achieve industrially reasonable, more than 60 000 h of lifetime.

6.3. Compressed air and hydrogen energy storage

One of the newest and also complex methods to store energy combines the traditional method of Compressed Air Energy Storage (CAES) with hydrogen fuel used to produce Synthetic Natural Gas (SNG). CAES system involves air compression during energy surplus, storage and then air expansion to receive energy in an analogous way as it takes place in pumped hydropower plants. CAES system can correspond with SNG from hydrogen to become an efficient energy storage system. Both components (compressed air and SNG produced from H_2) can be easily stored and used to produce energy, e.g., in gas turbines later, during energy demand valleys.

That kind of hybrid system, which relies indirectly on hydrogen production during energy storage, is called the Power to Gas to Power (P-t-G-t-P) system [68]. One of the newest ideas of energy storage called the Compression Air and Hydrogen Energy Storage (CAHES) system, combines both storage methods mentioned before, CAES and P-t-G-t-P system (or P-t-SNG-t-P for synthetic gas).

Figure 13 shows the scheme of the CAHES system. The entire system consists of several different devices with distinct roles. As a part of the P-t-SNG-t-P system, we can note water treatment installation, hydrogen generator, optional oxygen and hydrogen compressors, hydrogen tank, oxygen tank, mechanization unit, SNG and CO_2 compressor, combustion changer and finally, flue gas turbine. On the other side of this system, there is the CAES part, including an air compressor, heat exchangers, and compressed air turbine. There are also devices that fulfil the entire system and cannot be assigned as a part of only one subsystem; these are the water tank, generator, moisture separator, and compressed air tank. As Fig. 13 illustrates the CAHES system design scheme, it also represents three phases that feature most of the energy storage sub-systems.

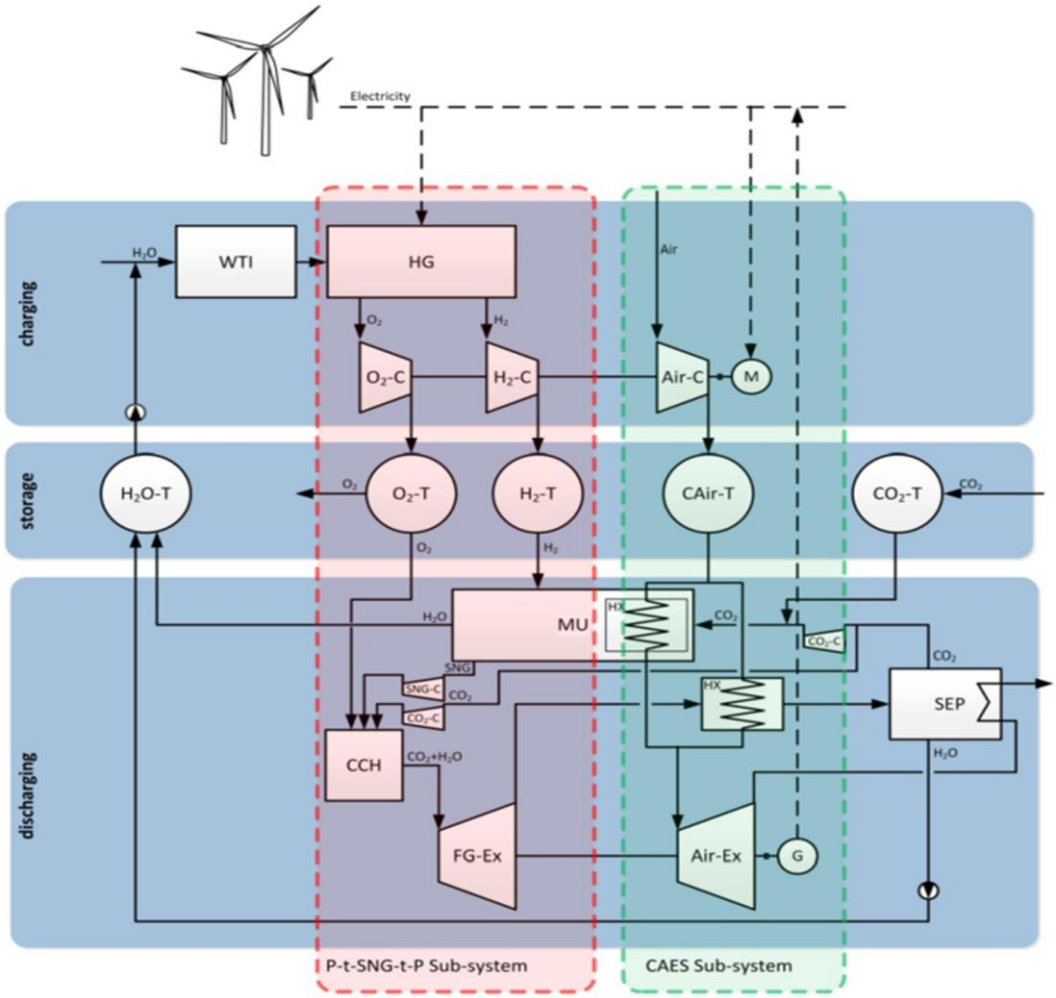


Fig. 13. CAHES system concept scheme.
CCH – Combustion Chamber, SEP – Moisture Separator, HG - Hydrogen Generator, MU - Methanation Unit, HX - Heat Exchanger, WTI – Water Treatment Installation, M – Motor, G - Generator Air-Ex (Air Expander), FG-Ex – Flue Gases Expander, O_2-T – Oxygen Tank, H_2-T – Hydrogen Tank, H_2O-T – Water Tank, CO_2-T – Carbon Dioxide Tank, Air-T – Compressed Air Tank, Air-C – Air Compressor, H_2-C – Hydrogen Compressor, O_2-C – Oxygen Compressor, CO_2-C – Carbon Dioxide Compressor, SNG-C – Synthetic Natural Gas Compressor [70].

The first subsystem consists of a hydrogen generator, water preparation installation, hydrogen and oxygen compressors, and storage tanks for hydrogen, oxygen, and water. The hydrogen generator operates during low electricity demand or increased renewable energy production. Hydrogen and oxygen are stored in H_2−T and O_2−T tanks at 30−40 bar. The hydrogen goes to the methanation unit, while oxygen is used as an oxidant for burned SNG in the SNGOCSs.

The Methanation Sub-system (MSs) receives a mixture of carbon dioxide and steam, a byproduct of flue gas drying during SNG oxycombustion. It includes three methanation reactors with heat exchangers. The Compressed Air Energy Storage Subsystem (CAESSs) includes a three-section air compressor (Air-C) with cooling sections. Atmospheric air is compressed to 4 000 kPa, and the pressure can be adjusted from 2 000 kPa to 6 000 kPa. The compressor's internal efficiency is 88%, with a 98% electromechanical efficiency. Compressed air can be stored in an underground tank and then divided into two streams: one is heated using the methanation process, and the other is heated by high-temperature flue gas. Both streams are directed into separate expanders.

The expanded air can be utilized to more efficiently dry exhaust gases before they enter the methanation process. The flue gases expander (FG-Ex) operates in the SNG Oxy-Combustion Sub-system, fuelled by SNG combustion in the combustion chamber (CCH). Oxygen from the electrolysis process is used for combustion. The expander's pressure is 4 000 kPa, and its temperature ranges from 800°C to 1 100°C.

The flue gases expand to 600 kPa, providing high-temperature gases for the HX exchanger inside MU (Methanation Unit) to heat the air in the CAESSs expander. The exhaust gas from the CCH is a mixture of CO_2 and H_2O. Under ideal conditions, the oxygen used for combustion matches the oxygen produced by the hydrogen generator in the MSs. The Drying Sub-system (DS) condenses water vapour in the flue gases from the FG-Ex by cooling them below the dew point. The flue gases are first cooled to 30°C in the standalone HX heat exchanger. Further cooling is achieved by optionally using the low temperature of the air, leaving the CAESS Air-Ex.

The first charging phase occurs during sunny weather and PV electricity generation surplus. The energy that cannot be used by residential devices right away is used to supply hydrogen electrolysers and air compressors. Both gases are then stored inside tanks.

However, according to Fig. 8 and section 6 of this paper, there is the possibility of implementing different methods of hydrogen storage. But those cases should be part of further research. Moreover, it could also be possible to use the produced hydrogen straightforwardly inside the mechanisation unit and then store SNG instead of H_2. As tanks are filled with PV energy surplus products, the second phase starts – storage itself. The last discharge stage is complex and covers several different processes like using hydrogen in methanization unit (if not performed in other phases), combustion of SNG inside the chamber, expansion of flue gases on the turbine, compressed air expansion, power generation from generator coupled with flue gas and compressed expanders, separation of moisture from flue gases. There are also minor processes which provide efficiency due to heat recovery in heat exchangers, like using heat generated inside the mechanisation unit to increase the temperature of compressed air heading to the air expander. According to research [69] CAHES system, presented in Fig. 13, can achieve an efficiency of 38.15% (2020 y), which is higher than P-t G(H2)-t-P sub-systems alone but is lower than CAES sub-system considered individually. The whole idea is covered by patent procedure [71]. Regarding efficiency of this CAHES system only puts many doubts to this idea and points to the superiority of energy storage methods like BESS or hydropower technology. However, as this technology is new and features with higher complexity, there are many parts that are under improvement and development, which can result in great efficiency grow as research continues.

7. Conclusions

The current global energy landscape is characterized by rapid energy price increases, frequent delivery disruptions, and geopolitical tensions, highlighting the urgent need for energy storage solutions to enhance energy sustainability. It is undeniable that energy storage systems will play a pivotal role in the future development of both residential and national energy grids. With the growing global electricity production from renewable but non-reliable sources, one of the major challenges in today's scientific landscape is to find the most efficient means to utilize any surplus energy that occurs and use it when needed by consumers. At the residential scale, energy storage solutions offer a promising avenue to improve the performance of photovoltaic installations, increasing the rate of auto-consumption. However, the range of energy storage methods discussed in this paper reveals that there is no one-size-fits-all approach for every application. While hydropower technology is well-suited for vast national grids, it presents technical limitations that make its implementation on a residential scale unfeasible.

Battery energy storage systems (BESS) emerge as a more accessible and effective solution for residential conditions. BESS boasts advantages such as low inertia, high reliability, and efficiency. Despite these benefits, the excessive cost and limited lifespan of BESS systems continue to hinder their widespread adoption for most domestic installations. Additionally, the environmental implications of batteries, containing substances harmful to the environment and generating considerable waste, raise concerns from an ecological standpoint.

The future of energy storage lies in innovative technologies based on hydrogen energy, which offer promising and environmentally friendly solutions when successfully implemented. However, the primary challenge surrounding hydrogen storage systems is their current implementation phase, with most hydrogen installations in early or mid-development stages. Accessibility to common consumers is limited, as certain devices required for such systems are not readily available. Furthermore, the investment cost (CAPEX) remains a significant barrier to widespread adoption. Nevertheless, the growing adoption of hydrogen energy technologies in the automotive and electrical sectors, coupled with mass production, is expected to drive down costs over time. Efforts to lower the cost of devices related to hydrogen energy, such as electrolysers and fuel cells, are witnessing a surge of research and publications. Scientists and researchers focus on optimizing hydrogen energy technologies to reduce expenses and promote broader accessibility. This research trend aims to replace precious materials like platinum with more readily available and cost-effective substances, contributing to cost reduction in hydrogen energy systems.

Lastly, the Compressed Air and Hydrogen Energy Storage (CAHES) method represents a unique combination of modern hydrogen-based technology with a more traditional compressed air-based approach. While CAHES is still under investigation and necessitates further research, it holds immense potential for significant improvement. This advancement could result in an efficient and cost-effective solution, viable for residential scale implementation alongside photovoltaic installations. A successful implementation of CAHES technology can lead to reduced energy costs and a more reliable and environmentally friendly energy system.

In conclusion, the current state of energy storage systems in residual installations presents a spectrum of viable options, each with its unique advantages and challenges. The increasing focus on hydrogen energy technologies, along with advancements in BESS and CAHES, represents a promising future for energy storage. Further research and innovation are necessary to optimize these solutions, making them more accessible, cost-effective, and environmentally friendly. As global demand for sustainable energy solutions intensifies, energy storage systems play a crucial role in shaping a greener and more resilient energy future.

Developing cost-effective solutions for long-duration storage systems is one of a key directions for the future researches in this field. While lithium-ion battery solutions dominate the market, they are not sufficient systems for extender storage requirements. Researchers should focus on alternative and innovative technologies. One of the crucial aspects that requires further investigation is post-lithium-ion battery technologies,

which will not rely on lithium as a basic material. This element is currently widely sped; however, the lithium mining procedure generates high criticism and inequalities (especially in the regions of Africa). Materials Science and Engineering play a pivotal role in advancing electrical energy storage technologies. Researching new materials for electrodes, electrolytes, and separators to enhance energy density, cycle life, and safety is imperative. Additionally, exploring recycling and second-life applications for retired batteries can minimize environmental impact and optimize the costs of installations.

Along with the great development of artificial intelligence we witness these days, the development of advanced control algorithms for optimal energy usage, dispatch, and grid stability will also be a huge part of the next research. Future research may focus on enhancing predictive analytics capabilities by leveraging computer algorithms. These solutions can analyse vast datasets, including historical energy usage patterns, weather forecasts, market trends, and grid conditions, to provide accurate predictions of energy demand and supply dynamics. AI-driven predictive analytics can enable more efficient energy storage planning and management by predicting energy fluctuations with higher precision.

Interdisciplinary Collaboration is a key to addressing the multifaceted challenges in energy storage. Technological, economic, and social challenges can be solved collectively by fostering collaboration between researchers, engineers, policymakers, and industry stakeholders. By fostering collaboration among these diverse stakeholders, energy storage challenges can be approached from multiple angles, leading to more comprehensive and effective solutions. For example, researchers may develop new battery chemistries with improved performance, engineers can design efficient storage systems based on these innovations, policymakers can create supportive policies and regulations to incentivize deployment, and industry stakeholders can implement and scale up these solutions in the marketplace. In summary, the future of residential electrical energy storage research is characterized by an interdisciplinary approach that encompasses advanced battery technologies, seamless integration with renewable energy sources, smart energy management systems, grid-interactive capabilities, and sustainability considerations. By advancing research in these directions, we can unlock the full potential of residential energy storage to drive the transition towards a more sustainable and resilient energy future.

References

[1] Bouzzine, Y., & Lueg, R. (2021). The Shareholder Value Effect of System Overloads: An Analysis of Investor Responses to the 2003 Blackout in the US. *International Journal of Energy Economics and Policy*, 11(6). doi: 10.32479/ijeep.11756

[2] Blaszke, M., Nowak, M., Śleszyński, P., & Mickiewicz, B. (2021). Investments in Renewable Energy Sources in the Concepts of Local Spatial Policy: The Case of Poland. *Energies*, 14(7902). doi: 10.3390/en14237902

[3] Central Statistical Office. *Environment, Energy*. https://stat.gov.pl/obszary-tematyczne/srodowisko-energia/ [accessed 17 Jan. 2022].

[4] Wciślik, S., & Kotrys-Działak, D. (2021). Thermal building upgrade with off-grid PV system: a Polish case. *Energy Efficiency*, 14, 70. doi: 10.1007/s12053-021-09980-x

[5] Gnatowska, R., & Moryń-Kucharczyk, E. (2021). The place of photovoltaics in Poland's energy mix. *Energies*, 14(5), 1471. doi: 10.3390/en14051471

[6] Jurasz, J. (2016). The impact of temperature variability on the demand for electric power in Poland in 2002−2015. *Przegląd Elektrotechniczny*, 1(9), 259–263. doi: 10.15199/48.2016.09.62 (in Polish).

[7] Jurasz, J., Krzywda, M., & Mikulik, J. (2016). How might residential PV change the energy demand curve in Poland. *E3S Web of Conferences*, 10, 00059. doi: 10.1051/e3sconf/20161000059

[8] Hittinger, E., & Ciez, R.E. (2020). Modeling costs and benefits of energy storage systems. *Annual Review of Environment and Resources*, 45(1), 445–469. doi: 10.1146/annurev-environ-012320-082101

[9] Zakeri, B., Cross, S., Dodds, P.E., & Gissey, G.C. (2021). Policy options for enhancing economic profitability of residential solar photovoltaic with battery energy storage. *Applied Energy*, 290, 116697. doi: 10.1016/j.apenergy.2021.116697

[10] PV Magazine International. *Germany has 200 000 solar-plus-storage systems*. https://www.pv-magazine.com/2020/04/21/germany-has-200000-solar-plus-storage-systems/ [accessed 18 Jan. 2022].

[11] Jarosiński, M., Godlewski, W., & Sierakowski, M. (2021). Cost-effectiveness of PV installations with battery energy storage and proposed changes in prosumer settlement. *Installation Market*, 9/2021 (in Polish).

[12] Popp, H., Attia, J., Delcorso, F., & Trifonova, A. (2014). Lifetime analysis of four different lithium ion batteries for (plug – in) electric vehicle. *Conference: TRA2014 Transport Research Arena,* 14−17 April 2014, Paris, France.

[13] Khalid, A., Stevenson, A., & Sarwat, A.I. (2021). Overview of technical specifications for grid-connected microgrid battery energy storage systems. *IEEE Access: Practical Innovations, Open Solutions*, 9, 163554–163593. doi: 10.1109/access.2021.3132223

[14] Wang, T., Zhao, Y., & Chen, J. (2018). A battery monitoring IC with an isolated communication interface for electric vehicles. *IEICE Electronics Express*, 15(12), 20180513–20180513. doi: 10.1587/elex.15.20180513

[15] Salkuti, S.R. (2020). Comparative analysis of electrochemical energy storage technologies for smart grid. *ELKOMNIKA (Telecommunication Computing Electronics and Control)*, 18. doi: 10.12928/telkomnika.v18i4.14039

[16] Simpson, A.G. (2024). *Parametric modelling of energy consumption in road vehicles*. University of Queensland Library.

[17] Dixon, J., Nakashima, I., Arcos, E.F., & Ortuzar, M. (2010). Electric vehicle using a combination of ultracapacitors and ZEBRA battery. *IEEE Transactions on Industrial Electronics (1982)*, 57(3), 943–949. doi: 10.1109/tie.2009.2027920

[18] Xie, P., Sun, F., Wang, L., & Liu, P. (2019). A review on China's Energy Storage Industry under the "Internet Plus" initiative. *International Journal of Energy Research*, 43(2), 717–741. doi: 10.1002/er.4234

[19] Yuqing, Y., Bremner, S., Menictas, C., & Kay, M. (2018). Battery energy storage system size determination in renewable energy systems: A review. *Renewable and Sustainable Energy Reviews*, 91(8), 109–125. doi: 10.1016/j.rser.2018.03.047

[20] Jingmei, S., Fang, D., Hong, Z., & Mei, C. (2015). Introduction to Electrochemical Energy Storage and Conversion. In book: *Electrochemical Energy: Advanced Materials and Technologies*, Chapter 1. CRC Press. doi: 10.1201/9781351228756

[21] Boparai, K., & Singh, R. (2018). Electrochemical Energy Storage Using Batteries, Superconductors and Hybrid Technologies. In

book K. Boparai, & R. Singh, *Reference Module in Materials Science and Materials Engineering*. doi: 10.1016/B978-0-12-803581-8.11277-9

[22] Bloomberg New Energy Finance. (2019). *A Behind the Scenes Take on Lithium-ion Battery Prices*. https://about.bnef.com/blog/behind-scenes-take-lithium-ion-battery-prices/ [accessed 17 Jan. 2022].

[23] Figgener, J., Stenzel, P., Kairies, K.P., Linßen, J., Haberschusz, D., Wessels, O., Robinius, M., Stolten, D., & Sauer, D.U. (2021). The development of stationary battery storage systems in Germany – status 2020. *Journal of Energy Storage*, 33, 101982. doi: 10.1016/j.est.2020.101982

[24] Stecca, M., Ramirez Elizondo, L., Batista Soeiro, T., Bauer, P., & Palensky, P. (2020). A comprehensive review of the integration of battery energy storage systems into distribution networks. *IEEE Open Journal of the Industrial Electronics Society*, 1, 46–65. doi: 10.1109/ojies.2020.2981832

[25] Lebrouhi, B.E., Djoupo, J.J., Lamrani, B., Benabdelaziz, K., & Kousksou, T. (2022). Global hydrogen development - A technological and geopolitical overview. *International Journal of Hydrogen Energy*, 47(11), 7016–7048. doi: 10.1016/j.ijhydene.2021.12.076

[26] Li, H., Ma, C., Zou, X., Li, A., Huang, Z., & Zhu, L. (2021). On-board methanol catalytic reforming for hydrogen Production: A review. *International Journal of Hydrogen Energy*, 46(43), 22303–22327. doi: 10.1016/j.ijhydene.2021.04.062

[27] Sdanghi, G., Maranzana, G., Celzard, A., & Fierro, V. (2019). Review of the current technologies and performances of hydrogen compression for stationary and automotive applications. *Renewable and Sustainable Energy Reviews*, 102, 150–170. doi: 10.1016/j.rser.2018.11.028

[28] Chouhan, K., Sinha, S., Kumar, S., & Kumar, S. (2021). Simulation of steam reforming of biogas in an industrial reformer for hydrogen production. *International Journal of Hydrogen Energy*, 46(53), 26809–26824. doi: 10.1016/j.ijhydene.2021.05.152

[29] Sanchez, N., Ruiz, R., Hacker, V., & Cobo, M. (2020). Impact of bioethanol impurities on steam reforming for hydrogen production: A review. *International Journal of Hydrogen Energy*, 45(21), 11923–11942. doi: 10.1016/j.ijhydene.2020.02.159

[30] Ma, Y., Wang, X. R., Li, T., Zhang, J., Gao, J., & Sun, Z.Y. (2021). Hydrogen and ethanol: Production, storage, and transportation. *International Journal of Hydrogen Energy*, 46(54), 27330–27348. doi: 10.1016/j.ijhydene.2021.06.027

[31] Scamman, D., & Newborough, M. (2016). Using surplus nuclear power for hydrogen mobility and power-to-gas in France. *International Journal of Hydrogen Energy*, 41(24), 10080–10089. doi: 10.1016/j.ijhydene.2016.04.166

[32] Zeng, K., & Zhang, D. (2010). Recent progress in alkaline water electrolysis for hydrogen production and applications. *Progress in Energy and Combustion Science*, 36(3), 307−326. doi: 10.1016/j.pecs.2009.11.002

[33] Khalid, F., & Bicer, Y. (2020). High temperature electrolysis of hydrogen bromide gas for hydrogen production using solid oxide membrane electrolyzer. *International Journal of Hydrogen Energy*, 45(9), 5629–5635. doi: 10.1016/j.ijhydene.2019.01.293

[34] Yoon, S., Ahmed, F., Zhang, W., Ryu, T., Jin, L., Kim, D., Kim, W., & Jang, H. (2020). Flexible blend polymer electrolyte membranes with excellent conductivity for fuel cells. *International Journal of Hydrogen Energy*, 45(51), 27611–27621. doi: 10.1016/j.ijhydene.2020.07.076

[35] Węcel, D., & Ogulewicz, W. (2011). Study on the possibility of use of photovoltaic cells for the supply of electrolysers. *Archives of Thermodynamics*, 32(4), 33–53. doi: 10.2478/v10173-011-0030-4

[36] Gago, A., Bürkle, J., Lettenmeier, P., Morawietz, T., Handl, M., Hiesgen, R., Burggraf F., Beltran P., Friedrich K.A.(2018). Degradation of Proton Exchange Membrane (PEM) Electrolysis: The Influence of Current Density. *ECS Transactions*, 86 (13). doi: 10.1149/08613.0695ecst

[37] Zivar, D., Kumar, S., & Foroozesh, J. (2021). Underground hydrogen storage: A comprehensive review. *International Journal of Hydrogen Energy*, 46(45), 23436–23462. doi: 10.1016/j.ijhydene.2020.08.138

[38] Wolf, E. (2015). Large-Scale Hydrogen Energy Storage. In *Electrochemical Energy Storage for Renewable Sources and Grid Balancing* (pp. 129–142). Elsevier doi: 10.1016/B978-0-444-62616-5.00009-7

[39] Olabi, A.G., Bahri, A.S., Abdelghafar, A.A., Baroutaji, A., Sayed, E.T., Alami, A.H., Rezk, H., & Abdelkareem, M.A. (2021). Large-vscale hydrogen production and storage technologies: Current status and future directions. *International Journal of Hydrogen Energy*, 46(45), 23498–23528. doi: 10.1016/j.ijhydene.2020.10.110

[40] Hassan, I.A., Ramadan, H.S., Saleh, M.A., & Hissel, D. (2021). Hydrogen storage technologies for stationary and mobile applications: Review, analysis and perspectives. *Renewable and Sustainable Energy Reviews*, 149, 111311. doi: 10.1016/j.rser.2021.111311

[41] Zheng, J., Zhou, H., Wang, C.G., Ye, E., Xu, J. W., Loh, X.J., & Li, Z. (2021). Current research progress and perspectives on liquid hydrogen rich molecules in sustainable hydrogen storage. *Energy Storage Materials*, 35, 695–722. doi: 10.1016/j.ensm.2020.12.007

[42] Andersson, J., & Grönkvist, S. (2019). Large-scale storage of hydrogen. *International Journal of Hydrogen Energy*, 44(23), 11901–11919. doi: 10.1016/j.ijhydene.2019.03.063

[43] Chi, J., & Yu, H. (2018). Water electrolysis based on renewable energy for hydrogen production. *Cuihua Xuebao/Chinese Journal of Catalysis*, 39(3), 390–394. doi: 10.1016/s1872-2067(17)62949-8

[44] Acar, C., & Dincer, I. (2014). Comparative assessment of hydrogen production methods from renewable and non-renewable sources. *International Journal of Hydrogen Energy*, 39(1), 1–12. doi: 10.1016/j.ijhydene.2013.10.060

[45] Lee, B., Heo, J., Kim, S., Sung, C., Moon, C., Moon, S., & Lim, H. (2018). Economic feasibility studies of high pressure PEM water electrolysis for distributed H2 refueling stations. *Energy Conversion and Management*, 162, 139–144. doi: 10.1016/j.enconman.2018.02.041

[46] Sun, Y., Shen, C., Lai, Q., Liu, W., Wang, D.W., & Aguey-Zinsou, K.F. (2018). Tailoring magnesium based materials for hydrogen storage through synthesis: Current state of the art. *Energy Storage Materials*, 10, 168–198. doi: 10.1016/j.ensm.2017.01.010

[47] Pinsky, R., Sabharwall, P., Hartvigsen, J., & O'Brien, J. (2020). Comparative review of hydrogen production technologies for nuclear hybrid energy systems. *Progress in Nuclear Energy*, 123(103317), 103317. doi: 10.1016/j.pnucene.2020.103317

[48] Shiva Kumar, S., & Lim, H. (2022). An overview of water electrolysis technologies for green hydrogen production. *Energy Reports*, 8, 13793–13813. doi: 10.1016/j.egyr.2022.10.127

[49] Balat, M. (2008). Possible methods for hydrogen production. *Energy Sources Part A Recovery Utilization and Environmental Effects*, 31(1), 39–50. doi: 10.1080/15567030701468068

[50] Rashid, M., Al Mesfer, M., Naseem, H., & Danish, M. (2015). Hydrogen production by water electrolysis: a review of alkaline

water electrolysis, PEM water electrolysis and high temperature water electrolysis. *International Journal of Engineering and Advanced Technology*. 4(3), 80–93.

[51] Ursua, A., Gandia, L.M., & Sanchis, P. (2012). Hydrogen production from water electrolysis: Current status and future trends. *Proceedings of the Institute of Electrical and Electronics Engineers*, 100(2), 410–426. doi: 10.1109/jproc. 2011.2156750

[52] Anwar, S., Khan, F., Zhang, Y., & Djire, A. (2021). Recent development in electrocatalysts for hydrogen production through water electrolysis. *International Journal of Hydrogen Energy*, 46(63), 32284–32317. doi: 10.1016/j.ijhydene.2021.06.191

[53] Cheng, J., Zhang, H., Chen, G., & Zhang, Y. (2009). Study of IrxRu1−xO2 oxides as anodic electrocatalysts for solid polymer electrolyte water electrolysis. *Electrochimica Acta*, 54(26), 6250–6256. doi: 10.1016/j.electacta.2009.05.090

[54] Grove, W.R. (1838). *On a new voltaic combination*: To the editors of the Philosophical Magazine and Journal. *The London and Edinburgh Philosophical Magazine and Journal of Science*, 13(84), 430–431. doi: 10.1080/14786443808649618

[55] Thomas, J.M. (2012). W.R. Grove and the fuel cell. *Philosophical Magazine*, 92(31), 3757–3765. doi: 10.1080/14786435. 2012.691216

[56] Mond, L., & Langer, C. (1890). A new Form of Gas Battery, *Proceedings of the Royal Society of London*, 52(46), 296–304.

[57] Jannelli, E., Minutillo, M., & Galloni, E. (2007). Performance of a polymer electrolyte membrane fuel cell system fueled with hydrogen generated by a fuel processor. *Journal of Fuel Cell Science and Technology*, 4(4), 435–440. doi: 10.1115/1.2756568

[58] Luo, Y., Shi, Y., & Cai, N. (2021). Bridging a bi-directional connection between electricity and fuels in hybrid multienergy systems. In *Hybrid Systems and Multi-energy Networks for the Future Energy Internet* (pp. 41–84). Elsevier.

[59] Sharaf, O.Z., & Orhan, M.F. (2014). An overview of fuel cell technology: Fundamentals and applications. *Renewable and Sustainable Energy Reviews*, 32, 810–853. doi: 10.1016/j.rser. 2014.01.012

[60] Magar, Y.N. (2006). *Convective Cooling and Thermal Management Optimization of Planar Anode-Supported Solid Oxide Fuel Cells*. M.S. Thesis. University of Cincinnati.

[61] Polat, C., & Kilinc-Ata, N. (2008). Market Opportunities for Hydrogen Solid Oxide Fuel Cells (SOFC): A Review of the Literature and the Future Market Trends. *Business & Economics Conferences (EABR) and Teaching & Education Conferences (TLC).* 23−26 June 2008, Salzburg, Austria.

[62] Vang, J.R., Andreasen, S.J., & Kær, S.K. (2012). A transient fuel cell model to simulate HTPEM fuel cell impedance spectra. *Journal of Fuel Cell Science and Technology*, 9(2). doi: 10.1115/1.4005609

[63] Breeze, P. (2017). An introduction to fuel cells. In *Fuel Cells* (pp. 1–10). Elsevier. doi: 10.1016/B978-0-08-101039-6.00001-7

[64] Baik, K.D., & Yang, S.H. (2020). Improving open-cathode polymer electrolyte membrane fuel cell performance using multi-hole separators. *International Journal of Hydrogen Energy*, 45(15), 9004–9009. doi: 10.1016/j.ijhydene.2020.01.040

[65] Wong, C.Y., Wong, W.Y., Ramya, K., Khalid, M., Loh, K.S., Daud, W.R. W., Lim, K.L., Walvekar, R., & Kadhum, A.A.H. (2019). Additives in proton exchange membranes for low- and high-temperature fuel cell applications: A review. *International Journal of Hydrogen Energy*, 44(12), 6116–6135. doi: 10.1016/ j.ijhydene.2019.01.084

[66] Tu, B., Qi, H., Yin, Y., Zhang, T., Liu, D., Han, S., Zhang, F., Su, X., Cui, D., & Cheng, M. (2021). Effects of methane processing strategy on fuel composition, electrical and thermal efficiency of solid oxide fuel cell. *International Journal of Hydrogen Energy*, 46(52), 26537–26549. doi: 10.1016/j.ijhydene.2021.05.128

[67] Gaines, L.L., Elgowainy, A., & Wang, M.Q. (2008). *Full fuel-cycle comparison of forklift propulsion systems*. Office of Scientific and Technical Information (OSTI), ID 946421. doi: 10.2172/946421

[68] Al Rafea, K., Elsholkami, M., Elkamel, A., & Fowler, M. (2017). Integration of decentralized energy systems with utility-scale energy storage through underground hydrogen–natural gas co-storage using the energy hub approach. *Industrial and Engineering Chemistry Research*, 56(8), 2310–2330. doi: 10.1021/acs.iecr.6b02861

[69] Bartela, Ł. (2020). A hybrid energy storage system using compressed air and hydrogen as the energy carrier. *Energy*, 196, 117088. doi: 10.1016/j.energy.2020.117088

[70] Bartela, Ł., Chmielniak, T., & Kotowicz, J. (2018). *A way of integration of energy storage systems using in hydrogen and compressed air*. Patent No. PL 235565 B1, Poland (in Polish).

Co-published by
Institute of Fluid-Flow Machinery
Polish Academy of Sciences
Committee on Thermodynamics and Combustion
Polish Academy of Sciences

Copyright©2024 by the Authors under licence CC BY 4.0

http://www.imp.gda.pl/archives-of-thermodynamics/

Parametric multi-response optimisation of various organic Rankine cycle configurations for geothermal heat source application using Taguchi – grey relational analysis

Dodeye Ina Igbong[a*], Mafel Obhuo[b], Oku Ekpenyong Nyong[a]

[a]University of Cross River State, Calabar, Cross River State, Nigeria
[b]Nigeria Maritime University, Okerenkoko, Delta State, Nigeria
*Corresponding author email: d.i.igbong@unicross.edu.ng

Received: 31.05.2023; revised: 6.12.2023; accepted: 19.04.2024

Abstract

In this study, statistical methods (Taguchi, analysis of variance (ANOVA), and grey relational analysis (GRA)) are used to evaluate the impact, contribution ratios, and order of importance of parameters on the energy and exergy efficiencies of the simple organic Rankine cycle (SORC) and dual pressure organic Rankine cycle (DORC). The parameters being investigated are the working fluid (A), pinch point temperature difference of the evaporator (B) and condenser (C), degree of superheating (D), evaporator temperature (E), condenser temperature (F), turbine isentropic efficiency (G), pump isentropic efficiency (H), and low-pressure evaporator temperature (J, for DPORC only). Whereas the Taguchi method determines the optimum parameter combination for maximum system performance, ANOVA weighs the influence of individual parameters on the performance of the target function, and GRA optimizes the multi-response characteristic function. The condenser and evaporator temperatures, pinch point temperature difference of the condenser and turbine isentropic efficiency are revealed as the major process parameters for multi-response performance characteristics of SORC, with an influence factor of 44.79%, 20.96%, 14.81% and 10.69%, respectively. While considering three different working fluids: HFE7000 (1), R245fa (2), and R141b (3), the combination $A_3B_2C_1D_1E_3F_1G_3H_3$ is determined as the optimum operating condition for multi-response performance characteristic of SORC with first- (energy) and second- (exergy) law efficiencies calculated as 18.64% and 51.69%, respectively. For DPORC, the turbine isentropic efficiency, condenser temperature, and pinch point temperature difference of the condenser and evaporator are the main process parameters for multi-response performance with 41.90%, 17.80%, 14.75%, and 10.47% impact factors, respectively. The best operating condition is obtained as $A_1B_1C_1D_3E_2F_1G_3H_3J_2$ with first- and second-law efficiencies computed as 13.17% and 57.33%, respectively.

Keywords: ANOVA; Dual pressure ORC; First- and second-law efficiencies; Grey relational analysis; Simple ORC; Taguchi.

Vol. 45(2024), No. 2, 231–246; doi: 10.24425/ather.2024.150868

Cite this manuscript as: Igbong, D.I., Obhuo, M., & Nyong, O.E. (2024). Parametric multi-response optimisation of various organic Rankine cycle configurations for geothermal heat source application using Taguchi-Grey Relational Analysis. *Archives of Thermodynamics*, 45(2), 231–246.

1. Introduction

The increased awareness of energy and environmental sustainability has spurred research interest in developing efficient and more environmentally friendly energy systems. Organic Rankine cycles (ORCs) are considered one of those technologies with promising potential for effective low-grade heat-to-electricity conversion, with wide application in exhaust waste heat

Nomenclature

$\dot{E}x$ – exergy, W
$\dot{E}x_D$ – exergy destruction, W
h – specific enthalpy, J/kg
h_0 – specific enthalpy at the reference state, J/kg
$\dot{m}$ – mass flow rate, kg/s
P – pressure, Pa
$\dot{Q}$ – heat rate, W
s – specific entropy, J/(kg K)
s_0 – specific entropy at a reference state, J/(kg K)
T – temperature, K, °C
w_A – actual enthalpy change in the turbine, J/kg
w_S – isentropic enthalpy change in the turbine, J/kg
$\dot{W}_{pump}$ – power to drive pump
$\dot{W}_{net,SORC}$ – net power of simple organic Rankine cycle, W
$\dot{W}_{net,DPORC}$ – net power of dual pressure organic Rankine cycle, W
$\dot{W}_{turb}$ – power produced from the turbine, W

Greek symbols

η – efficiency

Subscripts and Superscripts

ch – chemical
cond – condenser
cw – cooling water
ex – exergy
evap – evaporator
f – working fluid
heat – heat source
HP – high-pressure
in – inlet
IN – input
LP – low-pressure
out – outlet
pp – pinch point
PreH – preheater
Sat – saturation
SupH – superheater
sys – system
th – thermal
w – geothermal water

Abbreviations and Acronyms

ANOVA – analysis of variance
DOF – degree of freedom
DPORC – dual pressure organic Rankine cycle
GRA – grey relational analysis
GRG – grey relational grade
SORC – simple organic Rankine cycle

recovery, geothermal, solar, and biomass for electricity generation [1]. Instead of steam, it uses low-temperature organic working fluid, which makes it more flexible with good matching characteristics between a wide temperature range of heat sources and its working fluid, hence decreasing exergy losses in the evaporator and consequently improving the overall cycle exergy efficiency [2,3].

There are many studies in the literature that conduct analysis on the thermal and exergy efficiency performance of ORC. Some of them have focused on experimental and theoretical studies of ORC performance enhancement, while others have reported on the effect of different configurations on system performance.

In general, the ORC system has been widely utilised for electricity generation from low- and medium-temperature geothermal wells. Igbong et al. [1] performed an exergo-economic and optimization study of dual pressure ORC (DPORC) utilising geothermal sources. In that study, the system optimised for maximum efficiency obtained an exergy efficiency and a cost per unit exergy of 33% and 3.059 cent/kWh, respectively. Yamankaradeniz et al. [4] investigated the energy and exergy performance of ORC with an internal heat exchanger. The study assessed the effects of evaporator temperature and heat exchanger effectiveness on the operation of the ORC system and concluded that a maximum increase of 6.21% in exergy efficiency is achievable depending on the working conditions. Igbong et al. [5] carried out a comparative exergetic analysis of selecting working fluid for various operating conditions of simple and recuperative organic Rankine cycles. Sadeghi et al. [6] performed a comparative thermodynamic analysis of different ORC configurations (simple ORC (SORC), series two-stage ORC (STORC) and parallel two-stage ORC (PTORC)) using zeotropic mixtures and powered by a geothermal heat source of 100 C. The result revealed that STORC has better net power output when R407A refrigerant is used. Other interesting and useful pieces of literature on ORC systems utilising geothermal sources are those of Liu et al. [7], Mokhtari et al. [8], Sun et al. [9] and Zare [10].

The low- and medium-temperature waste heat from plants and industrial processes is being recovered and utilised by the ORC system to generate electricity [11–13]. Mansoury et al. [11] analyzed a two-stage ORC driven by waste heat recovered from the exhaust gas and cooling water from an engine operating under three modes. The authors carried out a parametric analysis to ascertain how parameters affect the energetic and exergetic performance of the system. Scardigno et al. [14] examined solar thermal ORC systems and optimised the design parameters to obtain maximum efficiencies (first and second law), and minimum cost of energy. The study revealed that the R32-based ORC system demonstrated higher performance over the R143a-based system for energy efficiency but lower for second-law efficiency. The performance and power produced by the ORC are directly affected by the system's operating condition. Moloney et al. [15] analyzed the effects of different turbine inlet temperatures and pressures on the performance of a supercritical ORC system. In that investigation, the system's first- and second-law performance was assessed using various refrigerants, and the system was optimised for maximum thermal and exergy efficiencies, including net output power. Many researchers have recently conducted parametric studies and optimization of ORC systems to improve their thermodynamic performance [16–18]. Wang et al. [18] investigated the effect of an increase in turbine inlet temperature on the ORC first- and second-law efficiencies,

net output power, and turbine sizing factor. A parametric study of the ORC was also performed using several hydrofluoroether refrigerants (HFE7500, HFE7100 and HFE7000) at the same operational conditions. Their results revealed that the HFE7000 showed better performance with regard to the first-law efficiency and net output power. Li [16] analyzed the performance of various ORC system configurations and computed the mass flow rate requirement for a 30kW turbine work ORC system using the energetic and exergetic approaches. The assessment suggested that the condenser temperature had a greater impact on the system's thermal efficiency than the evaporator temperature and the exergy destruction appeared to be in the region of low thermal efficiency.

The present study aims at utilising statistical methods for the optimisation of the first- and second-law efficiencies of different ORC system configurations. To effectively optimise the system's objective functions (performance or/and cost), the optimum parameter combination and impact of weight of an individual parameter must be established statistically. According to the literature, the Taguchi technique and the analysis of variance (ANOVA) method are widely used [19–21]. Bademlioglu et al. [19] utilised the Taguchi and ANOVA methods to investigate the optimum parameter combination and the impact of individual factors on the ORC thermal efficiency. In that study, the evaporator temperature, evaporator's pinch point temperature difference, superheating temperature, condenser's pinch point temperature difference, condenser temperature, turbine and pump isentropic efficiencies, and heat exchanger effectiveness were selected as the operating parameters and their weight on the cycle thermal efficiency were evaluated. The analysis concluded that three parameters (evaporator and condenser temperature, and turbine isentropic efficiency) account for 70% of the total impact ratio, and the best and worst operating conditions obtained produced a thermal efficiency of 18.1% and 9.6%, respectively. In another study, Kumar and Karimi [21] used the Taguchi and ANOVA techniques to obtain the optimum parameter combinations for optimising the energetic performance of the ORC, and the level of importance of individual parameters. Although these methods are well-established and widely used in other areas [22–25], only a few studies have been published on the application for ORC system performance improvement.

Whereas Taguchi and ANOVA techniques are deployed to obtain statistically optimum performance of a system, they are limited to linear objective functions and cannot determine the optimum parameter combinations for multi-response performance characteristics. Grey relational analysis (GRA) is another statistical method capable of evaluating multiple objective functions at the same time [20,27,28]. Bademlioglu et al. [20] performed a multi-objective parametric optimisation of ORC using the Taguchi-GRA method. In their study, the energetic and exergetic performance of the ORC were simultaneously optimised statistically. The multi-response performance characteristic of ORC was shown to be most influenced by the evaporator temperature, turbine efficiency, the effectiveness of the heat exchanger and condenser temperature, with an impact ratio of 31.37%, 19.53%, 16.64% and 16.61%, respectively. The best operating conditions for the multi-response performance of the ORC were calculated as 18.1% and 65.52% for the first and second-law efficiencies, respectively.

In the present study, parametric multi-response optimisation of various ORC configurations is evaluated and a comparative analysis is performed. The Taguchi-GRA statistical method is utilised to simultaneously optimise the first and second-law efficiencies, the contribution ratio of individual parameters, and the best parameter combination on the multi-response performance characteristics of different ORC configurations. The main contribution and benefit of this study can be summarized as follows:

- Perform multi-objective performance optimisation of different ORC configurations (SORC and DPORC) using statistical methods;
- Obtain the best parameter combination (operating conditions) for the multi-response performance characteristics and carry out a comparison of different ORC configurations;
- Investigate the impact of ORC configuration on the parameter contribution ratio to the multi-response performance characteristics of ORC.

2. Materials and methods

2.1. Description of system

Figures 1 and 2 show the schematic diagrams of the simple and dual pressure ORCs, respectively, for geothermal heat source utilization for electricity production. For the simple ORC (Fig. 1), the organic refrigerant fluid leaving the condenser (state 1) is compressed by the pump to the evaporator pressure (state 2). The fluid enthalpy is then increased in the preheater before entering the evaporator (state 3) as saturated liquid and exiting from it (state 4) as a saturated vapour. Geothermal heat is also used to superheat the saturated vapour in the superheater (state 5). The working fluid then undergoes expansion to condenser pressure in the turbine (state 6) and it is cooled in the condenser by the cooling water (state 7) into liquid (state 1).

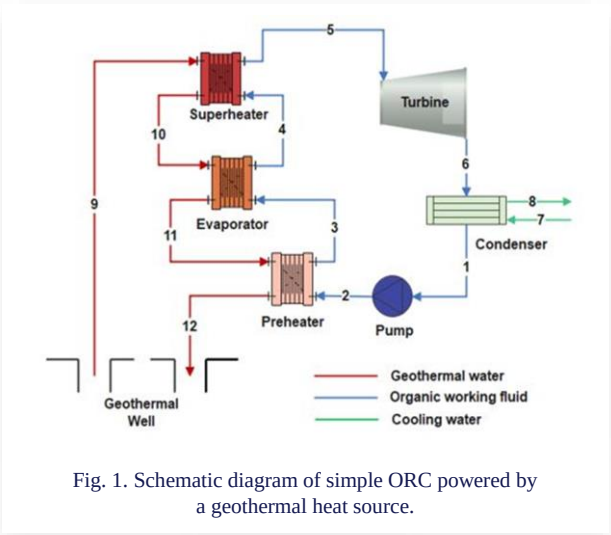


Fig. 1. Schematic diagram of simple ORC powered by a geothermal heat source.

In the dual pressure ORC (Fig. 2), after the refrigerant is pressurized in the low-pressure (LP) pump to LP evaporator pressure (P_{LP}) (state 2), the fluid flows through the preheater-1 where it is further heated and exits at P_{LP} saturated liquid temperature (state 3). The refrigerant flow is then divided into two parts. One part of the fluid is further compressed to high-pressure (HP) evaporator pressure in the (HP) pump (state 3b), while

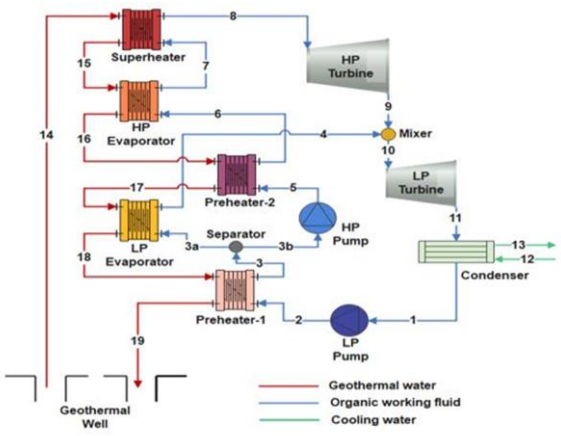


Fig. 2. Schematic diagram of dual pressure ORC powered by a geothermal heat source; LP – low pressure, HP – high pressure.

the other is transferred to the LP evaporator (state 3a). The high-pressure fluid exiting the HP pump (state 5) is channelled through preheater-2, where it absorbs heat before entering the HP evaporator (stage 6). Saturated liquid at P_{LP} temperature enters the HP evaporator and exits as saturated vapour (state 7). The fluid is further superheated before leaving the superheater (state 8) to be expanded in the HP turbine. The refrigerant exiting the HP turbine (state 9) mixes with the fluid from the LP evaporator (state 4) and then undergoes turbine expansion in the LP turbine (state 10). The working fluid vapour exiting the LP turbine (state 11) is condensed in the condenser by cooling water (state 12) into the liquid flow (state 1) exiting the condenser.

For the purpose of this study, to simplify the calculation, the following assumptions were adopted:

- The entire system undergoes steady-state flow conditions;
- Pressure drop and heat losses in the components are negligible;
- Changes in potential and kinetic energy are negligible;
- The range of values of parameters considered in the current study is based on an extensive literature survey by Bademlioglu et al. [20].

2.2. System modelling

Simple and dual-pressure ORC systems are modelled based on an energy and exergy balance at the system's component level. The performance calculation of the physical properties of the fluids utilised is achieved with the help of the Engineering Equation Solver (EES) [29].

2.2.1. Energy and exergy models

The mass and energy conservation relations, including the exergy balance equations for individual system components, are expressed as follows [30,31]:

$$\sum \dot{m}_{in} = \sum \dot{m}_{out}, \quad (1)$$

$$\sum \dot{m}_{in} h_{in} + \dot{Q}_{cv} - \sum \dot{m}_{out} h_{out} - \dot{W}_{cv} = 0, \quad (2)$$

$$\sum \dot{E}x_{in} - \sum \dot{E}x_{out} + \sum \dot{E}x_{heat} + \sum \dot{W}_J - \dot{E}x_{D,J} = 0, \quad (3)$$

where $\dot{m}$ represents mass flow rate, h is the specific enthalpy, $\dot{Q}_{cv}$ is the heat transferred and $\dot{W}_{cv}$ is the work rate. The quantities $\dot{E}x$ and $\dot{E}x_D$ stand for exergy and exergy destruction, respectively. Subscripts *in* and *out* refer to the inlet and outlet, respectively. Subscripts *heat* and *J* pertains to the heat source and *J*-th system component, respectively. The total exergy at each state point is the summation of the physical and chemical exergies when the potential and kinetic components are neglected. It can be expressed as [30]:

$$\dot{E}x = \dot{E}x_{ph} + \dot{E}x_{ch}. \quad (4)$$

The specific physical exergy is expressed as:

$$\dot{E}x_{ph} = \dot{m}[(h - h_0) - T_0(s - s_0)], \quad (5)$$

where s_0 and h_0 are the entropy and enthalpy at the reference state. The physical exergy determines the maximum useful work that can be done when the system state changes from the specific state *(T, P)* to the reference state *(T_0, P_0)*.

The net output power of the SORC and DPORC systems are defined as follows, respectively:

$$\dot{W}_{net,SORC} = \dot{W}_{turb} - \dot{W}_{pump}, \quad (6)$$

$$\dot{W}_{net,DPORC} = (\dot{W}_{HP_{turb}} + \dot{W}_{LP_{turb}}) - (\dot{W}_{HP_{pump}} + \dot{W}_{LP_{pump}}), \quad (7)$$

where $\dot{W}_{turb}$ is the power produced from the turbine and $\dot{W}_{pump}$ is the pump running power. Subscripts *HP* and *LP* refer to high pressure and low pressure, respectively.

The first-law (thermal) and second-law (exergy) efficiencies of the SORC system are defined as, respectively:

$$\eta_{th,SORC} = \frac{\dot{W}_{net,SORC}}{\dot{Q}_{IN}}, \quad (8)$$

$$\eta_{ex,SORC} = \frac{\dot{W}_{net,SORC}}{\dot{E}_{IN}}, \quad (9)$$

and for the DPORC system, they are expressed as:

$$\eta_{th,DPORC} = \frac{\dot{W}_{net,DPORC}}{\dot{Q}_{IN}}, \quad (10)$$

$$\eta_{ex,DPORC} = \frac{\dot{W}_{net,DPORC}}{\dot{E}_{IN}}, \quad (11)$$

where $\dot{Q}_{IN}$ and $\dot{E}_{IN}$ define the heat input and exergy input, respectively, for the SORC and DPORC systems from the geothermal heat source. The heat input $\dot{Q}_{IN}$ is equal to $\dot{Q}_9$ for SORC (Fig. 1) and $\dot{Q}_{14}$ for DPORC (Fig. 2).

The exergy input is defined as follows:

$$\dot{E}_{IN} = \dot{Q}_{IN}\left(1 - \frac{T_0}{T_{IN}}\right), \quad (12)$$

where T_{IN} represents the temperature of the stream at that state.

The energy and exergy equations for each component of the SORC and DPORC systems are shown in Table 1.

The thermodynamic models of SORC and DPORC systems used in this study were initially validated against literature data

[1,32–34]. The thermal efficiencies and evaporator and condenser temperatures of the systems are compared with those obtained from the literature and are presented in Table 2. Results reveal a good agreement between the present results obtained with those published in the literature.

Table 1. Energy and exergy destruction equations for individual components of the cycles.

Cycle	Component	Energy equations	Exergy destruction relations
SORC system	Superheater	$\dot{m}_{w,9}(h_9 - h_{10}) = \dot{m}_f(h_5 - h_4)$ $\dot{Q}_{SupH} = \dot{m}_{w,9}(h_9 - h_{10})$	$\dot{E}x_{D_{SupH}} = (\dot{E}x_9 + \dot{E}x_4) - (\dot{E}x_5 + \dot{E}x_{10})$
	Evaporator	$\dot{m}_{w,10}(h_{10} - h_{11}) = \dot{m}_f(h_4 - h_3)$ $\dot{Q}_{evap} = \dot{m}_{w,10}(h_{10} - h_{11})$	$\dot{E}x_{D_{evap}} = (\dot{E}x_{10} + \dot{E}x_3) - (\dot{E}x_4 + \dot{E}x_{11})$
	Turbine	$\eta_{turb} = \frac{w_A}{w_s} = \frac{h_5 - h_6}{h_5 - h_{6s}}$ $\dot{W}_{turb} = \dot{m}_f(h_5 - h_6)$	$\dot{E}x_{D_{turb}} = \dot{E}x_5 - (\dot{E}x_6 + \dot{W}_{turb})$
	Preheater	$\dot{m}_{w,11}(h_{11} - h_{12}) = \dot{m}_f(h_3 - h_2)$ $\dot{Q}_{PreH} = \dot{m}_{w,11}(h_{11} - h_{12})$	$\dot{E}x_{D_{PreH}} = (\dot{E}x_{11} + \dot{E}x_2) - (\dot{E}x_3 + \dot{E}x_{12})$
	Condenser	$\dot{m}_{w,8}(h_8 - h_7) = \dot{m}_f(h_6 - h_1)$ $\dot{Q}_{cond} = \dot{m}_f(h_6 - h_1)$	$\dot{E}x_{D_{cond}} = (\dot{E}x_6 + \dot{E}x_7) - (\dot{E}x_1 + \dot{E}x_8)$
	Pump	$\eta_{pump} = \frac{w_s}{w_A} = \frac{h_{2s} - h_1}{h_2 - h_1}$ $\dot{W}_{pump} = \dot{m}_f(h_2 - h_1)$	$\dot{E}x_{D_{pump}} = (\dot{E}x_1 + \dot{W}_{pump}) - \dot{E}x_2$
DPORC system	Superheater	$\dot{m}_{w,14}(h_{14} - h_{15}) = \dot{m}_f(h_8 - h_7)$ $\dot{Q}_{SupH} = \dot{m}_f(h_8 - h_7)$	$\dot{E}x_{D_{SupH}} = (\dot{E}x_7 + \dot{E}x_{14}) - (\dot{E}x_8 + \dot{E}x_{10})$
	HP Evaporator	$\dot{m}_{w,15}(h_{15} - h_{16}) = \dot{m}_f(h_7 - h_6)$ $\dot{Q}_{HP_evap} = \dot{m}_f(h_7 - h_6)$	$\dot{E}x_{D_{HP_evap}} = (\dot{E}x_{15} + \dot{E}x_6) - (\dot{E}x_{16} + \dot{E}x_7)$
	HP Turbine	$\eta_{turb} = \frac{w_A}{w_s} = \frac{h_8 - h_9}{h_8 - h_{9s}}$ $\dot{W}_{HP_turb} = \dot{m}_f(h_8 - h_9)$	$\dot{E}x_{D_{HP_turb}} = \dot{E}x_8 - (\dot{E}x_9 + \dot{W}_{HP_turb})$
	Preheater 2	$\dot{m}_{w,16}(h_{16} - h_{17}) = \dot{m}_f(h_6 - h_5)$ $\dot{Q}_{PreH2} = \dot{m}_f(h_6 - h_5)$	$\dot{E}x_{D_{PreH2}} = (\dot{E}x_{16} + \dot{E}x_5) - (\dot{E}x_{17} + \dot{E}x_6)$
	HP Pump	$\eta_{HP_pump} = \frac{w_s}{w_A} = \frac{h_{5s} - h_{3b}}{h_5 - h_{3b}}$ $\dot{W}_{HP_pump} = \dot{m}_f(h_5 - h_{3b})$	$\dot{E}x_{D_{HP_pump}} = (\dot{E}x_{3b} + \dot{W}_{HP_pump}) - \dot{E}x_5$
	LP Evaporator	$\dot{m}_{w,17}(h_{17} - h_{18}) = \dot{m}_f(h_4 - h_{3a})$ $\dot{Q}_{LP_evap} = \dot{m}_f(h_4 - h_{3a})$	$\dot{E}x_{D_{LP_evap}} = (\dot{E}x_{17} + \dot{E}x_{3a}) - (\dot{E}x_4 + \dot{E}x_{18})$
	LP Turbine	$\eta_{turb} = \frac{w_A}{w_s} = \frac{h_{10} - h_{11}}{h_{10} - h_{11s}}$ $\dot{W}_{LP_turb} = \dot{m}_f(h_{10} - h_{11})$	$\dot{E}x_{D_{LP_turb}} = \dot{E}x_{10} - (\dot{E}x_{11} + \dot{W}_{LP_turb})$
	Preheater 1	$\dot{m}_{w,18}(h_{18} - h_{19}) = \dot{m}_f(h_3 - h_2)$ $\dot{Q}_{PreH1} = \dot{m}_f(h_3 - h_2)$	$\dot{E}x_{D_{PreH1}} = (\dot{E}x_{18} + \dot{E}x_2) - (\dot{E}x_3 + \dot{E}x_{19})$
	LP Pump	$\eta_{pump} = \frac{w_s}{w_A} = \frac{h_{2s} - h_1}{h_2 - h_1}$ $\dot{W}_{LP_pump} = \dot{m}_f(h_2 - h_1)$	$\dot{E}x_{D_{LP_pump}} = (\dot{E}x_1 + \dot{W}_{LP_pump}) - \dot{E}x_2$
	Condenser	$\dot{m}_{cw}(h_{13} - h_{12}) = \dot{m}_f(h_{11} - h_1)$ $\dot{Q}_{cond} = \dot{m}_f(h_{11} - h_1)$	$\dot{E}x_{D_{cond}} = (\dot{E}x_{12} + \dot{E}x_{11}) - (\dot{E}x_1 + \dot{E}x_{13})$

Table 2. Validation of parameters and cycle efficiencies.

Performance parameters for SORC/ DPORC	SORC						DPORC					
	Isobutane			R245fa			Isobutane			R245fa		
	Ref. [33]	Present study	Error %	Ref. [34]	Present study	Error %	Ref. [34]	Present study	Error %	Ref. [34]	Present study	Error %
T_{Sat_HP}	-	-	-	-	-	-	113.3	113.3	0.00	133.9	133.9	0.00
T_{Sat_LP}	96.53	96.53	0.00	112.9	112.9	0.00	76.60	76.60	0.00	86.80	86.8	0.00
P_{HP}	-	-	-	-	-	-	2530	2525	-0.197	2520	2516	-0.158
P_{LP}	1861.4	1859	-0.128	1670	1672	+0.119	1230	1251	+1.707	935	935	0.00
$\dot{m}_{HP}$	-	-	-	-	-	-	62.90	62.96	+0.095	141.7	142.4	+0.494
$\dot{m}_{LP}$	82.53	82.92	+0.472	181.8	182	+0.110	32.80	32.62	-0.548	62.20	62.10	-0.161
η_{th}	10.00	10.21	+2.10	12.17	12.31	+1.150	10.22	10.23	+0.097	12.51	12.25	-2.078
η_{sys}	5.97	6.052	+1.373	8.064	8.060	-0.049	7.066	7.032	-0.481	9.306	9.092	-2.299
$\dot{W}_{net}$	3269.9	3324	+1.654	5294	5301	+0.132	3871	3865	-0.154	6108	5984	-2.030

2.3. Methodology

2.3.1. Taguchi optimisation and analysis of S/N ratio

Taguchi optimisation is a design of experiment (DOE) technique that proposes an efficient approach to solving design problems and uses analysis of variance (ANOVA) to rank the order of importance of different factors for a given target function. In the present work, the Taguchi–Grey relational method is applied to simple ORC (SORC) and dual pressure ORC (DPORC) to optimise the parameter factors and levels and determine their order of importance for different ORC configurations.

Figure 3 shows a flow chart representing the application of Taguchi–Grey relational analysis for parametric optimisation of different ORC configurations. In this work, the performance characteristics for the first (N = 1) ORC configuration are initially calculated to obtain the cycle thermal and exergy efficiencies. Different control parameters, levels, and objective functions for the considered ORC configuration are identified. The orthogonal array table for the optimum trial runs is selected based on the number of parameters (factors), levels, and the total degree of freedom (DOF), which is the summation of each parameter's degree of freedom (DOF). For the SORC, Table 3 shows the number of factors and levels used for the analysis. Since there are eight factors with three levels, the total DOF is 25, which is the individual DOF number for each factor of each factor level minus one [20,35]. Therefore, the orthogonal array of L27 (3^8) is used for SORC analysis as shown in Tables 4 and 5. The results from each run, which are the first- and second-law efficiencies of the cycles, are transformed into the S/N ratios. The purpose of the S/N ratio calculation is to estimate the effect of the noise factors on the response and minimize that effect. There are three performance characteristics for calculating the S/N ratios; the lower is better, the nominal is best, and the higher is the better criteria [36]. Since the study seeks the maximization of both target functions (the first- and second-law efficiencies), the S/N ratio of higher is better (HB) is selected for this analysis:

$$\mathrm{S/N_{HB}} = -10\log\left(\frac{1}{n}\sum_{i=1}^{n} 1/y_i^2\right), \qquad (13)$$

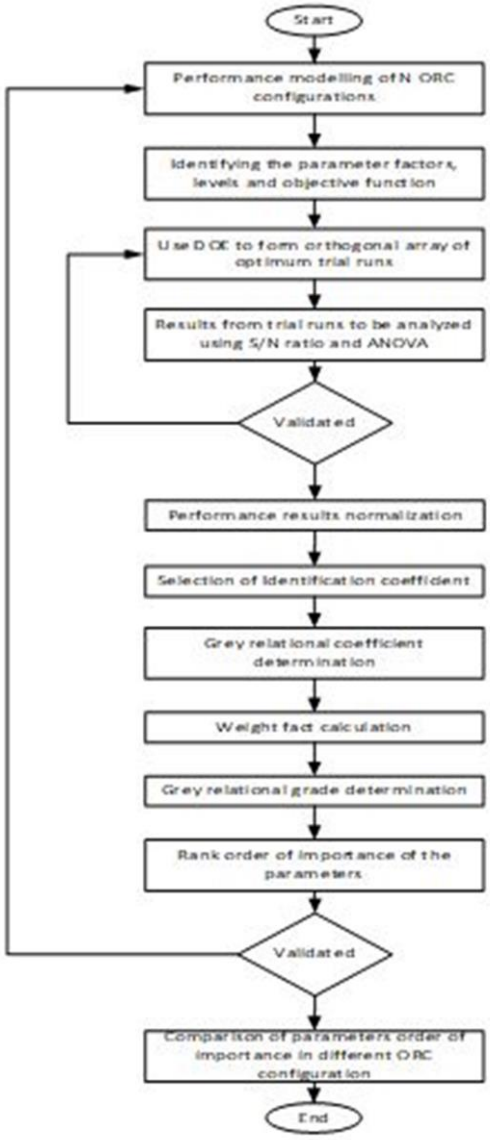


Fig. 3. Flow-chart for Taguchi – grey relational analysis.

Table 3. SORC and DPORC parameters and levels in the analysis.

SORC	DPORC	Parameters	Levels		
			1	2	3
A	A	Working fluid	HFE7000	R245fa	R141b
B	B	$\Delta T_{pp,evap}$	0	10	15
C	C	$\Delta T_{pp,cond}$	0	5	10
D	D	ΔT_{SH}	0	5	10
E	E	T_{evap}	110	130	150
F	F	T_{cond}	30	35	40
G	G	η_{turb}	0.75	0.8	0.85
H	H	η_{pump}	0.75	0.8	0.9
	J	$T_{LP,evap}$	75	80	85

where n refers to the number of cases, and y_i indicates the value of results for the i-th performance calculations.

The analysis of variance (ANOVA) is a good statistical tool for determining the contribution ratio to individual control parameters in the target functions. It is used alongside the Taguchi method to determine the contribution ratio and rank each parameter's significance.

2.3.2. Grey relational analysis

The Taguchi method is incapable of accurately determining the impact of parameters on multi-objective functions at the same time. Therefore, the grey relational analysis (GRA), which is more appropriate for achieving more than one target function simultaneously, is adopted in this study. There are six steps, as indicated in Fig. 3, and they enable the transformation of multi-response optimisation problems into single-response optimisation problems. The procedure begins with normalizing the analysis results of the target responses between the ranges of 0 and 1, also called grey relational generating.

The three common normalization procedures used are higher is better (HB), nominal is best (NB), and lower is better (LB) [26]. Since the aim of this study is the simultaneous maximization of the first- and second-law efficiencies, the HB criterion is selected as given:

$$y_i(k) = \frac{x_i^o(k) - \min x_i^o(k)}{\max x_i^o(k) - \min x_i^o(k)}, \tag{14}$$

where $y_i(k)$ refers to the normalised value of the response result, x^0 is the optimum value, and $\max x_i^o(k)$ and $\min x_i^o(k)$ represent the maximum and minimum values of $x_i^o(k)$, respectively.

After the identification coefficient ϕ has been selected, the grey relational coefficient (ξ_i) is then computed using equations:

$$\xi_i(k) = \frac{\Delta_{min} + \phi\Delta_{max}}{\Delta_{oi}(k) + \phi\Delta_{max}}, \tag{15}$$

$$\Delta_{oi}(k) = y_o(k) - y_i(k), \tag{16}$$

$$\Delta_{max} = \max_{\forall j \in i} \max_{\forall k} \left(y_o(k) - y_j(k) \right), \tag{17}$$

$$\Delta_{min} = \min_{\forall j \in i} \min_{\forall k} \left(y_o(k) - y_j(k) \right), \tag{18}$$

where $y_0(k)$ is the reference sequence, $y_i(k)$ is the comparative sequence, and Δ_{0i} is the difference between $y_0(k)$ and $y_i(k)$. Quantities Δ_{min} and Δ_{max} are the minimum and maximum values of Δ_{0i}, respectively. The value of the identification coefficient is in the range $0 < \phi < 1$ and is generally taken as 0.5. Grey relational coefficient (ξ_i) indicates the correlation between the target and actual normalized values [26].

Each factor/parameter of the objective function is weighted based on the degree of its influence on the first- and second-law efficiencies. For each response, the difference between the maximum and minimum values of each parameter's S/N ratio is known as *Delta* (see the fourth row in Table 5 and the fifth row in Table 7). The sum of the values of *Delta* for each parameter of each response is obtained (see the fifth row in Table 5 and the sixth row in Table 7). Then the weight factor is calculated as the ratio of the sum of the values of *Delta* from each parameter to the total value of *Delta* of the entire responses (see the seventh row in Tables 5 and 7) in accordance with the expression [37]:

$$w_i = \frac{\sum_{j=1}^{p} Delta_{ij}}{\sum_{i=1}^{m}\sum_{j=1}^{p} Delta_{ij}}, \tag{19}$$

where p is the number of parameters and m is the number of responses.

Finally, the grey relational grade (γ_i) for different weight factors, which indicates the degree of the relationship between the reference and comparative sequences is calculated. Since this study aims to maximize the first- and second-law efficiencies, the best result will correspond to the maximum grey relational grade.

The total grey relational grade for a given weight factor is expressed as follows:

$$\gamma_i = \frac{1}{2}\sum_{k=1}^{n} w_k \xi_i(k), \tag{20}$$

where n is the number of runs, w_k is the weight factor for k-th performance characteristics.

3. Results and discussion

As aforementioned, this work investigates the multi-parameter performance optimisation of SORC and DPORC, while simultaneously accounting for both the thermal and exergy efficiencies. The main aim of this work is to establish the order of importance and optimised parameter combination for both SORC and DPORC configurations and compare the results. The Taguchi method provides a quantitative impact of individual parameters on the cycle performance. The grey relational analysis (GRA) is then deployed for the optimisation of parameters affecting the cycles with multi-objective functions, such as thermal and exergy efficiencies. The parameters and levels of the SORC and DPORC are presented in Table 3. The L27 (3^8) and L27 (3^9) orthogonal arrays were designed for a standard three-level orthogonal array with 8 and 9 variables for SORC and DPORC, respectively. Tables 4 and 5 show 27 different cases with various combinations of factors in the orthogonal array. The analysis calculates the first- and second-law efficiencies for these cases, which are then transformed into S/N ratios, as shown in Tables 4 and 5.

Table 4. SORC L27 orthogonal array with their first and second-law efficiencies and S/N ratios.

	Parameters											
	A	B	C	D	E	F	G	H	Results		S/N Ratio	
Cases	Levels								η_{th}	η_{ex}	η_{th}	η_{ex}
1	1	1	1	1	1	1	1	1	11.53	62.11	-18.763	-4.137
2	1	1	1	1	2	2	2	2	12.99	59.82	-17.728	-4.463
3	1	1	1	1	3	3	3	3	14.20	58.45	-16.985	-4.664
4	1	2	2	2	1	1	1	2	10.84	60.63	-19.299	-4.346
5	1	2	2	2	2	2	2	3	12.37	58.52	-18.153	-4.654
6	1	2	2	2	3	3	3	1	13.35	57.03	-17.490	-4.878
7	1	3	3	3	1	1	1	3	10.16	59.23	-19.862	-4.549
8	1	3	3	3	2	2	2	1	11.56	57.14	-18.741	-4.861
9	1	3	3	3	3	3	3	2	12.74	55.80	-17.897	-5.067
10	2	1	2	3	1	2	3	1	12.40	53.60	-18.132	-5.417
11	2	1	2	3	2	3	1	2	11.82	50.83	-18.548	-5.878
12	2	1	2	3	3	1	2	3	15.33	51.02	-16.289	-5.845
13	2	2	3	1	1	2	3	2	11.63	57.31	-18.688	-4.835
14	2	2	3	1	2	3	1	3	11.17	54.70	-19.039	-5.240
15	2	2	3	1	3	1	2	1	14.07	55.14	-17.034	-5.171
16	2	3	1	2	1	2	3	3	13.26	55.11	-17.549	-5.175
17	2	3	1	2	2	3	1	1	12.36	52.04	-18.159	-5.673
18	2	3	1	2	3	1	2	2	15.76	52.35	-16.065	-5.622
19	3	1	3	2	1	3	2	1	10.85	49.55	-19.291	-6.099
20	3	1	3	2	2	1	3	2	15.47	50.55	-16.210	-5.926
21	3	1	3	2	3	2	1	3	14.49	47.90	-16.779	-6.393
22	3	2	1	3	1	3	2	2	12.49	48.88	-18.069	-6.217
23	3	2	1	3	2	1	3	3	17.12	50.33	-15.329	-5.963
24	3	2	1	3	3	2	1	1	15.72	47.31	-16.071	-6.501
25	3	3	2	1	1	3	2	3	11.70	50.86	-18.636	-5.872
26	3	3	2	1	2	1	3	1	16.18	51.67	-15.820	-5.735
27	3	3	2	1	3	2	1	2	15.01	48.75	-16.472	-6.241

Table 5. DPORC L27 orthogonal array with their first and second-law efficiencies and S/N ratios.

	Parameters												
	A	B	C	D	E	F	G	H	J	Results		S/N Ratio	
Case	Levels									η_{th}	η_{ex}	η_{th}	η_{ex}
1	1	1	1	1	1	1	1	1	1	11.14	58.10	-19.062	-4.716
2	1	1	1	1	2	2	2	2	2	11.99	58.46	-18.424	-4.662
3	1	1	1	1	3	3	3	3	3	11.94	59.77	-18.460	-4.470
4	1	2	2	2	1	1	1	2	2	10.30	57.62	-19.743	-4.788
5	1	2	2	2	2	2	2	3	3	10.91	58.57	-19.244	-4.646
6	1	2	2	2	3	3	3	1	1	8.382	62.34	-21.533	-4.104
7	1	3	3	3	1	1	1	3	3	9.627	57.09	-20.330	-4.868
8	1	3	3	3	2	2	2	1	1	8.938	59.67	-20.975	-4.484
9	1	3	3	3	3	3	3	2	2	7.179	63.83	-22.879	-3.899
10	2	1	2	3	1	2	3	1	2	11.76	50.83	-18.592	-5.877
11	2	1	2	3	2	3	1	2	3	10.63	49.97	-19.469	-6.025
12	2	1	2	3	3	1	2	3	1	11.98	50.76	-18.431	-5.889
13	2	2	3	1	1	2	3	2	3	11.01	53.18	-19.164	-5.485
14	2	2	3	1	2	3	1	3	1	9.009	52.35	-20.907	-5.621
15	2	2	3	1	3	1	2	1	2	10.40	52.57	-19.659	-5.585
16	2	3	1	2	1	2	3	3	1	12.11	51.62	-18.337	-5.743
17	2	3	1	2	2	3	1	1	2	10.16	50.54	-19.862	-5.927
18	2	3	1	2	3	1	2	2	3	11.23	51.05	-18.992	-5.840
19	3	1	3	2	1	3	2	1	3	10.09	46.24	-19.922	-6.699
20	3	1	3	2	2	1	3	2	1	12.38	47.43	-18.146	-6.478
21	3	1	3	2	3	2	1	3	2	9.545	45.54	-20.405	-6.832
22	3	2	1	3	1	3	2	2	1	11.02	45.80	-19.156	-6.782
23	3	2	1	3	2	1	3	3	2	13.95	47.70	-17.109	-6.429
24	3	2	1	3	3	2	1	1	3	10.54	45.48	-19.543	-6.843
25	3	3	2	1	1	3	2	3	2	10.40	46.64	-19.659	-6.624
26	3	3	2	1	2	1	3	1	3	13.21	48.02	-17.582	-6.371
27	3	3	2	1	3	2	1	2	1	7.719	44.56	-22.249	-7.021

To ensure the integrity of this study for both first and second-law analysis, the response table with average S/N ratios, the rank or order of importance of the parameters, and the graphs showing the parameter contribution ratios for SORC and DPORC are presented. Table 6 shows the average S/N ratios and parameter ranking (order of significance) on the SORC's first- and second-law efficiencies. The order of importance of parameters with regard to the first-law (thermal) efficiency is T_{evap} > working fluid > T_{cond} > η_{turb} > $\Delta T_{pp,\,cond}$ > η_{pump} > $\Delta T_{pp,evap}$ > ΔT_{SH}, and for the

Table 6. SORC average S/N ratios for the first and second-law efficiencies.

Parameters	First-law efficiency							
Levels	A	B	C	D	E	F	G	H
1	-18.32	-17.64	-17.19	-17.69	-18.70	-17.19	-18.11	-17.72
2	-17.72	-17.69	-17.65	-17.67	-17.53	-17.59	-17.78	-17.66
3	-16.96	-17.69	-18.17	-17.66	-16.79	-18.23	-17.12	-17.62
Delta (max-min)	1.36	0.05	0.98	0.03	1.91	1.05	0.99	0.10
Rank	2	7	5	8	1	3	4	6
$\sum Delta$	6.47							
Weight	68.66%							
	Second-law efficiency							
Levels	A	B	C	D	E	F	G	H
1	-4.624	-5.425	-5.380	-5.151	-5.183	-5.255	-5.440	-5.386
2	-5.428	-5.312	-5.430	-5.418	-5.377	-5.393	-5.423	-5.399
3	-6.105	-5.422	-5.349	-5.589	-5.598	-5.510	-5.296	-5.373
Delta (max-min)	1.481	0.113	0.080	0.438	0.415	0.255	0.144	0.026
Rank	1	6	7	2	3	4	5	8
$\sum Delta$	2.95							
Weight	31.33%							

Table 7. SORC ANOVA table for first- and second-law efficiency.

	Parameters	DOF	SS	MS	F	Contribution, %	DOF	SS	MS	F	Contribution, %
	First-law efficiency						Second-law efficiency				
A	Working fluid	2	8.3589	4.17944	474.60	21.34	2	9.8930	4.94649	8641.24	82.01
B	$\Delta T_{pp,evap}$	2	0.0160	0.00798	0.91	0.04	2	0.0745	0.03726	65.09	0.62
C	$\Delta T_{pp,cond}$	2	4.3294	2.16470	245.82	11.06	2	0.0297	0.01484	25.92	0.25
D	ΔT_{SH}	2	0.0031	0.00157	0.18	0.01	2	0.8767	0.43836	765.80	7.27
E	T_{evap}	2	16.7349	8.36746	950.18	42.73	2	0.7754	0.38768	677.25	6.43
F	T_{cond}	2	5.0378	2.51890	286.04	12.86	2	0.2935	0.14675	256.37	2.43
G	η_{turb}	2	4.5500	2.27499	258.34	11.62	2	0.1116	0.05578	97.45	0.92
H	η_{pump}	2	0.0437	0.02183	2.48	0.11	2	0.0031	0.00156	2.73	0.03
	Error	10	0.0881	0.00881		0.22	10	0.0057	0.00057		0.05
	Total	26	39.1618			100.00	26	12.0632			100.00

second-law (exergy) efficiency it is Working fluid > ΔT_{SH} > T_{evap} > T_{cond} > η_{turb} > $\Delta T_{pp,evap}$ > $\Delta T_{pp,cond}$ > η_{pump}, as shown in Table 6.

After the Taguchi analysis, analysis of variance (ANOVA) is performed to determine the contribution ratios of the parameters, and for the first-law efficiency, the parameters with the highest influence are found to be the evaporator temperature (E), working fluid (A), condenser temperature (F) and turbine efficiency (G), with contribution ratios of 42.73%, 21.34%, 12.73% and 11.62%, respectively, as presented in Table 7. The study concludes that the findings from the Taguchi and ANOVA methods are compatible with each other.

From Fig. 4, the optimum operating conditions are determined as working fluid = R141b (A_3), $\Delta T_{pp,evap}$ = 0°C (B_1), $\Delta T_{pp,\ cond}$ = 0°C (C_1), ΔT_{SH} = 10°C (D_3), T_{evap} = 150°C (E_3), T_{cond} = 30°C (F_1), η_{turb} = 85% (G_3) and η_{pump} = 90% (H_3), and under these conditions, the first-law efficiency of SORC is computed as 18.78%.

Similarly, the most effective parameters influencing the second-law efficiency of SORC are determined as working fluid, degree of superheating, evaporator temperature, and condenser temperature, with contribution ratios of 82.01%, 7.27%, 6.43% and 2.43%, respectively, as shown in Table 6. The optimum operating conditions for the second-law efficiency objective function of SORC are determined as working fluid = HFE7000 (A_1), $\Delta T_{pp,evap}$ = 5°C (B_2), $\Delta T_{pp,\ cond}$ = 10°C (C_3), ΔT_{SH} = 0°C (D_1), T_{evap} = 110°C (E_1), T_{cond} = 30°C (F_1), η_{turb} = 85% (G_3) and η_{pump} = 90% (H_3), as presented in Fig. 5. For these conditions (A_1 B_2 C_3 D_1 E_1 F_1 G_3 H_3), the second-law efficiency is calculated as 65.09%, which is clearly higher than the efficiencies of cases 1–27 (see Table 4). The contribution ratio or importance level of the different parameters on the target objective function, as determined by the ANOVA method, is presented in Table 6. It can be observed that the Taguchi and ANOVA methods are in complete agreement as regards the order of importance of the parameters. Indicating that the working fluid has the highest influence on the exergy efficiency with about 82.01%, ΔT_{SH}, T_{evap}, and T_{cond} have a total effect of 16.13%, and other parameters cumulatively account for 1.86% of the exergy efficiency.

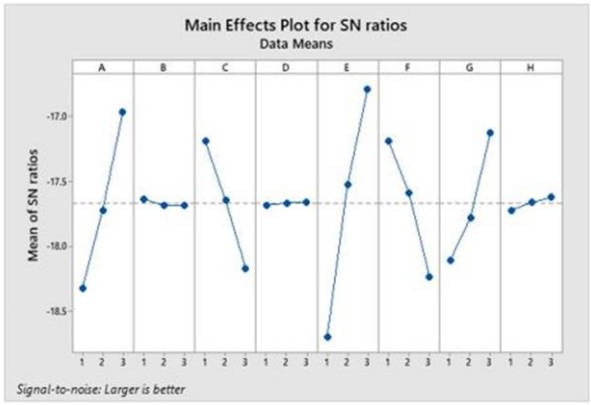


Fig. 4. Effect of each parameter on SORC first-law efficiency.

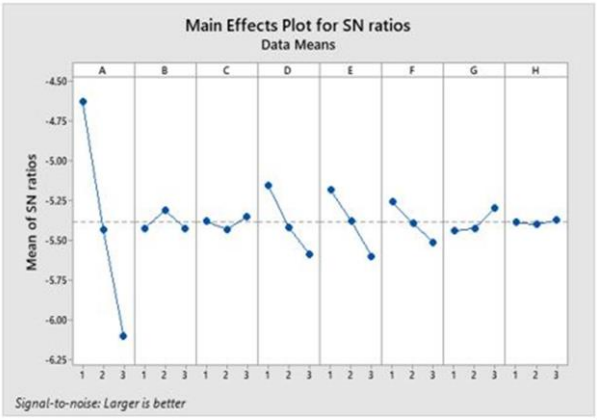


Fig. 5. Effect of each parameter on SORC second-law efficiency.

Table 8. DPORC average S/N ratios for the first- and second-law efficiencies.

Parameters	**First-law efficiency**								
Levels	A	B	C	D	E	F	G	H	J
1	-20.07	-18.99	-18.77	-19.46	-19.33	-18.78	-20.17	-19.64	-19.87
2	-19.27	-19.56	-19.61	-19.58	-19.08	-19.66	-19.38	-19.80	-19.59
3	-19.31	-20.10	-20.27	-19.61	-20.24	-20.21	-19.09	-19.21	-19.19
***Delta* (max-min)**	0.80	1.11	1.49	0.15	1.16	1.42	1.09	0.59	0.68
Rank	6	4	1	9	3	2	5	8	7
$\sum Delta$	8.49								
Weight	71.62%								
	Second-law efficiency								
Levels	A	B	C	D	E	F	G	H	J
1	-4.516	-5.739	-5.713	-5.618	-5.732	-5.663	-5.849	-5.623	-5.649
2	-5.777	-5.588	-5.706	-5.673	-5.628	-5.733	-5.691	-5.665	-5.625
3	-6.676	-5.642	-5.551	-5.678	-5.610	-5.573	-5.429	-5.681	-5.695
***Delta* (max-min)**	2.160	0.152	0.162	0.060	0.122	0.160	0.421	0.057	0.069
Rank	1	5	3	8	6	4	2	9	7
$\sum Delta$	3.363								
Weight	28.37%								

The Taguchi and ANOVA results of the DPORC system's parameters importance level are displayed in Tables 8 and 9, respectively. Result analysis indicates that the order of parameter influence on the DPORC first-law (thermal) efficiency is $\Delta T_{pp,cond} > T_{cond} > T_{evap} > \Delta T_{pp,evap} > \eta_{turb} >$ working fluid $> T_{LP,evap} > \eta_{pump} > \Delta T_{SH}$, and for the second-law (exergy) efficiency is working fluid $> \eta_{turb} > \Delta T_{pp,cond} > T_{cond} > \Delta T_{pp,evap} > T_{evap} > T_{LP,evap} > \Delta T_{SH} > \eta_{pump}$, as shown in Table 8.

As presented in Table 9, the parameters with the most significance on the first-law efficiency performance are $\Delta T_{pp,cond}$ (C), T_{cond} (F) and T_{evap} (E), with contribution ratios of 21.61%, 19.83% and 14.36%, respectively. For the second-law (exergy) efficiency, the parameters with significant influence are the working fluid (A) and turbine efficiency (G), with contribution ratios of 93.53% and 3.58%, respectively, and the other parameters cumulatively accounting for about 2.89%.

Table 9. DPORC ANOVA table for first- and second-law efficiency.

	Parameters	**DOF**	**SS**	**MS**	**F**	**Contribution, %**	**DOF**	**SS**	**MS**	**F**	**Contribution, %**
	First-law efficiency						Second-law efficiency				
A	Working fluid	2	3.696	1.8483	7.93	7.92	2	21.196	10.5981	585.55	93.53
B	$\Delta T_{pp,evap}$	2	5.508	2.7542	11.81	11.81	2	0.106	0.0531	2.94	0.47
C	$\Delta T_{pp,cond}$	2	10.088	5.0441	21.63	21.61	2	0.151	0.0756	4.18	0.67
D	ΔT_{SH}	2	0.106	0.0530	0.23	0.23	2	0.020	0.0102	0.56	0.09
E	T_{evap}	2	6.701	3.3503	14.37	14.36	2	0.078	0.0392	2.17	0.35
F	T_{cond}	2	9.254	4.6274	19.85	19.83	2	0.116	0.0580	3.20	0.51
G	η_{turb}	2	5.668	2.8442	12.15	12.15	2	0.811	0.4058	22.42	3.58
H	η_{pump}	2	1.688	0.8442	3.62	3.62	2	0.015	0.0079	0.44	0.07
J	$T_{LP,evap}$	2	2.084	1.0422	4.47	4.47	2	0.022	0.0111	0.62	0.10
	Error	8	1.865	0.2331		4.00	8	0.144	0.0181		0.64
	Total	26	46.661			100.00	26	22.662			100.00

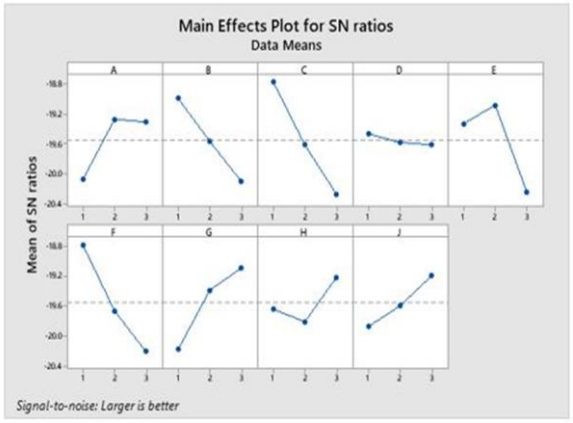


Fig. 6. Effect of each parameter on DPORC first-law efficiency.

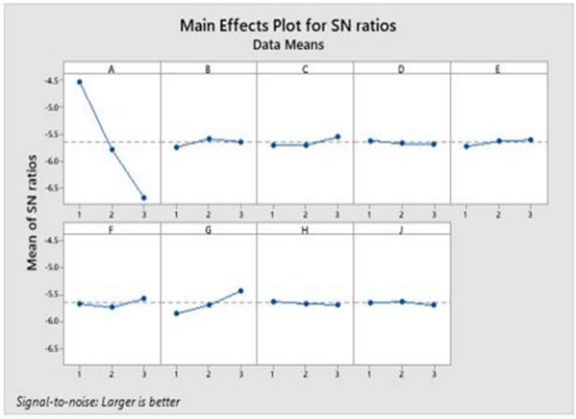


Fig. 7. Effect of each parameter on DPORC second-law efficiency.

The optimum operating condition of the DPORC system for maximum thermal and exergy efficiencies can be determined from Figs. 6 and 7, respectively. It is observed that the operating conditions of working fluid = R245fa (A_2), $\Delta T_{pp,evap}$ = 0°C (B_1), $\Delta T_{pp,cond}$ = 0°C (C_1), ΔT_{SH} = 0°C (D_1), T_{evap} = 130°C (E_2), T_{cond} = 30°C (F_1), η_{turb} = 85% (G_3) and η_{pump} = 90% (H_3), and $T_{LP,evap}$ = 85°C (J_3) produced the optimum first-law efficiency, and the operating conditions of working fluid = HFE7000 (A_1), $\Delta T_{pp,evap}$ = 10°C (B_2), $\Delta T_{pp,cond}$ = 10°C (C_3), ΔT_{SH} = 0°C (D_1), T_{evap} = 150°C (E_3), T_{cond} = 40°C (F_3), η_{turb} = 85% (G_3) and η_{pump} = 75% (H_1), and $T_{LP,evap}$ = 80°C (J_2) produced the optimum exergy efficiency of the DPORC system, as shown in Figs. 6 and 7, respectively. For the condition ($A_2B_1C_1D_1E_2F_1G_3H_3J_3$) the thermal efficiency is calculated as 14.64%, and for ($A_1B_2C_3D_1E_3F_3G_3H_1J_2$) the exergy efficiency is computed as 63.08%.

Up to this point in the analysis, the first- and second-law efficiencies have been optimised separately. However, to carry out the multi-response performance optimization, the grey relational

Table 10. Normalized results, grey relational coefficients, grey relational grade and order.

	SORC						DPORC					
Case	Normalized results		Grey relational coefficients		Grey relational grade	Order	Normalized results		Grey relational coefficients		Grey relational grade	Order
	η_{th}	η_{ex}	η_{th}	η_{ex}			η_{th}	η_{ex}	η_{th}	η_{ex}		
1	0.1968	1.0000	0.3837	1.0000	0.5767	8	0.5850	0.7026	0.5464	0.6270	0.5692	8
2	0.4066	0.8453	0.4573	0.7637	0.5532	9	0.7105	0.7213	0.6333	0.6421	0.6357	4
3	0.5733	0.7527	0.5395	0.6691	0.5800	6	0.7031	0.7893	0.6274	0.7035	0.6489	3
4	0.0977	0.9000	0.3566	0.8333	0.5059	13	0.4609	0.6777	0.4812	0.6081	0.5172	14
5	0.3132	0.7574	0.4213	0.6733	0.5002	14	0.5510	0.7270	0.5269	0.6468	0.5609	9
6	0.4583	0.6568	0.4800	0.5930	0.5154	12	0.1777	0.9227	0.3781	0.8661	0.5165	15
7	0.0000	0.8054	0.3333	0.7198	0.4544	19	0.3615	0.6502	0.4392	0.5884	0.4815	18
8	0.2011	0.6642	0.3849	0.5982	0.4517	20	0.2598	0.7841	0.4032	0.6984	0.4869	16
9	0.3707	0.5736	0.4428	0.5397	0.4731	17	0.0000	1.0000	0.3333	1.0000	0.5224	11
10	0.3218	0.4250	0.4244	0.4651	0.4371	21	0.6766	0.3254	0.6072	0.4257	0.5556	10
11	0.2385	0.2378	0.3964	0.3961	0.3963	25	0.5097	0.2807	0.5049	0.4101	0.4780	20
12	0.7428	0.2507	0.6603	0.4002	0.5787	7	0.7091	0.3217	0.6322	0.4243	0.5732	7
13	0.2112	0.6757	0.3880	0.6066	0.4564	18	0.5658	0.4473	0.5352	0.4750	0.5181	13
14	0.1451	0.4993	0.3690	0.4997	0.4099	23	0.2703	0.4043	0.4066	0.4563	0.4207	25
15	0.5618	0.5291	0.5329	0.5150	0.5272	11	0.4757	0.4157	0.4881	0.4611	0.4804	19
16	0.4454	0.5270	0.4741	0.5139	0.4865	16	0.7283	0.3664	06479	0.4411	0.5892	6
17	0.3161	0.3196	0.4223	0.4236	0.4227	22	0.4403	0.3103	0.4718	0.4203	0.4571	21
18	0.8003	0.3405	0.7146	0.4312	0.6257	3	0.5983	0.3368	0.5545	0.4298	0.5191	12
19	0.0991	0.1514	0.3569	0.3708	0.3612	27	0.4299	0.0872	0.4672	0.3539	0.4350	24
20	0.7629	0.2189	0.6783	0.3903	0.5880	5	0.7681	0.1489	0.6832	0.3701	0.5943	5
21	0.6221	0.0399	0.5695	0.3424	0.4983	15	0.3494	0.0509	0.4346	0.3450	0.4091	26
22	0.3348	0.1061	0.4291	0.3587	0.4070	24	0.5673	0.0644	0.5361	0.3483	0.4828	17
23	1.0000	0.2041	1.0000	0.3858	0.8075	1	1.0000	0.1629	1.0000	0.3739	0.8223	1
24	0.7989	0.0000	0.7132	0.3333	0.5941	4	0.4964	0.0477	0.4982	0.3443	0.4545	22
25	0.2213	0.2399	0.3910	0.3968	0.3928	26	0.4757	0.1079	0.4881	0.3592	0.4515	23
26	0.8649	0.2946	0.7873	0.4148	0.6705	2	0.8907	0.1796	0.8206	0.3787	0.6952	2
27	0.6968	0.0973	0.6225	0.3565	0.5391	10	0.0798	0.0000	0.3521	0.3333	0.3467	27

Table 11. SORC response table for grey relational grade.

Parameters								
Levels	A	B	C	D	E	F	G	H
1	-5.845	-6.016	-5.184	-5.748	-6.953	-4.653	-6.306	-6.057
2	-6.434	-5.778	-6.070	-6.112	-5.697	-6.029	-6.357	-6.030
3	-5.628	-6.113	-6.654	-6.047	-5.257	-7.225	-5.243	-5.820
Delta	0.806	0.336	1.470	0.365	1.696	2.572	1.114	0.237
Rank	5	7	3	6	2	1	4	8

Table 12. SORC ANOVA table for grey relational grade.

	Parameters	DOF	SS	MS	F	Contribution, %
A	Working fluid	2	3.1352	1.5676	13.43	4.71
B	$\Delta T_{pp,evap}$	2	0.5360	0.2680	2.28	0.81
C	$\Delta T_{pp,cond}$	2	9.8603	4.9301	41.96	14.81
D	ΔT_{SH}	2	0.6800	0.3400	2.89	1.02
E	T_{evap}	2	13.9512	6.9756	59.37	20.96
F	T_{cond}	2	29.8167	14.9084	126.88	44.79
G	η_{turb}	2	7.1188	3.5594	30.29	10.69
H	η_{pump}	2	0.3031	0.1515	1.29	0.46
	Error	10	1.1750	0.1175		1.76
	Total	26	66.5762			100.00

analysis (GRA) method is utilised to linearize the first and second-law efficiency target functions to a single multi-response performance function. As mentioned previously, the GRA method optimises the operating condition to obtain maximum first- and second-law efficiencies, simultaneously. The procedure for the GRA method is implemented as illustrated in the flowchart in Fig. 3, and the results, including order of importance, are shown in Table 10. The calculation of the weight factor of each target function (first- and second-law efficiency) has a strong effect in determining a realistic result of the multi-response performance and the grey relational grade (GRG). Based on Eq. (16), the weight factors of the first- and second-law efficiencies are 68.66% and 31.33% for SORC, and 71.62% and 28.37% for DPORC, respectively, as shown in Tables 6 and 8. Therefore, the equation of the grey relational grade (GRG) based on their weight factors for the SORC and DPORC systems can be expressed as, respectively:

$$\mathrm{GRG}_{SORC} = 0.6866\mathrm{GRC}_{\eta_{th,SORC}} + 0.3133\mathrm{GRC}_{\eta_{ex,SORC}}, \quad (21)$$

$$\mathrm{GRG}_{DPORC} = 0.7162\mathrm{GRC}_{\eta_{th,DPORC}} + 0.2837\mathrm{GRC}_{\eta_{ex,DPORC}} \quad (22)$$

where $\mathrm{GRC}_{\eta_{th,SORC}}$, $\mathrm{GRC}_{\eta_{ex,SORC}}$, $\mathrm{GRC}_{\eta_{th,DPORC}}$, $\mathrm{GRC}_{\eta_{ex,DPORC}}$ represent the first- and second-law efficiency's grey relational coefficients (GRCs) for SORC and DPORC systems, respectively.

The variation in grey relational grade (GRG) for the different multi-response performance cases (1 – 27) of the SORC and DPORC systems is illustrated in Table 10. It can be observed that case 23 ($A_3B_2C_1D_3E_2F_1G_3H_3$) and case 19 ($A_3B_1C_3D_2E_1F_3G_2H_1$) for the SORC system, and case 23 ($A_3B_2C_1D_3E_2F_1G_3H_3J_2$) and case 27 ($A_3B_3C_2\ D_1E_3F_2G_1H_2J_1$) for

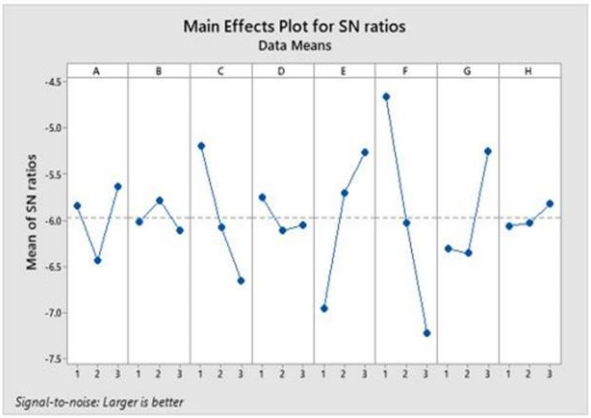


Fig. 8. Effect of each parameteron the multi-response characteristics for SORC system.

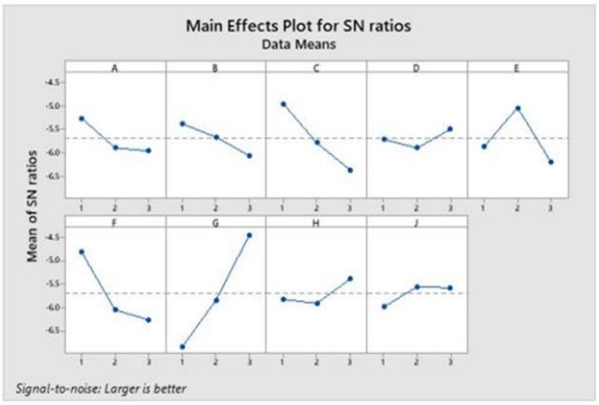


Fig. 9. Effect of each parameter on the multi-response characteristics for DPORC system.

the DPORC system, have the maximum and minimum values of GRG among cases 1 – 27, respectively.

From Figs. 8 and 9, the optimum parameter combinations for maximum first- and second-law efficiency (multi-response performance) for the SORC system are determined as working fluid = R141b (A_3), $\Delta T_{pp,evap}$ = 10°C (B_2), $\Delta T_{pp,cond}$ = 0°C (C_1), ΔT_{SH} = 0°C (D_1), T_{evap} = 150°C (E_3), T_{cond} = 30°C (F_1), η_{turb} = 85% (G_3) and η_{pump} = 90% (H_3), and for the DPORC system as working fluid = HFE7000 (A_1), $\Delta T_{pp,evap}$ = 0°C (B_1), $\Delta T_{pp,cond}$ = 0°C (C_1), ΔT_{SH} = 10°C (D_3), T_{evap} = 130°C (E_2), T_{cond} = 30°C (F_1), η_{turb} = 85% (G_3) and η_{pump} = 90% (H_3), and $T_{LP,evap}$ = 80°C (J_2). The first- and second-law efficiencies are calculated as 18.64% and 51.69% for SORC and 13.17% and 57.33% for DPORC, respectively, within these optimum conditions for the multi-response performance characteristics.

Furthermore, the response table for the grey relational grade (GRG) of SORC and DPORC systems is generated to determine the importance level of each parameter. For the SORC system, the order of importance of parameters is T_{cond} (44.79%) > T_{evap} (20.96%) > $\Delta T_{pp,cond}$ (14.81%) > η_{turb} (10.69%) > working fluid (4.71%) > ΔT_{SH} (1.02%) > $\Delta T_{pp,evap}$ (0.81%) > η_{pump} (0.46%), and the ANOVA results of the GRG of SORC are presented in Table 11 and 12. The order of importance of parameters for the multi-response performance characteristics of the DPORC system is η_{turb} > T_{cond} > $\Delta T_{pp,cond}$ > T_{evap} > working fluid > $\Delta T_{pp,evap}$ > η_{pump} > $T_{LP,evap}$ > ΔT_{SH}, as shown in Table 13, and with contribution ratios of 44.79%, 20.96%, 14.81%, 10.69%, 4.71%, 1.02%, 0.81% and 0.46%, respectively (Table 14**)**.

A comparison of parameter contribution ratios to the multi-performance characteristics for SORC and DPORC systems is shown in Figs. 10 and 11, respectively.

Table 13. DPORC response table for grey relational grade.

Parameters									
Levels	A	B	C	D	E	F	G	H	J
1	-5.257	-5.383	-4.950	-5.717	-5.871	-4.805	-6.835	-5.822	-5.987
2	-5.893	-5.662	-5.789	-5.899	-5.035	-6.048	-5.841	-5.907	-5.549
3	-5.961	-6.066	-6.373	-5.496	-6.205	-6.259	-4.436	-5.383	-5.576
Delta	0.704	0.683	1.423	0.403	1.170	1.454	2.399	0.524	0.437
Rank	5	6	3	9	4	2	1	7	8

Table 14. DPORC ANOVA table for grey relational grade.

	Parameters	DOF	SS	MS	F	Contribution, %
A	Working fluid	2	2.7170	1.3585	8.17	4.35
B	$\Delta T_{pp,evap}$	2	2.1208	1.0604	6.38	3.40
C	$\Delta T_{pp,cond}$	2	9.2062	4.6031	27.68	14.75
D	ΔT_{SH}	2	0.7335	0.3668	2.21	1.18
E	T_{evap}	2	6.5366	3.2683	19.66	10.47
F	T_{cond}	2	11.1119	5.5559	33.41	17.80
G	η_{turb}	2	26.1531	13.0766	78.64	41.90
H	η_{pump}	2	1.4245	0.7123	4.28	2.28
J	$T_{LP,evap}$	2	1.0819	0.5409	3.25	1.73
	Error	8	1.3302	0.1663		2.13
	Total	26	62.4158			100.00

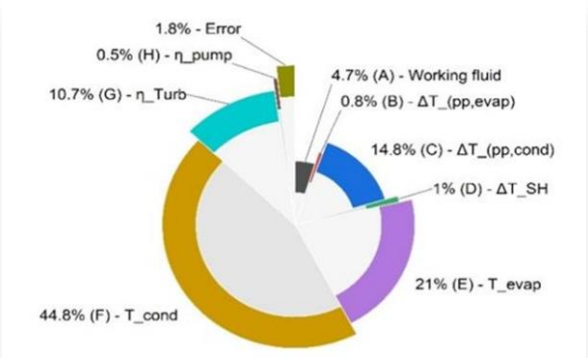


Fig. 10. Contribution ratio of each parameter to multi-response characteristics of SORC.

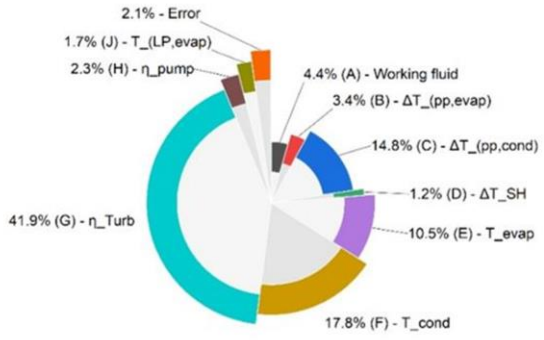


Fig. 11. Contribution ratio of each parameter to multi-response characteristics of DPORC.

4. Conclusions

This work uses the Taguchi–GRA method to optimise parameter combinations for maximum multi-response performance characteristics. The contribution ratios of parameters to the characteristics of SORC and DPORC systems are determined, and comparative analysis is performed. In this study, the fundamental parameters used for the analysis are working fluid, pinch

point temperature difference in the evaporator, pinch point temperature difference in the condenser, superheating temperature, evaporator temperature, condenser temperature, turbine and pump efficiencies for the SORC system. For the DPORC system, the LP turbine evaporation temperature is added to all parameters selected previously for SORC. The effects of these parameters on SORC and DPORC first and second law efficiencies are investigated. The grey relational analysis method is then deployed to linearize the first- and second-law efficiency functions to a single multi-response performance objective function, to determine the order of importance of these parameters and their contribution ratios to the multi-response performance process. It is worth noting, that the objective of this multi-response optimisation process is to optimise parameter combinations to simultaneously achieve an increase in the first and second-law efficiencies of SORC and DPORC systems.

Results obtained based on the methods discussed above are as follows:

- For the SORC system, the order of importance of the parameters on the first law (thermal) efficiency is T_{evap} > working fluid > T_{cond} > η_{turb} > $\Delta T_{pp,cond}$ > η_{pump} > $\Delta T_{pp,evap}$ > ΔT_{SH}, with the most significant parameters being found to be evaporator temperature (E), working fluid (A), condenser temperature (F) and turbine efficiency, with contribution ratios of 42.73%, 21.34%, 12.73% and 11.62%, respectively. The optimum operating condition determined is $A_3B_1C_1D_3E_3F_1G_3H_3$, which calculates the first-law (thermal) efficiency as 18.78%.
- The order of importance for the second law (exergy) efficiency is working fluid > ΔT_{SH} > T_{evap} > T_{cond} > η_{turb} > $\Delta T_{pp,evap}$ > $\Delta T_{pp,cond}$ > η_{pump}. The most effective parameters influencing the second-law efficiency of SORC are determined as working fluid, degree of superheating, evaporator temperature, and condenser temperature, with contribution ratios of 82.01%, 7.27%, 6.43% and 2.43%, respectively. The optimum operating conditions for the second-law efficiency objective function of SORC are determined as $A_1B_2C_3D_1E_1F_1G_3H_3$ with the second-law efficiency calculated as 65.09%.
- For the DPORC system, the parameters' level of importance on the thermal efficiency was determined as $\Delta T_{pp,cond}$ > T_{cond} > T_{evap} > $\Delta T_{pp,evap}$ > η_{turb} > working fluid > $T_{LP,evap}$ > η_{pump} > ΔT_{SH}, with the most influential parameters identified as $\Delta T_{pp,cond}$ (C), T_{cond} (F) and T_{evap} (E), with contribution ratios of 21.61%, 19.83% and 14.36%, respectively. The optimum condition observed was $A_2B_1C_1D_1E_2F_1G_3H_3J_3$ with an estimated cycle thermal efficiency of 14.64%.
- On the other hand, the order of importance of parameters for the second law (exergy) efficiency is working fluid > η_{turb} > $\Delta T_{pp,cond}$ > T_{cond} > $\Delta T_{pp,evap}$ > T_{evap} > $T_{LP,evap}$ > ΔT_{SH} > η_{pump}. The parameters with significant influence are the working fluid (A) and turbine efficiency (G), with contribution ratios of 93.53% and 3.58%, respectively, and other parameters cumulatively accounting for about 2.89%. An optimal exergy efficiency of 63.08% was obtained with the operating condition of $A_2B_2C_3D_1E_3F_3G_3H_1J_2$.
- The Grey relational analysis was implemented to simultaneously maximize both thermal and exergy efficiencies. For the SORC, the optimum operating condition for maximum first- and second-law efficiencies is $A_3B_2C_1D_1E_3F_1G_3H_3$, with 18.64% and 51.69% as the multi-response performance of the first- and second-law efficiency, respectively. For DPORC, 13.17% and 57.33% are the first- and second-law efficiency, respectively, obtained at the optimum operating condition of $A_1B_1C_1D_3E_2F_1G_3H_3J_2$.

Based on the analysis and thermodynamic comparison investigated in this study, SORC shows better thermal efficiency (+5.54%pt.) while DPORC represents a more advanced system in terms of exergy efficiency (+5.64%pt.). This could be attributed to the improved heat utilization due to the addition of LP turbine and heat exchangers (LP evaporator, Preheater 2, etc.). However, a more informed comparison will require the economic assessment of both systems, which is recommended for further research.

Acknowledgements

The authors appreciate the support of University of Cross River State under the 2023 Institution Based Research (IBR) project. This research project is funded by the Tertiary Education Trust Fund (TETFund) on the basis of the grant reference TETF/DR&D/CE/CRUTECH/IBR/2023/VOL.1.

References

[1] Igbong, D., Nyong, O., Enyia, J., Oluwadare, B., & Obhua, M. (2021). Exergoeconomic evaluation and optimization of Dual Pressure Organic Rankine Cycle (ORC) for geothermal heat source utilization. *Journal of Power and Energy Engineering*, 9(9), 19–40. doi: 10.4236/jpee.2021.99002

[2] Braimakis, K., & Karellas, S. (2018). Energetic optimization of regenerative Organic Rankine Cycle (ORC) configurations. *Energy Conversion and Management*, 159, 353–370. doi: 10.1016/j.enconman.2017.12.093

[3] Li, J., Ge, Z., Liu, Q., Duan, Y., & Yang, Z. (2018). Thermo-economic performance analyses and comparison of two turbine layouts for organic Rankine cycles with dual-pressure evaporation. *Energy Conversion and Management*, 164, 603–614. doi: 10.1016/j.enconman.2018.03.029

[4] Yamankaradeniz, N., Bademlioglu, A., & Kaynakli, O. (2018). Performance assessments of organic Rankine cycle with internal heat exchanger based on exergetic approach. *Journal of Energy Resources Technology*, 140, 102001–102008. doi: 10.1115/1.4040108

[5] Igbong, D., Nyong, O. E., Enyia, J., & Agba, A. (2021). Working fluid selection for simple and recuperative Organic Rankine Cycle operating under varying conditions : A comparative analysis. *Advances in Science and Technology Research Journal*, 15(4), 202–221. doi: 10.12913/22998624/142013

[6] Sadeghi, M., Nemati, A., & Yari, M. (2016). Thermodynamic analysis and multi-objective optimization of various ORC (organic Rankine cycle) configurations using zeotropic mixtures. *Energy*, 109, 791–802. doi: 10.1016/j.energy.2016.05.022

[7] Liu, Q., Chen, R., Yang, X., & Xiao, X. (2023). Thermodynamic analyses of sub- and supercritical ORCs using R1234yf, R236ea and their mixtures as working fluids for geothermal power generation. *Energies*, 16(15), 5676. doi: 10.3390/en16155676

[8] Mokhtari, H., Hadiannasab, H., Mostafavi, M., Ahmadibeni, A., & Shahriari, B. (2016). Determination of optimum geothermal Rankine cycle parameters utilizing coaxial heat exchanger. *Energy*, 102, 260–275. doi: 10.1016/j.energy.2016.02.067

[9] Sun, J., Liu, Q., & Duan, Y. (2018). Effects of evaporator pinch point temperature difference on thermo-economic performance of geothermal organic Rankine cycle systems. *Geothermics*, 75, 249–258. doi: 10.1016/j.geothermics.2018.06.001

[10] Zare, V. (2016). A comparative thermodynamic analysis of two tri-generation systems utilizing low-grade geothermal energy. *Energy Conversion and Management*, 118, 264–274. doi: 10.1016/j.enconman.2016.04.011

[11] Mansoury, M., Jafarmadar, S., & Khalilarya, S. (2018). Energetic and exergetic assessment of a two-stage organic Rankine cycle with reactivity controlled compression ignition engine as a low temperature heat source. *Energy Conversion and Management*, 166, 215–232. doi: 10.1016/j.enconman.2018.04.019

[12] Quoilin, S., Declaye, S., Tchanche, B. F., & Lemort, V. (2011). Thermo-economic optimization of waste heat recovery organic Rankine cycles. *Applied Thermal Engineering*, 31, 2885–2893. doi: 10.1016/j.applthermaleng.2011.05.014

[13] Roy, J. P., Mishra, M. K., & Misra, A. (2010). Parametric optimization and performance analysis of a waste heat recovery system using organic Rankine cycle. *Energy*, 35, 5049–5062. doi: 10.1016/j.energy.2010.08.013

[14] Scardigno, D., Fanelli, E., Viggiano, A., Bracco, G., & Magi, V. (2015). A genetic optimization of a hybrid organic Rankine plant for solar and low-grade energy sources. *Energy*, 91, 807–815. doi: 10.1016/j.energy.2015.08.066

[15] Moloney, F., Almatrafi, E., & Goswami, D. Y. (2017). Working fluid parametric analysis for regenerative supercritical organic Rankine cycles for medium geothermal reservoir temperatures. *Energy Procedia*, 129, 599–606. doi: 10.1016/j.egypro. 2017.09.216

[16] Li, G. (2016). Organic Rankine cycle performance evaluation and thermoeconomic assessment with various applications part I: Energy and exergy performance evaluation. *Renewable and Sustainable Energy Reviews*, 53, 477–499. doi: 10.1016/ j.rser. 2015.08.066

[17] Roy, J. P., & Misra, A. (2012). Parametric optimization and performance analysis of a regenerative Organic Rankine cycle using R123 for waste heat recovery. *Energy*, 39, 227–235. doi: 10.1016/j.energy.2012.01.026

[18] Wang, H., Li, H., Wang, L., & Bu, X. (2017). Thermodynamic analysis of organic Rankine cycle with hydrofluoroethers as working fluids. *Energy Procedia*, 105, 1889–1894. doi: 10.1016/j.egypro.2017.03.554

[19] Bademlioglu, A. H., Canbolat, A. S., Yamankaradeniz, N., & Kaynakli, O. (2018). Investigation of parameters affecting Organic Rankine Cycle efficiency by using Taguchi and ANOVA methods. *Applied Thermal Engineering*, 145, 221–228. doi: 10.1016/j.applthermaleng.2018.09.032

[20] Bademlioglu, A. H., Canbolat, A. S., & Kaynakli, O. (2020). Multi-objective optimization of parameters affecting Organic Rankine Cycle performance characteristics with Taguchi-Grey Relational Analysis. *Renewable and Sustainable Energy Reviews*, 117, 109483. doi: 10.1016/j.rser.2019.109483

[21] Kumar, U., & Karimi, M. N. (2014). Application of Taguchi's methods for optimizing organic Rankine cycle for recovering low grade industrial waste heat. *International Journal of Thermal & Environmental Engineering*, 8(2), 91–101. doi: 10.5383/ijtee. 08.02.005

[22] Kotcioglu, I., Cansiz, A., & Khalaji, M. (2013). Experimental investigation for optimization of design parameters in a rectangular duct with plate-fins heat exchanger by Taguchi method. *Applied Thermal Engineering*, 50, 604–613. doi: 10.1016/j.applthermaleng.2012.05.036

[23] Sahin, B. (2007). Taguchi approach for determination of optimum design parameters for a heat exchanger having circular-cross sectional pin fins. *Heat and Mass Transfer*, 45, 493–502. doi: 10.1007/s00231-006-0224-5

[24] Turgut, E., Cakmak, G., & Yildiz, C. (2012). Optimization of the concentric heat exchanger with injector turbulator by Taguchi method. *Energy Conversion and Management*, 53, 268–275. doi: 10.1016/j.enconman.2011.09.011

[25] Verma, V., & Murugesan, K. (2014). Optimization of solar assisted ground source heat pump system for space heating application by Taguchi method and utility concept. *Energy and Buildings*, 82, 296–309. doi: 10.1016/j.enbuild.2014.07.029

[26] Acir, A., Canli, M. E., Ata, I., & Cakiroglu, R. (2017). Parametric optimization of energy and exergy analyses of a novel solar air heater with grey relational analysis. *Applied Thermal Engineering*, 122, 330–338. doi: 10.1016/j.applthermaleng. 2017.05.018

[27] Chamoli, S., Yu, P., & Kumar, A. (2016). Multi-response optimization of geometric and flow parameters in a heat exchanger tube with perforated disk inserts by Taguchi grey relational analysis. *Applied Thermal Engineering*, 103, 1339–1350. doi: 10.1016/j.applthermaleng.2016.04.166

[28] Mia, M., Rifat, A., Tanvir, F., Gupta, M. K., Hossain, J., & Goswami, A. (2018). Multi-objective optimization of chip-tool interaction parameters using Grey-Taguchi method in MQL-assisted turning. *Measurement*, 129, 156–166. doi: 10.1016/ j.measurement.2018.07.014

[29] Klein, S. A. (2020). *Engineering Equation Solver* (V10.801-3D). F-Chart Software.

[30] Bejan, A., Tsatsaronis, G., & Moran, M. (1996). *Thermal Design & Optimization*. John Wiley & Sons Inc.

[31] Igbong, D. (2022). Energy and Exergy-based Performance Analysis of a Combined Recompression Supercritical Carbon Dioxide-Organic Rankine Cycle for Waste Heat Recovery. *Cleaner Energy Systems*, 100022. doi: 10.1016/j.cles. 2022.100022

[32] Delgado-Torres, A. M., & García-Rodríguez, L. (2010). Analysis and optimization of the low-temperature solar organic Rankine cycle (ORC). *Energy and Buildings*, 51, 2846–2856. doi: 10.1016/j.enconman.2010.06.022

[33] Yari, M. (2010). Exergetic analysis of various types of geothermal power plants. *Renewable Energy*, 35(1), 112–121. doi: 10.1016/j.renene.2009.07.023

[34] Wang, M., Chen, Y., Liu, Q., & Yuanyuan, Z. (2018). Thermodynamic and thermo-economic analysis of dual-pressure and single pressure evaporation organic Rankine cycles. *Energy Conversion and Management*, 177, 718–736. doi: 10.1016/ j.enconman.2018.10.017

[35] Tutar, M., Aydin, H., Yuce, G., Yavuz, N., & Bayram, A. (2014). The optimisation of process parameters for friction stir spot-welded AA3003-H12 aluminium alloy using a Taguchi orthogonal array. *Material Design*, 63, 789–797. doi: 10.1016/ j.matdes.2014.07.003

[36] Ross, P. J. (1996). *Taguchi techniques for quality engineering* (second). McGraw Hill.

[37] Yan, J., & Li, I. (2013). Multi-objective optimization of miling parameters - the trade-offs between energy, production rate and cutting quality. *Journal of Cleaner Production*, 52, 462–471. doi: 10.1016/j.jclepro.2013.02.030

Co-published by
Institute of Fluid-Flow Machinery
Polish Academy of Sciences
Committee on Thermodynamics and Combustion
Polish Academy of Sciences

Copyright©2024 by the Authors under licence CC BY 4.0

http://www.imp.gda.pl/archives-of-thermodynamics/

Darcy Forchheimer two-dimensional thin flow of Jeffrey nanofluid with heat generation/absorption and thermal radiation over a stretchable flat sheet

Saravanan Jagadha[a*], Batina Madhusudhan Rao[b], Putta Durgaprasad[c], Degavath Gopal[d], Putta Prakash[e], Naikoti Kishan[f], Krishnan Muthunagai[g]

[a]Institute of Aeronautical Engineering, Dundigal, Hyderabad, T.S. 500043, India
[b]Department of IT, Mathematics section, University of Technology and Applied Sciences, Muscat 324, Oman
[c]Vellore Institute of Technology, Kelambakkam - Vandalur Rd, Rajan Nagar, Chennai 600127, India
[d]Department of Mathematics, CMR Engineering College, Medchal, T.S. 501401, India
[e]Mohan Babu University, Sree Vidyanikethan Sree Sainath Nagar, Andhra Pradesh, Tirupati 517102, India
[f]Osmania University, Main road, Amberpet, Hyderabad, Telangana T.S. 500007, India
[g]Vellore Institute of Technology, Kelambakkam - Vandalur Rd, Rajan Nagar, Chennai, Tamil Nadu 600127, India

Received: 18.06.2023; revised: 23.12.2023; accepted: 19.04.2024

Abstract

This work aims to study the combined effects of concentration and thermal radiation on a steady flow of Jeffrey nanofluid under the Darcy-Forchheimer relation over a flat nonlinear stretching sheet of variable thickness. A varying magnetic field influences normal to the flow movement is considered to strengthen the Jeffery nanofluid conductivity. However, a little effect of the magnetic Reynolds number is assumed to eliminate the impact of the magnetic field range. The higher-order nonlinear partial differential equations (PDEs) and convective boundary conditions are transformed into nonlinear ordinary differential equations (ODEs) by applying corresponding transformations. Then the ODEs are numerically solved with Runge-Kutta method via shooting technique. This process is applied for convergent relations of nanoparticle temperature, concentration, and velocity distributions. The influence of different fluid parameters like thermophoresis, melting parameter, Deborah number, chemical reaction parameter, Brownian motion parameter, inertia parameter and Darcy number on the flow profiles is explained through graphical analysis. Thermal radiation is emitted by accelerated charged particles, and the enhanced particle motion at higher temperatures causes a more significant discharge of radiation. Also, it was concluded that the heat generation parameter enhances the momentum boundary layer thickness and reduces the thermal and solutal boundary layer thickness over a Jeffrey nanofluid.

Keywords: MHD; Jeffrey nanofluid; Chemical reaction; Darcy-Forchheimer; Stretchable flat sheet

Vol. 45(2024), No. 2, 247–259; doi: 10.24425/ather.2024.150869

Cite this manuscript as: Jagadha, S., Madhusudhan Rao, B., Durgaprasad, P., Gopal, D., Prakash, P., Kishan, N., & Muthunagai, K. (2023). Darcy Forchheimer two-dimensional thin flow of Jeffrey nanofluid with heat generation/absorption and thermal radiation over a stretchable flat sheet. *Archives of Thermodynamics*, 45(2), 247-259.

1. Introduction

The analysis of boundary layer flow along with the radiation parameter is significant in different materials such as glass fabrications, liquid metallic fluids, and high-temperature plasmas. The specific transport problems seem to be highly nonlinear when combined with thermal convection fluid flows.

Nomenclature

a_0, b_0 – constants
B_0 – stregth of magnetic field, kg/(s^2 A)
C – fluid concentration
C_{fx} – skin friction coefficient
C_p – specific heat capacity at constant pressure, J/(kg K)
C_∞ – fluid concentration in the free stream
D_B – diffusion coefficient due to Brownian effect, m^2/s
D_T – diffusion coefficient due to thermal effect, m^2/s
D_∞ – diffusion of the fluid far away from sheet, m^2/s
Da – Darcy number
F – dimensionless velocity
k – porosity parameter
K – Deborah number
k^* – absorption coefficient
Le – Lewis number
M – magnetic field parameter
n – shape parameter
Nb – Brownian motion parameter
Nt – thermophoresis parameter
Nu_x – Nusselt number
p – pressure, kg/(m s^2)
Pr – Prandtl number
R – radiation parameter
Re – local Reynolds number
Sh_x – Sherwood number
T – temperature, K
u – velocity component in x direction, m/s
v – velocity component in y direction, m/s
x – direction along the surface, m
y – direction normal to the surface, m

Greek symbols

α – thermal diffusivity, m^2/s
β – interaction parameter
β_s – heat generation parameter
ε – variable thermal conductivity
Γ – chemical reaction parameter
η – similarity variable (dimensionless)
θ – dimensionless fluid temperature
λ_s – concentration buoyancy parameter
λ_t – thermal buoyancy parameter
υ – kinematic viscosity, m^2/s
ξ – similarity variable
ρ – fluid density, kg m^{-3}
σ^* – Stefan-Boltzmann constant, W/(m^2 K^4)
τ – ratio of heat capacities
ψ – stream function,
Φ – concentration in dimensionless form

Subscripts and Superscripts

∞ – ambient condition
w – condition on surface
* – dimensionless properties
' – differentiation with respect to η

Abbreviations and Acronyms

BL – boundary layer
CNT – carbon nanotubes
IVP – initial value problem
MBL – momentum boundary layer
MHD– magnetohydrodynamic
ODE – ordinary differential equation
PDE – partial differential equations

The distribution of temperature in the boundary layer is altered by the presence of thermal radiation at high temperatures, which affects the heat transfer near the wall. Because of their unique industrial applications, non-Newtonian liquid flows have attracted the interest of many researchers and scientists. Non-Newtonian fluids entitle a non-linear relation between stress and strain. The study of non-Newtonian flows and their features is not easy when compared to Newtonian fluids. To investigate the characteristics of non-Newtonian fluid flows, the Navier-Stokes equations are crucial. It has also been suggested to use a variety of fluid models to describe the properties of non-Newtonian liquids. One of the non-Newtonian liquids whose behaviour is being examined by means of a variety of models is Jeffrey fluid. Viscous fluids are developed using a single constitutive equation. There are several models of non-Newtonian materials accessible because these fluids have a variety of features that no single constitutive expression can adequately describe. The differential and rate-type liquid categories have gained the attention of numerous scholars. A significant non-Newtonian liquid that can determine the impact of retardation and relaxation is Jeffrey fluid. In bioengineering, geophysics, oil reservoir process, and chemical and nuclear technologies, Jeffrey fluid models are widely used. Many investigators, like Waqas [1] and Pal et al. [2] have studied and analysed Jeffrey fluid under various characteristics. Abdullah et al. [3] examined the magnetohydrodynamic (MHD) Jeffrey nanofluid flow over a stretching sheet. Turkyilmazoglu and Pop [4] discussed the flow and heat transfer of a Jeffrey fluid near the stagnation point on a stretching or shrinking sheet with a parallel external flow by using an analytical method. They observed the skin friction coefficient decreases as the stretching parameter of the sheet increases. Hayat et al. [5] reported on the MHD stagnation point flow of Jeffrey fluid near a stretching sheet with variable sheet thickness. They examined that the thermal boundary layer thickness increases with an increase in the heat generation parameter. Mabood et al. [6] studied the features of the heat flux model for a stagnation point flow of Jeffrey fluid past a flat stretching sheet. They observed that the momentum boundary thickness increases with an increase in Deborah number while decreasing the thermal boundary layer thickness.

Few researchers worked towards the combination of stretching sheet and thermal radiation influences on Jeffrey nanofluid. Using active energy and nonlinear thermal radiation effects, Hayat et al. [7] investigated the entropy generation optimisation of MHD Jeffrey nanofluid along a flat stretched surface. Technologies and businesses have investigated how to use the melting phenomenon. Researchers have focused on enhancing efficient, environmentally friendly, and energy-efficient systems.

These technologies are associated with planetary power and the recovery of excess heat. Three procedures (latent, sensible heat and chemical energy) have been implemented for energy storage. The MHD stagnation point flow of a Casson nanofluid as well as the combined effects of heat radiation and velocity slip were discussed by Besthapu et al. [8]. Kumar [9] later studied the differential transform method for transient hydro-magnetic Jeffrey liquid flow with a flat stretched sheet.

Many different fields, including heat exchanger coils, based pumps, solidification, and welding operations, etc., involve the melting phenomena. In addition to Newtonian cooling and nonlinear thermal radiation, Sen et al. [10] observed a thermal distributed homogeneous–heterogeneous interaction inside the MHD flow of Jeffrey fluid. By using the Fourier law and an infinite plate, Asjad et al. [11] modified the extended heat flux flow in Jeffrey fluid. Muhammad et al. [12] investigated a Jeffrey nanofluid flow under convective heat or mass circumstances. Anitha and Gireesha [13] explored the thermal analysis of Jeffrey nanofluid through microchannel applying Buongiorno's model. A stretched cylinder has been employed to examine the heat transfer analysis of Jeffrey nanofluid by Hayat et al. [14] and Ur Rasheed et al. [15]. Khan et al. [16] and Dadhich et al. [17] also examined the impact of thermal radiation on Jeffrey fluid. The different engineering and industrial applications such as heat transformers, chemical reactors and geothermic systems are associated with a convective permeable channel. The mechanical phenomenon, i.e. effect of diffusion and drag force, is dealt with in the Darcy-Forchheimer model. At first, it was known as the Darcian flow model, and as a modified Darcy-Forchheimer model was later extended toward nanofluid flow. This model was developed to explain the mechanical phenomenon in the analysis of heat flow in a fluid stream. The extra velocity term and drag force parameter in the equation of momentum, both of which have a negative sign, result in the Darcy-Forchheimer model. Several applications such as natural compound recovery strategy, soil material science, living tissue transitions, and junk storage (specifically gas litter) are included in this model. A few earlier investigations on the Darcy-Forchheimer model are reported by many researchers [18–20]. Seth and Mandal [21] employed the Darcy-Forchheimer model to analyse the Casson fluid flow. In connection with the Darcy-Forchheimer model, the problems concentrating on the fluid flows over a radially stretching sheet have attracted a huge number of researchers.

A notable amount of research was carried out on the problems of fluid flows due to nonlinear radially stretched surfaces. Bilal Ashraf et al. [22] studied MHD Jeffrey nanoliquid over a radially stretching surface along with radiative and mixed convection. Hayat et al. [23] examined the flow characteristics of Jeffrey fluid due to the nonlinear surface that can be stretchable in the radial direction. Ali et al. [24] incorporated a porous Reynolds number and a contracting/relaxing parameter in their analysis of the mass/heat transfer flow around metallic oxide nanoparticles close to perpendicularly moving extremely permeable discs. For the numerical results, they also used a correct quasi-linearization technique. Much research has introduced nonlinear stretching sheets into the Darcy-Forchheimer model of flow. Lund et al. [25] deliberated stability analysis of Casson nanoliquid flow past a stretchable exponential sheet with the help of the Darcy-Forchheimer model. Furthermore, the obtained results showed that several solutions occur only for high suction. In addition, the effect of a magnetic field is very useful in many chemical and engineering applications of nanoliquids. properties. In industries like thermal engineering, geothermal operations, chemical and petroleum equipment, etc., flow-saturating porous media is important.

Darcy law pays particular attention to permeable space. The Darcy principle is not intended for places where permeable channels experience increased flow rates because of uneven surrounding wall surfaces. Therefore, a non-Darcian effect resulting from a porous media is required to study the heat transfer and flow analysis. Khani et al. [27] examined the case of fluid flow saturating a non-Darcy permeable media with heat transfer. Hayat et al. [28] took into consideration the convective carbon nanotubes (CNTs) nanofluid flow over a non-Darcy permeable media. Siddiq et al. [29] and Madhu et al. [30] used the non-Darcy Forchheimer principle to evaluate the MHD radiative flow of the Carreau fluid to a stretching surface. They observed the Darcy-Forchheimer flow of MHD Powell-Eyring nanofluid past stretchable non-linear radial disc under the influence of activating energy. Later, problems with Darcy-Forchheimer MHD fluid flows were reviewed by Madkhali et al. [31], Machireddy et al. [32], Ramesh et al. [33] and Eswaramoorthi et al. [34]. Recently, the two-dimensional mixed convection and radiative Al2O3-Cu/H2O hybrid nanofluid flow over a vertical exponentially shrinking sheet with partial slip conditions has been analysed by Asghar et al. [35]. For this study, a physical model of the influence of thermal radiation on the two-dimensional flow of a hybrid nanofluid was developed. Asghar et al. [36] also investigated the effect of thermal radiation and the three-dimensional magnetized rotating flow of a hybrid.

The heat generation/absorption parameter is non-dimensional and depends on the amount of heat generated or absorbed in the fluid. The dual solutions of MHD Al2O3+Cu hybrid nanofluid in the presence of Joule heating were studied by Sajjad et al. [37]. Teh and Asghar [38] explained three-dimensional MHD hybrid nanofluid flow in the presence of Joule heating with a rotating stretching sheet. Furthermore, Asghar et al. [39–41] investigated the two-dimensional hybrid nanofluid flow with the effects of thermal slip condition, Joule heating and heat generation/heat absorption. Moreover, Gohar et al. [42] studied heat and mass transfer of Darcy-Forchheimer hybrid nanofluid flow due to an extending curved surface. Satyanarayana et al. [43] investigated nanofluid under the influence of suction/injection in a convective medium. Mamatha et al. [44] discussed the mass transfer analysis of two-phase flow in a suspension of microorganisms. Finally, Madhusudhana Rao et al. [45] studied the heat and mass transfer mechanism on the three-dimensional flow of inclined magneto Carreau nanofluid with chemical reaction.

The goal of the current study, which was motivated by the research, is to identify a Darcy Forchheimer 2D thin flow of Jeffrey nanofluid with heat generation or absorption and thermal radiation over a stretchable flat sheet. Under the relevant boundary conditions, the coupled nonlinear PDEs can be numerically solved using the MATLAB solver with the help of the Runge-Kutta method via shooting technique. The effects of physical parameters on the fluid concentration ($\Phi(\xi)$) and temperature ($\theta(\xi)$), and the velocity field ($F'(\xi)$), are graphically displayed for numerous sets of physical parameter values. The thermophoresis parameter enhances the heat transfer rate and decelerates the mass transfer rate. Also, it was observed that the thermal radiation parameter increases the heat transfer rate.

2. Mathematical analysis

Let us consider a steady a two-dimensional laminar and incompressible magnetohydrodynamic flow of Jeffrey nanofluid with heat generation or absorption and thermal radiation over a stretchable flat sheet, as shown in Fig. 1.

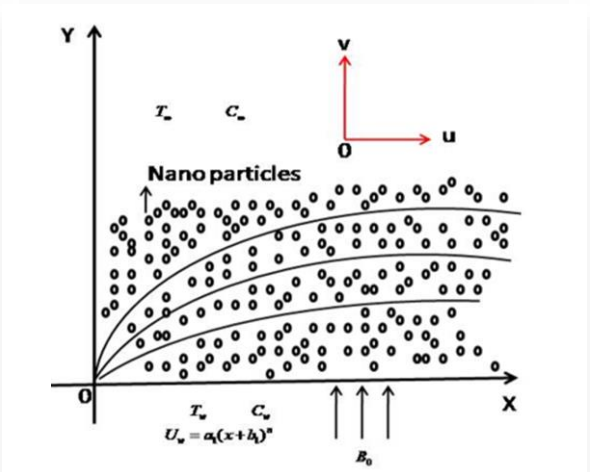


Fig. 1. Physical description of the problem.

After employing the usual boundary layer analysis, the basic partial differential equations governing the conservation of mass, momentum, energy, and concentration for the Jeffrey nanofluid flow can be written as, respectively [46].

$$u_x + v_y = 0, \tag{1}$$

$$u\,u_x + v\,u_y = \frac{\upsilon}{(1+\lambda_s)}\left[\upsilon\,u_{yy} + \lambda_t\left(v\,y_{yyy} + u\,u_{xyy} + u_y u_{xy}\right) - \left(\frac{\sigma^2 B_0^2}{\rho} + \frac{\upsilon\varepsilon}{k}\right)u - \frac{\varepsilon c_b}{\sqrt{k}}u^2 u_x u_{xy}\right], \tag{2}$$

$$\left(u\,T_x + v\,T_y\right) = \alpha T_{yy} + \tau\left(D_B C_y T_y + \frac{D_T}{T_\infty}T_y^2\right) + \frac{16\sigma^* T_\infty^3}{3k^*\rho c_p}T_{yy} + \frac{Q_0(T_0 - T_m)}{\rho c_p}, \tag{3}$$

$$\left(u\,C_x + v\,C_y\right) = D_B C_{yy} + \frac{D_T}{T_\infty}T_{yy} - K_n(C - C_w)^m, \tag{4}$$

where u and v represent the velocity vector components in x and y directions, respectively, υ is the kinematic viscosity, ρ is the fluid density, c_p is its specific heat, ε is the variable thermal conductivity, k is the permeability, B_0 is the strength of the magnetic field, c_b is the drag force, whereas λ_s and λ_t denote the concentration and thermal buoyancy parameters, respectively. Parameters D_B and D_T represent Brownian and thermal diffusivities, respectively, T is the field temperature, α denotes thermal diffusivity, C is the fluid concentration, Q_0 is the heat generation/absorption, τ is the ratio of heat capacities., σ^* and k^* represent the Stefan-Boltzmann constant and the absorption coefficient, respectively, and K_n stands for the n-th order chemical reaction. Subscripts ∞ and w refer to free stream (ambient) and surface (wall), respectively.

Boundary conditions near and away from the sheets surface were described as:

$$\begin{cases} u = u_w(x) = a_0(x + b_0)^n, v = 0, T = T_w, C = C_w & \text{at } y = \delta(x + b_0)^{\frac{(1-n)}{2}} \\ T \to T_\infty, C \to C_w, u \to 0 & \text{as } y \to \infty \end{cases}. \tag{5}$$

Introducing the non-dimensional quantities:

$$\psi(x, y) = \sqrt{\frac{2\upsilon a_0}{n+1}(x + b_0)^{n+1}}\, f(\eta), \tag{6a}$$

$$\eta = y\sqrt{\frac{(n+1)}{2\upsilon}(x + b_0)^{n-1}}, \tag{6b}$$

$$u = a_0(x + b_0)^n f'(\eta), \tag{6c}$$

$$v = -\sqrt{\frac{\upsilon(n+1)}{2}a_0(x + b_0)^{n-1}}\left(f(\eta) + \eta\left(\frac{n-1}{n+1}\right)\right)(x + b_0)^n f'(\eta), \tag{6d}$$

$$\theta(\eta) = \frac{T - T_w}{T - T_\infty},\ \ \Phi(\eta) = \frac{C - C_w}{C - C_\infty}, \tag{6e}$$

the set of dimensionless form of the governing Eqs. (2)–(4) along with the boundary conditions (Eq. (5)) are converted to the set of ODEs as:

$$F''' - \mathrm{K}\left[\left(\frac{n-1}{2}\right)F'F^{iv} - (n-1)F'F''' - \left(\frac{3n-1}{2}\right)F''^2\right] - \left(\frac{2n}{n+1}\right)(1+\lambda_s)F'^2 - \left(\frac{2}{n+1}\right)(1+\lambda_s)\left(MF' - \beta F'^2 - \mathrm{Da}F'\right) = 0, \quad (7)$$

$$\frac{1}{\mathrm{Pr}}\left(1+\frac{4R}{3}\right)\theta'' + f\theta' + Nt\theta'\Phi' + \frac{2}{n+1}\lambda\theta = 0, \quad (8)$$

$$\Phi'' + \mathrm{PrLe}\Phi' + \frac{Nt}{Nb}\theta'' + \Gamma\Phi^m = 0, \quad (9)$$

where K, Da, Pr, and Le are the Deborah, Darcy, Prandtl and Lewis numbers, respectively, *R* is a thermal radiation parameter, *M* is a magnetic field parameter, *Γ* denotes a chemical reaction parameter, *n* is a shape factor, whereas *Nt* and *Nb* are the thermophoresis and Brownian motion parameters. Parameter *β* represents inertia parameter.

The corresponding non-dimensional boundary conditions are:

$$\begin{cases} \Phi(0) = 0, F'(0) = 1, \theta(0) = 0, F(0) = 0 \\ F'(\infty) \to 0,\ \theta(\infty) \to 0, \Phi(\infty) \to 0 \end{cases}, \quad (10)$$

where the parameters in the Eqs. (7)–(9) are assumed as:

$$M = \sqrt{\frac{\sigma}{a\rho}}B_0, \mathrm{Pr} = \frac{\upsilon}{\alpha}, \mathrm{Le} = \frac{\alpha}{D_B}, \mathrm{Da} = \frac{\upsilon\varepsilon}{ka_0(x+b_0)^{n-1}},$$

$$Nt = \frac{\tau D_T(T_w - T_\infty)}{\upsilon T_\infty}, Nb = \frac{\tau D_B(C_w - C_\infty)}{\upsilon}, R = \frac{4\sigma^* T_\infty^3}{kk^*},$$

$$\beta = \frac{\varepsilon C_b(x+b_0)}{\sqrt{k}}, \Gamma = xK_n(C_w - C_\infty)^{n-1}.$$

For engineering interest, skin friction coefficient, Nusselt and Sherwood numbers are represented as, respectively:

$$C_{fx} = \frac{\tau}{\frac{1}{2}\rho u_w^2}, \mathrm{Nu}_x = \frac{(x+b_0)q_w}{k(T_w - T_\infty)}, \mathrm{Sh}_x = \frac{(x+b_0)q_m}{D_B(C_w - C_\infty)},$$

where q_w is the heat flux and q_m represents the mass flux.

With the help of non-dimensional variables (Eqs. (6)), the aforementioned C_{fx}, Nu_x and Sh_x are rewritten as:

$$\mathrm{Re}^{\frac{1}{2}} C_{fx} = \frac{1}{1+\lambda_s}\left(F''(0) + K\left(F'(0)\right)F''(0) + -\left(\frac{n+1}{2}\right)F(0)F'''(0)\right),$$

$$\mathrm{Re}^{-\frac{1}{2}}\mathrm{Nu}_x = -(1+R)\sqrt{\frac{n+1}{2}}\,\theta'(0);$$

$$\mathrm{Re}^{-\frac{1}{2}}\mathrm{Sh}_x = -\sqrt{\frac{n+1}{2}}\,\Phi'(0),$$

or

$$\mathrm{Re}^{-\frac{1}{2}}\mathrm{Sh}_x = -\frac{a_0(x+b_0)^{n+1}}{\upsilon}$$

where Sh_x is the local Sherwood number due to stretching velocity.

3. Solution methodology

The familiar numerical technique Runge-Kutta method of fourth order was employed to obtain solutions of non-linear governing flow ordinary differential equations (7)–(9) subjected to boundary conditions (10). The nonlinear derivative formations are reduced to simultaneous mathematical formulations. The initial input value of the similarity variable is taken as zero and the free streamline as infinity for (F',θ,Φ). An infinity condition was presented for the free streamline but in the calculation, the maximum value of η is taken as 7. This value is appropriate to satisfy the flow region conditions for all the physical significances of dimensionless parameters.

Higher-order differential equations are converted to linear formulations by introducing new variables:

$$(f_1 = F), (f_2 = F'), (f_3 = F''), (f_4 = F'''), (f_5 = \theta),$$

$$(f_6 = \theta'), (f_7 = \Phi), (f_8 = \Phi').$$

Equations (7)–(9) are transformed into the following first-order ODEs:

$$f_4' = \frac{1}{k\left(\frac{n+1}{2}\right)f_2}\left[f_4 - k\left(-(n-1)f_2f_4 - \left(\frac{3n-1}{2}\right)f_3^2\right)\left(\frac{2n}{n+1}\right)(1+\lambda_s)f_2^2 - \left(\frac{2}{n+1}\right)(1+\lambda_s)[Mf_2 - \beta f_2^2 - \mathrm{Da}f_2]\right], \quad (11)$$

$$f_6' = \frac{1}{Pr\left(1+\frac{4R}{3}\right)}\left[f_1f_6 + Ntf_6^2 + Nbf_6f_8 + \left(\frac{2}{n+1}\right)\lambda f_5\right], \quad (12)$$

$$f_8' = -\left[\mathrm{Pr}\,Le\,f_1f_8 + \frac{Nt}{Nb}f_6 + \Gamma f_7^m\right]. \quad (13)$$

The results of governing flow equations of Jeffrey nanofluid were approximated numerically using MATLAB bvp4c software [47] for the interpretation of dimensionless quantifiers.

4. Algorithm

The solution algorithm includes the following steps:

- First, the momentum, energy and conservation equations are converted into IVP (initial value problem) equations, as stated in Eqs. (11)–(13).
- The solvers continually call the ordinary differential equation (ODE) file to assess the system of differential equations at different times (for energy equations and momentum). These are the data (information) required to be defined for the ODE system to be computed.
- The switch statement governs the type of output required so that the ODE file can pass the appropriate information (data) to the solver. In the default initial conditions ('bvpinit') case, the ODE file returns basic information (time span, initial conditions, and options) to the solver.
- In the 'Jacobian' case, the MATLAB ODE45 file returns a Jacobian matrix to the solver. If the Jacobian value becomes an undefined value (infinity) an error is received, so there is a need to change the guess values and proceed further.
- The physical governing parameters are guessed based on existing information like magnetic field, thermal radiation, thermal buoyancy, etc.

Once all the initial conditions are found, the solver automatically gives the plots as well as values in the command window.

5. Results and discussion

In this work, the combined effects of heat generation/absorption, melting heat transfer, and thermal radiation were investigated for the 2-D Darcy Forchheimer flow of a Jeffrey nanofluid past a flat stretchable sheet. Using the Runge-Kutta and shooting technique, the basic Eqs. (7)–(9) and boundary conditions Eq. (10) were solved. For evaluating the consistency and accuracy of the solutions, numerical analysis of influence of the significant parameters are demonstrated through graphs in this section. To obtain the results, numerical computations are carried out by assuming different values of non-dimensional governing parameters such as: $R = 1.1$, $M = 0.2$, $Nt = 0.2$, $Nb = 0.1$, Da = 0.5, $\beta = 1$, $\beta_s = 0.6$, $n = 0.3$, and Pr = 0.3.

The significance of radiation parameter (R) on the temperature profile $\theta(\xi)$ is interpreted through Fig. 2. It may be observed that an increase in thermal radiation parameter raises the fluid temperature over a flat stretching sheet since thermal radiation powers the varying temperatures to exchange energy. The particles move more rapidly due to higher kinetic energy. More particle collisions and more significant acceleration of charged particles result from this increased heat radiation. Accelerated charged particles are the source of electromagnetic radiation or thermal radiation, and the enhanced particle motion at higher temperatures causes a more significant discharge of radiation.

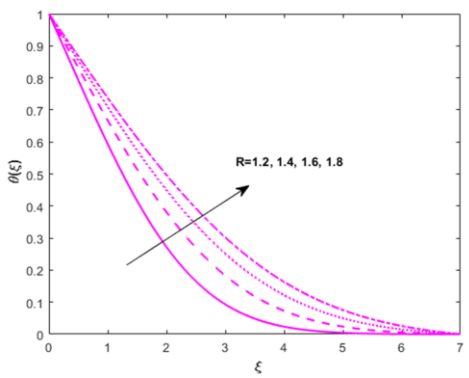
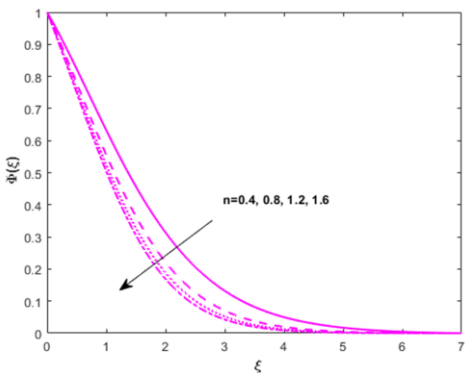


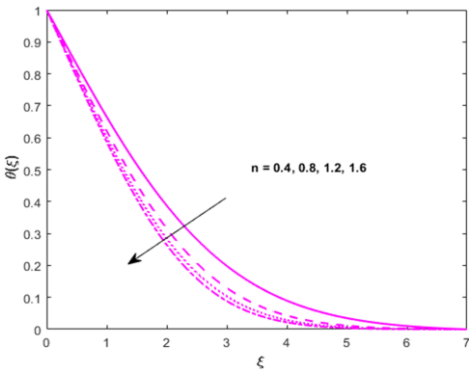
Fig. 2. Impact of R on $\theta(\xi)$.

Figures 3a and 3b show the effect of shape parameter n on the distributions of nanofluid concentration and temperature, respectively, in presence of stretching sheet. It is perceived that both concentration and temperature decrease for the incremental values of shape parameter.

From Figs. 4(a) and 4(b), illustrating the impact of thermophoresis quantity (Nt) on $\Phi(\xi)$ and $\theta(\xi)$, it is found that both profiles enlarge for improved values of Nt in the case of heat generation. Hence, it can be inferred that the amount of heat and mass exchange will be increased by enhancing Nt. In fact, solid nanoparticles in the nanofluid experience a force in the direction opposite to the imposed temperature gradient. Hence, the nanoparticles tend to move from hot to cold. It is important to note that the thermophoresis parameter is positive when the temperature of the wall is higher than the ambient temperature.



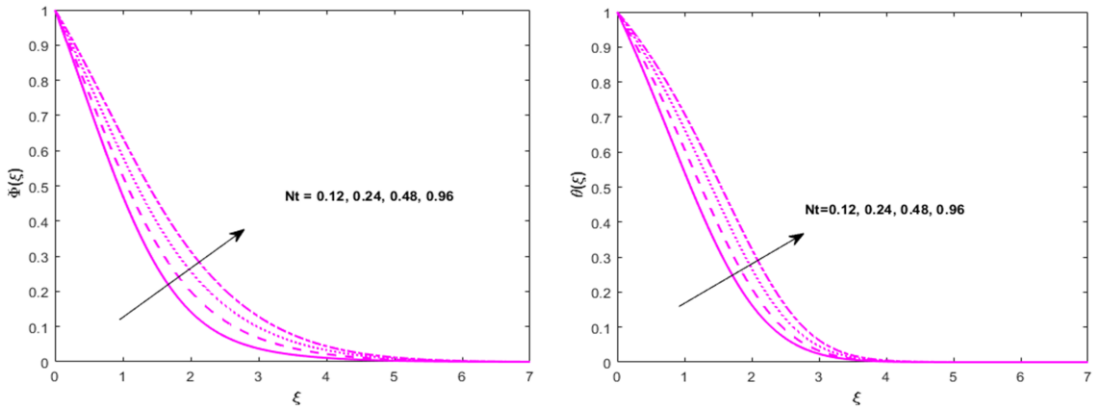
(a)



(b)

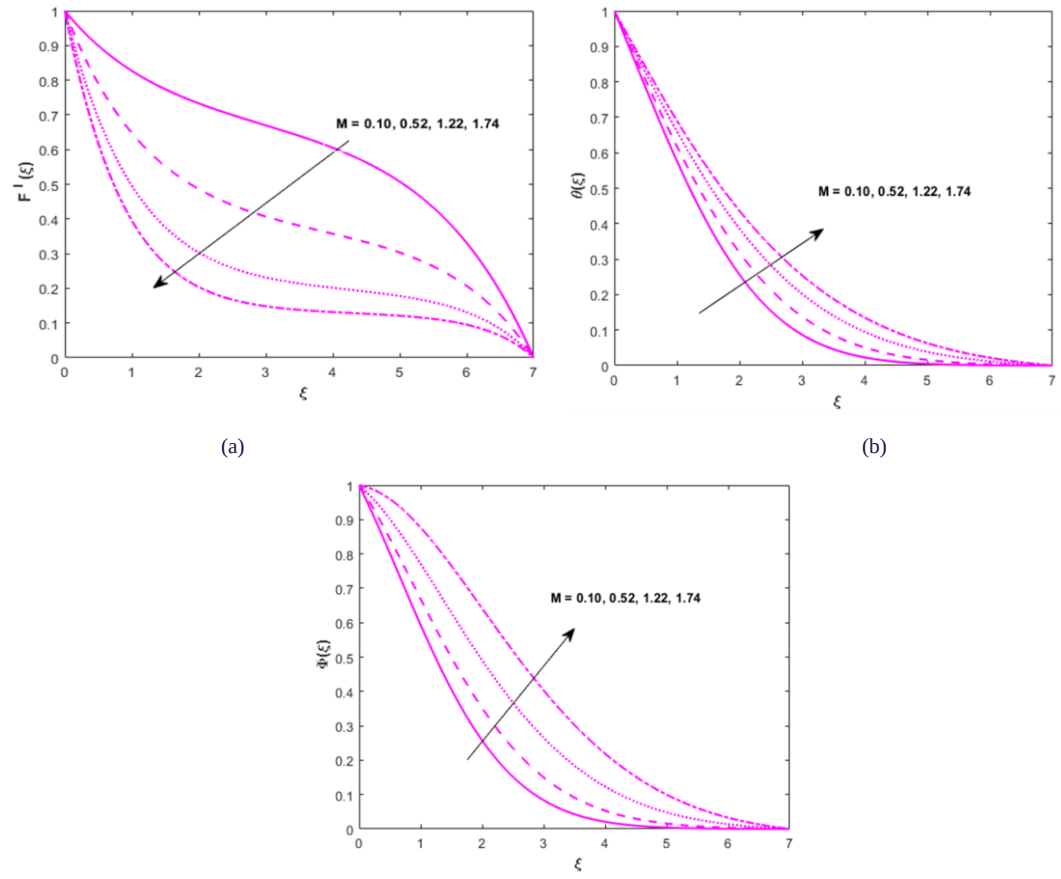
Fig. 3. Impact of n on: a) $\Phi(\xi)$, b) $\theta(\xi)$.

Through Figs. 5a, 5b and 5c, the effect of the magnetic field parameter (M) on the velocity field ($F'(\xi)$), temperature $\theta(\xi)$ and concentration ($\Phi(\xi)$), respectively, is illustrated and explained.



(a) (b)

Fig. 4. Effect of *Nt* on: a) $\Phi(\zeta)$, b) $\theta(\zeta)$.



(a) (b)

(c)

Fig. 5. Influence of *M* on: a) $F'(\zeta)$, b) $\theta(\zeta)$, and c) $\Phi(\zeta)$.

These results show that the magnetic field reduces the fluid velocity by lowering the resistive force, known as the Lorentz force, whereas $\theta(\zeta)$ and $\Phi(\zeta)$ rise for improved values of *M* in the presence of stretching sheet. It is also found that the increased magnetic parameter results in the concentration increase for both stretching and shrinking sheets.

The influence of Deborah number (K) on temperature and concentration profiles of Jeffrey nanofluid is presented in Figs. 6a and 6b, respectively. The increasing Deborah number enhances the temperature rise over the stretching sheet since the extrapolated temperature depends on the mechanical properties of polymers. The Deborah number increases the concentration of nanofluid, which causes a reduction in the momentum boundary layer (MBL) and a rise in the thermal boundary layer (TBL).

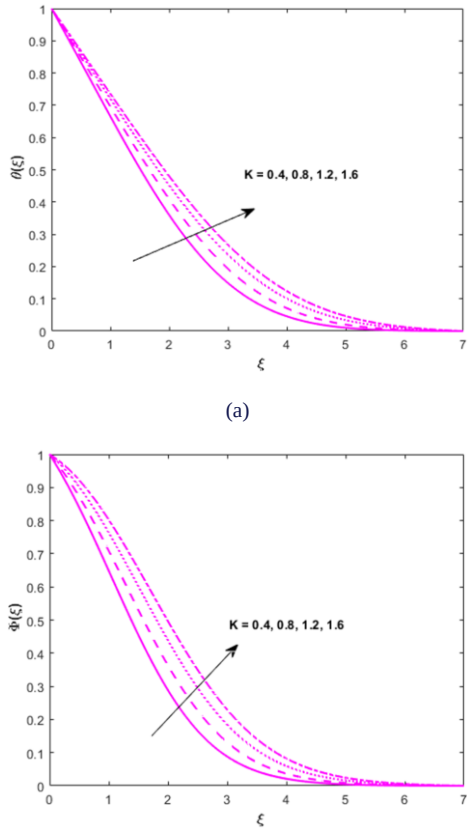


Fig. 6. Influence of K on: a) $\theta(\zeta)$, and b) $\Phi(\zeta)$.

The impact of Darcy number (Da) on flow velocity, temperature, and concentration of nanofluid past stretchable flat sheet is illustrated through Figs. 7a, 7b and 7c, respectively. It can be noticed noticed that the Darcy number accelerates the nanofluid flow and declines the temperature and concentration profiles of the nanofluid. Hence, it is concluded that an increasing Darcy number speeds up the motion of fluid particles, but it reduces the temperature of fluid near the stretching sheet.

The concentration of nanofluid flow via a flat stretching sheet is depicted in Fig. 8 exhibiting the effect of a chemical reaction parameter (Γ), which increases the concentration of nanofluid close to the wall. The concentration of nanoparticles close to the surface may be dominated by chemical processes if the chemical reaction parameter has a greater value. A lower value denotes a greater influence of other variables, such as convective transport.

It is observed from Figs. 9a and 9b that growing β raises up $\theta(\zeta)$ and $\Phi(\zeta)$ of a nanofluid over the stretching surface.

The influence of heat generation parameter β_s on $F'(\zeta)$, $\theta(\zeta)$ and $\Phi(\zeta)$ of the nanofluid past the stretchable non-linear flat sheet is displayed in Figs. 10a, 10b and 10c, respectively. It can be noticed that nanofluid velocity enlarges as the heat generation parameter increases. The impact of β_s results in reducing the temperature of the fluid. In addition, the direction of heat transfer is turned around all through heat generation.

The impact of heat generation or absorption through a stretched surface on the concentration of nanofluid and the

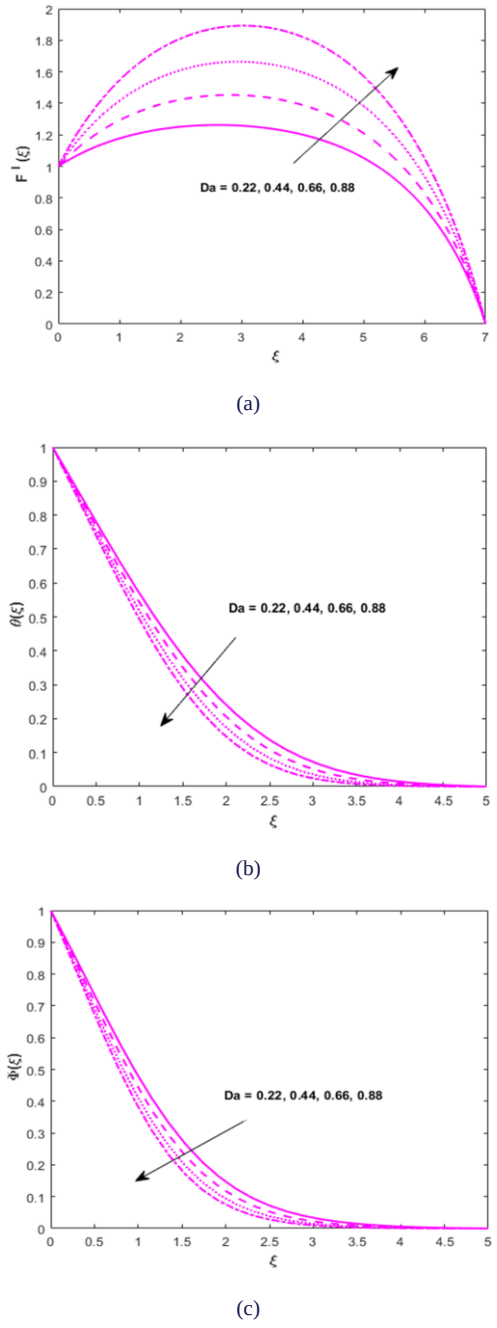


Fig. 7. Influence of M on: a) $F'(\zeta)$, b) $\theta(\zeta)$, and c) $\Phi(\zeta)$.

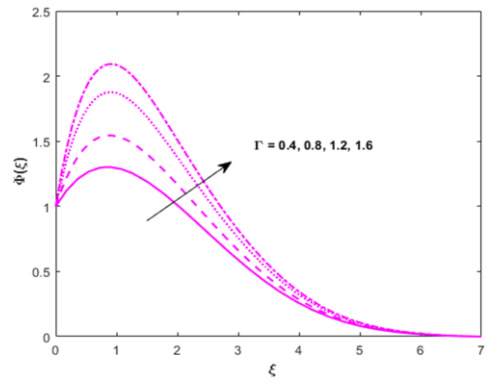
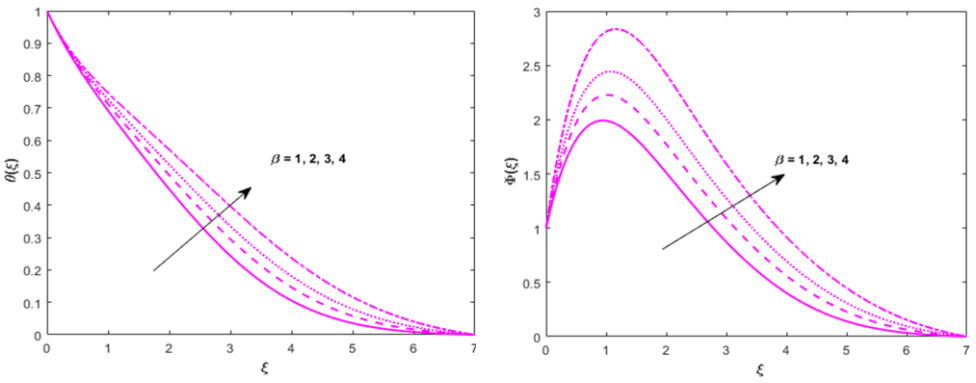
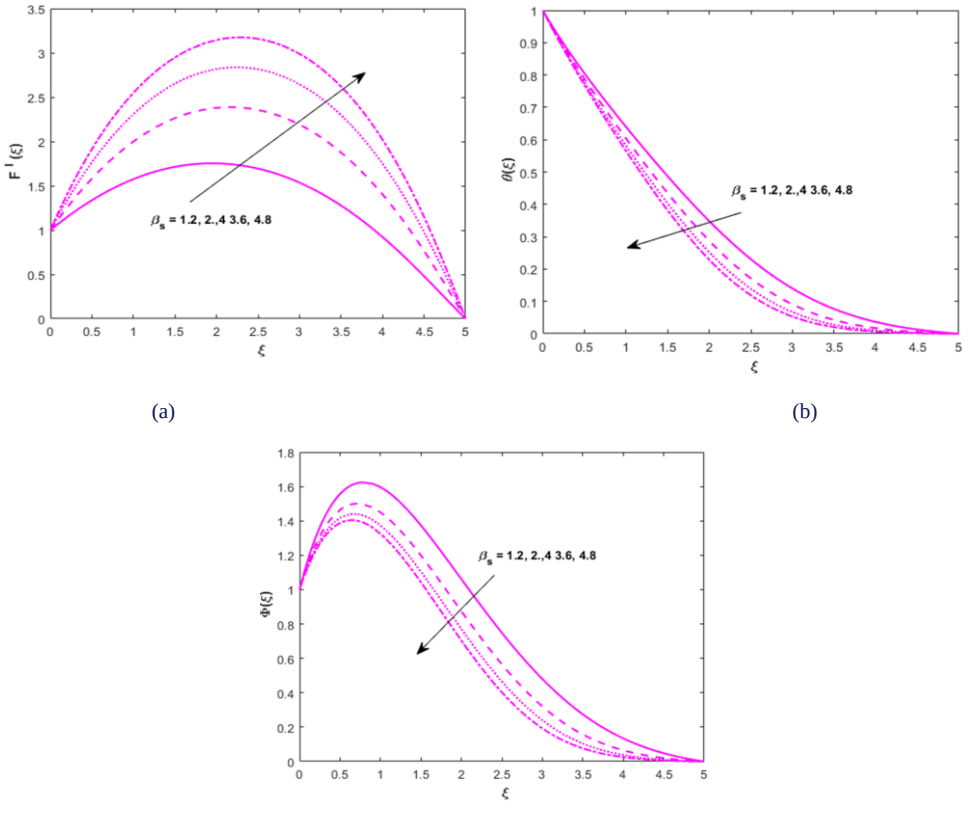


Fig. 8. Effect of Γ on $\Phi(\zeta)$.



(a) (b)

Fig. 9. Impact β on: a) $\theta(\zeta)$, and b) $\Phi(\zeta)$.



(a) (b)

(c)

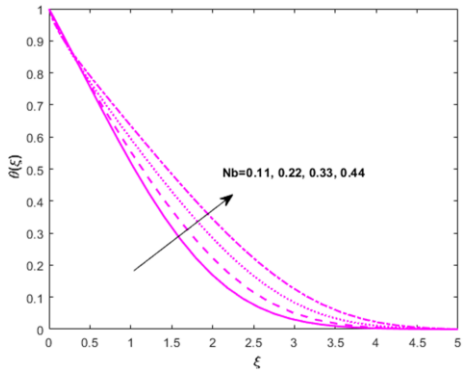
Fig. 10. Effect of β_s on: a) $F'(\zeta)$, b) $\theta(\zeta)$, and c) $\Phi(\zeta)$.

thickness of the thermal boundary layer is also examined. The impact of Brownian motion parameter (Nb) on $\theta(\zeta)$ and $\Phi(\zeta)$ is exhibited through the Figs. 11a and 11b, respectively. The results show that the augmented Brownian movement enhances the temperature profile whereas it decrements the concentration of Jeffrey nanofluid past the stretching sheet.

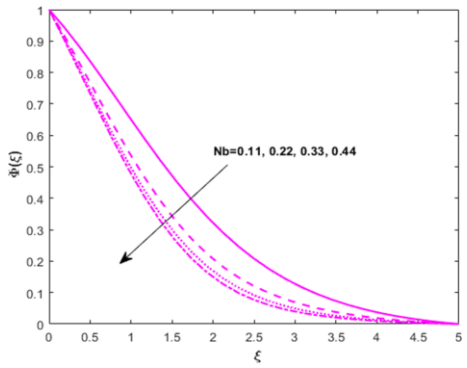
Figure 12 demonstrates the influence of Prandtl number (Pr) on $\Phi(\zeta)$ and $\theta(\zeta)$. The results show that an increase in Pr decreases the concentration $\Phi(\zeta)$ and it surges up the $\theta(\zeta)$ of the nanofluid along the stretching sheet.

Figure 13 displays the impact of the Lewis number (Le) on the concentration of nanofluid flow. A dimensionless number known as the Lewis number is defined as the ratio of the thermal boundary thickness to the concentration boundary layer thickness. The results reveal that the Lewis number reduces the concentration of nanofluid past the stretching surface. When it increases, the fraction of nanoparticle volume increases and the rate of mass transfer increases.

From Table 1 we can observe that M, β and Nt decrease the skin friction factor coefficient, and heat and mass transfer rates,

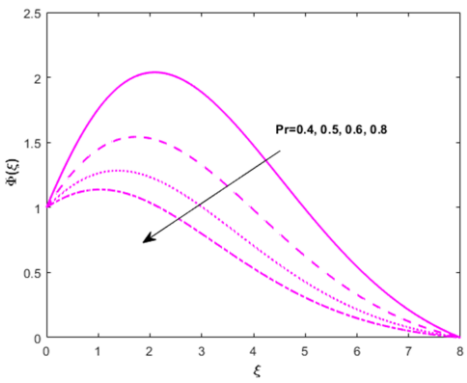


(a)

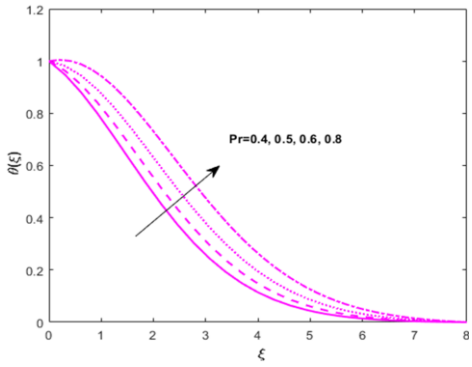


(b)

Fig. 11. Impact of *Nb* on: a) $\theta(\zeta)$, and b) $\Phi(\zeta)$.



(a)



(b)

Fig. 12. Effect of Pr on: a) $\Phi(\zeta)$, and b) $\theta(\zeta)$.

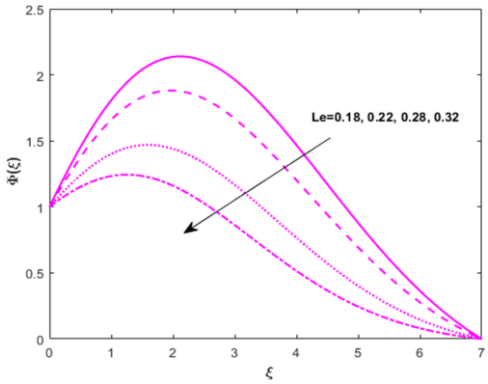


Fig. 13. Effect of Le on $\Phi(\zeta)$.

but the opposite trend can be observed as regards the impact of chemical reaction parameter. Darcy parameter and heat source parameter enhance the heat and mass transfer rates but diminish the skin friction coefficient. Finally, the Prandtl number and thermal radiation parameter enhance the heat transfer rate. The goal of this work is to show that the thermophoresis parameter impacts flat stretching sheet irrespective of additional physical characteristics. A comparison of previous findings was used to evaluate the validity of the present analysis. Heat generation, chemical reaction, thermal relaxation, thermal radiation, Lewis number, Prandtl number, and Brownian motion parameters are found to be in excellent agreement with those of Noghrehabadi et al. [48] and Rasool et al. [49], which are shown in Table 2.

6. Concluding remarks

The present work investigates the influence of the rate of heat and mass transfer on the boundary layer flow of a Jeffrey fluid. Some of the key findings of the study are listed below:

1) An increase in the thermal radiation parameter (R) leads to an increase in $\theta(\zeta)$ over the flat stretching sheet and the shape parameter (n) decreases both concentration and temperature profiles.
2) The concentration ($\Phi(\zeta)$) enlarges for improved metrics of thermophoresis parameter (Nt) in heat generation and hence, it could be inferred that the amount of heat and mass exchange increases by enhancing the thermophoresis parameter.
3) The magnetic field parameter (M) lessens the fluid velocity $F'(\zeta)$, whereas it increases both temperature and concentration in the presence of stretching sheet.
4) The fluid velocity increases, and both, temperature and concentration, decrease over the stretching sheet for increasing values of Deborah number (Da).
5) Da accelerates the flow and the interaction parameter (β) declines temperature and concentration profiles. The concentration of nanofluid near the wall enlarges as chemical reaction parameter (Γ) increases.
6) An increase in β augments the temperature and concentration of the nanofluid over stretching sheet.

Table 1. Numerical values of $\mathrm{Re}^{1/2}C_{fx}$, $-\mathrm{Re}^{-1/2}\mathrm{Nu}_x$ and $-\mathrm{Re}^{-1/2}\mathrm{Sh}_x$ for distinct values of n, M, λ, Le, Nb, Nt.

M	R	n	β	Nb	Nt	Pr	Da	β_s	Γ	$\mathrm{Re}^{1/2}C_{fx}$	$-\mathrm{Re}^{-1/2}\mathrm{Nu}_x$	$-\mathrm{Re}^{-1/2}\mathrm{Sh}_x$
0.2	1.1	0.3	1.0	0.2	0.1	0.3	0.5	0.6	0.3	-0.282825	0.470756	0.296402
0.4										-0.405691	0.447773	0.257508
0.8										-0.613039	0.407362	0.175855
	1.1									-0.462033	0.508971	0.260833
	2.2									-0.462132	0.627797	0.285551
	3.3									-0.462153	0.743016	0.299653
		0.3								-0.455331	0.834993	0.430956
		0.6								-0.232639	1.404371	0.623115
		0.9								-0.120835	1.983364	0.776368
			1.0							-0.911888	0.350850	0.144496
			1.5							-1.032867	0.340127	0.084824
			2.0							-1.141087	0.331808	0.022914
				0.2						-0.613312	0.373469	0.100882
				0.4						-0.725521	0.360514	0.022858
				0.8						-0.816602	0.339530	0.084342
					0.1					-0.816602	0.353799	0.100335
					0.3					-0.816602	0.346146	0.208557
					0.6					-0.816602	0.339346	0.701374
						0.3				-0.865965	0.293768	0.789873
						0.5				-0.865975	0.399425	0.369492
						0.7				-0.865985	0.468570	0.196080
							0.5			-0.692204	0.415457	0.301114
							0.7			-0.578540	0.436285	0.339561
							0.9			-0.451867	0.459372	0.381474
								0.6		-0.503356	0.502596	0.154077
								1.2		-0.503353	0.461514	0.156926
								1.8		-0.503350	0.454051	0.226907
									0.4	-0.503356	0.465296	0.159757
									0.8	-0.503355	0.527696	0.553727
									1.2	-0.428455	0.876910	0.929316

Table 2. Comparison of the present study results with other research findings, for $-\Phi'(0)$ and various values of Nt, with $R = M = Nt = \mathrm{Da} = \beta = \beta_s = \Gamma = 0$, $Nb = 0.2$, Pr = 10 and Le = 10.

Nt	$-\Phi'(0)$		
	Noghrehabadi et al. [48]	Rasool et al. [49]	Present results
0.2	1.76895455	1.76895455	1.76862
0.4	2.09565585	2.09565585	2.09544
0.6	2.50535461	2.50535461	2.50522

7) The velocity enlarges as heat generation parameter increases and the impact of heat absorption/generation outcomes in reducing $\theta(\zeta)$ and $\Phi(\zeta)$ distributions of the fluid over stretching sheet.
8) Chemical reaction parameter enhances the mass transfer rate in a Jeffrey nanofluid.
9) Thermophoresis and Brownian motion parameters decrease the heat transfer.

References

[1] Waqas, H. (2021). Numerical simulation for magnetic dipole in bio convection flow of Jeffrey nanofluid with swimming motile microorganisms. *Waves in Random and Complex Media*, 1–18. doi: 10.1080/17455030.2021.1948634

[2] Pal, D., Mondal, S., & Mondal, H. (2019). Entropy generation on MHD Jeffrey nanofluid over a stretching sheet with nonlinear thermal radiation using spectral quasilinearization Method. *International Journal of Ambient Energy*, 42(15), 1712–1726. doi: 10.1080/01430750.2019.1614984

[3] Abdullah Mohamed, R.A. (2020). MHD Jeffrey nanofluid flow over a stretching sheet through a porous medium in presence of nonlinear thermal radiation and heat generation/absorption. *Transport Phenomena in Nano and Micro Scales*, *8*(1), 9–22. doi: 10.22111/TPNMS.2019.29314.1172

[4] Turkyilmazoglu, M., & Pop, I. (2013). Exact analytical solutions for the flow and heat transfer near the stagnation point on a stretching/shrinking sheet in a Jeffrey fluid. *International Journal of Heat and Mass Transfer*, 57, 82–88. doi: 10.1016/ j.ijheatmasstransfer.2012.10.006

[5] Hayat, T. (2018). Simultaneous effects of melting heat and internal heat generation in stagnation point flow of Jeffrey fluid towards a nonlinear stretching surface with variable thickness. *International Journal of Thermal Sciences*, 132, 344–354. doi: 10.1016/j.ijthermalsci.2018.05.047

[6] Mabood, F., Imtiaz, M., & Hayat, T. (2020). Features of Cattaneo-Christov heat flux model for Stagnation point flow of a Jeffrey fluid impinging over a stretching sheet: A numerical study. *Heat Transfer*, 49(5), 2706–2716. doi: 10.1002/htj.21741

[7] Hayat, T., Kanwal, M., Qayyum, S., & Al Saedi, A. (2020). Entropy generation optimization of MHD Jeffrey nanofluid past a stretchable sheet with activation energy and non-linear thermal radiation. *Physica A*, 544, 123457. doi: 10.1016/j.physa.2019.123437

[8] Besthapu, P., Ul Haq, R., Bandari, S., & Al-Mdallal, Q.M. (2019). Thermal radiation and slip effects on stagnation point flow of

MHD non-Newtonian nanofluid over a convective stretching surface. *Neural Computing and Applications*, 31, 207–221. doi: 10.1007/s00521-017-2992-x

[9] Kumar, M. (2020). Study of differential transform technique for transient hydromagnetic Jeffrey fluid flow from a stretching sheet. *Nonlinear Engineering*, 9, 145–155. doi: 10.1515/nleng-2020-0004

[10] Sen, S.S.S., Das, M., & Shaw, S. (2021). Thermal dispersed homogeneous- heterogeneous reaction within MHD flow of a Jeffrey fluid in the presence of Newtonian cooling and nonlinear thermal radiation. *Heat Transfer*, 50(6), 5744–5759. doi: 10.1002/htj.22146

[11] Asjad, M.I., Basit, A., Akgul, A., & Muhammad, T. (2021). Generalized thermal flux flow for Jeffrey fluid with Fourier law over an infinite plate. *Mathematical Problems in Engineering*, 5403879. doi: 10.1155/2021/5403879

[12] Muhammad, K., Hayat, T., & Alsaedi, A. (2021). Stagnation point flow of Jeffrey nanofluid with activation energy and convective heat and mass conditions. In *Proceedings of the Institution of Mechanical Engineers, Part N: Journal of Nanomaterials, Nanoengineering and Nanosystems*, 236(2). doi: 10.1177/09544089211044245

[13] Anitha, L., & Gireesha, B. J. (2023). Convective flow of Jeffrey nanofluid along an upright microchannel with Hall current and Buongiorno model: an irreversibility analysis. *Applied Mathematics and Mechanics*, 44, 16131628. doi: 10.1007/s10483-023-3029-6

[14] Hayat, T., Habibullah, A., Ahmad, B., & Alhodaly, M. S. (2021). Heat transfer analysis in convective flow of Jeffrey nanofluid by vertical stretchable cylinder. *International Communications in Heat and Mass Transfer*, 120, 104965. doi: 10.1016/ j.icheatmasstransfer.2020.104965

[15] Ur Rasheed, H., AL-Zubaidi, A., Islam, S., Saleem, S, Khan, Z., & Khan, W. (2021). Effects of Joule heating and viscous dissipation on magnetohydrodynamic boundary layer flow of Jeffrey nanofluid over a vertically stretching cylinder. *Coatings*, 11(21), 353. doi: 10.3390/coatings11030353

[16] Ullah Khan, S., Ali Shehzadi, S., Munir Abbasi, F., & Hussain Arshad, S. (2021). Thermo diffusion aspects in Jeffrey nanofluid over periodically moving surface with time dependent thermal conductivity. *Thermoscience*, 25(1), 197–207. doi: 10.2298/TSCI190428312U

[17] Dadhich, Y., Jain, R., & Kaladgi, A.R. (2021). Thermally radiated Jeffery fluid flow with nanoparticles over a surface of varying thickness in the influence of heat source. *Case Studies in Thermal Engineering*, 28, 101549. doi: 10.1016/j.csite.2021.101549

[18] Hayat, T., Muhammad, T., Al-Mezal, S., & Liao, S. J. (2016). Darcy-Forchheimer flow with variable thermal conductivity and Cattaneo-Christov heat flux. *International Journal of Numerical Methods for Heat & Fluid Flow*, 26, 2355–2369. doi: 10.1108/HFF-08-2015-0333

[19] Alshomrani, A. S., & Ullah, M. Z. (2019). Effects of homogeneous-heterogeneous reactions and convective condition in Darcy-Forchheimer flow of carbon nanotubes. *Journal of Heat Transfer*, 141(1), 012405. doi: 10.1115/1.4041553

[20] Muhammad, T., Alsaedi, A., Shehzad, S.A., & Hayat, T. (2017). A revised model for Darcy Forchheimer flow of Maxwell nanofluid subject to convective boundary condition. *Chinese Journal of Physics*, 55(3), 963–976. doi: 10.1016/j.cjph.2017.03.006

[21] Mandal, P. K., & Seth, G. S. (2018). Hydromagnetic rotating flow of Casson fluid in Darcy-Forchheimer porous medium. *MATEC Web of Conferences*, 192, 02059. doi: 10.1051/matecconf/201819202059

[22] Bilal Ashraf, M., Hayat, T., Alsaedi, A., & Shehzad, S. A. (2015). Convective heat and mass transfer in MHD mixed convection flow of Jeffrey nanofluid over a radially stretching surface with thermal radiation. *Journal of Central South University*, 22, 1114-1123. doi: 10.1007/s11771-015-2623-6

[23] Hayat, T., Waqas, M., Ijaz Khan, M., & Alsaedi, A. (2017). Impacts of constructive and destructive chemical reactions in magnetohydrodynamic (MHD) flow of Jeffrey liquid due to non-linear radially stretched surface. *Journal of Molecular Liquids*, 225, 302–310. doi: 10.1016/j.molliq.2016.11.023

[24] Ali K., Akbar, M.Z, Farooq Iqbal, M., & Ashraf, M. (2014). Numerical simulation of heat and mass transfer in unsteady nanofluid between two orthogonally moving porous coaxial disks. *AIP Advances*, 4, 107113. doi: 10.1063/1.4897947

[25] Lund, L.A., Omar, Z., Khan, I., Raza, J., Bakouri, M., & Tlili, I. (2019). Stability analysis of Darcy-Forchheimer flow of Casson type Nanofluid over an exponential sheet: Investigation of critical points. *Symmetry*, 11(3), 412. doi: 10.3390/sym11030412

[26] Mabood, F. (2016). Numerical study of unsteady Jeffrey fluid flow with magnetic field effect and variable fluid. *Journal of Thermophysics and Heat Transfer*, 8, 041003. doi: 10.1115/1.4033013

[27] Khani, F., Farmany, A., Ahmadzadeh Raji, M., Aziz, A. & Samadi, F. (2009). Analytic solution for heat transfer of a third grade viscoelastic fluid in non-Darcy porous media with thermophysical effects. *Communications in Nonlinear Science and Numerical Simulation*, 14, 3867-3878. doi: 10.1016/j.cnsns.2009.01.031

[28] Hayat, T., Hussain, Z., Ahmad, B., & Alsaedi, A. (2017). Base fluids with CNTs as nanoparticles through non-Darcy porous medium in convectively heated flow: A comparative study. *Advanced Powder Technology*, 28, 855–865. doi: 10.1016/j.apt.2017.04.003

[29] Siddiq, M. K., Ashraf, M., & Mushtaq, T. (2021). MHD thermally radiative flow of Carreau fluid subjected to the stretching sheet by considering non-Darcy Forchheimer law. *Pramana - Journal of Physics*, 9, 164. doi: 10.1007/s12043-021-02192-z

[30] Madhu, M., & Prabhakar, B. (2021). Darcy-Forchheimer Flow of MHD Powell-Eyring nanoliquid over a nonlinear radially stretching disk with the impact of activation energy. *Discontinuity, Nonlinearity, and Complexity*, 10(14), 743–753. doi: 10.5890/DNC.2021.12.013

[31] Madkhali, H.A., Nawaz, M., Saif, R.S., Afzaal, M.F., Alharbi, S.O., & Kbiri Alaoui, M. (2021). Comparative analysis on the roles of different nanoparticles on mixed convection heat transfer in Newtonian fluid in Darcy-Forchheimer porous space subjected to convectively heated boundary. *International Communications in Heat and Mass Transfer*, 128, 105580. doi: 10.1016/ j.icheatmasstransfer.2021.105580

[32] Machireddy, G.R., Praveena, M.M., Rudraswamy N.G., & Kumar, G.K. (2021). Impact of Cattaneo-Christov heat flux on hydromagnetic flow of non-Newtonian fluids filled with Darcy-Forchheimer porous medium. *Waves in Random and Complex Media*, 1957178. doi: 10.1080/17455030.2021.1957178

[33] Ramesh, G.K., Madhukesh, J.K., Shah, N.A., & Yook, S.-J. (2023). Flow of hybrid CNTs past a rotating sphere subjected to thermal radiation and thermophoretic particle deposition. *Alexandria Engineering Journal*, 64, 969–979. doi: 10.1016/j.aej.2022.09.026

[34] Eswaramoorthi S., Loganathan, K., Faisal, M., Thongchai Botmart, T., & Shah, N.A. (2023). Analytical and numerical investigation of Darcy-Forchheimer flow of nonlinear-radiative non-

Newtonian fluid over a Riga plate with entropy optimization. *Ain Shams Engineering Journal*, 14, 101887. doi: 10.1016/j.asej. 2022.101887

[35] Asghar A., Teh, Y.Y., & Zaimi, K. (2022). Two-Dimensional Mixed Convection and Radiative Al2O3-Cu/H2O Hybrid Nanofluid Flow over Vertical Exponentially Shrinking Sheet with Partial Slip Conditions. *CFD Letters*, 14(13), 22–28. doi: 10.37934/cfdl.14.3.2238

[36] Asghar, A., Lund, L.A., Shah, Z., Vrinceanu, N., Deebani, W., & Shutaywi, M.. (2022). Effect of Thermal Radiation on Three-Dimensional Magnetized Rotating Flow of a Hybrid Nanofluid. *Journal of Nanomaterials*, 12(9), 1566. doi: 10.3390/ nano12091566

[37] Sajjad, M., Mujtaba, A., Asghar A., & Teh Y. Y. (2022). Dual Solutions of Magnetohydrodynamics Al2O3+Cu Hybrid Nanofluid Over a Vertical Exponentially Shrinking Sheet by Presences of Joule Heating and Thermal Slip Condition. *CFD Letters*, 14(8), 100−115. doi: 10.37934/cfdl.14.8.100115

[38] Teh Y.Y., & Asghar, A. (2021). Three Dimensional MHD Hybrid Nanofluid Flow with Rotating Stretching/Shrinking Sheet and Joule Heating. *CFD Letters*, 13(8), 1–19. doi: 10.37934/cfdl. 13.8.119

[39] Asghar, A., Teh, Y.Y., Zaimi, K.. (2022). Two-Dimensional Magnetized Mixed Convection Hybrid Nanofluid Over a Vertical Exponentially Shrinking Sheet by Thermal Radiation, Joule Heating, Velocity and Thermal Slip Conditions. *Journal of Advanced Research in Fluid Mechanics and Thermal Sciences*, 95(2), 159–179. doi: 10.37934/arfmts.95.2.159179

[40] Asghar A., Chandio A.F., Shah Z., Vrinceanu N., Deebani W., Shutaywi M., et al. (2023). Magnetized mixed convection hybrid nanofluid with effect of heat generation/absorption and velocity slip condition. *Heliyon*, 9(2), 13189. doi: 10.1016/j.heliyon. 2023.e13189

[41] Asghar, V., Vrinceanu, N., Teh, Y.Y., Lund, L.A., Shah, Z., & Tirt, V. (2023). Dual solutions of convective rotating flow of three-dimensional hybrid nanofluid across the linearstretching/shrinking sheet. *Alexandria Engineering Journal*, 75, 297–312. doi: 10.1016/j.aej.2023.05.089

[42] Gohar., Khan, T.S., Sene, N., Mouldi, A., & Brahmia, A.(2022). Heat and Mass transfer of the Darcy-Forchheimer Casson Hybrid Nanofluid Flow due to an Extending Curved Surface. *Journal of Nanomaterials*, 3979168. doi: 10.1155/2022/3979168

[43] Sathyanarayana, M., Ramakrishna Goud, T. (2023). Numerical study of MHD Williamson-nano fluid flow past a vertical cone in the presence of suction/injection and convective boundary conditions. *Archives of Thermodynamics*, 44(2), 115–138. doi: 10.24425/ather.2023.146561

[44] Mamatha, S. U., Ramesh Babu, K., Durga Prasad, P., Raju, C.S.K., & Varma, S.V.K. (2020). Mass transfer analysis of two-phase flow in a suspension of microorganisms. *Archives of Thermodynamics*, 41(1), 175-192. doi: 10.24425/ ather.2020.132954

[45] Madhusudhana Rao, B., Gopal, D., Kishan, N., Ahmed, S., & Durga Prasad, P. (2020). Heat and mass transfer mechanism on three-dimensional flow of inclined magneto Carreau nanofluid with chemical reaction. *Archives of Thermodynamics*, 41(2), 223–238. doi: 10.24425/ather.2020.133630

[46] Hayat, T., Shah, F., Hussain, Z., & Alsaedi, A. (2019). Darcy Forchheimer flow of Jeffrey nanofluid with heat generation/absorption and melting heat transfer. *Thermoscience*, 23(6B), 3833−3842. doi: 10.2298/TSCI171222314H

[47] Chandel, S., & Sood, S., (2023). Dynamics of Williamson hybrid nanofluid over an extending surface with non-linear convection and shape factors. *Journal of Nanofluids*, 12 (5), 1335-1350. doi: 10.1166/jon.2023.2022

[48] Nogrehabadi, A., Pourrajab, R., & Ghalembaz, M. (2012). Effect of partial slip boundary condition on the flow and heat transfer of nanofluids past stretching sheet prescribed constant wall temperature. *International Journal of Thermal Sciences*, 54, 253–261. doi: 10.1016/j.ijthermalsci.2011.11.017

[49] Rasool, G., Chamkha, A.J., Muhammad, T., Shafiq, A., & Khan, I. (2020). Darcy-Forchheimer relation in Casson type MHD nanofluid flow over non-linear stretching surface. *Propulsion and Power Research*, 9(2), 159–168. doi: 10.1016/j.jppr.2020.04.003

Co-published by
Institute of Fluid-Flow Machinery
Polish Academy of Sciences
Committee on Thermodynamics and Combustion
Polish Academy of Sciences

Copyright©2024 by the Authors under licence CC BY 4.0

http://www.imp.gda.pl/archives-of-thermodynamics/

Finite element analysis of femur bone fracture – modelling and analysis

Pranjal Sarmah[a], Ravi Kumar[a], Amrit Thakur[a], Mohit Sharma[a], Surendra Kumar Yadav [b*], Virendra Kumar[c*]

[a]Department of Mechanical Engineering, Dibrugarh University, Dibrugarh 786004, Assam, India
[b]Department of Mechanical Engineering, K. R. Mangalam University, Gurugram 122001, India
[c]Department of Mechanical Engineering, Harcourt Butler Technical University, Kanpur 208002, India
*Corresponding author email: s.k.yadav86@gmail.com, virendra.k@hbtu.ac.in

Received: 09.10.2023; revised: 12.12.2023; accepted: 10.04.2024

Abstract

Femoral fractures are frequent in adolescents and children, and most fractures occur within the centre of the bone, typically referred to as the femur shaft. Plate and screws are ideal fixation methods for femoral fractures close to the articular surfaces. When using plates and screws, estimating the load on the plates and screws before starting treatment is important. The primary focus of this paper is the examination of fixation plates utilized in the treatment of femur bone fractures. The study employs the finite element method to conduct this analysis. Initial modelling of the femur bone is executed through the utilization of CATIA V5 software. Subsequently, the investigation transitions to the ANSYS R14.5 environment, where more in-depth analysis is carried out. The modelling of the fracture fixation plates is done on commercially available CAD software CATIA V5. The stress distribution of different biomaterials in the bone plate system is calculated when the system is subjected to compressive loads with varying healing times. Here we have used stainless steel (SS316-L), titanium alloy (Ti6Al4V) and magnesium alloy (AZ31). More focus was given to the magnesium alloy. Here a fracture gap of 1mm gap was taken for analysis. A comprehensive compressive force amounting to 750 N was applied to the bone-plate assembly during the simulation. This force magnitude corresponds to the approximate weight of an average human body.

Keywords: Femur shaft; Simulation; Fixation plate; Finite element method.

Vol. 45(2024), No. 2, 261–268; doi: 10.24425/ather.2024.150870

Cite this manuscript as: Sarmah, P., Kumar, R., Thakur, A., Sharma, M., Yadav, S.K., & Kumar, V. (2024). Finite element analysis of femur bone fracture-modelling and analysis. *Archives of Thermodynamics*, 45(2), 261−268.

1. Introduction

Biomechanics is the branch of science that uses mechanical principles concerning all forces acting on the human body and the effects of the forces on the bone to analyse the biological system. It is a branch of science that deals with applying mechanical principles to biological things [1]. The biomechanical elements that determine the rate of healing efficiency of a fractured bone treated with plates and screws are given to the fractured bone in the form of (a) the level of bone contact that occurs at the fracture interface and (b) stability provided to the fractured bone in terms of reduced motion at the fracture interface, and (c) Necessary and adequate stress shielding of bone at and away from the fracture interface [2]. Studied ways to accurately predict the strength and risk of fractures in femurs with metastases using finite element modelling. However, there's a variety in the material models, loading conditions, and critical thresholds used in these models [3]. Orthopaedic surgeons are finding it challenging to treat bone fractures resulting from accidents. To address this issue, screws and locking compression plates are used

to externally stabilize fractured bones. In this study, we modelled the femur bone, locking compression plate, and screws. We then analysed the existing materials for joining plates using different materials [4]. Bones serve as the body's main structural support, protecting vital organs and giving us a sturdy frame for movement. Studying bone mechanics helps us understand how and why bones break. From an engineering perspective, fractures happen when the force or pressure on a bone exceeds its capacity to bear the load [5]. Bones are crucial tissues made of calcium and phosphorus. They grow quickly in their early years and repair themselves well. Bones are essential for the human skeleton, providing support for the softer parts of the body. When bones crack, a common way to treat them is by using bone joints to reconnect the broken parts [6].

The term "femur bone" pertains to a bone-like substance that is synthesized within a laboratory setting. This material finds application in bone graft procedures, serving as a replacement for human bone loss resulting from conditions such as severe fractures, illnesses, and related factors [6]. The femur bone stands as the longest and most robust bone within the human body, bridging the connection between the hip joint and the knee joint. [7]. The femur bone contains a linear elastic, isotropic and homogenous material of calcium phosphate. In the human body during static loading, femur bone supports weight in between the hip and knee joints. In femur mid shaft fracture is common [8]. It fractures due to the sudden impact of a large amount of force, for example accidents, fall from great height. In some cases, due to osteoporosis small amounts of force can also fracture the femur bone. To promote bone structure stabilisation, various types of internal fixation devices like bone plates are used [9]. The femur bone can bear 25% of the body weight of the person's height. It can bear 2 500 N force (which is 4 times the body weight) without any significant change in the factor of safety [10]. Figures 1 and 2 show the complete structure of the femur bone and the cut section of the bone respectively. The material properties of cortical and trabecular bone are shown in Tables 1 and 2, respectively.



Fig. 1. Femur bone.

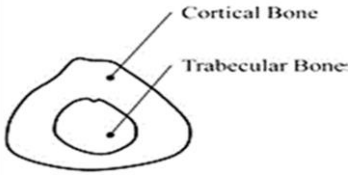


Fig. 2. Geometric view of femur bone.

Biomaterials are used in the manufacture of structures to replace broken or diseased biological structures or parts and restore their morphology and function. Biomaterials interact with cells and exhibit stereotypical responses. Biomaterials have to show bio-functionally and bio-compatibility properties. Biodegradable materials can get decomposed by the action of microorganisms such as bacteria. When considering biomedical uses, the choice of a biodegradable material becomes a pivotal aspect. This decision bears weight due to the material's density, mechanical characteristics, and rates of corrosion (biodegradation), all of which notably influence both the implant plate's design and its performance [11]. Over the span of the last six decades, substantial progress has been made in the development of novel materials characterized by excellent biocompatibility. This evolution encompasses three distinct generations: the initial generation marked by bioinert materials, the subsequent generation featuring bioactive and biodegradable materials, and the most recent third generation characterized by biologically adaptive materials [12].

Table 1. Material properties of cortical bone [19].

No.	Parameters	Value
1	Material	Cortical bone
2	Elastic modulus	16 700 MPa
3	Density	1 750 kg/m^3
4	Poisson's ratio	0.26

Table 2. Material properties of trabecular bone [19].

No.	Parameters	Value
1	Material	Trabecular bone
2	Elastic modulus	100 MPa
3	Density	1 750 kg/m^3
4	Poisson's ratio	0.3

A new era has dawned in the realm of developing implant materials that are both corrosion-resistant and biodegradable, tailored to harmonize with the physiological milieu. The imperative is for these implant materials to satisfy specific mechanical requisites, enabling them to effectively endure biomechanical forces. Implant materials that were used in this study are titanium alloy, stainless steel alloy and magnesium alloy. Research says that the best-suited material for orthopaedic implants is Magnesium alloy because of its biocompatibility, biodegradability, bioresorbable, closer density, Young modulus of bone (E = 10−30 GPa), low-stress shielding effect, and light in weight. The strain distribution of the callus generated between the fractured surfaces was considered the main criterion in determining the best bone plate performance. A connected study by [8,13] found that a gap strain of 2% to 10% was effective in creating and developing callus at the fracture site by stimulating healing tissue. Callus is also known to develop dramatically 4−8 weeks after surgery, which is generally considered to be the most important time for fracture healing [14−16]. The material properties of callus are shown in Table 3.

Fracture fixation can also be accomplished through secondary-type healing via callus formation, which takes place when new bone is produced at the location of the fracture site and its porosity is reduced as it develops into a mature structure. Inflammation, soft callus, hard callus, and bone remodelling are the four steps that take place, and during each stage, the mechanical stiffness and strength increase [17].

Table 3. Material properties of callus [21].

No.	Property	Callus 1%	Callus 50%	Callus 100%
1	Density (kg/m^3)	1 100	1 500	1 750
2	Elastic modulus E (MPa)	20	10 000	16 700
3	Poisson's ratio	0.3	0.3	0.3

Hence, it holds significance to offer the optimal gap or load on the callus during this phase. Upon completion of an eight-week healing interval, the callus reaches a state conducive to the formation of solid bone, heightening the importance of stabilizing the fractured site. This study aimed to explore the biomechanical viability of bone plates constructed from diverse biomaterials, aiming to establish an environment conducive to the effective development of callus.

2. Method: finite element method

The finite element analysis is a practical implementation of the finite element method, utilized to carry out detailed assessments through this methodology. To check developed structural stresses finite element analysis (FEA) is used. It also helps in identifying high-stress zones in implant design. Solid models of implant material such as bone plates and screws were created in CATIA software. The completed assembly was transferred to the ANSYS Workbench program for finite element analysis, with the export facilitated through the utilization of CATIA V5 software.

The Finite Element Method is a numerical approach used to get an approximate solution to problems such as boundary values using elliptical partial differential equations. Because the finite element approach transforms these elliptical partial differential equations into a set of algebraic equations, they are easily solved. FEA additionally establishes a correlation between the quantity of elements employed and the level of analytical accuracy achieved.

2.1. Selection of material and methodology

Biological internal fixation has no effect on early and complete restoration of bone, limb and patient function, but recognition of optimal requirements for bone healing is now preferred, with stable performance and less rigid mechanics while still allowing painless and reliable functional healing [13]. The biomaterials that are selected for this study are:

- Magnesium Alloy (AZ31), Table 4,
- Titanium (Ti-6Al-4V Alloy), Table 5,
- Stainless steel (SS316L Alloy), Table 6.

Here Table 4 represents the material properties of Mg Alloy, Table 5 represents the material properties of Ti-6Al-4V Alloy and Table 6 represents the material properties of SS316-L Alloy, respectively. Complete material properties along with the data showing the elastic modulus, shear modulus, density, and Poisson's ratio are represented in the tables below respectively. These materials are selected based on their metal compatibility, corrosion, strength and ductility.

Table 4. Material properties of Mg alloy [20].

No.	Parameters	Value
1	Material	Mg Alloy (AZ31)
2	Elastic modulus	45 000 MPa
3	Density	1 810 kg/m^3
4	Poisson's ratio	0.35
5	Shear modulus	16.67 GPa
6	Ultimate tensile strength	260 MPa

Table 5. Material properties of Ti-6Al-4V alloy [21].

No.	Parameters	Value
1	Material	Ti-6Al-4V Alloy
2	Elastic modulus	120 000 MPa
3	Density	4 500 kg/m^3
4	Poisson's ratio	0.32
5	Shear modulus	45 455 MPa
6	Ultimate tensile strength	397.2 MPa

Table 6. Material properties of SS316-L alloy [18].

No.	Parameters	Value
1	Material	SS316L Alloy
2	Elastic modulus	193 000 MPa
3	Density	7 750 kg/m^3
4	Poisson's ratio	0.31
5	Shear modulus	73 664 MPa
6	Ultimate tensile strength	570 MPa

Ti-6Al-4V is low-density material. So, it is used for implantation. Because of this, the patient can move his/her leg easily [18]. This alloy has excellent bio-compatibility and mechanical properties. Compared to Ti-alloy stainless steel is more economical. It has poor fatigue strength. Magnesium alloy is biodegradable. It has a low shielding effect and is light in weight.

3. CFD modelling

Within the scope of the finite element simulation, the configuration of the fractured long bone is portrayed as a pair of uniform hollow cylindrical structures, each measuring 280 mm in length and possessing an external diameter of 27 mm. Additionally, solid cylindrical forms with a length of 280 mm and an internal diameter of 13 mm are employed. For the analytical phase, a straightforward transverse fracture pattern, classified as a low-energy fracture, was chosen. The process encompassed the creation of bone and plate models through CATIA V5 software, followed by the assembly of distinct components. The length of the bone plates measures 145 mm, encompassing 8 holes, each featuring a diameter of 4.5 mm. These plates are affixed to the fractured bone using 8 implant alloy screws, each measuring 4.5

mm in diameter and 31 mm in length [8]. Figure 3 shows the geometry (3D models) of the femur bone, plates, and screw which are made in the CATIA software.

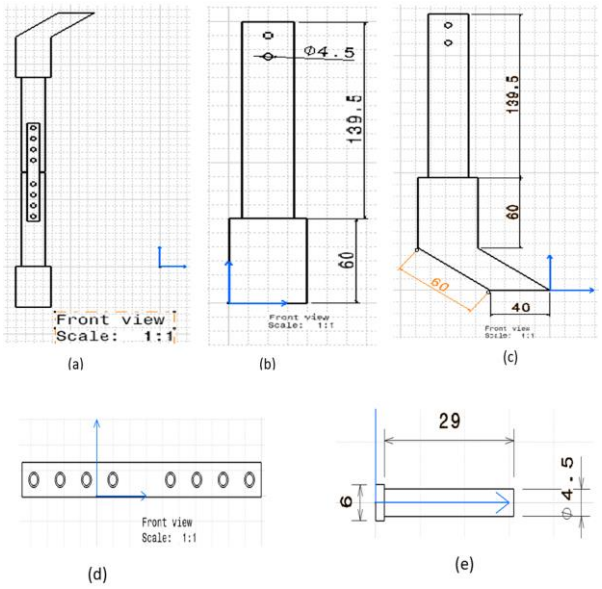


Fig. 3. CAD models of: (a) front view of femur bone with plate and screw, (b) lower part of cortical femur, (c) upper part of cortical femur, (d) bone plate, (e) screw.

Meshing: A mesh is defined as the process of dividing an entire component into a set of elements so that the load is evenly distributed each time the component is loaded. This is called a meshing. Components are analysed in two ways. One is meshed and the other is without meshed.

With Meshing: When a load is applied to a structure or body and the bodies are considered interlocked, the load is evenly distributed throughout the structure. After creating the mesh, the entire structure is divided into several elements, each of which has its stiffness under load.

Without Meshing: Applying loads to bodies in which mesh is not created can result in uneven load distribution and irregular or false results.

In our study, we used ANSYS Workbench R14.5 software to generate a mesh of the femur assembly model, as shown in Fig. 4. We used tetrahedral elements (5 mm) of the same size and shape for the meshing [16,21,22].

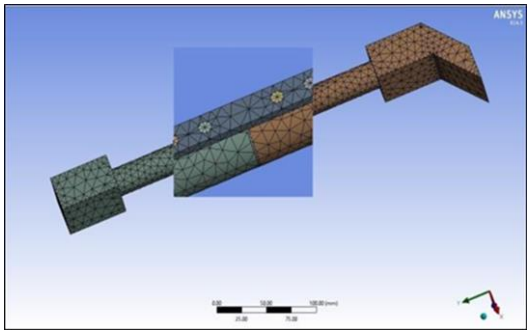


Fig. 4. Meshed model.

3.1. Loading and boundary conditions

A comprehensive compressive force amounting to 750 N was imposed on the cortical region of the femoral head within the assembly. The opposing side of the bone was maintained as a fixed support, resulting in a statically loaded model [20]. The implant plate should exhibit homogeneity, maintaining consistent mechanical and degradation characteristics throughout. The loading conditions for the implant plate are contingent on the two segments of the fractured bone. The fractured lower section of the bone is regarded as anchored by the lower limbs (legs). This signifies that one side of the lower segment can be treated as fixed, secured in place with a screw. Conversely, the upper part of the fractured bone is immobilized, and the upper section of the plate is affixed with screws to withstand the applied load [11]. Figure 5 shows how the assembly is kept in a fixed support from one end and Fig. 6 shows that a load is applied on the assembly from one end.

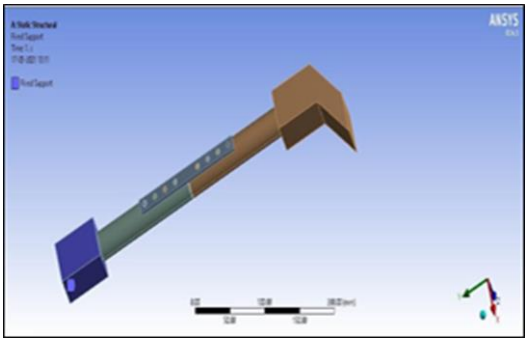


Fig. 5. Fixed support on assembly.

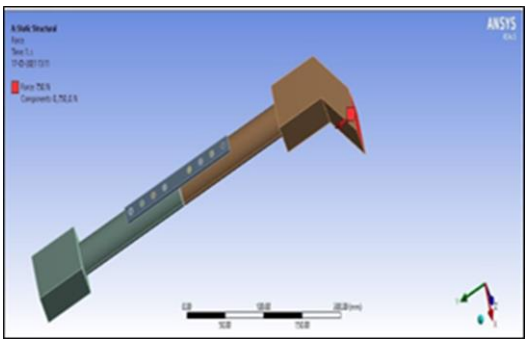


Fig. 6. Load on assembly.

4. Results and discussion

This investigation aimed to assess the levels of maximum and minimum stress, as well as maximum and minimum strain and deformation, resulting from the utilization of implants composed of different materials in a male individual weighing 75 kg, under standard anatomical conditions. The main fluctuations occurring in callus, are 1% and 50%. 100% of the healing phase is achieved with different implant materials and results for each category are calculated. Initially, at around 1%, there is minimal callus formation, characterized by soft fibrous tissue. As the

healing progresses, typically peaking around 50%, the callus transforms into a more rigid structure incorporating both cartilage and woven bone. This intermediate callus provides initial stability to the fractured site. Finally, at 100% the callus undergoes further remodelling, transitioning into mature, lamellar bone. This phase ensures the restoration of strength and function to the bone.

Here, the model was just statically loaded. The following Figures show the response of the bone plate system for a 1 mm gap compressive load using a variety of implant materials. Below Figs 7, 8 and 9 show the Von Mises stress distributions on the bone plate at 1%, 50%, and 100% callus for Ti-6Al-4V alloy. Figures 10−12 show the Von Mises stress distributions on the bone plate at 1%, 50%, and 100% callus for Mg AZ31 alloy. Figures 13−15 show the Von Mises stress distributions on the bone plate at 1%, 50%, and 100% callus SS316-L alloy. Figures 16−18 show the equivalent strain results for Ti-6Al-4V alloy, Mg AZ31 alloy, and SS316-L alloy respectively. Figures 19−21 show the Total deformation results for Ti-6Al-4V alloy, Mg AZ31 alloy, and SS316-L alloy respectively.

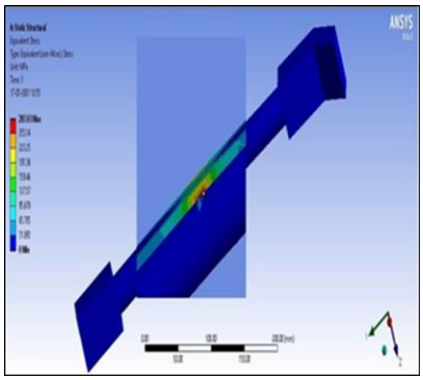


Fig. 7. Von Mises stress distributions on bone plate at 1% callus for Ti-6Al-4V alloy.

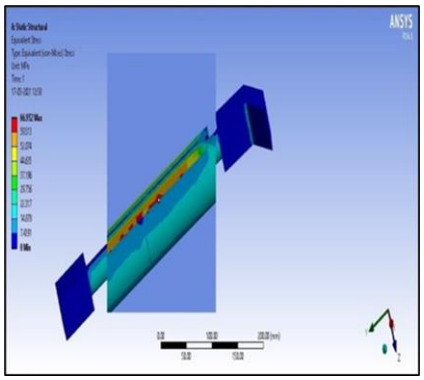


Fig. 8. Von Mises stress distributions on bone plate at 50% callus for Ti-6Al-4V alloy.

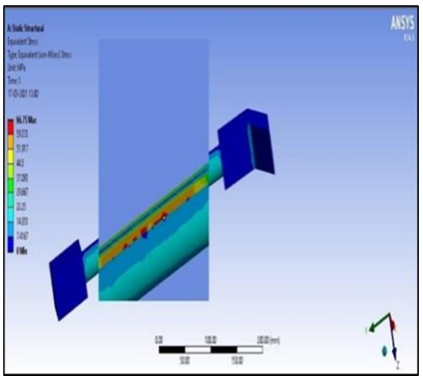


Fig. 9. Von Mises stress distributions on bone plate at 100% callus for Ti-6Al-4V alloy.

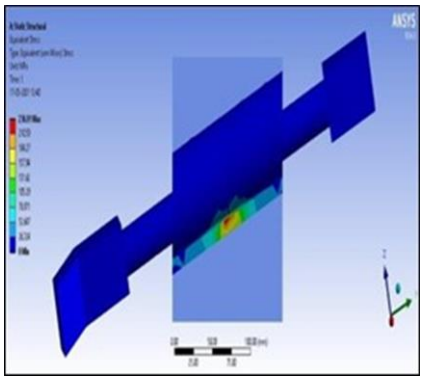


Fig. 10. Von Mises stress distributions on bone plate at 1%, callus for Mg AZ31 alloy.

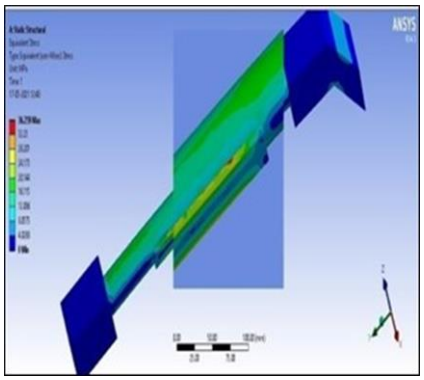


Fig. 11. Von Mises stress distributions on bone plate at 50%, callus for Mg AZ31 alloy.

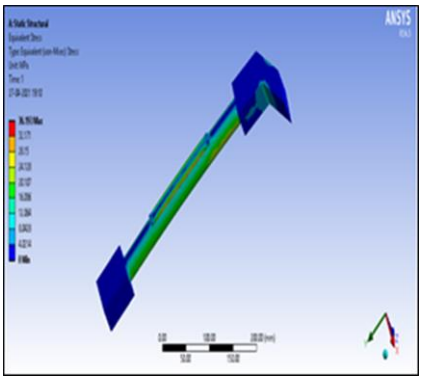


Fig. 12. Von Mises stress distributions on bone plate at 100%, callus for Mg AZ31 alloy.

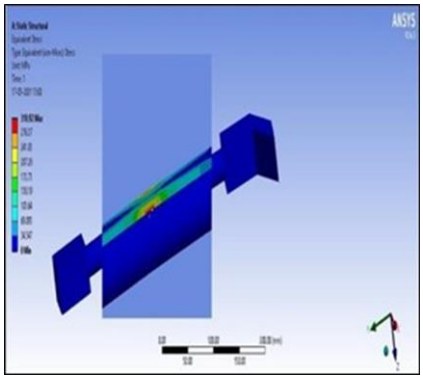


Fig. 13. Von Mises stress distributions on bone plate at 1% callus SS316-L alloy.

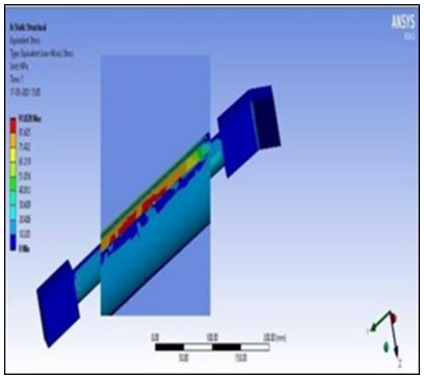


Fig. 14. Von Mises stress distributions on bone plate at 50% callus SS316-L alloy.

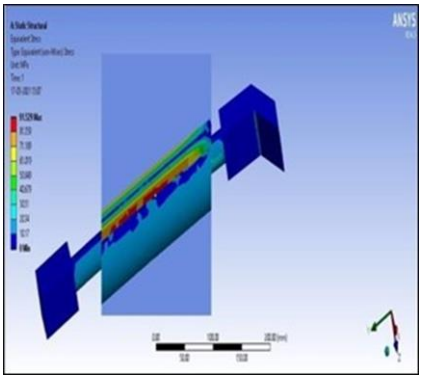


Fig. 15. Von Mises stress distributions on bone plate at 100% callus SS316-L alloy.

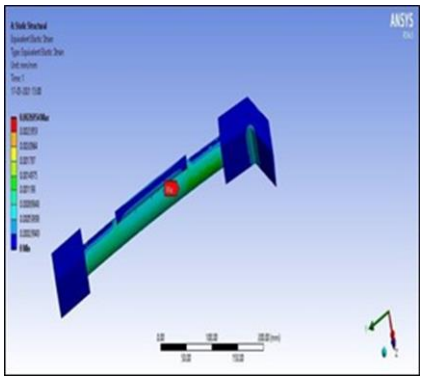


Fig. 16. Equivalent strain results for Ti-6Al-4V alloy.

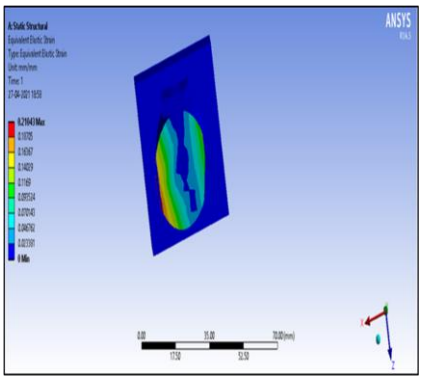


Fig. 17. Equivalent strain results for Mg AZ31 alloy.

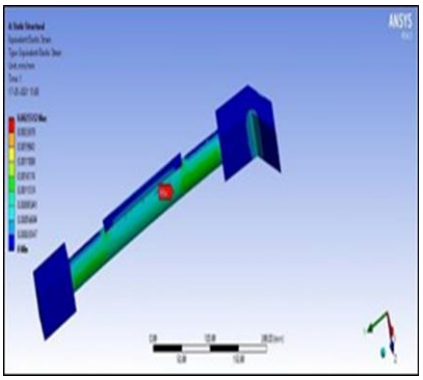


Fig. 18. Equivalent strain results for SS316-L alloy.

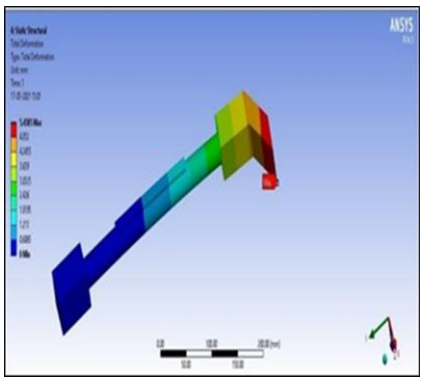


Fig. 19. Total deformation results for Ti-6Al-4V alloy.

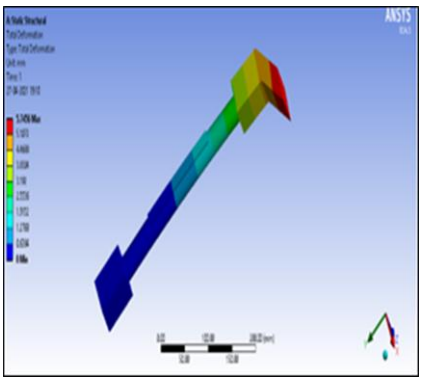


Fig. 20. Total deformation results for Mg AZ31 alloy.

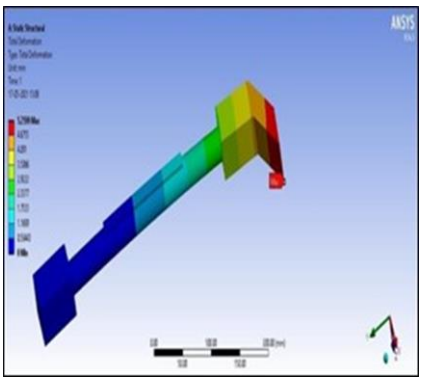


Fig. 21. Total deformation results for SS316-L alloy.

Since the fracture zone is immature compared to normal bone tissue, it is not possible to load the bone in the early stages of healing, so the load-bearing part includes only the bone plate. Callus has a low elastic modulus and cannot withstand the load. Therefore, the tension of the bone plate is also relatively higher in the magnesium plate. As the healing duration extends, the fracture zone gains increased strength in contrast to its initial healing phase, thus enabling enhanced load transmission to the bone. During the 50% and 100% healing stages, supplementary callus forms at the fracture junction, affording the bone greater load-bearing capacity. Consequently, the bone and plate function as a composite material, leading to heightened stress levels at the fracture location while concurrently alleviating stress on the bone plate. Figure 22 shows the Graphical representation of obtained stress results with different healing conditions using the three different implant materials which are Mg (AZ31) alloy SS316L alloy and Ti6Al-4V alloy.

In this study, the biomechanical performance of titanium alloys (Ti6Al4V), stainless steel (SS316L), and magnesium alloys used to heal femoral fractures is investigated through finite element analysis. The titanium alloy, stainless steel, and magnesium alloy implants are taken for analysis, various models of the assembly are designed on CATIA software, and the analysis is performed with Ansys R14.5. Previous studies have shown that Magnesium alloys are used in the field of orthopaedics because of their biodegradability, bioabsorbable, Young's modulus of bone (E = 10 GPa to 30 GPa), less stress shielding effect, and light in weight. It can be seen from Table 7, that the minimum stress that is obtained at various stages of callus formation is in the magnesium alloy. From the results, it is clear that at 1% callus, the value of Von-misses stress of magnesium implant is 236.91 MPa at 50% callus is 36.295 MPa and at 100% callus formation is 36.209 MPa. Therefore, if a fracture occurs in the femoral shaft of the femur, the magnesium alloy plate has the lowest stress compared to other implant materials and can be healed early with a magnesium implant.

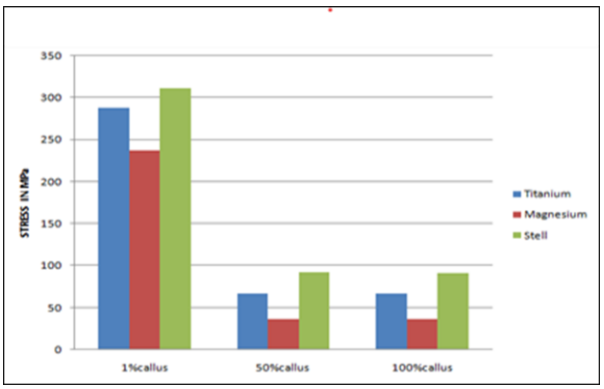


Fig. 22. Graphical representation of obtained stress results with different healing conditions.

Table 7. Finite element analysis (FEA) results for different bone plate material at different healing conditions (1%, 50%,100% callus).

Name of materials	Stress (MPa)			Strain			Deformation (mm)			LHV
	1%	50%	100%	1%	50%	100%	1%	50%	100%	[%]
Mg (AZ31)	236.91	36.259	36.209	0.23214	0.002899	0.00289	8.6621	5.76	5.75	4272
SS316L	310.92	91.828	91.529	0.12244	0.002556	0.00255	6.2695	5.26	5.25	24402
Ti6Al-4V	287.03	66.952	66.75	0.15242	0.002701	0.00269	6.9585	5.46	5.45	12960

Also, we can say that the stress rating of stainless steel (SS316L) is maximum. Therefore, if a fracture occurs, the stress generated by this implant is maximized at various stages of callus formation and should be avoided. This will take longer for the bone to heal and one can use magnesium or titanium instead. The other two implants are less than when using stainless steel. This is because it leads to better early healing of the fractured bone. And results of this analysis are then displayed in a graph showing the changes in the callus of different implant materials under load. By referring to the figures showing the values of the stress as the load changes when different implant materials being used, the surgeon understands that a better and earlier healing process is achieved when the implant material is used.

5. Conclusions

The test results obtained here provide an insight into the stresses achieved by varying the callus formation. More focus was paid to the stresses on the bone plate assembly. From the results, it is seen that the least stress is obtained in the bone plate assembly of magnesium alloy as compared to other implants. At 100% healing condition, the bone and plate act as a composite material i.e. at 100% healing condition the scar tissue becomes strong hence at the fracture zone it can bear a maximum load, which means if at the callus zone, maximum load is being transferred it means that at fracture zone also maximum stress takes place and it is in a completely healing condition which in turn will result in better bone remodelling.

In our analysis, it is seen that using Mg alloy at 100% callus formation or completely healing conditions minimum stress is obtained in the bone plate assembly as compared to titanium alloy and stainless-steel alloy. Hence at the fracture zone, it will result in maximum stress, and hence Mg alloy will show better bone healing. Also, it is seen that at 1% healing condition of magnesium alloy, 23% strain is not possible. Generally, load sharing should be there but not excess which results in the effect of callus. Also, as time passes by strain should not be high as it will result in slow bone healing and bone fractured bone mass will result in misalignment. New research can be done on strain analysis using different implant materials.

References

[1] Yousif, A.E., & Aziz M.Y. (2012). Biomechanical Analysis of the human femur bone during normal walking and standing up. *IOSR Journal of Engineering*, 2(8), 13–19. doi: 10.9790/3021-02851319

[2] Ganesh, V.K., Ramakrishna, K., & Ghista, D.N. (2005). Biomechanics of bone-fracture fixation by stiffness-graded plates in comparison with stainless-steel plates. *Biomedical Engineering*, 4(1), 46. doi: 10.1186/1475-925x-4-46

[3] O'Rourke, D., Johnson, L.J., Jagiello, J., & Taylor, M. (2023). Examining agreement between finite element modelling methodologies in predicting pathological fracture risk in proximal femurs with bone metastases. *Clinical Biomechanics (Bristol, Avon)*, 104, 105931. doi: 10.1016/j.clinbiomech.2023.105931

[4] Balasubramani, V., Gokul, D., & Gokul, R.K. (2023). Modelling and finite element analysis of fractured femur bone with locking compression plate under fatigue load condition. *Materials Today: Proceedings*. doi: 10.1016/j.matpr.2023.03.437

[5] Manubolu, V.N., & Reddy, D. (2022). Design aspects of femur bone fractures: A review. *Materials Today: Proceedings*, 68(6), 2676–2681. doi: 10.1016/j.matpr.2022.09.558

[6] Kalaiyarasan, A., Sankar, K., & Sundaram, S. (2020). Finite element analysis and modeling of fractured femur bone. *Materials Today: Proceedings*, 22(3), 649−653. doi: 10.1016/j.matpr.2019.09.036

[7] Manral, A.R., Gariya, N., & Kumar, K N. (2020). Material optimization for femur bone implants based on vibration analysis. *Materials Today: Proceedings*, 28(4), 2393−2399. doi: 10.1016/j.matpr.2020.04.714

[8] Fang, R., Ji, A., Zhao, Z., Long, D., & Chen, C. (2020). A regression orthogonal biomechanical analysis of internal fixation for femoral shaft fracture. *Biocybernetics and Biomedical Engineering*, 40(3), 1277−1290. doi: 10.1016/j.bbe.2020.07.006

[9] Fouad, H.J. (2011). Assessment of function-graded materials as fracture fixation bone-plates under combined loading conditions using finite element modelling. *Medical Engineering & Physics*, 33(4), 456−463. doi: 10.1016/j.medengphy.2010.11.013

[10] Innocenti, B., Bellemans, J., & Catani, F. (2016). Deviations from optimal alignment in TKA: Is there a biomechanical difference between femoral or tibial component alignment? *The Journal of Arthroplasty*, 31(1), 295−301. doi: 10.1016/j.arth.2015.07.038

[11] Chandra, G., Pandey, A., & Pandey, S. (2020). Design of a biodegradable plate for femoral shaft fracture fixation. *Medical Engineering & Physics*, 81, 86−96. doi: 10.1016/j.medengphy.2020.05.010

[12] Cheng, C.K., Wang, X.H., Luan, Y.C., Zhang, N.Z., Liu, B.L., Ma, X.Y., & Nie, M.D. (2019). Challenges of pre-clinical testing in orthopedic implant development. *Medical Engineering & Physics*, 72, 49−54. doi: 10.1016/j.medengphy.2019.08.006

[13] Perren, S.M. (2002). Evolution of the internal fixation of long bone fractures: The scientific basis of biological internal fixation: Choosing a new balance between stability and biology. *The Journal of Bone and Joint Surgery. British Volume*, 84-B(8), 1093−1110. doi: 10.1302/0301-620X.84B8.0841093

[14] Kim, S.H., Chang, S.H., & Jung, H.J. (2010). The finite element analysis of a fractured tibia applied by composite bone plates considering contact conditions and time-varying properties of curing tissues. *Composite Structures*, 92(9), 2109−2118. doi: 10.1016/j.compstruct.2009.09.051

[15] Gardnera, T.N., Stoll, T., Marks, L., Mishra, S., & Tate, M.K. (2000). The influence of mechanical stimulus on the pattern of tissue differentiation in a long bone fracture − an FEM study.

Journal of Biomechanics, 33(4), 415−425. doi: 10.1016/S0021-9290(99)00189-X

[16] Izzawati, B., Daud, R., Rojan, A., Majid, M.A., Najwa, M.N., Zain, N.A., & Azizan, A.F. (2019). The effect of bone healing condition on the stress of screw fixation in orthotropic femur bone for fracture stabilization. *Materials Today: Proceedings*, 16(4), 2160−2169. doi: 10.1016/j.matpr.2019.06.106

[17] Samiezadeh, S., Schemitsch, E. H., Zdero, R., & Bougherara, H. (2020). Biomechanical response under stress-controlled tension-tension fatigue of a novel carbon fiber/epoxy intramedullary nail for femur fractures. *Medical Engineering & Physics*, 80, 26−32. doi: 10.1016/j.medengphy.2020.04.001

[18] Amalraju, D., & Dawood, A.K. (2012). Mechanical strength evaluation analysis of stainless steel and titanium locking plate for femur bone fracture. *Engineering Science and Technology: An International Journal*, 2(3), 381−388.

[19] Dhason, R., Roy, S., & Datta, S. (2020). A biomechanical study on the laminate stacking sequence in composite bone plates for vancouver femur B1 fracture fixation. *Computer Methods and Programs in Biomedicine*, 196, 105680. doi: 10.1016/j.cmpb.2020.105680

[20] Kumar, K.N., Griya, N., Shaikh, A., Chaudhry, V., & Chavadaki, S. (2020). Structural analysis of femur bone to predict the suitable alternative material. *Materials Today: Proceedings*, 26, 364−368. doi: 10.1016/j.matpr.2019.12.031

[21] Das, S., & Sarangi, S.K. (2014). Finite element analysis of femur fracture fixation plates. *International Journal of Basic and Applied Biology*, 1(1), 1−5.

[22] Steiner, L., Synek, A., & Pahr, D.H. (2021). Femoral strength can be predicted from 2D projections using a 3D statistical deformation and texture model with finite element analysis. *Medical Engineering & Physics*, 93, 72−82. doi: 10.1016/j.medengphy.2021.05.012

Co-published by
Institute of Fluid-Flow Machinery
Polish Academy of Sciences
Committee on Thermodynamics and Combustion
Polish Academy of Sciences

Copyright©2024 by the Authors under licence CC BY 4.0

http://www.imp.gda.pl/archives-of-thermodynamics/

Thermophysical properties and microstructure of 32CrMoV12-28 hot-work tool steel

Piotr Koniorczyk[a], Mateusz Zieliński[a], Judyta Sienkiewicz[a*], Janusz Zmywaczyk[a]

[a]Military University of Technology, Faculty of Mechatronics, Armament and Aerospace, gen. Sylwestra Kaliskiego 2, 00-908 Warsaw, Poland
*Corresponding author email: judyta.sienkiewicz@wat.edu.pl

Received: 09.01.2024; revised: 21.02.2024; accepted: 03.03.2024

Abstract

Measurements of thermal diffusivity, heat capacity and thermal expansion of hot work tool steel 32CrMoV12-28 have been carried out in the temperature range from room temperature (RT) to 1000°C. 32CrMoV12-28 steel has been tested for military applications as steel for gun barrels. The thermophysical properties of this steel can be used as input data for numerical simulations of heat transfer in gun barrels. Both the LFA 427 laser flash apparatus in the RT–1000°C temperature range and the LFA 467 light flash apparatus in the RT–500°C temperature range were used for thermal diffusivity tests. Specific heat capacity was investigated in the range RT–1000°C. The specific heat was determined by two methods, i.e. the classical method, the so-called continuous-scanning method and the stepwise-scanning method according to EN ISO 11357-4. The paper compares both methods and assesses their suitability for testing the specific heat capacity of barrel steels. Thermal expansion was investigated in the range RT–1000°C. Inconel 600 was selected as the reference material during the thermal diffusivity test using LFA 467. Light microscopy (LM), scanning electron microscopy (SEM), and Vickers microhardness measurements were performed to detect changes in the microstructure before and after thermophysical measurements. We compared the results of measurements of the thermophysical properties of 32CrMoV12-28 steel with the results of our tests for other barrel steels with medium carbon content, i.e. X37CrMoV5-1 (1.2343), 38HMJ (1.8509) and 30HN2MFA. The comparison was made in terms of shifting the effect of material shrinkage towards higher temperatures.

Keywords: Microstructure; Thermal expansion; Thermal diffusivity; Specific heat capacity; 32CrMoV12-28 (1.2365) steel

Vol. 45(2024), No. 2, 269–277; doi: 10.24425/ather.2024.150871

Cite this manuscript as: Koniorczyk, P., Zieliński, M., Sienkiewicz, J., & Zmywaczyk, J. (2024). Thermophysical properties and microstructure of 32CrMoV12-28 hot-work tool steel. *Archives of Thermodynamics*, 45(2), 269–277.

1. Introduction

The durability of anti-aircraft guns in which gas flows at high pressure (of the order of hundreds of MPa) and high temperature (of the order of thousands of Kelvin) is influenced by mechanical erosion and changes in the thermophysical properties of steel. This damage manifests as a network of cracks as well as degradation of the Cr protective coating [1–5]. Thermal loads occurring during the operation of the barrel influence the microstructure, e.g. related to the ferrite-austenite phase transition of the barrel steel leading to a change in its mechanical properties [6–9]. The abovementioned phase transition during the heating and cooling of steel is associated with a sharp change in volume that in turn is caused by a transition from the BCC (body-

Nomenclature

A – thermal diffusivity, mm^2/s
c_p – specific heat, J/(kg K)
CLTE – coefficient of linear thermal expansion, 1/K
CR – cooling rate, K/min
d – diameter, mm
HR – heating rate, K/min
k – thermal conductivity, W/(m K)
L – length, mm
M – mass, mg
Q – pulse energy
t – time, s
T – temperature, K
T_∞ – corrected detector signal
V – gain of the detector signal amplitude

Greek symbols
α – ferrite
γ – austenite
ε – relative elongation (thermal expansion
ρ – density, g/cm^3

Subscripts and Superscripts
ref – reference material
s – sample
0 – initial
st – sapphire
bl – base line

Abbreviations and Acronyms
BCC – body-centred cubic
DSC – differential scanning calorimetry
EDS – energy dispersive spectroscopy
FCC – face-centred cubic
HV – Vickers hardness
LM – light microscopy
RT – room temperature
SEM – scanning electron microscopy

centred cubic) crystallographic lattice to the FCC (face-centred cubic) [6,7,9]. Additionally, during the operation of a barrel when pressure increases, denser phases are favoured and hence the FCC structure (γ-austenite) is more stable than the BCC structure (α-ferrite). In summary, the combined action of heat and pressure causes the formation and spread of deep cracks through the barrel and consequently leads to the destruction of the chrome coating on the inner surface of the barrel steel.

The authors' previous research on the coefficient of linear thermal expansion (CLTE) of similar barrel steels with medium carbon content, i.e. 30HN2MFA, 38HMJ (1.8509) and X37CrMoV5-1 (1.2343) showed that the ferrite-austenite phase transition and shrinkage effect occur at temperatures of 749.7 C, 808.4°C and 860.9°C [8,10,11]. Steels with a higher phase transformation temperature seem promising, i.e. X37CrMoV5-1 steel is better than 30HN2MFA steel. Heating such barrel steels to a temperature of 900°C and then slowly cooling causes irreversible changes in the ferrite and pearlite structure together with the characteristic Widmanstätten phases, resulting in reduced impact strength compared to the original steel [12,13]. Modern cannons fire according to a precisely defined sequence of shots, which is closely related to the shrinkage temperature of the cannon barrel steel. Therefore, designers of cannons and small arms look for steels in which this effect does not occur, or the shrinkage temperature of the barrel steel is as high as possible [10,14–20].

Another problem is the proper preparation of input data for the numerical simulation of heat transfer in the cannon barrel, especially thermal characteristics such as thermal conductivity k, specific heat c_p, density ρ and thermal diffusivity a. These parameters are related to each other through $a = k/(\rho c_p)$, and each can be measured separately or calculated from other parameters. When calculating the thermal conductivity k in the phase transition region, this effect is taken into account twice in both thermal diffusivity and specific heat. The authors of this paper suggest that the phase transition effect should only be included in the thermal conductivity characteristics [10,21].

The work aimed to investigate the thermophysical properties of the 32CrMoV12-28 (1.2365) hot work tool steel with the medium carbon content, in which, apart from the phase transition at the Curie point, there is a ferrite-austenite phase transition and the associated material shrinkage occurrence. To identify this transition, the DSC (differential scanning calorimetry) stepwise scanning method according to EN ISO 11357-4 was used, which allowed it to qualify as a first-order phase transition. According to the Ehrenfest nomenclature, the phase transition of the first kind is accompanied by the heat of the phase transition [6]. In addition to the specific heat, other thermophysical properties of this steel were also tested, i.e. thermal diffusivity and thermal expansion in the temperature range from RT (room temperature) to 1000°C. The thermophysical properties of the hot working 32CrMoV12-28 tool steel will be used as input data for the numerical simulation of heat transfer in a 35 mm cannon barrel, analogous to those of steels with medium carbon content, i.e. 30HN2MFA, 38HMJ (1.8509) and X37CrMoV5-1 (1.2343) [22–27]. As part of the paper, the authors also compared 32CrMoV12-5 steel with previously tested barrel steels with medium carbon content, looking for the relationship between the shrinkage temperature and the chromium content in these steels. This paper is a summary of research on the thermophysical properties of barrel steels with medium carbon content conducted by the authors from 2020 to the present [8,10,18,28].

2. Materials and methods

2.1. Materials

The 32CrMoV12-28 hot-work tool steel bar (Akrostal, Rogozno, Poland) supplied for testing was cylindrical with a length of 500 mm and a diameter of 71 mm. The tests were performed without additional heat treatment. The nominal composition (wt. %) of the test steel (32CrMoV12-28) is given in Table 1.

Table 1. Chemical composition of the hot-work tool (32CrMoV12-28) steel [7].

Component	Fe	C	Si	Mn
Concentration [wt. %]	92.88	0.32	0.25	0.30
Component	Cr	Mo	V	P
Concentration [wt. %]	3.00	2.75	0.55	0.03

32CrMoV12-28 is a high-alloy steel primarily used for making hot work tools, such as cutting and punching tools, dies and knives [29]. Generally, 32CrMoV12-28 is a high-performance tool steel engineered for applications where good toughness, wear resistance and high hardness are required, especially at lower temperatures. It can be heat-treated to achieve the desired mechanical properties for various tooling and cutting applications [7, 29]. As shown by the research described in this paper, compared to 38HMJ and 30HN2MFA steel, 32CrMoV12-28 steel is characterized by a higher ferrite-austenite transformation temperature, which is approximately 835.8°C. Only for X37CrMoV5-1 steel, shrinkage occurs at a higher temperature, i.e. 860.9°C.

2.2. Sample preparation

For the thermal diffusivity tests, cylindrical specimens with a thickness of 1.63 mm and a diameter of 12.70 mm were cut from a rod with a diameter of 71 mm. To increase the absorption of the energy of the heat pulse generated by the xenon lamp or laser, the samples were coated with a thin layer of graphite 2–3 µm thick (Graphit 33 Kontakt Chemie). The density of the materials was determined on a Sartorius MSA125P-1CE-DA analytical balance (accuracy [d]: 0.01 mg) using the double weighing method (in air and water). The result of measuring the density of the hot work tool steel at room temperature was 7.80 g/cm^3.

Cylindrical samples with a diameter of d = 6 mm and a mass of m = 191.3 mg for the test material and m = 114 mg for the reference material were used for DSC investigations. During the measurement, both samples were placed in a platinum crucible with a platinum lid (Pt crucible volume: 85 µl).

The samples for the dilatometric test had also cylindrical shapes with a diameter of 6.0 mm and length of 24.35 mm for hot-work tool steel (32CrMoV12-28). All samples were cut from the bar using a water-cooled cutting disc.

2.3. Microstructure analysis and Vickers micro-hardness measurements

The preparation of metallographic samples involved several steps. Initially, samples were cut using a precision cut-off machine and subsequently embedded in thermosetting Bakelite resin. Next, a sequence of abrasive treatments was applied, including grinding with 320-grit SiC paper and polishing using diamond pastes with particle sizes of 6, 3, and 1 µm. A final polishing step utilized 0.25 µm silica. The resulting microstructures were examined using two microscopy methods. The Keyence VHX-6000 digital (light) microscope was employed for initial analysis. Additionally, the Phenom Pro-X scanning electron microscope (Thermo Fisher Scientific) was used. SEM was equipped with an energy dispersive spectroscopy (EDS) chemical composition analyzer and operated at an acceleration voltage of 15 kV. To enhance the visibility of specific features, samples underwent etching with nital.

To validate the mechanical properties of the 32CrMoV12-28 steel, Vickers micro-hardness measurements at ambient temperature were conducted. This involved applying a load of 1000 g with a loading time of 10 s for each indentation. The measurements were performed using the Qness Q10 A+ Micro Hardness Tester from ATM Qness GmbH, which is a part of Verder Scientific, located in Maastricht, the Netherlands. The mean value for hardness was calculated based on a minimum of ten measurements for each sample.

2.4. Thermal analysis

2.4.1. Thermal diffusivity measurement

Thermal diffusivity measurements were performed using devices from Netzsch (Selb, Germany). To compare the results, tests were carried out on two devices: LFA 427 (laser flash apparatus) and LFA 467 HyperFlash (light flash apparatus). Thermal diffusivity testing using LFA devices refers to the Parker method and involves generating a heat impulse by a laser (LFA 427) or a xenon lamp (LFA 467) on one side of a plane-parallel sample and measuring the temperature change on the other side of the sample. Thermal diffusivity is calculated using the standard Cape-Lehman model with pulse correction for which a theoretical curve is fitted to the measurement points obtained on the IR (infrared) detector (CdHgTe) [30]. The standard model includes the effects of heat loss through surface radiation in the context of the temperature change of the analysed sample. Thermal diffusivity measurements were carried out independently on two instruments: LFA 467 at RT–500°C and LFA 427 at RT–1000°C. For each temperature step, two measurements were made in an atmosphere of argon as an inert gas at a flow rate of 50 ml/min. Unlike LFA 427, LFA 467 enables specific heat and thermal conductivity of the material under test to be measured, because the design of LFA 467 allows measurements to be made for several samples simultaneously. To determine the specific heat using the comparative method, Inconel 600 was used as a reference material [31]. In the comparative method, we use the following Eq. (1) to determine the specific heat:

$$c_p^s(T) = \frac{T_\infty^{ref}}{T_\infty^s}\frac{\rho^{ref}}{\rho^s}\frac{d^{ref}}{d^s}\frac{Q^s}{Q^{ref}}\frac{V^s}{V^{ref}}\frac{d^{2,s}_{\text{orifice}}}{d^{2,ref}_{\text{orifice}}}c_p^{ref}(T), \quad (1)$$

where there are such parameters as corrected detector signal (T_∞), density of sample material (ρ), sample diameter (d), pulse energy (Q), gain of the detector signal amplitude (V), diameter of IR detector measurement field (d with orifice index) and specific heat at constant pressure (c_p); superscripts: ref – reference material, s – sample. The T_∞ parameter is proportional to the adiabatic temperature and takes into account surface heat losses. In the context of Eq. (1) and the thermal diffusivity value of the

test sample $a(T)$ obtained from LFA 467, the thermal conductivity $k^s(T)$ was determined using Eq. (2):

$$k^s(T) = \frac{\rho_0}{[1+\varepsilon(T)]^3}\, a(T)\, c_p^s(T), \tag{2}$$

where $\varepsilon(T)$ stands for the relative elongation of the sample (thermal expansion).

2.4.2. Dilatometric measurements

A Netzsch pusher dilatometer (DIL402C) was used to measure the thermal expansion of 32CrMoV12-28 steel. The experiment was conducted in the range from room temperature (RT) to 1100°C. As a protective gas, nitrogen was supplied to the measurement chamber at a gas flow rate of 60 ml/min. The thermal expansion of the sample, expressed by the coefficient of linear thermal expansion (CLTE), is practically represented regarding the initial sample length $L(T_0)$ – denoted as CLTE* and represented by Eq. (3) [31,32]:

$$\mathrm{CLTE}^*(T) = \frac{1}{L(T_0)}\frac{\mathrm{d}L(T)}{\mathrm{d}T} = \frac{1}{L_0}\frac{\mathrm{d}L(T)}{\mathrm{d}T}. \tag{3}$$

The heating rate (HR) was 2 K/min. The relative elongation mentioned in Eq. (2) is related to CLTE* as follows:

$$\mathrm{CLTE}^*(T) = \frac{1}{\mathrm{d}T}\frac{\mathrm{d}L(T)}{L_0} = \frac{1}{\mathrm{d}T}\mathrm{d}\varepsilon. \tag{4}$$

2.4.3. Differential scanning calorimeter measurement

The specific heat capacity temperature characteristics were determined using a DSC 404 F1 Pegasus differential scanning calorimeter (Netzsch). Two methods were used, i.e. the classic method of the continuous-scanning - in the range of RT to about 1000°C and the stepwise-scanning method according to EN ISO 11357-4 – in the range of 490°C to about 910°C [33]. In the classical DSC approach, the temperature characteristics of the heat capacity of the test material were determined using the c_p-ratio method from three DSC curves (test sample line, sapphire line, baseline) [31]. The test was carried out at a heating/cooling rate (HR/CR) of 10 K/min. In the case of the stepwise DSC method, the temperature rise was achieved through a sequence of isothermal and dynamic segments. The dynamic segments heated up at a rate of 10 K/min, and the isothermal segments lasted 10 min. The temperature increase during the dynamic section was 20°C. An initial dynamic segment was used to reach a first isothermal temperature of 490°C. The next isothermal segments were: 510°C, 550°C, 590°C, 650°C, 690°C, 710°C, 730°C, 750°C, 770°C, 790°C, 810°C, 830°C, 850°C, 870°C, 890°C. To avoid damage to the crucible/DSC sensor system, the maximum isothermal temperature segment was limited to 910°C. Similarly, to the classic DSC method, in the stepwise DSC method, 3-DSC curves (baseline, sapphire line and line of the tested sample) were used to determine the specific heat. The specific heat of the sample was calculated from the peak integrals of the DSC signals during dynamic temperature steps according to Eq. (5) [33]:

$$c_p^s = c_p^{st}\frac{m_{st}}{m_s}\frac{\Delta Q_s - \Delta Q_{bl}}{\Delta Q_{st} - \Delta Q_{bl}}, \tag{5}$$

where c_p^s is the specific heat capacity of the sample; c_p^{st} is the specific heat capacity of the sapphire; *s*, *st* and *bl* indices denote the sample, sapphire and baseline; ΔQ_s, ΔQ_{bl}, ΔQ_{st} are the integrals of the peak-shaped DSC signals during a dynamic temperature step; m_{st} and m_s are the masses of the sapphire and the sample.

Both in the classic method and in the stepwise method, the tests were carried out in a protective atmosphere of argon at a flow of 20 ml/min. To obtain stable DSC signals, two evacuations of argon filling the furnace chamber were used along with 15-minute isothermal segments at the beginning of the measurement.

3. Thermal analysis

3.1. Microstructural analysis

The typical microstructure of 32CrMoV12-28 hot-work steel is dependent on the performed heat treatment, i.e. quenching and tempering temperatures and times. The final microstructure and hence properties can be tailored to meet the desired mechanical and thermal requirements for a particular application.

The examined microstructure of as-received 32CrMoV12-28 steel is composed of tempered martensite, as a matrix, and precipitations of carbides (Fig. 1). Generally, tempered martensite is obtained when quenched steel is subjected to a tempering process to reduce the brittleness and improve toughness. This process involves reheating the steel to a specific temperature range and holding it for a certain period to transform some of the martensite into tempered martensite, which is less brittle and has improved ductility compared to the as-quenched martensite. Observed carbides are compounds of carbon with various alloying elements, i.e. chromium, vanadium, molybdenum and silicon, see Fig. 1 (EDS – element distribution map).

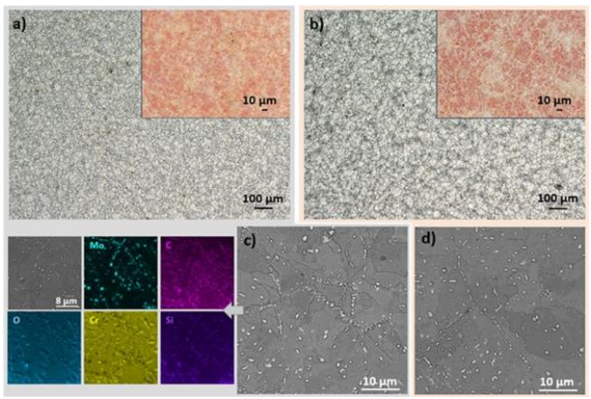


Fig. 1. Microstructure of 32CrMoV12-28 steel in a) initial state, b) after DCS measurement obtained by using a light microscope and c) initial state (together with an elements distribution map), d) after DCS measurement obtained by using SEM.

These carbides occur along grain boundaries as well as are dispersed throughout the tempered martensitic matrix. In both cases, they are elliptical or even spherical.

A slight reduction in hardness was observed after the DSC test. The hardness of the sample HV1 in the initial state was 194 ± 4, while it decreased to 190 ± 3 for the sample after the DSC measurement. This reduction may be due to an increase in the amount of martensite in the sample material after the DSC measurement.

3.2. Thermal properties investigations

The thermal expansion, specific heat capacity and thermal diffusivity of 32CrMoV12-28 steel were investigated from room temperature (RT) to about 1000°C. Measurements of the thermal diffusivity of the tested steel allowed for the identification of the Curie point temperature and changes in thermal diffusivity as a function of temperature. Only one measurement cycle was performed, as in the case of thermal expansion and specific heat using the classic continuous-scanning DSC method. In the case of stepwise scanning DSC method of the specific heat measurements (in the range 490–910°C), the tests were repeated twice to verify the measurement results.

Thermal diffusivity tests were carried out in stages. In the first stage, measurements were made from room temperature to 1000°C using an LFA 427 apparatus. The results of the thermal diffusivity measurements were obtained while the sample was being heated. In the second stage, thermal diffusivity measurements were also taken from room temperature to 480°C. For this purpose, the LFA 467 apparatus was used and the thermal diffusivity characteristics were determined during the heating of the samples. At the same time, for the steel sample, the thermal diffusivity of the reference material (Inconel 600) was also measured using LFA 467. This measurement was necessary to calculate the specific heat as a function of the temperature of the steel under test, using Eq. (1).

The DIL402C high-temperature dilatometer was used to measure thermal expansion. The measurements aimed to determine the thermal expansion characteristics of the test material from room temperature to 1000 °C during continuous heating at 2 K/min.

In the case of specific heat investigations, two methods were used, i.e. the classic continuous-scanning DSC method and the stepwise-scanning DSC method according to EN ISO 11357-4. In addition, a comparative method of measuring thermal diffusivity LFA 467 in the temperature range RT–500°C was used together with the apparent specific heat measurements DSC in the temperature range RT–1000°C, for specific heat calculations.

Netzsch Geräte GmbH guarantees the proper accuracy of its devices. This allows the determination of thermophysical properties of the tested material based on two to three measurements. To ensure sufficient accuracy, measurements on a reference material supplied by Netzsch with thermophysical characteristic tables must be performed before each measurement series. To verify the accuracy of the device, the thermophysical measurement results for the reference material are compared with the data from the tables. For thermal diffusivity measurements, the reference material was Inconel 600 and the deviation of the results did not exceed 5%. Sapphire was used in thermal expansion measurements. The deviation of the measurement results from Netzsch data did not exceed 4%. The same material was used in specific heat measurements. The accuracy did not exceed a 6% difference between the data provided by Netzsch and the data obtained from the reference sample measurements. Additionally, the device undergoes temperature calibration with the melting of pure elements (tin, zinc, silver, etc.) to improve measurement accuracy.

3.2.1. Thermal diffusivity investigations

The temperature characteristics of the thermal diffusivity of 32CrMoV12-28 steel obtained with both diffusometers (LFA427 and LFA467) are shown in Fig. 2. From the thermal diffusivity characteristics, it can be seen that at a temperature of about 764.8°C, there is a phase transition from the ferromagnetic to the paramagnetic state – the Curie point. As can be seen in Fig. 2, the thermal diffusivity of 32CrMoV12-28 decreases steadily with temperature up to the Curie point and reaches a minimum value of about 3 mm^2/s. Beyond the Curie point temperature, the thermal diffusivity increases with temperature.

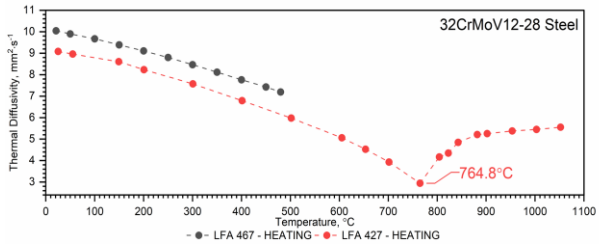


Fig. 2. Thermal diffusivity as a function of temperature for the 32CrMoV12-28 hot-work tool steel obtained from the first heating runs on LFA 467 and LFA 427 (based on [34]).

Figure 3 shows the dependence of thermal conductivity as a function of temperature, obtained by the comparative method in the RT–500°C range and using Eq. (2) in the RT–1000°C range. The differences between the two characteristics for the RT–500°C range are due to the lower accuracy of the thermal diffusivity determination (Fig. 2, black dashed line) using the LFA 467 apparatus.

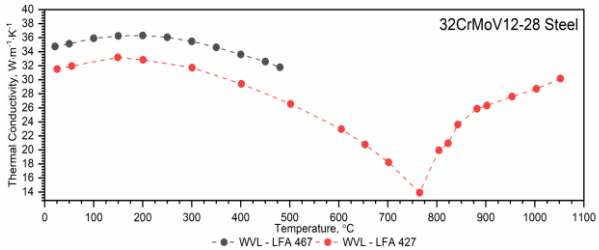


Fig. 3. Thermal conductivity as a function of temperature for the 32CrMoV12-28 hot-work tool steel obtained from the first heating runs on LFA 467 (black dotted line) and LFA 427 (red dotted line).

Figure 4 shows the dependence of specific heat as a function of temperature, obtained by a comparative method using LFA 467 from room temperature to 500°C, and obtained by approximation of experimental data from DSC in the RT–1000°C range.

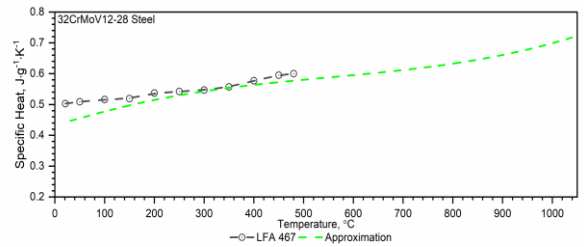


Fig. 4. Specific heat as a function of temperature for the 32CrMoV12-28 hot-work tool steel obtained from the first heating run on LFA 467 in the range from RT to about 500°C (dotted black line) and from the approximation of the experimental data on DSC in the range from RT to 1000°C (green dashed line).

3.2.2. Thermal expansion investigations

The DIL402C high-temperature dilatometer was used to measure the thermal expansion of the test steel from room temperature (RT) to 1000°C during continuous heating at a rate of 2 K/min. One measurement cycle was carried out for the sample. The temperature-dependent thermal expansion characteristics of 32CrMoV12-28 steel are shown in Fig. 5.

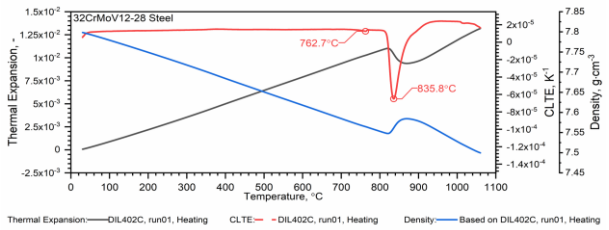


Fig. 5. Density, thermal expansion and CLTE as a function of temperature for the 32CrMoV12-28 hot-work tool steel obtained from the first heating run on DIL 402 C.

3.2.3. Differential scanning calorimeter investigations

The result of the classic continuous-scanning DSC method of the apparent specific heat investigations (calculated using the c_p-ratio method) based on the 3-DSC curves (baseline, sapphire line and tested sample line) for the 32CrMoV12-28 hot-work tool steel samples is shown in Fig. 6. One measuring cycle was carried out for the sample. The figure also shows the specific heat determined by the comparison method during thermal diffusivity measurements (LFA 467) in the RT–500°C range – dashed green line. The resulting specific heat was compared with the results of apparent specific heat measurements in the RT–1000°C range (DSC 404 F1 Pegasus – classic continuous-scanning method). The purple dashed line (Fig. 6) shows the specific heat as a function of temperature, described by Eq. (6). The thermal conductivity shown in Fig. 3 was calculated using Eq. (2) for which the specific heat values were determined from Eq. (6).

For 32CrMoV12-28 steel, a correlation formula was proposed for the specific heat capacity over the tested temperature range (RT–1000°C). The fitting curve for specific heat capacity as a function of temperature for the tested steel is shown in Fig. 6 as a dashed purple line, for which the proposed formula has the following form:

$$c_p(T) = a_0 + a_1 T + a_2 T^2 + a_3 T^3 + a_4 T^{\frac{1}{3}}, \qquad (6)$$

where the temperature is given in kelvins. The values of the coefficients are given in Table 2.

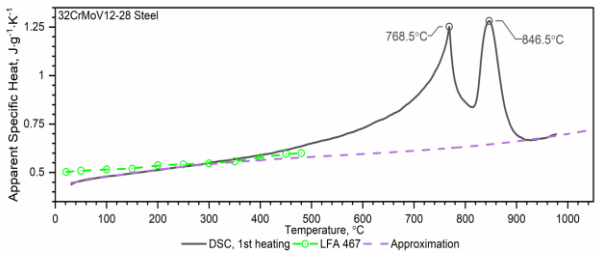


Fig. 6. Temperature characteristics of apparent specific heat for the 32CrMoV12-28 hot-work tool steel obtained from the first heating run: dotted green line—results obtained from LFA 467; dashed purple line—approximation of measurement from DSC; black line – results obtained from classic continuous-scanning DSC method.

Table 2. Coefficients for calculating specific heat capacity of 32CrMoV12-28 sample on Eq. (5).

Coefficient	Value	Coefficient	Value
a_0[J/(g K)]	4.1470×10^{-1}	a_3[J/(g K^4)]	4.8932×10^{-2}
a_1[J/(g K^2)]	6.0408×10^{-4}	a_4[J/(g K$^{2/3}$)]	4.5697×10^{-2}
a_2[J/(g K^3)]	-8.1376×10^{-7}		

To sum up, the input data for numerical simulations of heat transfer in the barrel related to the thermophysical properties of steel will be used: specific heat in the form of a polynomial Eq. (6), the dependence of thermal conductivity as a function of temperature presented in the form of a red dotted line in Fig. 3, and the dependence of density as a function of temperature illustrated in the form of a blue line in Fig. 5.

A comparison of the results of the stepwise-scanning DSC method with the results of the classic continuous-scanning DSC method for the same steel is shown in Fig. 7. Two measuring

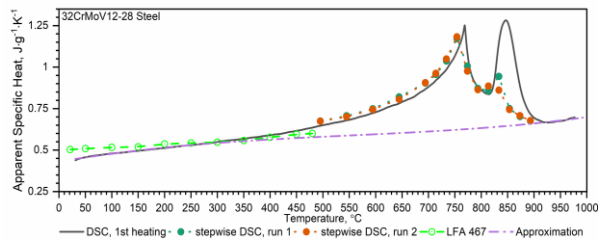


Fig. 7. Temperature characteristics of apparent specific heat for 32CrMoV12-28 obtained from: the first heating run by the classic continuous scanning DSC method – black line; the first and second heating runs by the stepwise-scanning DSC method – blue and red points together with the characteristic of specific heat obtained from LFA 467 – dashed green line.

cycles were carried out for the sample in the temperature range 490÷900°C in the case of the stepwise scanning DSC method.

Repeated thermostating of the sample in the stepwise-scanning DSC method removes the peak associated with the shrinkage temperature of the tested steel, i.e. 846.5°C, because this type of phase transformation requires the supply of heat. The first peak, i.e. 768.5°C, remains practically in the same place as in the classic continuous-scanning DSC method, because it is related to the phase transition at the Curie temperature.

Both methods of measuring apparent specific heat, i.e. the classic method, the so-called continuous-scanning DSC method and the stepwise DSC method – under the EN ISO 11357-4 standard, are complementary. Thermostating the sample also allows for a better understanding of the results of measurements of thermal diffusivity of barrel steels as a function of temperature.

3.2.4. Comparison of thermophysical properties of selected barrel steels

Figure 8 presents a summary of the results of measurements of thermophysical properties, i.e. thermal diffusivity, thermal expansion and apparent specific heat as a function of temperature for selected barrel steels with medium carbon content, i.e. 30HN2MFA, 38HMJ, X37CrMoV5-1, 32CrMoV12-28. All these measurements were performed using various methods [8–10]. Measurements of thermal diffusivity using the laser flash method (LFA 427) required thermostating the sample to the measurement temperature, which made it impossible to record changes in this parameter during the phase transition associated with the shrinkage effect of the steel. However, thermosetting the sample at the measurement temperature did not affect the registration of the thermal diffusivity of phase transitions at the Curie temperature. In the case of measurements of apparent specific heat using the continuous scanning DSC method and thermal expansion using the pushrod dilatometer method, peaks related to steel shrinkage were also recorded (Fig. 8). Thermostating of the sample did not prevent the recording of changes in thermal diffusivity as a function of temperature during the second type of phase transition, i.e. the transition of steel from the ferromagnetic state to the paramagnetic state at the Curie point, because the heat of this phase transition is zero. The identification of the phase transition at the Curie point as a phase transition of the second type was also confirmed by measurements of the apparent specific heat using the stepwise DSC method, which also required thermostating of the sample at the measurement temperature (Fig. 7).

In the case of 30HN2MFA steel, both transformations, i.e. Curie and shrinkage, coincide, which is confirmed by the measurements of thermal expansion of this steel (Fig. 8). It is also worth noting that despite the different heating rates of the sample using the DSC method, i.e. 10 K/min, and thermal expansion, i.e. 2 K/min, the shrinkage temperatures obtained by both methods practically coincide. Differences in the determination of shrinkage effect temperature reach approximately 3°C.

Figure 9 shows the steel shrinkage temperature as a function of the chromium content for selected barrel steels with medium carbon content, i.e. 30HN2MFA, 38HMJ, X37CrMoV5-1, 32CrMoV12-28. It is also worth noting that the higher the Cr content in the steel, the higher the shrinkage temperature (Fig. 8 and Table 3).

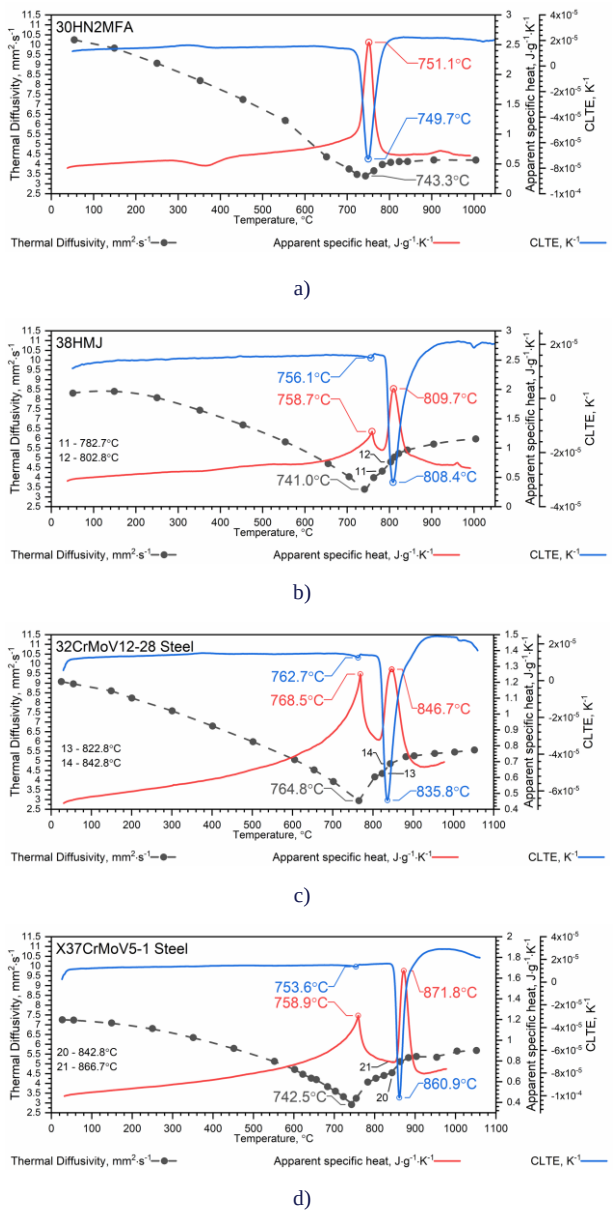


Fig. 8. Thermal diffusivity, CLTE and apparent specific heat of selected barrel steels (based on [8,10]).

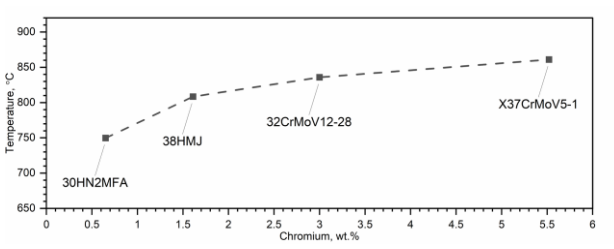


Fig. 9. Influence of chromium content on shrinkage temperature of selected barrel steels, i.e. 30HN2MFA, 38HMJ, 32CrMoV12-28, X37CrMoV5-1 [8,10,35,36].

Table 3. Chemical composition of tested steels [8,10].

Steel grade	Chemical composition [wt. %]				
	Fe	C	Si	Mn	Cr
30HN2MFA	96.42	0.29	0.26	0.36	0.65
38HMJ	95.21	0.44	0.24	0.54	1.61
32CrMoV12-28	92.88	0.32	0.25	0.30	3.00
X37CrMoV5-1	90.71	0.39	0.84	0.36	5.52
	Mo	Ni	V	Al	P
30HN2MFA	0.24	2.21	0.23	—	—
38HMJ	0.26	0.19	1.20	1.20	—
32CrMoV12-28	2.75	—	0.55	—	0.03
X37CrMoV5-1	1.30	0.40	0.45	—	0.012

4. Conclusions

The authors analyzed the thermophysical properties of medium-carbon barrel steel 32CrMoV12-28 and compared it with other previously measured barrel steels, i.e. 30HN2MFA, 38HMJ, X37CrMoV5-1, manufactured on behalf of arms factories. In all of them, apart from the phase transition associated with the Curie point, the ferrite-austenite phase transition occurs. This phenomenon is related to material shrinkage (the transformation into austenite) and occurs in the tested steels at various temperatures. It is widely known that chromium influences the shrinkage temperature in medium carbon hot-work steels which in turn refers to the phase transformation behavior of such steels. The transformation of ferrite into austenite is determined by several alloying elements, including chromium, and can affect the shrinkage temperature, which is the temperature at which this transformation occurs during cooling or heating. Chromium is a ferrite stabilizer which means, that it tends to promote the formation of ferrite in steel. Hence, it can increase the temperature at which austenite transforms into ferrite during cooling. It implies that the addition of chromium can lead to a higher shrinkage temperature, as the transformation from austenite to ferrite will occur at a higher temperature. Furthermore, chromium also has a strong affinity for carbon, and hence it forms carbides that can act as nucleation sites for phase transformations, affecting the kinetics of the transformation. Express differently, the presence of chromium carbides can potentially raise the shrinkage temperature. It should be borne in mind, however, that the exact influence of chromium on the shrinkage temperature in medium carbon hot-work steels can vary depending on the specific composition of the steel, including the presence of other alloying elements such as nickel, manganese, molybdenum, vanadium, and chromium. Additionally, the heat treatment process, cooling rate, and other factors can also have an impact on the transformation behaviour and shrinkage temperature. Summarizing this part, chromium in medium carbon hot-work steels raises the shrinkage temperature by promoting the formation of ferrite and influencing the nucleation of phase transformations. Nevertheless, it is important to remember that the precise effect depends on the overall steel composition and processing conditions.

Another problem is the measurement of the specific heat of the tested steel. According to Ehrenfest's classification, the effect of material shrinkage is a phase transition of the first type, i.e. a transition associated with the heat of transformation. To identify this effect, the authors used the stepwise scanning method in DSC studies. Thermostating of the measurement sample near the material shrinkage temperature, which is associated with the supply of phase transition heat, practically eliminates the peak associated with the characteristics of the apparent specific heat obtained in the classic method of continuous scanning DSC measurement. It should be noted that the thermostating of the sample does not affect the peak related to the Curie point temperature, because the heat of this transformation is equal to zero.

As a result, it can be concluded that an analogous character of temperature-dependent changes in thermophysical properties is observed in steels with medium carbon content. The thermal diffusivity and thermal conductivity of these steels decrease monotonically with increasing temperature until the Curie point is reached, for which they reach a minimum value. The values of both parameters increase above the ferromagnetic-paramagnetic phase transition temperature. However, the increase in the values of these parameters is small. Two peaks are observed in the apparent specific heat results. The first endothermic peak is related to the Curie point temperature (ferromagnetic-paramagnetic transition). The second peak is related to the ferrite-austenite phase transition. For 30HN2MFA steel, we observe the overlap of the peaks of these two transitions (Curie point temperature and ferrite-austenite transition).

The analysis of the influence of steel shrinkage temperature as a function of chromium content allowed for ranking the selected barrel steels with medium carbon content, i.e. 30HN2MFA, 38HMJ, X37CrMoV5-1, 32CrMoV12-28 in terms of their suitability for military applications. The least useful steel is currently the most commonly used, i.e. 30HN2MFA, because the shrinkage temperature of this steel is the lowest and is 749.7°C. The best steel for barrels is X37CrMoV5-1 because the shrinkage temperature of this steel is approximately 860.9°C, which allows for more heat impulses (shots). The 32CrMoV12-28 steel analyzed in this work has a shrinkage temperature of 835.8°C, which makes it as attractive as the X37CrMoV5-1 steel.

References

[1] Sopok, S., Rickard, C., & Dunn, S. (2005). Thermal-chemical-mechanical gun bore erosion of an advanced artillery system part one: Theories and mechanisms. *Wear*, 258(5-6), 659–670. doi: 10.1016/j.wear.2004.09.031

[2] Sopok, S., Rickard, C., & Dunn, S. (2005). Thermal–chemical–mechanical gun bore erosion of an advanced artillery system part two: Modeling and predictions. *Wear*, 258(5-6), 671–683. doi: 10.1016/j.wear.2004.09.030

[3] Li, H., Chen, G., Zhang, K., Luo, G., & Ye, Z. (2007). Degradation failure features of chromium-plated gun barrels with a laser-discrete-quenched substrate. *Surface and Coatings Technology*, 201(16-17), 9558–9564. doi: 10.1016/j.surfcoat.2007.04.034

[4] Sarraf, S. H., Soltanieh, M., & Aghajani, H. (2016). Repairing the cracks network of hard chromium electroplated layers using plasma nitriding technique. *Vacuum*, 127, 1–9. doi: 10.1016/j.vacuum.2016.02.001

[5] Dębski, A., Surma, Z., & Koperski, W. (2009). Material and technological optimization research in terms of increasing the durability of small arms. *Journal of Physics: Conference Series*, 2628, 012035. doi: 10.1088/1742-6596/2628/1/012035

[6] Bhadeshia, H.K.D.H. (2021). *Theory of transformations in steels*. Boca Raton: CRC Press.

[7] Blicharski, M. (2017). *Inżynieria materiałowa: Stal* (2nd ed., 1st reprint). Warszawa: Wydawnictwo WNT. ISBN 9788301189556.

[8] Koniorczyk, P., Zmywaczyk, J., Dębski, A., Zieliński, M., Preiskorn, M., & Sienkiewicz, J. (2020). Investigation of thermophysical properties of three barrel steels. *Metals*, 10(5), 573. doi: 10.3390/met10050573

[9] Koniorczyk, P., Zmywaczyk, J., Dębski, A., Zieliński, M., & Cegła, M. (2019). Investigations of thermal diffusivity and thermal expansion for three types of barrel steel. *Thermophysics 2019: 24th International Meeting of Thermophysics and 20th Conference REFRA* (p. 20006). Smolenice, Slovakia, AIP Publishing.

[10] Koniorczyk, P., Zieliński, M., Sienkiewicz, J., Zmywaczyk, J., & Dębski, A. (2023). Experimental studies of thermophysical properties and microstructure of X37CrMoV5-1 hot-work tool steel and maraging 350 steel. *Materials*, 16(3), 1206. doi: 10.3390/ ma16031206

[11] Kaschnitz, E., Hofer-Hauser, P., & Funk, W. (2020). Electrical resistivity measured by millisecond pulse-heating in comparison to thermal conductivity of the hot work tool steel AISI H11 (1.2343) at elevated temperature. *High Temperatures-High Pressures: Thermophysical Properties: Fundamentals and Applications*, 49, 75–87. doi: 10.32908/hthp.v49.825

[12] Souza, S. d. S. d., Moreira, P.S., & Faria, G.L. d. (2020). Austenitizing temperature and cooling rate effects on the martensitic transformation in a microalloyed-steel. *Materials Research*, 23, 322. doi: 10.1590/1980-5373-MR-2019-0570

[13] Coll Ferrari, M.T. (n.d.). Effect of austenitising temperature and cooling rate on microstructures of hot-work tool steels. https://www.diva-portal.org/smash/get/diva2:868510/ FULLTEXT01.pdf [accessed 27 Oct. 2023].

[14] Tewari, R., Mazumder, S., Batra, I.S., Dey, G.K., & Banerjee, S. (2000). Precipitation in 18 wt% Ni maraging steel of grade 350. *Acta Materialia*, 48, 1187–1200. doi: 10.1016/S1359-6454(99)00370-5

[15] Guo, Z., Sha, W., & Li, D. (2004). Quantification of phase transformation kinetics of 18 wt.% Ni C250 maraging steel. *Materials Science and Engineering: A*, 373, 10–20. doi: 10.1016/ j.msea. 2004.01.040

[16] Jarfors, A.E.W., Matsushita, T., Siafakas, D., Stolt, R. (2021). On the nature of the anisotropy of Maraging steel (1.2709) in additive manufacturing through powder bed laser-based fusion processing. *Materials & Design*, 204, 109608. doi: 10.1016/ j.matdes. 2021.109608

[17] Kapoor, R., Kumar, L., & Batra, I.S. (2003). A dilatometric study of the continuous heating transformations in 18wt.% Ni maraging steel of grade 350. *Materials Science and Engineering: A*, 352, 318–324. doi: 10.1016/S0921-5093(02)00934-6

[18] Koniorczyk, P., Sienkiewicz, J., Zmywaczyk, J., Dębski, A., Zieliński, M., & Preiskorn, M. (2021). Effect of microstructure on thermophysical properties of heat-treated duplex steel. *Materials (Basel)*, 14(20), 6043. doi: 10.3390/ma14206043

[19] Knyazeva, M., & Pohl, M. (2013). Duplex Steels: Part I: Genesis, Formation, Structure. *Metallography, Microstructure, and Analysis*, 2, 113–121. doi: 10.1007/s13632-013-0066-8

[20] Knyazeva, M., & Pohl, M. (2013). Duplex Steels. Part II: Carbides and Nitrides. *Metallography, Microstructure, and Analysis*, 2, 343–351. doi: 10.1007/s13632-013-0088-2

[21] Chen, H., Yue, Z., Ren, D., Zeng, H., Wei, T., Zhao, K., Yang, R., Qiu, P., Chen, L., & Shi, X. (2019). Thermal conductivity during phase transitions. *Advanced Materials*, 31(51), e1806518. doi: 10.1002/adma.201806518

[22] Zieliński, M., Koniorczyk, P., Surma, Z., Zmywaczyk, J., & Preiskorn, M. (2022). Numerical study of heat transfer in a gun barrel made of selected steels. *Energies*, 15(5), 1868. doi: 10.3390/ en15051868

[23] Fikus, B., Dorochowicz, A., Surma, Z., Kijewski, J., Leciejewski, Z., Michalski, J., & Trębiński, R. (2022). Investigations of middle-caliber anti-aircraft cannon interior ballistics including heat transfer problem in estimation of critical burst length. *Processes*, 10(3), 607. doi: 10.3390/pr10030607

[24] Dębski, A., Koniorczyk, P., Leciejewski, Z., Preiskorn, M., Surma, Z., & Zmywaczyk, J. (2016). Analysis of heat transfer in a 35 mm barrel of an anti-aircraft cannon. *Problems of Mechatronics: Armament, Aviation, Safety Engineering*, 7, 71–86. doi: 10.5604/01.3001.0009.2983

[25] Fikus, B., Surma, Z., Leciejewski, Z., & Trębiński, R. (2022). Influence of relations defining propellant gases-barrel heat transfer on critical burst length of 35 mm anti-aircraft cannon. *Proceedings of the 32nd International Symposium on Ballistics*, May 9-13, 2022 (pp. 71–86). DEStech Publications.

[26] Zieliński, M., Koniorczyk, P., Surma, Z., Preiskorn, M., & Sienkiewicz, J. (2023). Selected aspects of heat transfer study in a gun barrel of an anti-aircraft cannon. *Problems of Mechatronics: Armament, Aviation, Safety Engineering*, 14, 73–86. doi: 10.5604/ 01.3001.0053.6672

[27] Koniorczyk, P., Zieliński, M., & Surma, Z. (2023). Heat transfer in the anti-aircraft gun barrel during fire with training and combat ammunition – Comparison of calculation results. *Issues of Armament Technology*, 165(3), 23–39. doi: 10.5604/01.3001. 0053.9191

[28] Zieliński, M., & Koniorczyk, P. (2023). Thermophysical properties of selected barrel steels. *Issues of Armament Technology*, 164(2), 19–41. doi: 10.5604/ 01.3001.0053.7229

[29] Mesquita, R. A. (2016). *Tool steels*. CRC Press. ISBN 9781439881729.

[30] Cape, J.A., & Lehman, G.W. (1963). Temperature and finite pulse-time effects in the flash method for measuring thermal diffusivity. *Journal of Applied Physics*, 34(7), 1909–1913. doi: 10.1063/1.1729711

[31] Netzsch. (2023). *Proteus ver. 7.1 software manual*. https://www.netzsch-thermal-analysis.com/en/products-solutions/software/proteus/ (accessed 27 Oct. 2023).

[32] Ling, S.J., Sanny, J., & Moebs, W. (2018). *University physics, vol. 2*. OpenStax, Rice University.

[33] Schindler, A. (2023). *"Stepwise" According to EN ISO 11357-4*. https://analyzing-testing.netzsch.com/_Resources/Persistent/3/0/4/8/3048e6366e9773455694482cc4f15f72da7d65bd/SW%20Innovation%20014_English.pdf [accessed 27 Oct. 2023].

[34] Zieliński, M., & Koniorczyk, P. (2023). Thermal diffusivity and thermal expansion investigations of WLV steel. *Journal of Physics: Conference Series*, 2628(1), 012035. doi: 10.1088/1742-6596/2628/1/012035

[35] Chadha, K., Shahriari, D., Aranas, C., Lapierre-Boire, L.-P., & Jahazi, M. (2019). On the role of chromium in dynamic transformation of austenite. *Metals and Materials International*, 25, 559–569. doi: 10.1007/s12540-018-00227-6

[36] Jirková, H., Kučerová, L., & Mašek, B. (2015). The effect of chromium on microstructure development during Q-P process. *Materials Today: Proceedings*, 2, 627–630. doi: 10.1016/ j.matpr. 2015.07.362

Co-published by
Institute of Fluid-Flow Machinery
Polish Academy of Sciences
Committee on Thermodynamics and Combustion
Polish Academy of Sciences

Copyright©2024 by the Authors under licence CC BY 4.0

http://www.imp.gda.pl/archives-of-thermodynamics/

Thermodynamic analysis of the performance of an irreversible ammonia-fed solid oxide fuel cell

Hanlin Song[a], Zhanghao Lu[b], Zheshu Ma[a*], Xinjia Guo[a], Qilin Guo[a]

[a]College of Automobile and Traffic Engineering, Nanjing Forestry University, Nanjing, 210037, China
[b]School of Mechanical and Automobile Engineering, Jinken College of Technology, Nanjing, 211156, China
*Corresponding author email: mazheshu@njfu.edu.cn

Received: 24.11.2023; revised: 17.02.2024; accepted: 18.04.2024

Abstract

To investigate the performance of an irreversible direct ammonia-fed solid oxide fuel cell, the direct ammonia-fed solid oxide fuel cell based on oxygen ion conductivity was modeled using finite time thermodynamic theory. First, mathematical expressions for the output power, output efficiency, ecological objective function and ecological coefficient of performance of the direct ammonia-fed solid oxide fuel cell were derived. Further, the effects of parameters such as operating temperature, operating pressure, fuel utilization, and electrolyte thickness on the performance of direct ammonia-fed solid oxide fuel cell were numerically investigated. The results show that as the operating temperature of direct ammonia-fed solid oxide fuel cell increases, the performance of direct ammonia-fed solid oxide fuel cell including output power, output efficiency, ecological objective function and ecological coefficient of performance will be improved. Under certain conditions, increasing fuel utilization can improve output power, output efficiency and ecological performance. Increasing the electrolyte thickness will decrease the finite time thermodynamic performance of direct ammonia-fed solid oxide fuel cell. Moreover, the microstructure of the electrode also affects the performance of direct ammonia-fed solid oxide fuel cell, and the ecological objective function is increased by 16.9% when the electrode porosity is increased from 0.4 to 0.8.

Keywords: Direct ammonia-fed solid oxide fuel cell; FTT; Parametric study; Ecological coefficient of performance

Vol. 45(2024), No. 2, 279–290; doi: 10.24425/ather.2024.150872

Cite this manuscript as: Song, H., Lu, Z., Ma, Z., Guo, X., & Guo, Q. (2024). Thermodynamic analysis of the performance of an irreversible ammonia-fed solid oxide fuel cell. *Archives of Thermodynamics*, 45(2), 279−290.

1. Introduction

There is an urgent need to find new clean and renewable sources of energy for normal socio-economic development, so solar, wind, nuclear, tidal, hydrogen have become new options [1, 2]. Solar, wind and geothermal energy (tidal energy) have the advantages of being renewable and non-polluting. However, the climate, geographical location, time intermittency and other limitations make the large-scale popularization of the use of large-scale is hindered while solid oxide fuel cell (SOFC) is not limited by the above factors. The chemical energy of the fuel itself may be transformed into electricity at any moment as long as it is electrified. Fuel options include hydrogen, methanol, natural gas, and biomass gas [3]. Thus, it is characterized by fuel flexibility. But it is difficult to storage and transportation hydrogen for the case of requiring high pressure vessels and good tanks for storage of compressed hydrogen [4].

At present, ammonia is proposed to be used as a sustainable fuel [5−7]. Ammonia is less expensive per unit volume of stored energy than hydrogen, making it simpler to generate, store, and

Nomenclature

A_{cell} – active cell area, m^2
E_r – cell reversible voltage, V
E^0 – voltage at standard pressure, V
F – Faraday's constant, C/mol
G – Gibbs free energy, J
J_0 – exchange current density, A/m^2
J – current density, A/m^2
J_t – total battery current, A/m^2
LHV_{NH_3} – lower heating value of the ammonia fuel, kJ/mol
m_{NH_3} – mass flow rate, kg/h
N – number of single cells
$n_{H_2,equ}$ – equivalent molar flow rate of H_2 ,mol/s
$n_{H_2,consumed}$ – actual molar flow rate consumed of , mol/s
n_{fuel} – amount of fuel required, mol
p_i – partial pressures of *i*, atm
p_i^{TB} – partial pressures of at the three-phase boundary, atm
P – power density, W/m^2
R – gas constant, J/(mol·K)
R_Ω – electrolyte resistivity, Ω m
S_g – cyclic entropy increase
T – operating temperature, K
T_0 – ambient temperature, K
T_L – temperature of the low-temperature heat source, K
U_f – fuel utilization, %
$V_{act,an}$ – anodic activation overpotential, V
$V_{act,ca}$ – cathodic activation overpotential, V
V_{ohm} – ohmic overpotential, V
$V_{con,an}$ – anodic concentration overpotential, V
$V_{con,ca}$ – cathodic concentration overpotential, V
W – output power, W
z – number of electrons

Greek symbols

α – charge transfer coefficient
λ_{H_2} – mole fraction of hydrogen, %
σ – entropy production rate, W/(K·m^2)
σ_m – electrolyte thickness, mm
τ – cycle period
φ – output exergy, kJ/mol

Subscripts and Superscripts

0 – standard conditions
act – activation
an – anode
ca – cathode
con – concentration
H_2 – hydrogen H2
H_2O – water
O_2 – oxygen
ohm – Ohmic

Abbreviations and Acronyms

DA-SOFC – direct ammonia-fed solid oxide fuel cell
ECOP – ecological coefficient of performance
FTT – finite time thermodynamics
PEMFC – proton exchange membrane fuel cell
SOFC – solid oxide fuel cell

transport. Besides, Ammonia is relatively safe to use because its pungent odor is easily detected. Most importantly, liquid ammonia is not released when used as fuel cell fuel, which is cost effective [8]. As a result, there has been increasing research into the use of ammonia as a sustainable fuel in fuel cells, especially in SOFCs. Ammonia fuel and solid oxide fuel cells are an ideal combination to address decarbonization issues in transportation sectors such as shipping, heavy vehicles, and aviation [9]. For instance, Toyota's Mirai and Hyundai's Nexo have successfully passed testing using the direct ammonia-fed solid oxide fuel cell (DA-SOFC) system in Australia. In addition, Japanese company IHI has partnered with Toyota to commercialize small cogeneration systems based on DA-SOFC, which can be used for power generation in homes, factories, and other places to reduce fossil energy[10]. Therefore, it is of great significance to study DA-SOFC in order to achieve carbon-free transportation and other fields.

For now, researches on DA-SOFC mainly includes electrolyte types [11−13], electrolyte materials [14,15], electrode materials and parameter research [16]. Ni et al. [17] tested direct ammonia fuel cells with different electrolytes. Specifically SOFC based on proton conductivity (SOFC-H) and SOFC based on oxygen ion conductivity (SOFC-O) were tested separately. The large ohmic overpotential of the SOFC-H electrolyte results in a much lower practical performance of the proton conduction direct ammonia fuel cell than the oxygen ion conduction direct ammonia fuel cell. The electrolyte is an important structure of DA-SOFC, it transports oxygen ions or protons between the anode and cathode to complete the electrochemical reaction of DA-SOFC [18]. At the relevant working temperature of the fuel cell, an ideal electrolyte should be stable. Because it is highly conductive and stable in a variety of conditions, yttria-stabilized zirconia (YSZ) is the most often utilized electrolyte for direct ammonia fuel cells with oxygen ion conducting electrolyte (SOFC-O). Kaur and Singh [19] studied the influence of cathode materials on the operating temperature of fuel cells. The findings indicate that the cathode material significantly impedes the reduction of the fuel cell's operating temperature. This is primarily due to the dominance of cathode activation polarization when the fuel cell's operating temperature lowers. Jiang and Chan [20] analyzed the specific requirements of SOFC anode materials. The results show that the anode material must have sufficient electrical conductivity, chemical and mechanical stability and activity for electrochemical reactions. Li et al. [21] conducted a study to investigate the impact of operating temperature on the performance of DA-SOFCs. The findings indicate that the efficiency of the DA-SOFC is significantly influenced by the level of breakdown of the entering NH_3. Siddiqui and Dincer [8] conducted a study to examine the impact of electrolyte thickness and operating temperature on the performance of a DA-SOFC. According to the findings, the peak power density of the fuel cell and the performance of the battery are both able to be greatly

enhanced by reducing the electrolyte thickness and increasing the operating temperature, respectively. Yin et al.[22] showed through research that increasing the temperature can increase the reaction rate inside the fuel cell and then significantly improve the performance of the fuel cell.

Finite time thermodynamics is an extension and promotion of classical thermodynamics, a new branch of modern thermodynamic theory, mainly studying the laws of energy flow and entropy flow of non-equilibrium systems in finite time. In the development process of finite time thermodynamics, the research on internal reversible Carnot cycle model, efficiency at maximum power output, basic optimization relations, unified theory of internal reversible cycles, irreversible cycle theory and other aspects play an extremely important role. Traditional methods of studying fuel cells are usually based on idealized assumptions, such as equilibrium conditions under infinite time. Finite time thermodynamics (FTT) takes into account the irreversibility and actual operating conditions in the actual system, thus providing a more realistic model which reflects the actual Fuel cell performance accurately. The goal of finite time thermodynamics is to achieve the best performance in a given time, which is different from the traditional approach that focuses on the equilibrium state. This means finite time thermodynamics can optimize the power output and efficiency of the fuel cell in a specific time period, which is very important to many practical applications. The purpose of FTT is to minimize the irreversibility of a thermal system in a finite time constraint by seeking performance boundaries for thermodynamic processes. The use of finite time thermodynamics theory is to determine the best thermodynamic efficiency of a DA-SOFC under limited time limitations, with the objective of enhancing the actual output performance of the fuel cell [23−25].

Sieniutycz and Poświata [26] used finite time thermodynamic optimization method to study the ultimate output performance of fuel cells. Ye et al. [27] used exergy analysis theory to study the performance of two fuel cell systems under different operating conditions. The findings indicate that raising the operational temperature of the fuel cell leads to a corresponding enhancement in both the power output and efficiency of the system. Conversely, the influence of relative humidity and operating pressure on the performance of the system is found to be negligible. Ishak et al. [28] conducted their investigation of the ammonia fuel cell system using energy and exergy analysis methodologies. The findings indicate that there is a negative correlation between the amount of fuel use and the system's energy and exergy efficiency. By raising the temperature of the fuel cell, one may improve both its energy efficiency and its exergy efficiency. You et al. [29] analyzed the energy, energy efficiency, economic, and environmental aspects of the SOFC polygeneration system. They then used the NSGA-II technique to carry out two sets of multi-objective optimizations, with the goal of optimizing the system's performance in various situations. Xu et al. [30] developed a thermodynamic model for irreversible proton exchange membrane fuel cells (PEMFCs) and investigated the impact of several factors, including operating temperature, film thickness, and operating pressure, on the performance of the fuel cell. Enhancing the operating temperature and pressure of a PEMFC has been shown to have a positive impact on its performance. Similarly, it has been noted that the degree of phosphoric acid doping may greatly enhance the fuel cell's performance. This is mostly attributed to the influence of phosphoric acid doping on the proton exchange membrane's conductivity.

The main contribution of applying the FTT method in this paper is to establish various thermodynamic evaluation index models for performance analysis and optimization, as well as to study the irreversible process of DA-SOFC. Firstly, the irreversibility of DA-SOFC was analyzed from the perspective of finite-time thermodynamics, and a voltage model considering the irreversibility was established. From this, the finite time thermodynamic indexes such as power, efficiency, entropy production rate, ecological objective function and ecological coefficient of performance (ECOP) of DA-SOFC were derived. Then, the performance of DA-SOFC is analyzed, and the effects of operating temperature, operating pressure, fuel utilization, electrolyte thickness and electrode porosity on various finite time thermodynamic indexes of DA-SOFC are studied. We believe that this finite time thermodynamic model can provide new ideas for future fuel cell research. The irreversibility analysis of fuel cells can better identify the source of polarization loss in fuel cells and provide direction for future improvements in fuel cell performance. Evaluate the performance of DA-SOFC under different operating parameters, and the results obtained can provide theoretical guidance for the optimization design and practical application of fuel cells.

2. Finite time thermodynamic model of irreversible DA-SOFC

2.1. Working mechanisms

The operation of solid oxide fuel cells, which rely on oxygen ion conducting electrolytes, need the transportation of ions through the electrolyte. Introduce either pure oxygen gas or air to the cathode compartment of the fuel cell. At the boundary between the cathode and electrolyte, the process of oxygen reduction occurs, resulting in the formation of oxygen ions. The aforementioned ions traverse the electrolyte and engage in an electrochemical process with hydrogen gas at the boundary between the anode and electrolyte, resulting in the generation of water vapor. Ammonia fuel decomposes at the anode of an ammonia fuel cell. This decomposition process results in the formation of two distinct products, referred to as H_2 and N_2. The reaction equation is as follows:

$$NH_3 \leftrightarrow \frac{3}{2}H_2 + \frac{1}{2}N_2 \,. \tag{1}$$

The hydrogen gas produced by decomposition reacts with oxygen ions at the anode-electrolyte interface to produce water vapor. The fuel cell releases hydrogen, nitrogen, unreacted ammonia fuel, and produced water vapor. The hydrogen concentration is diluted as a result of the creation of nitrogen during the thermal breakdown of ammonia, which lowers the fuel cell's reversible cell potential. At low temperatures and without a catalyst, the decomposition rate is slower, but at high temperatures

and with a catalyst, the decomposition rate is faster. Figure 1 describes the working principle of the ammonia-fed. The electrochemical reactions on the anode and cathode of SOFC are as follows:

– anode reaction:

$$H_2 + O^{2-} \rightarrow H_2O + 2_{e^-} \quad (2)$$

– cathode reaction:

$$\frac{1}{2}O_2 + 2e^- \rightarrow O^{2-} \quad (3)$$

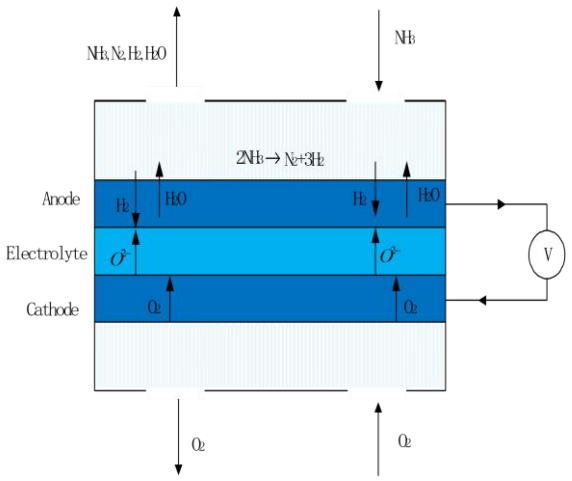


Fig. 1. Working mechanisms of SOFC-O.

2.2. Reversible potential of DA-SOFC

In order to calculate the maximum output power, efficiency of DA-SOFC, the voltage of the fuel cell consists of irreversible factors such as activation polarization, ohmic polarization, concentration polarization, and thermal irreversibility, which are not considered in the ideal model. Under situations when the circuit is open, the potential (voltage) may be characterized as:

$$E_r = E^0 + \frac{RT}{2F}\ln\left[\frac{p_{H_2}{p_{O_2}}^{1/2}}{p_{H_2O}}\right], \quad (4)$$

$$E^0 = \frac{-\Delta G}{zF}, \quad (5)$$

where E_r is the cell reversible voltage; E^0 is the voltage at standard pressure, R is the gas constant; T is the operating temperature; F is Faraday's constant; p_{H2}, p_{O2} and p_{H2O} are the partial pressures of hydrogen, oxygen, and water on the anode side, respectively; G is the Gibbs free energy; and z is the number of electrons involved in the chemical reaction, set to a value of 2.

The irreversibility within the cell leads to energy loss, which is represented by the overpotential. Thus, the single DA-SOFC voltage can be expressed as:

$$V = E_r - V_{act,an} - V_{act,ca} - V_{ohm} - V_{con,an} - V_{act,ca}, \quad (6)$$

where $V_{act,an}$ and $V_{act,ca}$ are the anodic and cathodic activation overpotentials, respectively; V_{ohm} is the ohmic overpotential at the electrolyte; $V_{con,an}$ and $V_{act,ca}$ are the anodic and cathodic concentration overpotentials, respectively.

2.3. Overpotential of DA-SOFC

Due to the irreversibility of electrode dynamics, the losses occurring in fuel cells are referred to as activation overpotentials. The correlation between the activation overpotential and the current density of a fuel cell is mathematically represented by the Butler-Volmer equation:

$$J = J_0\left[\exp\left(\frac{\alpha z F V_{act}}{RT}\right) - \exp\left(-\frac{(1-\alpha)zFV_{act}}{RT}\right)\right], \quad (7)$$

where J_0 is the exchange current density, z is the number of electrons involved per reaction.

This depends on the material and structure of the electrode used [31]. This effect is described by the charge transfer coefficient (α), which is numerically between 0 and 1. It is usually taken as 0.5. Thus, the activation overpotential can be expressed as:

$$V_{act,i} = \frac{\mathrm{RT}}{F}\sinh^{-1}\left(\frac{J}{zJ_{0,i}}\right), \quad i = \text{cathode or anode}. \quad (8)$$

The ohmic overpotential (V_{ohm}) illustrates the ionic resistance of the electrolyte. The ohmic overpotential can be evaluated according to Ohm's law [32]. The ohmic overpotential of DA-SOFC electrolyte is expressed as:

$$V_{ohm} = J\sigma_m R_\Omega, \quad (9)$$

where σ_m is the current density, R_Ω is the electrolyte thickness; is the electrolyte resistivity.

Water vapor is produced at the SOFC-O anode and the concentration at the electrode is related to the partial pressure of the gas. Thus the anode concentration overpotential and cathode concentration overpotential are expressed as:

$$V_{con,an} = \frac{RT}{2F}\ln\left(\frac{p_{H_2}^{TB}p_{H_2O}}{p_{H_2}p_{H_2O}^{TB}}\right), \quad (10)$$

$$V_{con,ca} = \frac{RT}{4F}\ln\left(\frac{p_{O_2}}{p_{O_2}^{TB}}\right), \quad (11)$$

where $p_{H_2}^{TB}$, $p_{O_2}^{TB}$ and $p_{H_2O}^{TB}$ are the partial pressures of H_2, O_2 and H_2O at the three-phase boundary, respectively.

The current density J is defined by [33]:

$$J = \frac{J_t}{NA_{cell}} = \frac{nU_f F x n_{H_2,equ}}{NA_{cell}}, \quad (12)$$

$$n_{H_2,equ} = n_{fuel}, \quad (13)$$

$$U_f = \frac{n_{H_2,consumed}}{n_{H_2,equ}}, \quad (14)$$

where J_t is the total battery current, N and A_{cell} are the number of single cells and the active cell area, respectively, U_f is the fuel utilization, $n_{H_2,equ}$ is the equivalent molar flow rate of H_2, n_{fuel} and λ_{H_2} are the amount of fuel required and the mole fraction of hydrogen, respectively, $n_{H_2,consumed}$ is the actual molar flow rate consumed.

2.4. Finite-time thermodynamic performance analysis of DA-SOFC

The output power density of DA-SOFC can be expressed as follows [34]:

$$P = JV = J\left(E_r - V_{act,an} - V_{act,ca} - V_{ohm} - V_{con,an} - V_{con,ca}\right)$$

$$= J\left[E^0 + \frac{RT}{2F}\ln\left(\frac{p_{\mathrm{H_2}}(p_{\mathrm{O_2}})^{\frac{1}{2}}}{p_{\mathrm{H_2O}}}\right) - \frac{RT}{F}\sinh^{-1}\left(\frac{J}{zJ_{ca}}\right) + \right. \quad (15)$$

$$\left. -\frac{RT}{F}\sinh^{-1}\left(\frac{J}{zJ_{an}}\right) - J\sigma_m R_\Omega - \frac{RT}{2F}\ln\left(\frac{p_{\mathrm{H_2}}^{TB}p_{\mathrm{H_2O}}}{p_{\mathrm{H_2}}p_{\mathrm{H_2O}}^{TB}}\right) - \frac{RT}{4F}\ln\left(\frac{p_{\mathrm{O_2}}}{p_{\mathrm{O_2}}^{TB}}\right)\right].$$

The output efficiency of an energy conversion device may be determined by dividing the energy output by the total energy intake. Therefore, the expression for the output efficiency of DA-SOFC may be represented by the following equation [35]:

$$n(\%) = \frac{P}{m_{\mathrm{NH_3}}\cdot LHV_{\mathrm{NH_3}}} =$$

$$\frac{J(E_r - V_{act,an} - V_{act,ca} - V_{ohm} - V_{con,an} - V_{con,ca})}{m_{\mathrm{NH_3}}\cdot LHV_{\mathrm{NH_3}}}, \quad (16)$$

where $m_{\mathrm{NH_3}}$ is the mass flow rate; is the lower heating value of the ammonia fuel.

Angulo-Brown [36] proposed an ecological objective function $E = P - T_L\sigma$ as an objective to discuss the performance of finite time Carnot engines (where T_L is the temperature of the low-temperature heat source, P is the output power of the finite time heat engine, and σ is the entropy production rate). By substituting T_L with T_0 in the mathematical model, the ecological objective function may be represented as [37]:

$$E = P - T_L\sigma, \quad (17)$$

$$\sigma = \frac{-\Delta H^0 - P}{T_0}, \quad (18)$$

where T_0 a represents the ambient temperature. Based on the analysis of FTT theory, references [38,39] provide unified ecological optimization indicators for thermodynamic cycles:

$$E = \frac{\varphi}{\tau} - \frac{T_e\Delta S}{\tau} = \frac{\varphi}{\tau} - T_0, \quad (19)$$

where φ represents the cycle output exergy, τ is the cycle period, T_0 is the ambient temperature, and ΔS is the entropy production of the entire cycle.

Chen et al. [37] proposed that the actual power dissipation is formulated as $T_0\sigma$. When seen from the perspective of exergy analysis, the ecological criteria function is defined as the difference between the rate at which exergy is produced and the amount of power that is lost in the process. The following is an expression that may be used to describe the ecological goal function of DA-SOFC:

$$E = p - T_0\sigma = (E_r - V_{act,an} - V_{act,ca} +$$

$$-V_{ohm} - V_{con,an} - V_{con,ca})\,J - T_0\sigma. \quad (20)$$

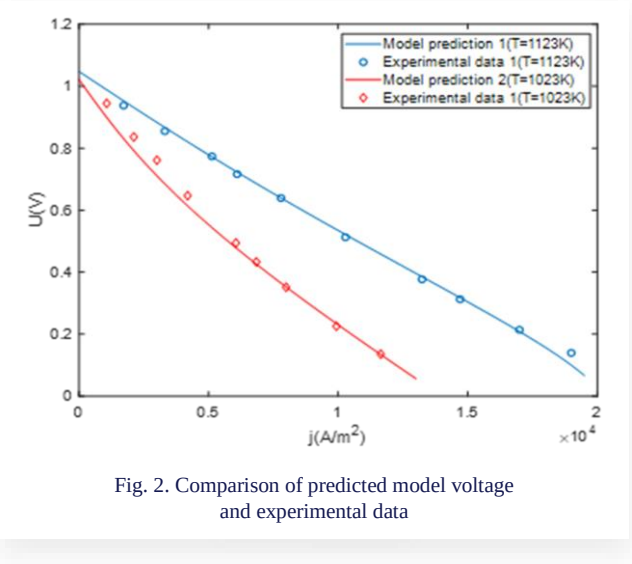


Fig. 2. Comparison of predicted model voltage and experimental data

Ust et al. [40] introduced the concept of the ECOP as a means to evaluate and enhance the efficiency of limited time irreversible dual cycles. The ecological coefficient of performance is a metric that quantifies the efficiency of a system by measuring the ratio of power production to the loss of availability. It may be mathematically represented as:

$$\mathrm{ECOP} = \frac{W}{T_0 S_g}. \quad (21)$$

Based on previous research, Ust et al. [40] proposed a new ecological objective function, called ECOP. In the context of DA-SOFC, the ecological performance coefficient refers to the proportion between the actual output power and power dissipation, which can be expressed as:

$$\mathrm{ECOP} = \frac{P}{T_0\sigma} = \frac{J(E_r - V_{act,an} - V_{act,ca} - V_{ohm} - V_{con,an} - V_{con,ca})}{T_0\sigma}. \quad (22)$$

The new ecological coefficient of performance optimizes the relationship between output power and power dissipation, and is an important evaluation index for DA-SOFC.

2.5. Model verification

Among various types of fuel cells, SOFC has obvious advantages in power generation efficiency, environmentally friendly power generation and fuel flexibility [41]. This characteristic makes SOFC technology attract much attention in practice. It can not only effectively reduce environmental pollution, but also have more flexible fuel options. While hydrogen is considered an ideal fuel, its production, storage and transportation present problems. Moreover, under different experimental conditions, the power difference between solid oxide fuel cells using ammonia fuel and hydrogen is less than 4%, so ammonia fuel is the best choice [42].

Figure 2 shows the comparison results of the voltage predicted by the established DA-SOFC model and experimental data at 1023 K and 1123 K [42]. The operating pressure is 1atm and the electrolyte thickness is 30 um. The results show that the established model agrees well with the experimental data with a maximum error of 5%.

3. Results and discussion

For SOFC to be widely commercialized, a suitable fuel should be selected. Among all fuels, ammonia has the best volume density and better hydrogen storage weight density. It has lower liquefaction requirements and is easier to store and transport. Ammonia is therefore especially suited for tiny, portable systems and applications in automobiles. A finite time thermodynamic evaluation index and the known model of irreversible DA-SOFC are used to study the influence of various parameters on the performance of DA-SOFC. Table 1 lists the fundamental characteristics of the cell that will be used in the ensuing computational investigation. The remaining parameters stay the same while one is altered to examine its impact.

Table 1. Relevant parameters involved in DA-SOFC single cell [42–48].

Parameters	Value
Fuel utilization (%)	85
Exchange current density of anode, J_{an} $(\mathrm{A/m^2})$	$7\times10^{9}\frac{P_{H_2}}{P_0}\frac{P_{H_2O}}{P_0}\exp(-\frac{100000}{RT})$
Exchange current density of cathode, J_{ca} $(\mathrm{A/m^2})$	$7\times10^{9}\left(\frac{P_{O_2}}{P_0}\right)^{0.25}\exp(-\frac{130000}{RT})$
Operating temperature, T (K)	1073
Operating pressure, p (atm)	1
Electrode porosity, ε	0.4
Electrode tortuosity, τ	4.25
Average pore radius of electrode, r_p (μm)	0.5
Resistivity of electrolyte, R_Ω (Ωm)	$2.94\times10^{-5}\exp(-\frac{10350}{T})$
Anode thickness (μm)	500
Electrolyte thickness (μm)	30
Cathode thickness (μm)	30

3.1. Effect of operating temperature on DA-SOFC performance

Figure 3 shows the effect of current density and temperature on the finite time thermodynamic index of DA-SOFC. Figure 3a illustrates the substantial impact of temperature escalation on the power output of the fuel cell. The output power exhibits an initial rise followed by a subsequent decline as the current density rises, given a certain operating temperature. The output power has a positive correlation with the operating temperature while the current density is constant. This phenomenon occurs due to the positive correlation between temperature and exchange current density, as well as the negative correlation between temperature and activation overpotential. Additionally, a rise in temperature leads to an enhanced rate of oxygen ion passage, resulting in a reduction of the irreversible effects caused by the ohmic overpotential. When the magnitude of power consumption is low, there will be a corresponding drop in the lowest entropy production, leading to a rise in the output power. Hence, it can be shown that the ideal output power density of a DA-SOFC may be efficiently enhanced by raising its operating temperature within a certain range. Figure 3b shows that the output efficiency of the fuel cell will become lower as the current density increases at a certain temperature. Because the increase in current density leads to an increase in irreversible losses within DA-SOFC, resulting in lower efficiency. In addition, under a certain current density, the battery energy efficiency increases with the increase of operating temperature.

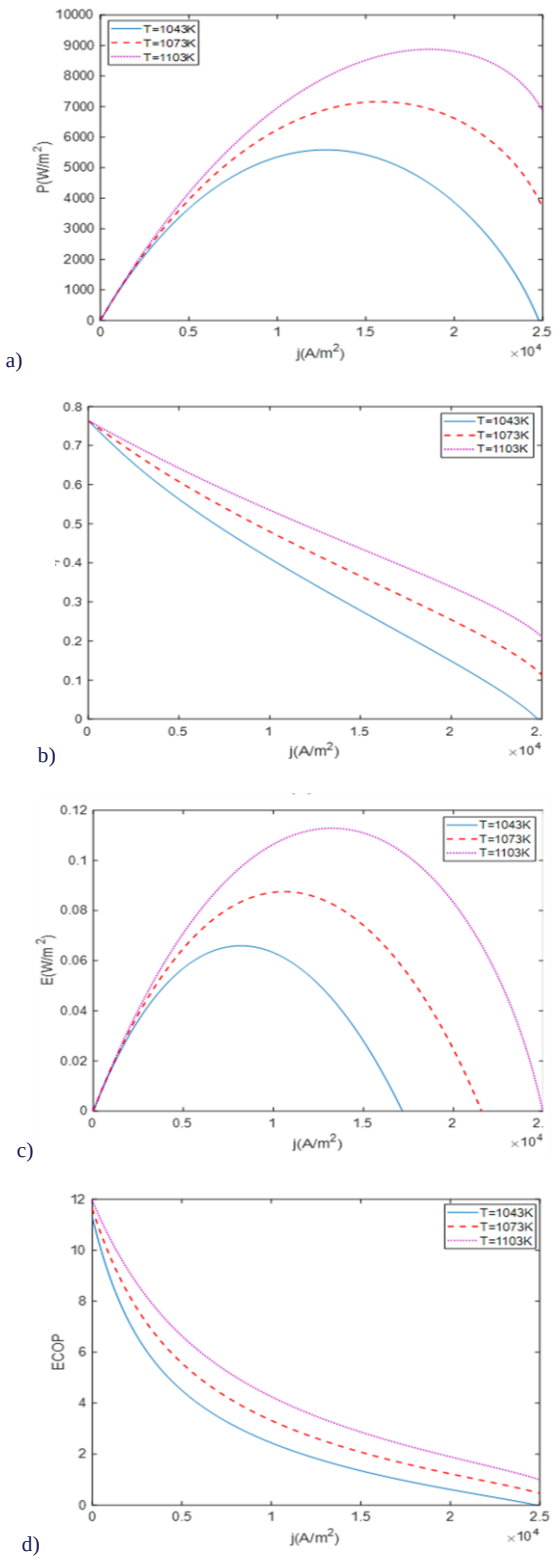


Fig. 3. Variation of P with operating temperature (a), variation of η with operating temperature (b), variation of E with operating temperature (c), variation of $ECOP$ with operating temperature (d).

It can be seen from Fig. 3c that when the operating temperature is kept constant, the ecological objective function first increases and then decreases as the current density increases. It can be explained that as the DA-SOFC reaction continues to proceed, the electrochemical reaction rate continues to increase, and the output power of DA-SOFC continues to increase. At this time, power dissipation is also increasing, but its amplitude is much smaller than the increase in output power, so the ecological objective function is increasing. As the current density continues to increase, power dissipation has been increasing, and the output power is decreasing, so the ecological objective function is gradually decreasing. An increase in the operating temperature leads to an increase in the ecological objective function. The main reason is that an increase in the operating temperature increases the output power of the irreversible DA-SOFC and reduces the power loss due to entropy formation. Therefore, when the operating temperature increases, the ecological objective function of DA-SOFC also increases.

The decrease in the ecological coefficient of performance is seen in Fig. 3d. The phenomenon of power dissipation is seen to be on the rise, while the output power is concurrently experiencing a decline. Furthermore, the ratio between the output power and power dissipation is also observed to be falling. Hence, the ecological coefficient of performance is seen to be diminishing as the operation of the DA-SOFC progresses. Raising the operational temperature has the ability to enhance the exchange current density, diminish the activation overpotential, and augment the rate of oxygen ion passage. Consequently, this mitigate the irreversible consequences associated with the ohmic overpotential. Consequently, increasing the operational temperature has the potential to enhance the ecological coefficient of performance.

3.2. Effect of operating pressure on DA-SOFC performance

Figure 4 shows the effect of operating pressure on the FTT index of DA-SOFC when the current density is 15 000 A/cm^2. It is clear from looking at Fig. 4a that when the operating pressure of the DA-SOFC is raised, the power density will also rise. This is due to the fact that if the operating pressure is increased, the exchange current density will keep growing, as will the reversible potential, and the irreversibility of the DA-SOFC will decrease. As a consequence of this, the power density of DA-SOFC continues becoming better. When the operating temperature is 1 073 K and the operating pressure is increased to 3 atm, the corresponding power density is 9 395.4 W/m^2. When the current density is 15 000 A/cm^2, the operating temperature is 1 073 K, and the DA-SOFC operating pressure is increased from 1atm to 3atm, the DA-SOFC power density increases by 33.8%. This observation demonstrates that the performance of DA-SOFC is significantly influenced by the operating pressure.

Figures 4b−4d illustrates how the DA-SOFC's output efficiency, ecological objective function, and ECOP will all improve with an increase in operating pressure. When the operating pressure of DA-SOFC with an operating temperature of 1 073 K and a current density of 15 000 A/cm^2 was increased from 1 atm to 3 atm (101.33 – 303.98 kPa), the output efficiency, ecological objective function, and the ecological coefficient of performance of DA-SOFC increased by 33.9%, 85.5%, and 65.3%, respectively.

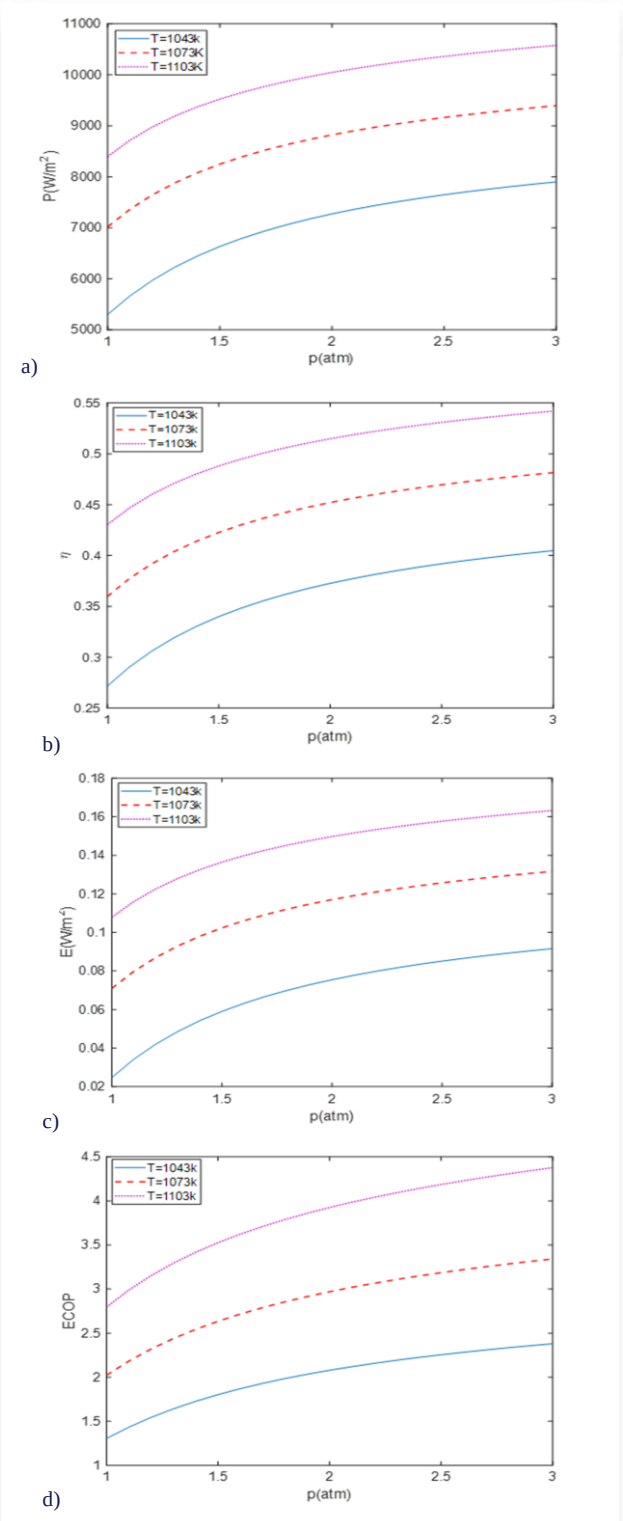


Fig. 4. Variation of P with operating pressure (a), variation of η with operating pressure (b), variation of E with operating pressure (c), variation of ECOP with operating pressure (d).

The ecological objective function increases with increased operating pressure. This is primarily because increasing operating pressure lowers power loss from entropy creation and boosts

the irreversible DA-SOFC's output power. As a result, as operating pressure increases, the ecological goal function of the DA-SOFC also increases. Increasing operating pressure can also mitigate the irreversible consequences associated with ohmic overpotentials, thereby improving ECOP.

Based on the numerical analysis, increasing the operating pressure significantly improves the finite time thermodynamic performance of the DA-SOFC. First, increasing operating pressure helps increase gas diffusion rates, making it easier for reactants to transport inside the cell. By enhancing gas transfer, cells can use fuel and oxygen more efficiently, increasing overall efficiency. Secondly, higher operating pressure helps reduce the resistance of the gas flow channel, thereby reducing internal resistance. This is critical to improving the battery's power output and response speed. However, it is important to note that excessive operating pressures may result in increased system engineering complexity as stronger materials and construction are required to withstand the greater pressures. In addition, increasing the operating pressure consumes the power of ancillary equipment such as compressor, which requires higher cost, and the cost of manufacturing and maintaining the system may also increase. Therefore, when considering increasing operating pressure, multiple factors such as performance improvement, system cost, and material strength must be comprehensively considered to find optimal operating parameters to meet the needs of specific application scenarios. Overall, optimizing operating pressure is one of the important strategies to improve fuel cell system performance, but requires a careful balance of various factors.

3.3. Effect of fuel utilization on DA-SOFC performance

Figure 5 illustrates the impact of fuel utilization on the finite time thermodynamic index of a DA-SOFC under the conditions of a current density of 15 000 A/cm^2 and an operating temperature of 1 073 K. The observed variations in power density exhibit distinct patterns at varying pressures, as seen in Fig 5a. The power density exhibits an upward trend as the fuel utilization ranges from 0.65 to 0.95, while maintaining a pressure of 1.5 atm (151.99 kPa) and 2 atm (202.65 kPa). As fuel utilization rises, it is seen that the output voltage lowers while the current density increases. The rise in current density surpasses the drop in voltage, resulting in an overall gain in power density. When the operating pressure is set at 1, a rise in fuel utilization from 0.65 to 0.95 results in a non-linear relationship with power density. Initially, the power density experiences an increase, followed by a subsequent reduction. The power density attains its greatest value when the fuel utilization is around 0.88. The primary factor contributing to this occurrence is the substantial drop in fuel mass flow into the fuel compressor under specified circumstances, resulting from the rise in fuel utilization. When the fuel mass flow reaches a certain value, the increase in polarization loss dominates the change in battery voltage and causes the battery output power to decrease.

Figures 5b–5d shows the corresponding output efficiency, ecological objective function and ECOP of DA-SOFC with fuel utilization at different pressures. The results indicate that the performance index of the DA-SOFC has a positive correlation with the fuel utilization, seen at both 1.5 atm and 2 atm pressures. When U_f = 0.65 and p = 1.5 atm, the output efficiency, ecological objective function and ecological coefficient of performance are 0.37, 0.15 and 2.14, respectively. When U_f = 0.95 and p = 1.5 atm, they are 0.43, 0.21 and 2.69, respectively, and the three finite time thermodynamic indexes are improved by 14.7%, 35.3% and 25.7%.

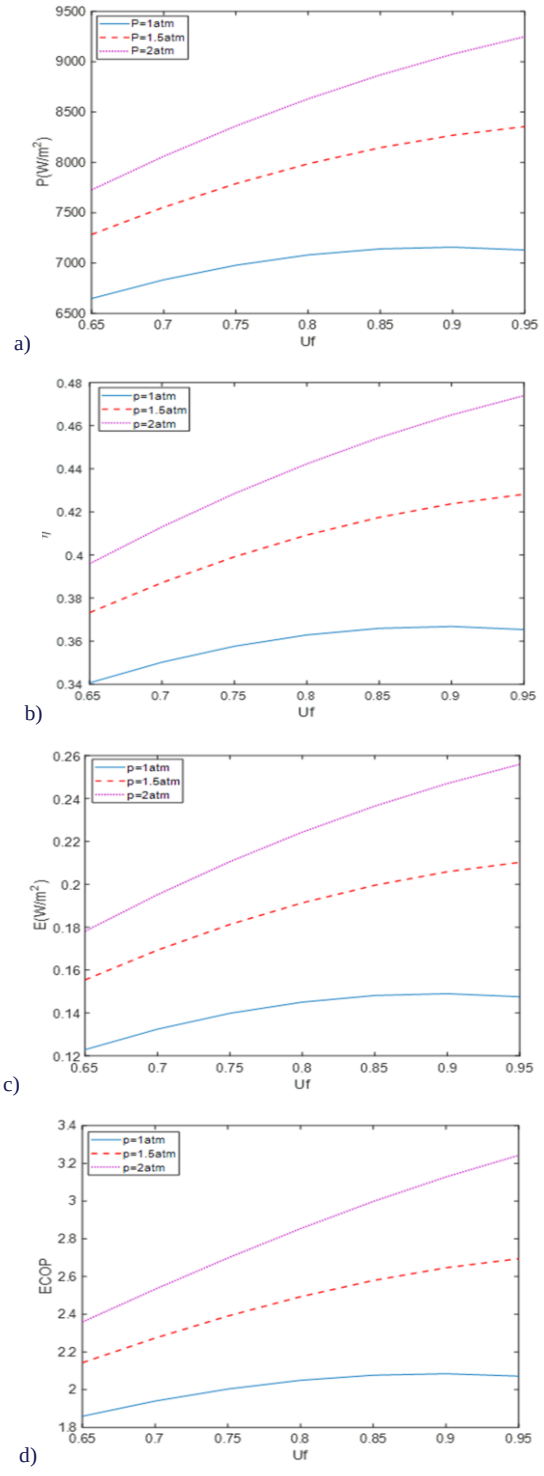


Fig. 5. Variation of P with fuel utilization (a), variation of η with fuel utilization (b), variation of E with fuel utilization (c), variation of ECOP with fuel utilization (d).

The ecological objective function increases with the increase in fuel utilization. This is mainly because an increase in fuel utilization increases the overall energy conversion efficiency of the fuel cell. Higher utilization means that more energy is efficiently converted from fuel to electricity, reducing energy waste, reducing entropy-generated power loss, and increasing the output power of the irreversible DA-SOFC. Therefore, the eco-objective function of the DA-SOFC increases as the operating pressure increases. In summary, under certain conditions, increasing the fuel utilization can improve the finite time thermodynamic performance of DA-SOFC.

Fuel utilization has an important impact on fuel cell performance. Higher fuel utilization means more efficient conversion of fuel into electricity, increasing the overall efficiency of the battery. By maximizing the use of available energy in the fuel, unnecessary waste of resources can be reduced, thereby improving the economy and sustainability of the system. High fuel utilization also helps reduce fuel costs, driving wider adoption of fuel cell technology in commercial and industrial applications. However, multiple aspects such as fuel supply, reaction kinetics, and system design need to be considered comprehensively to achieve optimal fuel utilization and maintain the long-term stability of the battery while improving efficiency. Therefore, in the development and optimization of fuel cell technology, maximizing fuel utilization is one of the key considerations to achieve efficient, economical and sustainable energy conversion.

3.4. Effect of electrolyte thickness on DA-SOFC performance

Figure 6 shows the effect of electrolyte thickness (σ_m) on the finite time thermodynamic index of DA-SOFC when the current density is 15000A/m^{2}and the operating temperature is 1073 K. As can be seen from Fig. 6(a), the power density and fuel cell performance significantly increase as the pressure increases and the electrolyte thickness decreases. When P=1atm and the electrolyte thickness is 30um, the power density of DA-SOFC is 7141.4W/m^2. When the electrolyte thickness is 90um, it is 1006.3.4W/m^2, which is reduced 7 times. This is mainly because an electrolyte layer that is too thick will produce a large ohmic resistance, and the number and speed of ions in the electrolyte passing through the electrolyte will be reduced. The ohmic loss increases, and the internal resistance generated by the ohmic overpotential increases. Since the entropy production rate caused by ohmic resistance becomes larger, the power dissipation becomes larger, so the output power density becomes smaller.

Figures 6b-6d shows the output efficiency, ecological objective function and ECOP corresponding to DA-SOFC with electrolyte thickness at different pressures. When the electrolyte thickness increases, the three finite time thermodynamic indexes decrease significantly. As the electrolyte thickness increases, the power dissipation due to ohmic resistance becomes larger, the output efficiency becomes smaller, and the irreversible DA-SOFC ecological objective function becomes smaller. Increasing the thickness of the electrolyte, the irreversible losses become larger and thus the ecological coefficient of performance

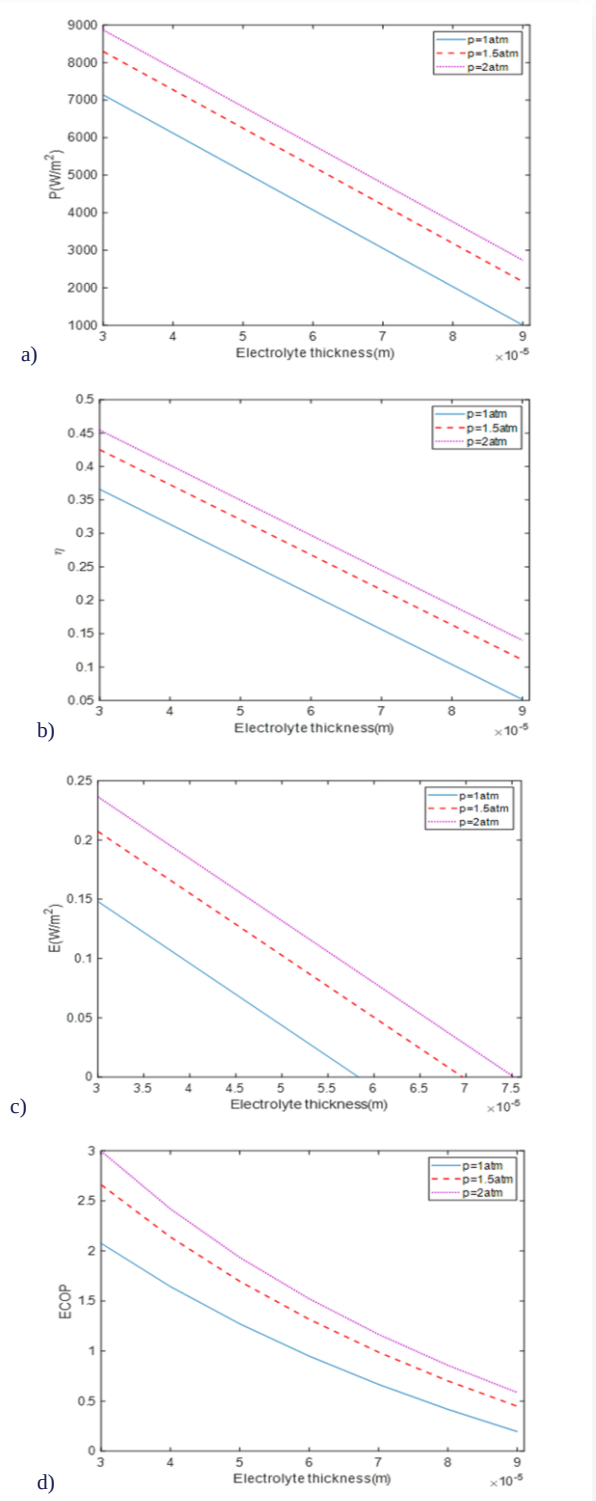


Fig. 6. Variation of P with electrolyte thickness (a), variation of η with electrolyte thickness (b), variation of E with electrolyte thick-ness (c), variation of ECOP with electrolyte thickness (d).

of the DA-SOFC decreases with increasing the thickness of the electrolyte.

Electrolyte thickness is a key design parameter in fuel cells and has a significant impact on cell performance. When the thickness of the electrolyte is too large, firstly, the resistance inside the battery also increases due to the increased ion transmission path. This will increase the resistance of current transmission in the electrolyte, reduce the overall conductivity of the bat-

tery, and thus affect the output power of the battery. Excessive electrolyte thickness may also lead to an increase in voltage drop between electrodes, thereby affecting battery efficiency. Secondly, an electrolyte that is too thick increases the path for gas diffusion, hindering the efficient transport of fuel and oxygen in the battery. This affects the battery's utilization efficiency of reactants and reduces the rate at which electrochemical reactions occur. As a result, the battery's response speed is slower, affecting its dynamic performance, which may be limited especially in applications that require fast response. Therefore, when designing fuel cells, the effects of electrolyte thickness on resistance and reaction rate need to be carefully balanced while considering improved stability and loss resistance to achieve optimal cell performance. This requires system engineers to make precise adjustments and optimizations based on specific application requirements when weighing these factors.

3.5. Effect of porosity on the performance of DA-SOFC

In addition to the operating parameters, the microstructure of the electrode also affects the performance of DA-SOFC. Figure 7 illustrates the impact of electrode porosity on the finite time thermodynamic index of DA-SOFC when the current density is 15 000 A/m^2 and the operating temperature is 1 073 K. As can be seen from Fig. 7a, the output power of DA-SOFC increases with the increase of porosity.

When the DA-SOFC operates in the low-current region, there is basically little change in the output power of the DA-SOFC as the porosity increases. Because the electrochemical reaction rate is slow at the beginning, the number of ions in the electrolyte is low and the operation speed is slow, so the impact of porosity on power density is minimal. As the electrochemical reaction proceeds, the effect on power density gradually becomes larger. The reason for this phenomenon is that the rise in porosity results in a corresponding rise in the diffusion coefficient. This increase in diffusion coefficient facilitates the movement of reactants towards the triple-phase boundary (TPB) located at the interface between the electrode and electrolyte. Additionally, it facilitates the outward transport of products from the TPB interface.

Figures 7b−7d shows the corresponding finite time thermodynamic indexes of the DA-SOFC with the change of current density at different porosities. When the current density is 15 000 A/m^2, the operating temperature is 1 073 K, and the porosity is increased from 0.4 to 0.8, the corresponding output efficiencies, ecological objective functions, and ecological coefficient of performance are increased by 8.3%, 16.9%, and 11.1%, respectively. Therefore, modifying the microstructure of the electrode may boost the efficiency of an irreversible DA-SOFC.

The porosity of fuel cell electrodes has an important impact on performance. Moderate porosity can improve gas diffusion and electron conduction, promote the effective transport of reactants in the electrode, and thus enhance the cell performance. Higher porosity helps to increase the passage of gases in the electrodes, providing more active surfaces and facilitating the catalytic reaction. However, too high a porosity may also lead to a loose electrode structure and reduce the effective electrode surface area, thereby affecting the rate of the reaction. In addition, an increase in porosity may lead to a prolongation of the gas flow path and an increase in the gas diffusion resistance.

Therefore, when optimizing the fuel cell electrode porosity, factors such as gas diffusion, electron conduction and reaction rate need to be considered comprehensively to achieve the best cell performance.

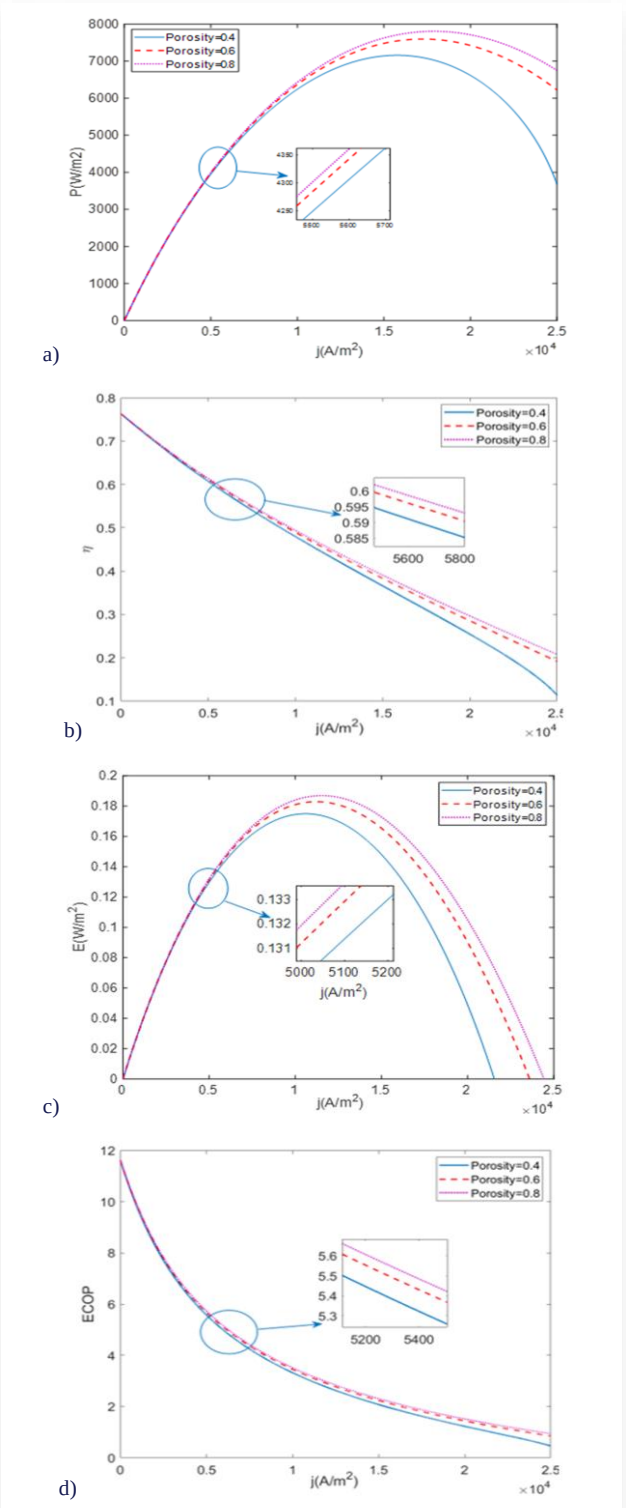


Fig. 7. Variation of P with porosity (a), variation of η with porosity (b), Variation of E with porosity; (d) Variation of $ECOP$ with porosity.

4. Conclusions

In this paper, a finite time thermodynamic model of DA-SOFC is developed after considering the effect of polarization loss. The effects of parameters such as operating temperature, operating pressure, fuel utilization, electrolyte thickness and electrode porosity on the finite time thermodynamic performance of DA-SOFC are investigated in detail.

When the current density of the irreversible DA-SOFC is 15 000 A/m^2, the output power density, output efficiency, ecological objective function and ECOP rise by 57.1%, 57.4%, 311% and 113%, respectively with the increase of operating temperature from 1 043 K to 1 103 K. When $p = 1$ atm (101.33 kPa), the power density first goes up and then decreases in the wake of fuel utilization. When the fuel utilization rate is about 0.88, the power density reaches the maximum value. Under certain conditions, improving fuel utilization can improve the finite time thermodynamic performance of DA-SOFC. When the electrolyte thickness increases from 30 um to 90 um, the power density decreases by nearly 7 times and it found that increasing the electrolyte thickness will reduce the finite time thermodynamic performance of DA-SOFC. The microstructure of the electrode also affects the performance of DA-SOFC. When the electrode porosity increases from 0.4 to 0.8, the corresponding output efficiency, ecological objective function and ecological coefficient of performance increase by 8.3%, 16.9% and 11.1% respectively.

Based on the finite time thermodynamic theory analysis, the finite time thermodynamic performance of DA-SOFC can be further improved when the operating temperature, operating pressure, the electrode porosity and fuel utilization increase and the thickness of the electrolyte decrease.

Acknowledgements

We gratefully acknowledge the financial support of the Scientific Research Foundation of Nanjing Forestry University (No. GXL2018004).

References

[1] Glenk, G., & Reichelstein, S. (2019). Economics of converting renewable power to hydrogen. *Nature Energy*, 4(3), 216–222. doi:10.1038/s41560-019-0326-1

[2] Comello, S., Reichelstein, S., & Sahoo, A. (2018). The road ahead for solar PV power. *Renewable and Sustainable Energy Reviews*, 92, 744–756. doi: 10.1016/j.rser.2018.04.098

[3] Nguyen, T., Sakamoto, M., Uchida, T., Doan, D., Dang, M., Tu, P., Sasaki, K., & Shiratori, Y. (2019). Development of paper-structured catalyst for application to direct internal reforming solid oxide fuel cell fueled by biogas. *International Journal of Hydrogen Energy*, 44(21), 10484–10497. doi: 10.1016/j.ijhydene.2019.02.134

[4] Zhao, Y., Setzler, B.P., Wang, J., Nash, J., Wang, T., Xu, B., & Yan, Y. (2019). An efficient direct ammonia fuel cell for affordable carbon-neutral transportation. *Joule*, 3(10), 2472–2484. doi: 10.1016/j.joule.2019.07.005

[5] Zamfirescu, C., & Dincer, I. (2008). Using ammonia as a sustainable fuel. *Journal of Power Sources*, 185(1), 459–465. doi: 10.1016/j.jpowsour.2008.02.097

[6] Fuerte, A., Valenzuela, R.X., Escudero, M. ., & Daza, L. (2009). Ammonia as efficient fuel for SOFC. *Journal of Power Sources*, 192(1), 170–174. doi: 10.1016/j.jpowsour.2008.11.037

[7] Zamfirescu, C., & Dincer, I. (2009). Ammonia as a green fuel and hydrogen source for vehicular applications. *Fuel Processing Technology*, 90(5), 729–737. doi: 10.1016/j.fuproc.2009.02.004

[8] Siddiqui, O., & Dincer, I. (2018). A review and comparative assessment of direct ammonia fuel cells. *Thermal Science and Engineering Progress*, 5, 568–578. doi: 10.1016/j.tsep.2018.02.011

[9] Rathore, S.S., Biswas, S., Fini, D., Kulkarni, A.P., & Giddey, S. (2021). Direct ammonia solid-oxide fuel cells: A review of progress and prospects. *International Journal of Hydrogen Energy*, 46(71), 35365–35384. doi: 10.1016/j.ijhydene.2021.08.092

[10] Sonker, M., Tiwary, S.K., Shreyash, N., Bajpai, S., Ray, M., Kar, S.K., & Balathanigaimani, M. (2022). Ammonia as an alternative fuel for vehicular applications: Paving the way for adsorbed ammonia and direct ammonia fuel cells. *Journal of Cleaner Production*, 376, 133960. doi: 10.1016/j.jclepro.2022.133960

[11] Ma, Q., Peng, R., Tian, L., & Meng, G. (2006). Direct utilization of ammonia in intermediate-temperature solid oxide fuel cells. *Electrochemistry Communications*, 8(11), 1791–1795. doi: 10.1016/j.elecom.2006.08.012

[12] Ni, M., Leung, D.Y., & Leung, M.K. (2008). Thermodynamic analysis of ammonia fed solid oxide fuel cells: Comparison between proton-conducting electrolyte and oxygen ion-conducting electrolyte. *Journal of Power Sources*, 183(2), 682–686. doi: 10.1016/j.jpowsour.2008.05.022

[13] Valera-Medina, A., Xiao, H., Owen-Jones, M., David, W.I., & Bowen, P. (2018). Ammonia for power. *Progress in Energy and Combustion Science*, 69, 63–102. doi: 10.1016/j.pecs.2018.07.001

[14] Pelletier, L., McFarlan, A., & Maffei, N. (2005). Ammonia fuel cell using doped barium cerate proton conducting solid electrolytes. *Journal of Power Sources*, 145(2), 262–265. doi: 10.1016/j.jpowsour.2005.02.040

[15] Fini, D., Badwal, S.P., Giddey, S., Kulkarni, A.P., & Bhattacharya, S. (2018). Evaluation of Sc_2O_3–CeO_2–ZrO_2 electrolyte-based tubular fuel cells using activated charcoal and hydrogen fuels. *Electrochimica Acta*, 259, 143–150. doi: 10.1016/j.electacta.2017.10.140

[16] Maffei, N., Pelletier, L., Charland, J.P., & McFarlan, A. (2005). An intermediate temperature direct ammonia fuel cell using a proton conducting electrolyte. *Journal of Power Sources*, 140(2), 264–267. doi: 10.1016/j.jpowsour.2004.08.020

[17] Ni, M., Leung, D.Y., & Leung, M.K. (2008). Mathematical modeling of ammonia-fed solid oxide fuel cells with different electrolytes. *International Journal of Hydrogen Energy*, 33(20), 5765−5772. doi: 10.1016/j.ijhydene.2008.07.021

[18] Rashid, N.L.R.M., Samat, A.A., Jais, A.A., Somalu, M.R., Muchtar, A., Baharuddin, N.A., & Isahak, W.N.R.W. (2019). Review on zirconate-cerate-based electrolytes for proton-conducting solid oxide fuel cell. *Ceramics International*, 45(6), 6605–6615. doi: 10.1016/j.ceramint.2019.01.045

[19] Kaur, P., & Singh, K. (2020). Review of perovskite-structure related cathode materials for solid oxide fuel cells. *Ceramics International*, 46(5), 5521–5535. doi: 10.1016/j.ceramint.2019.11.066

[20] Jiang, S.P., & Chan, S.H. (2004). A review of anode materials development in solid oxide fuel cells. *Journal of Materials Science*, 39, 4405–4439. doi: 10.1023/B:JMSC.0000034135.52164.6b

[21] Li, Z., Liu, R., Wang, J., Xu, Z., Xie, Y., & Wang, B. (2007). Preparation of double-doped BaCeO3 and its application in the

synthesis of ammonia at atmospheric pressure. *Science and Technology of Advanced Materials*, 8(7−8), 566. doi: 10.1016/j.stam.2007.08.009

[22] Yin, S., Xu, B., Zhou, X., & Au, C. (2004). A mini-review on ammonia decomposition catalysts for on-site generation of hydrogen for fuel cell applications. *Applied Catalysis A: General*, 277(1−2), 1–9. doi: 10.1016/j.apcata.2004.09.020

[23] Lai, H.Y., Li, Y.T., & Chan, Y.H. (2021). Efficiency enhancement on hybrid power system composed of irreversible solid oxide fuel cell and Stirling engine by finite time thermodynamics. *Energies*, 14(4), 1037. doi: 10.3390/en14041037

[24] Li, D., Ma, Z., Shao, W., Li, Y., & Guo, X. (2022). Finite Time Thermodynamic Modeling and Performance Analysis of High-Temperature Proton Exchange Membrane Fuel Cells. *International Journal of Molecular Sciences*, 23(16), 9157. doi: 10.3390/ijms23169157

[25] Ge, Y., Wu, H., Chen, L., Feng, H., & Xie, Z. (2023). Finite time and finite speed thermodynamic optimization for an irreversible Atkinson cycle. *Energy*, 270, 126856. doi: 10.1016/j.energy.2023.126856

[26] Sieniutycz, S., & Poświata, A. (2012). Thermodynamic aspects of power production in thermal, chemical and electrochemical systems. *Energy*, 45(1), 62–70. doi: 10.1016/j.energy.2011.12.040

[27] Ye, L., Jiao, K., Du, Q., & Yin, Y. (2015). Exergy analysis of high-temperature proton exchange membrane fuel cell systems. *International Journal of Green Energy*, 12(9), 917–929. doi: 10.1080/15435075.2014.892004

[28] Ishak, F., Dincer, I., & Zamfirescu, C. (2012). Energy and exergy analyses of direct ammonia solid oxide fuel cell integrated with gas turbine power cycle. *Journal of Power Sources*, 212, 73–85. doi: 10.1016/j.jpowsour.2012.03.083

[29] You, H., Han, J., Liu, Y., Chen, C., & Ge, Y. (2020). 4E analysis and multi-objective optimization of a micro poly-generation system based on SOFC/MGT/MED and organic steam ejector refrigerator. *Energy*, 206, 118122. doi: 10.1016/j.energy.2020.118122

[30] Xu, B., Li, D., Ma, Z., Zheng, M., & Li, Y. (2021). Thermodynamic optimization of a high temperature proton exchange membrane fuel cell for fuel cell vehicle applications. *Mathematics*, 9(15), 1792. doi:10.3390/math9151792

[31] Ni, M., Leung, D.Y., & Leung, M.K. (2009). Electrochemical modeling and parametric study of methane fed solid oxide fuel cells. *Energy Conversion and Management*, 50(2), 268–278. doi: 10.1016/j.enconman.2008.09.028

[32] Chan, S., Low, C., & Ding, O. (2002). Energy and exergy analysis of simple solid-oxide fuel-cell power systems. *Journal of Power Sources*, 103(2), 188–200. doi: 10.1016/S0378-7753(01)00842-4

[33] Tanim, T., Bayless, D.J., & Trembly, J.P. (2014). Modeling a 5 kWe planar solid oxide fuel cell based system operating on JP-8 fuel and a comparison with tubular cell based system for auxiliary and mobile power applications. *Journal of Power Sources*, 245, 986–997. doi: 10.1016/j.jpowsour.2013.07.008

[34] Ni, M., Leung, D.Y., & Leung, M.K. (2008). An improved electrochemical model for the NH_3 fed proton conducting solid oxide fuel cells at intermediate temperatures. *Journal of Power Sources*, 185(1), 233–240. doi: 10.1016/j.jpowsour.2008.07.023

[35] Afif, A., Radenahmad, N., Cheok, Q., Shams, S., Kim, J.H., & Azad, A.K. (2016). Ammonia-fed fuel cells: A comprehensive review. *Renewable and Sustainable Energy Reviews*, 60, 822−835. doi: 10.1016/j.rser.2016.01.120

[36] Angulo-Brown, F. (1991). An ecological optimization criterion for finite-time heat engines. *Journal of Applied Physics*, 69(11), 7465–7469. doi: 10.1063/1.347562

[37] Chen, L.G., Sun, F.R., & Chen, W.Z. (1994). On the ecological figures of merit for thermodynamic cycles. *Journal Engineering for Thermal Energy and Power*, 9(6), 374–376 (in Chinese).

[38] Zijun, Y. (1993). Comment on "An ecological optimization criterion for finite-time heat engines" [J. Appl. Phys. 69, 7465 (1991)]. *Journal of Applied Physics*, 73(7), 3583. doi: 10.1063/1.354041

[39] Chen, L., Xiaoqin, Z., Sun, F., & Wu, C. (2004). Ecological optimization for generalized irreversible Carnot refrigerators. *Journal of Physics D: Applied Physics*, 38(1), 113. doi: 10.1016/S0306-2619(03)00138-7

[40] Ust, Y., Sahin, B., & Sogut, O.S. (2005). Performance analysis and optimization of an irreversible dual-cycle based on an ecological coefficient of performance criterion. *Applied Energy*, 82(1), 23–39. doi: 10.1016/j.apenergy.2004.08.005

[41] Minh, N.Q. (1993). Ceramic fuel cells. *Journal of the American Ceramic Society*, 76(3), 563–588. doi: 10.1111/j.1151-2916.1993.tb03645.x

[42] Ma, Q., Ma, J., Zhou, S., Yan, R., Gao, J., & Meng, G. (2007). A high-performance ammonia-fueled SOFC based on a YSZ thin-film electrolyte. *Journal of Power Sources*, 164(1), 86–89. doi: 10.1016/j.jpowsour.2006.09.093

[43] Chen, F., Wang, P., Sørensen, O.T., Meng, G., & Peng, D. (1997). Preparation of Nd-doped $BaCeO_3$ proton-conducting ceramics by homogeneous oxalate coprecipitation. *Journal of Materials Chemistry*, 7(8), 1533–1539. doi: 10.1039/a608289k

[44] Li, P.W., & Chyu, M.K. (2005). Electrochemical and Transport Phenomena in Solid Oxide Fuel Cells. *Journal of Heat Transfer*, 127(12), 1344–1362. doi: 10.1115/1.2098828

[45] Akkaya, A.V. (2007). Electrochemical model for performance analysis of a tubular SOFC. *International Journal of Energy Research*, 31(1), 79–98. doi: 10.1002/er.1238

[46] Xie, K., Ma, Q., Lin, B., Jiang, Y., Gao, J., Liu, X., & Meng, G. (2007). An ammonia-fuelled SOFC with a BaCe0.9Nd0.1O3−δ thin electrolyte prepared with a suspension spray. *Journal of Power Sources*, 170(1), 38–41. doi: 10.1016/j.jpowsour.2007.03.059

[47] Ni, M., Leung, D.Y.C., & Leung, M.K.H. (2008). Electrochemical modeling of ammonia-fed solid oxide fuel cells based on proton conducting electrolyte. *Journal of Power Sources*, 183(2), 687–692. doi: 10.1016/j.jpowsour.2008.05.018

[48] Zhang, L., & Yang, W. (2008). Direct ammonia solid oxide fuel cell based on thin proton-conducting electrolyte. *Journal of Power Sources*, 179(1), 92–95. doi: 10.1016/j.jpowsour.2007.12.061

Co-published by
Institute of Fluid-Flow Machinery
Polish Academy of Sciences
Committee on Thermodynamics and Combustion
Polish Academy of Sciences

Copyright©2024 by the Authors under licence CC BY 4.0

http://www.imp.gda.pl/archives-of-thermodynamics/

ARCHIVES OF THERMODYNAMICS

Study on the effect of tab cooling on the lithium-ion battery pack life cycle

K. Muthukrishnan[a], C. Ramesh Kumar[a*]

[a]Automotive Research Center, Vellore Institute of Technology, Vellore, India
*Corresponding author email: crameshkumar@vit.ac.in

Received: 18.08.2023; revised: 22.09.2023; accepted: 18.03.2024

Abstract

Electric vehicles are the future of mobility. Electric vehicles have batteries to store energy and the most common type of batteries used in electric vehicle's battery packs are lithium-ion cells. These cells have very high energy density and dissipate heat during charging and discharging cycles. There is a need to have an efficient cooling system to dissipate this heat. Bigger-size batteries in four-wheelers use liquid cooling to ensure faster charging and longer battery life. Surface cooling and tab cooling are two popular types of liquid cooling systems for battery packs. Surface cooling is a preferred type of cooling system as it is less complex and cheaper, but it creates a temperature gradient inside the cell which is detrimental to cell life. This work proposes tab cooling as a solution to improve the life cycle of lithium-ion cells. Two sets of the battery pack, one with tab cooling and the other without a cooling system were tested under different conditions for multiple fast charging and discharging cycles until their initial capacity was reduced by 30%. The results show that with tab cooling the battery performed better and battery degradation was reduced.

Keywords: Lithium-ion; Battery pack; Thermal management; Tab cooling; Battery life

Vol. 45(2024), No. 2, 291–299; doi: 10.24425/ather.2024.150873

Cite this manuscript as: Muthukrishnan, K., & Ramesh Kumar, C. (2024). Study on the effect of tab cooling on the lithium-ion battery pack life cycle. *Archives of Thermodynamics*, 45(2), 291–299.

1. Introduction

Electric vehicles are the future of the automotive industry. One of the major issues that hinder the acceptance of an electric vehicle is the battery. It is a very expensive part of the vehicle and requires replacement at least once during the lifetime of the car. Lithium-ion batteries are widely used in electric vehicles (EVs). There are six types of lithium-ion battery chemistries available in the market. These are lithium-ion cobalt oxide, lithium-ion manganese oxide, lithium iron phosphate, lithium nickel manganese cobalt oxide, lithium nickel cobalt aluminium oxide and lithium titanate batteries. Lithium iron phosphate batteries which have a long life and lesser self-discharging are much preferred for two-wheelers. Lithium nickel manganese cobalt oxides are popularly used in bigger EVs as they have higher specific energy.

Lithium titanate and lithium nickel cobalt aluminium oxide batteries are also used in automotive applications. Most of the automotive industries are currently working on batteries that have higher energy density and can be charged quickly.

Battery thermal management is an emerging area in battery electric vehicles (BEV) where research work is carried out to improve the performance of the battery by optimizing the design of the cooling system [1,2]. As stated, lithium-ion batteries re-

Nomenclature

$C_{p\,cv}$ – specific heat capacity of calorimeter vessel material, kJ/(kg K)
$C_{p\,eg}$ – specific heat capacity of ethylene glycol, kJ/(kg K)
I_b – battery charging or discharging current
I_{loss} – current consumed by loss (heating due to resistance)
m_{cv} – mass of the calorimeter vessel, kg
m_{eg} – mass of ethylene glycol in the calorimeter, kg
q – power generated by the battery, W
SoC – state of charge of the battery
SoC_{to} – state of charge of the battery at the beginning of the charging or discharging
t_d – duration of the test, s
t_o – initial time at the beginning of the charging or discharging
T_f – temperature of EG at the end of test, K
T_{fcv} – temperature of CV at the end of the test, K
T_i – initial temperature of EG, K
T_{icv} – initial temperature of CV, K
τ – time at the end of charging or discharging

Abbreviations and Acronyms

BEV – battery electric vehicles
CV – calorimeter vessel
DC – direct current
EG – ethylene glycol
EV – electric vehicle
HEV – hybrid electric vehicles
HVAC– heating, ventilation and air conditioning
OCV – open circuit voltage
SOC – state of charge

ject heat during the charging and discharging cycle because of electrochemical reactions, phase changes and Joule's heating. If this rejected heat is not removed effectively, the temperature of the battery rises. Lithium-ion cells work very efficiently within the temperature range of 15°C to 45°C. The battery starts to degrade and lose its capacity when it operates at a lower or higher temperature range than the range that is recommended.

Generally, BEV battery life depends on the effectiveness of the thermal management system along with battery pack design, cell arrangement and operating conditions. A single lithium-ion cell provides around 3.6 V with a 2 500 mAh to 3 000 mAh rating. Present-day BEV requires a minimum of 48 V to a maximum of 800 V with a minimum of 10 kWh capacity. BEV battery pack capacity is rated in terms of kWh which is a product of total output voltage and Ah rating. To achieve such a high capacity, hundreds of cells are connected in series and parallel and are made in the form of a stack. Because of space restrictions in the vehicle, cells in the stack should be arranged as compactly as possible. In the stack, thermal management becomes challenging as spacing between cells and fluid flow through the battery stack has to be optimized to keep the battery at the desired operating temperature.

Air-cooled systems are a more attractive cooling technique for hybrid electric vehicles (HEV) and EV battery packs [3−9]. In air-cooled systems, the air is used as a cooling medium to maintain a uniform temperature and to control the temperature variation across the battery pack. The cooling effect is easily achieved by simply directing the airflow through the battery pack module. Air-cooled systems are effective when the battery pack is small and the ambient temperature is less than 20°C. As heat rejection per cell is less than 5 W [3], smaller packs have fewer cells arranged in series and parallel, and it generates less heat. Cooling can be improved with the addition of a cooling fan, cooling fins or heat sinks and proper air ducts [4]. Such systems can effectively function till 35°C of the ambient temperature.

Air-cooled systems are less expensive as the battery pack design is simple and it has a few components. However, in extreme conditions, especially at high discharge rates and higher ambient temperatures air-cooled systems are not preferred. Sometimes cells in the battery pack are cooled indirectly with the help of aluminium plates sandwiched between pairs of pouch cells. These plates have extended surfaces (cooling fins) which are exposed to airflow from the air conditioner [5]. Some studies also reveal that due to the better thermal conductivity and thermal diffusivity of the cooling plates, heat transfer of the cooling plate governs the cell temperature distribution by spreading the cell's heat over the surface [6−7]. Cylindrical cells cannot be cooled in this way, mostly they are stacked in the form of a matrix or arrays for the want of space.

Zhao et al. [9] investigated numerically the heat transfer characteristics of a cylindrical lithium-ion battery pack with air as a cooling medium. In their work, a parametric investigation was carried out to study the effect of different ventilation types, fluid velocities, spacing between adjacent batteries, the temperature of ambient air and the diameter of the cell on heat transfer. Though it was optimized, their study showed the temperature difference between cells arranged in the array. In addition, for better heat transfer, the spacing between the batteries should be optimized. Wang et al [10,11] studied the thermal performance of battery packs with different cell array arrangements. Air-cooling method was investigated by installing fans at different locations of the battery pack to obtain uniform temperature throughout the pack. Based on the simulation study, the effect of factors like cell array arrangement, spacing between the cell and fan location on cooling was discussed. Their study concluded variation in the temperature of the pack. So as to achieve better cooling, a fan should be placed on the top of the battery pack module with the cubical arrangement of cells (5 × 5 structure) in the battery pack [10]. Fan et al. [12] examined the effects of spacing and rate of airflow on the effective cooling of the air-cooled battery pack. It was inferred that decreasing the gap space or increasing the air flow rate will lead to a decrease in temperature rise and temperature difference. It is clear from the review that achieving uniform cell temperature across the battery pack of an air-cooled battery pack system needs proper spacing between the cells, uniform airflow and lower pressure drop.

In modern HEV and EV, a liquid-cooled system is a preferred mode of cooling because of its ability to absorb more heat than the air-cooled system due to the liquid's better thermal conductivity and specific heat [12]. In a liquid cooling system, a mixture of water and ethylene glycol or a dielectric fluid is used as a cooling medium to maintain a uniform temperature of the battery system. Liquid cooling effectively meets modern vehicle

drive demands. Though quieter during operation, it has a possibility of coolant leakage in joints, if not designed properly. Liquid cooling can be achieved in different ways such as through discrete tubing around each module, with a jacket around the module, submerging modules in a dielectric fluid for direct contact, or placing the modules on a liquid-cooled plate heat sink [13]. The heat transfer medium could be water, glycol, oil, acetone or even refrigerants.

Apart from leakage, liquid cooling systems increase the weight of the cooling system and hence it may impact the range of the vehicle. So, both the cooling requirements and weight reduction are important from the point of view of battery cooling design [14]. Zhao et al. [15] proposed a new kind of cooling method for the cylindrically shaped battery pack which is based on a mini-channel liquid-cooled cylinder. The dependence of channel quantity, rate of mass flow, the direction of flow and size of the inlet on heat dissipation was numerically investigated. Teng and Yeow [16] compared the designs of various direct and indirect liquid cooling systems, the paper describes the cooling system design along with all its calculations.

Janarthanam et al. [17] discussed the requirements of a cooling system in a vehicle and how a liquid cooling system is better than an air-cooling system. Their work presents a way to determine the requirements of battery cooling system design targets, pack configuration and cooling method determination. Their simulation results demonstrated clearly that direct liquid cooling has advantages over indirect liquid cooling from the battery thermal management point of view. Research also reveals that the heat transfer from the internal cell structure to positive and negative electrode terminals (tabs) is higher than that from the radial surface (circumferential surface of the cylindrical cell). The tab temperature is higher at least by 5°C compared to the cylindrical surface [18]. The study also reveals that the cathode registered a higher temperature than the anode. Researchers are exploring various ways by which the thermal management of lithium-ion batteries can be improved without complexity. Tab cooling is a type of liquid cooling system which has improved cooling performance; the cooling performance to weight ratio of the system is also higher [19]. A study also reveals that tab cooling reduces the thermal gradient within the pack and improves the temperature distribution [20,21]. Hunt et al. [22] explored the effects of cell surface cooling and cell tab cooling, reproducing two typical cooling systems that are used in real-world battery packs. The work also reports that surface cooling using liquid coolants deteriorates the capacity of the cell three times higher than tab cooling due to thermal gradients being perpendicular to the layers of the surface. Several studies also reveal that tab (axial cooling) cooling provides a uniform temperature distribution and a smaller thermal gradient within the cell, and the limitation of such cooling is the tab area [23−26]. This can be overcome by increasing the thickness of the tabs and the number of the electrode stacks.

The design of a good thermal management system for a battery pack should consider both the overall temperature of the pack and internal thermal gradients. Considering the temperature gradient, it is concluded that tab cooling is better than surface cooling.

2. Experimental setup

The battery used in this work is a Samsung ICR18650-26JM. The cell chemistry of this battery is LiNi-CoMnO_2. The specifications of the battery are given in Table 1.

Table 1. Battery cell specifications.

Parameter	Specification
Dimensions	18 mm diameter and 65 mm length
Capacity	2600 mAh
Nominal voltage	3.60 V
Standard charging current	1.07 A (0.5 C)
Maximum charging current	2.15 A (1 C)
Standard discharging current	0.43 A (0.2 C)
Maximum discharging current	3.225 A (1.5 C)
Weight	47 mg

According to the specifications given by the manufacturer, the upper and lower limit of the cut-off voltage is given as 4.2 V and 2.5 V. Three cells were stacked in a series to form a battery pack as shown in Figs. 1 and 2. Figure 1 shows the solid model of the battery pack which is used for theoretical study. Figures 2a and 2b show the actual construction of the pack with and without cooling tabs. To make the pack, cells of similar capacity with the same OCV are stacked together. Three cells in series give a maximum of 12.6 V to a minimum of 7.5 V. As most of the conventional automotive electrical and electronic systems are 12 V systems, three cells were combined in series in this study. Using thermocouples, current sensor, BK Precision 8610 electronic load and Keysight data logger, the temperature, current and voltage are measured and stored during the charging and discharging cycle.

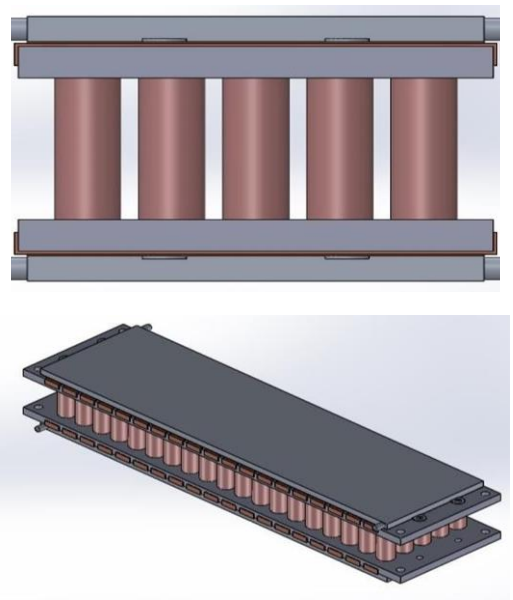


Fig. 1. CAD model of the pack.

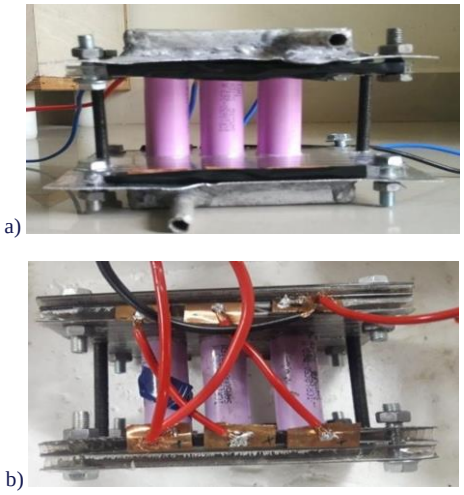


Fig. 2. Photographic view of the setup: (a) with cooling tabs; (b) without cooling tabs.

A two-way switch is used to ease switching between the charging and discharging state of the battery. An Imax B6AC lithium-ion battery charger is used to charge the batteries. It has a built-in balance socket in addition to configurable charge voltage output. Charging configuration can be programmed according to our requirements, using a software interface the charging data is acquired into the computer. The state of charge (SOC) is calculated using the coulomb counting method as given in Eqs. (1) and (2). Calculating the capacity of the battery ampere-hour (Ah) counting, or current integration, is the most common technique. This method employs battery current readings mathematically integrated over the usage period of charging or discharging and it is given by:

$$Capacity\ (\text{Ah}) = \int_{t_o}^{t_0+\tau} (I_b - I_{loss})\ , \tag{1}$$

$$\text{SOC} = \frac{\text{SOC}_{to} + \int_{t_o}^{t_0+\tau} (I_b - I_{loss})}{Rated\ Capacity\ (\text{Ah})}\ . \tag{2}$$

Figures 3a and 3b show the complete schematic and photographic view of the experimental setup used in this study. The battery packs are placed into a thermal chamber (isolation box) to replicate real-time conditions while charging and discharging the cells. To study the effect of cooling on the life of the cells, two sets of battery packs are made for each configuration and are tested under the same conditions to check the repeatability. Two configurations, without a cooling system and with tab cooling are tested. The tab cooling enclosure is manufactured inside the laboratory with available facilities and its physical properties are tested. A brief method of preparation of the tab enclosure is given here. To begin the fabrication of the tab cooling enclosure, a measured quantity of epoxy resin and hardener is added to a beaker. Nano-copper equivalent to 1% by mass of the total bled is added at a steady pace to the beaker and stirred continuously to make a blend. Followed by that, ripped strands of carbon fibre of 2% by weight are added to this mixture and stirred to make a blend. The first half of the prepared blend is poured into the mould which is already coated with a mould release agent. A woven carbon fibre sheet is placed on the mould and the remaining blend is poured into the mould. The prepared moulds are then placed inside the sintering furnace for 60 minutes and the temperature is set to 100°C. After 60 minutes the moulds are taken out and allowed to cool for five minutes before removing the casted component from the mould.

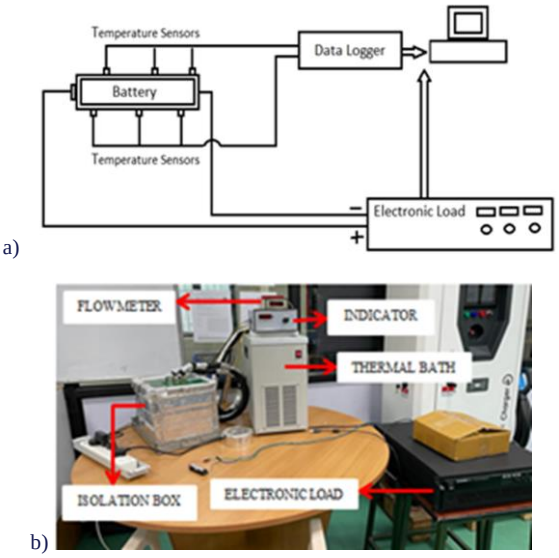


Fig. 3. Experimental setup: (a) schematic view; (b) photographic view.

The mineral oil that is used in electric transformers is used as a coolant for the battery pack. Mineral oil has good dielectric properties, chemical stability at high temperatures and moderate thermal conductivity. The coolant channel in the battery pack is supplied with mineral oil at a constant temperature of 35°C using a thermal bath. The flow rate can be varied from 0.5 lpm (litre per minute) to 2 lpm. The temperature was measured with a K type thermocouple. Thermocouples and sensors are connected to the Keysight 34970A data acquisition system. The flow rate of the coolant was measured using a turbine-type flow meter. The maximum possible error in the case of temperature and flowrate was calculated from the minimum values of the temperature and flowrate measured and the accuracy of the indicator as given by Holman (1973) [27]. The calculated error in the temperature and flowrate measurement was found to be 0.9 % and 0.5%, respectively.

The main factor in determining battery life is not only the battery temperature and discharging cycle but also the charging cycle as well. The research by Abousleiman et al. [28] compares the constant-current (CC) constant-voltage (CV) charging method against the time-pulsed charging method. The constant-current constant-voltage charging method is the most common approach that is used to charge li-ion batteries. The logic behind this approach is divided into two regions, a constant-current region followed by a constant-voltage region. The work by Xu et al. [29] suggests that both CC and pulse charging are good for fast charging and CV charging yields good efficiency.

The research by Musaliyarakam [30] compares different charging methods and enlists their advantages and disavantages.

The performance of each type of charger, namely battery resistance compensation (BRC), state of charge estimated technique (SET), fuzzy control based on battery temperature (FCST), fuzzy controller based on the active state of charge (FCASC) and sinusoidal ripple current technique (SRC) is compared with the conventional CC-CV type. BRC/FCASC can be used for low-power applications, where the battery packs are kept in a comparatively cooler area or where there is proper ventilation. FCST can be used if there is a tight tolerance for the temperature rise due to which the ambient temperature is close to the maximum operating temperature of the battery pack (55°C−60°C). SRC can be used for high-power/high-performance applications, where the battery charging efficiency plays a critical role along with the reduced charging time and battery temperature.

The charging method that was used in this work is a combination of CC and CV charging. Initially, the current supplied is high (1.5 A) until the voltage reaches 3.7 V, and subsequently migrates to CV until the voltage reaches 4.2 V (the charging current gradually decreases). After charging, the cells are left for two hours before starting the discharging cycle to allow the cells to reach thermal stability. The SOC for charging cycles was kept at 30% to avoid deep discharge.

2.1. Tab cooling design

Generally, electric vehicles use a separate cooling system which is linked with the vehicle's HVAC system to meet the operating temperature requirements of the battery pack. The HVAC system consumes energy from the battery pack [31]. Battery cooling system involves components of the HVAC system, coolant, coolant circuit, pumps and heat exchangers. These components consume a significant amount of energy from the battery and this study has not considered the energy consumed by the battery cooling system. The battery cooling system is an important subsystem of an electric vehicle as the optimal temperature range for the battery's efficient operation is between 15−45°C. Therefore, it is important to develop a highly competent battery cooling system to aid the high energy density cells. Tab cooling improves cell life but is difficult to implement. This is mainly because the surface that is the point of contact for the supply of electricity is also the surface that is supposed to transfer heat. Li-ion cells are made up of very thin layers of anode, cathode and separator rolled together or stacked together very close to each other to give the maximum energy density possible. These layers generate heat when charging or discharging due to the electrochemical reactions occurring in them. But the inner layers are generally hotter than the outer layers as they have a smaller surface area to dissipate heat. This temperature difference is the internal temperature gradient of the cell. Further, when the cell is cooled using either natural convection, air cooling or liquid surface cooling, cooling the curved surface of the battery cools only the outer surface. This further increases the internal temperature gradient of the cell.

A high internal temperature gradient either makes the inner layers much hotter than recommended or as the outer layers are much cooler than the inner layers, they end up providing most of the current supply. This results in the loss of available capacity of the cell and also accelerates the process of cell degradation. The primary objective of this work is to design and study the performance of a tab cooling system. Existing battery liquid cooling systems are either very intricate and segmented and difficult to manufacture or the ones which are easy to manufacture aren't very efficient. Moreover, ensuring that no leakage takes place adds to the difficulty and cost of manufacturing. To carry out the study, first, a battery pack with cylindrical lithium-ion batteries in series and parallel was modelled and analysed in ANSYS FLUENT. These include the initial model for 100 cells that gives 72 V and 25 A current ratings. The results are presented for a single battery, which could be representative of batteries in the battery pack.

To simulate the temperature distribution inside the cooling tab, a solid model of the enclosure is created. Sections were named as inlet, outlet, wall and battery. During mesh generation, certain surfaces need a sizing function to obtain a refined mesh to achieve accurate temperature distribution. The turbulence k–ε model is used for the analysis. The density, thermal conductivity and specific heat capacity of the composite material are taken as 1 760 kg/m^3, 3.91 W/(m K), 1 108 J/(kg K), respectively. The density of the composite is calculated based on the standard test piece of known volume and measured weight. The specific heat capacity is measured using the rule of mixtures and the thermal conductivity was calculated as per ASTM D5470-17 using a calorimeter. The governing equations used in this analysis are continuity, momentum, and energy equations. Coming to the solution step, the solver preferred for this analysis is the coupled solver with a second order upwind scheme. The number of iterations is varied till the convergence is reached.

The pack is designed specifically to achieve tab cooling in a battery pack that uses cylindrical li-ion cells. The cooling ducts of this design extract heat from the cell tabs more efficiently due to the larger contact area between the cooling fluid and cell tabs. The module was designed keeping in mind manufacturing constraints and addressing safety issues such as leakage of coolant. The tab cooling module is manufactured using composite material as it is an electrical insulator and has low thermal conductivity. Heat is transferred from the cell tabs to the coolant and the coolant is passed through the ducts or boxes.

3. Results and discussion

3.1. Simulation study

The flow and heat transfer analysis of the battery pack was done in the Ansys Fluent commercial software. The input parameters given for the analysis were: gravity in the negative Y-axis direction, inlet coolant temperature 303 K (30°C), inlet velocity 2 m/s and battery heat flux 1 100 W/m^2. The heat flux was calculated experimentally during the discharging of a battery in the calorimeter. For calculating the heat flux, a cell was discharged at 2 C inside a thermal bath filled with ethylene glycol and the temperature rise during the test duration was noted. Using Eqs. (3) and (4), the heat flux of the battery can be calculated. Figures 4 and 5 show velocity vectors in the enclosure and temperature distribution inside the battery tab. The theoretical study is

mainly conducted to see whether the proposed design yields a better result.

$$\dot{q} = \frac{m_{eg} * C_{p\ eg} * (T_i - T_f) + m_{cv} * C_{p\ cv} * (T_{icv} - T_{fcv})}{t_d}, \quad (3)$$

$$Heat\ flux\ of\ the\ cell = \frac{\dot{q}}{Battery\ surface\ area}. \quad (4)$$

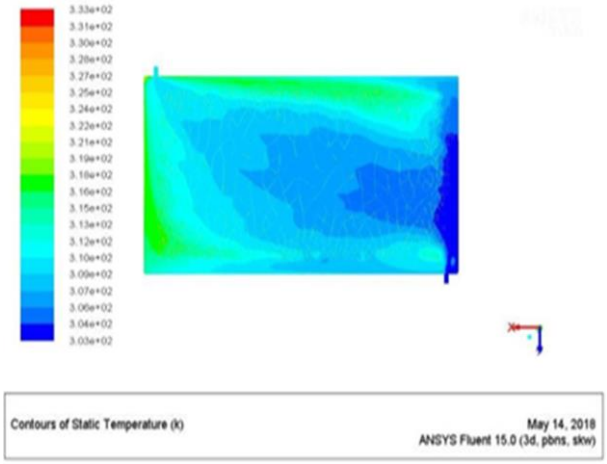


Fig. 4. Temperature contours in the coolant box.

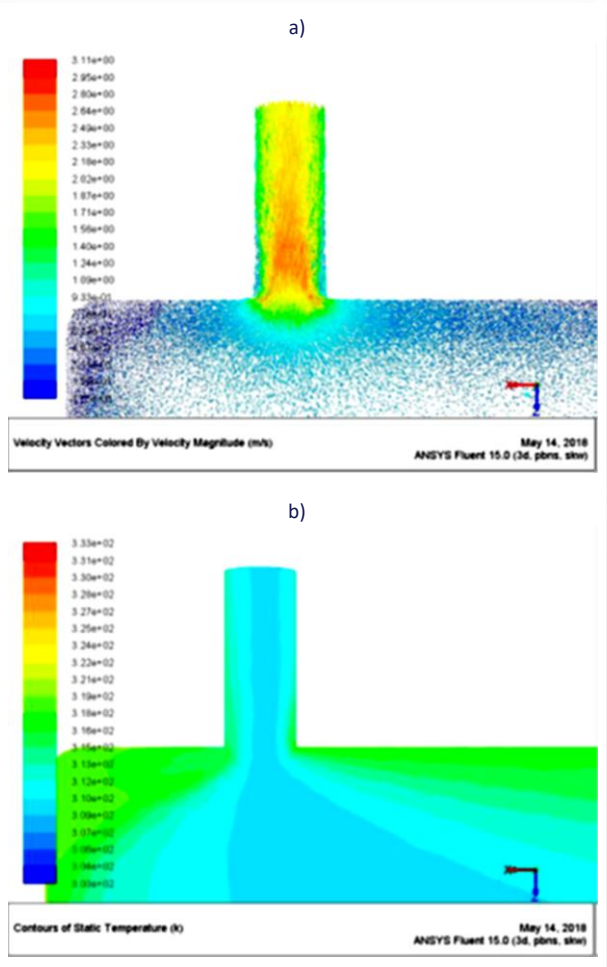


Fig. 5. Velocity vectors (a) and outlet temperature contours (b).

From the temperature contours it is observed that the overall temperature of the coolant remains about 313 K (40°C). Further, in the places where the temperature is high (shown in green), it is below 50°C. The average outlet temperature of the coolant is 38°C. From the velocity contours it is observed that the water loses its velocity as soon as it leaves the cylindrical inlet section of the coolant box and regains its velocity near the outlet region. As the results of the theoretical study are encouraging, battery tab enclosures are fabricated for experimental study.

3.2. Performance of battery pack without cooling

To benchmark the performance of the tab cooling, experiments were conducted using a battery pack without cooling tabs. It is very well known that the battery pack temperature will rise to a maximum level without the cooling system being incorporated. Heat is generated inside the spiral construction that involves multiple layers (known as a jelly roll) of the electrode assembly due to activation polarization, concentration polarisation and ohmic polarisation. If the generated heat is not removed from the cell/battery pack, the temperature of the cell rises. Without a cooling system, as the number of charging and discharging cycles increases, the temperature of the cell is also increased. The entire experiment is conducted at a thermal chamber temperature of 40°C. India is a tropical country, the central and southern parts of India experience hot weather for almost 9 months. The temperature reaches a maximum of 44°C during the peak summer. So, all the experiments are conducted at 40°C. A sample discharge profile (variation of voltage with respect to the capacity of the cell) of both packs with and without the cooling system is given in Fig. 6. During the entire course of the experiment, the battery was discharged at a 2 C current rating and the experiment was stopped after the battery reached 30% of the SOC to avoid deep discharge and damage.

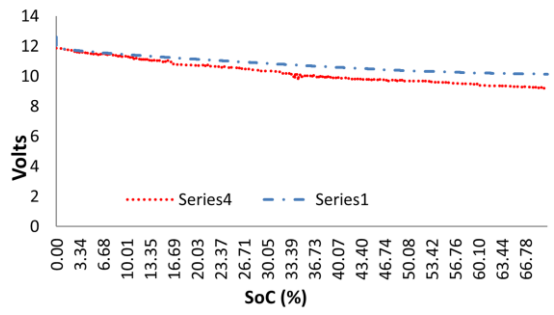


Fig. 6. Variation of discharge voltage with respect to capacity.

The temperature profile of the battery pack during the discharge test is given in Figs. 7 and 8. Figure 7 shows the temperature distribution of the surface of the cells. Each cell in the pack is installed with 6 thermocouples. A protocol is established to mount the thermocouples on the cells, i.e. locations of the thermocouples should be the same in all three cells of the pack. The locations are assigned numbers from 1 to 6 in each cell. T1 and T3 represent the locations of the thermocouple close to the positive and negative terminals of the cell. The average temperature

at specific locations of the thermocouple is plotted in Fig. 7. From Fig. 8, it is evident that the peak temperature of the cells gradually increased as the cycles progressed; initially, it was close to 50°C for cells without a cooling system. While the middle regions of the cell registered a temperature close to 60°C during the tests, the thermocouples near the positive and negative tabs registered a maximum of 71°C and 69°C after reaching 700 cycles.

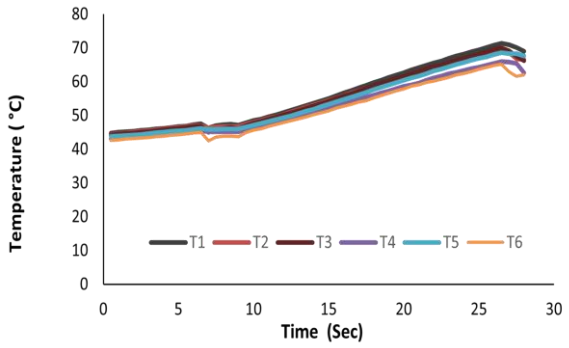


Fig. 7. Surface temperature at different locations on an 18 650 battery without a cooling system discharged at a rate of 2 C.

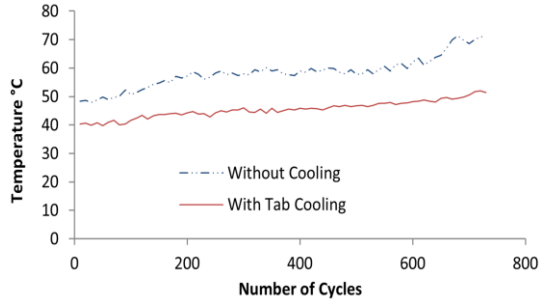


Fig. 8. Average peak temperature of the battery surface with respect to the number of cycles.

As mentioned earlier, during the loading cycle, cells are discharged till 30% of the SOC. When the cells in the pack are discharged at 2 C rating using a DC load, the duration of the test depends on the capacity (Ah rating) of the battery. It is also a known fact that the battery capacity fades with ageing (number of charge and discharge cycles executed). The capacity fading (effect of ageing) with respect to the number of charge and discharge cycles is studied and presented here. Figure 9 shows the comparison of test duration with respect to the number of cycles for both battery packs with and without cooling. For the pack without cooling, the pack reached 30% of the SOC within 25 minutes in the first few cycles and it was further reduced to 17 minutes at 700 cycles of charging and discharging. After 700 cycles the experiments were stopped as it represented a capacity loss of 30% of the nominal capacity. Generally, automotive battery packs will be replaced when there is a capacity fading of 30% of the nominal capacity. The rise in the discharge temperature and shortening of the test duration clearly represents the accelerated degradation of the cells in the pack without a cooling system. High discharge temperature also leads to a rise in internal resistance of the cells, which is also a sign of degradation.

3.3. Setup with cooling

The battery pack with a tab cooling system performed well when compared to the pack without a cooling system incorporated. Figure 6 very clearly shows that the discharge voltage of the tab cooling pack is higher than the pack without cooling by close to 1.5 V at the end of 700 cycles. It took almost 1 138 cycles to reach a 30% loss of initial capacity for the tab cooling pack, which is an indication of slower deterioration of the cells in the pack.

Figure 8 shows the peak temperature reached by the cells in the pack during the discharge. The maximum battery temperature was noted during charging and discharging cycles and the point at which the maximum temperature is registered with thermocouples (out of the six thermocouples) is taken as the maximum temperature of the cell and it is plotted in Fig. 8. As stated earlier, the temperature increased as the number of cycles increased. A maximum increase in temperature by around 5°C is registered with the tab cooling pack, whereas the maximum temperature rise by around 30°C is registered with the pack without a cooling system.

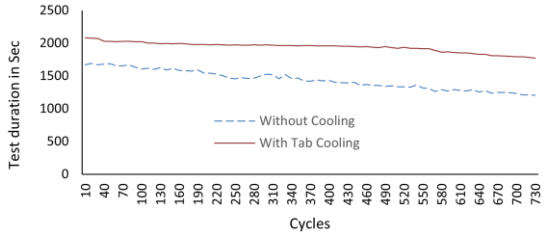


Fig. 9. Discharge time with respect to the number of cycles.

From Fig. 9, it is observed that the battery with a cooling system loses its power capacity much slower than the battery without a cooling system. This is primarily due to the heat extraction by the cooling system which allowed the temperature of the cells to remain below 50°C. The maximum temperature stays within 48°C for the battery pack with the cooling system. Further, it is also observed that the temperature of the battery starts increasing sharply when the circuit voltage drops below 9 V with both configurations. Concerning the capacity fading in Fig. 9, we can conclude that a 45% improvement in the cells' lifetime was achieved by implementing the tab cooling system.

4. Conclusions

The cooling system in battery modules is a very crucial sub-system of electric vehicles. Therefore, an attempt was made to study the performance of the tab (liquid) cooling system. A model was created and analysed in ANSYS, to confirm the merits of tab cooling.

For experimental validation, a miniature battery pack was made with 3 cells in a series. To compare the results of the cooling system, another battery pack with 3 cells in a series was made without a cooling system. Both the packs were charged

and discharged repeatedly until a 30% loss in power capacity occurred.

The results of the pack with tab cooling show improvement in the performance and cycle life of the pack. A close-to-45% improvement in the cycle life of the cells was achieved with the tab cooling when compared to that of the pack without cooling.

Further, the results also show a marginal rise in the surface temperature of the cell in the tab cooled pack which ascertains the safe operation of the cells in the pack.

References

[1] He, F., & Ma, L. (2016). Thermal management in hybrid power systems using cylindrical and prismatic battery cells. *Heat Transfer Engineering*, 37(6), 581−590. doi: 10.1080/01457632.2015.1060776

[2] Yang, Y., Wu, J., Song, X., & Gu, Z. (2022). Thermal management performance of lithium-ion battery using supercritical CO_2 as cooling fluid. *Heat Transfer Engineering*, 1−14 doi: 10.1080/01457632.2022.2134082

[3] Nelson, P., Dees, D., Amine, K., & Henriksen, G. (2002). Modeling thermal management of lithium-ion PNGV batteries. *Journal of Power Sources*, 110(2), 349−356. doi: 10.1016/s0378-7753(02)00197-0

[4] Mohammadian, S.K., & Zhang, Y. (2015). Thermal management optimization of an air-cooled Li-ion battery module using pin-fin heat sinks for hybrid electric vehicles. *Journal of Power Sources*, 273, 431−439. doi: 10.1016/j.jpowsour.2014.09.110

[5] Tennessen, P.T., Weintraub, J.C., & Hermann, W.A. (2014). *Extruded and ribbed thermal interface for use with a battery cooling system*. U.S. Patent 8758924B2. Washington, USA.

[6] Teng, H., Ma, Y., Yeow, K., & Thelliez, M. (2011). Thermal characterization of a Li-ion battery module cooled through aluminum heat-sink plates. *SAE International Journal of Passenger Cars - Mechanical Systems*, 4(3), 1331−1342. doi: 10.4271/2011-01-2248

[7] Mohammed, A.H., Alhadri, M., Zakri, W., Aliniagerdroudbari, H., Esmaeeli, R., Hashemi, SR., Nadkarni, G., & Farhad, S. (2018). Design and comparison of cooling plates for a prismatic lithium-ion battery for electrified vehicles. *SAE Technical Paper*, 2018-01-1188. doi: 10.4271/2018-01-1188

[8] Li, X., He, F., Zhang, G., Huang, Q., & Zhou, D. (2019). Experiment and simulation for pouch battery with silica cooling plates and copper mesh based air cooling thermal management system. *Applied Thermal Engineering*, 146, 866−880. doi: 10.1016/j.applthermaleng.2018.10.061

[9] Zhao, J., Rao, Z., Huo, Y., Liu, X., & Li, Y. (2015). Thermal management of cylindrical power battery module for extending the life of new energy electric vehicles. *Applied thermal engineering*, 85, 33−43. doi: 10.1016/j.applthermaleng.2015.04.012

[10] Wang, T., Tseng, K.J., Zhao, J., & Wei, Z. (2014). Thermal investigation of lithium-ion battery module with different cell arrangement structures and forced air-cooling strategies. *Applied energy*, 134, 229−238. doi: 10.1016/j.apenergy.2014.08.013

[11] Wang, T., Tseng, K. J., & Zhao, J. (2015). Development of efficient air-cooling strategies for lithium-ion battery module based on empirical heat source model. *Applied Thermal Engineering*, 90, 521−529. doi: 10.1016/j.applthermaleng.2015.07.033

[12] Fan, L., Khodadadi, J.M., & Pesaran, A.A. (2013). A parametric study on thermal management of an air-cooled lithium-ion battery module for plug-in hybrid electric vehicles. *Journal of Power Sources*, 238, 301−312. doi: 10.1016/j.jpowsour.2013.03.050.

[13] Kim, G.H., & Pesaran, A. (2007). Battery thermal management design modeling. *World Electric Vehicle Journal*, 1(1), 126−133. doi: 10.3390/wevj1010126

[14] Xie, J., Zang, M., Wang, S., & Ge, Z. (2017). Optimization investigation on the liquid cooling heat dissipation structure for the lithium-ion battery package in electric vehicles. *Proceedings of the Institution of Mechanical Engineers, Part D: Journal of Automobile Engineering*, 231(13), 1735−1750. doi: 10.1177/0954407016685457

[15] Zhao, J., Rao, Z., & Li, Y. (2015). Thermal performance of mini-channel liquid cooled cylinder based battery thermal management for cylindrical lithium-ion power battery. *Energy Conversion and Management*, 103, 157−165. doi: 10.1016/j.enconman.2015.06.056

[16] Teng, H., & Yeow, K. (2012). Design of direct and indirect liquid cooling systems for high-capacity, high-power lithium-ion battery packs. *SAE International Journal of Alternative Powertrains*, 1(2), 525−536. doi: 10.4271/2012-01-2017

[17] Janarthanam, S., Burrows, N., & Boddakayala, B.R. (2017). Factors Influencing Liquid over Air Cooling of High Voltage Battery Packs in an Electrified Vehicle. *SAE Technical Paper*, 2017-01-1171. doi: 10.4271/2017-01-1171

[18] Mevawalla, A., Panchal, S., Tran, M.K., Fowler, M., & Fraser, R. (2020). Mathematical Heat Transfer Modeling and Experimental Validation of Lithium-Ion Battery Considering: Tab and Surface Temperature, Separator, Electrolyte Resistance, Anode-Cathode Irreversible and Reversible Heat. *Batteries*, 6(4), 61. doi: 10.3390/batteries6040061

[19] Ham, S.H., Jang, D. S., Lee, M., Jang, Y., & Kim, Y. (2023). Effective thermal management of pouch-type lithium-ion batteries using tab-cooling method involving highly conductive ceramics. *Applied Thermal Engineering*, 220, 119790. doi: 10.1016/j.applthermaleng.2022.119790

[20] Liebertseder, J., Dollinger, A., Sorg, T., Berg, L.F., & Tübke, J. (2022). Battery Tab Cooling in Traction Battery Modules using Thermally Conductive Plastics, *IEEE Xplore, Vehicle Power and Propulsion Conference*, 1-4 November, Merced, USA, doi: 10.1109/VPPC55846.2022.10003372

[21] Ahmad, T., Mishra, A., Ghosh, S., & Casari, C.S. (2022). Identifying efficient cooling approach of cylindrical lithium-ion batteries. *Energy Technology*, 10(2). doi: 10.1002/ente.202100888

[22] Hunt, I.A., Zhao, Y., Patel, Y., & Offer, G.J. (2016). Surface cooling causes accelerated degradation compared to tab cooling for lithium-ion pouch cells. *Journal of The Electrochemical Society*, 163(9), A1846. doi: 10.1149/2.0361609jes

[23] Zhao, Y., Diaz, L.B., Patel, Y., Zhang, T., & Offer, G.J. (2019). How to cool lithium ion batteries: optimising cell design using a thermally coupled model. *Journal of The Electrochemical Society*, 166(13), A2849. doi: 10.1149/2.0501913jes

[24] Zhao, Y., Patel, Y., Zhang, T., & Offer, G.J. (2018). Modeling the effects of thermal gradients induced by tab and surface cooling on lithium ion cell performance. *Journal of The Electrochemical Society*, 165(13), A3169−A3178. doi: 10.1149/2.0901813jes

[25] Li, S., Kirkaldy, N., Zhang, C., Gopalakrishnan, K., Amietszajew, T., Diaz, L.B., & Marinescu, M. (2021). Optimal cell tab design and cooling strategy for cylindrical lithium-ion batteries. *Journal of Power Sources*, 492, 229594. doi: 10.1016/j.jpowsour.2021.229594

[26] Theinglim, K., & Poramapojana, P. (2019). Effect of Tab Cooling on Large-Format Lithium-Ion Pouch Cells. *SAE Technical Paper*, 2019-01-2261. doi: 10.4271/2019-01-2261

[27] Holman, J.P. (2011). *Experimental Methods for Engineers* (8th ed.). McGraw-Hill, New York, USA.

[28] Abousleiman, R., Al-Refai, A., & Rawashdeh, O. (2013). Charge capacity versus charge time in CC-CV and pulse charging of Li-ion batteries. *SAE Technical* Paper, 2013-01-1546. doi: 10.4271/2013-01-1546

[29] Xu, X., Wei, X., Gao, H., Zhu, J., Yang, J., & Liu, Y. (2015). Research on Charging Strategy of Lithium-ion Battery. *SAE Technical Paper*, 2015-01-1192. doi: 10.4271/2015-01-1192

[30] Musaliyarakam, N.A. (2016). A Road Map for Li-Ion Battery Charger based on Charging Time, Battery Life and Safety. *SAE Technical Paper*, 2016-28-0150. doi: 10.4271/2016-28-0150

[31] Canteros, M.L., & Polansky, J. (2022). Study of the heat pump for a passenger electric vehicle based on refrigerant R744. *Archives of Thermodynamics*, 43(2), 17–36, doi: 10.24425/ather.2022.141976

Co-published by
Institute of Fluid-Flow Machinery
Polish Academy of Sciences
Committee on Thermodynamics and Combustion
Polish Academy of Sciences

Copyright©2024 by the Authors under licence CC BY 4.0

http://www.imp.gda.pl/archives-of-thermodynamics/

Effects of cooling methods and key parameters on the cooling performance of oil-cooling motor with hairpin windings

Y.X. Liu[ab*], H. Wu[b], J. Zhang[b], P.X. Xu[c], S. Chen[c], X.H. He[a], Z.D. Sun[d]

[a]School of Smart Health, Chongqing College of Electronic Engineering, Chongqing, 401331, China
[b]Department of Technology, Chongqing Tsingshan Industrial Co. Ltd., Chongqing, 402776, China
[c]College of Mechanical Engineering, Chongqing University of Technology, Chongqing 400044, China
[d]Hubei University of Automotive Technology, Shiyan Hubei, 442002, China
*Corresponding author: liugw215@126.com

Received: 11.12.2023; revised: 21.02.2024; accepted: 22.04.2024

Abstract

Based on the electromagnetic thermal coupling analysis method, the cooling performance of different motor cooling models and the influence of key parameters of the cooling system on the cooling effect of the motor are investigated. First, the losses of various parts of the permanent magnet synchronous motors are obtained through electromagnetic calculations; the analysis results show that the stator core loss, winding copper loss, and eddy current loss of permanent magnets exceed 95% of the total loss of the motor. Second, the cooling performance of the three motor was compared and analyzed. The axial housing liquid cooling and oil spray cooling (Model B) has a better cooling performance and a higher cooling efficiency. Compared with the other two motor models, Model B can reduce the time to reach steady-state temperature by about 81.8%.Then the effects of coolant volume flow rate, coolant inlet temperature, and ambient temperature on the cooling effect of the motor are investigated. The results show that within a certain range, the rate of coolant inlet temperature change is approximately proportional to the internal temperature rise of the motor. The oil spray cooling system of Model B is less affected by ambient temperature and can be used for motor cooling in complex environments. The results of this study can provide a useful guidance for the design of the cooling system and the selection of coolant volume flow rate for oil-cooling motor with hairpin windings.

Keywords: Hairpin winding; Electromagnetic-thermal coupling; Permanent magnet synchronous motors; Cooling performance; Oil spray cooling

Vol. 45(2024), No. 2, 301–309; doi: 10.24425/ather.2024.150874

Cite this manuscript as: Liu, Y.X., Wu, H., Zhang, J., Xu, P.X., Chen, S., He, X.H., & Sun Z.D. (2024). Effects of cooling methods and key parameters on the cooling performance of oil-cooling motor with hairpin windings. *Archives of Thermodynamics*, 45(2), 301−309.

1. Introduction

Due to fluctuations in fuel prices, emission restrictions, and increasing public awareness of global warming, electric vehicles (EVs) have been welcomed as the future of passenger car and light transport vehicle industry [1−2]. In this case, motors with high power density are needed to reduce weight and extending the travel range of EVs. Due to its ability to increase motor power density, hairpin windings are being increasingly adopted in EV drive motors and have become a research hotspot in recent years [3−5].

Permanent magnet synchronous motors (PMSM) is one of

Nomenclature

B_m – amplitude of the magnetic flux density, T
f – frequency, Hz
I – effective value of phase current pressure, A
k_c – additional locc coefficient,
k_e – eddy current loss coefficient,
k_h – hysteresis locc coefficient,
m – number of phases in the motor,
P_{AC1} – AC copper loss caused by skin effect, W
P_{AC2} – AC copper loss caused by proximity effect, W
P_c – additional loss, W
P_{Cu} – total winding loss of the motor, W
P_{DC} – DC copper loss, W
P_e – eddy current loss, W
P_h – hysteresis loss, W
P_{pm} − eddy current loss in permanent magnets, W
r – winding resistance, Ω

Greek symbols

σ − electrical conductivity, S/m

Abbreviations and Acronyms

AC − alternating current
DC − direct current
EV – electric vehicle
PMSM − permanent magnet synchronous motors

the most commonly used types of motors in the power transmission system of electric vehicles. The motor cooling method for a PMSM can be air cooling, water cooling, or oil cooling [6−8]. Although air cooling [9,10] and water jacket cooling [11,12] are widely used for thermal management of motors, they cannot meet the demanding requirements of higher heat flux in future motors due to the poor thermal conductivity of laminations and insulation materials. Modern EVs require the smallest weight to achieve high power, thereby increasing heat generation and reducing heat dissipation space [13]. The performance of motors is thus typically limited by their ability to remove heat from critical components, requiring an efficient cooling system [14]. To meet the cooling performance of high-power density motors, various advanced cooling methods and design concepts have been proposed. Lindh et al. [15] combined cooling tubes with the slot winding and tested its performance with three real drive cycles, the cooling capability was extremely promising, and the motors winding average temperature reaches only 77°C temperatures. Madonna et al. [16] developed a novel thermal management method, their modelling and experimental results show that a 25% hot-spot temperature reduction on a particular application can be achieved. Liu et al. [17] conducted experimental research on oil spray cooling for end winding and discussed the effects of spray parameters and nozzle structure, hot spots on end-windings can be expected within the top half, from the 10 o'clock to the 2 o'clock positions, and the cooling performances of full-cone nozzles are generally better than the hollow-cone nozzle. Wang et al. [18] have designed three kinds of novel PMSM integrated with heat pipe, the heat transfer performance between the heat pipe and the end cap is significantly improved compared to traditional PMSM cooling systems, the highest temperatures of the end winding are 149.9°C, 140.1°C, 133.5°C, and 139.6°C for the traditional PMSM and the three new PMSMs, respectively. Wang et al. [19] investigated a novel direct cooling structure for the primary core and windings, integrated with the advantage of a filler with high thermal conductivity, which can greatly reduce the thermal resistances between the heat source and the coolant and thus improves the cooling performance. Wang et al. [20] studied the thermal management of the end winding of oil spray and established a prediction model for heat transfer performance, the predicted results of the model coincided with experimental data very well with the MSE and correlation coefficient of 7.28 and 0.93, respectively. Guo et al. [21] proposed a novel hybrid cooling method for high-speed high-power permanent magnet assisted synchronous reluctance starter/generator, which can decrease 10% and 35.7% temperature compared with the cooling method of the oil circulation in the housing, oil spray at winding ends and the cooling method of the oil spray at rotor end surface. According to studying the oil spray cooling parameters of end windings [22], it was found that around 75% increase of the total heat transfer coefficient and 8 times decrease of the uniformness of wall temperature can be achieved by increasing around half the flow rate of the coolant liquid. Zhao et al. [23] proposed a water-cold plate cooling structure between the axial laminations of the motor stator. Compared with the outer spiral water jacket cooling structure, the maximum and average temperatures of the water-cooled plate structure were reduced by 25.5% and 30.5%, respectively. The thermal losses of PMSMs are primarily caused by mechanical, magnetic, copper losses and bearing friction losses [24]. Copper losses occur in the winding conductors and can be evaluated through Joule loss relation [25]. The mechanical losses are caused by friction between the rotor and air inside the air gap [26]. Magnetic loss or iron loss, including hysteresis and eddy current losses of the rotor and stator, can be estimated by constants related to motor material and electromagnetic configuration [27]. Due to many details often being unknown, significant errors often occur when using theoretical calculations to calculate the heat loss value of a motor. Therefore, modeling software and electromagnetic thermal calculation software are usually used for numerical evaluation, such as Altair Flux [28] or Ansys Motor-CAD [29].

Research on hairpin winding oil cooled motors mainly focuses on optimizing the cooling system. However, more comprehensive research is needed on the impact of key parameters of the cooling system on the cooling performance of the motor. On this basis, taking a PMSM with hairpin windings as the research object, a motor loss solution model was established based on the theory of electromagnetism and heat transfer. In addition, based on the electromagnetic thermal coupling analysis method, the cooling performance of different motor cooling models and the influence of key parameters of the cooling system on the cooling effect of the motor were investigated. The research results can provide a useful guidance for the design of cooling system and key parameters for PMSM with hairpin windings.

2. Material and method

2.1. Motor model and parameters

The research object is the permanent magnet synchronous drive motor for EVs, which adopts a hairpin winding. The axial structure and composition of the motor are shown in Fig. 1, and the basic parameters of the motor are shown in Table 1.

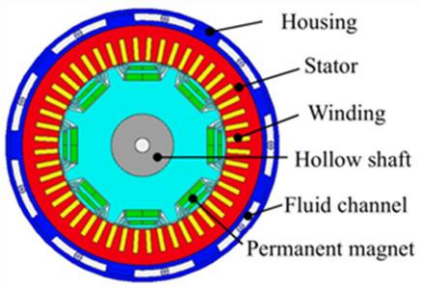


Fig. 1. PMSM with hairpin windings.

Table 1. Basic parameters of PMSM.

Parameters	Values
Rated speed (r/min)	6 000
Rated power (kW)	150
Number of stator slots	48
Pair of poles	8
Outer diameter of stator(mm)	250
Inner diameter of stator(mm)	175
Cooling method	Oil cooling
Number of winding layers	6
Coil type	Hairpin winding

To analyse the influence of different cooling systems on the cooling performance of the motor, three cooling models were created based on the prototype model (Fig. 1): axial housing liquid cooling model (Model A), axial housing liquid cooling and oil spray cooling model (Model B), and axial housing liquid cooling and hollow shaft cooling model (Model C). In Model A, there are 9 evenly distributed coolant flow channels along the circumference of the housing. The coolant enters from the front inlet of the motor and flows out from the rear outlet along the axial direction (see Fig. 3a). In addition, to better compare and analyse the cooling performance of the three different cooling systems, ATF134 coolant is selected, with a thermal conductivity of 0.1338 W/(m·K), a specific heat capacity of 2.26 J/(kg·K), and a density of 811.8 kg/m^3.

2.2. Losses analysis of motor with hairpin windings

1) Iron core loss

Iron core loss (referred to as iron loss) is a general term for power losses caused by hysteresis and eddy currents in the core during AC magnetic circuits. The iron loss inside the motor can be divided into three parts: eddy current loss, hysteresis loss and additional loss. Based on the Bertotti iron loss calculation model, the iron loss per unit mass can be express as follows [30]:

$$P_{\mathrm{Fe}} = P_h + P_c + P_e = k_h f B_m^2 + k_c f^2 B_m^2 + k_e f^{1.5} B_m^{1.5}, \quad (1)$$

where P_h is hysteresis loss, W; P_c is additional loss, W; P_e is eddy current loss, W; B_m is the amplitude of the magnetic flux density, T; f is the frequency, Hz; k_h, k_c and k_e are the hysteresis loss coefficient, additional loss coefficient and eddy current loss coefficient, respectively.

2) Winding copper loss

For conventional round wire motors, the AC copper loss during motor operation can be ignored. The total copper loss in the motor can be represented by the DC copper loss, which is proportional to the square of the current and the resistance. However, for hairpin winding motors, the skin effect and proximity effect in the windings are more significant, resulting in larger eddy current losses. Therefore, the copper loss in hairpin windings can be divided into three parts: DC copper loss, AC copper loss caused by skin effect, and AC copper loss caused by proximity effect:

$$P_{\mathrm{Cu}} = P_{\mathrm{DC}} + P_{\mathrm{AC1}} + P_{\mathrm{AC2}}\ , \quad (2)$$

where P_{Cu} is the total winding loss of the motor; P_{DC} is the DC copper loss; P_{AC1} is the AC copper loss caused by skin effect; P_{AC2} is the AC copper loss caused by proximity effect:

$$P_{\mathrm{DC}} = mI^2 r\ , \quad (3)$$

where m is the number of phases in the motor; I is the effective value of phase current; r is the winding resistance.

The factors that affect the copper loss of hairpin winding motors can be divided into two categories: winding structural parameters and winding energization parameters. In practical calculations, analytical calculation methods are often unable to accurately calculate the copper loss. Therefore, finite element simulation is commonly used to calculate the winding copper loss.

3) Eddy current loss in permanent magnets

During the actual operation of the motor, there are certain harmonic components in the air gap magnetic field. These harmonic components induce eddy currents within the permanent magnets, resulting in a certain eddy current loss. The loss can be calculated as follows [31]:

$$P_{pm} = \int_V^{\cdot} \delta E^2 \mathrm{d}V = \int_V^{\cdot} J^2/\sigma \mathrm{d}V, \quad (4)$$

where P_{pm} is the eddy current loss in permanent magnets, W; σ is the electrical conductivity, S/m; J is the eddy current density, W/m^3; E is the electric field strength, N/C, and V is the spatial integration area.

3. Results and discussion

3.1. Motor loss calculation

During the operation of a PMSM, due to electromagnetic and mechanical losses, its internal components will convert electrical energy into thermal energy, resulting in an increase in motor

temperature. The electromagnetic-thermal coupling method allows the motor losses obtained from electromagnetic calculations to be directly input into the temperature field calculation of the motor. In the calculation process, the heat transfer between the various components of the motor mainly occurs through conduction and convection, while the influence of thermal radiation between the components is ignored. To simplify the analysis, the following assumptions are made in the electromagnetic thermal coupling calculation:

1) the influence of heat dissipation from the motor end cover on the motor temperature is ignored, and only the heat transfer between the motor housing and the external air is considered,
2) only conduction and convection are considered between the various components and between the components and the air or cooling liquid,
3) the variation in thermal conductivity, heat transfer coefficient, and heat transfer coefficient within the motor due to temperature changes are ignored,
4) the insulation material of the winding is uniformly distributed, and the thermal conductivity between the different parts is consistent.

Based on the above assumptions, the losses of each component of the PMSM with hairpin windings under rated operating conditions can be obtained through electromagnetic calculations, as shown in Table 2.

Table 2. Motor losses under rated operating conditions (W).

Name	Stator iron loss	DC copper loss	Rotor iron loss	Eddy current loss of magnet
Loss value	710.6	2 529	107.4	64.98

From the calculation results, it can be seen that the stator iron core losses, winding copper losses and permanent magnet eddy current losses account for over 95% of the total motor losses.

3.2. Temperature characteristics of housing axial liquid cooling

To compare and analyse the influence of the cooling system on the temperature field distribution of the motor, the temperature field distribution of the housing axial cooling model (Model A) is calculated first based on the electromagnetic thermal coupling method. During the analysis, the coolant volume flow rate, inlet temperature, and ambient temperature are set as10 L/min, 65°C, and 40°C, respectively. Due to the axial symmetry of the studied motor model, half of the motor model A is taken as the research object. Through calculation, it can be concluded that under rated operating conditions, the steady-state temperature distribution along the axial direction of Model A is shown in Fig. 2a, and the relationships between the transient temperature and time of each component is shown in Fig. 2b. It can be seen from Fig. 2a that the highest temperature inside the motor is found in the end winding, with a steady-state temperature of 213.91°C, and the steady-state temperatures of the stator core and permanent magnet are 195.74°C and 195.01°C, respectively. It can be observed from Fig. 2b that the transient temperatures of different components of the motor increase overtime. After approximately 3 000 s, the temperature increase rate of the winding and stator iron core gradually decreases. The temperatures of the permanent magnet, rotor and shaft gradually reach a steady-state stage after about 5 000 s. The above analysis results indicate that for housing liquid-cooled motors, the temperature rise of the winding, stator core, and permanent magnet is relatively large, and they are the main heat source for the internal temperature rise of the motor. In addition, for the housing liquid-cooled motor, during operation, the temperature of the stator and winding in direct contact with the housing reaches a steady-state stage first.

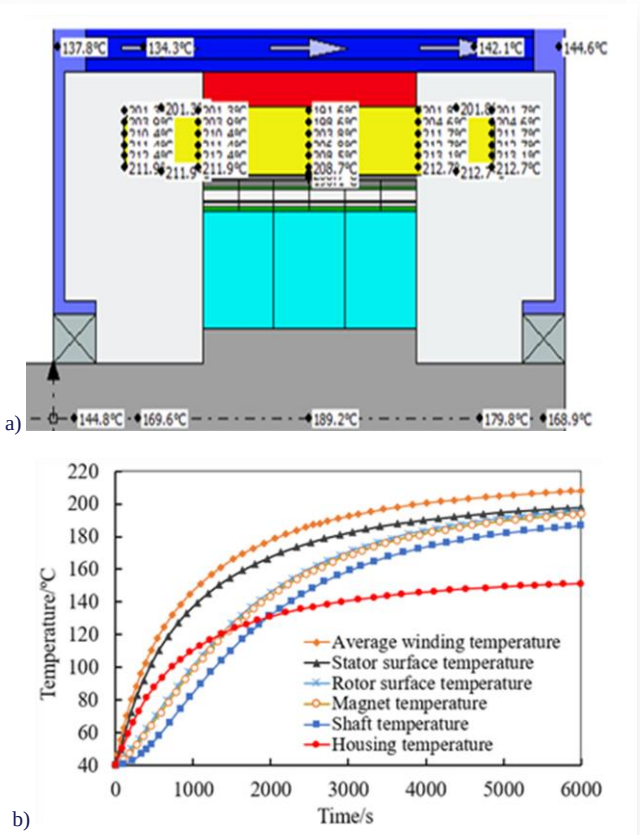


Fig. 2. Steady state temperature distribution and transient temperature variation curve of Model A: a) the steady-state temperature distribution along the axial direction, b) the relationships between the transient temperature of the motor and time.

The operating temperature of neodymium iron boron magnets in PMSM should generally not exceed 200°C. The maximum temperature of the stator and rotor iron cores should not exceed 250°C, and the maximum operating temperature of the shaft is 200°C. When the temperature is too high, irreversible demagnetization can occur in the permanent magnet, and excessive temperatures in the stator and rotor iron cores can lead to insulation layer damage, increased iron losses, and decreased mechanical strength. The insulation class of the motor here is Class H, with a maximum allowable temperature for the stator winding of 180°C and a reference temperature of 145°C. Therefore, for the hairpin winding motor in this study, using only liq

uid cooling in the housing is not sufficient to maintain the temperature rise within an acceptable limit, and the motor will not be able to operate normally. Hence, further optimization of the cooling system is necessary to control the temperature of the permanent magnet below 180°C and the temperature of the stator winding below the reference temperature of 145°C.

3.3. Impact of cooling system on cooling performance

This section mainly compares and analyses the structural characteristics and cooling performance of three cooling systems: Model A, Model B, and Model C. According to the calculation results of the steady-state and transient temperatures of components in Model A (Fig. 1), it can be seen that the average temperature of the windings, the surface temperature of the stator core, and the temperature of the permanent magnets vary significantly during motor operation. When comparing the three models, the focus is on studying the variation of the average temperature of the windings, the surface temperature of the stator core, and the temperature of the permanent magnets under the same boundary conditions, as well as the cooling performance of the three different cooling systems.

The structures of the three motor cooling models are shown in Fig. 3.

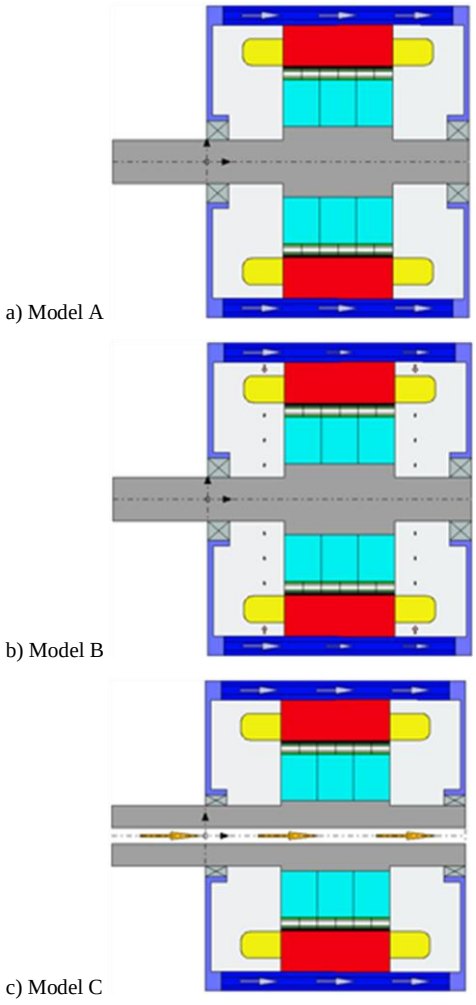


Fig. 3. Structure comparison of three cooling models.

An axial oil channel is used in Model A, where the coolant flows along the axial direction in the housing (the arrow indicates the direction of coolant flow (Fig. 3a). Model B (Fig. 3b) has ring-shaped oil grooves arranged at the front and rear end windings, with 16 oil spray holes evenly distributed on the grooves. The oil sprayed from the spray holes fall onto the shaft, and under the action of centrifugal force, some of the coolant is thrown onto the end windings, enhancing the cooling effect of the end windings. Model B and Model C (Fig. 3c) are two cooling models based on the structural optimization of Model A. The cooling structure of the housing of Model C is the same as that of Model A, and in addition, a hollow shaft cooling is added. The coolant flows from the front end of the hollow shaft to the rear end. The structural parameters of the axial oil passage in the motor housing for the three models are the same. The key structural parameters of Model B and Model C are shown in Table 1.

The main parameter settings for steady-state temperature rise calculation in the three motor models are as follows: the coolant inlet flow rate is 10 L/min; the inlet temperature is 65°C; the ambient temperature is 40°C, and the rated speed is 6 000 r/min. The internal coolant volume flow rate of the shaft in Model C is 2 L/min. The steady-state temperatures of typical components in the three motor models are shown in Fig. 4. From the results of Fig. 4, it can be visually seen that Model B has the best cooling performance, with a steady-state temperature rises of 126.44°C, 119.79°C, and 79.69°C for the windings, stator core and permanent magnets, respectively. Compared with Model A, the steady-state temperature of the windings and the steady-state temperature of the permanent magnets in Model B decrease by 38.19% and 58.55%, respectively. Therefore, based on the above analysis results, it can be concluded that among the three motor cooling models, Model B has better cooling performance because the coolant in Model B can directly contact the internal components of the motor, quickly absorbing their heat.

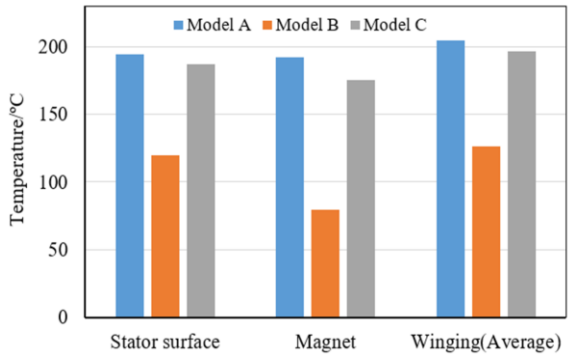


Fig. 4. Steady-state temperatures of typical components in three motor models.

Figure 4 presents the steady-state temperatures of typical components in the three motor models. To more accurately evaluate the cooling performance of different motor models, transient temperature calculations are performed on the motor. In the calculation process, the parameter settings for coolant volume flow rate, inlet temperature, and ambient temperature are the

same as those for steady-state calculations. Under rated operating conditions, the transient temperature variation curves of the windings and permanent magnets in the three motor cooling models are shown in Fig. 5. From the transient temperature analysis results of the three models, it can be observed that after approximately 1 000 seconds of motor operation, the average winding temperature and permanent magnet temperature of Model B tend to stabilize and enter a stable state. The average winding temperature and permanent magnet temperature of Model A and Model C tend to stabilize after about 5 500 seconds of motor operation. It can be seen from the transient temperature changes of the three motor models that the internal temperature of Model B is significantly lower than that of the other two models. The above analysis results indicates that among the three motor cooling models, the oil spray cooling in Model B can achieve fast cooling of various components of the motor, with a higher cooling rate. Compared with the other two motor cooling models, Model B can reduce the time to reach steady-state temperature by about 81.8%. Additionally, due to the presence of an oil spray cooling system, the winding temperature at the end is slightly lower than that of the winding inside the slots.

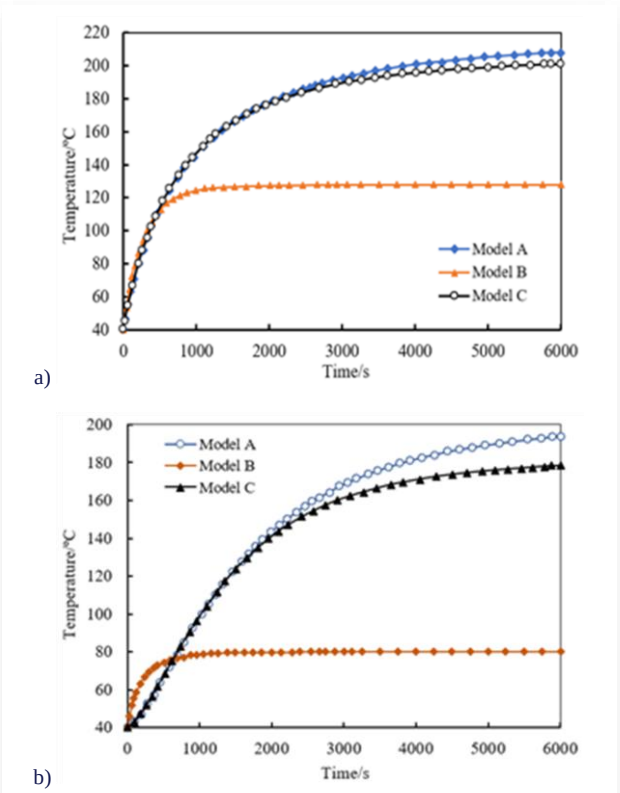


Fig. 5. Transient temperature variation curve with time: a) average winding temperature,(b) permanent magnet temperature.

3.4. Effect of coolant volume flow rate on cooling performance

The magnitude of the coolant flow rate directly determines the selection of the coolant pump. A scientifically and reasonably chosen coolant pump can reduce energy consumption and also contribute to weight and cost reduction. Therefore, it is necessary to conduct a systematic study on the volume flow rate of the coolant inlet. According to comparing and analyzing the motor temperature characteristics of the three cooling systems, the influence of coolant volume flow rate on steady-state temperature reduction in the motor was investigated. All three motor cooling models use ATF134 as the cooling medium, with a coolant inlet temperature of 65°C. The influence of coolant volume flow rate on internal motor temperature can be obtained through calculations, as shown in Fig. 6.

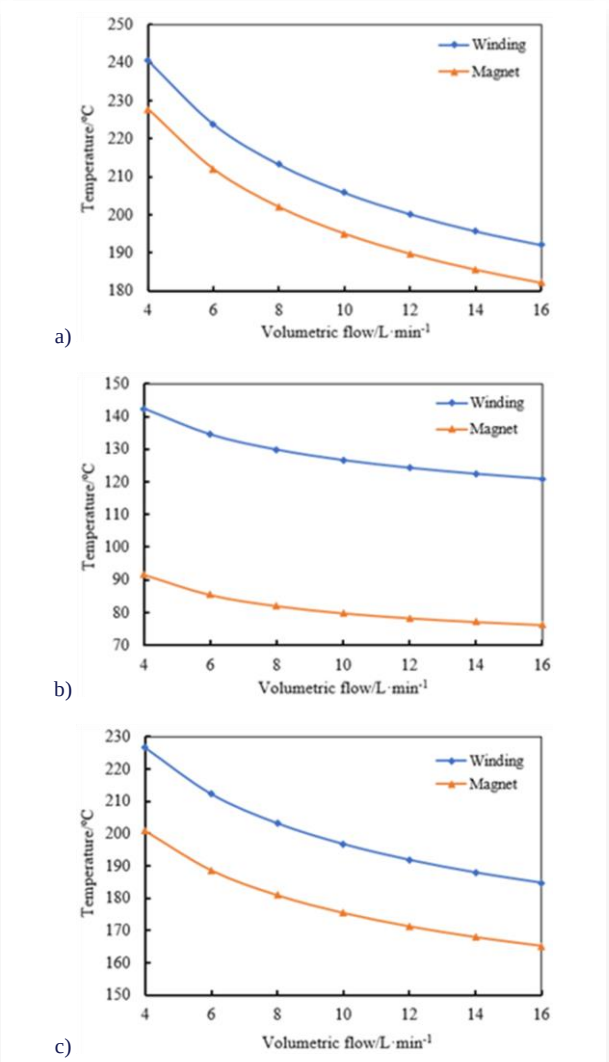


Fig. 6. Relationships between steady-state temperature of different cooling systems and coolant volume flow rate: a) Model A, b) Model B, c) Model C.

From the analysis results in Fig. 6, it can be seen that:

1) As the coolant volume flow rate changes, the temperature of the stator winding is consistently higher than that of the permanent magnets. When designing the motor cooling system, special attention should be paid to the temperature of the stator winding;
2) For Model B, a coolant flow rate of 6 L/min can meet the performance temperature allowance for Class H, with good economy. However, Model A and Model C require a larger coolant volume flow rate;
3) With the same coolant volume flow rate, oil spray cooling can significantly reduce the motor temperature;

4) The relationship between coolant flow rate and motor temperature is nonlinear. When the coolant flow rate increases to a certain value, the influence of coolant flow rate on motor temperature gradually decreases. These findings provide a valuable guidance for selecting the coolant volume flow rate for motor cooling.

3.5. Effect of coolant inlet temperature on cooling performance

At a coolant flow rate of 10 L/min and an ambient temperature of 40°C, the variation of the temperature field of the three motors is investigated as the coolant inlet temperature changes from 40°C to 80°C. The calculated results are shown in Fig. 7.

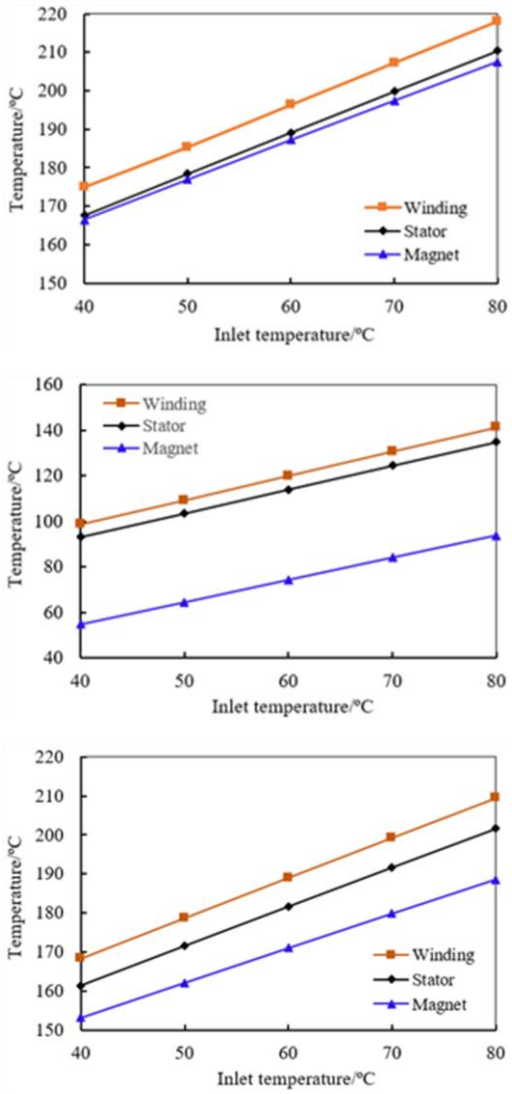


Fig. 7. The relationship between the internal temperature of motor and the inlet temperature of the coolant.

From the analysis results, it can be seen that the rate of change of coolant inlet temperature is directly proportional to the internal temperature rise of the motor, meaning that a higher inlet temperature results in a higher internal temperature of the motor. As the inlet temperature increases, the internal temperature rise of Model B exhibits greater variation compared to the other models. Under the same coolant inlet temperature, the internal temperature of the motor shows more pronounced changes. For Model B, for every 1°C increase in coolant inlet temperature, the stator winding temperature increases by approximately 1.076°C, and the permanent magnet temperature increases by approximately 0.984°C. The above analysis indicates that the coolant inlet temperature directly affects the temperature rise inside the motor. During the design process of the motor cooling system, reducing the coolant inlet temperature can effectively lower the internal temperature of the motor.

3.6. Effect of ambient temperature on cooling performance

This section investigates the variations in the steady-state temperature field of three types of motors as the ambient temperature fluctuates between 20°C and 60°C. The impact of ambient temperature on the steady-state temperature rise of key components of the motor is shown in Fig. 8.

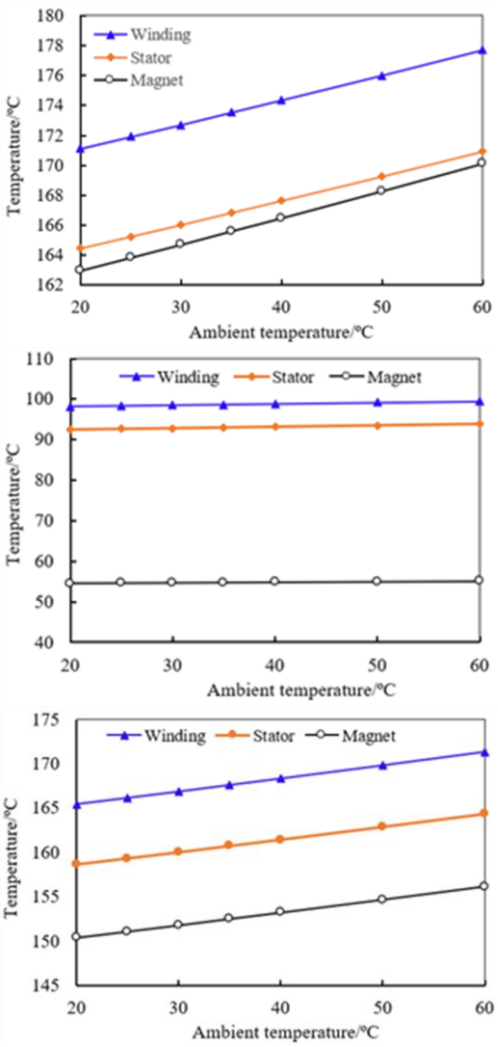


Fig. 8. The relationship between the internal temperature of motor and ambient temperature.

The main parameters used in the calculations are a coolant flow rate of 10 L/min, a coolant inlet temperature of 40°C, and an inner coolant volume flow rate of 2 L/min. From the analysis results, it can be seen that in Model A and Model C, as the ambient temperature increases, the temperature of each internal component of the motor tends to rise, and the degree of influence varies among different components. In Model B, however, the temperatures of the internal components hardly change with increasing ambient temperature.

These analysis results indicate that the different motor cooling systems are affected to varying degrees by the ambient temperature. The spray cooling system in Model B is less affected by the ambient temperature and can be used for motor cooling in complex environments.

4. Conclusions

A PMSM with hairpin windings is investigated in this paper. The influences of key parameters of the cooling system on motor cooling performance are studied based on the electromagnetic-thermal coupling analysis method. The following conclusions are drawn:

1) The thermal losses of the PMSM with hairpin windings primarily originate from the stator iron core and the copper losses in the windings. The permanent magnet eddy current loss accounts for more than 95% of the total motor losses, making it the primary heat sources within the motor.
2) The Model B has the best cooling performance in the three models. Compared with the other two motor models, the steady-state temperature of Model B's winding and permanent magnet is decreased by 38.19% and 58.55%, respectively, and the time to reach steady-state temperature also decreased by about 81.8%.
3) The coolant flow rate and temperature in the motor exhibits a non-linear relationship. For Model B, when the coolant flow rate is greater than 6 L/min, the temperature change inside the motor is relatively small and the economy is weakened.
4) The coolant inlet temperature has an impact on the cooling performance of the motor. For the three studied motor models, the rate of change of the coolant inlet temperature is directly proportional to the internal temperature rise of the motor.
5) The oil spray cooling system in Model B is less influenced by the ambient temperature, making it suitable for motor cooling in complex environments. For models A and C, as the ambient temperature increases, the internal temperature of the motor significantly increases. However, in Model B, the temperature of the internal components hardly changes as the ambient temperature increase.

Acknowledgements

This work was supported by the Natural Science Foundation of Chongqing (Grant No.: CSTB2023NSCQ-MSX0255), and Science and Technology Research Program of Chongqing Municipal Education Commission (Grant No.: KJQN202203110 and KJZD-K202203404).

References

[1] Kumar, A., Chandekar, A., Deshmukh, P.W., & Ugale, R.T. (2023). Development of electric vehicle with permanent magnet synchronous motor and its analysis with drive cycles in MATLAB/Simulink. *Materials Today: Proceedings*, 72, 643−651. doi: 10.1016/j.matpr.2022.08.304

[2] Gammaidoni, T., Zembi, J., Battistoni, M., Biscontini, G., & Mariani, A. (2023). CFD analysis of an electric motor's cooling system: Model validation and solutions for optimization. *Case Studies in Thermal Engineering*, 49, 103349. doi: 10.1016/j.csite.2023.103349

[3] Ha, T., & Kim, D.K. (2021). Study of injection method for maximizing oil-cooling performance of electric vehicle motor with hairpin winding. *Energies*, 14(3), 747. doi: 10.3390/en14030747

[4] Zhang, F., Gerada, D., Xu, Z., Liu, C., Zhang, H., Zou, T., Chong, Y.C., & Gerada, C. (2021). A thermal modeling approach and experimental validation for an oil spray-cooled hairpin winding machine. *IEEE Transactions on Transportation Electrification*, 7(4), 2914–2926. doi: 10.1109/tte.2021.3067601

[5] Ha, T., Kang, Y., Kim, N.S., Park, S.H., Lee, S.H., Kim, D.K., & Ryou, H.S. (2021). Cooling effect of oil cooling method on electric vehicle motors with hairpin winding. *Journal of Mechanical Science and Technology*, 35(1), 407–415. doi: 10.1007/s12206-020-1240-y

[6] Gai, Y., Kimiabeigi, M., Chuan Chong, Y., Widmer, J.D., Deng, X., Popescu, M., Goss, J., Staton, D.A., & Steven, A. (2019). Cooling of automotive traction motors: Schemes, examples, and computation methods. *IEEE Transactions on Industrial Electronics*, 66(3), 1681–1692. doi: 10.1109/tie.2018.2835397

[7] Carriero, A., Locatelli, M., Ramakrishnan, K., Mastinu, G., & Gobbi, M. (2018). A review of the state of the art of electric traction motors cooling techniques. *SAE Technical Paper*, 2018-01-0057. doi: 10.4271/2018-01-0057

[8] Liange, H., Hongling, C., & Wenjun, S. (2022). Erratum to "Boiling heat transfer-based temperature rise characteristics of automotive permanent magnet synchronous motors at peak operating conditions". *Journal of Mechanical Science and Technology*, 36(8), 4335–4335. doi: 10.1007/s12206-022-0750-1

[9] Ulbrich, S., Kopte, J., & Proske, J. (2018). Cooling fin optimization on a TEFC electrical machine housing using a 2-D conjugate heat transfer model. IEEE *Transactions on Industrial Electronics (1982)*, 65(2), 1711–1718. doi: 10.1109/tie.2017.2748051

[10] Peng, H.S., & Lai, F.H. (2019). Investigation of parameters affecting heat transfer and fluid flow of a TEFC electric motor by using Taguchi method. *IOP Conference Series. Materials Science and Engineering*, 491, 012021. doi: 10.1088/1757-899x/491/1/012021

[11] Li, J., Lu, Y., Cho, Y.H., & Qu, R. (2019). Design, analysis, and prototyping of a water-cooled axial-flux permanent-magnet machine for large-power direct-driven applications. *IEEE Transactions on Industry Applications*, 55(4), 3555–3565. doi: 10.1109/tia.2019.2907890

[12] Wu, P.S., Hsieh, M.F., Cai, W.L., Liu, J.H., Huang, Y.T., Caceres, J.F., & Chang, S.W. (2019). Heat transfer and thermal management of interior permanent magnet synchronous electric motor. *Inventions*, 4(4), 69. doi: 10.3390/inventions4040069

[13] Li, Y., Li, Q., Fan, T., & Wen, X. (2023). Heat dissipation design of end winding of permanent magnet synchronous motor for electric vehicle. *Energy Reports*, 9, 282–288. doi: 10.1016/j.egyr.2022.10.416

[14] Gai, Y., Ma, C., Xu, Y., & Chong, Y.C. (2021). Numerical prediction and measurement of pressure drop and heat transfer in

a water-cooled hollow-shaft rotor for a traction motor application. *IET Electric Power Applications*, 15(4), 476–486. doi: 10.1049/elp2.12042

[15] Lindh, P., Petrov, I., Pyrhonen, J., Scherman, E., Niemela, M., & Immonen, P. (2019). Direct liquid cooling method verified with a permanent-magnet traction motor in a bus. *IEEE Transactions on Industry Applications*, 55(4), 4183–4191. doi: 10.1109/tia.2019.2908801

[16] Madonna, V., Walker, A., Giangrande, P., Serra, G., Gerada, C., & Galea, M. (2019). Improved thermal management and analysis for Stator end-windings of electrical machines. *IEEE Transactions on Industrial Electronics (1982)*, 66(7), 5057–5069. doi: 10.1109/tie.2018.2868288

[17] Liu, C., Xu, Z., Gerada, D., Li, J., Gerada, C., Chong, Y.C., Popescu, M., Goss, J., Staton, D., & Zhang, H. (2020). Experimental investigation on oil spray cooling with hairpin windings. *IEEE Transactions on Industrial Electronics (1982)*, 67(9), 7343–7353. doi: 10.1109/tie.2019.2942563

[18] Wang, X., Wan, Z., & Wen, W. (2021). Heat dissipation of three permanent magnet synchronous motors integrated with heat pipes. *International Journal of Thermophysics*, 42(5). doi: 10.1007/s10765-021-02819-8

[19] Wang, Z., Huang, X., & Liu, J. (2023). Comparative investigation and optimization of a direct cooling structure for the primary core and windings in permanent magnet synchronous linear motors. *Applied Thermal Engineering*, 228, 120499. doi: 10.1016/j.applthermaleng.2023.120499

[20] Wang, X., Li, B., Huang, K., Yan, Y., Stone, I., & Worrall, S. (2022). Experimental investigation on end winding thermal management with oil spray in electric vehicles. *Case Studies in Thermal Engineering*, 35, 102082. doi: 10.1016/j.csite.2022.102082

[21] Guo, H., He, X., Xu, J., Tian, W., Ding, X., Ju, L., & Li, D. (2023). Design and analysis of a novel hybrid cooling method of high-speed high-power permanent magnet assisted synchronous reluctance starter/generator in aviation applications. *Chinese Journal of Aeronautics*, 36(3), 285–302. doi: 10.1016/j.cja.2022.08.017

[22] Zhao, A., Duwig, C., Liu, C., Gerada, D., & Leksell, M. (2023). Parameter study for oil spray cooling on end windings of electric machines via Eulerian–Lagrangian simulation. *Applied Thermal Engineering*, 235, 121281. doi: 10.1016/j.applthermaleng.2023.121281

[23] Zhao, X., Cui, H., Teng, Y., Chen, Z., & Liu, G. (2023). Design and analysis of a high loss density motor cooling system with water cold plates. *Global Energy Interconnection*, 6(3), 343–354. doi: 10.1016/j.gloei.2023.06.008

[24] Gundabattini, E., Kuppan, R., Solomon, D.G., Kalam, A., Kothari, D.P., & Abu Bakar, R. (2021). A review on methods of finding losses and cooling methods to increase efficiency of electric machines. *Ain Shams Engineering Journal*, 12(1), 497–505. doi: 10.1016/j.asej.2020.08.014

[25] Zhang, Y., Wang, L., Zhang, Y., & Zhang, Y. (2021). Design and thermal characteristic analysis of motorized spindle cooling system. *Advances in Mechanical Engineering*, 13(5), 168781402110208. doi: 10.1177/16878140211020878

[26] Bossmanns, B., & Tu, J.F. (1999). A thermal model for high speed motorized spindles. *International Journal of Machine Tools and Manufacture*, 39(9), 1345–1366. doi: 10.1016/s0890-6955(99)00005-x

[27] Madhavan, S., Devdatta, R., Gundabattini, E., & Mystkowski, A. (2022). Thermal analysis and heat management strategies for an induction motor, a review. *Energies*, 15(21), 8127. doi: 10.3390/en15218127

[28] Credo, A., Tursini, M., Villani, M., Di Lodovico, C., Orlando, M., & Frattari, F. (2021). Axial flux PM in-wheel motor for electric Vehicles: 3D multiphysics analysis. *Energies*, 14(8), 2107. doi: 10.3390/en14082107

[29] Jie, D. (2019). Thermal performance analysis of motor based on motor-CAD. *AIP Conference Proceedings*, 2073(1), 020049. *3rd International Conference on Advances in Materials, Machinery, Electronics*, 19−20 January, Wuhan, China. doi: 10.1063/1.5090703

[30] Xie, Y., Fan, Y., Cai, W., & Xin, W. (2023). Oil circuit structure optimization design and temperature field calculation of oil cooled motor with hairpin winding. *Electric Machines and Control*, 27, 37–45. doi: 10.15938/j.emc.2023.05.005

[31] Wang, C., Zhang, Z., & Liu, Y. (2021). Optimization of rotor eddy-current loss and heat dissipation for high torque density hybrid excitation synchronous motor with magnetic shunting rotor. *Proceedings of the of the Chinese Society of Electrical Engineering*, 41(21), 7476–7486 (in Chinese). doi: 10.13334/j.0258-8013.pcsee.201100

Co-published by
Institute of Fluid-Flow Machinery
Polish Academy of Sciences
Committee on Thermodynamics and Combustion
Polish Academy of Sciences

Copyright©2024 by the Authors under licence CC BY 4.0

http://www.imp.gda.pl/archives-of-thermodynamics/

Thermo-physical properties, heat transfer characteristics and performance of nano-enhanced refrigerants: A review

B.S. Bibin[a], Elena Ionela Chereches[b], Arkadiusz Mystkowski[c], Kamil Śmierciew[d], Adam Dudar[d], Edison Gundabattini[a*]

[a]Department of Thermal and Energy Engineering, School of Mechanical Engineering, Vellore Institute of Technology, Vellore-632 014, India
[b]Faculty of Materials Science and Engineering, Technical University "Gheorghe Asachi" of Iasi, Iasi, Romania
[c]Department of Automatic Control and Robotics, Faculty of Electrical Engineering, Bialystok University of Technology, Wiejska 45D, 15-351, Bialystok, Poland
[d]Department of Thermal Engineering, Faculty of Mechanical Engineering, Bialystok University of Technology, Wiejska 45C, 15-351, Bialystok, Poland
*Corresponding author email: edison.g@vit.ac.in

Received: 15.02.2024; revised: 20.03.2024; accepted: 28.03.2024

Abstract

To boost the efficacy of a refrigeration system, researchers have imported nanoparticles into refrigerants in recent years. This paper comprehensively reviewed the properties, heat transfer performance, and system performance of nano-added refrigerants in recent years. This article likewise assists with recognizing the gap in past research works and explores the possibilities for additional work. Refrigerant R134a charged with the nanoparticles TiO_2 has the highest value of coefficient of performance which is 63.5% higher than that of Al_2O_3 nanoparticle charged R134a. Charging of the nano-refrigerants has enhanced the heat transfer performance of vapour compression refrigeration systems, particularly in the pool and nucleate boiling heat transfer. The heat transfer coefficient of R134a-based nano-refrigerant is enhanced by 42% and 30.2% with CuO and TiO_2 nanoparticles respectively. The inclusions of nanomaterials, concerning their physical phenomena, influencing the vapour compression refrigeration system are confined in this paper.

Keywords: Nano-refrigerants; Vapour compression refrigeration; Heat transfer enhancement; Coefficient of performance; Coefficient of heat transfer

Vol. 45(2024), No. 2, 311–322; doi: 10.24425/ather.2024.150875

Cite this manuscript as: Bibin, B.S., Chereches, E.I., Mystkowski, A., Śmierciew, K., Dudar, A., & Gundabattini, E. (2024). Thermo-physical properties, heat transfer characteristics and performance of nano-enhanced refrigerants: A review, *Archives of Thermodynamics*, 45(2), 311–322.

1. Introduction

Energy is the main input to the social, economic, industrial, and technological development of every country. Its demand is increasing with the rise in the population and enhancement in the standards of living. The energy crisis and environmental issues are the major problems facing all over the world. In these problems, the refrigeration system takes a vital role. In the current situation, the refrigeration system consumes around 20 % of the total production of energy. The substances used in these systems are causing the ozone layer thinning and increase the temperature of the atmosphere. Based on recent reports, in India, 23%

Nomenclature

c_p – specific heat capacity
k – thermal conductivity
Nu – Nusselt number
r_p – radius of nanoparticles
Re – Reynolds number
t – thickness of the interfacial layer

Greek symbols

μ – viscosity
ρ – density
ϕ – volume fraction of the nanoparticle

Subscripts and Superscripts

l – interfacial layer
nr – nano-refrigerant
p – nanoparticle
r – refrigerant

Abbreviations and Acronyms

CHT – coefficient of heat transfer
COP – coefficient of performance
GWP – global warming potential
HC – hydrocarbons
HFO – hydro fluoro olefin
HT – heat transfer
HTF – heat transfer fluid
MO – mineral oil
ODP – ozone depletion potential
PAG – polyalkyleneglycol
PDT – pull downtime
POE – polyol ester
PVD – physical vapour deposition
RE – refrigerating effect
VCR – vapour compression refrigeration

of the overall energy is utilized by the refrigerator and 2% by the air conditioner [1]. In Poland, the energy consumption of refrigerators and freezers accounts for about 5% of the total electricity consumption in households, while the energy consumption of air conditioners accounts for about 4% of the total electricity consumption. According to Eurostat data, in 2020 the energy consumption for heating, ventilation, and air conditioning (HVAC) equipment accounted for approximately 33% of the total energy consumption in buildings in the European Union [2]. The latest analysis indicated that since increasing household appliances the energy utilization by the refrigeration system rose continuously. In various countries around the globe, the Government has put forward policies related to energy efficiency to minimize the usage of energy; consequently, the usage of refrigeration systems becomes economical and nature friendly [3]. Reducing the energy and environmental effect of substances used in refrigerant systems lead to new research. Nanotechnology also involves a new kind of research. Nanotechnology makes it possible to produce metal or metal oxide with sizes ranging from 1 to 100 nm called nanoparticles. By the inclusion of nanomaterials in the standard fluid, the thermal conductivity (k) of the fluid could be improved [4]. The volume concentration and the type of nanoparticles used are the key factors for improvement in heat transfer (HT) performance [5]. Generally, nanoparticles are the build-up of metals, oxides, or carbides, due to their small size and large surface area. Nanofluids should have better thermal properties, less sedimentation, and decline clogging flow lines [6].

Refrigeration is the action of reducing the temperature of a confined area by removing heat. In the vapour compression refrigeration (VCR) system, the phase change of the working fluid will produce the cooling effect and the performance of these systems could be enhanced by using a water-cooled condenser and by using a heat exchanger at the end of the compressor [7]. Nowadays refrigeration becomes a human necessity, but it leads to global warming. For refrigeration purposes, varieties of refrigerators and various compositions of refrigerants were used [3].

Choi and Eastman [8] developed a novel kind of HTF by adding nanoparticles to the base fluid. These conceptual studies indicated that the HT is enhanced extremely when nanoparticles are added to base fluids. Nanofluids are engineering fluids that possess a high specific surface area. Due to this property, nanofluids have a higher transfer capacity between particles and fluids. It also possesses high dispersion stability, reduced particle clogging, and reduced pumping power [9–12]. Nanoparticles act differently from their parental materials in properties such as molecular interaction and nature of reaction for mass and energy usage. The thermophysical properties such as thermal conductivity, convective HT, viscosity, and thermal diffusivity of standard fluids are enlarged by nanoparticles [13].

Nano-refrigerant is a type of nanofluid that is prepared by nanoparticles and is perfectly mixed with the base refrigerant. Since it has better thermo-physical properties, the rate of HT can be boosted. Because of these, the use of nano-refrigerant in the refrigeration system can develop a compact and lighter system; raise the 'k' of the refrigerant and upgrade the HT features of the entire thermodynamic system [14, 15]. The utilization of nanoparticles in the base fluid could boost the miscibility between the refrigerant and lubricant [16, 17]. The nanoparticles in the nano-refrigerant remain to put up for more time than microparticles and remain in suspension almost forever [18]. Also, the nanoparticle increases the solubility between the lubricants and refrigerants [19] (Fig. 1).

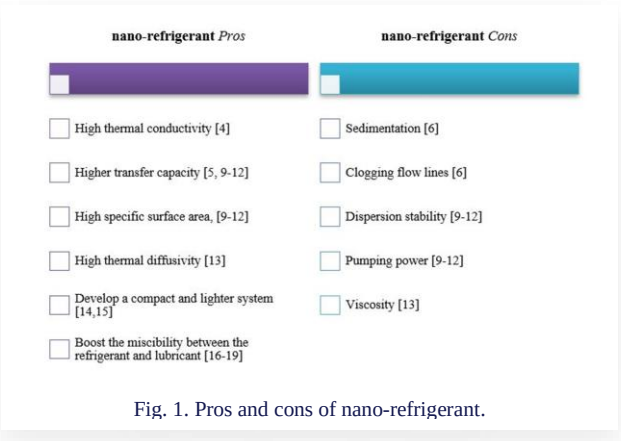


Fig. 1. Pros and cons of nano-refrigerant.

The goal of the current article is to present an extensive review of the development of nano-refrigerants for different categories of refrigerant-based and their performance. This paper explores and analyses the types of nano-refrigerants in refrigeration systems. The properties such as HT performance based on the HT coefficient; system efficacy in respect of coefficient of performance (COP); energy efficiency and exergy efficiency are reviewed in this article.

2. Preparation of nano-refrigerant

The nano-refrigerant is prepared by dispersing the nanoparticles spread over the refrigerant, and then it straight away boosts up the refrigerant thermal properties and hence improves the refrigeration system performance [3]. In preparation for nano-enhanced refrigerant, there are two ways to add nanoparticles to the working fluid. It is known as the charging of nanoparticles. Based on this there are two categories, one is nano-refrigerant and the other one is nano-lubricant. In nano-refrigerant, the nanoparticles are dispersed directly to the refrigerant, whereas in nano-lubricant the particles are added to the compressor's lubricant. This is shown in Fig. 2.

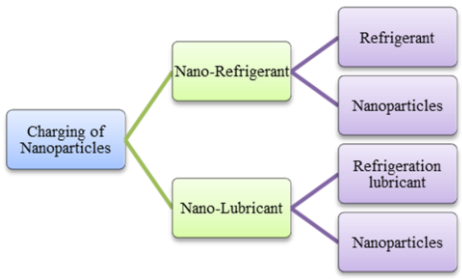


Fig. 2. Methods of charging nanoparticles.

Nano-refrigerants and nano-lubricants are alike in the way of operation; meanwhile, there are remarkable differences between both. The refrigeration system that works with nano-refrigerant will have a boost in the heat transport features in contrast to tribology characteristics. While nano-lubricant provides an improvement as far as tribology as the nanoparticles are more massed in the compressor lubricant contrasted with the refrigerant. The nanoparticle addition of both refrigerant and lubricant was demonstrated to raise the energy efficiency in the system remarkably. The nano refrigerant is prepared in two ways: a single-stage technique and a double-stage technique.

2.1. Single-stage technique

The single-stage technique combines the preparation of nanoparticles with the blend of nano-refrigerants in a single stage, with nanoparticles formed directly by PVD or liquid chemical treatment [3].

2.2. Double-stage technique

The double-stage technique is the step-by-step process of the production of nano-refrigerant from the preparation of nanoparticles. The nanoparticles are involved in each step, mainly in the action of dying, storage, and transportation. Ultrasonic stirring or additions of surfactants to the fluids are employed to reduce particle collection and enhance dispersion capacity. To ensure the proper blending of nanomaterial with standard fluid, an ultrasonic agitator or higher shear mixing devices were used [3].

Mohan et al. [20] also adopted the double-stage technique to prepare the nano-refrigerant with a probe sonicator. They produced nanoparticles into dry powder and were kept in the hot oven at 80°C for 24 hrs. At that point, nanoparticles completely blended in with polyalkyleneglycol utilizing an ultrasonic vibrator with a frequency of about 40 Hz. Subhedar et al. [21] prepared the samples by two-step method with oleic acid as the surfactant. To get the stable nano-refrigerant they used sonics and made a VCX500 probe sonicator to apply ultrasonic agitation force. The sonication was done for 1 hr at the frequency of 50 Hz to homogenize the 1 L sample. Chauhan et al. [22] used a double-stage technique with no surfactant added all over the making process of nano-refrigerant. This process was finished by employing the magnetic agitator for 2 hrs followed by ultrasonic homogenization of nano-refrigerant for a determined period. Subramani and Prakash [23] used two unique techniques for sonication for the preparation of nano-refrigerants. Firstly, the ultrasonic bath technique was utilized with a vortex blender as the initial stage and this method failed in the sedimentation test. Secondly, they used a probe sonicator with a magnetic stirrer.

The double-stage technique is a commonly used process in the combination of nano-refrigerants by blending base fluid with industrially accessible nanoparticles acquired from various chemical, physical, and mechanical processes like grinding, milling, and sol-gel and vapor phase techniques [3].

3. Analysis of nano-refrigerants concerning the thermo-physical properties

The thermo-physical properties are necessary for estimating the nano-refrigerant's efficiency. The viscosity, density, thermal conductivity, surface tension, specific heat, and latent heat are some of the important thermal and physical properties of the fluid. The thermophysical properties were studied numerically using some relations. The values of nano-refrigerant's thermal conductivity were determined by Sitprasert et al. [24] correlation

$$k_{nr} = \frac{(k_p - k_l)\phi k_l[2\beta^3 - \beta^3 + 1] + (k_p + 2k_l)\beta_1^3[\phi\beta^3(k_l - k_r) + k_r]}{\beta_1^3(k_p + 2k_l) - (k_p - k_l)\phi[\beta_1^3 + \beta^3 - 1]}, \quad (1)$$

where: $\beta = 1 + \frac{t}{r_p}$, $\beta_1 = 1 + \frac{t}{2r_p}$, $k_l = C\frac{t}{r_p}k_p$, k_P is the conductivity of the nanoparticle, k_l is the thermal conductivity of the base liquid, ϕ is the volume fraction of the nanoparticle.

The Brinkman model [25] was used to measure the dynamic viscosity of nano-refrigerant as follows:

$$\mu_{nr} = \mu_r \frac{1}{(1 - \phi)^{0.25}}, \quad (2)$$

where: μ_r is the viscosity of the base refrigerant.

Pak and Cho's [26] relationship was used to calculate the density of nano-refrigerant:

$$\rho_{nr} = \phi\rho_p + (1 - \phi)\rho_r, \quad (3)$$

where: ρ_p is the density of the nanoparticle, ρ_r is the density of the base refrigerant.

Pak and Cho's [26] relationship may be used to determine the specific heat of nano-refrigerant

$$c_{p,nr} = \phi c_{p,p} + (1 - \phi) c_{p,r}. \quad (4)$$

3.1. Viscosity of the nano-refrigerant

The concentration of nanoparticles and temperature has a significant effect on the viscosity of the nano-refrigerants. According to the studies, the viscosity on the discharged side is lesser than on the suction side. The rise in the fluid temperature causes lowered cohesive and adhesive forces between the molecule and would lead to the reduction in fluid viscosity [27]. Mahbubul et al. [28] identified the dynamic viscosity of R134a/Al_2O_3 with enhancement in its value by 28.58%. A similar result was obtained by Zawawi et al. [29] and found that the viscosity was enhanced with volume concentration and declined with temperature. Chauhan et al. [22] studied the viscosity of R134a/TiO_2/POE (where POE - polyol ester) and discovered that the maximum value was 0.38 mPa·s on the suction side and 0.2 mPa·s on the discharge side at 0.3% TiO_2 concentration. The viscosity test conducted by Ajayi et al. [30] revealed that the existence of nanoparticles in the refrigerants reduces the viscosity. The reduced viscosity affected the heat generation directly and reduced its value. According to Ambhore et al. [3], increasing nanoparticle concentration increases nano-refrigerant viscosity.

The viscosity of the nano-refrigerant was also affected by the viscosity of the base refrigerant, according to the report by Subhedar et al. [21] studies show that the volume concentration of nanoparticles depends on viscosity. The viscosity of nano-refrigerant was increased with the volume fraction of nanomaterials present in it. They were used by Anton Paar's viscometerto determine the viscosity. The viscosity of Al_2O_3/R141b nano-refrigerant was evaluated by Soheel et al. [31] using the Brinkman model. They found that the viscosity and degradation declined with increasing temperature, depending on the quantity of nanoparticles. The kinematic viscosity of the nano-refrigerant is directly affecting the overall energy consumption. When the viscosity value is low, then the energy losses are also less [30].

3.2. Thermal conductivity of the nano-refrigerant

The thermal conductivity (k) value of the fluid is related to convective HT and boiling coefficients. Therefore, it is one of the most influential thermo-physical properties of a nano-refrigerant. As a result, recent studies have placed a strong emphasis on thermal conductivity, with non-linear thermal conductivity enhancement being verified as the temperature rises [22]. Based on the studies Brownian motion of nano-sized particles gets raised with the increase in temperature contributing to the rise in micro-convective HT. This process enhanced the thermal conductivity finally [32].

Jiang et al. [33] identified that the enhancement in the nanomaterial concentration causes thermal conductivity improvement. Mahbubul et al. [28] studied the thermal conductivity of R134a/Al_2O_3 and they found that its value increased by 28.58%. Likewise, Patil et al. [34] discovered that the effective value of k declined with the particle size. According to Zawawi et al. [29], the thermal conductivity of nanoparticles is affected by their volume concentration and temperature. The value of k was improved with the concentration of nanomaterial and it declined with temperature. Liu and Hu. [35] found that increasing the volume fraction of TiO_2 increased the value of k of R134a/TiO_2. When 5% of the volume concentration of TiO_2 was introduced to the standard fluid, the value of k increased by 30%. They also discovered that as the temperature rose, so did the thermal conductivity. Soheel et al. [31] explored the thermal conductivity of the R134a-based nano-refrigerant. They used Al_2O_3, SiO_2, ZrO_2, and CNT as nano inhibitors with different mass concentrations. From these, they identified that the thermal conductivity was improved with the nanomaterial concentration in the refrigerant. Figure 3 depicts the thermal conductivity of R134a nano-refrigerant with various nanoparticles at different concentrations. From the figure, it is clear that R134a with SiO_2 gives more thermal conductivity than that of the other nanoparticles such as Al_2O_3, ZrO, and CNT.

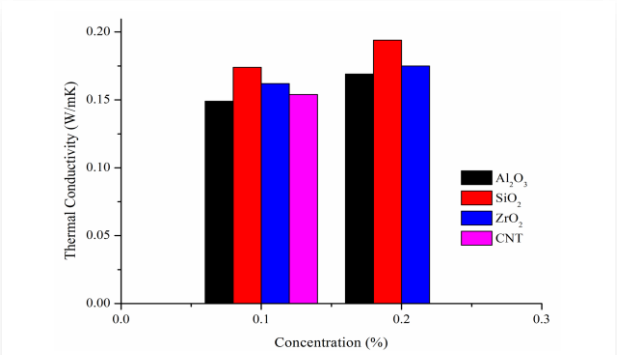


Fig. 3. Thermal conductivity of different R134a-based nano-refrigerants [31].

Ambhore et al. [3] concluded that conventional refrigerants have lower thermal conductivities than nano-refrigerants. The thermal conductivity of R134a/TiO_2/POE was obtained by Chauhan et al. [22] and their highest values were 0.107 W/(m K) and 0.125 W/(m K) at 0.3 % concentration of nanoparticle on suction and discharge sides respectively. According to Alawi et al. [36], variation in the value of 'k' of R141b/Al_2O_3 nano-refrigerant is linear with temperature and volume fracture. As per the studies, as the temperature rises, the Brownian motion of nanoparticles and the effect of micro-convection in HT boost up, increasing thermal conductivity [32,37]. At 305 K, Rahman et al. [38] discovered that the values of 'k' of R407c/SWCNT nano-refrigerant were 15.6% higher than the conventional refrigerant.

3.3. Nano-refrigerant specific heat capacity and latent heat

According to Ajayi et al. [39] the existence of bio-based nanoparticles in the fluid enhanced the value of c_p and latent heat of the working fluid, resulting in an improvement in heat transportability. When the temperature and volume fraction increase

from 10 ºC to 35ºC and 1 vol% to 4 vol% the heat capacity of R141b/Al_2O_3 increases, according to Alawi et al. [36]. They also discovered that the nano-refrigerant had the lowest specific heat value at a particular volume fraction. The lower value of c_p of integrated materials contributed to this reduction. Alawi and Sidik [37] found that the value of c_p of the R141b refrigerant was 2.6% less than the R141b/Al_2O_3 nano-refrigerant. This was because of the enhancement in heat capacity leading to an increase in the system's internal energy. On the other hand, an increase in temperature will result in the variation of the value of liquid around its equilibrium value. This would increase the system's heat capacity since a greater amount of energy would be available. The specific heat capacities of nano-fluids have been reported to be lower than the base fluid [40].

Alawi et al. [36] found that increasing the temperature at the output resulted in a noticeable increase in specific heat. It was discovered that refrigeration systems that used nano-refrigerants were able to have better performance as a result of their higher production temperature. The existence of nanoparticles in the base fluid resulted in a higher output temperature. Hence, the specific heat was known as "the necessary heat to increase the temperature of a unit mass of a substance by one unit of temperature." As a result, any material with a lesser specific heat will produce a greater output temperature with the same amount of heat flow. According to Rahman et al. [38], with the inclusion of nanoparticles, the specific heat of the R407c/SWCNT nano-refrigerant decreased. This is attributable to the SWCNT nanoparticle's lower specific heat. When opposed to R407c refrigerant, the R407c/SWCNT nano-refrigerant reduced the value of c_p by 4.1% and 4.93% at 283 K and 308 K, respectively. They also found out that the system's internal energy was enhanced with an increase in the specific heat values.

3.4. Density

Solid particles have a much greater density than fluids, so the solid-fluid suspension has more density, in contrast, to the base fluid. If the concentration of nanomaterials in the standard fluid rises, the temperature rises and the density falls linearly [22]. According to Mahbubul et al. [28], the density of R134a/Al_2O_3 increased by 11%. Chauhan et al. [22] found that the density of the nano-refrigerant R134a/TiO_2/POE was observed to be greatest at 0.3% nanoparticle concentration, with values of 1 660 kg/m^3 and 1 370 kg/m^3 at 10ºC suction and 80ºC discharge temperature respectively.

As the temperature and volume fraction rose, Alawi et al. [36] discovered that the density of R141b/Al_2O_3 nano-refrigerant and R141b refrigerant decreased. The atoms of the refrigerant begin to vibrate as the temperature rises, increasing the refrigerant volume while decreasing the density.

4. HT performance with the nanoparticles

Researchers used a variety of approaches to improve the refrigeration system's HT efficiency in the experiments. Active and passive methods for improving HT efficiency have been identified [41]. HT was improved by an active technique of HT enhancement methods. This involved surface area modification and boundary layer adjustments. Heat transport was improved in passive methods by optimizing the thermal properties of working fluids [42]. Nano-refrigeration is a passive process for improving the system's HT. This is because, in nano-refrigeration, the nanoparticles are added to the refrigerants for improving the thermal properties of working fluids.

Bartelt et al. [43] researched on R134a-CuO nano-refrigerant and discovered that adding a 1% volume concentration of CuO improved the coefficient of Heat transfer (CHT) by 42%. Coumaressin and Palaniradja [44] found that the heat fluxes changed from 10 kW/m^2 to 40 kW/m^2 when CuO concentration varied from 0.5% to 1% and particle diameter from 10 nm to 70 nm. Furthermore, it was discovered that the evaporative CHT boost sup when CuO nano particle was added up to 0.55% concentration after that it was declining.

Besides, Coumaressin and Palaniradja [44] used GAMBIT software to illustrate an augmentation in the CHT for the R134a/CuO nano-refrigerant. Soheel et al. [31] considered the HT performance of CuO/R134a nano-refrigerant using a two folds channels heat exchanger. They have seen progress in HT characteristics. They identified that HT coefficient increased to 0.55% of the convergence of nano molecules and decreases for all properties. Also, they found out that the higher value of the CHT was 1 755.8 W/(m^{2}K) for a 5% volume concentration of nanoparticles.

According to Ajayi et al. [39], the inclusion of bio-based nanoparticles had a beneficial impact on the heat-carrying efficiency of the evaporator and condenser. They discovered that adding nanoparticles improves intermolecular reactions and alters fluids into heat-carrying fluids with high heat capacity. This ensures that the materials behave in such a manner that the fluids' capability to absorb a massive amount of heat from the requisite area per unit degree rise in temperature is increased, and so heat is transferred to the heat sink through enhanced intermolecular interaction.

The studies of Eid et al. [45] identified that the CHT of nano-refrigerant decreases with the rise in nanomaterials concentration. They also discovered that by raising the concentration of Al_2O_3 nanoparticles in R134a refrigerant to 0.25%, the CHT could be doubled and that when the concentration exceeded this amount, the coefficient was decreased.

Naas [46] identified that the CHT was enhanced by 50 % by adding TiO_2 nanoparticles from 0.05% to 1% to the R134 refrigerant. The HT characteristics of R134a/TiO_2 nano-refrigerant were investigated by Sanukrishna et al. [47]. They discovered that when the nanoparticle concentration is 1.5%, the CHT increases by 30.2%. Pasha [48] investigated the evaporator's variance, the Nusselt number's relationship to the Reynolds number, as well as the heat flux and nanoparticle concentration in the refrigeration device. The rise in Nusselt (Nu) number leads to the rise in Reynolds (Re) number, heat flux, and nanoparticle concentration up to 0.5, according to the research. They also discovered that the value of Nu was increased by a maximum of 67% while the value of Re were increased by 98% of its lowest value.

4.1. Flow condensation

Sheikholeslami et al. [49] investigated the flow within a horizontal plain tube in an experimental environment for identifying the condensation HT of nano-added refrigerant. They used R600a/POE/CuO nano-refrigerant. They identified that the coefficient of condensation HT depends on vapour quality, mass flux, and nanoparticle concentration in the working fluid. The value of HT was enhanced by vapour quality because of the reduction of liquid film thickness on the inner wall of the tube which lessened the internal thermal resistance. Another work of these authors [50] investigated the condensation activities inside a horizontal tube for identifying the development of entropy and loss of exergy in nano-refrigerant. They deduced that increasing mass flux, vapour quality, or nanoparticle concentration resulted in a modest increase in the development of entropy on account of HT. This is because the condensation CHT and Nu numbers have improved. They also discovered that nanoparticles did not affect the Bejan number, which was a ground-breaking research finding. The Bejan number is the ratio of HT entropy to overall HT and friction.

4.2. Pool boiling

Pool boiling is a technique of transferring heat on the surface into a huge matter of stagnant liquid. This is a form of boiling process in which the surface temperature is moderately higher than the fluid's saturated temperature. The nucleation and subsequent development of fluid vapour bubbles on the surface, followed by their growth from the surface, define this mechanism. In general, the growth of bubbles in a pool boiling is influenced by temperature, surface type, fluid thermodynamic properties, and surface tension. Pool boiling is used in heat-carrying devices in the process and refrigeration industries as a critical method of HT [51]. The optimum configuration of the evaporator in a refrigeration process necessitates the precise calculation of the refrigerant's pool boiling CHT [52]. HT on pool boiling was investigated by Park and Jung [53,54] using a carbon nanotube–halocarbon refrigerant nanofluid. The experiments were carried out with a 1% volume nanoparticle concentration and a pool temperature of 7°C, and remarkable pool boiling HT augmentation was observed. The study in R113/CNT/ VG68 nano-refrigerant indicated that the improvement of nucleate pool boiling could reach 61% in contrast to without nanotube refrigerant and oil mixture [28]. Peng et al. [55] conducted the pooling boiling HT experiment with R113/diamond nano-refrigerant. They discovered that HT promotion caused by diamond nanoparticle augmentation on pool boiling is higher than nanoparticles of CuO augmentation under related conditions.

The experiments on pool boiling of R141b/TiO_2 nano-refrigerant were done by Trisaksri and Wongwises [56]. They discovered that at strong heat fluxes, the increase in nanoparticle concentration improved pool boiling. Ray et al. [57] studied the pool boiling of R134a on flat copper surfaced with TiO_2 and thin film coating of thickness 100 nm and 200 nm. From this, they identified that the maximum enhancement in CHT was achieved with the 200 nm coating thickness and uncoated copper surface. They also resolved that the improvement in CHT was because of increased surface irregularity and improved dynamic nucleation site concentration. Ray and Bhaumik [58] analyzed the pool boiling of R134a at 100°C on a smooth copper surface coated with a smaller layer of TiO_2 nanoparticles. The boiling HT acquires 87.5% of improvement with the high thickness of TiO_2-coated surface than the surface without copper. They concluded that nanoporosity (*surface roughness* = 12.4 nm), nucleation site density, and area of heating surface influence the improvement of CHT. Kedzierski and Gong [59] established the pool boiling HT characteristics of the R134a/CuO nano-refrigerant. According to the findings, a CuO-based nano-refrigerant would improve HT.

5. Performance studies on refrigeration systems

The performance of the refrigeration system is evaluated by various parameters such as COP, pull downtime (PDT), refrigerating effect (RE), and power consumption. The ratio of the heat consumed by the refrigerated area to the compressor work is known as the COP. The cooling effect is the rate at which heat is removed from a refrigerated space and is proportional to the refrigeration system's cooling ability. The pull-down time is the amount of time it takes to reach a certain temperature in the refrigerated space. By improving the heat absorption rate in the evaporator or lowering the compressor's power, it could be enhanced the refrigeration system’s performance.

5.1. Vapour compression refrigeration system

The VCR cycle is a version of the refrigeration system in which a circulating liquid working fluid serves as the channel for absorbing and removing heat from a confined area, producing a cooling effect, and then rejecting the heat to the environment [3]. The performance examination of VCR systems with nano-refrigerant is studied by many researchers. Based on their studies we have comprehensively concluded the results from various researchers.

According to the values of enthalpy at the inlet and outlet of the VCR system elements, the theoretical COP of the system was determined. To identify the system’s actual COP, the work absorbed by the compressor and the heat released from the evaporator was used [20]. Figure 4 shows the variation of power consumption with different nano additives to the refrigerants. The power consumption is very less in the case of ZnO nano-sized particles added to the base refrigerant. While the Al_2O_3-added nano-refrigerant takes more power to run the system.

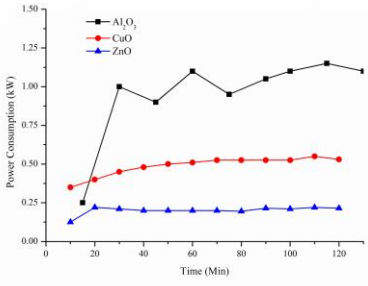


Fig. 4. Power consumption of different R134a-based nano-refrigerants.

Wang et al. [60] conducted the first experiment in the VCR system with nano-added refrigerant in 2003. The researchers discovered that nano-refrigerants improved the refrigeration system's COP and cooling effect.

The capability study of a VCR system was carried out by different analyses. PDT analysis, exergetic analysis, energy utilization analysis, and cooling load analysis were used by Ajayi et al. [30]. The PDT is the amount of time it takes to vary the temperature of the evaporator compartment from ambient to final. According to the PDT analysis, the nano-refrigerant achieves low temperatures three times faster than ordinary refrigerants. Ajayi and his colleagues found that the Al_2O_3-based nano-refrigerant system was more efficient with a lower cooling effect. The impact of R410a/Al_2O_3/MO nano-refrigerant on VCR was analyzed by Peyyala et al. [7]. The compressor exit temperature reduced and the coefficient of performance increased when the nanoparticle concentration increased. The studies of Mohan et al. [20] revealed that the actual COP depends on the evaporator temperature. The actual COP gradually increases as the evaporator temperature increases. Figure 5 indicates the fluctuation of evaporator temperature with time for various nano-refrigerants. From the Fig. 5, it is clear that after a certain time, all nano-refrigerant gives a constant evaporator temperature. The ZnO nanoparticle added to R152a refrigerant attained a very low evaporator temperature and it stabilized very quickly.

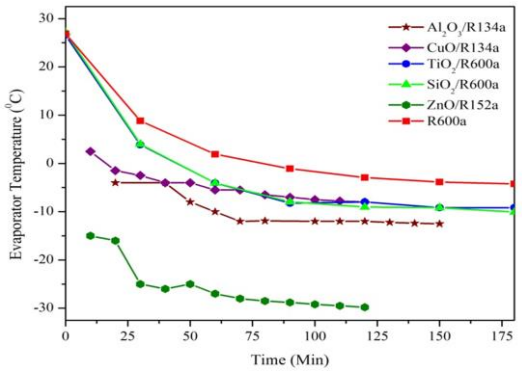


Fig. 5. Evaporator temperature with time for different nano-refrigerant.

The studies of Subhedar et al. [21] had revealed that the compressor power and coefficient of performance depend on the volume concentration of nanoparticles. They found around 27% reductions in compressor power using 0.075 % volume concentration R134a/Al_2O_3/MO nano-refrigerant. Chauhan et al. [22] discovered that as the concentration of TiO_2 increases, the temperature decreases. The lowest temperature of −16.7°C is obtained with 0.3% volume concentration of nanoparticle, whereas it is observed at −13.5°C for the base fluid used. Also, it was identified that freezing capacity depends on nanoparticle concentration. Since at higher concentrations, the drop in evaporator temperature is moderately high, therefore the freezing capacity increased as the TiO_2 concentration increased. Figure 6 shows the dependency of COP, Input power, and freezing capacity with the concentration of nanoparticle addition.

According to Prasad et al. [61] the COP of the system decreases and the energy consumption of the system increases with room temperature. According to Adelekan et al. [62], improving the concentration of nano-particles in the refrigerant or base fluid improves the refrigeration system's efficiency by reducing compressor work and increasing the HT rate. The condenser's performance degrades when a system operates at high pressure in hot and dry conditions.

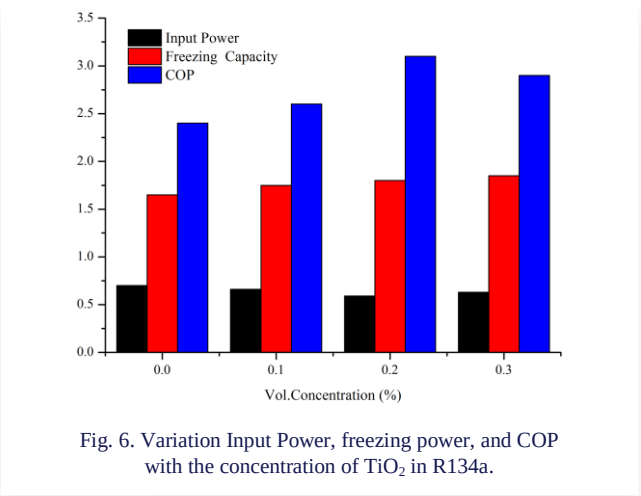


Fig. 6. Variation Input Power, freezing power, and COP with the concentration of TiO_2 in R134a.

The maximum exergy loss with R134a/Al_2O_3 identified by Dhondge and Kalbande [63], occurred in the evaporator and compressor and the values were lies between 36% to 37% of the whole losses in the system. And also, found that the highest sustainability index in R134a with 0.5 nanoparticle concentration. Generally, the exergy analysis revealed that the energy cannot be built nor be demolished; it could be degraded in quality. Exergy analysis can help us figure out what's causing process inefficiencies, where they're coming from, and how big they are. Dhondge and Kalbande [63] found that the evaporator temperature declined the exergy efficiency which means that the cooling efficiency of the system increased and the percent exergy destruction of the compressor decreases as the compressor has to do minimum work for maintaining the maximum temperature inside the evaporator. Table 1 tabulates the overview of performance in the VCR system. According to Yong et al. [64], TiO_2 increases the compatibility of mineral oil and R134a. Figure 7 illustrates the variation of COP with different nanoparticles. From the figure, it is clear that when 0.1 % of TiO_2 nanoparticle was added to R134a gave higher COP.

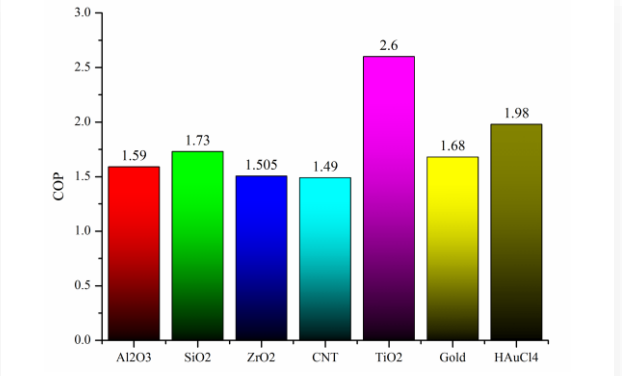


Fig. 7. Variation of COP with different nanoparticles.

Table 1. Summary of performance studies in vapour compression refrigeration system.

Author	Refrigerant	Nanoparticle	Lubrication oil	Main points
Wang et al. [60]	R134a	TiO_2	Mineral oil	• The system's performance was enhanced by the inclusion of nanomaterials in the refrigerant.
Padmanabhan and Palanisamy [65]	R134a, R436A, R436B	TiO_2	Mineral oil, Polyol ester (POE)	• R134a/TiO_2/MO achieve higher COP as compared to R436A/TiO_2/lubricant and R436B/TiO_2/lubricant
Patil et al. [34]	R134a	TiO_2	Polyol ester (POE)	• When 0.1% of nanoparticles are added, energy usage is decreased by 26.1%.
Yong et al. [64]	R134a	TiO_2	Mineral oil	• The energy utilization decreased by 26.1% when 0.1% of nanoparticle concentration and 50 nm particle size.
Chauhan et al. [22]	R134a	TiO_2	Polyol ester (POE)	• At 0.2% concentration, the least compressor power input and greatest COP are obtained. • The compressor uses 15.8% less electricity and the COP increases by 29.1% at 0.2% concentration.
Subramani and Prakesh [23]	R134a	Al_2O_3	Mineral oil	• The freezing capacity has increased, although the power consumption has decreased by 25%.COP was increased by 33%.
Kumar and Elansezhian [66]	R134a	Al_2O_3	Mineral oil	• Improvement in energy absorption by 10.32%.
Raghavalu et al.[68]	R134a	Al_2O_3	Ethylene glycol	• The system's COP increased by 12.08%.
Ajayi et al. [30]	R134a	Al_2O_3	Capella D	• The Al_2O_3 nanoparticles improve the system's freezing capacity. Higher values of exergy were obtained. • The system with nano-refrigerant consumed less power. • The presence of Al_2O_3 nanoparticles enhances the cooling, reduced energy consumption, and improved the performance of the system.
Dhondge and Kalbande [63]	R134a	Al_2O_3	-	• With the inclusion of nanoparticles, the COP rises, improving the system's overall performance.
Subhedar et al. [21]	R134a	Al_2O_3	Mineral oil	• The maximum improvement in COP is around 85% for 0.075% volume concentration of nano-refrigerant. • The highest COP was 3.68 at 0.075% volume concentration. • 27 % of compressor power saved.
Ambhore et al. [3]	R134a	Al_2O_3	-	• The addition of 0.5% of Al_2O_3 nanoparticles will lead to an enhancement in the overall performance.
Mohan et al. [20]	R134a	Gold, $HAuCl_4$, CNT	Polyalkyleneglycol (PAG)	• 31.7 % of enhancement in actual COP was attained with 0.1% Au + 0.005% CNT. • The loss of exergy for 0.1%Au + 0.005%CNT declined by 8%.
Harichandran et al. [68]	R134a	h-BN	Polyolester (POE)	• At 0.3 % volume concentration of nanoparticle, the COP improved by 60%
Peyyala et al. [7]	R140a	Al_2O_3	Mineral oil	• Reduction in compressor exit temp, improvement in COP, energy efficiency ratio, and pressure ratio when the percentages of nanoparticle concentrations were increased.
Pico et al. [69]	R410A	Diamond	Polyol ester (POE)	• Maximum enhancement in COP is 8%. • A reduction in compressor discharge temperature by 4°C causes a reduction in compressor power.
Sabareesh et al. [70]	R12	TiO_2	Mineral oil	• Power consumption of the system declined by 11%. • The COP improved by 17%.
Kumar and Elansezhian [71]	R152a	ZnO	PAG	• At 0.5% ZnO volume, energy consumption decreased by 21%. • Evaporation temperature declined by 6%.
Ajuka et al. [72]	R600a	TiO_2	Mineral oil	• At 1.5% mass concentration of nano addition, COP enhanced by 14.3% • The energy consumption was reduced by 35.15% at a 1.5% mass concentration of nanoparticles.
	LPG	TiO_2	Mineral oil	• The COP increased by 27.6% at 1.5% of mass concentration. • At a 1.5% mass concentration of nanoparticles, the energy consumption declined by 34.6%.

5.2. Domestic refrigeration system

To find a replacement for R134a, Ajayi et al. [39] examined the effect of nanomaterial produced from agriculture waste of Citrullus Lanatus peels in refrigerant R600a on domestic refrigeration systems. Despite the findings of the COP and PDT for the R134a refrigerant fluid device, the R600a, and its nano-refrigerant versions perform superior with referring to energy consump-

tion, cooling capability, and heat absorbed and emitted, according to the studies. The experiment presented that the nanoparticle concentration has a substantial impact on the compressor's output. The working fluid, which included 0.1% bio-based nanoparticles spread in nano-refrigerant, reduced the system's energy consumption by 71.38%. Similarly, Bi et al. [73] investigated the impact of TiO_2 on R600a and discovered that at a concentration of 0.5 g/L, the system performance boosts up by 9.5%. Bondre et al. [13] concluded that the increased COP and lower energy consumption indicate the need for a more compact and energy-efficient refrigeration system in the future.

Table 2 summarizes the performance of the domestic refrigeration system.

Table 2. Summary of performance studies in domestic refrigeration system.

Author	Refrigerant	Nanoparticle	Lubrication oil	Main points
Bi et al. [74]	R134a	TiO_2	Mineral oil	• The better performance at 0.1% mass concentration of nanoparticle with 26.1% reduction in energy usage.
Jayadi and Saidur [75]	R134a	TiO_2, Al_2O_3	Mineral oil	• The energy-saving using nanoparticles would be greater than without using nanoparticles with a 10 863 MWh reduction in energy consumed by the year 2030. • The maximum energy saving of 25% was obtained.
Ohunakin et al. [76]	LPG	TiO_2, SiO_2, Al_2O_3	Mineral oil	• Based on LPG, the nanoparticle TiO_2 and SiO_2 reduced the power consumption by 13% and 12% respectively.
Gill et al. [77]	LPG	TiO_2	Mineral oil	• The system's cooling capacity and COP grew by 18.74–32.72% and 10.15–61.49%, respectively. • Compressor energy usage and pressure ratio were reduced by 3.20–18.1 % and 2.33–8.45%.
Bondre et al.[13]	R134a	Al_2O_3	Polyol ester (POE)	• The system's COP was increased by 17.27%. • The amount of energy consumption decreased by 32.48%. • Cooling capacity was increased when nanoparticles were added to the base fluid.
Bi et al.[73]	R600a	TiO_2		• Obtained an energy saving of 9.65%, when 0.5 g/L nanoparticle was added to the refrigerant.

6. Conclusions

Nano-refrigerants have a major effect on the refrigeration mechanism. The properties, HT efficiency, and applications of nano-refrigerants are all examined in depth in this article. Nano-refrigerant research may aid the refrigeration and air conditioning industry in making a smooth alternative to sustainability. The industry has been pushed to embrace a novel kind of low-GWP refrigerants, such as HC and HFO refrigerants, as a result of growing foreign worries about refrigerants' global warming capacity. This article may be very useful in acquiring knowledge about the application and performance of nano-refrigerants during this period of transformation from high global warming potential systems to eco-friendly systems. While further research is required to understand nano-refrigerants' possible use in refrigeration systems, their impact on the thermodynamic efficiency of refrigerants and lubricants suggests that they would be widely used in the future. Based on previous research, we discovered certain benefits and merits that should be considered in future work. The utilization of nano-refrigerants enhanced the HT efficiency of VCR systems, especially in the HT of the pool and nucleate boiling.

The HT coefficient of R134a-based nano-refrigerant was enhanced by 42% and 30.2% with CuO and TiO_2 nanoparticles respectively.

The inclusion of nano-materials into the refrigerant-oil mixture has little effect on the solubility of the mixture, which aids in the oil return ratio in VCRs. The inclusion of nano-materials in the refrigerant improved the overall performance of VCRs, including cooling capacity and system coefficient of performance.

When TiO_2 was added to R134a, it obtained the highest value of COP, which was 63.5% higher than that of the Al_2O_3 nanoparticle added to R134a.

Acknowledgements

The authors are thankful to the management of the Vellore Institute of Technology, India, and Technical University ”Gheorghe Asachi” of Iasi, Romania for their continued support.

References

[1] Chunekar, A., Varshney, S., & Dixit, S. (2016). Residential Electricity Consumption in India: What do we know. *Prayas (Energy Group)*. https://energy.prayaspune.org/our-work/research-report/residential-electricity-consumption-in-india-what-do-we-know [accessed 09 Jan. 2024].

[2] Ministry of Climate and Environment. (2021). *Energy in Numbers 2021*. Republic of Poland.

[3] Ambhore, D., Tiwari, A., Patel, U., Patil, J., & Ramachandran, M. (2020). Effect of Aluminium oxide Nano filler in Tetrafluoroethane (R-134a) Refrigerant. *IOP Conference Series: Materials Science and Engineering*, 810(1), 012018. doi: 10.1088/1757-899X/810/1/012018

[4] Subhedar, D., & Ramani, B. (2016). Experimental Investigation On Thermal Conductivity And Viscosity Of Al_2O_3/Mono Ethylene Glycol And Water Mixture Nanofluids As A Car Radiator Coolant. *Advances and Applications in Fluid Mechanics*, 19(3), 575. doi: 10.17654/FM019030575

[5] Gugulothu, S., & Pasam, V.K. (2020). Experimental investigation to study the performance of CNT/MoS_2 hybrid nanofluid in turning of AISI 1040 steel. *Australian Journal of Mechanical Engineering*, 20(3), 814–824. doi: 10.1080/14484846.2020.1756067

[6] Krishnan, R.S., Arulprakasajothi, M., Logesh, K., Raja, N.D., & Rajendra, M. (2018). Analysis and feasibility of nano-lubricant in vapour compression refrigeration system. *Materials Today: Proceedings*, 5(9), 20580−20587. doi: 10.1016/j.matpr.2018.06.437

[7] Peyyala, A.M., Sri, N.S., Sudheer, N., & Kumar, K.C.K. (2020). Experimental investigation on the effect of Nano lubrication in a VCR system using R410A Refrigerant with Al_2O_3 nanoparticles. *International Journal of Mechanical and Production Engineering Research and Development*, 10(3), 1761−1768.

[8] Choi, S.U.S., & Eastman, J.A. (1995). Enhancing thermal conductivity of fluids with nanoparticles. *Argonne National Laboratory, ASME International Mechanical Engineering Congress & Exposition*, No. ANL/MSD/CP-84938; CONF-951135-29. 12−17 November, San Francisco, USA.

[9] Saidur, R., Kazi, S.N., Hossain, M.S., Rahman, M.M., & Mohammed, H.A. (2011). A review on the performance of nanoparticles suspended with refrigerants and lubricating oils in refrigeration systems. *Renewable and Sustainable Energy Reviews*, 15(1), 310−323. doi: 10.1016/j.rser.2010.08.018

[10] Ajayi, O.O., Ibia, D.E., Ogbonnaya, M., Attabo, A., & Michael, A. (2017). CFD analysis of nano-refrigerant through adiabatic capillary tube of vapour compression refrigeration system. *Procedia Manufacturing*, 7, 688−695. doi: 10.1016/j.promfg.2016.12.102

[11] Kostic, M. (2004). *Advanced flow and heat transfer fluids*. Department of Mechanical Engineering, Northern Illinois University, Illinois, Chicago.

[12] Vaishali, P.M., & Kale, N.W. (2017). Experimental analysis of vapour compression refrigeration system using nano-refrigerant. In *Proceedings of 68th IRF International Conference*, (pp. 90−94) 29 January, Pune, India.

[13] Bondre, D., Joshi, A., Shinde, T., Deshmukh, A., & Dhanawade, K. (2019). Experimental performance and analysis of domestic refrigeration system using nano-refrigerants. In *Proceedings of International Conference on Intelligent Manufacturing and Automation* Lecture Notes in Mechanical Engineering (pp. 389−399). Springer, Singapore.

[14] Nair, V., Tailor, P.R., & Parekh, A.D. (2016). Nano-refrigerants: A comprehensive review on its past, present and future. *International Journal of Refrigeration*, 67, 290−307. doi: 10.1016/j.ijrefrig.2016.01.011

[15] Jiang, W., Ding, G., & Peng, H. (2009). Measurement and model on thermal conductivities of carbon nanotube nano-refrigerants. *International Journal of Thermal Sciences*, 48(6), 1108−1115. doi: 10.1016/j.ijthermalsci.2008.11.012

[16] Alawi, O.A., Sidik, N.A.C., & Kherbeet, A.S. (2016). The effects of nano-lubricants on boiling and two-phase flow phenomena: a review. *International Communications in Heat and Mass Transfer*, 75, 197−205. doi: 10.1016/j.icheatmasstransfer.2016.04.001

[17] Alawi, O.A., & Sidik, N.A.C. (2015). Applications of nano-refrigerant and nano-lubricants in refrigeration, air-conditioning and heat pump systems: A review. *International Communications in Heat and Mass Transfer*, 68, 91−97. doi: 10.1016/j.icheatmasstransfer.2015.08.014

[18] Sarkar, J., Ghosh, P., & Adil, A. (2015). A review on hybrid nanofluids: recent research, development and applications. *Renewable and Sustainable Energy Reviews*, 43, 164−177. doi: 1016/j.rser.2014.11.023

[19] Wang, R.X., Zou, D.B., & Zhang, Q.L. (2003). An investigation on refrigerating system using HFC134a and mineral lubricant mixed with nano-particles TiO_2(a) as working fluids. In *Proceedings of the 4th International Conference on Compressor and Refrigeration* (pp. 313−319). Xian Jiaotong University Press.

[20] Mohan, K., Sundararaj, S., Kannan, K.G., & Kannan, A. (2020). Experimental analysis on refrigeration system using CNT, gold and HAUCL4 nanofluids. *Materials Today: Proceedings*, 33, 360–366. doi: 10.1016/j.matpr.2020.04.156

[21] Subhedar, D.G., Patel, J.Z., & Ramani, B.M. (2020). Experimental studies on vapour compression refrigeration system using Al_2O_3/mineral oil nano-lubricant. *Australian Journal of Mechanical Engineering*, 20(4), 1136−1141. doi: 10.1080/14484846.2020.1784558

[22] Chauhan, S.S., Kumar, R., & Rajput, S P.S. (2019). Performance investigation of ice plant working with R134a and different concentrations of POE/TiO_2 nano-lubricant using experimental method. *Journal of the Brazilian Society of Mechanical Sciences and Engineering*, 41(4), 163. doi: 10.1007/s40430-019-1657-3

[23] Subramani, N., & Prakash, M.J. (2011). Experimental studies on a vapour compression system using nano-refrigerants. *International Journal of Engineering, Science and Technology*, 3(9), 95−102. doi: 10.4314/ijest.v3i9.6

[24] Sitprasert, C., Dechaumphai, P., & Juntasaro, V. (2009). A thermal conductivity model for nanofluids including effect of the temperature-dependent interfacial layer. *Journal of Nanoparticle Research*, 11(6), 1465−1476. doi: 10.1007/s11051-008-9535-4

[25] Brinkman, H. C. (1952). The viscosity of concentrated suspensions and solutions. *The Journal of Chemical Physics*, 20(4), 571−571. doi:10.1063/1.1700493

[26] Pak, B.C., & Cho, Y.I. (1998). Hydrodynamic and heat transfer study of dispersed fluids with submicron metallic oxide particles. *Experimental Heat Transfer: An International Journal*, 11(2), 151−170. doi: 10.1080/08916159808946559

[27] Kole, M., & Dey, T.K. (2011). Effect of aggregation on the viscosity of copper oxide–gear oil nanofluids. *International Journal of Thermal Sciences*, 50(9), 1741−1747. doi: 10.1016/j.ijthermalsci.2011.03.027

[28] Mahbubul, I.M., Saadah, A., Saidur, R., Khairul, M.A., & Kamyar, A. (2015). Thermal performance analysis of Al_2O_3/R-134a nano-refrigerant. *International Journal of Heat and Mass Transfer*, 85, 1034−1040. doi: 10.1016/j.ijheatmasstransfer.2015.02.038

[29] Zawawi, N.N.M., Azmi, W.H., Redhwan, A A.M., Sharif, M.Z., & Sharma, K.V. (2017). Thermo-physical properties of Al2O3-SiO_2/PAG composite nano-lubricant for refrigeration system. *International Journal of Refrigeration*, 80, 1−10. doi: 10.1016/j.ijrefrig.2017.04.024

[30] Ajayi, O.O., Ukasoanya, D.E., Ogbonnaya, M., Salawu, E.Y., Okokpujie, I.P., Akinlabi, S.A., & Owoeye, F.T. (2019). Investigation of the Effect of R134a/Al_2O_3–Nanofluid on the Performance of a Domestic Vapour Compression Refrigeration System. *Procedia Manufacturing*, 35, 112−117. doi: 10.1016/j.promfg.2019.05.012

[31] Soheel, A.H., Salih, M.M.M., & Mohammed, K.H. (2020). Energy observation technique for vapour absorption using nano fluid refrigeration. *International Journal of Advanced Science and Technology*, 29(12s), 1268−1281.

[32] Mahbubul, I.M., Fadhilah, S.A., Saidur, R., Leong, K.Y., & Amalina, M.A. (2013). Thermophysical properties and heat transfer performance of Al_2O_3/R-134a nano-refrigerants.

International Journal of Heat and Mass Transfer, 57(1), 100−108. doi: 10.1016/j.ijheatmasstransfer.2012.10.007

[33] Jiang, W., Ding, G., Peng, H., Gao, Y., & Wang, K. (2009). Experimental and model research on nano-refrigerant thermal conductivity. *HVAC&R Research*, 15(3), 651−669. doi: 10.1080/10789669.2009.10390855

[34] Patil, M.S., Kim, S.C., Seo, J.H., & Lee, M.Y. (2016). Review of the thermo-physical properties and performance characteristics of a refrigeration system using refrigerant-based nanofluids. *Energies*, 9(1), 22. doi: 10.3390/en9010022

[35] Liu, Y., & Hu. Y. (2017). Toward TiO_2 nanofluids − Part 2: applications and challenges. *Nanoscale Research Letters*, 12, 446, 1−21. doi: 10.1186/s11671-017-2185-7

[36] Alawi, O.A., Salih, J.M., & Mallah, A.R. (2019). Thermo-physical properties effectiveness on the coefficient of performance of Al_2O_3/R141b nano-refrigerant. *International Communications in Heat and Mass Transfer*, 103, 54−61. doi: 10.1016/j.icheatmasstransfer.2019.02.011

[37] Alawi, O.A., & Sidik, N.A.C. (2014). Influence of particle concentration and temperature on the thermophysical properties of CuO/R134a nano-refrigerant. *International Communications in Heat and Mass Transfer*, 58, 79−84. doi: 10.1016/j.icheatmasstransfer.2014.08.038

[38] Rahman, S., Issa, S., Said, Z., Assad, M.E.H., Zadeh, R., & Barani, Y. (2019). Performance enhancement of a solar powered air conditioning system using passive techniques and SWCNT/R-407c nano refrigerant. *Case Studies in Thermal Engineering*, 16, 100565. doi: 10.1016/j.csite.2019.100565

[39] Ajayi, O.O., Aba-Onukaogu, C.C., Salawu, E.Y., Owoeye, F.T., Akinlabu, D.K., Popoola, A.P.I., & Abioye, A.A. (2019). Effect of Biomaterial (Citrullus Lanatus Peels) Nano-lubricant on the Thermal Performance and Energy Consumption of R600a in Refrigeration System. *In Energy Technology 2019* (pp. 91−102). Springer, Cham. doi: 10.1007/978-3-030-06209-5_9

[40] Sanukrishna, S.S., Murukan, M., & Jose, P.M. (2018). An overview of experimental studies on nano-refrigerants: recent research, development and applications. *International Journal of Refrigeration*, 88, 552−577. doi: 10.1016/j.ijrefrig.2018.03.013

[41] Dewan, A., Mahanta, P., Raju, K.S., & Kumar, P.S. (2004). Review of passive heat transfer augmentation techniques. *Proceedings of the Institution of Mechanical Engineers, Part A: Journal of Power and Energy*, 218(7), 509−527. doi: 10.1243/0957650042456953

[42] Bianco, V., Manca, O., Nardini, S., & Vafai, K. (2015). *Heat transfer enhancement with nanofluids* (1 st ed.). CRC Press. doi: 10.1201/b18324

[43] Bartelt, K., Park, Y., Liu, L., & Jacobi, A. (2008). Flow-boiling of R-134a/POE/CuO nanofluids in a horizontal tube. *International Refrigeration and Air Conditioning Conference*, Purdue University e-Pubs (paper no. 928), 14−17 July, West Lafayette, Indiana, USA.

[44] Coumaressin, T., & Palaniradja, K. (2014). Performance analysis of a refrigeration system using nanofluid. *International Journal of Advanced Mechanical Engineering*, 4(4), 459−470. Research India Publications.

[45] Eid, E.I., Khalaf-Allah, R.A., Taher, S.H., & Al-Nagdy, A.A. (2017). An experimental investigation of the effect of the addition of nano Aluminum oxide on pool boiling of refrigerant 134A. *Heat and Mass Transfer*, 53(8), 2597−2607. doi: 10.1007/s00231-017-2010-y

[46] Naas, K.S.M. (2016). *Heat transfer enhancement in vapor compression refrigeration system using nanofluid with R-134a.* Doctoral dissertation, Benha University, Faculty of Engineering, Mechanical Engineering Department.

[47] Sanukrishna, S.S., Ajmal, N., & Prakash, M.J. (2018). Thermophysical and heat transfer characteristics of R134a-TiO_2 nanorefrigerant: A Numerical Investigation. *Journal of Physics: Conference Series*, 969(1), 012015. IOP Publishing. doi: 10.1088/1742-6596/969/1/012015

[48] Pasha, K.M.K. (2019). Controlling the Nusselt Number in a TiO_2/R134a Nano-refrigerant System. International Journal of Heat and Technology, 37(1), 179−187. doi: 10.18280/ijht.370122

[49] Sheikholeslami, M., Darzi, M., & Sadoughi, M.K. (2018). Heat transfer improvement and pressure drop during condensation of refrigerant-based nanofluid; an experimental procedure. *International Journal of Heat and Mass Transfer*, 122, 643−650. doi: 10.1016/j.ijheatmasstransfer.2018.02.015

[50] Sheikholeslami, M., Darzi, M., & Li, Z. (2018). Experimental investigation for entropy generation and exergy loss of nano-refrigerant condensation process. *International Journal of Heat and Mass Transfer*, 125, 1087−1095. doi: 10.1016/j.ijheatmasstransfer.2018.04.155

[51] Bayareh, M., & Mohammadi, M. (2016). Multi-objective optimization of a triple shaft gas compressor station using Imperialist Competitive Algorithm. *Applied Thermal Engineering*, 109, 384−400. doi: 10.1016/j.applthermaleng.2016.08.089

[52] Zendehboudi, A., & Tatar, A. (2017). Utilization of the RBF network to model the nucleate pool boiling heat transfer properties of refrigerant-oil mixtures with nanoparticles. *Journal of Molecular Liquids*, 247, 304−312. doi: 10.1016/j.molliq.2017.09.105

[53] Park, K.J., & Jung, D. (2007). Boiling heat transfer enhancement with carbon nanotubes for refrigerants used in building air-conditioning. *Energy and Buildings*, 39(9), 1061−1064. doi: 10.1016/j.enbuild.2006.12.001

[54] Park, K.J., & Jung, D. (2007). Enhancement of nucleate boiling heat transfer using carbon nanotubes. *International Journal of Heat and Mass Transfer*, 50(21−22), 4499−4502. doi: 10.1016/j.ijheatmasstransfer.2007.03.012

[55] Peng, H., Ding, G., Hu, H., Jiang, W., Zhuang, D., & Wang, K. (2010). Nucleate pool boiling heat transfer characteristics of refrigerant/oil mixture with diamond nanoparticles. *International Journal of Refrigeration*, 33(2), 347−358. doi: 10.1016/j.ijrefrig.2009.11.007

[56] Trisaksri, V., & Wongwises, S. (2009). Nucleate pool boiling heat transfer of TiO_2–R141b nanofluids. *International Journal of Heat and Mass Transfer*, 52(5−6), 1582−1588. doi: 10.1016/j.ijheatmasstransfer.2008.07.041

[57] Ray, M., Deb, S., & Bhaumik, S. (2017). Experimental investigation of nucleate pool boiling heat transfer of R134a on TiO_2 coated TF surface. *Materials Today: Proceedings*, 4(9), 10002−10009. doi: 10.1016/j.matpr.2017.06.310

[58] Ray, M., & Bhaumik, S. (2019). Nucleate pool boiling heat transfer of hydro-fluorocarbon refrigerant R134a on TiO_2 nanoparticle coated copper heating surfaces. *Heat Engineering*, 40(12), 997-1006. doi: 10.1080/01457632.2018.1450333

[59] Kedzierski, M.A., & Gong, M. (2009). Effect of CuO nanoparticle on R134a pool boiling heat transfer. *International Journal of Refrigeration*, 32(5), 791−799. doi: 10.1115/1.3072926

[60] Wang, R.X., Hao, B., Xie, G.Z., & Li, H.Q. (2003, October). A refrigerating system using HFC134a and mineral lubricant appended with n-TiO_2 (R) as working fluids. In *Proceedings of the 4th international symposium on HAVC*, Tsinghua University Press, Beijing, China (pp. 888-892).

[61] Prasad, T.H., Reddy, R.P., & Rami Reddy, D.R. (2009). Exergy analysis of vapor compression refrigeration system. *International*

Journal of Applied Engineering Research, 4, 2505−2526. doi: 10.1016/S1164-0235(02)00079-1

[62] Adelekan, D.S., Ohunakin, O.S., Babarinde, T.O., Odunfa, M.K., Leramo, R.O., Oyedepo, S.O., & Badejo, D.C. (2017). Experimental performance of LPG refrigerant charges with varied concentration of TiO_2 nano-lubricants in a domestic refrigerator. *Case Studies in Thermal Engineering*, 9, 55−61. doi: 10.1016/j.csite.2016.12.002

[63] Dhondge, A.J., & Kalbande, S.R. (2019). *Energy and Exergy analysis of SPV Powered Vapor compression Refrigeration system*. International conference on EARES 2019.

[64] Yong, H., Bi, S.S., & Shi, L. (2006). Refrigerator with R134a/TiO2 nanoparticle system, *Huagong Xuebao. Journal of Chemical Industry and Engineering (China)*, 57, 141−145.

[65] Padmanabhan, V.M.V., & Palanisamy, S. (2012). The use of TiO2 nanoparticles to reduce refrigerator irreversibility. *Energy Conversion and Management*, 59, 122−132. doi: 10.1016/ j.enconman.2012.03.002

[66] Kumar, D.S., & Elansezhian, R. (2012). Experimental study on Al2O3-R134a nano refrigerant in refrigeration system. *International Journal of Modern Engineering Research*, 2(5), 3927−3929.

[67] Raghavalu, K.V., Reddy, P.S., Khan, A.R., Kumar, D.V., & Prashanth, T. (2016). Improvement of COP of vapor compression refrigeration system by using nanorefrigerants. In *IJSRD| National Conference on Recent Trends and Innovations in Mechanical Engineering* (pp. 172−175).

[68] Harichandran, R., Paulraj, P., Raja, S.M.P., & Raman, J.K. (2019). Effect of h-BN solid nano-lubricant on the performance of R134a–polyolesteroil-based vapour compression refrigeration system. *Journal of the Brazilian Society of Mechanical Sciences and Engineering*, 41(3), 140. doi: 10.1007/s40430-019-1645-7

[69] Pico, D.F.M., da Silva, L.R.R., Schneider, P.S., & Bandarra Filho, E. P. (2019). Performance evaluation of diamond nanolubricants applied to a refrigeration system. *International Journal of Refrigeration*, 100, 104−112. doi: 10.1016/j.ijrefrig. 2018.12.009

[70] Sabareesh, R.K., Gobinath, N., Sajith, V., Das, S., & Sobhan, C.B. (2012). Application of TiO_2 nanoparticles as a lubricant-additive for vapor compression refrigeration systems–An experimental investigation. *International Journal of Refrigeration*, 35(7), 1989−1996. doi: 10.1016/j.ijrefrig.2012. 07.002

[71] Kumar, D.S., & Elansezhian, R. (2014). ZnO nano-refrigerant in R152a refrigeration system for energy conservation and green environment. *Frontiers of Mechanical Engineering*, 9(1), 75−80. doi: 10.1007/s11465-014-0285-y

[72] Ajuka, L.O., Odunfa, M.K., Ohunakin, O.S., & Oyewola, M.O. (2017). Energy and exergy analysis of vapour compression refrigeration system using selected eco-friendly hydrocarbon refrigerants enhanced with TiO_2-nanoparticle. *International Journal of Engineering and Technology*, 6(4), 91−97. doi: 10.14419/ijet.v6i4.7099

[73] Bi, S., Guo, K., Liu, Z., & Wu, J. (2011). Performance of a domestic refrigerator using TiO_2-R600a nano-refrigerant as working fluid. *Energy Conversion and Management*, 52(1), 733−737. doi: 10.1016/j.enconman.2010.07.052

[74] Bi, S.S., Shi, L., & Zhang, L.L. (2008). Application of nanoparticles in domestic refrigerators. *Applied Thermal Engineering*, 28(14−15), 1834−1843. doi: 10.1016/ j.applthermaleng.2007.11.018

[75] Javadi, F. S., & Saidur, R. (2013). Energetic, economic and environmental impacts of using nano-refrigerant in domestic refrigerators in Malaysia. *Energy Conversion and Management*, 73, 335−339. doi: 10.1016/j.enconman.2013.05.013

[76] Ohunakin, O.S., Adelekan, D.S., Babarinde, T.O., Leramo, R.O., Abam, F.I., & Diarra, C.D. (2017). Experimental investigation of TiO_2-, SiO_2-, and Al_2O_3-lubricants for a domestic refrigerator system using LPG as working fluid. *Applied Thermal Engineering*, 127, 1469−1477. doi: 10.1016/j.applthermaleng. 2017.08.153

[77] Gill, J., Singh, J., Ohunakin, O.S., & Adelekan, D.S. (2019). Energy analysis of a domestic refrigerator system with ANN using LPG/TiO_2–lubricant as replacement for R134a. *Journal of Thermal Analysis and Calorimetry*, 135(1), 475−488. doi: 10.1007/s10973-018-7327-3